Advances in Polymer Science 275

Klaus Werner Stöckelhuber
Amit Das
Manfred Klüppel *Editors*

Designing of Elastomer Nanocomposites: From Theory to Applications

Springer

275
Advances in Polymer Science

Aims and Scope

The series Advances in Polymer Science presents critical reviews of the present and future trends in polymer and biopolymer science. It covers all areas of research in polymer and biopolymer science including chemistry, physical chemistry, physics, material science.

The thematic volumes are addressed to scientists, whether at universities or in industry, who wish to keep abreast of the important advances in the covered topics.

Advances in Polymer Science enjoys a longstanding tradition and good reputation in its community. Each volume is dedicated to a current topic, and each review critically surveys one aspect of that topic, to place it within the context of the volume. The volumes typically summarize the significant developments of the last 5 to 10 years and discuss them critically, presenting selected examples, explaining and illustrating the important principles, and bringing together many important references of primary literature. On that basis, future research directions in the area can be discussed. Advances in Polymer Science volumes thus are important references for every polymer scientist, as well as for other scientists interested in polymer science - as an introduction to a neighboring field, or as a compilation of detailed information for the specialist.

Review articles for the individual volumes are invited by the volume editors. Single contributions can be specially commissioned.

Readership: Polymer scientists, or scientists in related fields interested in polymer and biopolymer science, at universities or in industry, graduate students.

Special offer:
For all clients with a standing order we offer the electronic form of Advances in Polymer Science free of charge.

More information about this series at http://www.springer.com/series/12

Klaus Werner Stöckelhuber • Amit Das •
Manfred Klüppel
Editors

Designing of Elastomer Nanocomposites: From Theory to Applications

With contributions by

D. Basu · R. Behnke · A.K. Bhowmick · J.J.C. Busfield · N. Chatti · A. Das · F. Fleck · R. Ghosal · T. Horst · I. Ivaneiko · M. Kaliske · C.W. Karl · M. Klüppel · M. Koishi · A. Lang · B. Lorenz · T. Mondal · M.M. Möwes · R. Mukhopadhyay · B.N.J. Persson · J. Plagge · K. Reincke · M. Saphiannikova · N. Schönmehl · M. Shimizu · R. Stoček · K.W. Stöckelhuber · V. Toshchevikov · L.B. Tunnicliffe · T.A. Vilgis · S. Westermann · S. Wießner · M. Wunde · B.I. Zielbauer

Springer

Editors
Klaus Werner Stöckelhuber
Leibniz Institut für Polymerforschung
Dresden, Germany

Amit Das
Leibniz Institut für Polymerforschung
Dresden, Germany

Manfred Klüppel
Dt. Inst. für Kautschuktechnologie e.V.
Hannover, Germany

ISSN 0065-3195 ISSN 1436-5030 (electronic)
Advances in Polymer Science
ISBN 978-3-319-47695-7 ISBN 978-3-319-47696-4 (eBook)
DOI 10.1007/978-3-319-47696-4

Library of Congress Control Number: 2016956875

Printed on acid-free paper

This Springer imprint is published by Springer Nature
The registered company is Springer International Publishing AG
The registered company address is: Gewerbestrasse 11, 6330 Cham, Switzerland

Dedication

Gert Heinrich (Photo by Kai Uhlig, Dresden)

To sum up Gert Heinrich's scientific lifetime achievement in one word, "networks" would be the most accurate description. The molecular networks he worked on during his career were mostly those in filled elastomers and his studies ranged from their theoretical physical description to the testing of tire materials, so we titled this special issue in honor of Gert Heinrich "*Designing of Elastomer Nanocomposites: From Theory to Applications*."

Gert Heinrich's roots are in the Vogtland, a region reaching across the German free states of Bavaria, Saxony, and Thuringia, where he was born in 1950. Even when busy in other parts of the world, he kept faith with his origins, for example, by holding an annual extended weekend with his PhD students in his home town of Pausa. After finishing school and an apprenticeship as bricklayer, he started studies in physics at the Friedrich Schiller University in Jena and graduated as physicist in theoretical physics (applied quantum physics) in 1973. At the Technical University (TH) Merseburg, Department of Polymer Physics, G. Heinrich gained his doctorate in 1978 on the topic "Mechanical properties of polymer networks and statistical-mechanical approaches." As assistant professor at the TH Merseburg he taught polymer physics, experimental physics, and theoretical physics, qualifying as full professor (*Habilitation* and *facultas docendi*) in 1986 with the post-doctoral dissertation "Theory of polymer networks and topological constraints of network chains." He continued his teaching activities as Associate Professor for Theoretical Physics until 1990. After the political changes in East Germany and German reunification, he was eager to apply his extensive and comprehensive knowledge of polymer physics to more application-oriented tasks and accepted a position at the tire manufacturer Continental AG in Hanover as senior research scientist. In addition to his tasks as Head of Materials Research/Strategic Technology at Continental, G. Heinrich also continued his academic activities as lecturer in "Physics and technology of polymers" at the University of Hanover and "Elastomer materials and testing" at the Martin Luther University Halle/Wittenberg. In 2003, he was appointed as full professor for "Polymer materials science" at the Technical University Dresden and, simultaneously, as head of the Institute of Polymer Materials at the Leibniz Institute of Polymer Research Dresden e. V. (IPF). Gert Heinrich was also offered the Professorship for Micro- and Nanostructure-Based Polymer Composites at the Martin Luther University Halle/Wittenberg and the Fraunhofer Institute for Mechanics of Materials (IWM) in 2009. However, he declined the position because his chair at TU Dresden became more distinguished and was designated "Professorship for Polymer Materials and Rubber Technology." In 2015 he was honored three times, receiving the George Stafford Whitby Award for distinguished teaching and research from the Rubber Division of the American Chemical Society; the Colwyn Medal for outstanding services to the rubber industry from the Institute of Materials, Minerals and Mining (IOM3); and the Carl Dietrich Harries Medal from the Deutsche Kautschuk-Gesellschaft (German Rubber Society).

Gert Heinrich's contribution to elastomer research covers several topics. The most prominent works in polymer physics are probably his contributions on the non-affine tube model of rubber elasticity, developed during his time in Merseburg [1]. A first rigorous statistical-mechanical network theory for filled rubbers was published together with Thomas Vilgis [2]. An extension of the Merseburg model to account for the finite extensibility of network chains was made in his first collaboration with Manfred Klüppel, showing that the non-affine tube deformation is well suited for describing the stress–strain response of technical sulfur-cured rubbers [3, 4]. Later, together with Michael Kaliske in Hanover, the non-affine tube model was

further extended and implemented into a finite element code [5, 6]. In a comparison of 20 hyperelastic models for rubber-like materials [7] this extended tube model gave the best fit to experimental data and, moreover, involves only four parameters and its derivation is physically motivated. In his work on the physics of tires, Gert Heinrich authored several papers that generated the interest of specialists across the broad field of tire and rubber technology. His high-impact contributions on this topic range from the influence of filler networking on tire performance [2, 8] to the wet skid, wear, and rolling resistance of tire materials [9, 10], to name just a few. Within this framework, a rigorous and fundamental theory of rubber friction on rough surfaces was also developed that accounts for the multiscale excitation of skidding tires on wet tracks [11]. It is less well known that several fundamental results in all these fields were incorporated into R&D projects of Continental AG, recorded in more than 40 internal research reports by G. Heinrich and in several patent applications. In Dresden, intense activity began together with A. Das and K. W. Stöckelhuber on the development and understanding of new elastomeric materials incorporating several species of nanoparticles (layered silicates [12], carbon nanotubes [13], layered double hydroxides [14], haloysite nanotubes [15], graphene nanoplatelets [16]) as fillers. In addition, G. Heinrich delivered significant contributions on the fracture mechanics of elastomers [17] as organizer and spokesperson of research unit FOR 597, Fracture Mechanics and Statistical Mechanics of Reinforced Elastomeric Blends, of the German Research Foundation (DFG). Evaluation of the dynamic properties of rubber composites based on a theoretical, physically motivated multiscale approach [18] is another important point on his scientific agenda. Finally, it should be noted that in Dresden G. Heinrich supervised dozens of graduate students in engineering science and more than 40 PhD students in several branches of polymer materials, polymer processing, and modeling, with topics ranging from elastomers, thermoplastics, thermoplastic elastomers and vulcanizates, and biopolymer materials to composites for lightweight applications.

When Gert Heinrich was awarded the Colwyn Medal, it was stated about his time in Dresden: “He has grown the activity in elastomer research from a relatively modest beginning to be the largest academic group of researchers in Europe. He currently has the greatest publication record of any researcher in the EU with more than 330 journal papers listed on the Web of Science and he has the highest *h*-index of any academic in the EU who works in traditional elastomer/rubber materials.” For the magazine *Tire Technology International*, he was just “Mr. Tire Materials.”

Gert Heinrich has been married to his wife Nelly since 1975 and has two grown-up daughters.

For the up-coming stage of life, we wish him an ideal balance between repose and relaxation in his private life and continuing professional activities as advisor and consultant for science and industry.

References

1. Heinrich G, Straube E, Helmis G (1988) Adv Polym Sci 85:33–87
2. Heinrich G, Vilgis TA (1993) Macromolecules 26:1109–1119
3. Klüppel M, Heinrich G (1994) Macromolecules 27:3596–3603
4. Klüppel M (1994) Macromolecules 27:7179–7184
5. Kaliske M, Heinrich G (1999) Rubber Chem Technol 72:602–632
6. Heinrich G, Kaliske M (1997) Comput Theor Polym Sci 7:227–241
7. Marckmann G, Verron E (2006) Rubber Chem Technol 79:835–858
8. Heinrich G, Klüppel M (2002) In: Filled elastomers drug delivery systems. Springer, Heidelberg, pp 1–44
9. Heinrich G (1992) In: Physics of polymer networks. Steinkopff, Darmstadt, pp 16–26
10. Heinrich G, Klüppel M (2008) Wear 265:1052–1060
11. Klüppel M, Heinrich G (2000) Rubber Chem Technol 73:578–606
12. Rooj S, Das A, Stöckelhuber KW, Wang D-Y, Galiatsatos V, Heinrich G (2013) Soft Matter 9:3798–3808
13. Das A, Stöckelhuber KW, Jurk R, Saphiannikova M, Fritzsche J, Lorenz H, Klüppel M, Heinrich G (2008) Polymer 49:5276–5283
14. Basu D, Das A, Stöckelhuber KW, Wagenknecht U, Heinrich G (2014) Prog Polym Sci 39:594–626
15. Raman VS, Rooj S, Das A, Stöckelhuber KW, Simon F, Nando GB, Heinrich G (2013) J Macromol Sci A 50:1091–1106
16. Das A, Kasaliwal GR, Jurk R, Boldt R, Fischer D, Stöckelhuber KW, Heinrich G (2012) Compos Sci Technol 72:1961–1967
17. Horst T, Heinrich G, Schneider M, Schulze A, Rennert M (2013) In: Grellmann W, Heinrich G, Kaliske M, Klüppel M, Schneider K, Vilgis T (eds) Fracture mechanics and statistical mechanics of reinforced elastomeric blends. Springer, Heidelberg, pp 129–165
18. Ivaneiko I, Toshchevikov V, Saphiannikova M, Stöckelhuber KW, Petry F, Westermann S, Heinrich G (2016) Polymer 82:356–365

Preface

Rubber plays an important role as a material in modern technologies for mobility, production, and resource extraction. The unique elastic properties of this material facilitate a multitude of technologies to produce items as diverse as car tires, conveyor belts, sealings, bushes, and bearings. It is not the rubber polymers alone that give elastomeric materials their special elastomeric properties, but the combination of crosslinked macromolecules and solid, reinforcing nanoscale filler particles that confer these outstanding characteristic profiles to modern rubber parts for a multitude of applications. Any industrially used rubber can, therefore, be considered a nanocomposite material.

This special issue of *Advances in Polymer Science*, "Designing of Elastomer Nanocomposites: From Theory to Applications," is dedicated to Gert Heinrich, one of the great researchers in the field of elastomeric materials, on the occasion of his 65th birthday.

The first chapter of this book is devoted to the non-affine tube model of rubber elasticity, derived by Gert Heinrich during his time in Merseburg. The model has been extended to account for the finite extensibility of network chains and implemented into a finite element code. Various engineering applications of this model are reviewed by Behnke and Kaliske.

The reinforcement of rubber is examined in terms of filler network dynamics at small strains in the chapter by Tunnicliffe and Busfield. The concepts of filler networking, breakage, Payne effect, and physical ageing are discussed in the context of thermoviscoelasticity and taken as the basis for explanation of results for filled systems.

Persson et al. contribute a chapter on the contact mechanics, friction, and adhesion of rubber at rough surfaces. Using the approach of multiscale contact mechanics, the authors discuss different important practical applications such as the leak rate of static seals and the friction force of dynamics seals, as well as friction experiments and the interpretation of the resulting friction coefficients in dry and lubricated states.

A multiscale approach for the modeling of dynamic-mechanical properties of unfilled and filled elastomers is presented in the chapter by Ivaneiko et al. The proposed theoretical approach allows simultaneous and precise modeling of the frequency dependence of the dynamic-mechanical moduli of elastomer nanocomposites across a broad frequency domain, giving so-called master curves.

Not only rubbers show viscoelastic behavior, these properties are also of great importance in our daily food. Zielbauer, Vilgis et al. investigate network theories for unfilled and filled rubbers and compare these soft materials with the structure and properties of food systems. The common points between elastic materials and food gels are fundamentally discussed and the close connections are explained.

Most rubber materials are crosslinked by covalent bonds. However, Basu et al. give a review of elastomers that are crosslinked by a different mechanism. Nanostructured ionomeric elastomers show fascinating properties; maybe one of the most impressive examples is the self-healing ability of some of these rubbers.

Modern nanoparticles are very promising filler particles for novel elastomeric nanocomposites, providing outstanding features. Graphene is the youngest member of the carbon allotrope family and is sometimes referred to as the mother of all carbon nanomaterials. Two contributions in this issue of *Advances in Polymer Science* deal with this nanofiller system. Mondal et al. describe techniques for functionalization of graphene-like nanofillers by means of small molecules and macromolecules. Different strategies, in particular mixing in latex, solution mixing, and melt mixing, are introduced and the morphology and physical properties of the obtained graphene-based elastomeric nanocomposites are presented. The chapter by Klüppel et al. gives an overview of the potential of nanocomposites based on graphene nanoplatelets and their hybrid systems with industrial fillers. A variety of different application-oriented experimental methods such as static gas adsorption, gas permeation measurements, fracture mechanics, and friction experiments show the potential of these new materials for different purposes.

The fracture of materials is mostly an undesirable process that dramatically reduces the service life of structural components. Stoček et al. review advanced experimental methods for characterizing crack initiation in technical rubbers, crack propagation, and rubber wear under practical loading conditions.

Finally, we would personally like to express our thanks for the time, passion, and energy devoted by all contributing authors, from both academia and industry. Also very deserving of thanks are the reviewers for their excellent service and feedback, as well as the editorial team of *Advances in Polymer Science*, who assisted all of us through the editing and processing of manuscripts.

We are confident that the readers of this volume will find valuable and useful information on various aspects of such a fascinating material as elastomeric nanocomposites.

Dresden, Germany — Klaus Werner Stöckelhuber
Dresden, Germany and Tampere, Finland — Amit Das
Hanover, Germany — Manfred Klüppel

Contents

Adv Polym Sci (2017) 275: 1–70
DOI: 10.1007/12_2016_9

Published online: 23 September 2016

The Extended Non-affine Tube Model for Crosslinked Polymer Networks: Physical Basics, Implementation, and Application to Thermomechanical Finite Element Analyses

Ronny Behnke and Michael Kaliske

Abstract This chapter is devoted to a summary of the so-called extended non-affine tube model. First, general model approaches for representation of the behavior of elastomers within numerical simulations are discussed. Second, the extended non-affine tube model is considered in the context of hyperelastic material models. Starting from molecular-statistical considerations, a Helmholtz free energy function is derived and formulated in terms of continuum mechanical quantities of the macroscale. Furthermore, combination with a model approach to represent continuum damage and time-dependent effects is addressed. The free energy function of the model approach is further set into the context of thermomechanics to account for temperature-dependent behavior of elastomers within numerical simulations. Finally, finite element implementation of the extended non-affine tube model and its application to uniaxial and biaxial tension tests performed on elastomer specimens are presented.

Keywords Continuum damage • Elastomers • Finite element analysis • Hyperelasticity • Temperature dependency • Tube model • Viscoelasticity

R. Behnke and M. Kaliske (✉)
Institut für Statik und Dynamik der Tragwerke, Technische Universität Dresden, 01062 Dresden, Germany
e-mail: michael.kaliske@tu-dresden.de

Contents

1 Introduction

Elastomers offer favorable mechanical characteristics to engineers; polymer science even allows the specific design of outstanding characteristics by blending different elastomer compounds or adding different types of fillers. It has become obvious that a deep understanding of their polymer structure and mechanical behavior can only be reached by a combination of polymer science, to describe the molecular scale, and computational mechanics, to predict the mechanical behavior of complex elastomer components at the structural scale.

The outline of this chapter is as follows: In Sect. 2, different model approaches for representation of the mechanical behavior of elastomers are described. In this context, the polymer-physical origin of the extended non-affine tube model is discussed in Sect. 3. In Sect. 4, combination of the extended non-affine tube model with a representation of inelastic material properties is demonstrated. To be specific, continuum damage and time-dependent effects of nonlinear viscoelasticity are addressed. The presence of inelastic features leads to energy dissipation

during loading of elastomer components. To account for the triggered self-heating of cyclically loaded elastomer components and to take into account their temperature-dependent behavior, a non-isothermal framework is discussed in Sect. 5. In Sect. 6, application of the extended non-affine tube model within finite element (FE) analyses of elastomer specimens is shown. Finally, conclusions and an outlook are provided in Sect. 7.

2 Constitutive Descriptions of Elastomers

In this section, attention is paid to the molecular structure of elastomers to allow a physical model interpretation. Different model approaches for representation of the mechanical behavior of elastomers within numerical simulations are discussed.

2.1 Molecular Background of Elastomers

The microstructure of elastomers can explain, from a physical point of view, their material characteristics on the macroscale, as outlined by Behnke et al. [1] and Kaliske and Behnke [2]. Elastomers show both geometrical and physical strongly nonlinear mechanical behavior upon loading. Experiments on elastomers reveal that the main features of elastomers are:

- Nonlinear finite elasticity
- Stress softening
- Rate-dependent inelasticity
- Rate-independent inelasticity

2.1.1 Unfilled Elastomers

Elastomers are amorphous polymeric materials, formed by macromolecules on the molecular scale. Macromolecules are composed of chain-forming monomers, which are long entangled chains of hydrocarbons or other molecules. Chemical crosslinks between the molecules give rise to a wide-meshed network of polymer chains. These crosslinks are formed during the vulcanization process (heating of the uncured elastomer material). The crosslink density can be designed by adding crosslink-forming elements (e.g., sulfur) to the uncured elastomer material and by selecting an appropriate curing time for the vulcanization process. At the end of the vulcanization process, the characteristic network of polymer chains is formed, which is subjected to further topological changes during the elastomer's lifetime. These alterations of the inner structure are triggered, for example, by externally applied mechanical constraints, transport of chemical agents via diffusion, ultraviolet radiation, and temperature.

The mechanical properties of elastomers are a function of temperature. One can distinguish between the glassy brittle state, the rubbery state, and the liquid state. The glass transition temperature Θ_G separates the glassy state of the elastomer from its rubbery state. In analogy, the melting temperature Θ_M separates the rubbery state from the liquid state. We focus on the rubbery state of the elastomer, in which rubberlike behavior is observable. Hence, the temperature range of $\Theta_G < \Theta < \Theta_M$ is considered for the model setup.

Despite the network structure of crosslinked or entangled polymer chains, free molecular chain segments can rotate in combination with Brownian motion as a result of the free volume in the network. The corresponding energetic interpretation of these configurational changes of polymer chains in the temperature range of $\Theta_G < \Theta < \Theta_M$ leads to a large entropy elasticity. Furthermore, molecular chains can be constrained by the presence of crystallized domains, which are formed by aligned polymer chains in an amorphous environment of disordered polymer chains. The crystallization is dependent on temperature and can be also triggered by externally applied mechanical constraints (strain-induced crystallization).

2.1.2 Filled Elastomers

Elastomer blends can be reinforced by adding fillers. Fillers (e.g., carbon black, silica) enable the enhancement of a specific property of the final elastomer (e.g., wear resistance). In contrast to the polymer chains, fillers show mechanical behavior that is characteristic of solids. The fillers consist of primary particles, which form aggregates when they are added to the elastomer blend. The final properties of the elastomer are strongly influenced by the chemical reactivity of the fillers (active or inactive), their size, and the shape of filler aggregates.

The free volume of the polymer network is partially occupied by the nearly rigid filler. In consequence, polymer chains are more extended during external loading because the free relative motion of polymer chains is restricted by chemical or physical links. Filler–elastomer links are formed by molecular chain bonds, chemical bonds, or entanglements of chain segments with filler aggregates, which lead to physical bonds. It becomes obvious that the crosslinking density of the filled elastomer increases and the length of free chain segments decreases. Furthermore, filler–filler linkages appear as a result of interaction of filler particles with filler particles.

2.2 Material Properties

Material properties on the macroscale originate from the molecular structure and related micromechanical processes such as chain reptations, rearrangement of crosslinks between polymer chains, and irreversible sliding of filler–filler and filler–matrix contacts during external loading.

After the vulcanization process, the elastomer can be regarded on the macroscale as an isotropic, homogeneous solid. In the temperature range of $\Theta_G < \Theta < \Theta_M$, elastomers show a pronounced nonlinear elastic behavior upon large deformation, which can be explained by entropy elasticity. Entropy elasticity originates from the relative motion of polymer chains of the disordered polymer network. As a result of the applied deformation, a more ordered state of the initially unordered polymer network is reached. In consequence, the order of the system increases, which leads to a decrease in its entropy by nearly unchanged inner molecular energy.

With rising temperature, the stiffness of unfilled elastomers increases as a result of enforced Brownian molecular motions, which lead to an increased degree of order of the system. The presence of fillers in the network can partially or completely remove this property. In this case, the filler–chain interactions prevent relative motions of the polymer chains and a loss of stiffness with increasing temperature occurs if the energy elasticity of the filler network is more pronounced.

The processes of relative chain motions and rearrangement of the inner network structure are of dissipative nature; internal friction occurs, which is linked to a loss of mechanical energy. On the macroscale, these processes give rise to a nonlinear inelastic material behavior because the relaxation kinematics of the chains are nonlinear with respect to the deformation state and the temperature state.

If fillers are present in the polymer network, their interaction with polymer chains triggers stress softening (Mullins effect) during the first loading of the elastomer. Stress softening is caused by breakage and re-formation of highly stretched polymer chains, changes in the filler–chain contacts, and rupture of the filler network. After several load cycles at constant deformation amplitude, the mechanical properties stabilize and the polymer–filler network reaches a new dynamic equilibrium.

Furthermore, the so-called Payne effect is observable for filled elastomers. The Payne effect describes the viscoelastic behavior of filled elastomers, which is characterized by an amplitude dependency. With increasing deformation amplitude, the dynamic stiffness decreases as a result of changes in the filler network. Hence, the relaxation kinematics depend on the deformation state nonlinearly. In consequence, the Payne effect leads to a distinct dynamic material response in the case of small and large dynamic excitations.

Another characteristic belonging to the inelastic properties of filled elastomers is rate-independent and yield-surface-free plasticity. Plasticity is related to the time-independent and irreversible breakage and modification of the filler–chain and filler–filler contacts. Typical yield-surface-free plasticity originates from the relative slip of polymer chains on the filler particles and plastic deformations of filler particles. Another explanation of the yield-surface-free plasticity is that polymer chains in the network have different lengths and, in consequence, different critical lengths at which sliding and irreversible network rearrangements start.

In summary, filled elastomers show nonlinear stress–strain dependencies, stress softening, rate-dependent inelasticity, and rate-independent inelasticity. For more details, the reader is referred to, for example, Grambow [3].

2.3 Model Approaches

With the help of a numerical model, the experimentally observable material behavior can be represented by numerical simulations in a continuous manner for arbitrary loading conditions within a defined range of verification and validation of the model. In general, only a limited set of pairs (input and output quantities) can be provided by experimental measurements. Furthermore, the model is an idealization of real material behavior, in which assumptions with respect to the most significant material characteristics have to be made. In consequence, the material characteristics to be represented are task-specific.

The model defines the qualitative description of the most significant phenomena of the material behavior, whereas the model parameters allow quantitative calibration of the qualitative model response to experimental measurements. Several approaches exist for establishing a link between input quantities and output quantities of the model. Figure 1 illustrates several modeling approaches and strategies.

Phenomenological models use the framework of rheological elements to represent distinct properties of elastomers, as discussed in Sect. 2.2, on the macroscale.

Models that consider the inner structure and the related processes of its evolution on the micro- or mesoscale offer the advantage of being able to directly take into account specific properties stemming from the microstructure of the material (e.g., anisotropy, voids, and defects). Furthermore, the model parameters might be directly related to measurable physical quantities. As an example of this model approach, the extended non-affine tube model for elastomer hyperelasticity and its continuum mechanical formulation are addressed in Sect. 3. To formulate a macroscopic model, different homogenization techniques are available to accomplish the micro-to-macroscale transition. The molecular-statistical theory of polymer networks, considering one single molecular chain with respect to possible positions and deformation characteristics via statistical thermodynamics, can be used to analytically bridge the gap between micro- and macroscales. Gaussian statistics, Langevin statistics, and tube concepts are used to describe the free motion of single

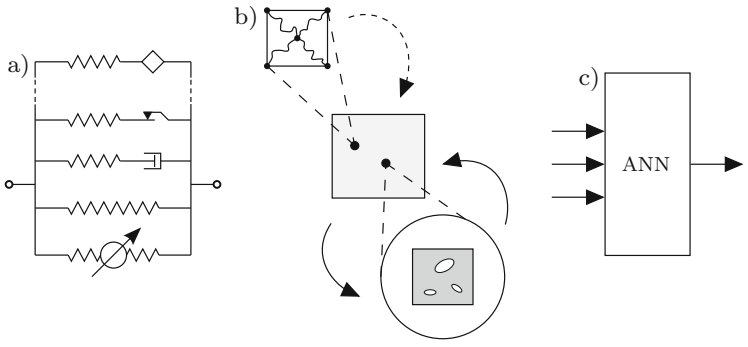

Fig. 1 Constitutive approaches: (**a**) generalized model with rheological elements; (**b**) analytical model derivation (micro–macro transition) or numerical homogenization via a representative unit; (**c**) artificial neural network

chains with or without constraints resulting from entanglements with surrounding polymer chains. First, micromechanical quantities are used for the description. Second, the micromechanical quantities are finally related to continuum-mechanical quantities on the macroscale.

Another formulation is the so-called model-free approach (e.g., in the form of artificial neural networks (ANN) with or without memory effects), which does not require the selection of properties to be modeled because input and output information are related without any underlying physical model.

3 The Extended Non-affine Tube Model for Elastomer Hyperelasticity and Its Continuum Mechanical Formulation

The extended non-affine tube model takes into account topological constraints as well as the limited chain extensibility of network chains. Similar to the tube model, the extended non-affine tube model offers a physical interpretation of the strain energy function on the macroscale in terms of quantities associated with the polymer network on the molecular scale.

The extended non-affine tube model requires a different formulation than used for the basic tube model (Heinrich et al. [4], Edwards and Vilgis [5]), to which the Valanis–Landel hypothesis [6] is only applicable. In the contributions by Heinrich and Kaliske [7, 8], the FE formulation and its implementation into FE analysis codes have been addressed. In many of today's commercial codes, the extended non-affine tube model for hyperelasticity is implemented as a basic constitutive law for elastomer hyperelasticity (see, for example, Bergström [9]).

Other important developments of the extended non-affine tube model are reported, for example, by Klüppel and Schramm [10], who discuss combination with a damage model of stress-induced filler cluster breakdown (stress softening). The framework of the model takes into account the tubelike topological constraints (packing effects) as well as the finite chain extensibility of filler-reinforced polymer networks. Further details are also provided by Klüppel [11].

The following section first summarizes the polymer-physical basics of the extended non-affine tube model, based on the original contributions from Heinrich and Kaliske [7, 8]. Second, the Helmholtz free energy function for isothermal elastomer hyperelasticity is derived, which sets the basis for FE implementation in terms of continuum mechanical quantities.

3.1 Polymer-Physical Basics of the Extended Non-affine Tube Model

The basic property of elastomers, hyperelasticity, is first addressed. In the extended non-affine tube model, the elastomer hyperelasticity can be derived from

molecular-statistical concepts. In general, affine or phantom networks are thought to explain fundamental relations. More advanced molecular-statistical concepts include the network theories of constraint junction fluctuations and different theories of constraint segment fluctuations (see, for example, Heinrich and Straube [12]). Within the latter group of concepts, a tube model of elastomer hyperelasticity has been proposed (see, for example, Heinrich et al. [4], Edwards and Vilgis [5], Heinrich and Straube [12–14]). Furthermore, experimental results obtained from small angle neutron scattering (SANS), mechanical testing, and numerical simulations have proved the admissibility of the extended non-affine tube model for elastomer hyperelasticity.

To highlight the polymer-physical background of the extended non-affine tube model, the basic ideas are briefly summarized next. Unfilled polymer networks with elastic characteristics are regarded as disordered systems with a constant topology of crosslinks and entanglements. The crosslinks and entanglements originate from the vulcanization process and do not change during the deformation process, according to the theory of elasticity.

The tube model for elastomer hyperelasticity considers a topology $\mathbf{T}$ given by a set of wormlike network-chain paths $\mathbf{R}(s)$, as depicted in Fig. 2. The wormlike network chain paths are parametrized by the contour variable s and crosslink positions $\mathbf{R}_i$, where the latter can be interpreted as average conformations or positions. The current conformations of the chains are analogously represented by the quantities $\mathbf{r}(s)$ and $\mathbf{r}_i$. The Helmholtz free energy

$$F(\lambda) \equiv \ll F(\lambda) \gg = \sum_{T} w_{\mathrm{T}} < F(\lambda) >_{\mathrm{T}} \rightarrow \int \mathrm{d}w_{\mathrm{T}} < F(\lambda) >_{\mathrm{T}} \tag{1}$$

for a macroscopic specimen in its deformed state is introduced according to Edwards [15] as the statistical averaging, where $\ll \ldots \gg$ stands for the structure and the thermodynamic averaging and $< \ldots >_{\mathrm{T}}$ denotes the thermodynamic average for the considered topology $\mathbf{T}$. The deformation-independent probability of the occurrence of topology $\mathbf{T}$ is termed w_{T}. Furthermore, the expression $<F(\lambda)>_{\mathrm{T}}$ characterizes the free energy of a network with topology $\mathbf{T}$. The symbol λ stands for the stretches in the principal directions, assuming incompressibility (i.e., $\lambda_1\lambda_2\lambda_3 \equiv 1$). From this basic assumption, the tube model assumes that topology $\mathbf{T}$ is given by a set of wormlike network chain paths $\mathbf{R}(s)$.

The tube approach is motivated by the large degree of coil interpenetration of network chains, which increases the Flory number N_{F} in the case of moderately

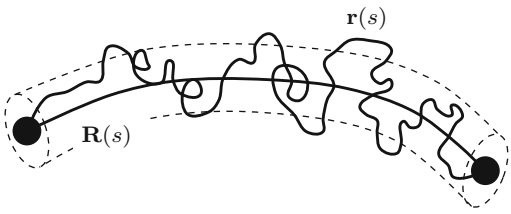

Fig. 2 Average tube conformation $\mathbf{R}(s)$ and current network chain conformation $\mathbf{r}(s)$

crosslinked networks. The Flory number is the number of network chains within a coil volume of a network chain of size $\sqrt{< r^2 >_0}$. The Flory number can be calculated in terms of molecular quantities,

$$N_{\mathrm{F}} = n_s b^3 \sqrt{N}, \tag{2}$$

where b stands for the Kuhn statistical segment length, n_s characterizes the number of statistical segments per unit volume, and N denotes the average number of statistical segments of a network chain. According to the model approach introduced by Edwards [15], a chain is confined to the neighborhood of its initial or mean conformation $\mathbf{R}(s)$ by a (harmonic) constraining potential. For the case $N_{\mathrm{F}} \gg 1$, it can be assumed that the contributions to the confining potential are controlled by the local topology of the neighboring chains. In this case, the probability of the conformation $\mathbf{R}(s)$ is represented by the random walk distribution

$$P(\mathbf{R}(s)) \sim \exp\left(-\frac{3}{2b} \int_0^L \mathrm{d}s \left(\frac{\partial \mathbf{R}(s)}{\partial s} \right)^2 \right) \tag{3}$$

with L being the stretched contour length of the polymer under consideration.

The constraints stemming from the neighboring chains, as depicted in Fig. 3, are represented by an entropic harmonic potential. The free energy

$$< F(\lambda) >_{\mathrm{T}} = -k_{\mathrm{B}} \Theta \ln(Z_{\mathrm{T}}(\lambda)) \tag{4}$$

is expressed with the help of the canonical partition integral,

$$Z_{\mathrm{T}}(\lambda) = \int\limits_{\text{fixed T}} D[\mathbf{r}(s)] \exp\left(-\frac{H}{k_{\mathrm{B}}\Theta} \right), \tag{5}$$

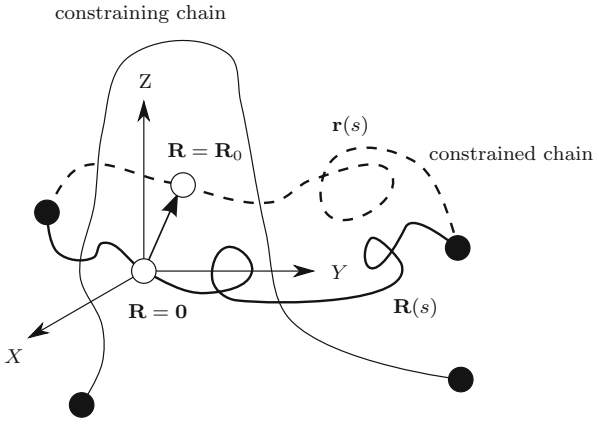

Fig. 3 Displaced segment of a tube-constrained network chain from position $\mathbf{R} = \mathbf{0}$ to $\mathbf{R} = \mathbf{R}_0$

which makes use of the Hamiltonian

$$\frac{H}{k_{\mathrm{B}}\Theta} = \frac{3}{2b}\int_0^L \mathrm{d}s\left(\frac{\partial \mathbf{r}(s)}{\partial s}\right)^2 + \sum_{\mu=x,\,y,\,z}\int_0^L \mathrm{d}s\,\Omega_\mu^2\big(r_\mu(s) - R_\mu(s)\big)^2, \tag{6}$$

where k_{B} is the Boltzmann constant and Θ the absolute temperature. The potential parameters Ω_μ take into account the change in entropy of the constraining chains as a result of displacement of a segment of the chain under consideration,

$$\Omega_\mu = \frac{\sqrt{b}}{d_\mu^2}, \tag{7}$$

see Heinrich and Straube [12–14] for more details. In the case of tube models, the parameter d_μ^2 can be calculated by the square root of the mean square deviation of the position of a segment $\mathbf{r}(s)$ from its average position $\mathbf{R}(s)$

$$d_\mu^2 = \ll \big(r_\mu(s) - \lambda_\mu R_\mu(s)\big)^2 \gg \tag{8}$$

with the limits $0 < s < bN$. According to Heinrich and Straube [12–14], the deformation dependency of the tube parameter can be given as the power law

$$d_\mu = d_0\,\lambda_\mu^{\alpha\beta}, \qquad \mu = x,\ y,\ z \tag{9}$$

with $\alpha = 1/2$, an empirical fit parameter β physically bounded by $0 < \beta \leq 1$, and the relation

$$\frac{d_0}{b} = a\left(n_s b^3\right)^{-\frac{1}{2}}. \tag{10}$$

The theory of tubelike constraints leads to the basic result of $\alpha = 1/2$, also known as the square root deformation law of the deformed confining tube. The value of the parameter α reflects the non-affine relation between the lateral tube dimension and the local stretch ratios at the microscale in terms of λ_μ (change in the radius of gyration of network chains in the case of a macroscopically imposed deformation with λ).

The parameter β represents the influence of the global rearrangements of crosslinks upon deformation and, in consequence, the release of topological constraints. The parameter β can be physically derived for a given polymer network as a function of the amount of solvent, sol fraction, network defects, and filler. In this case, the physically imposed limits $0 < \beta \leq 1$ hold. As a result, the parameter β acts as an indicator of the completeness of the crosslinking reaction. As suggested by Kaliske and Heinrich [8], other values with $0 < \beta$ can be selected for β during the

parameter identification process. It should be pointed out that this wider range clearly contradicts the physical explanation of the parameter (i.e., for $\beta > 1$), but still satisfies the thermodynamic admissibility of the model. In this case, β becomes a fitting parameter (phenomenological parameter) of a generalized model approach.

3.2 Helmholtz Free Energy Function of the Extended Non-affine Tube Model

The elastic free energy can be derived with the help of the statistical mechanics of unfilled polymer networks. Details are provided by Heinrich et al. [4] and Heinrich and Straube [12–14]. For weakly and moderately crosslinked networks, the elastic free energy change per unit volume is obtained as

$$\begin{aligned} W &= \Delta F(\lambda_1,\ \lambda_2,\ \lambda_3) \equiv F(\lambda_1,\ \lambda_2,\ \lambda_3) - F(1,\ 1,\ 1) \\ &= \frac{G_c}{2}\sum_{A=1}^{3}\left(\lambda_A^2 - 1\right) + \frac{2G_e}{\beta^2}\sum_{A=1}^{3}\left(\left(\frac{d_0}{d_A}\right)^2 - 1\right) \\ &= \frac{G_c}{2}\sum_{A=1}^{3}\left(\lambda_A^2 - 1\right) + \frac{2G_e}{\beta^2}\sum_{A=1}^{3}\left(\lambda_A^{-\beta} - 1\right) \\ &= W^e + L^e, \end{aligned} \tag{11}$$

which is composed of two additive terms. G_c stands for the crosslink contribution and G_e takes into account the constraint contribution to the total shear modulus. From the previously discussed molecular considerations, these parameters can be linked to the molecular network parameters by

$$G_c = A k_B \Theta \left(\nu \ -\frac{2}{f-2}\frac{\rho N_A}{M_n}\right) \tag{12}$$

and

$$G_e = \frac{k_B \Theta}{4\sqrt{6}}\beta^2 n_s \left(\frac{b}{d_0}\right)^2. \tag{13}$$

It can be observed that the shear modulus G_e results from the deformation dependency of the tube diameter as a function of the network chain density ν, the number of average molecular mass M_n of the primary chains, the number of statistical segments n_s per unit volume, and the fluctuation range of a segment or tube diameter d_0. In addition, the microstructure factor A is a function of the ratio between the fluctuation range d_c of a crosslink and the end-to-end distance R_c of a network chain,

$$A = 1 - \frac{2}{f}\left(1 - \frac{2}{\sqrt{\pi}}\frac{K\exp\left(-K^2\right)}{\operatorname{erf}(K)}\right), \quad K = \sqrt{\frac{3f}{2}}\,\frac{d_c}{R_c} \tag{14}$$

with the Gauss error function erf(K). Furthermore, the length of the fluctuation range of a chemical junction is given by d_c, whereas R_c and f stand for the end-to-end distance of a network chain and the functionality of a crosslink, respectively.

For the case of small strains characterized by $\lambda \to 1$, the small-strain modulus

$$G = G_c + G_e = (\nu - h\mu)k_{\mathrm{B}}\Theta + G_e^{*}\beta^2 \tag{15}$$

is obtained, where

$$G_e^{*} = \frac{1}{4\sqrt{6}} n_s\, k_{\mathrm{B}}\,\Theta \left(\frac{b}{d_0}\right)^2 = \frac{1}{2} k_{\mathrm{B}}\,\Theta\, n_e \tag{16}$$

includes n_e as the apparent number of elastically effective physical crosslinks per unit volume stemming from the conformational constraints with

$$n_e = \frac{1}{2\sqrt{6}}\, n_p \frac{bL}{d_0^2} = \frac{1}{2\sqrt{6}}\,\frac{\rho N_A}{M_n}\,\frac{R^2}{d_0^2}. \tag{17}$$

In the latter relation, n_p is the number of primary chains per unit volume, L is the contour length of a primary chain, and R^2 denotes the mean squared end-to-end distance of the chain. Furthermore, the polymer density is given by ρ and Avogadro's number by N_A.

To take into account the effect of strain amplification induced by the presence of filler particles within the basics of tube theory, the simplest model for the singularity in the chain entropy was proposed by Edwards and Vilgis [16] as

$$P(\mathbf{R}(s)) = \mathcal{N}\exp\left(-\frac{3}{2\,b}\int_0^L \mathrm{d}s\left(\frac{\left(\mathbf{R}'(s)\right)^2}{1-\left(\mathbf{R}'(s)\right)^2} + \gamma\left(\mathbf{R}'(s)\right)^2\right)\right), \tag{18}$$

where $\mathcal{N}$ denotes an outstanding normalization and $\mathbf{R}'$ denotes the partial derivative of $\mathbf{R}$ with respect to s. The quantity γ represents the constant chain stiffness (see Freed [17]). If $\mathbf{R}'^2$ is replaced in the denominator by its mean values, as proposed by Edwards and Vilgis [16],

$$P(\mathbf{R}(s)) = \frac{\exp\left(-\frac{3}{2b}\int_0^L \mathrm{d}s\left(\frac{\left(\mathbf{R}'(s)\right)^2}{1-<\mathbf{R}'^2>} + \gamma\left(\mathbf{R}''(s)\right)^2\right)\right)}{\int D\left[\mathbf{R}(s)\right]\exp\left(-\frac{3}{2b}\int_0^L \mathrm{d}s\left(\frac{\left(\mathbf{R}'(s)\right)^2}{1-<\mathbf{R}'^2>} + \gamma\left(\mathbf{R}''(s)\right)^2\right)\right)} \tag{19}$$

is obtained, where the normalization is included to be consistent with the model. The mean value of $\mathbf{R}'^2$ is computed via

$$< P(\mathbf{R}(s)) > = \frac{\int D[\mathbf{R}(s)]\mathbf{R}'^2 \exp\left(-\frac{3}{2b}\int_0^L \mathrm{d}s\left(\frac{(\mathbf{R}'(s))^2}{1-<\mathbf{R}'^2>}+\gamma\left(\mathbf{R}''(s)\right)^2\right)\right)}{\int D[\mathbf{R}(s)] \exp\left(-\frac{3}{2b}\int_0^L \mathrm{d}s\left(\frac{(\mathbf{R}'(s))^2}{1-<\mathbf{R}'^2>}+\gamma\left(\mathbf{R}''(s)\right)^2\right)\right)}. \tag{20}$$

Finally, the relation

$$\delta^2 \equiv <\mathbf{R}'^2> \approx q_0^2 b^2 = \alpha^2\left(\frac{b}{d_0}\right)^2 \tag{21}$$

is derived, where α is an additional parameter of the model and a measure of the inextensibility of the network chains. The crosslinking part of the free energy or entropy under deformation can be calculated from

$$\frac{F_c(\lambda_1,\lambda_2,\lambda_3)}{k_\mathrm{B}\Theta} \sim -\int d^3\mathbf{R}\, P(\mathbf{R}) \ln(P(\lambda_1 R_1, \lambda_2 R_2, \lambda_3 R_3)) \tag{22}$$

by substituting $\mathbf{R}$ with the relations $P(\lambda_1 R_1, \lambda_2 R_2, \lambda_3 R_3)$ in $\ln(P)$. Evaluation of the integral in the finite condition $q < q_0$ (see Edwards and Vilgis [16]) yields the final result for the crosslinking part of the strain energy function

$$\begin{aligned} W^e &= \Delta F_c(\lambda_1,\ \lambda_2,\ \lambda_3) \equiv F_c(\lambda_1,\ \lambda_2,\ \lambda_3) - F_c(1,\ 1,\ 1) \\ &= \frac{G_c}{2}\left[\frac{\left(1-\delta^2\right)(D-3)}{1-\delta^2(D-3)} + \ln\left(1-\delta^2(D-3)\right)\right] \end{aligned} \tag{23}$$

with

$$D \equiv \sum_{A=1}^{3} \lambda_A^2. \tag{24}$$

It should be pointed out that with the help of the continuum mechanical quantity D, a Helmholtz free energy function on the continuum scale is obtained.

To summarize, the final expression of the elastic energy of deformation of filled networks is given by the equation

$$W = W^e + L^e = \frac{G_c}{2}\left[\frac{\left(1-\delta^2\right)(D-3)}{1-\delta^2(D-3)} + \ln\left(1-\delta^2(D-3)\right)\right] + \frac{2G_e}{\beta^2}\sum_{A=1}^{3}\left(\lambda_A^{-\beta}-1\right). \quad (25)$$

4 Combination of the Extended Non-affine Tube Model with Inelastic Material Properties

In this section, the derived Helmholtz free energy function for isothermal conditions is used to represent the ground state hyperelasticity of elastomers, in combination with other inelastic material properties as discussed in Sect. 2.2. To be more specific, continuum damage and time-dependent phenomena in the form of finite nonlinear viscoelasticity are addressed and modeled by the concept of internal variables, which is briefly introduced.

4.1 Macroscopic Modeling and the Concept of Internal Variables

As outlined in Sect. 2.2, elastomers are characterized by nonlinear elasticity, local damage, rate-dependent and rate-independent dissipative properties, and resulting thermomechanical coupling phenomena. Various constitutive material models for elastomers have been developed that mainly focus on representation of the mechanical material behavior. A brief overview is provided next.

4.1.1 Hyperelasticity

Hyperelastic constitutive models are suitable for representation of the equilibrium ground state elastic response of elastomers. Treloar [18] gives an overview of hyperelastic material models for elastomers, the kinetic theory of chain motions, and network theory. As one of the basic constitutive models for elastomers, the Neo–Hooke material formulation can be derived from polymer-physical considerations. Arruda and Boyce [19] proposed the eight-chain model, which represents the macromolecular network of elastomers by eight chains and only two material parameters. As discussed before, the tube model (Heinrich et al. [4], Edwards and Vilgis [5]) considers the interactions of a polymer chain with its surroundings (termed tube confinement), which stem from crosslinks and other restrictions such as entanglements. Derived from molecular-statistical considerations, the tube model has been applied to numerical mechanics by Heinrich and Kaliske [7]

and has been further developed to the extended non-affine tube model (Kaliske and Heinrich [8]) to account for the limited chain extensibility of network chains. The comparison of several elastic models for elastomers by Marckmann and Verron [20] revealed the very good predictive capabilities of the extended non-affine tube model. Other models for hyperelasticity are the Ogden model (Ogden [21]) and the microsphere model (Miehe et al. [22]). A more detailed overview of constitutive models for hyperelasticity of elastomers is provided, for example, by Bergström [9] and Kaliske and Behnke [2].

4.1.2 Viscoelasticity

To describe the time-dependent material behavior of elastomers, two approaches have been developed. Transient-network theory explains stress relaxation as a result of the breakage and re-formation of crosslinks (see Drozdov and Dorfmann [23]). Originally introduced by Green and Tobolsky [24], several authors developed this theory further (e.g., Tanaka and Edwards [25, 26]). Reptation-type tube models (De Gennes [27], Doi and Edwards [28]) focus on the behavior of a single chain in a polymer gel. The motion of the chain is restricted by tubelike constraints, whereby Brownian motion appears within the tube and reptational motion along the tube.

The mathematical representation of viscous phenomena in the form of evolution equations on the macroscale is another challenging task. Bergström and Boyce [29] applied reptational motion to finite viscoelasticity and derived an evolution law describing the experimentally observed elastomer behavior. The theoretical and numerical aspects of this approach as well as its FE implementation are discussed by Dal and Kaliske [30]. Furthermore, a newly proposed FE formulation for viscoelasticity has been given by Areias and Matouš [31]. Miehe and Göktepe [32] represented the time-dependent material behavior by means of two microkinematic scalar internal variables within the microsphere approach (Miehe et al. [22]). An overview of nonlinear viscoelastic elastomers and solids is given by Wineman [33]. Recently, Freund et al. [34] proposed a microstructure-based one-dimensional (1D) material model for the uniaxial inelastic mechanical behavior of filled elastomers, which is similar to the microsphere approach. In this context, the concept of representative directions was employed for the generalization to three dimensions.

To propose models for the small and finite viscoelasticity of elastomers, different computational approaches have been made. An overview is provided, for example, by Kaliske [35]. In general, one can distinguish between stress- and strain-type internal variables for modeling deviations away from equilibrium (ground state response). Stress-type internal variables were used by Simo [36], Govindjee and Simo [37] and Kaliske and Rothert [38]. Strain-type internal variables require the additive or multiplicative decomposition of total strain. A multiplicative decomposition of the deformation gradient stems from the field of elastoplasticity (see Lee [39]) and has also been applied to viscoelasticity (see,

for example, Sidoroff [40], Lubliner [41], Simo [42], Reese and Govindjee [43], and Dal and Kaliske [30]).

4.1.3 Continuum Damage Mechanics

The formation of microcracks leads to irreversible alteration of the material. Microcracks can evolve further to form macrocracks. In the ultimate state, material failure occurs. As an irreversible thermodynamic process, material damage is another source of energy dissipation and results in an additional thermal contribution to the total energy balance.

Continuum damage mechanics (CDM) describes the formation of microdamage in a material using a continuum approach. The theory goes back to Kachanov [44], Chaboche [45, 46], and Lemaitre [47] among others. Chagnon et al. [48] gave a critical overview of the use of CDM, in particular for describing the Mullins effect in elastomers. An elastoplastic damage model with internal state variables as a strain- or stress-based formulation was developed by Simo and Ju [49, 50]. Kaliske et al. [51] discussed the evolution of scalar damage, where the approach for continuous softening makes use of spline functions (polynomial damage functions). This approach was motivated by Nasdala et al. [52]. Göktepe and Miehe [53] developed the microsphere network model further to also represent deformation-induced softening effects in elastomers by a micromechanically motivated two-network-based constitutive approach for anisotropic damage.

Next, we present an isothermal viscoelastic material model based on the extended non-affine tube model potential. The model includes a CDM approach to account for irreversible thermodynamic processes related to the ground state elasticity of the material. Subsequently, Sect. 5 is dedicated to the temperature-dependent formulation for thermomechanical coupling based on the isothermal terms derived in Sect. 4.

It is worth mentioning that the model development described is only one possible way to combine the extended non-affine tube model with other model parts, taking into account stress softening, damage, viscoelasticity, temperature dependence, etc.

4.2 Continuum Mechanical Basis of Isothermal Viscoelasticity

An isotropic and undeformed body $\mathfrak{B}$ is considered. The body is formed by material points with the position vector $\mathbf{X} \in \mathfrak{B} \subset \mathbb{R}^3$ of the so-called reference, initial, or material configuration at time $t = 0$. The position vector $\mathbf{X}$ is expressed via the fixed Cartesian basis $\mathbf{E}_I$. At time $t > 0$, the material points of the deformed body $\mathfrak{b}$ occupy the positions $\mathbf{x} \in \mathfrak{b} \subset \mathbb{R}^3$ of the so-called current or spatial configuration. The

position vector $\mathbf{x}$ is associated with the Cartesian basis $\mathbf{e}_i$. The position vectors $\mathbf{x}$ and $\mathbf{X}$ of a material point in both configurations are related by

$$\mathbf{x} = \varphi(\mathbf{X},\, t), \tag{26}$$

where $\varphi(\mathfrak{B},\, t) : \mathfrak{B} \times \mathbb{R}^3 \rightarrow \mathfrak{b} \times \mathbb{R}^3$ denotes mapping of the motion and associated deformation. As a result, the material configuration and the current configuration are linked by the relations $\mathbf{x} = \varphi(\mathbf{X},\, t)$ and $\mathfrak{b} = \varphi(\mathfrak{B},\, t)$. The deformation gradient $\mathbf{F}$ is introduced as the gradient of the mapping,

$$\mathbf{F} = \nabla_{\mathbf{X}}\, \varphi(\mathbf{X},\, t) = \frac{\partial x_i}{\partial X_J}\, \mathbf{e}_i \otimes E_J = F_{iJ}\, \mathbf{e}_i \otimes \mathbf{E}_J, \tag{27}$$

and is used as a basic kinematic quantity for constitutive material modeling. The operator $\nabla_{\mathbf{X}}\square$ denotes the gradient operator with respect to the reference configuration, whereas $\nabla_{\mathbf{x}}\square$ stands for the gradient operator with respect to the current configuration. The determinant of the deformation gradient

$$J = \det \mathbf{F} > 0 \tag{28}$$

can be interpreted as the ratio of volume change

$$J = \frac{\mathrm{d}v}{\mathrm{d}V} \quad \text{or} \quad J\,\mathrm{d}V = \mathrm{d}v, \tag{29}$$

where the infinitesimal volume element $\mathrm{d}v$ of the current configuration is compared with its counterpart (i.e., the infinitesimal volume element $\mathrm{d}V$ of the reference configuration).

To describe the distinct volumetric and isochoric material behaviors of elastomers, the deformation gradient is multiplicatively decomposed into a volume-preserving, isochoric (deviatoric) part $\overline{\mathbf{F}}$ and a volumetric (spherical) part $\mathbf{F}_{\mathrm{vol}}$,

$$\mathbf{F} = \overline{\mathbf{F}}\,\mathbf{F}_{\mathrm{vol}}, \quad \overline{\mathbf{F}} = J^{-\frac{1}{3}}\,\mathbf{F}, \quad \mathbf{F}_{\mathrm{vol}} = J^{\frac{1}{3}}\mathbf{1}, \tag{30}$$

where isochoric quantities are marked by an overline. The idea of the multiplicative decomposition of the deformation gradient goes back to Flory [54], Simo et al. [55], and other authors. Finite viscous material behavior with finite deviations far away from the equilibrium is represented by a further multiplicative split of the isochoric part $\overline{\mathbf{F}}$ into elastic and inelastic contributions,

$$\overline{\mathbf{F}} = \overline{\mathbf{F}}_e\,\overline{\mathbf{F}}_i. \tag{31}$$

As a result, an intermediate fictitious elastic configuration is introduced, as shown in Fig. 4. In the present approach, the viscosity is assumed to be purely isochoric in nature because a further multiplicative split is only applied to $\overline{\mathbf{F}}$.

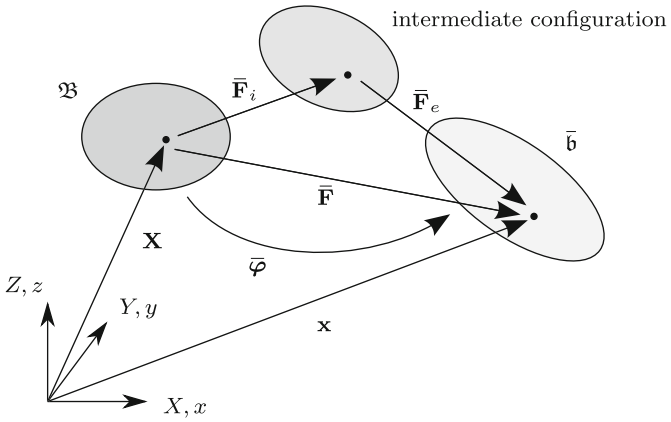

Fig. 4 Configurational setting (isochoric deformation part)

4.3 Stress Response and Rheology

A unit reference volume at constant temperature is considered. Its isothermal volumetric-isochoric Helmholtz free energy function is the sum of the volumetric and isochoric free energies,

$$\Psi_0 = U_0(J) + \overline{\Psi}_0\big(\overline{\mathbf{F}}_i, \overline{\mathbf{F}}_e,\, d\big). \tag{32}$$

In Eq. (32) and in the following, subscript 0 denotes evaluation of the quantities at a fixed reference temperature Θ_0. In analogy to the further split of the isochoric deformation, the isochoric free energy function is composed of equilibrium and non-equilibrium contributions,

$$\overline{\Psi}_0 = (1-d)\overline{\Psi}_0^e\big(\overline{\mathbf{C}}\big(\overline{\mathbf{F}}_i, \overline{\mathbf{F}}_e\big)\big) + \overline{\Psi}_0^v\big(\overline{\mathbf{C}}_e\big(\overline{\mathbf{F}}_e\big)\big)\,, \tag{33}$$

where $\overline{\mathbf{C}} = \overline{\mathbf{F}}^{\mathrm{T}}\overline{\mathbf{F}}$ and $\overline{\mathbf{C}}_e = \overline{\mathbf{F}}^{\mathrm{T}}\overline{\mathbf{F}}_e$ are the unimodular parts of the right Cauchy–Green tensor and the elastic right Cauchy–Green tensor, respectively. $0 \leq d \leq 1$ denotes a scalar damage variable, which is used to represent isotropic damage of the equilibrium material response.

The material stress response to deformation is the sum of volumetric and isochoric Kirchhoff stresses,

$$\boldsymbol{\tau}_0 = \boldsymbol{\tau}^e_{\mathrm{vol},0} + \boldsymbol{\tau}_{\mathrm{iso},0}, \tag{34}$$

which results from the introduced isochoric-volumetric split and Eq. (32) with

$$\begin{aligned} \boldsymbol{\tau}^{e}_{\mathrm{vol},\,0} = J p_0 \mathbf{1}, \quad \boldsymbol{\tau}_{\mathrm{iso},\,0} &= (1-d)\,\boldsymbol{\tau}^{e}_{\mathrm{iso},0} + \boldsymbol{\tau}^{v}_{\mathrm{iso},0} \\ &= (1-d)\mathbb{P} : \overline{\boldsymbol{\tau}}^{e}_{0} + \mathbb{P} : \overline{\boldsymbol{\tau}}^{v}_{0} \\ &= (1-d)\ \mathrm{dev}\ \overline{\boldsymbol{\tau}}^{e}_{0} + \mathrm{dev}\ \overline{\boldsymbol{\tau}}^{v}_{0}. \end{aligned} \tag{35}$$

In this case, $p_0 = U_0'(J)$ denotes the volumetric pressure and $\overline{\boldsymbol{\tau}}_0$ stands for the fictitious Kirchhoff stresses. With the help of the fourth order deviatoric projection tensor $\mathbb{P}_{abcd} = \frac{1}{2}\left[\delta_{ac}\delta_{bd} + \delta_{ad}\delta_{bc}\right] - \frac{1}{3}\delta_{ab}\delta_{cd}$, the Helmholtz free energy functions are directly evaluated with respect to the unimodular quantities (e.g., $\overline{\mathbf{C}}$, $\overline{\mathbf{C}}_e$). The isochoric stresses $\boldsymbol{\tau}_{\mathrm{iso},0}$ are obtained by a deviatoric projection applied to the fictitious stresses $\overline{\boldsymbol{\tau}}^{e}_{0}$ and $\overline{\boldsymbol{\tau}}^{v}_{0}$ (see, for example, Miehe [56]). δ_{ab} denotes the Kronecker symbol, which is associated with the current configuration. The fictitious stresses

$$\overline{\boldsymbol{\tau}}^{e}_{0} = 2\,\partial_{\overline{\mathbf{b}}}\,\overline{\Psi}^{e}_{0}\left(\overline{\mathbf{b}}\right)\overline{\mathbf{b}} \ \text{ and} \tag{36}$$

$$\overline{\boldsymbol{\tau}}^{v}_{0} = 2\,\partial_{\overline{\mathbf{b}}_e}\,\overline{\Psi}^{v}_{0}\left(\overline{\mathbf{b}}_e\right)\overline{\mathbf{b}}_e \tag{37}$$

originate from the further multiplicative decomposition of $\overline{\mathbf{F}}$ into elastic and inelastic parts. $\overline{\mathbf{b}} = \overline{\mathbf{F}}\overline{\mathbf{F}}^{\mathrm{T}}$ and $\overline{\mathbf{b}}_e = \overline{\mathbf{F}}_e\overline{\mathbf{F}}_e^{\mathrm{T}}$ denote the unimodular left Cauchy–Green tensor and the elastic left Cauchy–Green tensor, respectively. The relation

$$\overline{\mathbf{b}}_e = \overline{\mathbf{F}}\,\overline{\mathbf{C}}_i^{-1}\,\overline{\mathbf{F}}^{\mathrm{T}} \tag{38}$$

can be verified using Eq. (31) together with the definition of the unimodular inverse inelastic right Cauchy–Green tensor

$$\overline{\mathbf{C}}_i^{-1} = \overline{\mathbf{F}}_i^{-1}\,\overline{\mathbf{F}}_i^{-\mathrm{T}}. \tag{39}$$

In Fig. 5, the isochoric part of the material model is illustrated together with the stresses in the equilibrium and non-equilibrium branches. The equilibrium branch is formed by a hyperelastic spring, and the non-equilibrium branch consists of a Maxwell element with a nonlinear dashpot. The evolution law of the dashpot is discussed in Sect. 4.6.

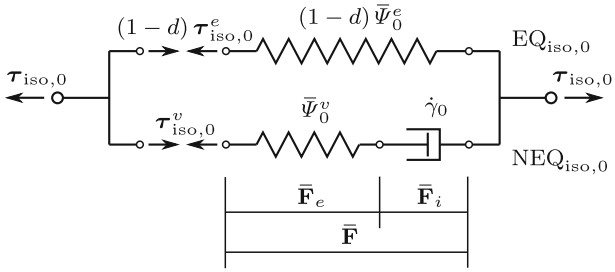

Fig. 5 Rheology of the isochoric part of the material model

4.4 Free Energy Function

For the Helmholtz free energy function $U_0(J)$ of the volumetric part, a standard expression

$$U_0(J) = \kappa_0(J - \ln J - 1) \tag{40}$$

is used; see, for example, Simo and Taylor [57] for more details and admissible function types. κ_0 denotes the bulk modulus evaluated at the reference temperature. In this approach, the bulk modulus has to be large enough to enforce the rubberlike incompressibility.

The isothermal isochoric free energy functions are

$$\overline{\Psi}^e_0(\overline{\mathbf{C}}) = W^e\left(I_{\overline{\mathbf{b}}}\right) + L^e\left(\overline{\lambda}_a\right), \tag{41}$$

$$\overline{\Psi}^v_0(\overline{\mathbf{C}}_e) = W^v\left(I^e_{\overline{\mathbf{b}}}\right), \tag{42}$$

where the functions $W^e\left(I_{\overline{\mathbf{b}}}\right)$ and $L^e\left(\overline{\lambda}_a\right)$ were derived by Kaliske and Heinrich [8] in the form of the extended non-affine tube model. Thus, the following expressions are used for the equilibrium branch

$$W^e\left(I_{\overline{\mathbf{b}}}\right) = \frac{G_c}{2}\left[\frac{\left(1-\delta^2\right)\left(I_{\overline{\mathbf{b}}}-3\right)}{1-\delta^2\left(I_{\overline{\mathbf{b}}}-3\right)} + \ln\left(1-\delta^2\left(I_{\overline{\mathbf{b}}}-3\right)\right)\right], \tag{43}$$

$$L^e\left(\overline{\lambda}_a\right) = \frac{2G_e}{\beta^2}\sum_{a=1}^{3}\left(\overline{\lambda}_a^{-\beta} - 1\right) \tag{44}$$

and for the non-equilibrium branch

$$W^v = \frac{G^v_c}{2}\left[\frac{\left(1-\delta^2_v\right)\left(I^e_{\overline{\mathbf{b}}}-3\right)}{1-\delta^2_v\left(I^e_{\overline{\mathbf{b}}}-3\right)} + \ln\left(1-\delta^2_v\left(I^e_{\overline{\mathbf{b}}}-3\right)\right)\right] \tag{45}$$

to describe the stress response of particle-reinforced elastomers according to the results obtained in Eq. (25). As already introduced in Eq. (24), $D = I_{\overline{\mathbf{b}}} = \operatorname{tr}\overline{\mathbf{C}} = \overline{\lambda}_1^2 + \overline{\lambda}_2^2 + \overline{\lambda}_3^2 = \operatorname{tr}\overline{\mathbf{b}}$ and $I^e_{\overline{\mathbf{b}}} = \operatorname{tr}\overline{\mathbf{C}}_e = \overline{\lambda}_1^{e2} + \overline{\lambda}_2^{e2} + \overline{\lambda}_3^{e2} = \operatorname{tr}\overline{\mathbf{b}}_e$ are the first invariants of the unimodular and elastic Cauchy–Green tensors, respectively. G_c, G_e, β, and δ are material parameters of the equilibrium part $\overline{\Psi}^e\left(\overline{\mathbf{C}}\right)$. The elastic isothermal potential of the non-equilibrium part contains G^v_c and δ_v as material parameters. For the non-equilibrium branch in the present model, only a function in terms of $W^v\left(I^e_{\overline{\mathbf{b}}}\right)$ is chosen as a simple ansatz. $\overline{\lambda}_a$ denotes the principal unimodular stretch

corresponding to the eigenvector $\mathbf{N}_a$ of the unimodular right Cauchy–Green tensor $\overline{\mathbf{C}}$ in the reference configuration,

$$\overline{\mathbf{C}} = \sum_{a=1}^{3} \overline{\lambda}_a^2 \mathbf{N}_a \otimes \mathbf{N}_a. \tag{46}$$

The corresponding eigenvector in the current configuration is termed $\mathbf{n}_a$ and belongs to the eigenspace of $\overline{\mathbf{b}}$,

$$\overline{\mathbf{b}} = \sum_{a=1}^{3} \overline{\lambda}_a^2 \mathbf{n}_a \otimes \mathbf{n}_a. \tag{47}$$

The influence of the model parameters of the free energy functions on the stress response is studied in Figs. 6 and 7. As an example, a uniaxial extension test of an incompressible elastomer cube is addressed. The stress contribution of part $W^e\left(I_{\overline{\mathbf{b}}}\right)$ at constant temperature is depicted in Fig. 6 for variation of parameter δ, whereas Fig. 7 shows the stress contribution of part $L^e\left(\overline{\lambda}_a\right)$ for variation of parameter β.

4.5 Thermodynamic Consistency for Constant Temperature

The second axiom of thermodynamics, also known as the dissipation inequality, for an isothermal setting reads

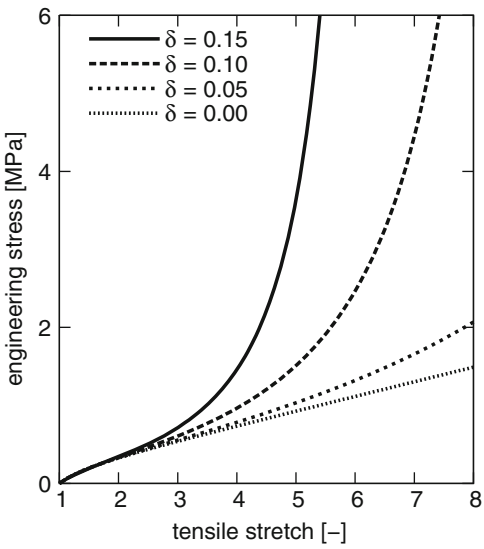

Fig. 6 Stress response of a uniaxial extension test on an incompressible elastomer cube: engineering stress contribution of part $W^e\left(I_{\overline{\mathbf{b}}}\right)$ as a function of parameter δ ($G_c = 0.1867$ MPa)

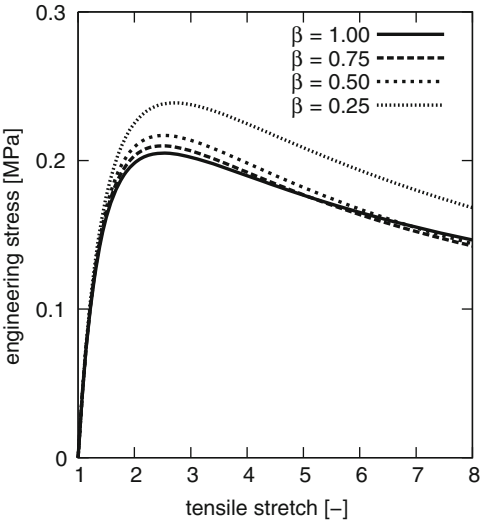

Fig. 7 Stress response of a uniaxial extension test on an incompressible elastomer cube: engineering stress contribution of part $L^e\left(\overline{\lambda}_a\right)$ as a function of parameter β ($G_e = 0.2169$ MPa)

$$\mathcal{D} = \boldsymbol{\tau}_0 : \mathbf{d} - \dot{\Psi}_0 \geq 0 \tag{48}$$

and stipulates that the external power ($\boldsymbol{\tau}_0 : \mathbf{d}$) in the form of the overall Kirchhoff stress tensor $\boldsymbol{\tau}_0$ and the deformation rate tensor

$$\begin{aligned} \mathbf{d} &= \frac{1}{2}\left(\mathbf{l} + \mathbf{l}^{\mathrm{T}}\right) = \frac{1}{2}\left(\left[\mathbf{l}_{\mathrm{iso}} + \mathbf{l}_{\mathrm{vol}}\right] + \left[\mathbf{l}_{\mathrm{iso}} + \mathbf{l}_{\mathrm{vol}}^{\mathrm{T}}\right]\right) \\ &= \frac{1}{2}\left(\mathbf{l}_{\mathrm{vol}} + \mathbf{l}_{\mathrm{vol}}^{\mathrm{T}}\right) + \frac{1}{2}\left(\mathbf{l}_{\mathrm{iso}} + \mathbf{l}_{\mathrm{iso}}{}^{\mathrm{T}}\right) = \mathbf{d}_{\mathrm{vol}} + \mathbf{d}_{\mathrm{iso}} \end{aligned} \tag{49}$$

has to be larger or equal to the rate of the free energy $\dot{\Psi}_0$ stored in the material during the applied deformation. Ψ is the Helmholtz free energy per unit reference volume.

The dissipation inequality can be separately considered for isochoric and volumetric processes

$$\mathcal{D} = \mathcal{D}_{\mathrm{vol}} + \mathcal{D}_{\mathrm{iso}} \geq 0, \tag{50}$$

which is an even stronger restriction than that formulated in Eq. (48). Hence, the volumetric and isochoric notation of Eq. (48) are written as

$$\mathcal{D}_{\mathrm{vol}} = \boldsymbol{\tau}^e_{\mathrm{vol},0} : \mathbf{d}_{\mathrm{vol}} - \dot{U}_0(J) \geq 0, \tag{51}$$

$$\mathcal{D}_{\mathrm{iso}} = \boldsymbol{\tau}_{\mathrm{iso},0} : \mathbf{d}_{\mathrm{iso}} - \dot{\overline{\Psi}}_0 \geq 0. \tag{52}$$

The volumetric dissipation inequality can be instantaneously verified,

$$\begin{aligned}\mathcal{D}_{\text{vol}} &= \boldsymbol{\tau}^{e}_{\text{vol},0} : \mathbf{d}_{\text{vol}} - \partial_{\mathbf{b}} U_0(J) : \dot{\mathbf{b}} \geq 0 \\ &= \boldsymbol{\tau}^{e}_{\text{vol},0} : \mathbf{d}_{\text{vol}} - \partial_{\mathbf{b}} U_0(J) \;\; : \;\; \left[\mathbf{l}\mathbf{b} + \mathbf{b}\mathbf{l}^{\text{T}}\right] \geq 0 \\ &= \boldsymbol{\tau}^{e}_{\text{vol},0} : \mathbf{d}_{\text{vol}} - \left[2\partial_{\mathbf{b}} U_0(J)\mathbf{b}\right] : \mathbf{d} \geq 0 \\ &= \boldsymbol{\tau}^{e}_{\text{vol},0} : \mathbf{d}_{\text{vol}} - \boldsymbol{\tau}^{e}_{\text{vol},0} : \mathbf{d}_{\text{vol}} = 0,\end{aligned} \tag{53}$$

noting that $\boldsymbol{\tau}^{e}_{\text{vol},0}$ is only a spherical second-order tensor and that viscous or damage effects are only considered in the isochoric part of the material model. To evaluate the isochoric dissipation inequality stated in Eq. (52), the material time derivative of the isochoric potential is carried out

$$\dot{\overline{\Psi}}_0 = (1-d)\,\partial_{\overline{\mathbf{b}}}\overline{\Psi}^{e}_0 : \dot{\overline{\mathbf{b}}} - \overline{\Psi}^{e}_0\,\dot{d} + \partial_{\overline{\mathbf{b}}_e}\overline{\Psi}^{v}_0 : \dot{\overline{\mathbf{b}}}_e. \tag{54}$$

A further evaluation of Eq. (54) yields

$$\begin{aligned}\dot{\overline{\Psi}}_0 &= (1-d)\partial_{\overline{\mathbf{b}}}\overline{\Psi}^{e}_0 : \left[\mathbf{l}_{\text{iso}}\overline{\mathbf{b}} + \overline{\mathbf{b}}\mathbf{l}^{\text{T}}_{\text{iso}}\right] - \overline{\Psi}^{e}_0\,\dot{d} + \partial_{\overline{\mathbf{b}}_e}\overline{\Psi}^{v}_0 \\ &\quad : \left[\mathbf{l}_{\text{iso}}\overline{\mathbf{b}}_e + \overline{\mathbf{b}}_e\mathbf{l}^{\text{T}}_{\text{iso}} + \overline{\mathcal{L}}_v\left(\overline{\mathbf{b}}_e\right)\right],\end{aligned} \tag{55}$$

where the material time derivative of $\overline{\mathbf{b}}_e$ is used,

$$\dot{\overline{\mathbf{b}}}_e = \mathbf{l}_{\text{iso}}\overline{\mathbf{b}}_e + \overline{\mathbf{b}}_e\mathbf{l}^{\text{T}}_{\text{iso}} + \overline{\mathcal{L}}_v\left(\overline{\mathbf{b}}_e\right). \tag{56}$$

The spatial time derivative $\overline{\mathcal{L}}_v\left(\overline{\mathbf{b}}_e\right)$ of the elastic stretch $\overline{\mathbf{b}}_e$ is calculated by a volume-preserving pull-back operation of $\overline{\mathbf{b}}_e$ to the reference configuration, differentiation with respect to time of this material quantity, and a push-forward operation to obtain the spatial time derivative. This procedure is commonly referred to as the Lie time derivative. In the present case, a modified form of the Lie time derivative is employed, which uses the isochoric deformation gradient $\overline{\mathbf{F}}$,

$$\begin{aligned}\overline{\mathcal{L}}_v\left(\overline{\mathbf{b}}_e\right) &= \overline{\Phi}_*\left[\frac{\mathrm{d}}{\mathrm{d}t}\left(\overline{\Phi}^*\left[\overline{\mathbf{b}}_e\right]\right)\right] = \overline{\Phi}_*\left[\frac{\mathrm{d}}{\mathrm{d}t}\left(\overline{\mathbf{F}}^{-1}\overline{\mathbf{b}}_e\overline{\mathbf{F}}^{-\text{T}}\right)\right] = \overline{\Phi}_*\left[\dot{\overline{\mathbf{C}}_i^{-1}}\right] \\ &= \overline{\mathbf{F}}\,\dot{\overline{\mathbf{C}}_i^{-1}}\,\overline{\mathbf{F}}^{\text{T}}.\end{aligned} \tag{57}$$

By recalling Eq. (55), a further manipulation yields

$$\begin{aligned}\dot{\overline{\Psi}}_0 &= (1-d)\left[2\partial_{\overline{\mathbf{b}}}\overline{\Psi}^{e}_0\overline{\mathbf{b}}\right] : \mathbf{d}_{\text{iso}} - \overline{\Psi}^{e}_0\,\dot{d} + \left[2\partial_{\overline{\mathbf{b}}_e}\overline{\Psi}^{v}_0\overline{\mathbf{b}}_e\right] : \left[\mathbf{d}_{\text{iso}} + \frac{1}{2}\overline{\mathcal{L}}_v\left(\overline{\mathbf{b}}_e\right)\overline{\mathbf{b}}_e^{-1}\right] \\ &= (1-d)\overline{\boldsymbol{\tau}}^{e}_0 : \mathbf{d}_{\text{iso}} - \overline{\Psi}^{e}_0\dot{d} + \overline{\boldsymbol{\tau}}^{v}_0 : \left[\mathbf{d}_{\text{iso}} + \frac{1}{2}\overline{\mathcal{L}}_v\left(\overline{\mathbf{b}}_e\right)\overline{\mathbf{b}}_e^{-1}\right].\end{aligned} \tag{58}$$

If the obtained result of Eq. (58) is inserted into the isochoric dissipation inequality given in Eq. (52),

$$\mathcal{D}_{\text{iso}} = \overline{\Psi}_0^e \dot{d} + \overline{\boldsymbol{\tau}}_0^v : \left[-\frac{1}{2} \overline{\mathcal{L}}_v \left(\overline{\mathbf{b}}_e \right) \overline{\mathbf{b}}_e^{-1} \right] \geq 0 \tag{59}$$

$$= \overline{\Psi}_0^e \dot{d} - \boldsymbol{\tau}_{\text{iso},0}^v : \frac{1}{2} \overline{\mathcal{L}}_v \left(\overline{\mathbf{b}}_e \right) \overline{\mathbf{b}}_e^{-1} \geq 0 \tag{60}$$

$$= \overline{\Psi}_0^e \dot{d} + \boldsymbol{\tau}_{\text{iso},0}^v : \widetilde{\mathbf{d}}_i \geq 0 \tag{61}$$

is obtained. With the expression of Eq. (57), the inelastic deformation rate tensor $\overline{\mathbf{d}}_i$ is formulated in terms of the inelastic velocity tensor, $\overline{\mathbf{l}}_i = \dot{\overline{\mathbf{F}}}_i \overline{\mathbf{F}}_i^{-1}$,

$$\begin{aligned} \frac{1}{2} \overline{\mathcal{L}}_v \left(\overline{\mathbf{b}}_e \right) \overline{\mathbf{b}}_e^{-1} &= \frac{1}{2} \left[\overline{\mathbf{F}}_e \overline{\mathbf{F}}_i \left(\dot{\overline{\mathbf{F}}_i^{-1}} \overline{\mathbf{F}}_i^{-\mathrm{T}} + \overline{\mathbf{F}}_i^{-1} \dot{\overline{\mathbf{F}}_i^{-\mathrm{T}}} \right) \overline{\mathbf{F}}_i^{\mathrm{T}} \overline{\mathbf{F}}_e^{\mathrm{T}} \right] \overline{\mathbf{b}}_e^{-1} \\ &= -\frac{1}{2} \overline{\mathbf{F}}_e \left(\overline{\mathbf{l}}_i + \overline{\mathbf{l}}_i^{\mathrm{T}} \right) \overline{\mathbf{F}}_e^{-1} \\ &= -\widetilde{\mathbf{d}}_i. \end{aligned} \tag{62}$$

The following section discusses a constitutive evolution law for the inelastic network stretches governed by the fictitious inelastic deformation rate tensor $\widetilde{\mathbf{d}}_i$.

4.6 Evolution Law of the Inelastic Deformation

On the macroscale, the observable viscous material behavior is represented by a constitutive evolution law. Different phenomenologically and physically motivated approaches have been proposed in the literature, as mentioned in Sect. 4.1. The approach proposed by Bergström and Boyce [29] describes evolution of the inelastic deformation rate tensor in the current configuration

$$\widetilde{\mathbf{d}}_i = \dot{\gamma}_0 \mathbf{N}_{\mathrm{P}} \tag{63}$$

by a physically based derivation for the effective creep rate $\dot{\gamma}_0 > 0$.

$$\mathbf{N}_{\mathrm{P}} = \frac{\boldsymbol{\tau}_{\text{iso},0}^v}{\| \boldsymbol{\tau}_{\text{iso},0}^v \|} \text{ with } \boldsymbol{\tau}_{\text{iso},0}^v = \mathbb{P} : \overline{\boldsymbol{\tau}}_0^v, \tag{64}$$

$$\| \boldsymbol{\tau}_{\text{iso},0}^v \| = \sqrt{\boldsymbol{\tau}_{\text{iso},0}^v : \boldsymbol{\tau}_{\text{iso},0}^v} \tag{65}$$

projects the creep process to the viscous stress directions. Because $\boldsymbol{\tau}_{\text{iso},0}^v$ is a function of the elastic left Cauchy–Green tensor, its eigenspace coincides with the eigenspace of $\overline{\mathbf{b}}_e$ and $\mathbf{b}_e$.

Dal and Kaliske [30] describe the micromechanical motivation and show the derivation of the effective creep rate expression on the macroscale,

$$\dot{\gamma}_0 = \dot{\gamma}_{\mathrm{R}} \left[\lambda^i_{\mathrm{chain}} - 1\right]^c \left(\frac{\tau_{v,0}}{\hat{\tau}}\right)^m. \tag{66}$$

In this case, the effective creep rate considers contributions stemming from the inelastic deformation, represented by the inelastic network stretch $\lambda^i_{\mathrm{chain}}$, and the isochoric viscous stresses in the form of $\tau_{v,0}$,

$$\lambda^i_{\mathrm{chain}} = \sqrt{\frac{I^i_{\overline{\mathbf{b}}}}{3}}, \quad \tau_{v,0} = \frac{\| \boldsymbol{\tau}^v_{\mathrm{iso},0} \|}{\sqrt{2}}. \tag{67}$$

$I^i_{\overline{\mathbf{b}}} = \mathrm{tr}\,\overline{\mathbf{C}}_i$ is the first invariant of the inelastic right Cauchy–Green tensor $\overline{\mathbf{C}}_i = \overline{\mathbf{F}}_i^T \overline{\mathbf{F}}_i$. $\dot{\gamma}_{\mathrm{R}}$ denotes the reference effective creep rate and $\hat{\tau}$ is a parameter with stress units to render the $\left(\frac{\tau_{v,0}}{\hat{\tau}}\right)$ ratio non-dimensional. The power terms c and m govern the kinetics of chain relaxation and the energy-activated inelastic flow, respectively. The thermodynamic consistency is satisfied for $\dot{\gamma}_{\mathrm{R}}/\hat{\tau}^m > 0$ and $m > 0$. In contrast to Doi and Edwards [28] and Bergström and Boyce [29], Dal and Kaliske [30] proposed a less restrictive choice for c, with $c < 0$. Alternatively, Dal and Kaliske [30] discussed the substitution of $\lambda^i_{\mathrm{chain}}$ by the ratio of the total and elastic network stretches,

$$\lambda^i_{\mathrm{chain}} = \frac{\lambda}{\lambda^e}, \quad \lambda = \sqrt{\frac{I_{\overline{\mathbf{b}}}}{3}}, \quad \lambda_e = \sqrt{\frac{I^e_{\overline{\mathbf{b}}}}{3}}. \tag{68}$$

Again, the first invariants can be calculated by $I_{\overline{\mathbf{b}}} = \mathrm{tr}\,\overline{\mathbf{C}}$ and $I^e_{\overline{\mathbf{b}}} = \mathrm{tr}\,\overline{\mathbf{C}}_e$. However, the quantities $\overline{\mathbf{C}}$ and $\overline{\mathbf{C}}_i$ do not lie in the same eigenspace as $\boldsymbol{\tau}^v_{\mathrm{iso},0}$ and $\overline{\mathbf{b}}_e$. To overcome this numerical problem, a further development of the evolution law has been recently proposed by Dal [58].

In the present contribution, in contrast to Dal and Kaliske [30], a modified effective creep rate expression

$$\boxed{\dot{\gamma}_0 = \dot{\gamma}_{\mathrm{R}} \lambda_e^c \left(\frac{\tau_{v,0}}{\hat{\tau}}\right)^m} \tag{69}$$

is introduced with quantities lying in the same eigenspace. In the following, $\dot{\gamma}_0$ always refers to the definition given in Eq. (69). In this case, the thermodynamic consistency is fulfilled for $\dot{\gamma}_{\mathrm{R}}/\hat{\tau}^m > 0$ and $m > 0$. From Eqs. (66) and (68), it can be concluded that for the modified effective creep rate in Eq. (69), $c \geq 0$ holds. In addition, the inelastic network flow directly depends on the elastic network stretch in its absolute value and is not scaled by the total deformation in the form of $\overline{\mathbf{C}}$. For the parameter combination $c = 0$ and $m = 1$, an evolution law is obtained that linearly depends on the isochoric stresses.

Figures 8 and 9 show the influence of the evolution law model parameters c and m. As an example, an elastomer unit cube was considered. After an initial uniaxial tensile loading applied within 1 s, a subsequent relaxation phase of 10 s at constant deformation level was used to demonstrate the relaxation behavior. The isothermal material model parameters (ground state elastic response) are summarized in Table 1. The evolution law parameter c is varied in Fig. 8, whereas the influence of the parameter m is shown in Fig. 9.

To reveal the different shapes of the hystereses as a function of the parameters c and m during cyclic uniaxial loading, a cyclic tension–compression test was carried out. Again, a unit elastomer cube was considered and subjected to an

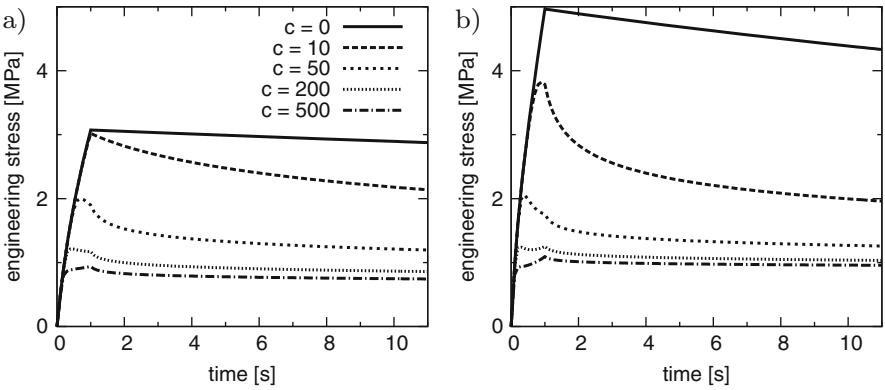

Fig. 8 Uniaxial tension test on an elastomer cube (see Table 1 for varying parameter c and constant parameter $m = 1$) with loading phase of 1 s and relaxation phase of 10 s: (**a**) maximum tensile stretch $\lambda = 2$; (**b**) maximum tensile stretch $\lambda = 3$

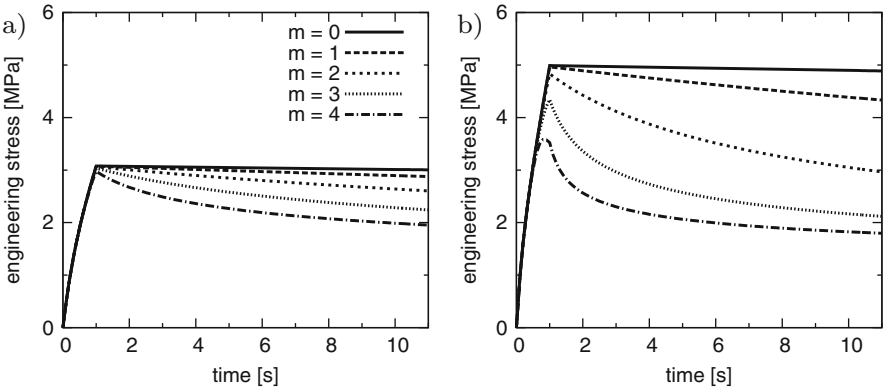

Fig. 9 Uniaxial tension test on an elastomer cube (see Table 1 for constant parameter $c = 0$ and varying parameter m) with loading phase of 1 s and relaxation phase of 10 s: (**a**) maximum tensile stretch $\lambda = 2$; (**b**) maximum tensile stretch $\lambda = 3$

Table 1 Model parameters for study of relaxation behavior

Mass density	ρ_0 (g/cm^3)				
	1.120				
Equilibrium branch	κ_0 (MPa)	G_c (MPa)	δ (−)	G_e (MPa)	β (−)
	1,000.0	0.1867	0.09693	0.2169	0.2
Non-equilibrium branch i	G_c^v (MPa)	δ_v (−)	$\dot{\gamma}_0/\hat{\tau}^m$ (MPa^{-m}s^{-1})	c (−)	m (−)
1	1.45	0.0	0.00145	Variable	Variable
Damage parameters	η_α (−)	η_β (−)	$f_{d,\alpha}$ (−)	$f_{d,\beta}$ (−)	
	1.0	1.0	0.0	0.0	

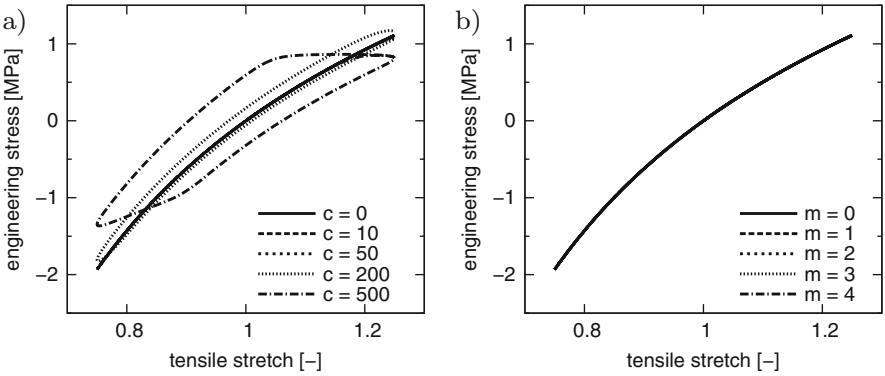

Fig. 10 Cyclic uniaxial tension-compression test on an elastomer cube (see Table 1), with loading frequency $f = 1.0$ Hz: (**a**) for varying parameter c and constant parameter $m = 1$; (**b**) for constant parameter $c = 0$ and varying parameter m

excitation frequency of $f = 1$ Hz. The resulting engineering stress response as a function of the strain state is depicted in Fig. 10.

4.7 Algorithmic Setting for the Isothermal Constitutive Model

A closed-form description of the resulting stress response as well as the consistent tangent moduli are next derived for the equilibrium and the non-equilibrium parts. By considering volumetric and isochoric decomposition, the total stress response

$$\boldsymbol{\tau}_0 = \boldsymbol{\tau}^e_{\mathrm{vol},0} + \boldsymbol{\tau}_{\mathrm{iso},0} \tag{70}$$

is computed, where the isochoric stresses have already been given in Eq. (35) as

$$\boxed{\boldsymbol{\tau}_{\mathrm{iso},0} = (1-d)\boldsymbol{\tau}^{e}_{\mathrm{iso},0} + \boldsymbol{\tau}^{v}_{\mathrm{iso},0}.} \tag{71}$$

The total tangent moduli in their volumetric and isochoric decomposition read

$$\mathbb{C}_0 = \mathbb{C}^{e}_{\mathrm{vol},0} + \mathbb{C}_{\mathrm{iso},0}. \tag{72}$$

Furthermore, the deviatoric tangent moduli of the isochoric equilibrium and non-equilibrium branches are

$$\boxed{\mathbb{C}_{\mathrm{iso},0} = (1-d)\mathbb{C}^{e}_{\mathrm{iso},0} + \mathbb{C}^{e}_{\mathrm{iso},d,0} + \mathbb{C}^{v}_{\mathrm{iso},0},} \tag{73}$$

with

$$\mathbb{C}^{e}_{\mathrm{iso},0} = \mathbb{P} : \overline{\mathbb{C}}^{e}_{0} : \mathbb{P} + \frac{2}{3}\mathrm{tr}\left[\overline{\boldsymbol{\tau}}^{e}_{0}\right]\mathbb{P} - \frac{2}{3}\left[\mathrm{dev}\left(\overline{\boldsymbol{\tau}}^{e}_{0}\right) \otimes \mathbf{1} + \mathbf{1} \otimes \mathrm{dev}\left(\overline{\boldsymbol{\tau}}^{e}_{0}\right)\right], \tag{74}$$

$$\mathbb{C}^{v}_{\mathrm{iso},0} = \mathbb{P} : \overline{\mathbb{C}}^{v}_{0} : \mathbb{P} + \frac{2}{3}\mathrm{tr}\left[\overline{\boldsymbol{\tau}}^{v}_{0}\right]\mathbb{P} - \frac{2}{3}\left[\mathrm{dev}\left(\overline{\boldsymbol{\tau}}^{v}_{0}\right) \otimes \mathbf{1} + \mathbf{1} \otimes \mathrm{dev}\left(\overline{\boldsymbol{\tau}}^{v}_{0}\right)\right]. \tag{75}$$

The total isochoric tangent moduli are obtained as the sum of the isochoric equilibrium response $(1-d)\mathbb{C}^{e}_{\mathrm{iso},0} + \mathbb{C}^{e}_{\mathrm{iso},d,0}$ and the isochoric non-equilibrium response $\mathbb{C}^{v}_{\mathrm{iso},0}$. The additional tangent term $\mathbb{C}^{e}_{\mathrm{iso},d,0}$ stems from the $(1-d)$ CDM approach. In the following steps, the stress and moduli expressions of the equilibrium response are given for the free energy functions defined in Eqs. (43) and (44). Subsequently, the stress and moduli terms of the non-equilibrium response are analogously derived.

4.7.1 Stress and Moduli Terms for the Equilibrium Branch

First, the equilibrium response, which consists of volumetric and isochoric parts, is investigated. Emphasis is given to the volumetric response and the isochoric response of the equilibrium branch.

The volumetric Kirchhoff stresses and the Eulerian tangent moduli as derivatives of $U_0(J)$ are

$$\boldsymbol{\tau}^{e}_{\mathrm{vol},0} = 2\partial_{\mathbf{b}}U_0(J)\mathbf{b}, \tag{76}$$

$$\mathbb{C}^{e}_{\mathrm{vol},0} = 4\mathbf{b}\partial^{2}_{\mathbf{bb}}U_0(J)\mathbf{b}. \tag{77}$$

Evaluation of the derivatives in Eqs. (76) and (77) results in

$$\boldsymbol{\tau}^{e}_{\mathrm{vol},0} = J p_0 \mathbf{1} \quad \text{and} \tag{78}$$

$$\mathbb{C}^{e}_{\mathrm{vol},0} = \left(J\,p_0 + J^2\,s_0\right)\mathbf{1}\otimes\mathbf{1} - 2J\,p_0\mathbb{I}, \tag{79}$$

where $\mathbb{I}_{abcd} = \frac{1}{2}[\delta_{ac}\delta_{bd} + \delta_{ad}\delta_{bc}]$ is the fourth order identity tensor. The scalars $J\,p_0$ and $J^2\,s_0$ denote the hydrostatic Kirchhoff stresses (negative pressure) and the corresponding modulus, respectively. They are defined as derivatives of $U_0(J)$ with respect to J,

$$p_0 = U_0'(J) \quad \text{and} \quad s_0 = U_0''(J). \tag{80}$$

If the derivatives are carried out by exploiting Eq. (40),

$$p_0 = \kappa_0\frac{(J-1)}{J} \quad \text{and} \quad s_0 = \frac{\kappa_0}{J^2} \tag{81}$$

are obtained.

To represent continuously distributed, isotropic damage of the material in the isochoric response of the equilibrium branch, a CDM approach with a scalar damage variable d,

$$0 \le d = f_{d,\alpha}d_\alpha(\alpha) + f_{d,\beta}\,d_\beta(\beta) \le 1 \tag{82}$$

is applied. Figure 11 depicts a 1D representation of the $(1-d)$ CDM approach. $d=0$ corresponds to a virgin, undamaged material, whereas $d=1$ represents total failure of the equilibrium branch. Limiting coefficients $0 \le f_{d,\alpha} \le 1 - f_{d,\beta}$ and $0 \le f_{d,\beta} \le 1 - f_{d,\alpha}$ are introduced to scale the discontinuous damage

$$d_\alpha(\alpha) = 1 - \exp\left(-\frac{\alpha}{\eta_\alpha}\right), \quad d_\alpha(\alpha) \in [0,1], \tag{83}$$

and the continuous damage,

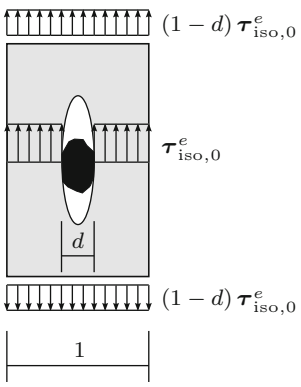

Fig. 11 Modeling of stress softening as a result of formation of microdefects (e.g., around filler aggregates)

$$d_\beta(\beta) = 1 - \exp\left(-\frac{\beta}{\eta_\beta}\right), \quad d_\beta(\beta) \in [0,1], \tag{84}$$

see, for example, Miehe [59]. In the present case, simple exponential softening functions have been chosen as defined in Eqs. (83) and (84), where more sophisticated and more material-appropriate monotonic function types are also possible (see, for example, Kaliske et al. [51]). η_α and η_β are material-specific shape parameters of the softening functions, while the softening parameters α and β

$$\alpha(t) = \max_{s\in[0,t]} \left[\overline{\Psi}_0^e(s)\right], \tag{85}$$

$$\beta(t) = \int_0^t \left|\frac{\partial \overline{\Psi}_0^e(s)}{\partial s}\right| \mathrm{d}s, \tag{86}$$

evolve with time t as a function of the isothermal isochoric potential $\overline{\Psi}_0^e(t)$. An algorithmic representation of Eqs. (85) and (86) for a finite time step $\Delta t = t_{n+1} - t_n$ yields

$$\alpha^{t_{n+1}} = \begin{cases} \overline{\Psi}_0^{e,t_{n+1}} & \text{if} \quad \overline{\Psi}_0^{e,t_{n+1}} > \alpha^{t_n} \\ \alpha^{t_n} & \text{else} \end{cases} \tag{87}$$

and

$$\beta^{t_{n+1}} = \beta^{t_n} + \left|\overline{\Psi}_0^{e,t_{n+1}} - \overline{\Psi}_0^{e,t_n}\right|. \tag{88}$$

Figure 12, shows the influence of the model parameters governing discontinuous damage evolution. For a purely elastic unit elastomer cube at constant temperature, a uniaxial tension test and a uniaxial compression test were carried out. The

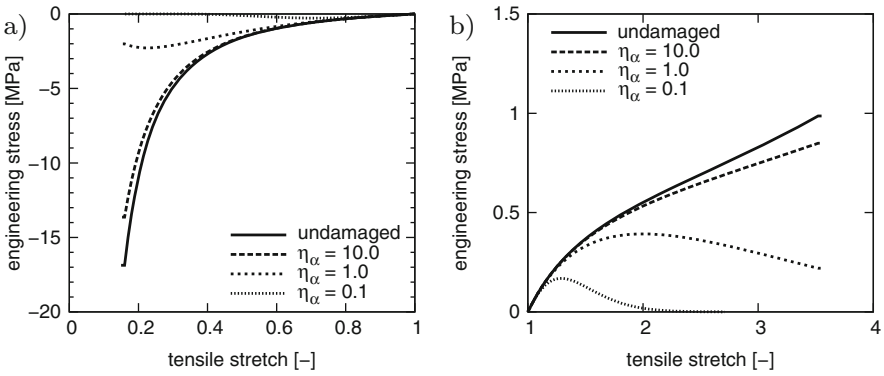

Fig. 12 Uniaxial tension test on an elastomer cube with discontinuous damage – variation of η_α (constant parameters $\eta_\beta = 0, f_{d,\alpha} = 1, f_{d,\beta} = 0$): (**a**) compression; (**b**) tension

isothermal ground state response of the material is represented by the model parameters summarized in Table 2.

Furthermore, to highlight the influence of the parameters governing the continuous damage approach, uniaxial cyclic loading of the unit elastomer cube is addressed in Fig. 13. It can be observed that the damage and, in consequence, the stress softening evolves with each loading and unloading process although a previously seen maximum loading situation is not exceeded during the cyclic test at constant deformation amplitude.

Table 2 Model parameters for study of stress softening

Mass density	ρ_0 (g/cm^3)				
	1.120				
Equilibrium branch	κ_0 (MPa)	G_c (MPa)	δ (−)	G_e (MPa)	β (−)
	1,000.0	0.1867	0.09693	0.2169	0.2
Damage parameters	η_α (−)	η_β (−)	$f_{d,\alpha}$ (−)	$f_{d,\beta}$ (−)	
	Variable	Variable	Variable	Variable	

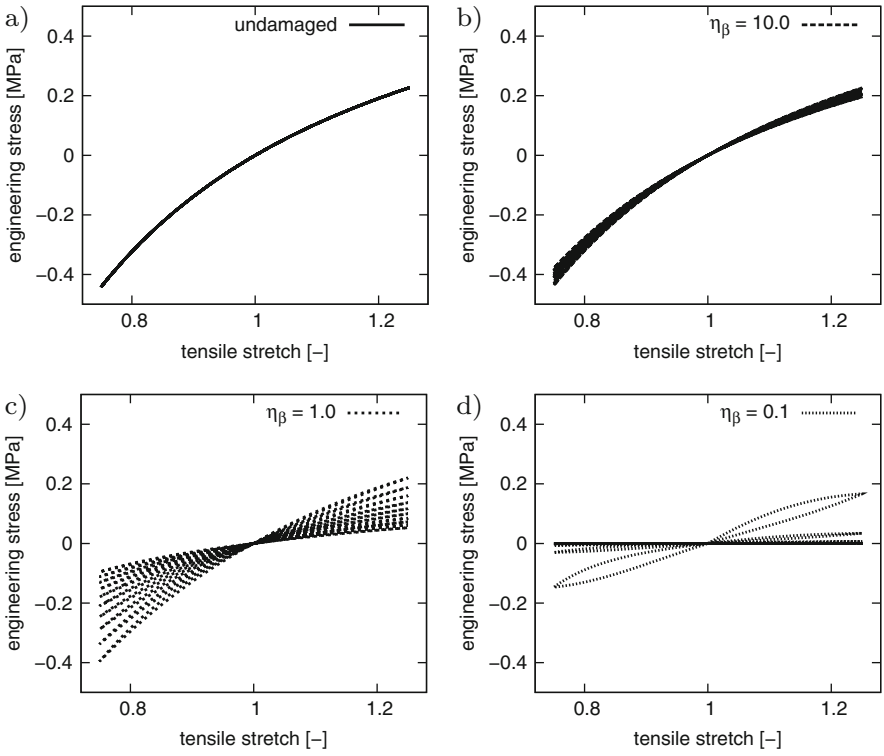

Fig. 13 Cyclic uniaxial tension-compression test on an elastomer cube with continuous damage – variation of η_β (constant parameters $\eta_\alpha = 0$, $f_{d,\alpha} = 0$, $f_{d,\beta} = 1$), with loading frequency $f = 1$ Hz, 10 cycles: (**a**) undamaged material; (**b**) $\eta_\beta = 10$; (**c**) $\eta_\beta = 1$; (**d**) $\eta_\beta = 0.1$

For further derivations, the isochoric dissipation inequality given in Eq. (52) for an isothermal isochoric free energy function $\overline{\Psi}_0\big(\overline{\mathbf{F}}_e, \overline{\mathbf{F}}_i, d\big)$ is recalled,

$$\begin{aligned}\mathcal{D}_{\text{iso}} = \boldsymbol{\tau}_{\text{iso},0} : \mathbf{d}_{\text{iso}} - (1-d)\partial_{\overline{\mathbf{b}}}\overline{\Psi}_0^e : \left[\mathbf{l}_{\text{iso}}\overline{\mathbf{b}} + \overline{\mathbf{b}}\mathbf{l}_{\text{iso}}^{\mathrm{T}}\right] + \overline{\Psi}_0^e \dot{d} \\ - \partial_{\overline{\mathbf{b}}_e}\overline{\Psi}_0^v : \left[\mathbf{l}_{\text{iso}}\overline{\mathbf{b}}_e + \overline{\mathbf{b}}_e\mathbf{l}_{\text{iso}}^{\mathrm{T}} + \overline{\mathcal{L}}_v\big(\overline{\mathbf{b}}_e\big)\right],\end{aligned} \tag{89}$$

where the free energy rate expression of Eq. (55) has been inserted. By defining $\mathcal{D}_{\text{EQ,iso}}$ as the dissipation related to the equilibrium branch, the use of Eq. (89) yields

$$\begin{aligned}\mathcal{D}_{\text{EQ,iso}} &= \boldsymbol{\tau}_{\text{EQ,iso},0} : \mathbf{d}_{\text{iso}} - (1-d)\ \partial_{\overline{\mathbf{b}}}\overline{\Psi}_0^e : \left[\mathbf{l}_{\text{iso}}\overline{\mathbf{b}} + \overline{\mathbf{b}}\mathbf{l}_{\text{iso}}^{\mathrm{T}}\right] + \overline{\Psi}_0^e \dot{d} \\ &= \left[\boldsymbol{\tau}_{\text{EQ,iso},0} - \mathbb{P} : \big(2(1-d)\ \partial_{\overline{\mathbf{b}}}\overline{\Psi}_0^e\overline{\mathbf{b}}\big)\right] : \mathbf{d}_{\text{iso}} + \overline{\Psi}_0^e \dot{d} \\ &= \overline{\Psi}_0^e \dot{d}\,.\end{aligned} \tag{90}$$

The equilibrium stresses of the equilibrium branch are

$$\begin{aligned}\boldsymbol{\tau}_{\text{EQ,iso},0} &= (1-d)\mathbb{P} : \big(2\partial_{\overline{\mathbf{b}}}\overline{\Psi}_0^e\overline{\mathbf{b}}\big) \\ &= (1-d)\boldsymbol{\tau}_{\text{iso},0}^e,\end{aligned} \tag{91}$$

which renders the first term in brackets of Eq. (90) zero and yields the stress definition (see, for example, Coleman and Gurtin [60]). The thermodynamic remaining dissipation inequality of the equilibrium branch,

$$\overline{\Psi}_0^e \dot{d} \geq 0, \tag{92}$$

is related to the CDM approach and quantifies the irreversibly dissipated rate of mechanical energy during microdamage formation.

The tangent moduli of the isochoric equilibrium branch $\mathbb{C}_{\text{EQ,iso},0}$ in the reference configuration are defined by the time derivative of the second Piola–Kirchhoff stresses $\dot{\mathbf{S}}_{\text{EQ,iso},0} = \mathbb{C}_{\text{EQ,iso},0} : \frac{1}{2}\dot{\mathbf{C}}$. The material time derivative reads

$$\begin{aligned}\dot{\mathbf{S}}_{\text{EQ,iso},0} &= 2\partial_{\mathbf{C}}\mathbf{S}_{\text{EQ,iso},0} : \frac{1}{2}\dot{\mathbf{C}} + \partial_d \mathbf{S}_{\text{EQ,iso},0}\ \dot{d} \\ &= \left[2\partial_{\mathbf{C}}\mathbf{S}_{\text{EQ,iso},0} + 2\partial_d \mathbf{S}_{\text{EQ,iso},0}\partial_{\mathbf{C}} d\right] : \frac{1}{2}\dot{\mathbf{C}} \\ &= \left[(1-d)\mathbb{C}_{\text{iso},0}^e + \mathbb{C}_{\text{iso},d,0}^e\right] : \frac{1}{2}\dot{\mathbf{C}} \\ &= \mathbb{C}_{\text{EQ,iso},0} : \frac{1}{2}\dot{\mathbf{C}},\end{aligned} \tag{93}$$

where the chain rule has been employed for the material time derivative $\dot{d} = \partial_{\mathbf{C}} d : \dot{\mathbf{C}}$. By recalling Eqs. (73) and (74) and evaluating the free energy functions given in Eqs. (43) and (44), a loading-independent part

$$\overline{\mathbb{C}}_0^e = \left(\overline{\mathbb{C}}_W^e + \overline{\mathbb{C}}_L^e\right) \tag{94}$$

and a second loading-dependent part can be identified, which for the case of loading is $\alpha^{t_{n+1}} > \alpha^{t_n}$

$$\begin{aligned}\mathbb{C}_{\mathrm{iso},d,0}^e &= -\left[\frac{\partial d_\alpha}{\partial \alpha} + \frac{\partial d_\beta}{\partial \beta}\operatorname{sign}\left(\overline{\Psi}_0^{e,t_{n+1}} - \overline{\Psi}_0^{e,t_n}\right)\right] \\ &\quad \cdot \operatorname{dev}\left(\overline{\boldsymbol{\tau}}_W^e + \overline{\boldsymbol{\tau}}_L^e\right) \otimes \operatorname{dev}\left(\overline{\boldsymbol{\tau}}_W^e + \overline{\boldsymbol{\tau}}_L^e\right)\end{aligned} \tag{95}$$

and for the case of unloading is $\alpha^{t_{n+1}} = \alpha^{t_n}$

$$\begin{aligned}\mathbb{C}_{\mathrm{iso},d,0}^e &= -\left[\frac{\partial d_\beta}{\partial \beta}\operatorname{sign}\left(\overline{\Psi}_0^{e,t_{n+1}} - \overline{\Psi}_0^{e,t_n}\right)\right] \\ &\quad \cdot \operatorname{dev}\left(\overline{\boldsymbol{\tau}}_W^e + \overline{\boldsymbol{\tau}}_L^e\right) \otimes \operatorname{dev}\left(\overline{\boldsymbol{\tau}}_W^e + \overline{\boldsymbol{\tau}}_L^e\right).\end{aligned} \tag{96}$$

$\overline{\boldsymbol{\tau}}_0^e = \overline{\boldsymbol{\tau}}_W^e + \overline{\boldsymbol{\tau}}_L^e$ represents the isothermal fictitious Kirchhoff stress of the undamaged equilibrium branch. A straightforward exploitation of Eq. (36) yields

$$\overline{\boldsymbol{\tau}}_W^e = 2W^{e'}\left(I_{\overline{\mathbf{b}}}\right)\overline{\mathbf{b}}, \tag{97}$$

$$\overline{\boldsymbol{\tau}}_L^e = -\frac{2G_e}{\beta}\sum_{a=1}^{3}\overline{\lambda}_a^{-\beta}\mathbf{n}_a \otimes \mathbf{n}_a. \tag{98}$$

For the sake of completeness, the corresponding tangent moduli in the current configuration are

$$\overline{\mathbb{C}}_W^e = 4W^{e''}\left(I_{\overline{\mathbf{b}}}\right)\overline{\mathbf{b}} \otimes \overline{\mathbf{b}} \tag{99}$$

and

$$\begin{aligned}\overline{\mathbb{C}}_L^e &= \sum_{a=1}^{3}\sum_{b=1}^{3}(\widetilde{c}_{ab} - 2\widetilde{\tau}_a\delta_{ab})\mathbf{n}_a \otimes \mathbf{n}_a \otimes \mathbf{n}_b \otimes \mathbf{n}_b \\ &\quad + \frac{1}{2}\sum_{a=1}^{3}\sum_{b\neq a}^{3}2\frac{\widetilde{\tau}_a\overline{\lambda}_b^2 - \widetilde{\tau}_b\overline{\lambda}_a^2}{\overline{\lambda}_a^2 - \overline{\lambda}_b^2}\mathbf{n}_a \otimes \mathbf{n}_b \otimes (\mathbf{n}_a \otimes \mathbf{n}_b + \mathbf{n}_b \otimes \mathbf{n}_a),\end{aligned} \tag{100}$$

with

$$\widetilde{c}_{ab} = 2G_e\overline{\lambda}_a^{-\beta}\delta_{ab}, \quad \widetilde{\tau}_a = -\frac{2G_e}{\beta}\overline{\lambda}_a^{-\beta}. \tag{101}$$

The derivatives with respect to $I_{\overline{\mathbf{b}}}$ are given as

$$W^{e'}\left(I_{\overline{\mathbf{b}}}\right) = \partial_{I_{\overline{\mathbf{b}}}} W^{e}\left(I_{\overline{\mathbf{b}}}\right) = \frac{G_c}{2}\left[\frac{1-2\delta^2+\delta^4\left(I_{\overline{\mathbf{b}}}-3\right)}{\left(1-\delta^2\left(I_{\overline{\mathbf{b}}}-3\right)\right)^2}\right], \tag{102}$$

$$W^{e''}\left(I_{\overline{\mathbf{b}}}\right) = \partial^2_{I_{\overline{\mathbf{b}}} I_{\overline{\mathbf{b}}}} W^{e}\left(I_{\overline{\mathbf{b}}}\right) = \frac{G_c}{2}\left[\frac{2\delta^2-3\delta^4+\delta^6\left(I_{\overline{\mathbf{b}}}-3\right)}{\left(1-\delta^2\left(I_{\overline{\mathbf{b}}}-3\right)\right)^3}\right]. \tag{103}$$

Note that Eqs. (98) and (100) are written in terms of the spatial eigenvectors $\mathbf{n}$ of $\overline{\mathbf{b}}$. For equal principal stretches $\overline{\lambda}_b \to \overline{\lambda}_a$, the second term of Eq. (100) can be evaluated via l'Hôpital's rule to give

$$\lim_{\overline{\lambda}_b \to \overline{\lambda}_a} \frac{\widetilde{\tau}_a \overline{\lambda}_b^2 - \widetilde{\tau}_b \overline{\lambda}_a^2}{\overline{\lambda}_a^2 - \overline{\lambda}_b^2} = \frac{1}{2}\widetilde{c}_{aa} - \widetilde{\tau}_a. \tag{104}$$

Note that the tensor defined in Eq. (100) is expressed with respect to the eigenspace $\mathbf{n}_a$. For transformation of the tensor components to the Cartesian basis $\mathbf{e}_i$, the relation

$$\mathbf{n}_a = \sum_{i=1}^{3} T_{ai}\mathbf{e}_i \tag{105}$$

is used, where T_{ai} are the Cartesian components of $\mathbf{n}_a$ (see, for example, Bonet and Wood [61]).

4.7.2 Stress and Moduli Terms of the Non-equilibrium Branch

The fictitious viscous Kirchhoff stresses are derived from Eq. (42),

$$\overline{\boldsymbol{\tau}}_0^v = 2\partial_{\overline{\mathbf{b}}_e} \overline{\Psi}_0^v\left(\overline{\mathbf{b}}_e\right)\overline{\mathbf{b}}_e = 2W^{v'}\left(I_{\overline{\mathbf{b}}}^e\right)\overline{\mathbf{b}}_e, \tag{106}$$

where the derivatives of the free energy function $W^v\left(I_{\overline{\mathbf{b}}}^e\right)$ are defined as

$$W^{v'}\left(I_{\overline{\mathbf{b}}}^e\right) = \partial_{I_{\overline{\mathbf{b}}}^e} W^v\left(I_{\overline{\mathbf{b}}}^e\right) = \frac{G_c^v}{2}\left[\frac{1-2\delta_v^2+\delta_v^4\left(I_{\overline{\mathbf{b}}}^e-3\right)}{\left(1-\delta_v^2\left(I_{\overline{\mathbf{b}}}^e-3\right)\right)^2}\right], \tag{107}$$

$$W^{v''}\left(I_{\overline{\mathbf{b}}}^e\right) = \partial^2_{I_{\overline{\mathbf{b}}}^e I_{\overline{\mathbf{b}}}^e} W^v\left(I_{\overline{\mathbf{b}}}^e\right) = \frac{G_c^v}{2}\left[\frac{2\delta_v^2-3\delta_v^4+\delta_v^6\left(I_{\overline{\mathbf{b}}}^e-3\right)}{\left(1-\delta_v^2\left(I_{\overline{\mathbf{b}}}^e-3\right)\right)^3}\right]. \tag{108}$$

Computation of the fictitious Kirchhoff stresses in Eq. (106) involves the current value of $\overline{\mathbf{b}}_e$ in the time step $t = t_{n+1}$. The current isochoric elastic stretches $\overline{\mathbf{b}}_e$ are

computed by considering the elastic stretches of the previous time step at $t = t_n$ and their evolution up to the time $t = t_{n+1}$, which is defined by the proposed evolution law given in Eqs. (63) and (69). Next, the time integration is addressed and considered in more detail.

For integration of the evolution law, an operator split of the material time derivative of $\overline{\mathbf{b}}_e$ is employed. It consists of an elastic predictor (EPRE) and an inelastic corrector step (ICOR),

$$\dot{\overline{\mathbf{b}}}_e = \underbrace{\mathbf{l}^{\mathrm{iso}}\overline{\mathbf{b}}_e + \overline{\mathbf{b}}_e\mathbf{l}^{\mathrm{iso}^{\mathrm{T}}}}_{\text{EPRE}} + \underbrace{\overline{\mathcal{L}}_v\left(\overline{\mathbf{b}}_e\right)}_{\text{ICOR}}. \tag{109}$$

In Fig. 14, the operator split technique is illustrated for a 1D setting. During the elastic trial step depicted in Fig. 14b, the inelastic deformation is considered to be fixed and, as a result, its material time derivative is zero,

$$\text{EPRE}: \quad \dot{\overline{\mathbf{C}}}_i^{-1} = 0. \tag{110}$$

Hence, the unimodular operator $\overline{\mathcal{L}}_v\left(\overline{\mathbf{b}}_e\right)$ defined in Eq. (57) is also zero,

$$\text{EPRE}: \quad \overline{\mathcal{L}}_v\left(\overline{\mathbf{b}}_e\right) = \overline{\mathbf{F}}\,\dot{\overline{\mathbf{C}}}_i^{-1}\overline{\mathbf{F}}^{\mathrm{T}} = 0. \tag{111}$$

The elastic trial or estimation for $\overline{\mathbf{b}}_e$ at time t_{n+1} can be obtained by making use of Eq. (38)

$$\text{EPRE}: \quad \overline{\mathbf{b}}_e^{\mathrm{tr}} = \overline{\mathbf{F}}^{t_{n+1}}\overline{\mathbf{C}}_i^{-1,t_n}\overline{\mathbf{F}}^{\mathrm{T},t_{n+1}} \tag{112}$$

with the unchanged inelastic right Cauchy–Green tensor

$$\text{EPRE}: \quad \overline{\mathbf{C}}_i^{-1,\mathrm{tr}} = \overline{\mathbf{C}}_i^{-1,t_n}. \tag{113}$$

In the inelastic corrector step illustrated in Fig. 14c, $\mathbf{l}^{\mathrm{iso}}$ is set to zero because $\overline{\mathbf{F}}$ does not evolve any further in the considered iteration in the time step t_{n+1}. This means that, with the help of Eq. (62), the material time derivative in Eq. (109) becomes

$$\text{ICOR}: \quad \dot{\overline{\mathbf{b}}}_e = 0 + \overline{\mathcal{L}}_v\left(\overline{\mathbf{b}}_e\right)\Big|_{\overline{\mathbf{b}}_e^{\mathrm{tr}}} = -2\widetilde{\mathbf{d}}_i\overline{\mathbf{b}}_e\Big|_{\overline{\mathbf{b}}_e^{\mathrm{tr}}} \tag{114}$$

If the constitutive evolution law defined in Eq. (63) is inserted for the inelastic deformation rate tensor $\widetilde{\mathbf{d}}_i$, the expression for the inelastic corrector step yields

$$\text{ICOR}: \quad \dot{\overline{\mathbf{b}}}_e = [-2\dot{\gamma}_0\mathbf{N}_{\mathrm{P}}]\overline{\mathbf{b}}_e\Big|_{\overline{\mathbf{b}}_e^{\mathrm{tr}}}, \tag{115}$$

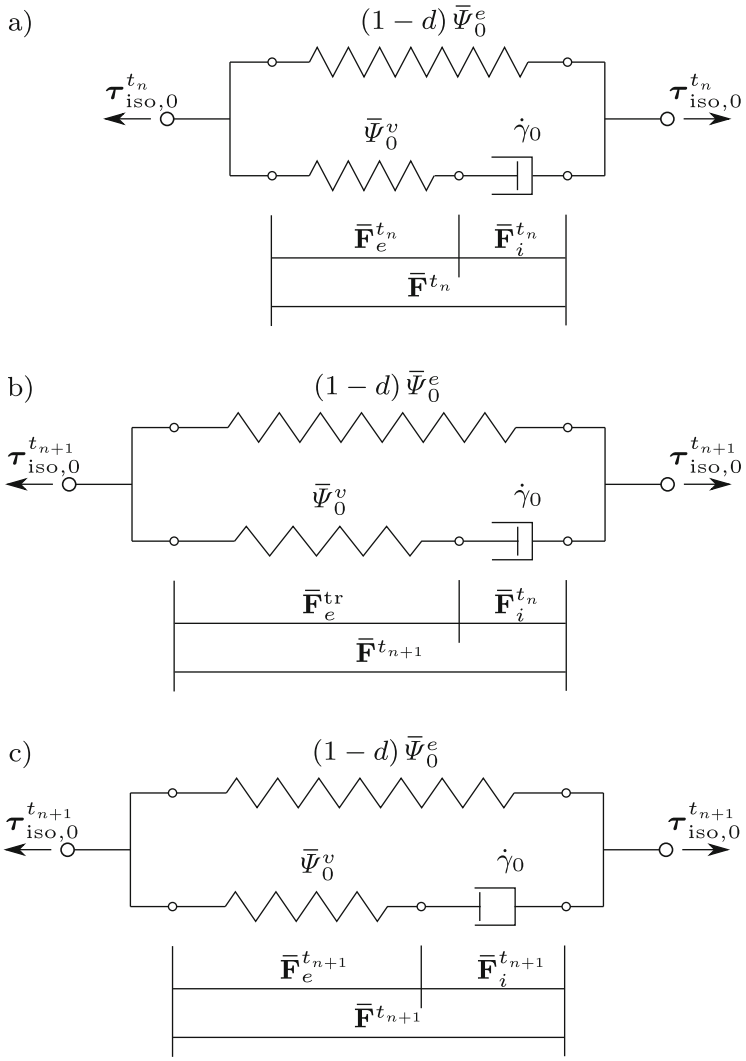

Fig. 14 Elastic trial and inelastic corrector step for evolution of the elastic and inelastic deformation parts: (**a**) $t = t_n$; (**b**) EPRE $t = t_{n+1}$; (**c**) ICOR $t = t_{n+1}$

which is an ordinary first-order differential equation with respect to time, with the initial condition $\bar{\mathbf{b}}_e^{\mathrm{tr}}$ from the elastic trial step. As proposed, for example, by Weber and Anand [62] or Simo [42], Eq. (115) can be solved by exponential mapping

$$\text{ICOR}: \quad \bar{\mathbf{b}}_e = \exp\left[-2\int_{t_n}^{t_{n+1}} \dot{\gamma}_0 \mathbf{N}_{\mathrm{P}}\ \mathrm{d}t\right] \bar{\mathbf{b}}_e^{\mathrm{tr}}, \tag{116}$$

where an integration in time from t_n to t_{n+1} is carried out and the result obtained by the elastic trial step [see Eq. (112)] is used. A linear approximation of the time integral yields

$$\text{ICOR}: \quad \overline{\mathbf{b}}_e \approx \exp[-2\dot{\gamma}_0 \mathbf{N}_\text{P} \ \Delta t] \overline{\mathbf{b}}_e^{\text{tr}}, \tag{117}$$

where $-2\dot{\gamma}_0 \mathbf{N}_\text{P}$ is assumed to be constant with respect to time in the current iteration in the time increment $[t_n, t_{n+1}]$. As a result of the assumption of an isotropic body, $\boldsymbol{\tau}^v_{\text{iso},0}$ and, therefore, $\mathbf{N}_\text{P}$ commutes with $\overline{\mathbf{b}}_e$ and also with $\overline{\mathbf{b}}_e^{\text{tr}}$

$$\overline{\mathbf{b}}_e^{\text{tr}} = \sum_{a=1}^{3} \overline{\lambda}_a^{e\text{tr}^2} \mathbf{n}_a \otimes \mathbf{n}_a, \tag{118}$$

$$\overline{\mathbf{b}}_e = \sum_{a=1}^{3} \overline{\lambda}_a^{e^2} \mathbf{n}_a \otimes \mathbf{n}_a. \tag{119}$$

In this case, Eq. (116) can be written in principal stretch directions $\mathbf{n}_a$ of $\overline{\mathbf{b}}_e^{\text{tr}}$,

$$\lambda_a^{e2} \approx \exp\left[-2\Delta t \ \dot{\gamma}_0 \frac{\left[\text{dev}\overline{\boldsymbol{\tau}}_0^v\right]_a}{\sqrt{2}\tau_v}\right] \lambda_a^{e\text{tr}^2}, \tag{120}$$

where

$$\mathbf{N}_\text{P} = \frac{\boldsymbol{\tau}^v_{\text{iso},0}}{\left\|\boldsymbol{\tau}^v_{\text{iso},0}\right\|} = \sum_{a=1}^{3} \frac{\left[\text{dev}\boldsymbol{\tau}_0^v\right]_a}{\sqrt{2}\tau_v} \mathbf{n}_a \otimes \mathbf{n}_a \tag{121}$$

is a function of $\overline{\mathbf{b}}_e$ and is expressed in its eigenspace by making use of Eqs. (64), (65), and (69). If the logarithm is applied to Eq. (120) and if principal logarithmic stretches $\varepsilon_a^e = \ln\overline{\lambda}_a^e$ and $\varepsilon_a^{\text{tr}} = \ln\overline{\lambda}_a^{e\text{tr}}$ are used, we obtain the form

$$\varepsilon_a^e \approx -\frac{\Delta t}{\sqrt{2}} \frac{\dot{\gamma}_0}{\tau_v} \left[\text{dev}\boldsymbol{\tau}_0^v\right]_a + \varepsilon_a^{e\text{tr}}. \tag{122}$$

Equation (122) is a nonlinear equation because $\overline{\tau}_a$ and $\dot{\gamma}_0$ are both functions of the principal stretches $\overline{\lambda}_a^e$. The residual expression for the iterative solution technique by a Newton–Raphson scheme is defined as

$$r_a = \varepsilon_a^e + \frac{\Delta t}{\sqrt{2}} \frac{\dot{\gamma}_0}{\tau_v} \left[\text{dev}\overline{\boldsymbol{\tau}}_0^v\right]_a - \varepsilon_a^{e\text{tr}} = 0. \tag{123}$$

The steps of the local Newton–Raphson iteration are summarized in Table 3. Note that $\varepsilon_a^{e\,\text{tr}}$ is constant during the iteration.

Table 3 Steps of the local Newton–Raphson iteration

1. Set initial values	$k = 0, \quad \varepsilon_a^{e,k} = \varepsilon_a^{e\mathrm{tr}}$
DO	
2. Residual equation	$r_a = \varepsilon_a + \frac{\Delta t}{\sqrt{2}} \frac{\dot{\gamma}_0}{\tau_v} \left[\mathrm{dev}\overline{\boldsymbol{\tau}}_0^v\right]_a - \varepsilon_a^{e\mathrm{tr}} = 0$
3. Linearization	$\mathrm{Lin} \; r_a = r_a\big\vert_{\varepsilon^{e,k}} + \frac{\partial r_a}{\partial \varepsilon_b^e}\Big\vert_{\varepsilon^{e,k}} \Delta\varepsilon_b^{e,k} = 0$
4. Computation	$\mathcal{K}_{ab} = \frac{\partial r_a}{\partial \varepsilon_b^e}\Big\vert_{\varepsilon^{e,k}}$
5. Solve	$\Delta\varepsilon_b^{e,k} = -(\mathcal{K}_{ab})^{-1} r_a$
6. Update	$\varepsilon_a^{e,k+1} \leftarrow \varepsilon_a^{e,k} + \Delta\varepsilon_a^{e,k}$ $k \leftarrow k + 1$
WHILE	$\mathrm{TOL} \leq \Vert r_a \Vert$

Once the current unimodular elastic left Cauchy–Green tensor $\overline{\mathbf{b}}_e$ is known from the result of the Newton–Raphson iteration (Table 3) and Eq. (119), the viscous stresses $\boldsymbol{\tau}_{\mathrm{iso},0}^v$ can be computed. In addition, the consistent tangent moduli for the non-equilibrium branch have to be formulated, as shown by Reese and Govindjee [43], Wriggers [63], and Dal and Kaliske [30]. The formulation is briefly summarized next.

In accordance with Eq. (118), the unimodular trial elastic deformation tensor in its spectral decomposition is given by

$$\overline{\mathbf{F}}_e^{\mathrm{tr}} = \sum_{a=1}^{3} \overline{\lambda}_a^{e\mathrm{tr}} \, \mathbf{n}_a \otimes \widetilde{\mathbf{N}}_a. \tag{124}$$

A fictitious second Piola–Kirchhoff stress tensor is defined from Eq. (106) in principal directions as

$$\widetilde{\mathbf{S}}_0^v = \overline{\mathbf{F}}_e^{\mathrm{tr}^{-1}} \overline{\boldsymbol{\tau}}_0^v \overline{\mathbf{F}}_e^{\mathrm{tr}^{-\mathrm{T}}} = \sum_{a=1}^{3} \frac{\overline{\tau}_a^v}{\overline{\lambda}_a^{e\mathrm{tr}^2}} \widetilde{\mathbf{N}}_a \otimes \widetilde{\mathbf{N}}_a, \tag{125}$$

which is based in the intermediate reference configuration with the eigenvectors $\widetilde{\mathbf{N}}_a$. Furthermore, the incremental rate equation in terms of the consistent tangent moduli $\overline{\mathbb{C}}_0^v$ is defined by

$$\Delta\widetilde{\mathbf{S}}_0^v = \overline{\mathbb{C}}_0^v : \frac{1}{2} \Delta \overline{\mathbf{C}}_e^{\mathrm{tr}} \quad \text{with} \quad \overline{\mathbb{C}}_0^v = 2 \frac{\partial \widetilde{\mathbf{S}}_0^v}{\partial \overline{\mathbf{C}}_e^{\mathrm{tr}}}. \tag{126}$$

The expression for the moduli in principal directions can be found by a straightforward evaluation of Eq. (126),

$$\begin{aligned}\overline{\mathbb{C}}_0^{v} &= \sum_{a=1}^{3}\sum_{b=1}^{3}\frac{\overline{c}_{ab}^{v}-2\overline{\tau}_a^{v}\delta_{ab}}{\overline{\lambda}_a^{e\mathrm{tr}^2}\overline{\lambda}_b^{e\mathrm{tr}^2}}\widetilde{\mathbf{N}}_a\otimes\widetilde{\mathbf{N}}_a\otimes\widetilde{\mathbf{N}}_b\otimes\widetilde{\mathbf{N}}_b \\ &\quad+\frac{1}{2}\sum_{a=1}^{3}\sum_{b\neq a}^{3}2\frac{\widetilde{s}_a^{v}-\widetilde{s}_b^{v}}{\overline{\lambda}_a^{e\mathrm{tr}^2}-\overline{\lambda}_b^{e\mathrm{tr}^2}}\widetilde{\mathbf{N}}_a\otimes\widetilde{\mathbf{N}}_b\left(\widetilde{\mathbf{N}}_a\otimes\widetilde{\mathbf{N}}_b+\widetilde{\mathbf{N}}_b\otimes\widetilde{\mathbf{N}}_a\right) \qquad (127)\\ &= \sum_{a=1}^{3}\sum_{b=1}^{3}\sum_{c=1}^{3}\sum_{d=1}^{3}\widetilde{L}_{abcd}\widetilde{\mathbf{N}}_a\otimes\widetilde{\mathbf{N}}_b\otimes\widetilde{\mathbf{N}}_c\otimes\widetilde{\mathbf{N}}_d \qquad (128)\end{aligned}$$

with $\widetilde{s}_a^{v}=\overline{\tau}_a^{v}/\overline{\lambda}_b^{e\mathrm{tr}^2}$. The term is evaluated as

$$\overline{c}_{ab}^{v}=\frac{\partial\overline{\tau}_a^{v}}{\partial\varepsilon_b^{e\mathrm{tr}}}=\frac{\partial\overline{\tau}_a^{v}}{\partial\varepsilon_c^{e}}\frac{\partial\varepsilon_c^{e}}{\partial\varepsilon_b^{e\mathrm{tr}}}, \qquad (129)$$

where the principal fictitious isothermal Kirchhoff stress $\overline{\tau}_a^{v}$ is obtained from the notation in its eigenbasis according to Eq. (106),

$$\overline{\tau}_a^{v}=2W^{v'}\left(I_{\overline{\mathrm{b}}}^{e}\right)\overline{\lambda}_a^{e2}. \qquad (130)$$

If the residual expression of the local Newton–Raphson iteration is considered again, the total derivative of the residual expression with respect to the trial stretches is

$$\frac{\mathrm{d}r_a}{\mathrm{d}\varepsilon_b^{e\mathrm{tr}}}=\frac{\partial r_a}{\partial\varepsilon_b^{e\mathrm{tr}}}+\frac{\partial r_a}{\partial\varepsilon_c^{e}}\frac{\partial\varepsilon_c^{e}}{\partial\varepsilon_b^{e\mathrm{tr}}}=0. \qquad (131)$$

With the help of the intermediate result,

$$0=-\delta_{ab}+\mathcal{K}_{ac}+\frac{\partial\varepsilon_c^{e}}{\partial\varepsilon_b^{e\mathrm{tr}}}, \qquad (132)$$

the relation

$$\frac{\partial\varepsilon_a^{e}}{\partial\varepsilon_b^{e\mathrm{tr}}}=(\mathcal{K}_{ba})^{-1}=\left(\mathcal{K}^{-1}\right)_{ab}=\mathcal{K}_{ab}^{-1} \qquad (133)$$

is computed by taking into account the property of the Kronecker symbol δ_{ab}. With the abbreviation $\mathcal{T}_{ac}$, Eq. (129) becomes

$$\overline{c}_{ab}^{v}=\mathcal{T}_{ac}\mathcal{K}_{cb}^{-1}. \qquad (134)$$

In Eq. (127), one observes a singularity of the second term for equal eigenvalues $\overline{\lambda}_b^{e\mathrm{tr}} \rightarrow \overline{\lambda}_a^{e\mathrm{tr}}$, which leads to an undetermined expression $\frac{0}{0}$. Again, in analogy to Eq. (104), the second term of Eq. (127) is evaluated via l'Hôpital's rule to give

$$\lim_{\overline{\lambda}_b \rightarrow \overline{\lambda}_a} \frac{\widetilde{s}_a^v - \widetilde{s}_b^v}{\overline{\lambda}_a^{e\mathrm{tr}^2} - \overline{\lambda}_b^{e\mathrm{tr}^2}} = \frac{1}{2} \frac{c_{aa}^v - 2\overline{\tau}_a^v}{\overline{\lambda}_a^{e\mathrm{tr}^4}}. \tag{135}$$

The consistent tangent moduli for the current configuration are formulated via a push forward in terms of $\overline{\mathbf{F}}_e^{\mathrm{tr}}$ from the intermediate reference configuration to the current configuration,

$$\overline{\mathbb{C}}_0^v = \sum_{a=1}^{3} \sum_{b=1}^{3} \sum_{c=1}^{3} \sum_{d=1}^{3} \widetilde{L}_{abcd} \overline{\lambda}_a^{e\mathrm{tr}} \overline{\lambda}_b^{e\mathrm{tr}} \overline{\lambda}_c^{e\mathrm{tr}} \overline{\lambda}_d^{e\mathrm{tr}} \mathbf{n}_a \otimes \mathbf{n}_b \otimes \mathbf{n}_c \otimes \mathbf{n}_d. \tag{136}$$

Note that the consistent tangent moduli expression, given in Eq. (136), is still based in the eigenspace $\mathbf{n}_a$. For a transformation of the tensor components to the Cartesian basis $\mathbf{e}_i$, the relation

$$\mathbf{n}_a = \sum_{i=1}^{3} T_{ai}^{\mathrm{tr}} \mathbf{e}_i \tag{137}$$

is used again, where T_{ai}^{tr} are the Cartesian components of $\mathbf{n}_a$ (see, for example, Bonet and Wood [61]). The eigenvectors in the different configurational settings are represented in Fig. 15.

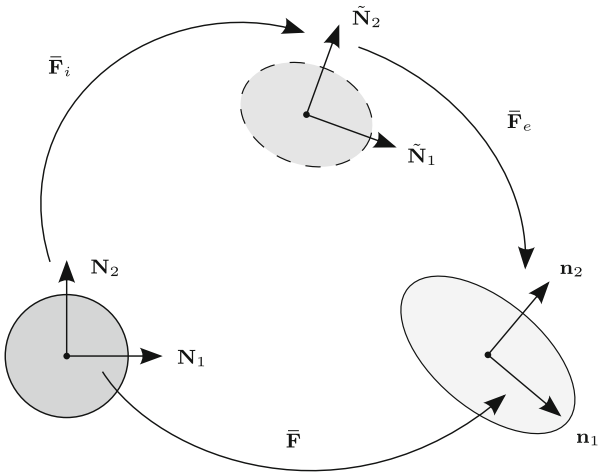

Fig. 15 Transformation of the eigenvectors in the case of multiplicative decomposition of the isochoric deformation gradient $\overline{\mathbf{F}} = \overline{\mathbf{F}}_e \overline{\mathbf{F}}_i$: eigenvectors $\mathbf{N}_a$ of the reference configuration, eigenvectors $\tilde{\mathbf{N}}_a$ of the inelastic intermediate configuration, and eigenvectors $\mathbf{n}_a$ of the current configuration

5 Non-isothermal Framework for Temperature-Dependent Material Behavior

The previous section outlined an isothermal setting for finite viscoelasticity. In this section, the temperature dependency of the material is addressed. The isothermal setting for finite viscoelasticity introduced in Sect. 4.2 is generalized to coupled thermomechanics. For the coupling of mechanical and thermal material behavior in the material model, the strategy proposed by Reese and Govindjee [64] is adapted and modified with respect to the heat capacity coefficient of the material model.

5.1 Thermoelasticity and Thermoviscoelasticity

The distinct entropic behavior of elastomers results in a strong coupling between the mechanical and thermal response, which also holds for polymer networks (regarded as purely elastic). As an example, the thermoelasticity of tubelike constrained polymer networks has been discussed by Heinrich [65]. Miehe [66] provided the basics of the numerical treatment of related thermomechanical processes and also discussed [67] the closed-form description for thermoelasticity with temperature changes upon deformation as a result of thermoelastic coupling. In the case of inelastic material behavior, the released thermal energy contributes to dissipative heat build-up in the material. The mechanical and thermal responses of a filler-reinforced tread compound were investigated, for example, by Lion [68] and a geometrically nonlinear constitutive theory for thermomechanical behavior has been presented [69]. Furthermore, thermoviscoelasticity for large deformations has been considered by Berardi et al. [70], who showed that the source term of viscous friction cannot be independent of temperature.

The effect of deformation on temperature is much less studied. For bidirectional coupling, a thermodynamic consistent form of the Helmholtz free energy function must be derived (Allen et al. [71, 72], Chadwick et al. [73, 74]). The theory of linear viscoelasticity has been addressed by Haupt [75] and is characterized by small deviations away from the thermodynamic equilibrium. Viscoelastic models for small deformations have been proposed by, for example, Morland and Lee [76] and models for large deformations by Holzapfel and Simo [77], where internal stress-based (Simo [36]) or strain-based (Reese and Govindjee [64]) variables were employed. Reese and Govindjee [64] have presented a general framework for fully coupled thermoviscoelasticity and evaluated the derived general expressions for the Ogden material model. Reese [78] has discussed a micromechanically motivated material model. More recently, thermomechanical coupling in elastomers has been experimentally and numerically studied by Dippel et al. [79].

Internal strain-type variables enable the derivation of an evolution equation comparable to that presented by Simo and Miehe [80] in the context of associative elastoplasticity. For its solution, an exponential mapping algorithm (Weber and

Anand [62], Eterovic and Bathe [81]) is commonly employed, whereas former methodologies are only applicable for small deformations and small deviations away from the thermodynamic equilibrium.

Reese and Govindjee [64] proposed a theory for fully coupled finite thermoviscoelasticity and showed its algorithmic FE implementation to be suitable for a simultaneous solution scheme. Temperature functions $f_{\mathrm{EQ}}(\Theta)$ and $f_{\mathrm{NEQ}}(\Theta)$ were introduced to represent the temperature dependency of the equilibrium (EQ) and non-equilibrium (NEQ) branches by multiplying them by the free energy functions evaluated at a reference temperature Θ_0. This theory proposed by Reese and Govindjee [64] is adopted in this contribution (see also Behnke [82]). However, in contrast to Reese and Govindjee [64], the extended non-affine tube model is used here for the hyperelastic features of the model. In addition, a CDM approach is incorporated in the context of finite thermomechanics. Furthermore, the reference heat capacity is no longer considered to be constant and can also be a function of temperature, which is commonly the case, as deduced from experiments.

5.2 Constitutive Equations for Thermomechanics

The second law of thermodynamics, also known as the Clausius–Duhem inequality or dissipation inequality, is given in the reference configuration by

$$\mathbf{S} : \frac{1}{2}\dot{\mathbf{C}} - \dot{\Psi} - \eta\dot{\Theta} - \frac{1}{\Theta}\mathbf{Q} \cdot \nabla_{\mathbf{X}}\Theta \geq 0 \tag{138}$$

and in the current configuration by

$$\boldsymbol{\tau} : \mathbf{d} - \dot{\Psi} - \eta\dot{\Theta} - \frac{1}{\Theta}\hat{\mathbf{q}} \cdot \nabla_{\mathbf{x}}\Theta \geq 0. \tag{139}$$

Ψ and η denote the Helmholtz free energy and the entropy per unit reference volume, respectively. $\mathbf{S}$ denotes the second Piola–Kirchhoff stress tensor, $\mathbf{C}$ the right Cauchy–Green tensor, and Θ the absolute temperature. The heat flux $\mathbf{Q}$ in the reference configuration is related to the heat flux $\mathbf{q}$ of the current configuration via the relation

$$\begin{aligned} \mathbf{Q} = J\ \mathbf{F}^{-1}\mathbf{q} \quad &= \mathbf{F}^{-1}\hat{\mathbf{q}} \\ &= \mathbf{F}^{-1}\left(-k\nabla_{\mathbf{x}}\Theta\right) \\ &= \mathbf{F}^{-1}\left(-k\,\mathbf{F}^{-T}\nabla_{\mathbf{X}}\Theta\right) \\ &= -k\,\mathbf{C}^{-1}\nabla_{\mathbf{X}}\Theta. \end{aligned} \tag{140}$$

The spatial Kirchhoff heat flux $\hat{\mathbf{q}}$ is written as

$$\hat{\mathbf{q}} = J\ \mathbf{q} = -k\nabla_{\mathbf{x}}\Theta, \tag{141}$$

where the constitutive relation of Fourier's law is applied on the Kirchhoff setting. In this case, the Cauchy heat flux $\mathbf{q}$ is identified as

$$\mathbf{q} = -\frac{1}{J} k \nabla_{\mathbf{x}} \Theta. \tag{142}$$

The constitutive parameter $k \geq 0$ stands for the heat conductivity coefficient of the material, which is assumed to be independent of temperature and deformation. To build up a thermomechanical coupled material model for finite thermoviscoelasticity, including continuum damage, the following dependencies are assumed:

$$\Psi = \Psi_{\mathrm{EQ}}(\mathbf{C}, d, \Theta) + \overline{\Psi}_{\mathrm{NEQ}}\big(\overline{\mathbf{C}}_e, \Theta\big), \tag{143}$$

$$\mathbf{S} = \mathbf{S}_{\mathrm{EQ}}(\mathbf{C}, d, \Theta) + \mathbf{S}_{\mathrm{NEQ}}\big(\overline{\mathbf{C}}_e, \Theta\big), \tag{144}$$

$$\eta = \eta_{\mathrm{EQ}}(\mathbf{C}, d, \Theta) + \eta_{\mathrm{NEQ}}\big(\overline{\mathbf{C}}_e, \Theta\big), \tag{145}$$

$$\mathbf{q} = \frac{1}{J} \mathbf{F} \mathbf{Q}(\mathbf{C}, \Theta). \tag{146}$$

Note that, for example, Ψ stands for the temperature-dependent Helmholtz free energy function, whereas the isothermal Helmholtz free energy function Ψ_0 (defined in Sect. 4.2) is labeled with the subscript 0. In Eqs. (143) to (146), the subscripts EQ and NEQ characterize quantities of the equilibrium and the non-equilibrium branches, respectively. $\mathbf{C}$ and Θ represent the functional dependency of Ψ, $\mathbf{S}$, η, and $\mathbf{Q}$ on deformation (mechanical field) and temperature (thermal field), respectively. $\overline{\mathbf{C}}_e$ and the scalar damage variable d are internal variables of the material model. Equation (138) is formulated with the help of Eqs. (143) to (146), which in the reference configuration yields

$$\begin{aligned} &\left(\mathbf{S} - 2\frac{\partial \Psi_{\mathrm{EQ}}}{\partial \mathbf{C}}\bigg|_{d=\mathrm{const.}}\right) : \frac{1}{2}\dot{\mathbf{C}} \\ &- \frac{\partial \overline{\Psi}_{\mathrm{NEQ}}}{\partial \overline{\mathbf{C}}_e} : \frac{1}{2}\dot{\overline{\mathbf{C}}}_e - \frac{\partial \Psi_{\mathrm{EQ}}}{\partial d}\dot{d} - \left(\frac{\partial \Psi}{\partial \Theta} + \eta\right)\dot{\Theta} \\ &- \frac{1}{\Theta}\mathbf{Q} \cdot \nabla_{\mathbf{X}} \Theta \geq 0 \end{aligned} \tag{147}$$

or in the current configuration

$$\begin{aligned} &\left(\boldsymbol{\tau} - 2\frac{\partial \Psi_{\mathrm{EQ}}}{\partial \mathbf{b}}\bigg|_{d=\mathrm{const.}}\mathbf{b}\right) : \mathbf{d} \\ &- \frac{\partial \overline{\Psi}_{\mathrm{NEQ}}}{\partial \overline{\mathbf{b}}_e} : \overline{\mathbf{b}}_e - \frac{\partial \Psi_{\mathrm{EQ}}}{\partial d}\dot{d} - \left(\frac{\partial \Psi}{\partial \Theta} + \eta\right)\dot{\Theta} \\ &- \frac{1}{\Theta}\hat{\mathbf{q}} \cdot \nabla_{\mathbf{x}} \Theta \geq 0. \end{aligned} \tag{148}$$

In Eqs. (147) and (148), the partial derivatives with respect to the strain field in the form of $\mathbf{C}$ or $\mathbf{b}$ are carried out for a fixed evolution of d. The evolution of d over time is taken into account by the partial derivative with respect to the internal variable d itself. Via the material time derivative of

$$\overline{\mathbf{C}}_e = \overline{\mathbf{F}}_i^{-\mathrm{T}} \overline{\mathbf{C}} \overline{\mathbf{F}}_i^{-1} \tag{149}$$

and Eq. (56), the dissipation inequalities given in Eqs. (147) and (148) become

$$\begin{aligned} &\left(\mathbf{S} - 2 \frac{\partial \Psi_{\mathrm{EQ}}}{\partial \mathbf{C}} \bigg|_{d=\mathrm{const.}} - \mathbb{P} : \left[2 \overline{\mathbf{F}}_i^{-1} \frac{\partial \overline{\Psi}_{\mathrm{NEQ}}}{\partial \overline{\mathbf{C}}_e} \overline{\mathbf{F}}_i^{-\mathrm{T}} \right] \right) : \frac{1}{2} \dot{\mathbf{C}} \\ &- \mathbb{P} : \left[2 \overline{\mathbf{F}}_i^{-1} \frac{\partial \overline{\Psi}_{\mathrm{NEQ}}}{\partial \overline{\mathbf{C}}_e} \overline{\mathbf{F}}_i^{-\mathrm{T}} \right] : \frac{1}{2} \left[- \overline{\mathbf{F}}_i^{\mathrm{T}} \left(\overline{\mathbf{I}}_i^{\mathrm{T}} \overline{\mathbf{C}}_e + \overline{\mathbf{C}}_e \overline{\mathbf{I}}_i \right) \overline{\mathbf{F}}_i \right] \\ &- \frac{\partial \Psi_{\mathrm{EQ}}}{\partial d} \dot{d} - \left(\frac{\partial \Psi}{\partial \Theta} + \eta \right) \dot{\Theta} - \frac{1}{\Theta} \mathbf{Q} \cdot \nabla_{\mathbf{X}} \Theta \geq 0 \end{aligned} \tag{150}$$

and

$$\begin{aligned} &\left(\boldsymbol{\tau} - 2 \frac{\partial \Psi_{\mathrm{EQ}}}{\partial \mathbf{b}} \bigg|_{d=\mathrm{const.}} \mathbf{b} - \mathbb{P} : \left[2 \frac{\partial \overline{\Psi}_{\mathrm{NEQ}}}{\partial \overline{\mathbf{b}}_e} \overline{\mathbf{b}}_e \right] \right) : \mathbf{d} \\ &- \mathbb{P} : \left[2 \frac{\partial \overline{\Psi}_{\mathrm{NEQ}}}{\partial \overline{\mathbf{b}}_e} \overline{\mathbf{b}}_i^{-1} \right] : \left[\frac{1}{2} \overline{\mathcal{L}}_v (\overline{\mathbf{b}}_e) \overline{\mathbf{b}}_e^{-1} \right] \\ &- \frac{\partial \Psi_{\mathrm{EQ}}}{\partial d} \dot{d} - \left(\frac{\partial \Psi}{\partial \Theta} + \eta \right) \dot{\Theta} - \frac{1}{\Theta} \hat{\mathbf{q}} \cdot \nabla_{\mathbf{x}} \Theta \geq 0, \end{aligned} \tag{151}$$

respectively. Because the inequality stated in Eqs. (150) and (151) must be fulfilled for arbitrary deformation rates ($\dot{\mathbf{C}}$, $\mathbf{d}$) and temperature rates ($\dot{\Theta}$), the terms in the brackets of Eq. (150) and Eq. (151) should vanish for an arbitrary strain and temperature evolution. This leads to the general stress and entropy definition,

$$\begin{aligned} \mathbf{S} &= 2 \frac{\partial \Psi_{\mathrm{EQ}}}{\partial \mathbf{C}} \bigg|_{d=\mathrm{const.}} + \mathbb{P} : \left[2 \overline{\mathbf{F}}_i^{-1} \frac{\partial \overline{\Psi}_{\mathrm{NEQ}}}{\partial \overline{\mathbf{C}}_e} \overline{\mathbf{F}}_i^{-\mathrm{T}} \right] \\ &= \mathbf{S}_{\mathrm{EQ}} + \mathbf{S}_{\mathrm{NEQ,iso}}, \end{aligned} \tag{152}$$

$$\eta = - \frac{\partial \Psi}{\partial \Theta}. \tag{153}$$

The remaining inequality, for example, in the current configuration

$$- \frac{\partial \Psi_{\mathrm{EQ}}}{\partial d} \dot{d} - \frac{1}{\Theta} \hat{\mathbf{q}} \cdot \nabla_{\mathbf{x}} \Theta \geq 0 \tag{154}$$

is fulfilled by enforcing

$$\frac{\partial \Psi_{\mathrm{EQ}}}{\partial d} \leq 0 \quad \text{and} \quad \dot{d} \geq 0, \tag{155}$$

$$\frac{1}{\Theta}\hat{\mathbf{q}} \cdot \nabla_{\mathbf{x}}\Theta = -\frac{1}{\Theta}k\nabla_{\mathbf{x}}\Theta \cdot \nabla_{\mathbf{x}}\Theta \leq 0 \quad \text{with} \quad k \geq 0. \tag{156}$$

The condition $\dot{d} \geq 0$ in Eq. (155) enforces that the material damage can only be constant or increase monotonically with time. In Eq. (156), the constitutive relation for the heat flux defined in Eq. (141) has been inserted.

5.3 Temperature-Dependent Helmholtz Free Energy

In Sect. 4.2, an approach for the Helmholtz free energy of a material model is given for an isothermal setting, where the functions are evaluated for one special temperature (i.e., the reference temperature Θ_0). The Helmholtz free energy is formulated as a function of temperature and, as a result, the stresses and tangent moduli also include temperature dependency. Therefore, the approach presented by Reese and Govindjee [64] is applied and adapted with modifications (see also Behnke [82]).

The Helmholtz free energy Ψ is one part of the internal energy e per unit reference volume of a body, which represents the mechanical energy stored as a mechanically reversible energy potential during deformation

$$\Psi = e - \Theta\eta = e + \Theta\frac{\partial \Psi}{\partial \Theta}. \tag{157}$$

In Eq. (157), η is the entropy per unit reference volume for which the relation given in Eq. (153) has been used. Equation (157) is derived with respect to temperature

$$\frac{\partial \Psi}{\partial \Theta} = \frac{\partial e}{\partial \Theta} + \frac{\partial \Psi}{\partial \Theta} + \Theta\frac{\partial^2 \Psi}{\partial \Theta \partial \Theta}. \tag{158}$$

Equation (158) is simplified to

$$0 = \frac{\partial e}{\partial \Theta} - c_v \rightarrow c_v = \frac{\partial e}{\partial \Theta} \tag{159}$$

with the heat capacity c_v per unit reference volume defined as

$$c_v = -\Theta\frac{\partial^2 \Psi}{\partial \Theta \partial \Theta} = c_{\mathrm{EQ}} + c_{\mathrm{NEQ}}. \tag{160}$$

From Eqs. (159) and (160), the internal energy is written as the integral of the heat capacity

$$e = \int_{\Theta_0}^{\Theta} c_v \mathrm{d}\widetilde{\Theta} + e_0 = e_{\mathrm{EQ}} + e_{\mathrm{NEQ}} \tag{161}$$

with e_0 as the internal energy per unit reference volume at the reference temperature Θ_0. Equation (160) also permits rewriting the Helmholtz free energy Ψ as

$$\frac{\partial^2 \Psi}{\partial \Theta \partial \Theta} = -\frac{c}{\Theta}. \tag{162}$$

Integration with respect to temperature yields

$$\frac{\partial \Psi}{\partial \Theta} = \int_{\Theta_0}^{\Theta} \left(-\frac{c}{\widetilde{\Theta}} \right) \mathrm{d}\widetilde{\Theta} + \left. \frac{\partial \Psi}{\partial \Theta} \right|_{\Theta_0}. \tag{163}$$

Equation (157) is formulated with the help of the terms derived in Eqs. (161) and (163) to become

$$\begin{aligned} \Psi &= \int_{\Theta_0}^{\Theta} c_v \mathrm{d}\widetilde{\Theta} + e_0 + \Theta \left(\int_{\Theta_0}^{\Theta} \left(-\frac{c}{\widetilde{\Theta}} \right) \mathrm{d}\widetilde{\Theta} + \left. \frac{\partial \Psi}{\partial \Theta} \right|_{\Theta_0} \right) \\ &= e_0 + \Theta \left. \frac{\partial \Psi}{\partial \Theta} \right|_{\Theta_0} + \int_{\Theta_0}^{\Theta} c_v \left(1 - \frac{\Theta}{\widetilde{\Theta}} \right) \mathrm{d}\widetilde{\Theta}. \end{aligned} \tag{164}$$

If the terms of Eq. (164) are compared with the terms of Eq. (157), the Helmholtz free energy at the reference temperature Θ_0 is

$$\Psi_0 = e_0 + \Theta_0 \left. \frac{\partial \Psi}{\partial \Theta} \right|_{\Theta_0}. \tag{165}$$

Via the definition of Ψ_0, Eq. (165) is reformulated to

$$\Theta \left. \frac{\partial \Psi}{\partial \Theta} \right|_{\Theta_0} = \frac{\Theta}{\Theta_0} \Psi_0 - \frac{\Theta}{\Theta_0} e_0 \tag{166}$$

and finally inserted into Eq. (164) to give the Helmholtz free energy per unit reference volume

$$\Psi = \frac{\Theta}{\Theta_0}\Psi_0\left(1-\frac{\Theta}{\Theta_0}\right)e_0 + \int_{\Theta_0}^{\Theta} c_v\left(1-\frac{\Theta}{\widetilde{\Theta}}\right)\mathrm{d}\widetilde{\Theta} \tag{167}$$

as a function of the isothermal quantities Ψ_0, e_0, and the temperature-dependent heat capacity c_v. It is assumed that the heat capacity c_v is a function of the temperature and current deformation via the isothermal free energy functions $\Psi_{\mathrm{EQ},0}$ and $\overline{\Psi}_{\mathrm{NEQ},0}$

$$c_v = \overline{c}(\Theta) - \Theta\frac{\partial^2 g_{\mathrm{EQ}}}{\partial\Theta\partial\Theta}\Psi_{\mathrm{EQ},0} - \Theta\frac{\partial^2 g_{\mathrm{NEQ}}}{\partial\Theta\partial\Theta}\overline{\Psi}_{\mathrm{NEQ},0}. \tag{168}$$

$\overline{c}(\Theta)$ is a continuously differentiable positive function of Θ and can be regarded as the heat capacity per unit reference volume of the stress-free body characterized by $\Psi_{\mathrm{EQ},0}=0$ and $\overline{\Psi}_{\mathrm{NEQ},0}=0$. In this case, Eq. (168) reduces to $c_v=\overline{c}(\Theta)$, independently of the choice of the temperature functions g_{EQ} and g_{NEQ}. Note that the function $\overline{c}(\Theta)\geq 0$ can easily be obtained from experimental measurements on stress-free material. For further derivation, the integral in Eq. (167) is split into two parts:

$$\int_{\Theta_0}^{\Theta} c_v\left(1-\frac{\Theta}{\widetilde{\Theta}}\right)\mathrm{d}\widetilde{\Theta} = \underbrace{\int_{\Theta_0}^{\Theta} c_v\mathrm{d}\widetilde{\Theta}}_{\mathrm{I}} \underbrace{-\Theta\int_{\Theta_0}^{\Theta}\frac{c}{\widetilde{\Theta}}\mathrm{d}\widetilde{\Theta}}_{\mathrm{II}}. \tag{169}$$

The first integral on the right-hand side of Eq. (169) can be evaluated as

$$\begin{aligned}\int_{\Theta_0}^{\Theta} c_v\mathrm{d}\widetilde{\Theta} \;=\; & \int_{\Theta_0}^{\Theta}\overline{c}\left(\widetilde{\Theta}\right)\mathrm{d}\widetilde{\Theta} - \left[\widetilde{\Theta}\frac{\partial g_{\mathrm{EQ}}}{\partial\widetilde{\Theta}}\Psi_{\mathrm{EQ},0}\right]_{\Theta_0}^{\Theta} + \int_{\Theta_0}^{\Theta}\frac{\partial g_{\mathrm{EQ}}}{\partial\widetilde{\Theta}}\Psi_{\mathrm{EQ},0}\mathrm{d}\widetilde{\Theta} \\ & - \left[\widetilde{\Theta}\frac{\partial g_{\mathrm{NEQ}}}{\partial\widetilde{\Theta}}\overline{\Psi}_{\mathrm{NEQ},0}\right]_{\Theta_0}^{\Theta} + \int_{\Theta_0}^{\Theta}\frac{\partial g_{\mathrm{NEQ}}}{\partial\widetilde{\Theta}}\overline{\Psi}_{\mathrm{NEQ},0}\mathrm{d}\widetilde{\Theta},\end{aligned} \tag{170}$$

where integration by parts has been applied to Eq. (169) after inserting the expression for heat capacity defined in Eq. (168). The general antiderivative $\overline{C}\left(\widetilde{\Theta}\right)$ to $\overline{c}\left(\widetilde{\Theta}\right)$ is introduced as

$$\overline{C}\left(\widetilde{\Theta}\right) = \int\overline{c}\left(\widetilde{\Theta}\right)\mathrm{d}\widetilde{\Theta}. \tag{171}$$

With this definition at hand, Eq. (170) is simplified to give

$$\begin{aligned}\int_{\Theta_0}^{\Theta} c_v \mathrm{d}\widetilde{\Theta} = \overline{C}(\Theta) - \overline{C}(\Theta_0) \\ - \Theta \frac{\partial g_{\mathrm{EQ}}}{\partial \Theta}\bigg|_{\Theta} \Psi_{\mathrm{EQ},0} + \Theta_0 \frac{\partial g_{\mathrm{EQ}}}{\partial \Theta}\bigg|_{\Theta_0} \Psi_{\mathrm{EQ},0} \\ + g_{\mathrm{EQ}}(\Theta)\Psi_{\mathrm{EQ},0} - g_{\mathrm{EQ}}(\Theta_0)\Psi_{\mathrm{EQ},0} \\ - \Theta \frac{\partial g_{\mathrm{NEQ}}}{\partial \Theta}\bigg|_{\Theta} \overline{\Psi}_{\mathrm{NEQ},0} + \Theta_0 \frac{\partial g_{\mathrm{NEQ}}}{\partial \Theta}\bigg|_{\Theta_0} \overline{\Psi}_{\mathrm{NEQ},0} \\ + g_{\mathrm{NEQ}}(\Theta)\overline{\Psi}_{\mathrm{NEQ},0} - g_{\mathrm{NEQ}}(\Theta_0)\overline{\Psi}_{\mathrm{NEQ},0}.\end{aligned} \tag{172}$$

The second integral term of Eq. (169) is now considered

$$\begin{aligned}\Theta \int_{\Theta_0}^{\Theta} \frac{c}{\widetilde{\Theta}} \mathrm{d}\widetilde{\Theta} = \Theta \int_{\Theta_0}^{\Theta} \overline{g}\left(\widetilde{\Theta}\right) \mathrm{d}\widetilde{\Theta} - \Theta \int_{\Theta_0}^{\Theta} \frac{\partial^2 g_{\mathrm{EQ}}}{\partial \widetilde{\Theta} \partial \widetilde{\Theta}} \Psi_{\mathrm{EQ},0} \mathrm{d}\widetilde{\Theta} \\ - \Theta \int_{\Theta_0}^{\Theta} \frac{\partial^2 g_{\mathrm{NEQ}}}{\partial \widetilde{\Theta} \partial \widetilde{\Theta}} \overline{\Psi}_{\mathrm{NEQ},0} \mathrm{d}\widetilde{\Theta},\end{aligned} \tag{173}$$

where

$$\overline{g}\left(\widetilde{\Theta}\right) = \frac{\overline{c}\left(\widetilde{\Theta}\right)}{\widetilde{\Theta}} \tag{174}$$

has been introduced. In analogy to Eq. (171), the general antiderivative $\overline{G}\left(\widetilde{\Theta}\right)$ to $\overline{g}\left(\widetilde{\Theta}\right)$ yields

$$\overline{G}\left(\widetilde{\Theta}\right) = \int \overline{g}\left(\widetilde{\Theta}\right) \mathrm{d}\widetilde{\Theta} \tag{175}$$

and Eq. (173) can be rewritten as

$$\begin{aligned}\Theta \int_{\Theta_0}^{\Theta} \frac{c}{\widetilde{\Theta}} \mathrm{d}\widetilde{\Theta} = \Theta\left(\overline{G}(\Theta) - \overline{G}(\Theta_0)\right) - \Theta\left(\frac{\partial g_{\mathrm{EQ}}}{\partial \Theta}\bigg|_{\Theta} - \frac{\partial g_{\mathrm{EQ}}}{\partial \Theta}\bigg|_{\Theta_0}\right) \Psi_{\mathrm{EQ},0} \\ - \Theta\left(\frac{\partial g_{\mathrm{NEQ}}}{\partial \Theta}\bigg|_{\Theta} - \frac{\partial g_{\mathrm{NEQ}}}{\partial \Theta}\bigg|_{\Theta_0}\right) \overline{\Psi}_{\mathrm{NEQ},0}.\end{aligned} \tag{176}$$

The total expression of Eq. (169) reads after simplification and taking care of the minus sign

$$\int_{\Theta_0}^{\Theta} c_v \left(1 - \frac{\Theta}{\widetilde{\Theta}}\right) \mathrm{d}\widetilde{\Theta} = \mathrm{I} - \mathrm{II} =$$

$$\begin{aligned} & g_{\mathrm{EQ}}(\Theta)\Psi_{\mathrm{EQ},0} + \left(\left.\frac{\partial g_{\mathrm{EQ}}}{\partial \Theta}\right|_{\Theta_0} (\Theta_0 - \Theta) - g_{\mathrm{EQ}}(\Theta_0)\right)\Psi_{\mathrm{EQ},0} \\ & + g_{\mathrm{NEQ}}(\Theta)\overline{\Psi}_{\mathrm{NEQ},0} + \left(\left.\frac{\partial g_{\mathrm{NEQ}}}{\partial \Theta}\right|_{\Theta_0} (\Theta_0 - \Theta) - g_{\mathrm{NEQ}}(\Theta_0)\right)\overline{\Psi}_{\mathrm{NEQ},0} \\ & + \left[\overline{C}(\Theta) - \overline{C}(\Theta_0)\right] - \Theta\left[\overline{G}(\Theta) - \overline{G}(\Theta_0)\right]. \end{aligned} \tag{177}$$

Often, the heat capacity $\overline{c}(\Theta)$ is assumed to be constant,

$$\overline{c}^*(\Theta) = \overline{c}_0, \quad \overline{g}^*(\Theta) = \frac{\overline{c}_0}{\Theta}, \tag{178}$$

where $\overline{c}_0$ denotes the heat capacity per unit reference volume, evaluated at the reference temperature for a stress-free specimen. In this case, the general antiderivatives from Eqs. (171) and (175) become

$$\overline{C}^*\left(\widetilde{\Theta}\right) = \int \overline{c}_0 \ \mathrm{d}\widetilde{\Theta} = \overline{c}_0 \widetilde{\Theta}, \tag{179}$$

$$\overline{G}^*\left(\widetilde{\Theta}\right) = \int \frac{\overline{c}_0}{\widetilde{\Theta}} \ \mathrm{d}\widetilde{\Theta} = \overline{c}_0 \ln \widetilde{\Theta}. \tag{180}$$

Using Eqs. (179) and (180) to evaluate the heat capacity terms of Eq. (177) yields the standard heat capacity term

$$\left[\overline{C}^*(\Theta) - \overline{C}^*(\Theta_0)\right] - \Theta\left[\overline{G}^*(\Theta) - \overline{G}^*(\Theta_0)\right] = \overline{c}_0\left(\Theta - \Theta_0 - \Theta \ln\frac{\Theta}{\Theta_0}\right) \tag{181}$$

of the Helmholtz free energy Ψ (see, for example, Reese and Govindjee [64]). In this case, the temperature-dependent free energy function of Eq. (167) takes the form

$$\begin{aligned} \Psi = {} & (e_{\mathrm{EQ},0} + e_{\mathrm{NEQ},0})\left(1 - \frac{\Theta}{\Theta_0}\right) + \left[\overline{C}(\Theta) - \overline{C}(\Theta_0)\right] - \Theta\left[\overline{G}(\Theta) - \overline{G}(\Theta_0)\right] \\ & + \left(\frac{\Theta}{\Theta_0} + g_{\mathrm{EQ}}(\Theta) - g_{\mathrm{EQ}}(\Theta_0) + \left.\frac{\partial g_{\mathrm{EQ}}}{\partial \Theta}\right|_{\Theta_0} (\Theta_0 - \Theta)\right)\Psi_{\mathrm{EQ},0} \\ & + \left(\frac{\Theta}{\Theta_0} + g_{\mathrm{NEQ}}(\Theta) - g_{\mathrm{NEQ}}(\Theta_0) + \left.\frac{\partial g_{\mathrm{NEQ}}}{\partial \Theta}\right|_{\Theta_0} (\Theta_0 - \Theta)\right)\overline{\Psi}_{\mathrm{NEQ},0}, \end{aligned} \tag{182}$$

where the integral expression of Eq. (177) has been used. The equilibrium part of the free energy function Ψ is identified as

$$\Psi_{\mathrm{EQ}}(\mathbf{C}, d, \Theta) = t(\Theta) e_{\mathrm{EQ},0} + f_{\mathrm{EQ}}(\Theta)\Psi_{\mathrm{EQ},0} + \overline{C}(\Theta) \tag{183}$$

and the non-equilibrium part as

$$\Psi_{\mathrm{NEQ}}\left(\overline{\mathbf{C}}_e, \Theta\right) = t(\Theta) e_{\mathrm{NEQ},0} + f_{\mathrm{NEQ}}(\Theta)\overline{\Psi}_{\mathrm{NEQ},0}, \tag{184}$$

where the temperature dependency of the free energy function is written in a more compact form by introducing temperature evolution functions $f_{\mathrm{EQ}}(\Theta)$ and $f_{\mathrm{NEQ}}(\Theta)$, which are multiplied by the reference free energy functions $\Psi_{\mathrm{EQ},0}$ and $\overline{\Psi}_{\mathrm{NEQ},0}$. These functions can be found by comparing Eq. (182) with Eqs. (183) and (184),

$$f_{\mathrm{EQ}}(\Theta) = \frac{\Theta}{\Theta_0} + g_{\mathrm{EQ}}(\Theta) - g_{\mathrm{EQ}}(\Theta_0) + \left.\frac{\partial g_{\mathrm{EQ}}}{\partial \Theta}\right|_{\Theta_0} (\Theta_0 - \Theta), \tag{185}$$

$$f_{\mathrm{NEQ}}(\Theta) = \frac{\Theta}{\Theta_0} + g_{\mathrm{NEQ}}(\Theta) - g_{\mathrm{NEQ}}(\Theta_0) + \left.\frac{\partial g_{\mathrm{NEQ}}}{\partial \Theta}\right|_{\Theta_0} (\Theta_0 - \Theta), \tag{186}$$

$$t(\Theta) = 1 - \frac{\Theta}{\Theta_0} \tag{187}$$

and the general heat capacity term $\overline{C}(\Theta)$,

$$\overline{C}(\Theta) = \left[\overline{C}(\Theta) - \overline{C}(\Theta_0)\right] - \Theta\left[\overline{G}(\Theta) - \overline{G}(\Theta_0)\right]. \tag{188}$$

As dimensionless functions $g_{\mathrm{EQ}}(\Theta)$ and $g_{\mathrm{NEQ}}(\Theta)$, a wide range of different function types are possible for representing the temperature dependency of the investigated material. For more details, see Reese and Govindjee [64]. With the help of Eq. (182), the internal energy e is given by

$$\begin{aligned} e = {} & e_{\mathrm{EQ},0} + \Psi_{\mathrm{EQ},0}\left(f_{\mathrm{EQ}} - \Theta\frac{\partial f_{\mathrm{EQ}}}{\partial \Theta}\right) + \overline{C}(\Theta) - \Theta\frac{\partial \overline{C}(\Theta)}{\partial \Theta} \\ & + e_{\mathrm{NEQ},0} + \overline{\Psi}_{\mathrm{NEQ},0}\left(f_{\mathrm{NEQ}} - \Theta\frac{\partial f_{\mathrm{NEQ}}}{\partial \Theta}\right). \end{aligned} \tag{189}$$

For the reference internal energy $e_{\mathrm{EQ},0}$, the form

$$e_{\mathrm{EQ},0} = \kappa_0 \alpha_0 \Theta_0 \ln J \tag{190}$$

is chosen, where κ_0 and α_0 are the bulk modulus and the thermal volume expansion coefficient of the equilibrium branch at reference temperature Θ_0, respectively. The same approach,

$$e_{\mathrm{NEQ},0} = \kappa_0^v \alpha_0^v \Theta_0 \ln J_e, \tag{191}$$

could be assumed for the non-equilibrium branch, where the superscript v denotes the viscous parameters in the case of viscous volumetric material behavior with

$$\mathbf{F}_{\mathrm{vol}} = J^{\frac{1}{3}}\mathbf{1} = \mathbf{F}_{\mathrm{vol},e}\mathbf{F}_{\mathrm{vol},i} = J_e^{\frac{1}{3}} J_i^{\frac{1}{3}}\mathbf{1}. \tag{192}$$

However, in the proposed material model, only purely isochoric viscous material behavior is considered as mentioned before; hence, $J = J_e$, $J_i = 1$ and $\kappa_0^v = \alpha_0^v = 0$, which leads to $e_{\mathrm{NEQ},0} = 0$.

Figure 16 depicts the volumetric part of the proposed material model by simple rheological elements. The rheological interpretation of the volumetric part is given by an equilibrium branch, which is composed of the potentials $U_0(J)$ and $e_{\mathrm{EQ},0}(J)$ at reference temperature Θ_0. Note that $e_{\mathrm{EQ},0}$ is also part of the volumetric material response as a result of its dependence on the volumetric deformation in the form of J. As a result, the internal energy $e_{\mathrm{EQ},0}$ can be seen as the potential of a second volumetric spring in parallel to the first defined by the potential $U_0(J)$. An alternative approach for the equilibrium branch is depicted in Fig. 17, in which the determinant of the deformation gradient J is also multiplicatively decomposed into a purely stress-free volume change J_Θ as a result of a temperature increase or decrease and a stress-generating volume change J_m as

$$\mathbf{F}_{\mathrm{vol}} = J^{\frac{1}{3}}\mathbf{1} = \mathbf{F}_{\mathrm{vol},m}\mathbf{F}_{\mathrm{vol},\Theta} = J_m^{\frac{1}{3}} J_\Theta^{\frac{1}{3}}\mathbf{1}. \tag{193}$$

For this alternative approach, the constitutive equation for the volume dilatation as a result of a temperature change

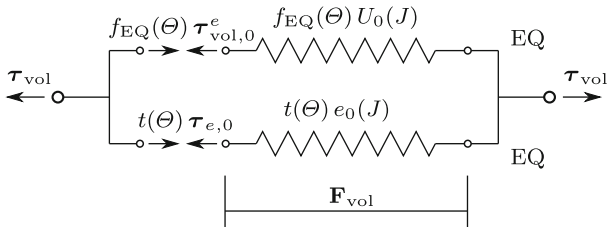

Fig. 16 Rheology of the volumetric part of the material model

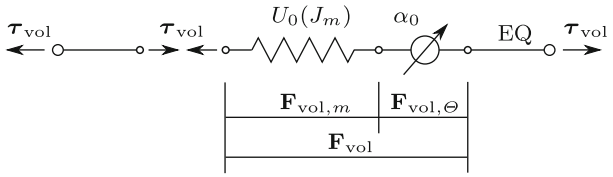

Fig. 17 Alternative rheology for volumetric part

$$J_\Theta = 1 + \alpha_0(\Theta - \Theta_0) = 1 + \alpha_0 \Delta\Theta \tag{194}$$

is given via the thermal volume expansion coefficient α_0.

If a stress-free state of the volumetric rheology depicted in Fig. 16 and a homogeneous temperature increase of $\Delta\Theta = \Theta - \Theta_0$ are considered, the body dilates, which leads to $J > 1$ and, hence, to a volumetric stress response stemming from the potential $U_0(J)$. However, the total stress response must remain zero,

$$\boldsymbol{\tau}_{\text{vol}} = J p \mathbf{1} = f_{\text{EQ}}(\Theta)\boldsymbol{\tau}^e_{\text{vol},0} + t(\Theta)\boldsymbol{\tau}_{e,0} = 0 \tag{195}$$

or, for one direction, the hydrostatic Cauchy pressure

$$\begin{aligned} p &= f_{\text{EQ}}(\Theta)\frac{\partial U_0(J)}{\partial J} + t(\Theta)\frac{\partial e_{\text{EQ},0}(J)}{\partial J} \\ &= f_{\text{EQ}}(\Theta)U_0'(J) + t(\Theta)e'_{\text{EQ},0}(J) \\ &= f_{\text{EQ}}(\Theta)\kappa_0\frac{J-1}{J} + \frac{-\kappa_0\alpha_0\Delta\Theta}{J} \end{aligned} \tag{196}$$

can be derived, where Eqs. (32), (40), (183) and (190) have been used. Multiplication by J yields the volumetric Kirchhoff stress

$$J p = f_{\text{EQ}}(\Theta)\kappa_0(J-1) + (-\kappa_0\alpha_0\Delta\Theta) = 0. \tag{197}$$

A further reordering of the terms in Eq. (197) results in

$$\alpha_0\Delta\Theta = (J-1)f_{\text{EQ}}(\Theta) \tag{198}$$

with

$$\Delta\Theta = \Theta - \Theta_0. \tag{199}$$

Finally, the unknown volume dilatation is derived as

$$J = 1 + \frac{1}{f_{\text{EQ}}(\Theta)}\alpha_0\Delta\Theta. \tag{200}$$

For the given relation

$$J = 1 + \alpha_v(\Theta)\Delta\Theta, \tag{201}$$

the temperature-dependent constitutive parameter $\alpha_v(\Theta)$ denotes the thermal volume expansion coefficient and can be identified for the present model approach by comparison with Eq. (200) as

$$\alpha_v(\Theta) = \frac{1}{f_{\mathrm{EQ}}(\Theta)}\alpha_0. \tag{202}$$

The volumetric response to a temperature change $\Delta\Theta$ of the second rheology given in Fig. 17 would lead to

$$J = J_m J_\Theta = 1 + \alpha_0 \Delta\Theta, \tag{203}$$

where $J_m = 1$. It can be seen that the result of the first approach from Eq. (200) corresponds to the result obtained from the second approach given in Eq. (203), besides the inverse factor $f_{\mathrm{EQ}}(\Theta)$. Hence, it can be concluded that the derivative of the internal energy with respect to deformation acts as a negative pressure [see Eq. (197)] and also that the volume expansion is governed by the temperature function $f_{\mathrm{EQ}}(\Theta)$, as stated in Eq. (200).

5.4 Balance Equations

The general balance equations of thermodynamics are addressed next. These must be fulfilled for any material, no matter what constitutive material law is assumed. First, their strong or local forms are presented and developed for the given constitutive material equations. Second, the strong forms are integrated over the volume of the body to derive their weak forms.

5.4.1 Strong Form

Investigation of a thermomechanical problem involves the linear and angular balance of momentum (displacement field)

$$J\,\mathrm{div}\left(\frac{\boldsymbol{\tau}}{J}\right) + \rho_0(\mathbf{g}_v - \ddot{\mathbf{u}}) = 0 \text{ with } \boldsymbol{\tau} = \boldsymbol{\tau}^{\mathrm{T}} \tag{204}$$

and also the balance of energy (temperature field)

$$\dot{e} - \boldsymbol{\tau} : \mathbf{d} - r + J\,\mathrm{div}\,\mathbf{q} = 0, \tag{205}$$

which has to satisfy the restrictions with respect to energy flux and energy transformation given by the dissipation inequality. In Eq. (204), $\boldsymbol{g}_v$ denotes the acceleration due to gravity and $\ddot{\mathbf{u}}$ stands for the acceleration vector of a material point. In Eq. (205), e and r represent the internal energy and a heat source per unit reference volume, respectively. The relation $e = \Psi + \Theta\,\eta$ and Eq. (153) lead together to

$$\begin{aligned}\dot{e} &= \dot{\Psi} + \dot{\Theta}\eta + \Theta\dot{\eta} = \dot{\Psi} - \dot{\Theta}\frac{\partial \Psi}{\partial \Theta} + \Theta\dot{\eta} \\ &= (\boldsymbol{\tau}_{\mathrm{EQ}} + \boldsymbol{\tau}_{\mathrm{NEQ,iso}}) : \mathbf{d} + \boldsymbol{\tau}_{\mathrm{NEQ,iso}} : \frac{1}{2}\overline{\mathcal{L}}_v(\overline{\mathbf{b}}_e)\overline{\mathbf{b}}_e^{-1} \\ &\quad + \frac{\partial \Psi}{\partial d}\dot{d} + \frac{\partial \Psi}{\partial \Theta}\dot{\Theta} - \dot{\Theta}\frac{\partial \Psi}{\partial \Theta} + \Theta\dot{\eta}\end{aligned} \tag{206}$$

with

$$\begin{aligned}\Theta\dot{\eta} = -\Theta\frac{\partial \dot{\Psi}}{\partial \Theta} \quad &= -\Theta\left(\frac{\partial \boldsymbol{\tau}_{\mathrm{EQ}}}{\partial \Theta} + \frac{\partial \boldsymbol{\tau}_{\mathrm{NEQ,iso}}}{\partial \Theta}\right) : \mathbf{d} \\ &\quad - \Theta\frac{\partial \boldsymbol{\tau}_{\mathrm{NEQ,iso}}}{\partial \Theta} : \frac{1}{2}\overline{\mathcal{L}}_v(\overline{\mathbf{b}}_e)\overline{\mathbf{b}}_e^{-1} \\ &\quad - \Theta\frac{\partial^2 \Psi}{\partial d \partial \Theta}\dot{d} \underbrace{- \Theta\frac{\partial^2 \Psi}{\partial \Theta \partial \Theta}}_{+c_v}\dot{\Theta}.\end{aligned} \tag{207}$$

If the expressions of Eqs. (206) and (207) are inserted into Eq. (205), the balance of energy becomes finally

$$\begin{aligned}&- \Theta\left(\frac{\partial \boldsymbol{\tau}_{\mathrm{EQ}}}{\partial \Theta} + \frac{\partial \boldsymbol{\tau}_{\mathrm{NEQ,iso}}}{\partial \Theta}\right) : \mathbf{d} \\ &+ \left(\boldsymbol{\tau}_{\mathrm{NEQ,iso}} - \Theta\frac{\partial \boldsymbol{\tau}_{\mathrm{NEQ,iso}}}{\partial \Theta}\right) : \frac{1}{2}\overline{\mathcal{L}}_v(\overline{\mathbf{b}}_e)\overline{\mathbf{b}}_e^{-1} \\ &+ \left(\frac{\partial \Psi}{\partial d} - \Theta\frac{\partial^2 \Psi}{\partial d \partial \Theta}\right)\dot{d} \\ &+ c_v\dot{\Theta} - r + J \operatorname{div} \mathbf{q} = 0,\end{aligned} \tag{208}$$

where the external power w_{ext} is identified as

$$\begin{aligned}w_{\mathrm{ext}} &= \Theta\left(\frac{\partial \boldsymbol{\tau}_{\mathrm{EQ}}}{\partial \Theta} + \frac{\partial \boldsymbol{\tau}_{\mathrm{NEQ,iso}}}{\partial \Theta}\right) : \mathbf{d} \\ &= \Theta\frac{\partial \boldsymbol{\tau}}{\partial \Theta} : \mathbf{d},\end{aligned} \tag{209}$$

the internal viscous power w_v as

$$w_v = -\left(\boldsymbol{\tau}_{\mathrm{NEQ,iso}} - \Theta\frac{\partial \boldsymbol{\tau}_{\mathrm{NEQ,iso}}}{\partial \Theta}\right) : \frac{1}{2}\overline{\mathcal{L}}_v(\overline{\mathbf{b}}_e)\overline{\mathbf{b}}_e^{-1} \tag{210}$$

and the internal damage power w_d stemming from the CDM approach as

$$w_d = -\left(\frac{\partial \Psi}{\partial d} - \Theta\frac{\partial^2 \Psi}{\partial d \partial \Theta}\right)\dot{d}. \tag{211}$$

As a result, the total internal power w_{int} is reformulated as

$$w_{\text{int}} = w_v + w_d \tag{212}$$

and represents the inner dissipation rate, which stems from the viscous branch and damage evolution. The expression w_v is the thermodynamic coupling term of the system and vanishes for purely entropy viscoelasticity ($f_{\text{NEQ}}(\Theta) = \Theta/\Theta_0 \rightarrow w_v = 0$). However, w_{ext} also includes a viscous stress term of the non-equilibrium branch because $\boldsymbol{\tau}_{\text{NEQ,iso}}$ is involved. The contribution of $\boldsymbol{\tau}_{\text{EQ}}$ results in thermoelastic coupling, whereas the contribution of $\boldsymbol{\tau}_{\text{NEQ,iso}}$ constitutes thermoviscoelastic coupling. With the introduced abbreviations, the balance of energy becomes

$$w_{\text{ext}} + w_v + w_d + r - c_v\dot{\Theta} - J \operatorname{div} \mathbf{q} = 0. \tag{213}$$

5.4.2 Weak Form

The balance equations stated in Eqs. (204) and (213) are solved on the FE level by means of a weak formulation. Therefore, test functions $\delta\mathbf{u}$ and $\delta\Theta$ for the displacement and temperature field, respectively, are introduced, fulfilling the boundary conditions of the body. The global weak formulation of the strong local form is obtained by multiplication by the test functions and integration over the volume of the body. As a result, the weak form of the governing equation of the balance of momentum becomes

$$\begin{aligned} G_{\text{M}}(\mathbf{u}, \ddot{\mathbf{u}}, \Theta) = &\int \mathbf{S} : \frac{1}{2}\text{D}\mathbf{C}[\delta\mathbf{u}]\text{d}V \\ &- \int \rho_0(\mathbf{g}_v - \ddot{\mathbf{u}}) \cdot \delta\mathbf{u}\text{d}V - \int \mathbf{T} \cdot \delta\mathbf{u} \ \text{d}A = 0 \end{aligned} \tag{214}$$

with $\mathbf{T} = \mathbf{FSN}$ and the directional derivative $\text{D}\mathbf{C}[\delta\mathbf{u}]$ of $\mathbf{C}$ in the direction $\delta\mathbf{u}$. The weak form of the balance of energy is given by

$$\begin{aligned} G_{\text{T}}\left(\mathbf{u}, \dot{\mathbf{u}}, \Theta, \dot{\Theta}\right) = &\int \mathbf{Q} \cdot \nabla_{\mathbf{X}}\delta\Theta\text{d}V + \int \left(w_{\text{ext}} + w_v + w_d + r - c_v\dot{\Theta}\right)\delta\Theta \, \text{d}V \\ &- \int \mathbf{Q} \cdot \mathbf{N}\delta\Theta \, \text{d}A = 0. \end{aligned} \tag{215}$$

The numerical integration is carried out over the reference volume V and reference boundary A of the body in the reference configuration. $\mathbf{N}$ denotes the unit outward normal to a surface element $\text{d}A$. $G_{\text{M}}(\mathbf{u}, \ddot{\mathbf{u}}, \Theta)$ and $G_{\text{T}}(\mathbf{u}, \dot{\mathbf{u}}, \ddot{\mathbf{u}}, \Theta, \Theta)$ also depend on $\delta\mathbf{u}$ and $\delta\Theta$, respectively. It is worth mentioning that the test functions $\delta\mathbf{u}$ and $\delta\Theta$ are constant and non-zero for any changes in $\mathbf{u}, \dot{\mathbf{u}}, \ddot{\mathbf{u}}, \Theta$, or Θ.

Different solution schemes for the unsymmetric system of equations resulting from thermomechanical analysis within the finite element method (FEM) exist. In staggered solution schemes, the displacement field is solved first during an isothermal predictor step, followed by an isochoric corrector step for the temperature field (Felippa and Park [83], Armero and Simo [84]). In simultaneous solution schemes, the incremental changes in displacement and temperature field are simultaneously computed, which requires a fully derived system of linearized equations with respect to displacement and temperature.

Because elastomers in general and particle-reinforced elastomers in particular are nearly incompressible, an unnatural stiffening of the discretized body under shear and inhomogeneous deformation modes can appear in the FE simulation, which is called "locking." Formulations to overcome this disadvantage of standard isoparametric displacement-based FE approximations are mixed element approaches. One of the simplest forms is the mean pressure-dilatation method, in which the hydrostatic pressure stemming from the volumetric part is assumed to be constant over the FE volume. The FE formulation is commonly referred to as Q1P0, which is a standard formulation for the treatment of purely mechanical problems (see, for example, Bathe [85], Bonet and Wood [61], Dal and Kaliske [86], Miehe [56], Simo et al. [55], Zienkiewicz and Taylor [87]). For thermomechanically coupled problems, the pressure is a function of the displacements and the temperature. Therefore, the standard mean-pressure method has to be modified (see, for example, Simo and Miehe [80], Simo et al. [88]).

Further details regarding the FE formulation (Q1P0 with a mean-pressure approach depending on temperature) and implementation of the extended non-affine tube model in the context of thermomechanics are provided by Behnke [82].

6 Applications Based on the Finite Element Method

The extended non-affine tube model can be used in the context of finite thermoviscoelasticity to represent the thermomechanical behavior of elastomer specimens. In the first example, a cyclic uniaxial extension test of an elastomer specimen is considered. The second example deals with a so-called three-branch specimen subjected to biaxial loading, which causes heterogeneous displacement and temperature fields upon loading.

In addition to these two examples, a thermomechanical study of cyclically loaded dumbbell-shaped elastomer specimens has been provided by Behnke et al. [89].

6.1 Uniaxial Extension Test

A thermomechanical simulation of an elastomer specimen is addressed as outlined by Behnke et al. [90]. The force and temperature response of an elastomer specimen to cyclic uniaxial loading is experimentally and numerically investigated. Thermal interactions with the environment are taken into account by using a special finite surface element formulation (see, for example, Behnke [82] for more details). In this element formulation, convective phenomena arising from relative surface motion with respect to the surroundings are captured by a modified Stefan–Boltzmann law with the constitutive heat flux equation

$$q_n = \overline{q} + [h_c + h_{cv}(\Theta, \dot{u}_{cv})\dot{u}_{cv}](\Theta - \Theta_a), \tag{216}$$

where q_n is the norm of the normal outward heat flux $\mathbf{q}_n$ per unit surface da in the current configuration,

$$\mathbf{q}_n = q_n\mathbf{n} = \mathbf{q}\cdot\mathbf{n}, \quad \mathbf{n} = \frac{\mathbf{x}_{,\xi}\times\mathbf{x}_{,\eta}}{\|\mathbf{x}_{,\xi}\times\mathbf{x}_{,\eta}\|} = \begin{pmatrix} n_1 \\ n_2 \\ n_3 \end{pmatrix} \tag{217}$$

with the tangent vectors

$$\mathbf{x}_{,\xi} = \frac{\partial\mathbf{x}}{\partial\xi}, \quad \mathbf{x}_{,\eta} = \frac{\partial\mathbf{x}}{\partial\eta}. \tag{218}$$

$\dot{u}_{cv}$ denotes the norm of the tangential surface velocity vector $\dot{\mathbf{u}}_{cv}$,

$$\dot{u}_{cv} = \|\dot{\mathbf{u}}_{cv}\| \geq 0. \tag{219}$$

In Eq. (216), $\overline{q}$ denotes a static prescribed heat flux, $h_c \geq 0$ is the static heat conduction coefficient of the linear Stefan–Boltzmann law, and $h_{cv}(\Theta, \dot{u}_{cv}) \geq 0$ refers to the dynamic heat conduction coefficient, which is assumed to be a function of the surface temperature Θ of the body and its tangential surface velocity $\dot{u}_{cv}$. As a result, different convective heat exchanges can be phenomenologically modeled by assuming different functional dependencies for $h_{cv}(\Theta, \dot{u}_{cv})$.

6.1.1 Test Setup

The test setup is depicted in Fig. 18 and allows simultaneous recording of the reaction force and the surface temperature of the specimen during the test. A cuboidal elastomer specimen with cross-sectional dimensions $a = 2$ mm and $b = 4$ mm is placed between the grips of a testing machine with an initial undeformed length of $l = 22$ mm. Information about the material composition of

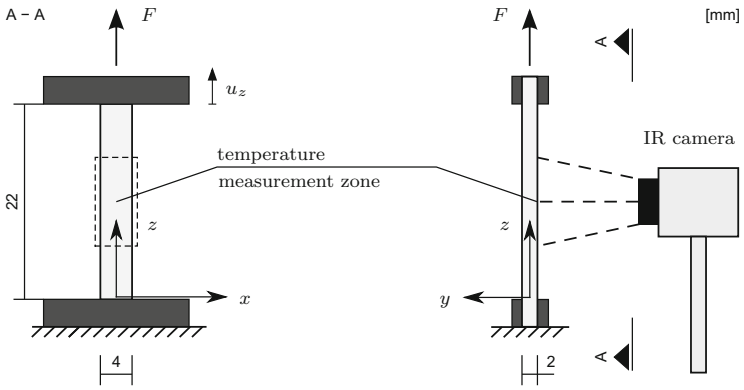

Fig. 18 Test setup for cyclic tensile test on elastomer specimen

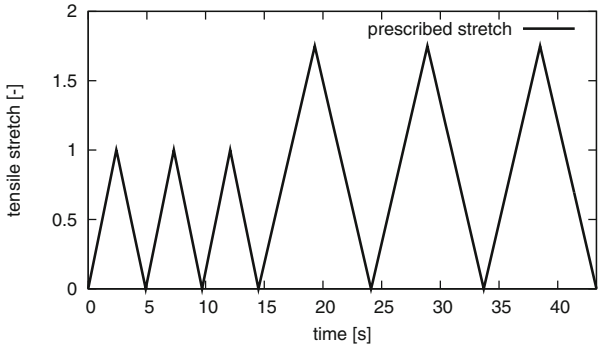

Fig. 19 Prescribed tensile stretch (strain–time diagram)

the elastomer was taken from Pottier et al. [91]. During the test, the reaction force at the upper moving grip and the surface temperature in the center of the specimen's length are recorded by a load cell and an infrared (IR) camera, respectively, as shown in Fig. 18. The test was carried out at Laboratoire de Méchanique et Ingénieries (LaMI) in France, and recorded test data were provided for comparison with the numerically simulated model response obtained by the research group of J.-B. Le Cam (IFMA, France).

During the displacement-controlled test, the upper grip of the testing machine is moved according to the displacement–time diagram given in Fig. 19.

6.1.2 Model Parameters

The measured data for reaction force and surface temperature change are used for model parameter identification. Additional thermal material characteristics are reported by Pottier et al. [91]. Because of the lack of additional test data, the

following second-order conditions were used during the parameter identification process (consisting of the execution of FE simulations of the whole test setup):

- Bulk modulus set to $\kappa_0 = 100$ MPa, representing nearly incompressible material behavior ($\nu \approx 0.49$)
- Shear modulus G_e set to zero (phenomenological approach)
- Viscoelastic behavior modeled with the help of one non-equilibrium branch
- Parameter δ_v of the non-equilibrium branch set to zero

To be precise, G_e was intentionally set to zero from a pragmatic point of view because neither polymer-physical data nor additional test data were available for its physical derivation (as discussed in Sect. 3.1). If parameter G_e is set to zero, the value of parameter β has no effect on the result (multiplication by zero). Therefore, the upper physical limit of $\beta = 1$ is used in the numerical example. As temperature coefficient function,

$$f_{\mathrm{EQ}}(\Theta) = \frac{\Theta}{\Theta_0} - \frac{\Theta[\tanh(b(\Theta - \Theta_0))]^3}{\Theta_0 + a} \tag{220}$$

is used for the equilibrium branch, whereas $f_{\mathrm{NEQ}}(\Theta) = 1$ is chosen for the non-equilibrium branch. Regarding the reference heat capacity of the undeformed material, a quadratic ansatz of type

$$\overline{c}(\Theta) = p_2\Theta^2 + p_1\Theta + p_0 \tag{221}$$

is included in the numerical model, see also Eq. (168). The defined and identified model parameters are summarized in Table 4.

Thermal boundary conditions on the side faces of the specimen are represented in the model by finite surface elements with enforced heat convection. The model parameters of the constitutive heat flux law are summarized in Table 5. The clamped edges of the test specimen are considered to be thermally insulated.

Table 4 Model parameters for uniaxial extension test

Mass density	ρ_0 (g/cm^3)				
	1.130				
Equilibrium branch	κ_0 (MPa)	G_c (MPa)	δ (−)	G_e (MPa)	β (−)
	100.0	2.750	0.25	0.0	1.0
Non-equilibrium branch i	G_c^v (MPa)	δ_v (−)	$\dot{\gamma}_0/\hat{\tau}^m$ (MPa^{-m}s^{-1})	c (−)	m (−)
1	0.350	0.0	0.27202	10.0	1.65
Temperature dependency parameters	a (K)	b (K^{-1})	Θ_0 (K)	Θ_{ref} (K)	
	69.84	0.196	253.0	292.0	
	p_0 (MPa/K)	p_1 (MPa/K^2)	p_2 (MPa/K^3)	α_0 (K^{-1})	k (W/m K)
	2.373	0.0	0.0	0.0001854	0.8
Damage parameters	η_α (−)	η_β (−)	$f_{d,\alpha}$ (−)	$f_{d,\beta}$ (−)	
	4.0	4.0	0.25	0.25	

Table 5 Model parameters for thermal boundary condition for uniaxial extension test

Heat exchange	$\overline{q}$ (W/m^2)	h_c (W/m^{2}K)	h_{cv} (W s/m^{3}K)	$\Delta\Theta_{initial}$ (K)
	0.0	10.0	2,000.0	0.0

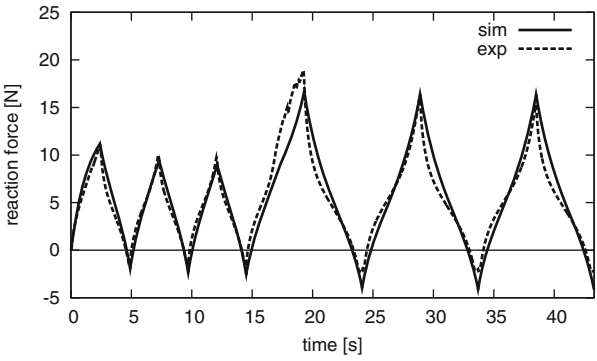

Fig. 20 Reaction force (force–time diagram)

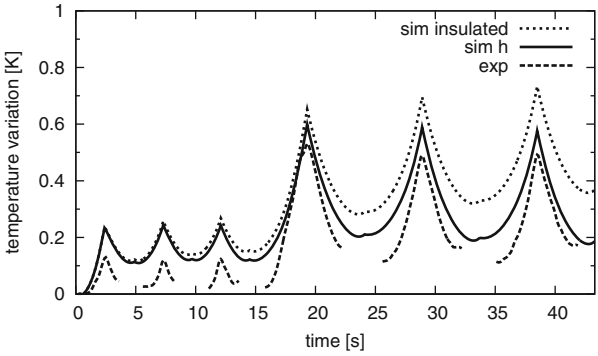

Fig. 21 Variation of surface temperature in the center of the specimen's length (temperature–time diagram): experimental measurement (*exp*) and simulated response for perfectly insulated specimen (*sim insulated*) and specimen with thermal boundary conditions (*sim h*) according to Table 5

6.1.3 Results of Simulation and Experiment

The force–time response and the surface temperature–time response in experiment and simulation are given in Figs. 20 and 21, respectively. The numerical simulation was carried out with the model parameter set summarized in Table 4 and time steps of $\Delta t = 0.05$ s. Good agreement between measurement and simulation is observable.

During the unloading phase to regain the specimen's initial position, buckling of the specimen occurred as a result of its viscoelastic properties. Hence, IR measurement was not possible for the period when buckling of the specimen and, in consequence, deflection of its surface occurred. In consequence, data gaps in the measurement of surface temperature are observable in the temperature–time plot (see Fig. 21). Via simulation of the surface temperature evolution, the temperature evolution can be predicted for these time periods. For comparison, the simulation result for the completely insulated specimen (no heat exchange with ambient air) is also plotted in Fig. 21.

Figure 22 depicts the surface temperature evolution from the beginning of the fourth cycle up to the maximum loading of 175 % strain amplitude. Because convection phenomena have been included in the modeling, the surface temperature field is slightly heterogeneous, depending on the relative velocity of the considered point during loading of the specimen. In consequence, the upper part of the specimen near the moving grip shows a slightly lower surface temperature than the lower part of the specimen near the fixed grip.

Figure 23 shows evolution of the damage variable d as the sum of discontinuous (d_α) and continuous (d_β) damage contributions at a point in the center of the specimen.

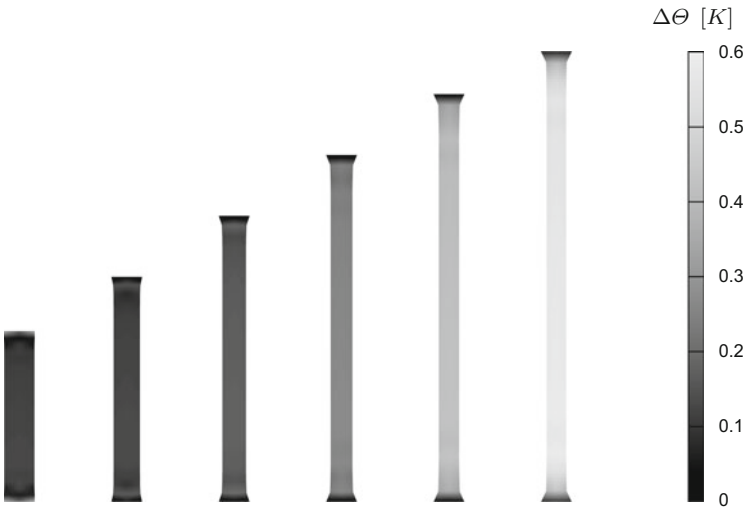

Fig. 22 Simulation result for surface temperature variation during displacement-controlled loading (displacement rate of 500 mm/min)

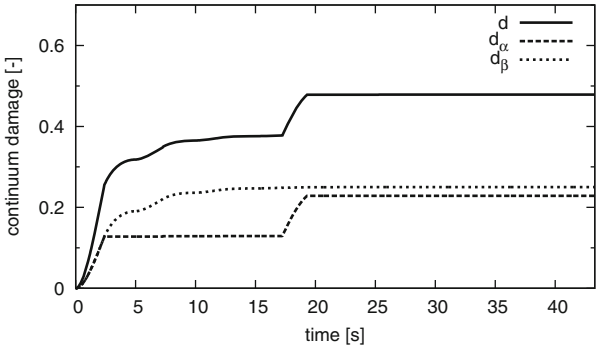

Fig. 23 Continuum damage (damage–time diagram): total damage d, discontinuous damage d_α, continuous damage d_β

6.2 Three-Branch Test

In the presented example, a so-called three-branch specimen was subjected to a multiaxial loading state, as reported by Balandraud et al. [92]. During the deformation process, the displacement and temperature field were recorded by full-field measurement. Finally, simulation results of the test were compared with experimental measurements.

6.2.1 Test Setup

The geometry of the elastomer specimen and the boundary conditions formed by the test machine are depicted in Fig. 24. Experimental investigation of the three-branch specimen was realized at LaMI (France) and recorded test data was provided for comparison with the numerically simulated model response obtained by J.-B. Le Cam and his research group. The special test setup of the three-branch specimen was proposed by Guelon et al. [93]. To achieve loading of the specimen at each of its branches, a tensile test machine was modified to apply biaxial loading in the form of equibiaxial tension and pure shear in the center of the specimen. The lower branch is clamped to a fixed grip while displacements in x- and y-directions are prescribed to the other two branches during two load steps. In the first step, a displacement of $u_y = 12$ mm is applied in the y-direction and a displacement of $u_x = 30$ mm is applied in the x-direction. Subsequently, a relaxation phase follows. In the first step, a heterogeneous displacement field is generated by deformation of the specimen. The deformation field on the surface of the sample is recorded by a

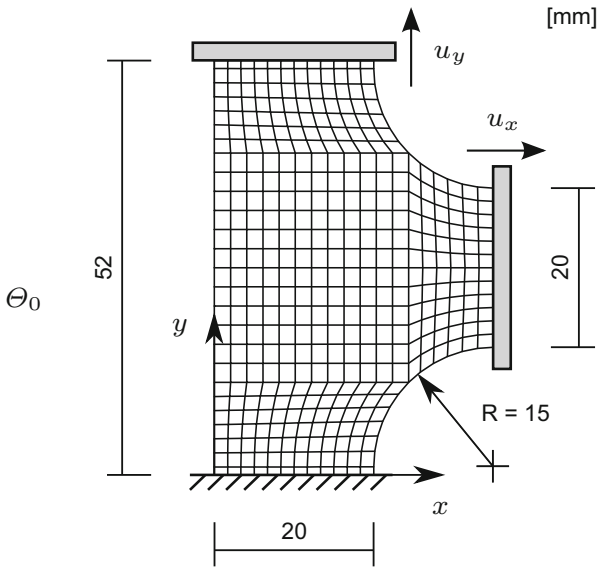

Fig. 24 FE mesh of the three-branch specimen and boundary conditions; initial temperature of the specimen and surroundings $\Theta_0 = 292$ K

digital camera, which observes the white paint-sprayed surface of the three-branch specimen. The configuration at the end of the first step and the subsequent relaxation phase is referred to as the intermediate configuration. In the second step, a displacement of $u_y = 47$ mm is applied in the y-direction in the form of a displacement rate of 15.66 mm/s to obtain a final global stretch of $\varepsilon_x = 2.13$ and $\varepsilon_y = 1.85$ in x- and y-directions, respectively. During the second loading step, digital and IR images are recorded over time.

Because finite displacements occur during the test, the material points of the surface of the specimens are tracked with the help of a motion compensation technique, as described by Pottier et al. [91]. Via digital image correlation (DIC) as a full-field measurement technique (see, for example, Sutton et al. [94]), the displacement field on the surface of the specimen can be computed. For further details, the reader is referred to Sasso et al. [95] and Chevalier et al. [96]. In analogy, temperature variations $\Delta\Theta$ are computed and plotted with respect to the initial temperature state and position of points of the reference configuration. Figure 25c depicts the temperature variation computed for the end of the second loading step. The maximum temperature rise is located at the edge between the two moving grips, which coincides with the zone where the highest strain rate is observable in uniaxial tension mode.

6.2.2 Model Parameters

The material and model parameters for simulation of the three-branch specimen are taken from the uniaxial extension test described in Sect. 6.1. The model parameters are summarized in Tables 4 and 6.

6.2.3 Numerical Simulation of the Thermomechanical Response

Using the same model parameters as identified in Sect. 6.1, a thermomechanically coupled simulation of the three-branch specimen can be carried out.

Figure 24 illustrates the FE mesh and the boundary conditions. Symmetry with respect to the x- and y-planes is taken into account by only modeling one half of the specimen in the thickness direction (z-direction) via a layer of finite continuum elements. The FE mesh includes 384 Q1P0 finite volume elements and 436 finite surface elements to represent thermal boundary conditions on the free surfaces of the three-branch specimen. During numerical simulation, adaptive time step control was used with time steps of $\Delta t = 0.1$ s for the loading phases and up to $\Delta t = 100.0$ s for the intermediate relaxation phase.

With the help of a post-processing algorithm, the simulation results for displacement field and temperature field are projected to the intermediate configuration. Figure 25 depicts the simulation results computed for the end of the second loading step. By comparing experimental and simulation results, good agreement between

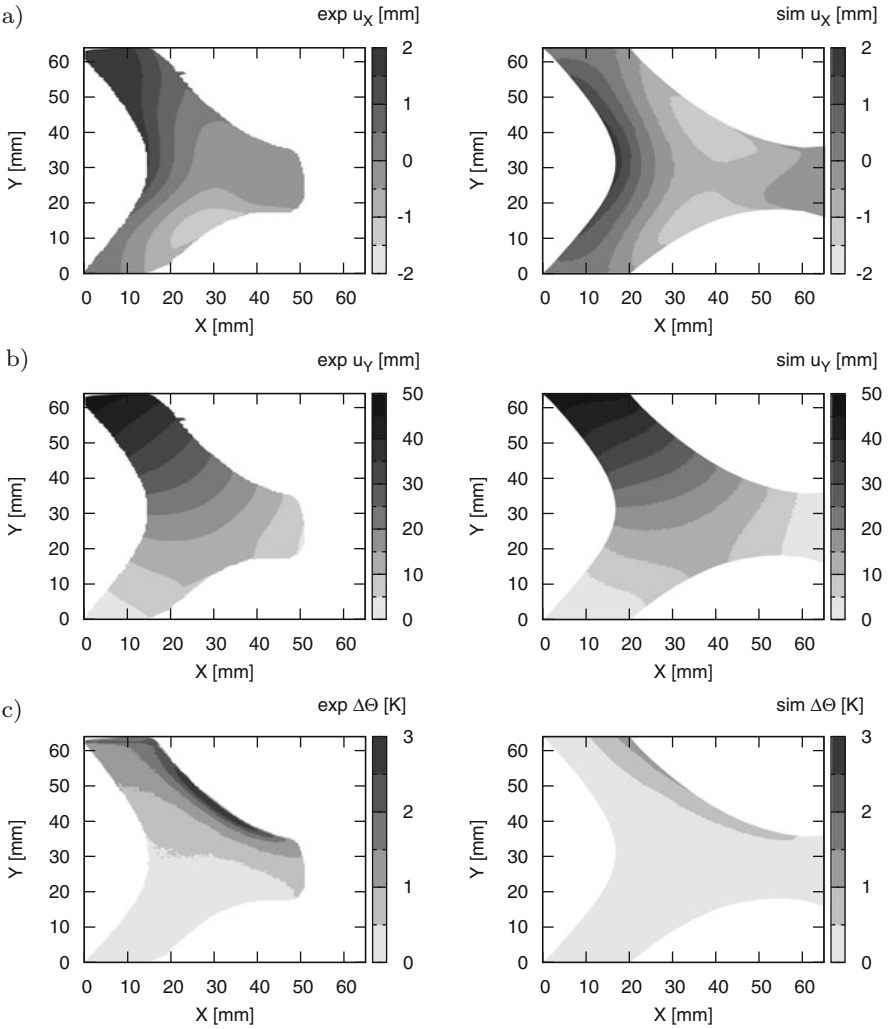

Fig. 25 Full-field measurement (*left*), simulated displacement (*right*), and temperature variation fields at the end of the second loading step: (**a**) horizontal displacement; (**b**) vertical displacement; (**c**) temperature variation

Table 6 Model parameters for thermal boundary condition for three-branch test

Heat exchange	$\overline{q}$ (W/m^2)	h_c (W/m^{2}K)	h_{cv} (W s/m^{3}K)	$\Delta\Theta_{initial}$ (K)
	0.0	10.0	0.0	0.0

measured and simulated fields is observable. Differences between experimental results and numerical results might be explained by a relative slip occurring between the specimen and upper grip. In consequence, a larger displacement in the x-direction at the upper grip is observable in the experimental measurements

compared with the computed displacement field in Fig. 25a, which is based on ideal boundary conditions throughout the whole test.

7 Conclusions and Outlook

The extended non-affine tube model combines both a molecular physically based derivation and a numerically attractive and efficient application within the FEM to represent the hyperelastic behavior of elastomers in a successful way. The extended non-affine tube model approach for isothermal hyperelasticity can be combined with other model approaches to account for inelastic phenomena, giving a more advanced description of time-dependent and time-independent characteristics. With the help of the FEM, local description of the material response can be integrated to predict the response of complex and arbitrary elastomer components on the structural scale, ranging from simple elastomer samples to cord-reinforced pneumatic tires (as illustrated in Fig. 26). It has become obvious that other fields, such as elastomer friction and wear, elastomer degradation, and elastomer fracture should also be considered to physically understand and numerically predict the behavior of such complex elastomer structures. Application of the extended non-affine tube model in such advanced thermomechanical simulations of steady-state rolling tires is described, for example, by Behnke and Kaliske [97, 98].

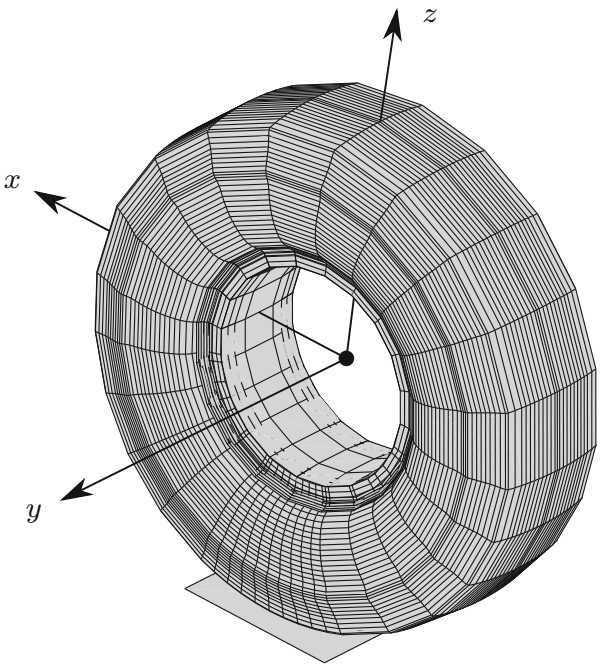

Fig. 26 Perspective view of a FE tire model

In the design process of future elastomer devices, advanced numerical simulations will play an important role in reducing prototype costs and speeding up the development of new components. However, these simulations must be reliable in terms of their predictability and capacity to represent all significant material and structural phenomena of the problem considered. By using physically inspired models, such as the extended non-affine tube model, this challenge can be faced more easily.

Acknowledgements Some of the research results reported herein are partially supported by the Deutsche Forschungsgemeinschaft (DFG) under grant KA 1163/16. The financial support is gratefully acknowledged. The authors thank J.-B. Le Cam (IFMA, France) and his research group for their experimental-numerical cooperation.

References

1. Behnke R, Dal H, Geißler G, Näser B, Netzker C, Kaliske M (2013) Macroscopical modeling and numerical simulation for the characterization of crack and durability properties of particle-reinforced elastomers. In: Grellmann W, Heinrich G, Kaliske M, Klüppel M, Schneider K, Vilgis T (eds) Fracture mechanics and statistical mechanics of reinforced elastomeric blends. Lecture notes in applied and computational mechanics, vol 70. Springer, Berlin, pp 167–226
2. Kaliske M, Behnke R (2015) Material laws of rubbers. In: Kobayashi S, Müllen K (eds) Encyclopedia of polymeric nanomaterials. Springer, Berlin, pp 1187–1197
3. Grambow A (2002) Determination of material parameters for filled rubber depending on time, temperature and loading condition. Ph.D. Thesis, Rheinisch-Westfälische Technische Hochschule Aachen, Germany
4. Heinrich G, Straube E, Helmis G (1988) Rubber elasticity of polymer networks: theories. Adv Polym Sci 85:33–87
5. Edwards S, Vilgis T (1988) The tube model theory of rubber elasticity. Rep Prog Phys 51:243–297
6. Valanis K, Landel R (1967) The strain-energy function of a hyperelastic material in terms of the extension ratios. J Appl Phys 38:2997–3002
7. Heinrich G, Kaliske M (1997) Theoretical and numerical formulation of a molecular based constitutive tube-model of rubber elasticity. Comput Theor Polym Sci 7:227–241
8. Kaliske M, Heinrich G (1999) An extended tube-model for rubber elasticity: statistical-mechanical theory and finite element implementation. Rubber Chem Technol 72:602–632
9. Bergström J (2015) Mechanics of solid polymers. Theory and computational modeling. Elsevier, San Diego
10. Klüppel M, Schramm J (2000) A generalized tube model of rubber elasticity and stress softening of filler reinforced elastomer systems. Macromol Theory Simul 9:742–754
11. Klüppel M (2003) Hyperelasticity and stress softening of filler reinforced polymer networks. Macromol Symp Funct Netw Gels 200:31–44
12. Heinrich G, Straube E (1987) A theory of topological constraints in polymer networks. Polym Bull 17:247–253
13. Heinrich G, Straube E (1984) On the strength and deformation dependence of tube-like topological constraints in polymer networks, melts and concentrated solutions I. The polymer network case. Acta Polym 34:589–594
14. Heinrich G, Straube E (1984) On the strength and deformation dependence of tube-like topological constraints in polymer networks, melts and concentrated solutions II. Polymer melts and concentrated solutions. Acta Polym 35:115–119

15. Edwards S (1965) The statistical mechanics of polymers with excluded volume. Proc Phys Soc 85:613–624
16. Edwards S, Vilgis T (1986) The effect of entanglements in rubber elasticity. Polymer 27:483–492
17. Freed K (1972) Functional integrals and polymer statistics. Adv Chem Phys 22:1–128
18. Treloar L (1975) The physics of rubber elasticity. Clarendon, Oxford
19. Arruda E, Boyce M (1993) A three-dimensional constitutive model for the large stretch behavior of rubber elastic materials. J Mech Phys Solids 41:389–412
20. Marckmann G, Verron E (2006) Comparison of hyperelastic models for rubberlike materials. Rubber Chem Technol 79:835–858
21. Ogden R (1972) Large deformation isotropic elasticity – on the correlation of theory and experiment for incompressible rubberlike solids. Proc R Soc A 326:565–584
22. Miehe C, Göktepe S, Lulei F (2004) A micro-macro approach to rubber-like materials. Part I: The non-affine micro-sphere model of rubber elasticity. J Mech Phys Solids 52:2617–2660
23. Drozdov A, Dorfmann A (2002) Finite viscoelasticity of filled rubbers: the effects of preloading and thermal recovery. Continuum Mech Thermodyn 14:337–361
24. Green M, Tobolsky A (1946) A new approach to the theory of relaxing polymeric media. J Chem Phys 14:80–92
25. Tanaka F, Edwards S (1992) Viscoelastic properties of physically crosslinked networks. Part 1. Non-linear stationary viscoelasticity. J Non-Newton Fluid Mech 43:247–271
26. Tanaka F, Edwards S (1992) Viscoelastic properties of physically crosslinked networks. Part 2. Dynamic mechanical moduli. J Non-Newton Fluid Mech 43:273–288
27. De Gennes P (1971) Reptation of a polymer chain in the presence of fixed obstacles. J Chem Phys 55:572–579
28. Doi M, Edwards S (1986) The theory of polymer dynamics. Clarendon, Oxford
29. Bergström J, Boyce M (1998) Constitutive modeling of the large strain time-dependent behavior of elastomers. J Mech Phys Solids 46:931–954
30. Dal H, Kaliske M (2009) Bergström-Boyce model for nonlinear finite rubber viscoelasticity: theoretical aspects and algorithmic treatment for the FE method. Comput Mech 44:809–823
31. Areias P, Matouš K (2008) Finite element formulation for modeling nonlinear viscoelastic elastomers. Comput Methods Appl Mech Eng 197:4702–4717
32. Miehe C, Göktepe S (2005) A micro-macro approach to rubber-like materials. Part II: The micro-sphere model of finite rubber viscoelasticity. J Mech Phys Solids 53:2231–2258
33. Wineman A (2009) Nonlinear viscoelastic solids – a review. Math Mech Solids 14:300–366
34. Freund M, Lorenz H, Juhre D, Ihlemann J, Klüppel M (2011) Finite element implementation of a microstructure-based model for filled elastomers. Int J Plast 27:902–919
35. Kaliske M (2000) A formulation of elasticity and viscoelasticity for fibre reinforced material at small and finite strains. Comput Methods Appl Mech Eng 185:225–243
36. Simo J (1987) On a fully three-dimensional finite-strain viscoelastic damage model: formulation and computational aspects. Comput Methods Appl Mech Eng 60:153–173
37. Govindjee S, Simo J (1992) Mullins' effect and the strain amplitude dependence of the storage modulus. Int J Solids Struct 29:1737–1751
38. Kaliske M, Rothert H (1997) Formulation and implementation of three-dimensional viscoelasticity at small and finite strains. Comput Mech 19:228–239
39. Lee E (1969) Elastic-plastic deformation at finite strains. J Appl Mech 36:1–6
40. Sidoroff F (1974) Un modèle viscoélastique nonlinéaire avec configuration intermédiaire. Journal de Mécanique 13:697–713
41. Lubliner J (1985) A model of rubber viscoelasticity. Mech Res Commun 12:93–99
42. Simo J (1992) Algorithms for static and dynamic multiplicative plasticity that preserve the classical return mapping schemes of the infinitesimal theory. Comput Methods Appl Mech Eng 99:61–112
43. Reese S, Govindjee S (1998) A theory of finite viscoelasticity and numerical aspects. Int J Solids Struct 35:3455–3482

44. Kachanov L (1986) Introduction to continuum damage mechanics. Martinus Nijhoff, Dordrecht
45. Chaboche JL (1981) Continuous damage mechanics – a tool to describe phenomena before crack initiation. Nucl Eng Des 64:233–247
46. Chaboche JL (1988) Continuum damage mechanics: Part I – General concepts. Part II – Damage growth, crack initiation and crack growth. J Appl Mech 55:59–72
47. Lemaitre J (1984) How to use damage mechanics. Nucl Eng Des 80:233–245
48. Chagnon G, Verron E, Gornet L, Marckmann G, Charrier P (2004) On the relevance of continuum damage mechanics as applied to the Mullins effect in elastomers. J Mech Phys Solids 52:1627–1650
49. Simo J, Ju J (1987) Strain- and stress-based continuum damage models – II. Computational aspects. Int J Solids Struct 23:841–869
50. Simo J, Ju J (1987) Strain- and stress-based continuum damage models – I. Formulation. Int J Solids Struct 23:821–840
51. Kaliske M, Nasdala L, Rothert H (2001) On damage modelling for elastic and viscoelastic materials at large strain. Comput Struct 79:2133–2141
52. Nasdala L, Kaliske M, Rothert H, Becker A (1999) A realistic elastic damage model for rubber. In: Dorfmann A, Muhr A (eds) Constitutive models for rubber. Balkema, Rotterdam, pp 151–158
53. Göktepe S, Miehe C (2005) A micro-macro approach to rubber-like materials. Part III: The micro-sphere model of anisotropic Mullins-type damage. J Mech Phys Solids 53:2259–2283
54. Flory P (1961) Thermodynamic relations for high elastic materials. Trans Faraday Soc 57:829–838
55. Simo J, Taylor R, Pister K (1985) Variational and projection methods for the volume constraint in finite deformation elasto-plasticity. Comput Methods Appl Mech Eng 51:177–208
56. Miehe C (1994) Aspects of the formulation and finite element implementation of large strain isotropic elasticity. Int J Numer Methods Eng 37:1981–2004
57. Simo J, Taylor R (1982) Penalty function formulations for incompressible nonlinear elastostatics. Comput Methods Appl Mech Eng 35:107–118
58. Dal H (2011) Approaches to the modeling of inelasticity and failure of rubberlike materials. Theory and numerics. Ph.D. Thesis, TU Dresden, Germany
59. Miehe C (1995) Discontinuous and continuous damage evolution in Ogden-type large-strain elastic materials. Eur J Mech A/Solids 14:697–720
60. Coleman B, Gurtin M (1967) Thermodynamics with internal state variables. J Chem Phys 47:597–613
61. Bonet J, Wood R (1997) Nonlinear continuum mechanics for finite element analysis. Cambridge University Press, Cambridge
62. Weber G, Anand L (1990) Finite deformation constitutive equations and a time integration procedure for isotropic, hyperelastic-viscoplastic solids. Comput Methods Appl Mech Eng 79:173–202
63. Wriggers P (2001) Nichtlineare Finite-Element-Methoden. Springer, Berlin
64. Reese S, Govindjee S (1998) Theoretical and numerical aspects in the thermoviscoelastic material behaviour of rubber-like polymers. Mech Time Dependent Mater 1:357–396
65. Heinrich G (1987) Thermoelasticity of tube-like constrained polymer networks. Acta Polym 38:637–638
66. Miehe C (1988) Zur numerischen Behandlung thermomechanischer Prozesse. Ph.D. Thesis, Universität Hannover, Germany
67. Miehe C (1995) Entropic thermoelasticity at finite strains. Aspects of the formulation and numerical implementation. Comput Methods Appl Mech Eng 120:243–269
68. Lion A (1997) On the large deformation behaviour of reinforced rubber at different temperatures. J Mech Phys Solids 45:1805–1834
69. Lion A (1997) A physically based method to represent the thermo-mechanical behaviour of elastomers. Acta Mech 123:1–25

70. Bérardi G, Jaeger M, Martin R, Carpentier C (1996) Modelling of a thermoviscoelastic coupling for large deformations through finite element analysis. Int J Heat Mass Transfer 39:3911–3924
71. Allen G, Bianchi U, Price C (1963) Thermodynamics of elasticity of natural rubber. Trans Faraday Soc 59:2493–2502
72. Allen G, Kirkham M, Padget J, Price C (1971) Thermodynamics of rubber elasticity at constant volume. Trans Faraday Soc 67:1278–1292
73. Chadwick P (1974) Thermo-mechanics of rubberlike materials. Philos Trans R Soc Lond Ser A Math Phys Sci 276:371–403
74. Chadwick P, Creasy C (1984) Modified entropic elasticity of rubberlike materials. J Mech Phys Solids 32:337–357
75. Haupt P (1993) On the mathematical modelling of material behavior in continuum mechanics. Acta Mech 100:129–154
76. Morland L, Lee E (1960) Stress analysis for linear viscoelastic materials with temperature variation. Trans Soc Rheol 4:233–263
77. Holzapfel G, Simo J (1996) A new viscoelastic constitutive model for continuous media at finite thermomechanical changes. Int J Solids Struct 33:3019–3034
78. Reese S (2003) A micromechanically motivated material model for the thermoviscoelastic material behaviour of rubber-like polymers. Int J Plast 19:909–940
79. Dippel B, Johlitz M, Lion A (2015) Thermo-mechanical couplings in elastomers – experiments and modelling. Zeitschrift für Angewandte Mathematik und Mechanik 95:1117–1128
80. Simo J, Miehe C (1992) Associative coupled thermoplasticity at finite strains: formulation, numerical analysis and implementation. Comput Methods Appl Mech Eng 98:41–104
81. Eterovic A, Bathe KJ (1990) A hyperelastic-based large strain elasto-plastic constitutive formulation with combined isotropic-kinematic hardening using the logarithmic stress and strain measures. Int J Numer Methods Eng 30:1099–1114
82. Behnke R (2015) Thermo-mechanical modeling and durability analysis of elastomer components under dynamic loading. Ph.D. Thesis, TU Dresden, Germany
83. Felippa C, Park K (1980) Staggered transient analysis procedures for coupled mechanical systems: Formulation. Comput Methods Appl Mech Eng 24:61–111
84. Armero F, Simo J (1992) A new unconditionally stable fractional step method for non-linear coupled thermomechanical problems. Int J Numer Methods Eng 35:737–766
85. Bathe KJ (1996) Finite element procedures. Prentice-Hall, New Jersey
86. Dal H, Kaliske M (2005) Q1P0-brick element for thermomechanical analysis. Leipzig Annu Civil Eng Rep 10:105–115
87. Zienkiewicz O, Taylor R (2000) The finite element method, vol 2; Solid mechanics, 5 edn. Butterworth-Heinmann, Oxford
88. Simo J, Armero F, Taylor R (1993) Improved versions of assumed enhanced strain tri-linear elements for 3D finite deformation problems. Comput Methods Appl Mech Eng 110:359–386
89. Behnke R, Kaliske M, Klüppel M (2016) Thermo-mechanical analysis of cyclically loaded particle-reinforced elastomer components: Experiment and finite element simulation. Rubber Chem Technol 89:154–176
90. Behnke R, Dal H, Kaliske M (2011) An extended tube model for thermoviscoelasticity of rubberlike materials: theory and numerical implementation. In: Jerrams S, Murphy N (eds) Constitutive models for rubber VII. CRC, London, pp 87–92
91. Pottier T, Moutrille MP, Le Cam JB, Balandraud X, Grédiac M (2009) Study on the use of motion compensation techniques to determine heat sources. Application to large deformations on cracked rubber specimens. Exp Mech 49:561–574
92. Balandraud X, Toussaint E, Le Cam J, Grédiac M, Behnke R, Kaliske M (2011) Application of full-field measurements and numerical simulations to analyze the thermo-mechanical response of a three-branch rubber specimen. In: Jerrams S, Murphy N (eds) Constitutive models for rubber VII. CRC, London, pp 45–50

93. Guélon T, Toussaint E, Le Cam JB, Promma N, Grédiac M (2009) A new characterisation method for rubber. Polym Test 28:715–723
94. Sutton M, Wolters W, Peters W, Ranson W, McNeil S (1983) Determination of displacements using an improved digital correlation method. Image Vis Computating 1:133–139
95. Sasso M, Palmieri G, Chiappini G, Amodio D (2008) Characterization of hyper-elastic rubber-like materials by biaxial and uniaxial stretching tests based on optical methods. Polym Test 27:995–1004
96. Chevalier L, Calloch S, Hild F, Marco Y (2001) Digital image correlation used to analyze the multiaxial behavior of rubber-like materials. Eur J Mech A/Solids 2:169–187
97. Behnke R, Kaliske M (2014) Thermo-mechanical finite element analysis of steady state rolling off-the-road tires with respect to thermal damage. In: Proceedings international rubber conference, Beijing, 16–18 Sept 2014, pp 1455–1460
98. Behnke R, Kaliske M (2015) Thermo-mechanically coupled investigation of steady state rolling tires by numerical simulation and experiment. Int J Non Linear Mech 68:101–131

Adv Polym Sci (2017) 275: 71–102
DOI: 10.1007/12_2016_7

Published online: 24 July 2016

Reinforcement of Rubber and Filler Network Dynamics at Small Strains

Lewis B. Tunnicliffe and James J.C. Busfield

Abstract Carbon black particulate reinforcement of rubber is examined in terms of linear viscoelasticity and the dynamics of the filler particle network. First, it is demonstrated that for the case of purely hydrodynamic reinforcement, the dynamics of the filled rubber are equivalent to those of the corresponding unfilled material. A breakdown in thermorheological simplicity is observed with the onset of filler networking in reinforced compounds. The dynamics of the filler network are initially examined by strain sweep/recovery experiments performed on uncrosslinked materials. The role of the surface activity of carbon black in defining the rate and magnitude of flocculation is explored and various models to describe this process are reviewed. The dynamics of carbon black filler networks in crosslinked materials are probed using small strain torsional creep experiments. Physical ageing (structural relaxation) of filled compounds at temperatures well above the glass transition temperature of the rubber matrix is observed and the ageing rate is found to scale with the level of filler networking in the various compounds. Physical ageing is the result of non-equilibrium, slow dynamics, which sheds light on the physical origin of the filler network. Furthermore, the implications of physical ageing of highly filled rubbers on typical linear viscoelastic time–temperature superposition experiments are discussed.

Keywords Carbon black • Dynamics • Reinforcement • Rubber

L.B. Tunnicliffe
Materials Research Institute & School of Engineering and Materials Science, Queen Mary University of London, Mile End Road, London E1 4NS, UK

Present address:
Birla Carbon Technical Centre, 1800 West Oak Commons Court, Marietta, GA 30062, USA

J.J.C. Busfield (✉)
Materials Research Institute & School of Engineering and Materials Science, Queen Mary University of London, Mile End Road, London E1 4NS, UK
e-mail: j.busfield@qmul.ac.uk

Contents

1 Introduction

The reinforcement of rubber by particulate fillers is an important phenomenon that has enabled the development of almost all engineering rubber products. However, despite the ubiquity of filler particles as reinforcing agents, the precise physical mechanisms underpinning the observed reinforcement phenomena are still only partially understood. The term ‘reinforcement’ itself can be used to describe a wide range of modifications of rubber material properties including linear/non-linear viscoelastic behaviour, electrical and dielectric properties, and fracture and fatigue responses.

Considering viscoelastic behaviour, the works of Fletcher and Gent [1, 2] and Payne [3–5] identified the non-linear strain dependence of the dynamic moduli imparted to rubber by the incorporation of carbon black (CB). Payne attributed this effect to the breakdown of a ‘filler network’ under progressive straining, resulting in softening of the material with concomitant dissipation of energy. The magnitude of this strain dependence of the viscoelastic moduli (Payne effect) and the reinforcement observed at small strain, $G'_{\text{filled}}/G'_{\text{unfilled}}$, are influenced by the filler particle volume fraction and quality of dispersion; the particle morphology, surface area and surface activity [2, 6–8]; and the strain history of the filled rubber [9]. Intriguingly, it has also been shown that the magnitude of the small strain linear viscoelastic reinforcing effect and, consequently, the magnitude of the Payne effect, are strongly temperature dependent in the transition and rubbery regions [3, 10], even at temperatures far in excess of the bulk polymer glass transition temperature (T_g) [11] (illustrated in Fig. 1 using data collected on materials studied in this paper).

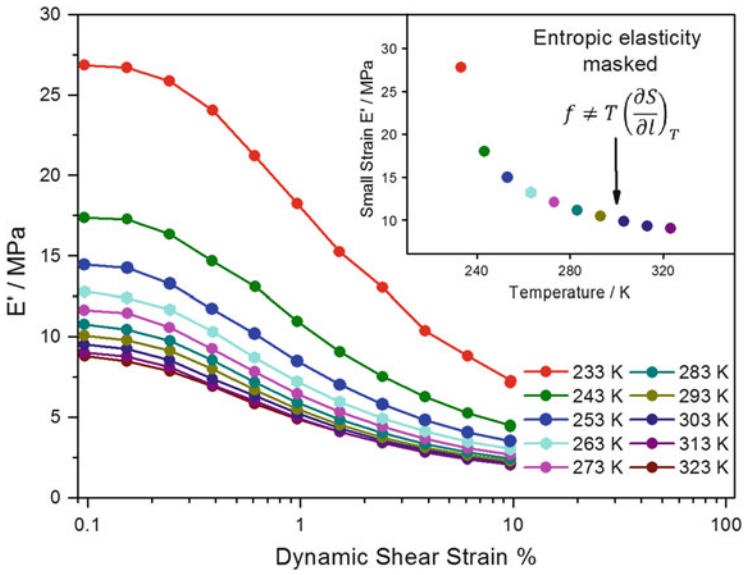

Fig. 1 Temperature dependence of the Payne effect for natural rubber filled with 20% volume N330 CB and crosslinked with 2 phr dicumyl peroxide. Each strain sweep was collected under isothermal conditions at a deformation frequency of 1 Hz. The lowest temperature strain sweep was taken at roughly 20 K above the rubber T_g. The data plotted here are the results after five preconditioning cycles. *Inset*: Small strain dynamic tensile modulus plotted versus temperature, illustrating the masking of entropy elasticity by the filler network

Because the magnitude of the Payne effect can dictate the dynamic performance of rubber products under various service conditions, a sound physical interpretation of this particular aspect of reinforcement is imperative.

The thermal sensitivity of the Payne effect and small strain reinforcement cannot be understood by considering the dynamics of unfilled rubber matrix alone because the modulus of the unfilled rubber increases with increasing temperature as a result of the entropic origins of rubber elasticity. Various mechanisms have been proposed to account for this behaviour, including thermal dependence of rubber chain–filler bonding (phase coupling) [12–15], thermal softening of interphase polymer of restricted segmental mobility located between filler aggregates [7, 16, 17] and the unjamming of flocculated filler aggregate networks [18] potentially caused by thermal expansion of the rubber matrix.

The magnitude of these reinforcement effects is dependent on the volume concentration of filler [8]. It is well established that filler particles such as CB have a tendency to flocculate during rubber processing, even if the dispersion states achieved during initial high shear compounding are optimal [19–23]. Approaches to modelling filler networking have been extensively reviewed elsewhere [24]. In commercial materials, the filler phase is generally present at a volume fraction such that a percolating/jammed filler network is established, as evident in reported dc conductivity and small strain studies [25–28]. The dynamics of such filler

networks are crucial for the resulting reinforcement and, as such, have been the subject of intensive study [16, 29, 30].

This paper explores the small strain dynamics of filled rubbers at temperatures above T_g, using model reinforced rubbers and rubbers reinforced with highly flocculated CB networks.

2 Hydrodynamic Reinforcement and the Breakdown of Thermorheological Simplicity

The simplest mechanism of reinforcement of rubber by rigid particles is described by an analogy with hydrodynamics. In this approach, the reinforcement of rubber elasticity is, at small strains, shown to be equivalent to the viscosity equation developed by Einstein, which predicts the viscosity of Newtonian fluids filled with spherical particles by accounting for the perturbation of the stress field in the liquid around the rigid inclusion [31, 32]. This viscosity–elasticity analogy has been the subject of many studies of the reinforcement of rubber, where attempts have been made to predict, using various analytical equations, the observed small strain stiffening effect of idealised and commercial reinforcing particles and to explore boundary condition effects [33–37]. A more general ramification of the hydrodynamic analogy is that the work of deforming the reinforced rubber is associated solely with the rubber phase of the composite. Consequently, the dynamic response of the reinforced rubber must be entirely dictated by the rubber matrix. In practice, it is difficult to evaluate the validity of this assertion using high surface area, commercial filler materials where the boundary condition between filler and rubber is the subject of much debate and the tendency of the filler aggregates to interact with one another within the rubber matrix is pronounced. As an alternative, it is very useful to consider the dynamics of model reinforced rubbers where the filler particle size, shape and boundary condition within the matrix are strictly defined and filler networking is suppressed. Rubbers reinforced with glass microspheres fulfil these criteria.

2.1 Dynamics of Unfilled and Model Reinforced Rubbers

Rubber networks reinforced with spherical glass microspheres were prepared by open milling (Carter laboratory two-roll mill) SMR CV(60) natural rubber (NR) with E-glass microspheres of 4 μm average diameter (Potter's Europe, Spheriglass 7010) at a volume fraction of 0.20. Crosslinked rubber compounds were prepared by addition of a typical sulphur-based vulcanisation package (zinc oxide 5 phr, stearic acid 1 phr, *N*-cyclohexyl-2-benzothiazol sulphenamide 1.5 phr, elemental sulphur, 1.5 phr) on a two-roll mill and compression moulding 2 mm

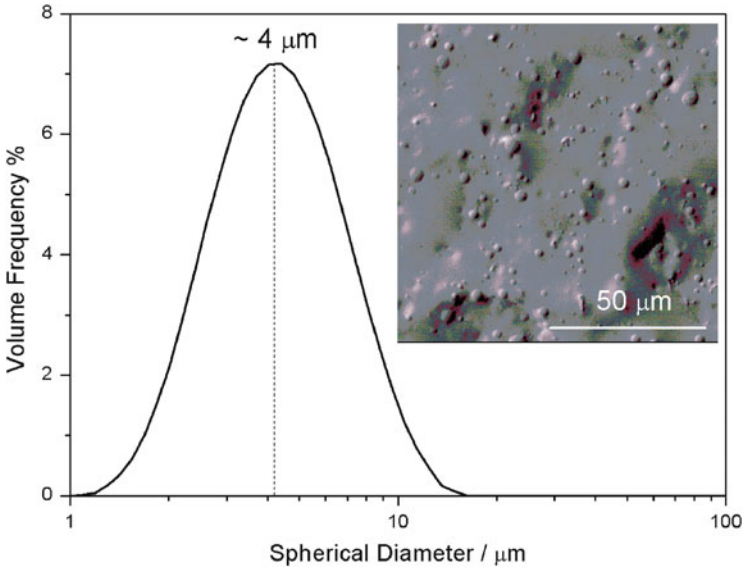

Fig. 2 Particle size distribution of glass microspheres in the model rubber network, as determined from light scattering experiments. *Inset*: SEM micrograph of a cryogenic fracture surface of the model reinforced rubber showing the random distribution of microspheres within the rubber matrix

thick sheets on a hot press at 160°C to T_{100} (the time required for full reaction of peroxide). An unfilled control material was also prepared.

CB-filled rubber was also prepared by internal mixing of N330 grade CB in a Banbury-type internal mixer to a volume fraction of 0.20. Further details of the compounding process are reported elsewhere [20]. A master batch was diluted through the addition of unfilled NR to provide compounds with various volume fractions as required. This blending method ensured effective dispersion of filler, which can be difficult to achieve when compounding at low volume fraction loadings as a result of reduced mixing torques. Addition of curatives on a two-roll mill and vulcanisation of the compounds were identical to the procedures used for microsphere-filled materials.

The particle size distribution of the microspheres, as determined from light scattering experiments (Malvern Mastersizer 2000), is shown in Fig. 2. The inset is a scanning electron microscopy (SEM) image of a cryogenic fracture surface of the crosslinked compound, showing the distribution of microspheres within the rubber matrix. The micrograph shows a random distribution of spherical particles within the matrix, with no evidence of microsphere agglomeration or networking.

The dynamics of the unfilled and model microsphere-reinforced materials were examined by performing time–temperature superposition (TTS) experiments to construct viscoelastic master curves. TTS was performed on a TA Instruments

Q800 DMA in tensile deformation mode at a dynamic strain of 0.2%, with a pre-load force of 0.5 N. A dynamic strain of 0.2% is well within the linear viscoelastic region for unfilled and microsphere-reinforced compounds and is at the upper limit of linear viscoelasticity for CB-filled compounds. Frequency sweeps were performed from 10 to 0.1 Hz at stepped isotherms from 0 to −70°C in −5°C steps, with a 2 min equilibration time prior to the start of each measurement.

A consequence of purely hydrodynamic reinforcement of rubber is that the viscoelastic spectrum of the reinforced rubber is solely dictated by the dynamics of the rubber matrix. Experimental confirmation of this for microsphere-reinforced rubber is found in the satisfactory TTS of the isothermal frequency domain data of model reinforced rubbers using the shift factors derived from the unfilled control material using the Williams–Landel–Ferry (WLF) equation (Eq. 1):

$$\log(a_t) = \frac{C_1(T - T_{ref})}{C_2 + (T - T_{ref})} \tag{1}$$

where a_t is the horizontal shift factor, C_1 and C_2 are material constants, T is the temperature and T_{ref} is the reference temperature.

Figure 3a, b shows the raw isotherm data and viscoelastic master curves for the unfilled rubber constructed via TTS, with the extracted horizontal shifting factors shown in the inset of Fig. 3b. Figure 3c shows equivalent master curves constructed for the microsphere-reinforced rubber. Satisfactory superpositioning is achieved in the rubbery region, demonstrating that the dynamics and reinforcement of such model compounds are dominated by the behaviour of the rubber matrix alone. Furthermore, the equilibrium modulus, E', is in good agreement with the Einstein–Smallwood hydrodynamic equation, confirming that hydrodynamics is the predominant reinforcement mechanism in microsphere-filled compounds.

2.2 *Onset of Filler Networking and Breakdown of Time–Temperature Superposition*

Commercially relevant filler particles are usually geometrically complex, often branched and highly structured pseudo-fractal aggregates with chemically and physically active surfaces and average aggregate sizes on the sub-micrometre length scale [38]. At volume fractions of commercial significance, CBs readily form percolated/flocculated networks, resulting in more complex thermomechanical behaviours such as the Payne effect and significant strain history effects. Figure 4 is adapted from the literature [20] and highlights evidence for CB filler networking by plotting the conductivity of N330-reinforced NR as a function of volume fraction. At the percolation threshold, φ_C, a conductive network of filler particles is established.

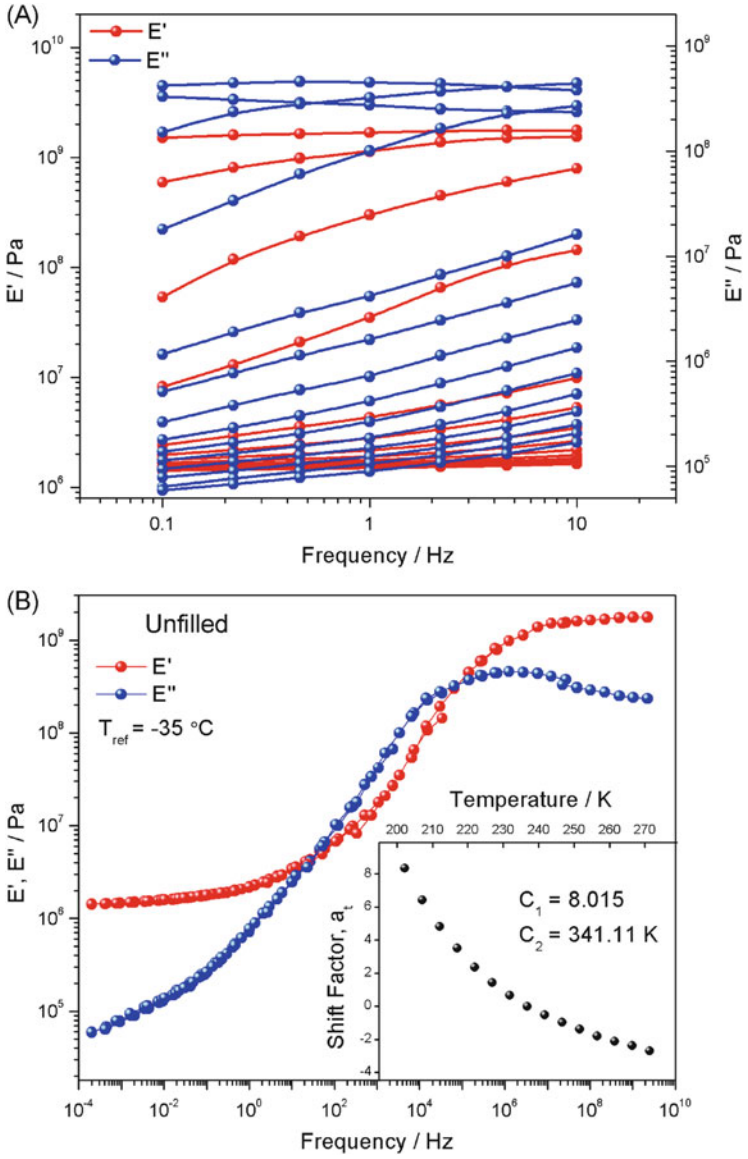

Fig. 3 (**a**) Isothermal frequency sweep data for the unfilled material. (**b**) Full viscoelastic master curves for the unfilled material. *Inset*: Horizontal shift factors required to construct the master curves. (**c**) Viscoelastic master curves for the microsphere-reinforced material in the rubbery region, showing satisfactory superpositioning. *Inset*: Full viscoelastic master curves

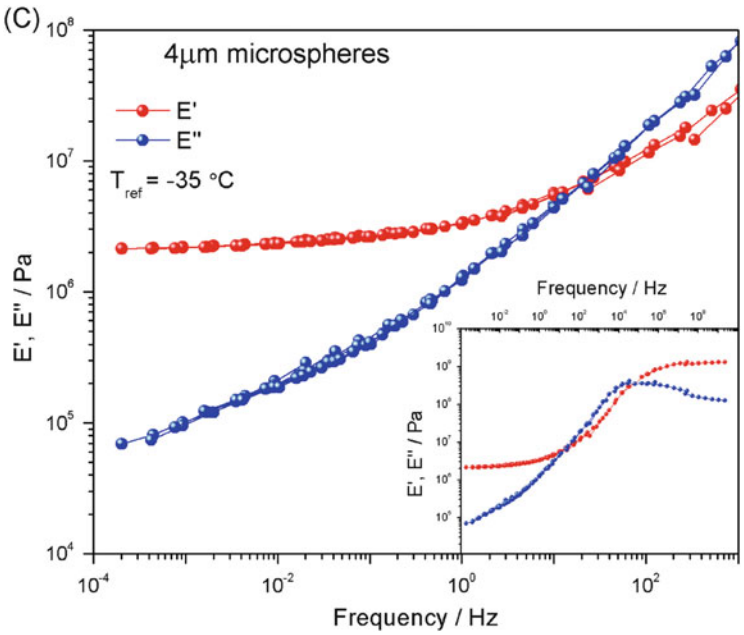

Fig. 3 (continued)

Consequently, the presence of filler networking also modifies the viscoelastic spectrum of the compound, resulting in incomplete horizontal superposition of isothermal behaviour in the rubbery region. Figure 5a–d shows master curves for N330-reinforced NR at various volume fractions (as indicated in Fig. 4), where horizontal shifting has been applied using the shift factors determined from the unfilled matrix. Clear 'feathering' of the master curves in the rubbery region can be observed, the severity of which increases with increasing N330 volume fraction. To correct for this effect, either additional horizontal shifting must be applied [29, 39] or independent vertical shifting of the dynamic moduli is required [40, 41]. Figure 5d shows the result of vertical shifting of one of the master curves, resulting in a continuous master curve. Figure 6 shows the vertical shift factors, v_t, of the storage and loss moduli required for each CB-filled compound, which clearly scale with the volume fraction of filler.

The collapse of the TTS principle in the rubbery region is the result of a separate dynamic response arising from the filler network, meaning that the work of deformation can no longer be solely associated with the rubber phase and implying that reinforcement is no longer purely hydrodynamic.

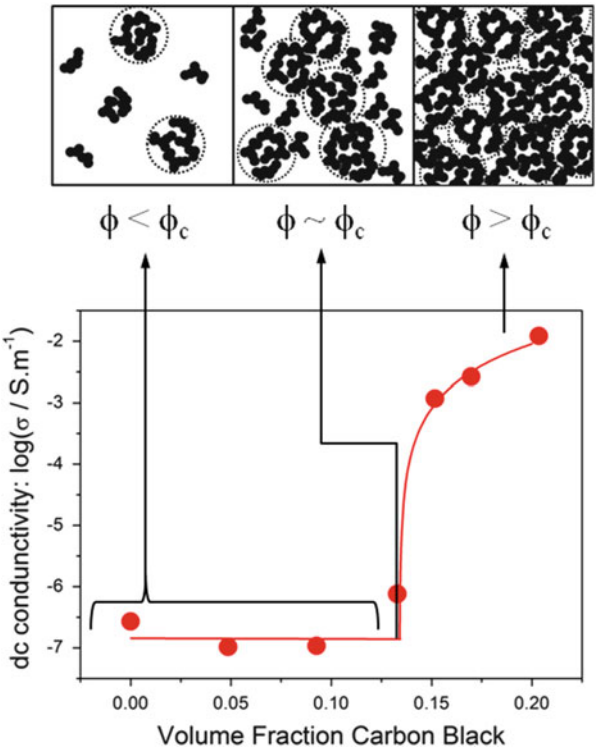

Fig. 4 The dc conductivity of NR filled with various volume fractions of N330 CB. At low volume concentrations, the CB is present as isolated aggregates or local aggregate subclusters (localised networks are indicated by *dashed circles*). At a critical volume fraction, an increase in conductivity of several orders of magnitude is observed. This dc percolation threshold corresponds to the percolation of aggregate clusters – permitting charge transfer through the material. Data is adapted from Tunnicliffe et al. [20]

3 Flocculation Dynamics of CB-Filled, Uncrosslinked Compounds

3.1 Characterisation of Flocculation in CB-Filled Rubbers

It is clear from the preceding section that the onset of filler networking is a key reason for the breakdown of the hydrodynamic description of rubber reinforcement. To probe the dynamics of the filler network in greater detail, a series of CB-reinforced NR compounds were prepared using N990, N330 and N134 grades of CB. Physicochemical data for these fillers are given in Table 1. N990 is a non-reinforcing, mid-thermal grade with very low aggregate branching and structure, leading to a near-spherical particle morphology, the average diameter of the particles being roughly 500 nm. N330 and N134 grades consist of much smaller, highly structured reinforcing aggregates.

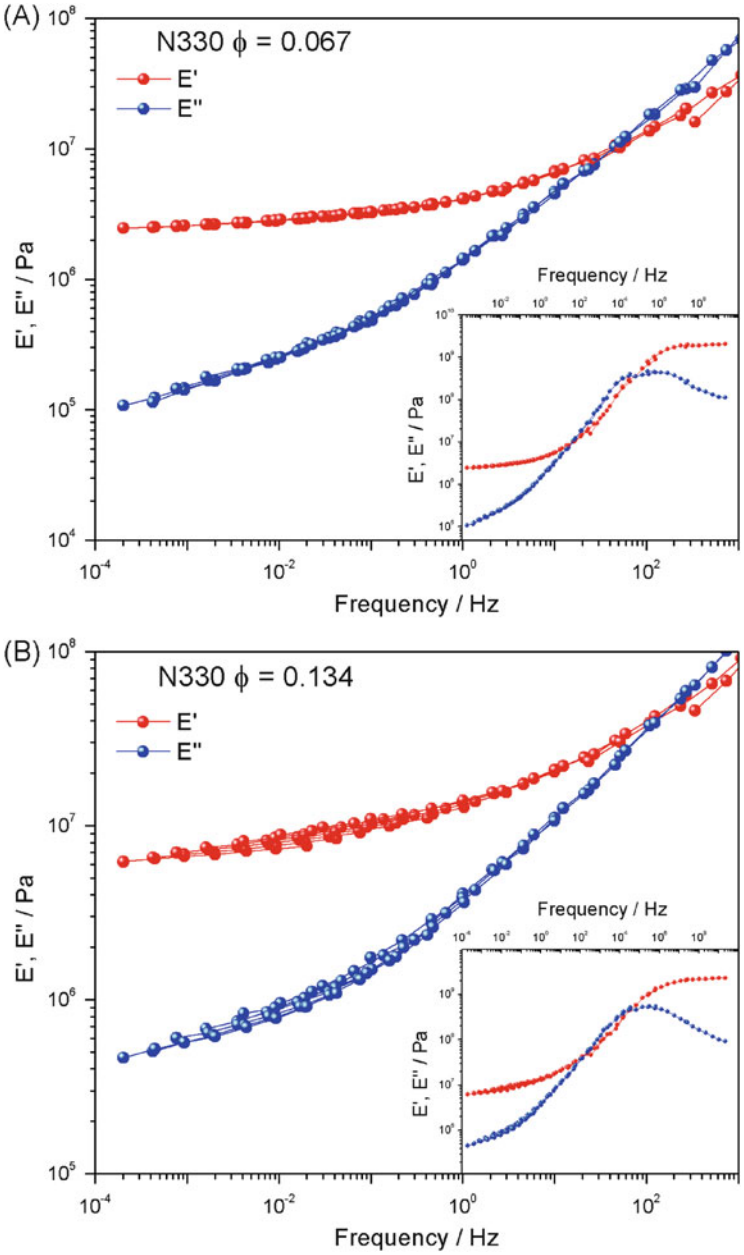

Fig. 5 (**a**) Master curves of NR/N330, $\varphi = 0.067$. Rubbery region is highlighted. (**b**) Master curves of NR/N330, $\varphi = 0.134$. (**c**) Master curves of NR/N330, $\varphi = 0.2$. Breakdown of TTS in the rubbery region is highlighted. (**d**) Master curves of NR/N330, $\varphi = 0.2$ after application of vertical shifting

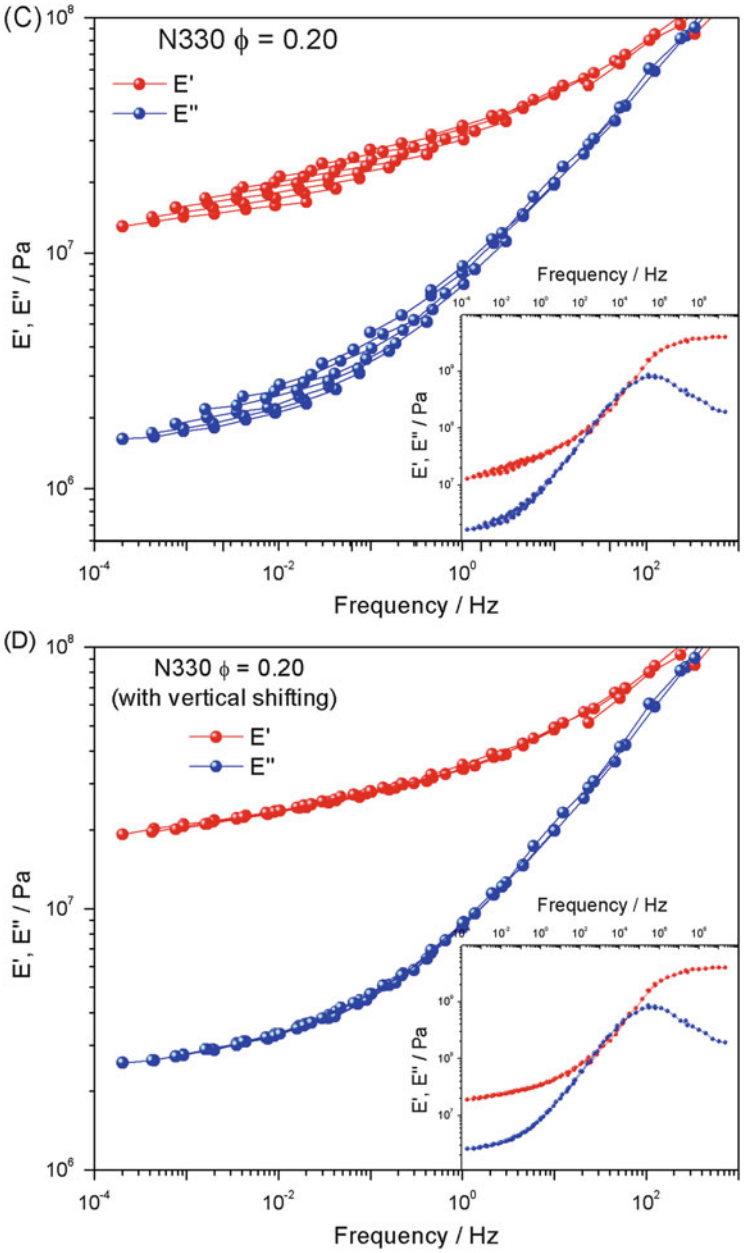

Fig. 5 (continued)

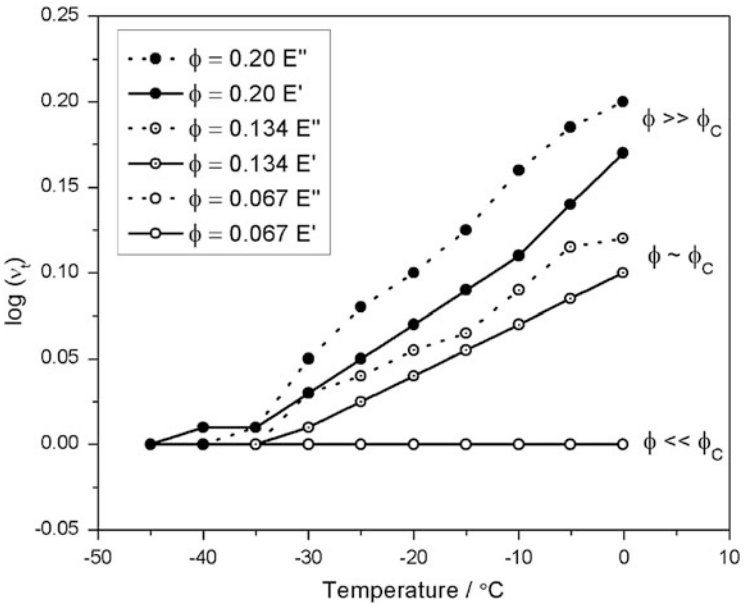

Fig. 6 Vertical shift factors as a function of temperature for NR filled with various volume fractions of N330 CB. *Labels* indicate the volume fraction of filler relative to the dc percolation threshold, φ_C

Table 1 Physicochemical properties of the carbon blacks used

Carbon black	N_2 surface area ($m^2\ g^{-1}$)	Average aggregate diameter[a] (nm)	dc percolation volume fraction	Average surface free energy (mJ m^2)
N134	134	70	0.094	39.1
N134g	136	–	0.007	5.2
N330	78	133	0.135	19.0
N330g	78	–	0.042	1.6
N990	8	436	≫0.20	17.5
N990g	8	–	≫0.20	6.9

Values reproduced from [20, 38]
[a]Average spherical aggregate diameter from disk centrifuge photosedimentometry [38]

The spatial distribution of free energy at the surface of regular tyre grade CBs is highly heterogeneous and predominantly dictated by thermal history in the industrial production method [38, 42]. Depending on the grade of CB there exist, to varying extents, regions of amorphous carbon interspersed with graphitic crystal layers and edges. Schröder et al. [43] identified four discrete types of energetic sites: (i) isolated at the lateral surface of the graphitic crystals, (ii) the amorphous carbon regions between crystallites, (iii) at the crystallite edges and (iv) within slit-shaped cavities between graphitic layers present on the surfaces of a range of different CBs. In addition, oxygen-containing chemical functionalities such as carboxyl, quinonic, phenol and lactone groups have been identified on the CB

surface. Both physical and chemical activities have been investigated in terms of physical interactions with polymer chains, although a quantitative description of these interactions is still lacking [38]. Several investigations into rubber reinforcement by CB have made use of the 'graphitisation' technique to modify the physicochemical activity of the CB surface and alter the nature of the filler–rubber interfacial interaction [20, 38, 44, 45]. During the graphitisation process, CB is exposed to high temperatures under an inert atmosphere. This results in a reduction in the number of high energy sites on the particle surface by crystallisation of amorphous carbon regions, producing a growth of graphitic layers that results in a net reduction in the concentration of crystallite edges. The removal of high energy sites is detrimental to the interaction between CB and rubber polymer.

In addition to the unmodified CB (N134, N330, N990) series, a corresponding series of compounds containing thermally deactivated (graphitised) CB was also produced. In the graphitisation process, 200 g of CB was placed inside a Carbolite STF tube furnace, which was connected to a flushing nitrogen supply. The furnace chamber containing the CB was purged with nitrogen for a minimum of 6 h before the temperature was ramped to 1250°C at a rate of 10 K/min. The peak temperature was held for 1 h before cooling to room temperature. Samples were removed from the furnace and stored under a nitrogen atmosphere until they were compounded with rubber. Physicochemical data for the graphitised CBs (N134g, N330g, N990g) are presented in Table 1 and additional details can be found in a separate publication. This thermal treatment resulted in significant reduction in the surface activity of the CB, without measurable changes to the morphology of the particles [20].

CB-filled NR compounds were prepared to a volume fraction of 0.20 in a Banbury-type internal mixer, as detailed in Sect. 2.1 of this paper and in a separate publication [20]. CB macrodispersion was qualitatively examined using SEM imaging of cryogenic fracture surfaces of the compounds, as shown in Fig. 7. The SEM images show little qualitative difference in macrodispersion state between compounds filled with CB and graphitised CB. Note that here the term 'macrodispersion' is used to refer to poorly dispersed micrometre-sized agglomerates of filler. For N990-based fillers, the CB particles are (relatively) large, near-spherical particles of between 250 and 1,000 nm diameter and can clearly be distinguished as individual particles within the rubber matrix.

In highly filled rubber compounds the filler network predominantly develops during the thermal vulcanisation process [46]. In this process, the thixotropic response of the compound to processing shear (such as that encountered during injection moulding) and to an increase in temperature are apparently underpinned by a particle flocculation mechanism. This section examines flocculation effects in uncrosslinked CB-filled compounds by probing the rheology of uncrosslinked compounds.

Rheological characterisation of the filled NR compounds prior to the incorporation of curing chemicals was performed using an Alpha Technologies Rubber Process Analyser (RPA) 2000. The plate temperature was set to 150°C and samples were loaded at room temperature. In an attempt to ameliorate strain and the thermal histories of the samples, a rest period of 10 min was incorporated into the test procedure prior to the initiation of dynamic testing. Subsequently, a dynamic shear strain sweep was performed between 0.067 and 10% strain. The shear strain was

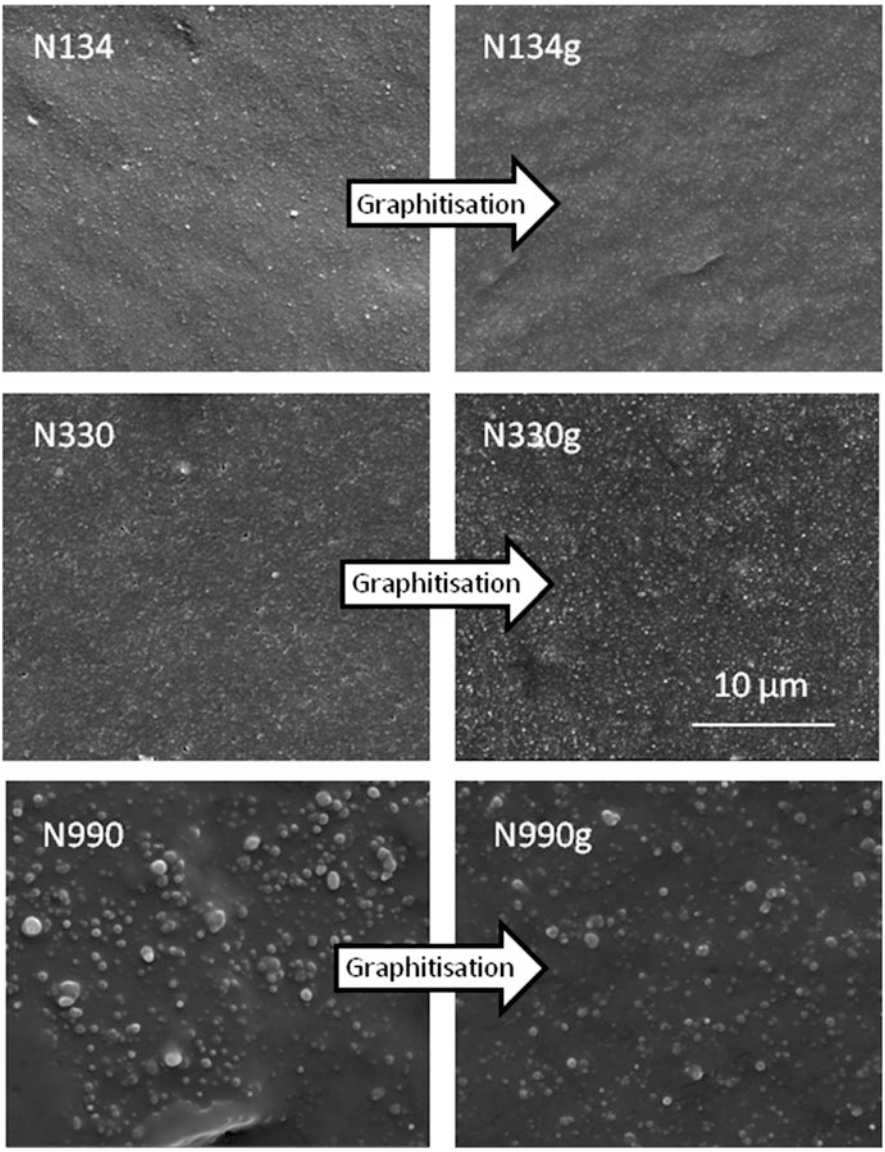

Fig. 7 SEM micrographs of cryogenic fracture surfaces of CB-filled compounds. The 10 µm *scale bar* is valid for all images

immediately dropped to 0.1% and the dynamic properties were monitored for 20 min. The frequency for all testing was fixed at 1 Hz.

The resulting data are presented in Fig. 8, which plots the recovery of the storage moduli of the materials following a dynamic shear strain sweep up to 10%.

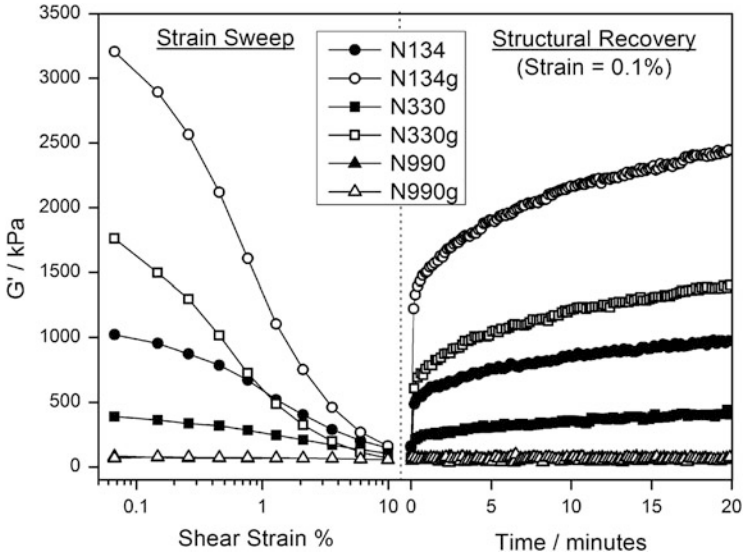

Fig. 8 Strain sweep/structural recovery test data. Plate temperature was 150°C and test frequency was 1 Hz

Materials filled with N134 and N330 grades of CB (as well as their graphitised analogues) all demonstrated an initially rapid thixotropic recovery following the imposed shear, which progressively slowed with time. Such a time dependence cannot therefore be captured by a single exponential process The precise physical mechanisms underpinning this thixotropy are still somewhat unclear but there is substantial evidence to suggest that it is related to dynamic flocculation of the filler aggregates [19] and a progressive, self-limiting jamming of the filler network [21–23, 47]. The strain sweep/recovery tests shown in Fig. 8 are strong evidence for the existence, at a volume fraction of 0.20, of localised or percolating filler networks within these rubber materials. In contrast, the N990-based CBs impart no detectable time-dependent characteristics to the rheology of the uncrosslinked rubber. This suggests that the filler networking capacity of this non-reinforcing CB is negligible. The thixotropic recovery of the filler network is far larger and more rapid for the graphitised CBs than for their unmodified counterparts, indicating a greater extent of filler flocculation and network development for these compounds.

3.2 Modelling and Physical Origins of Flocculation

The time-dependent nature of this structural recovery/evolution of the filler network has been the subject of recent studies [20–23, 48]. Meier and Klüppel [19] observed similar effects induced by thermal annealing of CB-filled solution styrene-

butadiene rubber (S-SBR) and captured the time dependence using a bi-exponential deconvolution (Eq. 2):

$$G^{'} = G_1^{'}\left(1 - e^{-k_{\text{fast}}t}\right) + G_2^{'}\left(1 - e^{-k_{\text{slow}}t}\right) \tag{2}$$

where t is the experimental time, k_{fast} is the rate constant corresponding to the initial rapid contribution and k_{slow} is the rate constant for the slower contribution. Meier and Klüppel proposed that the two fitting constants could be attributed to fast and slow structural reorganisations of aggregate clusters over different length scales. Such a model is also found to capture the data presented here (example given in Fig. 9a, b), indicating that there is a microstructural equivalence between flocculation effects induced by a step change in temperature (annealing) and those induced by pre-shearing

More recently, Robertson [23] examined flocculation in filled rubbers and critically reviewed models for capturing the form of the time-dependent recovery of the filler network, including exponential, stretched exponential and bi-exponential models. Robertson pointed out that the physical motivation for a bi-exponential model is still not fully understood and proposed a new model to capture this time dependence. The model is based on self-limiting jamming of the filler network through an analogy with physical ageing in glass-forming materials. Experimental evaluation of Robertson's model requires a more extensive rheological characterisation which is based on the experimental procedure established by Richter and co-workers [47].

A key observation from Fig. 8 is that where filler networking is apparent, graphitisation of the CB results in an increase in flocculation magnitude, which implies a greater extent of filler networking. Additionally, an increase in flocculation rate and corresponding decrease in the electrical percolation threshold are observed with graphitisation (these aspects are discussed in more detail in a separate publication [20]). One microstructural rationalisation of these observations is that the flocculation process is diffusion driven and strongly dependent on the attractive forces between filler aggregates to drive aggregate clustering. This process is also dependent on the boundary condition at the filler–rubber interface, which defines the effective Brownian diffusion coefficient, δ, of the aggregate [49]. This is given by Eq. (3), the Stokes–Einstein equation for the case of a spherical particle where η_{eff} is the effective viscosity experienced at the aggregate surface and r is the particle radius:

$$\delta = \frac{\mathbf{k}T}{\eta_{\text{eff}} 6\pi r} \tag{3}$$

Given the temperatures and timescales relevant for rubber compound processing, the viscosity of the rubber matrix and average filler aggregate size, it is apparent that the diffusion distances required to stiffen the matrix must be small, of the order of a few nanometres.

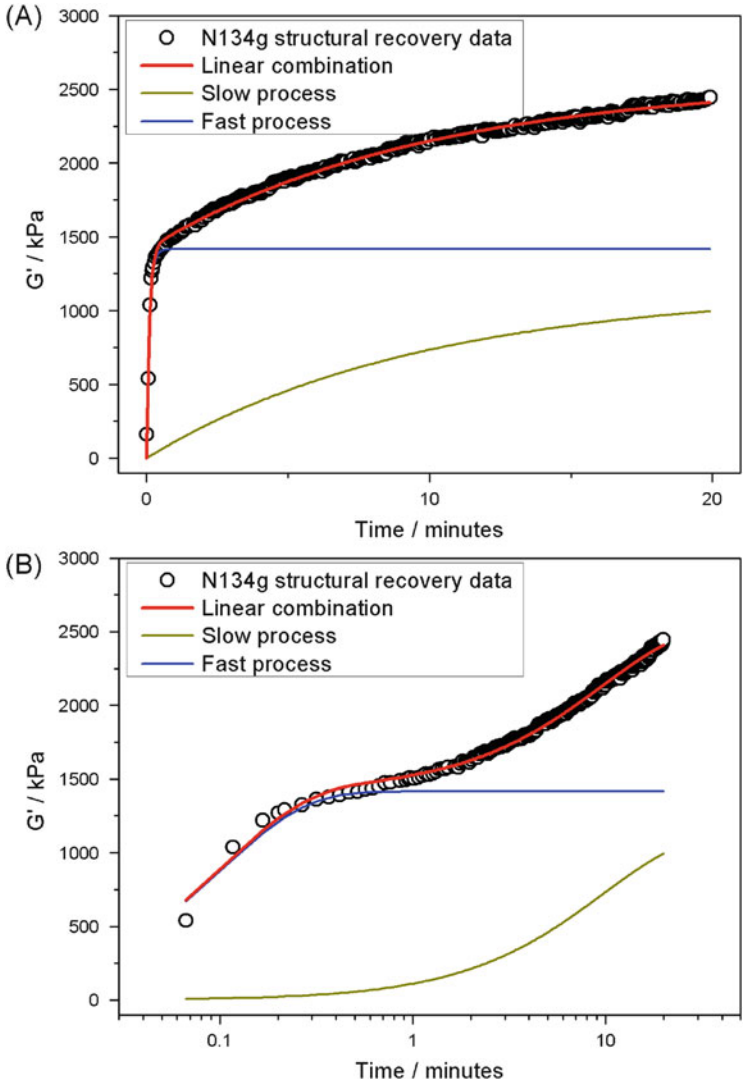

Fig. 9 Bi-exponential flocculation model fitted to structural recovery data for N134g-filled compound (**a**) with a linear time axis and (**b**) with a logarithmic time axis

The inference from this hypothesis is that post graphitisation, sufficient aggregate–aggregate interactions remain to drive a dynamic flocculation process, even though graphitisation reduces the polymer–filler interaction and thereby reduces the effective Brownian drag of rubber chains on the aggregate surface in the uncrosslinked melt and increases the aggregate diffusion coefficient. The net result of these effects is the development of a more flocculated small strain filler network [7, 20]. This is correlated with reduced interaggregate gap distances for

graphitised CB compared with unmodified CB-filled materials, as determined from dielectric spectroscopy data [45]. However, it should be reiterated that the exact mechanism of flocculation is still the subject of debate. For example, Schwartz et al. [50] carried out TEM microscopy studies and found no evidence of CB aggregate mobility in uncrosslinked rubber.

Rheological experiments provide further evidence that the dynamics of the filler network are crucial for understanding the observed effects of particle reinforcement of rubber. The filler network is predominantly established during thermal crosslinking of filled rubbers through a flocculation process that is highly dependent on aggregate–aggregate interactions and polymer–filler interactions. The temperature and strain dependence of the resulting flocculated filler network in the crosslinked compound is intimately related to the performance of rubber components and, as such, has been the subject of much research.

In practice, flocculated filler networks have been found to demonstrate a range of phenomena reminiscent of glass-forming materials. Such phenomena include strain memory effects [51, 52], asymmetric network kinetics and moduli crossover effects [18]. Furthermore, as part of his seminal work on structural relaxation in various glass-forming materials, Struik demonstrated very clear physical ageing effects in highly filled rubbers at temperatures well above the polymer T_g, using small strain creep tests to probe the temporal evolution of their retardation spectra following thermal quenching [53–55]. This simple observation has far-reaching implications for the reinforcement of rubber.

4 Physical Ageing of Filled Rubbers: The Role of Flocculation and the Filler Network

4.1 Physical Ageing in Non-equilibrium Materials

Physical ageing is a phenomenon associated with non-equilibrium and is observed in a wide range of different materials, such as colloidal suspensions [56, 57], gels [58, 59], granular powders [60] and, most obviously, polymeric materials [61]. Figure 10 plots an intrinsic material parameter versus temperature, illustrating physical ageing as typified by an unfilled, amorphous polymer. In this example, volume is taken as the parameter but mechanical or thermodynamic properties could equally be used as a descriptor. In the higher temperature regime, the polymer is in equilibrium. When the material is rapidly cooled from equilibrium temperature T_1 down to temperature T_2, which is below T_g, the timescales for structural reorganisation within the material increase by several orders of magnitude and deviation from the projected equilibrium values are observed. Physical ageing (also called structural relaxation) is observed as a slow approach towards equilibrium of the material parameter at temperature T_2 as a function of time. Physical ageing can be observed in a wide range of materials using various experimental techniques such as volumetric studies

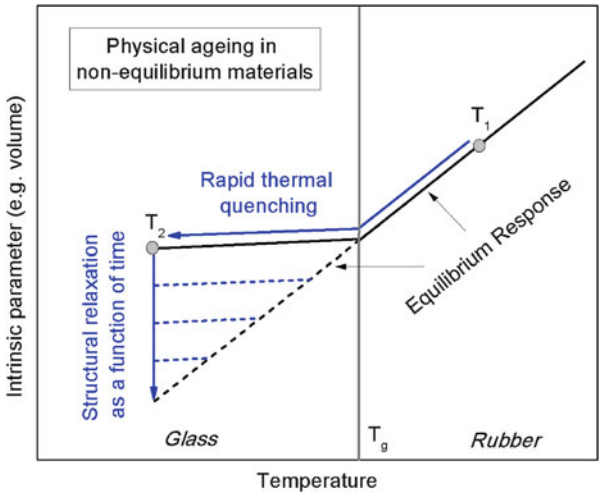

Fig. 10 Schematic of physical ageing in non-equilibrium materials. The illustrated example is for an unfilled, amorphous polymer. *Black dashed line* indicate the projected equilibrium values

[60], calorimetric measurements, small angle X-ray scattering [58] and dynamic light scattering [59]. Similarly, rheological or mechanical measurements can be used to track the evolution of the material retardation spectrum towards equilibrium [55].

The prerequisite for physical ageing is the transition from equilibrium (fast dynamics) to non-equilibrium (slow dynamics). In polymeric materials this condition is satisfied by structural arrest at the T_g. In non-polymeric materials such as colloids or granular materials, such a transition can occur after cessation of high shear deformations or through changes in material density.

Struik's observation of physical ageing in filled rubbers at thermal quenches far above the polymer T_g is therefore intriguing and is of major significance for particle reinforcement (although it is seldom directly discussed in the literature) [54, 55]. The implication is that the composite material is in a non-equilibrium condition and exhibits slow dynamics, even at temperatures well above the T_g of the polymer phase where one would expect the polymer part of the composite to be in equilibrium. It is important to note that at the filler loadings used by Struik (e.g., 30% volume of HAF grade CB), the filler phase would certainly be present in the form of a flocculated particle network ($\varphi > \varphi_c$), even though this is not explicitly stated in the text of the reference. Given that the previous section of this paper and many other investigations reported in the literature have inferred that the dynamics of the filler network are distinct from that of the unfilled rubber matrix [7, 16, 24, 29], it is of interest to probe the correlation between filler networking and physical ageing in filled rubbers at temperatures above T_g.

The materials used in this section of the study are crosslinked analogues of the materials prepared for the previous flocculation experiments. Compounds were crosslinked using 2 phr of dicumyl peroxide added on a two-roll mill. Crosslinking with peroxide yielded a simple two-phase rubber compound (NR/CB) without the

extraneous non-network material that can be associated with sulphur-based vulcanisation systems.

4.2 Experimental Characterisation of Physical Ageing of Filled Rubbers

Small strain creep tests were performed on the crosslinked CB-filled materials using a custom-built torsional creep apparatus. Strains were small enough to reliably probe the linear region of the material response – below the onset of the Payne effect (see Appendix 1 for discussion). A small, constant torsional force was applied to cylindrical specimens measuring 12 mm diameter and 150 mm in height using a calibrated non-contact induction mechanism (explained in detail in Appendix 1). The resulting elastic and inelastic responses of the samples were recorded using a non-contact displacement sensor. Calibrations were performed to ensure that data were collected in the linear stress–strain response regime for each material (see Appendix 1).

An experimental program similar to that defined by Struik [55] was used to examine physical ageing effects in the CB-filled materials at small strains. Cylindrical samples of material were held isothermally at 70°C for 18 h before being rapidly quenched to 25°C and mounted in the torsional creep rig. Note that this 'quench' sequence is performed at temperatures well above the glass transition of the materials (corresponding to $T_g + 130$ K $\rightarrow T_g + 80$ K). Creep tests lasting 10^3 s were performed at specified time intervals after the thermal quench. Note that the creep experiment timescale was short in contrast to the ageing time steps between sequential creep tests, allowing any superposition of the test histories to be ruled out. Time steps for the creep experiments post-quench, t_e, were 0.75, 1.5, 3, 6, 12 and 24 h. The constant torsional stress imposed on the samples during creep testing was 835 Pa for the least compliant samples (N134, N134g, N330, N330g) and 148 Pa for the more highly compliant samples (N990, N990g).

It is crucial to note that all the creep tests were performed at small strains (between 0.009 and 0.04% maximum strain during any individual creep experiment) and that the sample cylinders were not subjected to deformation during handling and mounting of the samples. Appendix 1 gives an extended discussion of how the materials were handled and mounted without straining. It is therefore possible to rule out any contributions to the apparent physical ageing response arising from strain-induced damage and subsequent structural recovery (thixotropy) of the materials.

4.3 Physical Ageing of the Creep Response of Filled Rubbers

Compliance–time data are presented in Fig. 11b–f for each material in this study together with data digitised from Struik [55] for comparison (Fig. 11a). Creep data

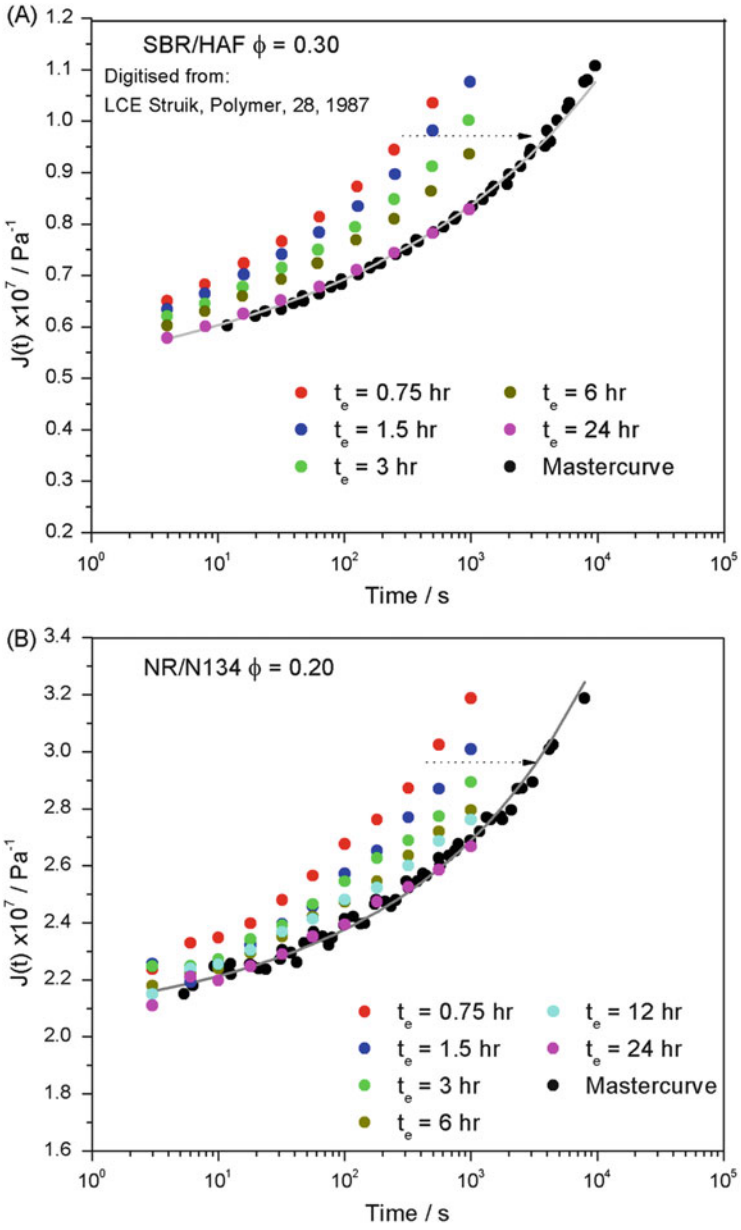

Fig. 11 (**a**) Data reproduced from Struik [54] for CB-filled SBR at a filler volume fraction of 0.30. (**b**–**f**) Creep data for material filled with (**b**) N134, (**c**) N134g, (**d**) N330, (**e**) N330g and (**f**) N990 and N990g

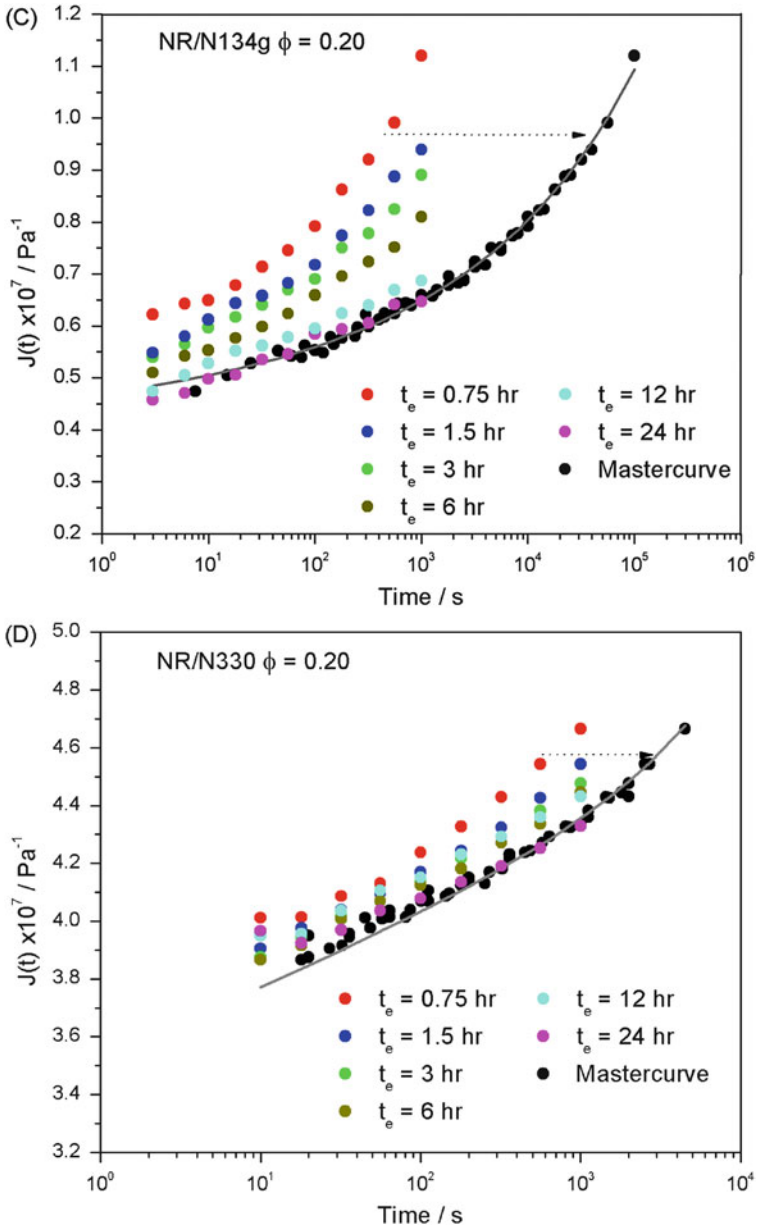

Fig. 11 (continued)

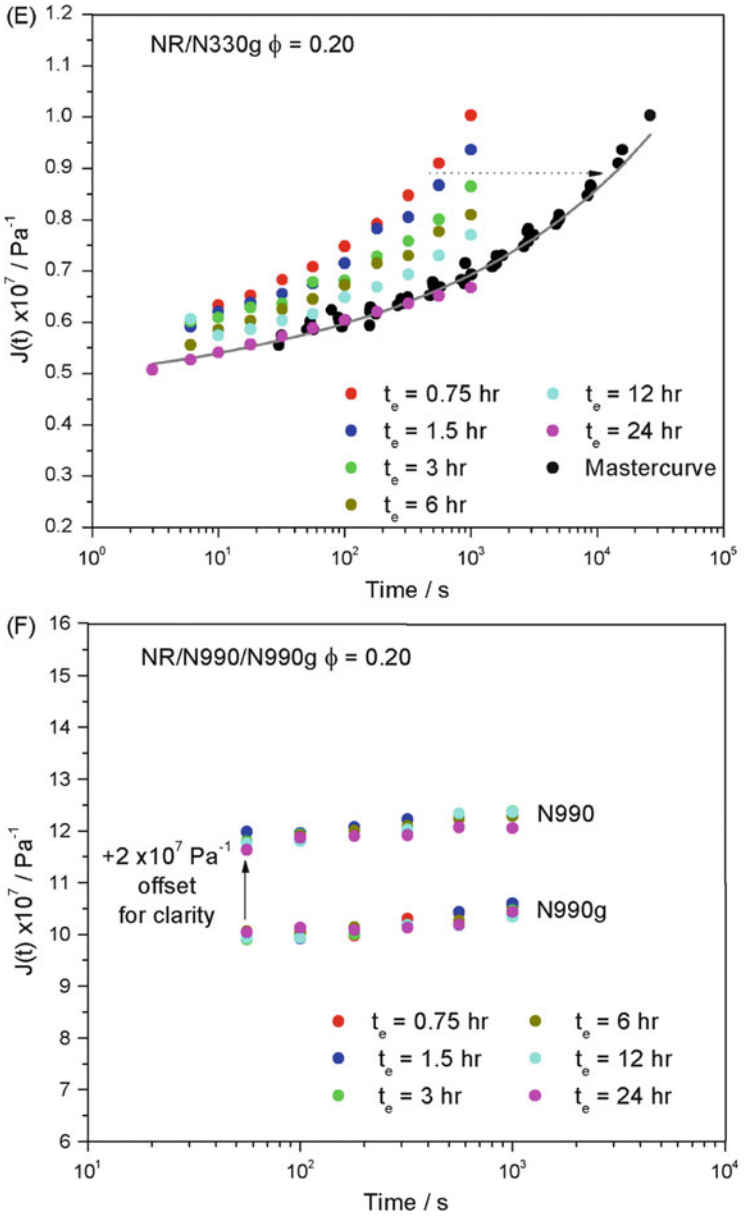

Fig. 11 (continued)

are presented for each ageing time. Physical ageing is identified as a shift to longer timescales of the creep response with increasing ageing time, t_e. This corresponds to a progressive shifting of the retardation spectrum of the material towards equilibrium. Also shown are creep master curves produced by horizontal shifting of each creep data set by a shift factor, a_t, relative to the $t_e = 24$ h data set (shifting is simply achieved using Eq. (4), where the shift in ageing time is from t_e to $t_e^{'}$):

$$J_{t_e'}(t) = J_{t_e}(a_t t) \tag{4}$$

All materials displayed clear physical ageing except materials filled with N990 and N990g, which displayed no evidence of physical ageing within the precision of the experiment. Note that data for the most compliant materials (N990 and N990g) was curtailed at short timescales as a result of inertial ringing from the experimental equipment.

The physical ageing rate, μ, is calculated for each material from the gradient of the plots of $\log(a_t)$ versus $\log(t_e)$ in Fig. 12a. The obtained rate of physical ageing is plotted in Fig. 12b against a filler networking parameter, $\Delta G'$. This parameter is determined from the rheological data of Fig. 8. Here, the value of the storage modulus measured at high strain (10%) in the strain sweep step represents the level of reinforcement of the material apparent upon strain-induced breakup of the filler network. This is subtracted from the value of G' apparent after 20 min of structural recovery following the shear sweep. The resulting parameter, $\Delta G'$, is taken as indicative of the magnitude of filler networking in each material. A clear correlation between physical ageing of the materials and the extent of filler networking is apparent. A similar correlation is observed between the physical ageing rate, μ, and the small strain dynamic shear modulus of the compounds determined from free vibration analysis (Fig. 12c). The small strain dynamic shear modulus is also indicative of the level of filler networking. See Appendix 2 for details of the determination of the small strain shear modulus from torsion pendulum equipment.

The two material variables in Fig. 12b, c are the filler surface area and the degree of particle flocculation. The volume fraction is fixed at $\varphi = 0.2$. Low surface area N990-based fillers are incorporated well below their dc percolation thresholds [20], with no evidence of filler networking from rheometry and no physical ageing observed within the error of the measurement. Higher surface area fillers introduce more filler–rubber contact area and more filler–filler contacts. In these cases significant physical ageing is observed. More flocculated materials (graphitised CBs) result in even greater rates of physical ageing than their dispersed analogues. The presence of filler networking appears to be a prerequisite for physical ageing of filled rubbers above their T_g (at least within the precision of the experiments performed). The filler network is therefore in a state of non-equilibrium above the rubber T_g following thermal quenching.

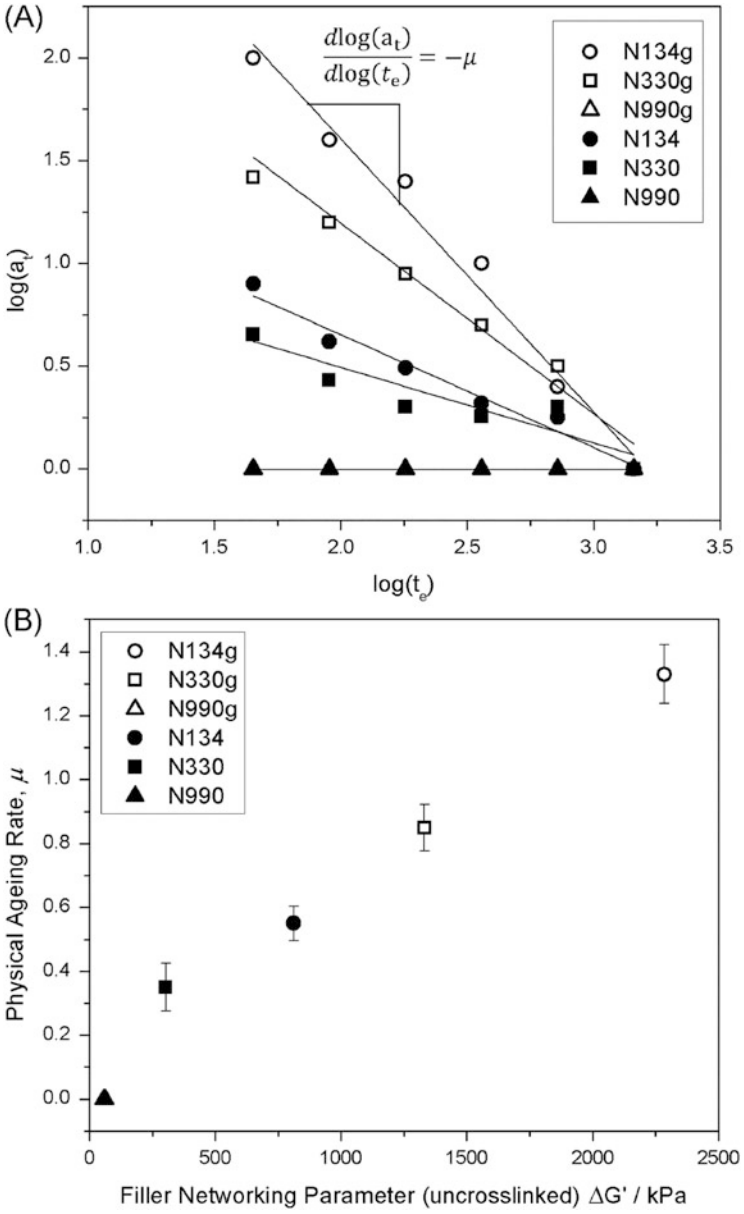

Fig. 12 (**a**) Dependence of the horizontal shift factors of each material on the ageing time, t_e. The ageing rate is taken from the gradient of the linear regressions. (**b**) Relationship between the rate of physical ageing, μ, and $\Delta G'$, which is the filler networking parameter determined from rheology experiments on uncrosslinked compounds at 150°C. (**c**) Relationship between μ and the small strain dynamic shear modulus, G', of the crosslinked compounds at 25°C

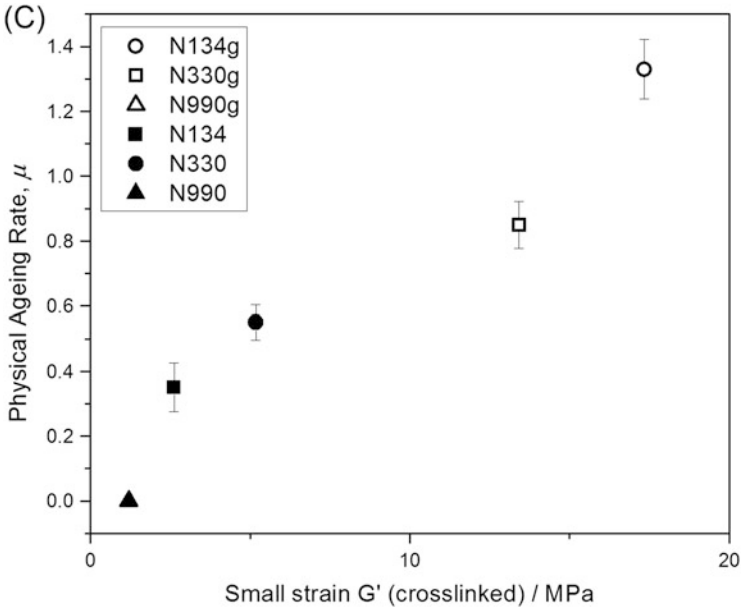

Fig. 12 (continued)

4.4 Microstructural Origins of Physical Ageing in Particle-Reinforced Rubber

The microstructural basis for the non-equilibrium nature of the filler network is of major significance for particle reinforcement of rubber. Figure 13 contrasts the observed ageing of the compliance of a filled rubber above the percolation threshold with the segmental relaxation time of the corresponding unfilled rubber. Clearly, the unfilled rubber is in equilibrium above the T_g and cannot undergo physical ageing until the relaxation time increases by several orders of magnitude at and below the T_g.

Struik [54, 55] attributed physical ageing in filled rubbers at temperatures above T_g to a filler-induced broadening of the rubber glass transition into the rubbery region, in which the observed physical ageing effects originate from a localised slowing down of the dynamics of the polymer in the vicinity of the filler particles. Potentially, this provides a qualitative understanding of the observed physical ageing effects. The mechanics of fractal aggregate cluster networks are governed by the force constant of bonds between filler particles [19, 62]; therefore, confined 'glassy bridges' of polymer between filler aggregates could dictate the total physical ageing response of the filler network. However, it is important to stress that direct experimental confirmation of such a glassy, immobilised polymer is difficult to obtain in commercially relevant materials [63]. Our previous investigations using

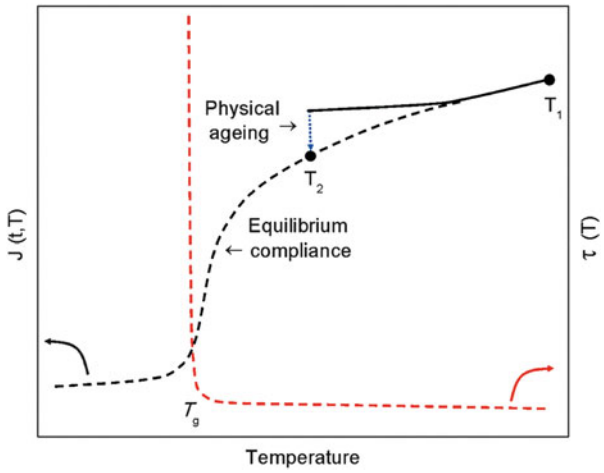

Fig. 13 Correlation between segmental relaxation of an unfilled rubber and equilibrium compliance in filled rubber. The *dashed red line* corresponds to the segmental relaxation time of the unfilled rubber, τ, as a function of temperature. The *dashed black line* corresponds to the small strain temperature-dependent equilibrium compliance of the filled rubber. The experiments correspond to a quench from T_1 to T_2 (both above the onset of slow dynamics in the unfilled rubber), with the observation of a slow relaxation towards equilibrium (physical ageing)

calorimetry and dielectric spectroscopy found no evidence for any effect of the presence of filler on the rubber glass transition in the materials considered here [64].

An alternative explanation for this apparent glass-like behaviour is potentially found in the analogous non-equilibrium behaviour (including physical ageing) of traditional polymeric glass formers with colloidal glasses, gels and granular materials. The onset of non-equilibrium in highly concentrated particle systems can be described by the general concept of the jamming transition, where changes in temperature, volume concentration of the rigid component or mechanical energy result in changes from fluid to solid-like behaviour of the material and vice versa [65, 66]. From studies on the rheology and dynamics of fractal aggregate suspensions, colloids and gels it is clear that particle suspensions can display complex glass-like behaviour and slow dynamics, even in the absence of a glass-forming matrix [56–60, 67, 68]. It may be possible to explain the observed physical ageing effects if we consider the flocculated filler network simply as a subset of such systems, without the need to invoke any drastic changes in the dynamics of the polymer matrix.

The concept of the jamming transition and the non-equilibrium of particle networks in filled rubbers has been explored in the strain domain by considering flocculation of filler networks following high shearing conditions [23]. The extent to which jamming/flocculation of the filler network can explain the temperature domain effects highlighted in this paper are issues for further study. This could include studies of CB suspensions in Newtonian fluids—to observe any physical ageing behaviour in systems in the absence of a polymeric matrix—or a study of

physical ageing of filled rubbers using dielectric spectroscopy, whose observable experimental behaviour is dominated by the dynamics of the conductive CB particles.

4.5 Relevance of Physical Ageing to the Breakdown of Time–Temperature Superposition

Small strain physical ageing of highly filled rubbers has implications for the stepped isothermal data collection typically used for construction of master curves (note that these isothermal steps are essentially small thermal quench steps towards the T_g). The breakdown of superpositioning of isothermal data is related to a significant temperature dependence of the filler network in the rubbery region. Physical ageing effects upon thermal quenching, as detailed in this paper, reflect a substantial increase in the non-equilibrium nature of the filler network as temperatures are reduced. Thus, the breakdown of TTS seems to originate from a slowing down of filler structural dynamics as the temperature is reduced, which results in significant physical ageing of the dynamic moduli at each isotherm. One could anticipate a correlation between horizontal shifts of creep curves in physical ageing experiments and vertical shifts of TTS isotherms, which can be used to ameliorate the temperature sensitivity of the filler network during construction of master curves.

5 Conclusions

Changes in the dynamic nature of rubber compounds as a result of introduction of reinforcing filler particles were examined using various dynamic and static mechanical techniques. The linear viscoelastic dynamics of compounds reinforced with model microsphere filler particles can be ascribed to the dynamics of the rubber matrix. This is a result of the hydrodynamic origin of reinforcement in such compounds. This is no longer the case once significant volumes of high surface area CB aggregates are introduced. The collapse of thermorheological simplicity indicates a new dynamic contribution to the viscoelastic response of the filled rubber, which is distinct from that of the corresponding unfilled rubber and is attributable to the formation of a filler network. The dynamic nature of the filler network was probed using simple strain sweep/recovery tests to probe flocculation in uncrosslinked materials. The role of the surface activity of CB in the flocculation process was highlighted. For crosslinked CB-filled compounds, small strain torsional creep tests revealed significant physical ageing effects at temperatures well above the T_g of the rubber matrix. The observation that the rate of physical ageing scales with the degree of filler networking in the various compounds (at least for the series of compounds studied here) suggests that filler networking is a prerequisite for physical ageing in filled rubbers. Physical ageing is associated with

non-equilibrium and, as such, is evidence that the filler network possesses glass-like dynamics. The potential microstructural origins of these dynamics were discussed. The effect of physical ageing on linear viscoelastic time–temperature superposition experiments was also discussed. The breakdown of thermorheological simplicity in highly filled rubbers originates from a slowing down of the filler network structural dynamics as the temperature is reduced.

Appendix 1: Torsional Creep Equipment and Experiments

Torsional creep apparatus is illustrated in Fig. 14.

Filled rubbers were compression moulded into cylinders of 150 mm length and 12 mm diameter. To minimise straining caused by sample handling, the mould design included thin flanges of excess crosslinked material attached to either side of the sample cylinder. This allowed the sample to be removed from the mould and subsequently handled without excessive pre-straining. Silicone-based mould release agent was also applied to the sample moulds prior to curing to lubricate removal of the samples from the mould. Cylindrical samples were then bonded by one end-face to a steel plate and by the other to a threaded screw using Loctite 480 adhesive. Once bonded in place, the flanges could then be trimmed from the

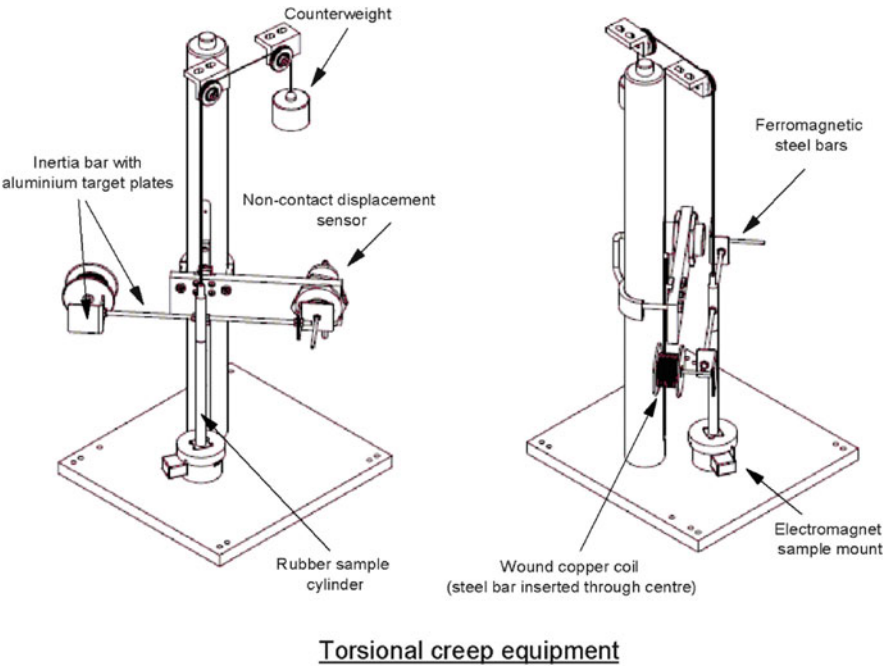

Fig. 14 Torsional creep rig setup, showing two different views of the equipment

sample using a scalpel. The samples were attached to the inertia bar via a screw thread and located and fixed to the bottom of the pendulum using an electromagnet locator system. Two aluminium plates were located at each end of the inertia bar and the bar was counter-balanced in the vertical direction using a pulley system. The central cylinder of the inertia bar seen in Fig. 14 had a diameter of 15 mm and a length of 65 mm. The arms and sensor target panels were constructed of stainless steel, giving the inertia bar a total length of 240 mm. Small steel side arms were attached at the extremities of the inertia bar projecting along the torsional plane of motion. One of these side arms passed through a wound copper coil. Passing a small, constant current through the coil induced a small, constant torsional force across the sample. The consequent elastic and inelastic creep displacements were measured by a non-contact displacement sensor for 1,000 s, after which the force was removed by cutting the current to the coil. The magnitude of the applied current depended on the sample in question. For the more compliant samples (N990, N990g), a current of 20 mA was required to produce an initial elastic deformation and creep behaviour that could be resolved by the sensor. For the stiffer samples (N330, N330g, N134, N134g), a current of 80 mA was required. Strain–time data were calculated from the raw voltage–time output by suitable calibration of the non-contact displacement sensor and calculation of the torsional strain, γ, in the sample by Eq. (5):

$$\gamma = \theta\left(\frac{r_{\max}}{l}\right) \tag{5}$$

where θ is the angular deflection in radians, $r_{\max}$ is the radius at the extremity of the sample cylinder and l is the length of the cylinder. Maximum torsional creep strain values were found to be in the range of 0.009–0.04%, depending on the compound, which is well below the onset of non-linear effects.

The torsional stress applied to the samples during the creep experiments was calculated by calibrating the force exerted by the copper coil on the side arm as a function of coil current. Force was converted to torsional stress, τ, using Eq. (6):

$$\tau = \frac{T_q d}{2I} \tag{6}$$

where T_q is the torque, d is the diameter of the sample cylinder and I is the second moment of area of the cylinder. Values of τ were used to convert shear strain into compliance.

Appendix 2: Free Vibration Experiments

The small strain linear viscoelastic storage moduli of the CB-filled compounds were determined by applying a small excitation across the sample cylinders via the inertia bar. The subsequent decay in free vibration was recorded by a non-contact displacement sensor. The vibration trace was analysed using Eq. (7):

$$G' = \left(\frac{2If^2}{\pi}\right)\left(\frac{l}{r^4}\right) \tag{7}$$

where I is the inertia of the pendulum, f is the frequency of oscillation, l is the length of the sample cylinder and r is the cylinder radius. The strain range of these experiments was between 0.001 and 0.01% shear strain (relative to the exterior radius of the cylinder), which is well below the onset strains of non-linear responses.

References

1. Fletcher WP, Gent AN (1953) Rubber Chem Technol 26:181–187
2. Fletcher WP, Gent AN (1953) Rubber Ind Trans Inst 27:209–222
3. Payne AR (1963) Rubber Chem Technol 36:432–443
4. Payne AR (1963) Rubber Chem Technol 36:444–450
5. Payne AR (1957) Rubber Chem Technol 30:218–241
6. Robertson CG, Lin CJ, Rackaitis M, Roland CM (2008) Macromolecules 41:2727–2731
7. Wang MJ (1998) Rubber Chem Technol 71:520–589
8. Payne AR, Whittaker RE (1971) Rubber Chem Technol 44:440–478
9. Chazeau L, Brown JD, Yanyo LC, Sternstein SS (2000) Polym Compos 21:202–222
10. Roland CM (1990) J Rheol 34:25–34
11. Clément F, Bokobza L, Monnerie L (2005) Rubber Chem Technol 78:211–231
12. Göritz D, Raab H, Frohlich J, Maier PG (1999) Rubber Chem Technol 72:929–945
13. Maier PG, Göritz D (1996) Kautschuk Gummi Kunststoffe 49:18–21
14. Sternstein SS, Zhu AJ (2002) Macromolecules 35:7262–7273
15. Busfield JJC, Jha V, Hon AA, Thomas AG (2005) Investigation of interfacial slippage on filler reinforcement in carbon-black filled elastomers. In: Austrell PE, Kari L (eds) Constitutive models for rubber IV: Proceedings of fourth European conference on constitutive models for rubber, Stockholm, June 2005. Balkema, London, pp 459–464
16. Fritzsche J, Klüppel M (2011) J Phys Condens Matter 23:035104
17. Merabia S, Sotta P, Long DR (2008) Macromolecules 41:8252–8266
18. Wang XR, Robertson CG (2005) Phys Rev E 72:031406
19. Meier JG, Klüppel M (2008) Macromol Mater Eng 293:12–38
20. Tunnicliffe LB, Kadlcak J, Shi Y, Morris MD, Thomas AG, Busfield JJC (2014) Macromol Mater Eng 299:1474–1483
21. Richter S, Kreyenschulte H, Saphiannikova M, Gotze T, Heinrich G (2011) Polym Networks 306–307:9
22. Richter S, Saphiannikova M, Heinrich G (2010) Flocculation kinetics in the light of jamming physics: new insights into the Payne-effect in filled rubbers. In: Heinrich G, Kaliske V, Lion A, Reese S (eds) Constitutive models for rubber VI: Proceedings of the sixth European conference on constitutive models for rubber, Dresden, September 2009. Balkema, Leiden, pp 205–210
23. Robertson CG (2015) Rubber Chem Technol 88:463–474
24. Heinrich G, Klüppel M (2002) Adv Polym Sci 160:1–44
25. Klüppel M (2003) Adv Polym Sci 164:1–86
26. Busfield JJC, Thomas AG, Yamaguchi K (2004) J Polym Sci Part B Polym Phys 42:2161–2167
27. Yamaguchi K, Busfield JJC, Thomas AG (2003) J Polym Sci Part B Polym Phys 41:2079–2089
28. Busfield JJC, Thomas AG, Yamaguchi K (2005) J Polym Sci Part B Polym Phys 43:1649–1661

29. Mujtaba A, Keller M, Ilisch S, Radusch HJ, Beiner M, Thurn-Albrecht T, Saalwächter K (2014) ACS Macro Lett 3:481–485
30. Mujtaba A, Keller M, Ilisch S, Radusch HJ, Thurn-Albrecht T, Saalwächter K, Beiner M (2012) Macromolecules 45:6504–6515
31. Einstein A (1906) Ann Phys 19:289
32. Smallwood HM (1945) Rubber Chem Technol 18:292–305
33. Guth E (1945) J Appl Phys 16:20–25
34. Wolff S, Donnet J-B (1990) Rubber Chem Technol 63:32–45
35. Hon AA, Busfield JJC, Thomas AG (2003) Filler reinforcement in rubber carbon black systems. In: Busfield J, Muhr A (eds) Constitutive models for rubber III: Proceedings of the third European conference on constitutive models for rubber, London, September 2003. Balkema, Lisse, pp 301–308
36. Jha V, Hon AA, Thomas AG, Busfield JJC (2008) J Appl Polym Sci 107:2572–2577
37. Fukahori Y, Hon AA, Jha V, Busfield JJC (2013) Rubber Chem Technol 86:218–232
38. Donnet JB, Bansal RC, Wang MJ (eds) (1993) Carbon black: science and technology, 2nd edn. Marcel Dekker, New York
39. Lorenz B, Pyckhout-Hintzen W, Persson BNJ (2014) Polymer 55:565–571
40. Klüppel M (2009) J Phys Condens Matter 21:10
41. Arai K, Ferry JD (1986) Rubber Chem Technol 59:592–604
42. Donnet JB (1998) Rubber Chem Technol 71:323–341
43. Schröder A, Klüppel M, Schuster RH (2007) Macromol Mater Eng 292:885–916
44. Dannenberg E (1975) Rubber Chem Technol 48:410–444
45. Geberth E, Klüppel M (2012) Macromol Mater Eng 297:914–922
46. Randall AM, Robertson CG (2014) J Appl Polym Sci 131:10
47. Richter S, Saphiannikova M, Stöckelhuber KW, Heinrich G (2010) Macromol Symp 291–292:193–201
48. Stöckelhuber KW, Svistkov AS, Pelevin AG, Heinrich G (2011) Macromolecules 44:4366–4381
49. Wyart FB, de Gennes PG (2000) Eur Phys J E 1:93–97
50. Schwartz GA, Cerveny S, Marzocca AJ, Gerspacher M, Nikiel L (2003) Polymer 44:7229–7240
51. Wang XR, Robertson CG (2010) J Polym Sci Part B Polym Phys 48:859–869
52. Wang XR, Robertson CG (2010) Rubber Chem Technol 83:149–159
53. Struik LCE (1987) Polymer 28:1521–1533
54. Struik LCE (1987) Polymer 28:1534–1542
55. Struik LCE (1978) Physical aging in amorphous polymers and other materials. Elsevier, Amsterdam
56. Peng XG, McKenna GB (2014) Phys Rev E 90:6
57. Di XJ, Peng XG, McKenna GB (2014) J Chem Phys 140:9
58. Cipelletti L, Ramos L (2002) Curr Opin Colloid Interf Sci 7:228–234
59. Cipelletti L, Manley S, Ball RC, Weitz DA (2000) Phys Rev Lett 84:2275–2278
60. Josserand C, Tkachenko AV, Mueth DM, Jaeger HM (2000) Phys Rev Lett 85:3632–3635
61. Hutchinson JM (1995) Prog Polym Sci 20:703–760
62. Kantor Y, Webman I (1984) Phys Rev Lett 52:1891–1894
63. Robertson CG, Roland CM (2008) Rubber Chem Technol 81:506–522
64. Huang ML, Tunnicliffe LB, Thomas AG, Busfield JJC (2015) Eur Polym J 67:232–241
65. van Hecke M (2010) J Phys Condens Matter 22:24
66. Trappe V, Prasad V, Cipelletti L, Segre PN, Weitz DA (2001) Nature 411:772–775
67. Pusey PN, Vanmegen W (1986) Nature 320:340–342
68. Pusey PN, Vanmegen W (1987) Phys Rev Lett 59:2083–2086

Adv Polym Sci (2017) 275: 103–156
DOI: 10.1007/12_2016_4

Published online: 17 August 2016

Multiscale Contact Mechanics with Application to Seals and Rubber Friction on Dry and Lubricated Surfaces

B.N.J. Persson, B. Lorenz, M. Shimizu, and M. Koishi

Abstract Fluid leakage out of mechanical equipment such as gearboxes, hydraulic systems, or fuel tanks could cause serious problems and thus should be avoided. Seals are extremely useful devices for preventing such fluid leakages. We have developed a theoretical approach for calculation of the leak rate of stationary rubber seals and the friction force for dynamic seals. The theory is based on a recently developed theory of contact mechanics, which we briefly review. To test the theory, we have performed both simple model experiments and experiments on engineering seal systems. We have found good agreement between the calculated and measured results, and hence our theory has the potential to improve the future design of efficient seals.

We briefly review the processes that determine rubber friction on lubricated smooth and rough substrate surfaces. We present experimental friction results for lubricated surfaces, obtained using a simple Leonardo da Vinci setup. The data is analyzed using the Persson rubber friction and contact mechanics theory.

Keywords Contact mechanics • Leakage • Rubber friction • Seals • Surface roughness

B.N.J. Persson (✉)
School of Chemistry, Tel Aviv University, 69978 Tel Aviv, Israel

PGI, FZ-Jülich, Jülich, Germany
e-mail: b.persson@fz.juelich.de; http://www.MultiscaleConsulting.com

B. Lorenz
PGI, FZ-Jülich, Jülich, Germany
http://www.MultiscaleConsulting.com

M. Shimizu and M. Koishi
The Yokohama Rubber Company, 2-1 Oiwake, Hiratsuka, Kanagawa 254-8601, Japan

Contents

1 Personal Introduction by Bo Persson: On My Contact with Gert Heinrich and His Influence on My Research Activity

My first contact with Gert Heinrich was in 1997 when Gert was still at the Continental Tire Company. I had just received the Walter Schottky Prize in Physics for my contributions to surface science (including friction) and I think this was why Gert knew I was working on friction-related problems. Gert invited me to give a presentation at Continental about sliding friction (not rubber friction). During this visit I told Gert that I was working on a book about sliding friction.

A year later, I had almost finished writing the first edition of my book on sliding friction [1], and I was preparing the final material during a visit to Oak Ridge National Laboratory (USA). I sent Gert a copy of the book manuscript and he wrote back suggesting that I include some material on rubber friction. I though this was an interesting idea and over the next few days I read many classical (experimental) papers on this topic (e.g., papers by Tabor, Roberts, and Grosch), as well as an important reprint I received from Gert [2]. The result was a new section for my book on rubber friction. I also published the same material in an article for *Surface Science* (my first article about rubber friction) [3].

Later, I developed my most important contribution to tribology, namely my multiscale contact mechanics theory, published in the *Journal of Chemical Physics* [4]. This turned out to be the basis for an understanding of a large number of practical topics such as rubber friction, adhesion, contact stiffness, electric and thermal contact resistance, seal leak rate, fluid dynamics at interfaces, and several other topics of technological importance. This theory also gained the interest of many companies and resulted in the formation of Multiscale Consulting (see www.MultiscaleConsulting.com), where the knowledge I have obtained in tribology (in particular the tribology of rubber-like materials) is transferred to companies. All the tribology-related activities described above are a direct result of the suggestion by Gert Heinrich to include a discussion of rubber friction in my book on sliding friction.

I have been in steady contact with Gert Heinrich ever since our first meeting in 1997, and have followed his important contributions to rubber physics and tribology, for example, his work with Klüppel and others on rubber friction [5–8]. During this long and wonderful interaction, he has always been extremely stimulating and supportive of my own research activities. We have also written some papers together, such as a review paper on crack propagation in rubber-like materials [9]. It is my hope Gert will continue to stay active in rubber tribology science and that we will have many more years of wonderful interaction.

The following text is divided into two parts. The first part is a very brief review of contact mechanics theories for randomly rough surfaces, and my own theory of contact mechanics with application to the leak rate of seals. The second part presents new results for rubber friction on wet (lubricated) surfaces, obtained in collaboration with the Yokohama tire company.

2 Contact Mechanics Theory

Nearly all surfaces have roughness, usually extending from the linear size of the object down to atomistic length scales, say from centimeters to nanometers. This can involve about seven decades in length scales, corresponding to about 10^{21} degrees of freedom if one wants to simulate the contact using numerical methods such as the finite element method (FEM). Thus, the contact between solids with surface roughness cannot be studied numerically on all relevant length scales without further simplification, and it is very important to develop analytical approaches to the contact between solids with rough surfaces.

Contact mechanics has a very long history [10]. The first work was presented by Hertz in 1882 (*Über die Berührung fester elastischer Körper*), in which he studied the frictionless contact between elastic solids with smooth surface profiles, which could be approximated as parabolic close to the contact area. This theory predicts a nonlinear increase in contact area A with the squeezing force F. The simplest model of a rough surface consists of a regular array of spherical bumps with equal radius of

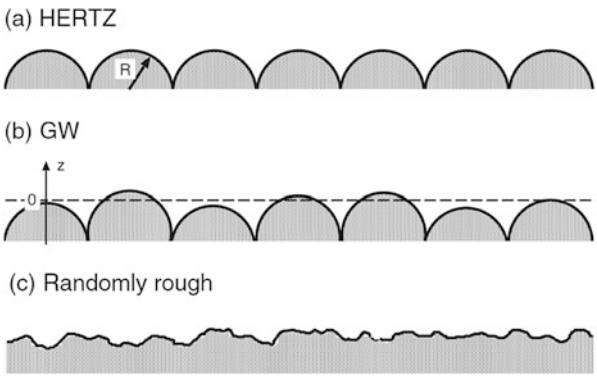

Fig. 1 Three different models of a "rough" surface. (**a**) All the asperities are equally high and have identical radius of curvature. (**b**) Introducing asperities with a random height distribution gives the Greenwood–Williamson approach towards contact mechanics. (**c**) In a real, randomly rough surface the asperities are of different heights and curvature radii

curvature R and equal height (see Fig. 1a). If such a surface is squeezed against an elastic solid with a flat surface, one can approximately apply the Hertz contact theory to each asperity. Thus, from this simple approach one expects that the real area of contact scales nonlinearly with F. However, this is not in accordance with experiments, which show that the real area of contact is proportional to F as long as $A << A_0$, where A_0 is the nominal contact area. This is also the reason why the friction force is usually proportional to the load (Coulomb friction law).

Greenwood and Williamson (GW) proposed that the contact problem between two elastic rough surfaces could be reduced to the problem of one infinitely hard rough surface acting on a flat elastic counter-surface. Within their model, the rough topography was described by a large collection of hemispherical asperities of uniform radius (which individually satisfied the Hertzian approximation) with a height distribution that followed a Gaussian law (see Fig. 1b). This model relies on the definition of "asperity." The asperity concept itself has proved to be quite controversial and depends on the resolution of the instrument used to measure the surface profile. In addition, the long-range elastic coupling between the asperity contact regions, which is neglected in the GW model, is now known to strongly influence contact mechanics (see Fig. 2). Thus, if an asperity is pushed downwards at a certain location, the elastic deformation field extends a long distance away from the asperity, influencing contact involving other asperities further away. This results in a more open contact morphology than expected if the long-range elastic coupling is neglected. This is illustrated in Fig. 3, which shows the contact between an elastic solid with a flat surface and a rigid solid with a randomly rough surface. Figure 3a is the result of an exact numerical treatment and Fig. 3b shows the result obtained neglecting the long-range elastic coupling. Note that the first case results in a more open contact morphology. This difference in contact morphology has a huge effect on some properties such as the leak rate of seals. In Fig. 3a there is no

Fig. 2 (**a**) When a high asperity makes contact with the substrate, the elastic solid in its neighborhood is displaced upwards, making it less likely for nearby smaller asperities to make contact with the substrate. This results in a more open contact morphology than expected if the long-range elastic coupling is neglected (see (**b**)), as is the case in the GW (and most other) asperity contact mechanics models

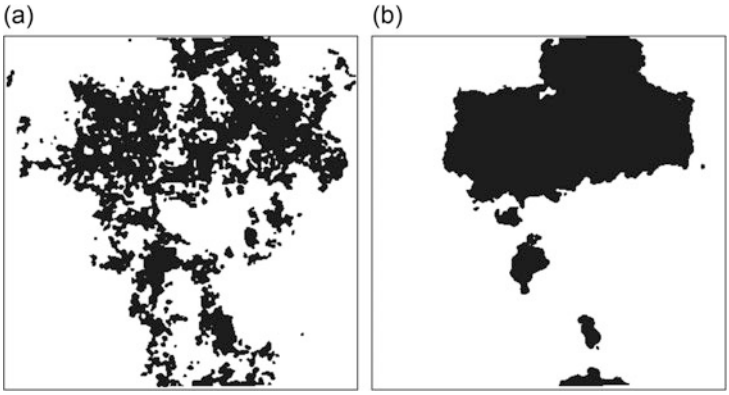

Fig. 3 Contact between an elastic solid with a flat surface and a rigid solid with a randomly rough surface: (**a**) numerically exact treatment and (**b**) results obtained neglecting the long-range elastic coupling. Note that case (**a**) results in a more open contact morphology. Adopted from [11]

noncontact channel, taking one from the right to the left, through which fluid could flow, whereas large noncontact channels can be seen in Fig. 3b.

Thus, neglect of long-range elastic coupling in the GW theory significantly limits its prediction capabilities when applied to most real surfaces. Additionally, in the GW model the asperity contact regions are assumed to be circular (or elliptical), whereas the actual contact regions (at sufficiently high experimental resolution) show fractal-like boundary lines. Therefore, one should try to avoid explicitly invoking the nature of the contact regions when searching for an analytical methodology to solve the contact problem of two rough elastic surfaces.

More recently, an analytical contact mechanics model that does not use the asperity concept and becomes exact in the limit of complete contact was developed by Persson [4]. The theory accounts for surface roughness on all relevant length scales and includes (in an approximate way) the long-range elastic coupling between asperity contact regions. In this theory, information about the surface enters via the surface roughness power spectrum, which depends on all the surface roughness wavevector components.

3 The Contact Mechanics Theory of Persson

The contact mechanics formalism developed by Persson [4] is based on study of the interface between two contacting solids at different magnifications ζ. When the system is studied at magnification ζ it appears as if the contact area equals $A(\zeta)$, but when the magnification increases, it is observed that the contact is incomplete and that the surfaces in the apparent contact area $A(\zeta)$ are in fact only in partial contact (see Fig. 4). The theory can be used to calculate the interfacial stress distribution, $P(\sigma, \zeta)$, from which one can obtain the area of contact as a function of the magnification ζ using:

$$\frac{A(\zeta)}{A_0} = \int_0^\infty d\sigma P(\sigma, \zeta), \tag{1}$$

where A_0 is the nominal contact area. The magnification ζ refers to some (arbitrary) chosen reference length scale. This could be, for example, the lateral size L of the nominal contact area, in which case $\zeta = L/\lambda = q/q_L$, where λ is the shortest wavelength roughness that can be resolved at magnification ζ. We often denote $A(\zeta)/A_0$ by $P(\zeta)$, and sometimes by $P(q)$ (where $q = q_L\zeta$).

An expression has been derived [4] for the stress distribution $P(\sigma, \zeta)$ at the interface when the interface is studied at magnification ζ. Assuming complete contact, one can show that $P(\sigma, \zeta)$ satisfies the diffusion-like equation:

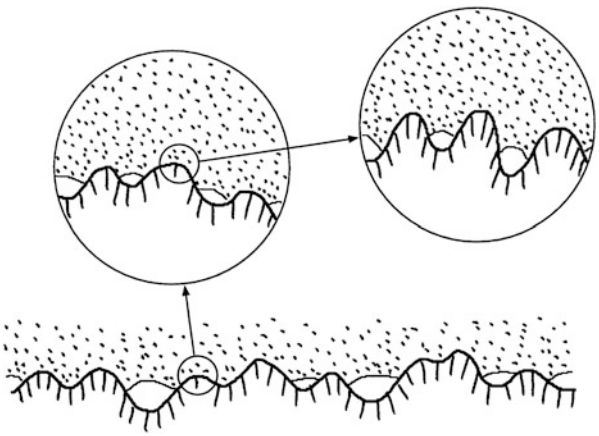

Fig. 4 An elastic block (*dotted area*) in adhesive contact with a rigid rough substrate (*dashed area*). The substrate has roughness on many different length scales, and the block makes partial contact with the substrate on all length scales. When a contact area is studied, at low magnification it appears as if complete contact occurs, but when the magnification is increased it is observed that, in reality, only partial contact has taken place

$$\frac{\partial P}{\partial \zeta} = f(\zeta)\frac{\partial^2 P}{\partial \sigma^2}, \tag{2}$$

where

$$f(\zeta) = \frac{\pi}{4}\left(\frac{E}{1-\nu^2}\right)^2 q_L q^3 C(q), \tag{3}$$

$q_L = 2\pi/L$, and $q = \zeta q_L$. In (3), the surface roughness power spectrum $C(q)$ is the Fourier transform of the height–height correlation function:

$$C(\boldsymbol{q}) = \frac{1}{(2\pi)^2}\int d^2x \ \langle h(\boldsymbol{x})h(0)\rangle e^{-i\boldsymbol{q}\cdot\boldsymbol{x}}. \tag{4}$$

Here, $z = h(\boldsymbol{x})$ is the height of the surface at the point $\boldsymbol{x} = (x, y)$ above a flat reference plane chosen so that $\langle h(\boldsymbol{x})\rangle = 0$ (here angular bracket $\langle \dots \rangle$ stands for ensemble averaging). In the following, we consider only surfaces for which the statistical properties are isotropic so that $C(\boldsymbol{q}) = C(q)$ only depends on the magnitude $|\boldsymbol{q}|$ of the wavevector $\boldsymbol{q}$.

It is now assumed that (2) also holds locally when only partial contact occurs at the interface. The calculation of the stress distribution in the latter case involves solving (2) with appropriate boundary conditions. If a rectangular elastic block is squeezed against the substrate with (uniform) stress p_0, then at the lowest magnification $\zeta = 1$, where the substrate appears flat, we have:

$$P(\sigma, 1) = \delta(\sigma - p_0), \tag{5}$$

which forms an "initial" condition. In addition, two boundary conditions along the σ-axis are necessary in order to solve (2). For elastic contact, $P(\sigma, \zeta)$ must vanish as $\sigma \to \infty$. In the absence of an adhesion interaction, the stress distribution must also vanish for $\sigma < 0$ because no tensile stress is possible without adhesion. In fact, one can show that $P(\sigma, \zeta)$ must vanish continuously as $\sigma \to 0$. One can also derive boundary conditions for elastoplastic contact, and for elastic contact with adhesion. The theory can also be applied to surfaces with anisotropic roughness and to layered materials.

Equation (2) is easy to solve with the initial condition (5) and the boundary conditions $P(0, \zeta) = 0$ and $P(\infty, \zeta) = 0$. The area of (apparent) contact when the system is studied at the magnification ζ is given by:

$$\frac{A(\zeta)}{A_0} = \frac{1}{\sqrt{\pi}}\int_0^{1/\sqrt{G}} dx \ e^{-x^2/4} = \mathrm{erf}\left(\frac{1}{2\sqrt{G}}\right), \tag{6}$$

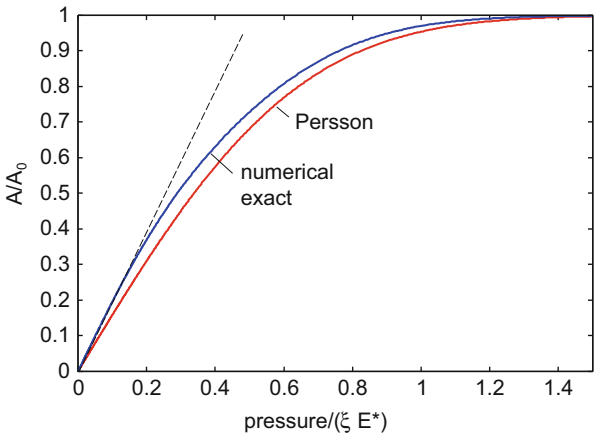

Fig. 5 Normalized (projected) contact area A/A_0 as a function of nominal applied pressure p_0 in units of ξE^*, where ξ is the surface root-mean-square (rms)-slope and $E^* = E/(1-\nu^2)$. The *blue line* is the exact numerical result (M. Müser, private communication) and the *red line* is the prediction according to the Persson contact mechanics theory. The *dashed line* has a slope of ≈ 2.0 [12, 13]

where

$$G(\zeta) = \frac{1}{8}\left(\frac{E}{(1-\nu^2)p_0}\right)^2 \xi(\zeta) \tag{7}$$

and

$$\xi^2 = 2\pi \int_{q_L}^{\zeta q_L} dq \; q^3 C(q)$$

is the surface mean-square slope. Using $\mathrm{erf}(x) \approx 2x/\sqrt{\pi}$ for $x << 1$ one can show that when the squeezing force $F_N = p_0 A_0$ is so small that $A << A_0$, Eq. (7) reduces to $A/A_0 \approx \kappa p/\left(\xi E^*\right)$ where $E^* = E/(1-\nu^2)$ and $\kappa = (8/\pi)^{1/2} \approx 1.6$. Thus, the Persson theory predicts that the contact area is a universal function of $p_0/(\xi E^*)$ and that it increases linearly with the squeezing force F_N as long as the contact area is small compared with the nominal contact area. Figure 5 shows the normalized (projected) contact area A/A_0 as a function of the nominal applied pressure p in units of ξE^*. The blue line is the exact numerical result (M. Müser, private communication and [12, 13]) and the red line is the prediction of the Persson contact mechanics theory [Eq. (6)]. Note that the initial slope of the $A(p_0/(\xi E^*))$ relation is about 20 % larger in the exact numerical study than in the Persson theory (≈ 2.0 compared with ≈ 1.6). This is the result of overestimation of the elastic energy stored in the asperity contact regions in the Persson theory, and can be corrected for in a phenomenological way [14].

Figure 6 shows the normalized (projected) contact area A/A_0 as a function of the magnification $\zeta = q/q_0$ obtained from (6) and (7) for $E^* = E/(1-\nu^2) = 5$ MPa and for the nominal contact pressure $p_0 = 0.2$ MPa. The inset shows the surface roughness power spectrum used in the calculation. The contact between solids can sometimes (for transparent material) be studied using optical methods. However, optical measurements have a resolution determined by the wavelength of light

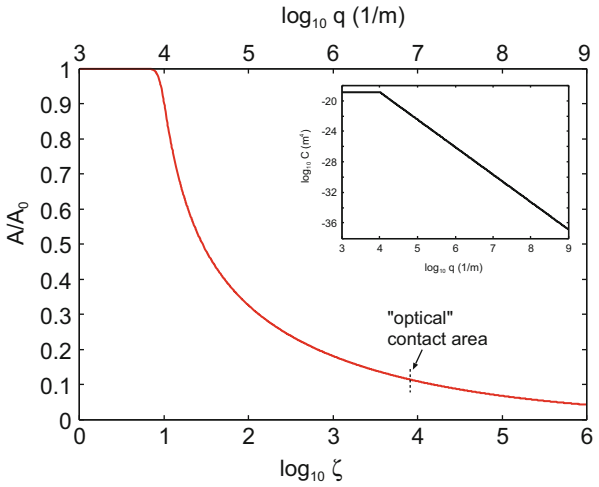

Fig. 6 The normalized (projected) contact area A/A_0 as a function of the magnification $\zeta = q/q_0$ for $E^* = E/(1-\nu^2) = 5$ MPa and nominal contact pressure $p_0 = 0.2$ MPa. The *inset* shows the surface roughness power spectrum used in the calculation. The surface has rms-roughness amplitude of 10 μm and the *straight line* corresponds to a self-affine fractal surface with the fractal dimension $D_f = 2.2$

(i.e., in the order of 1 μm). This correspond to the wavenumber $q = 2\pi/\lambda \approx 10^7$ m^{-1}. Hence, the contact area determined using an optical method is larger than the true atomic contact area (see Fig. 6). In general, the contact area measured using an optical method (and most other methods) cannot be directly related to, for example, the friction force, which is usually determined by the area of atomic contact.

Extension of the theory presented above also predicts the average interfacial surface separation $\bar{u}$ (see [15]), and the distribution of interfacial separation $P(u)$ (see [11, 16]), which is very important for the leak rate and friction of seals.

To summarize, the contact mechanics theory of Persson [4] is accurate and very flexible, and has been applied to a large number of important topics, including elastic, viscoelastic, and elastoplastic contact mechanics; rubber friction; adhesion; capillary adhesion; thermal and electric contact resistance; mixed lubrication; and seal leak rate. Here, we present applications to the leak rate of stationary seals and rubber friction.

4 Role of Different Length Scales

An extremely important result of the theory of contact mechanics is the prediction of how different physical quantities depend on different length scales (see Fig. 7). Thus, unless the nominal contact pressure is very high, the contact stiffness and the thermal and electric contact resistances depend mainly on the long-range part of the surface roughness. That is, for these quantities it is usually irrelevant how the roughness looks above some critical magnification ζ_c or, equivalently, below the critical length scale $\lambda_c = L/\zeta_c$. Similarly, the leak rate of a seal is mainly determined by surface roughness observed at the magnification where the first

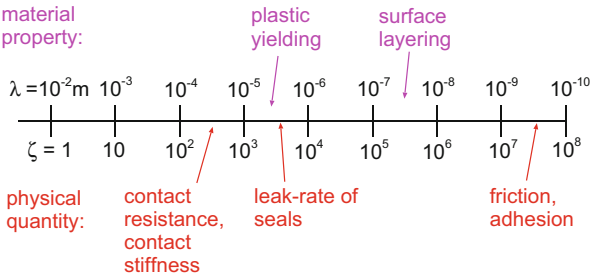

Fig. 7 Different physical quantities depend on different ranges of length scales

noncontact channel is observed (see below). Other quantities such as adhesion and friction generally depend on all length scales, down to atomic distances.

A particular interesting problem is the role of surface roughness on different length scales for adhesion, and whether adhesion influences other physical properties such as the leak rate of seals. The latter problem reduces to the question of whether adhesion influences contact mechanics at the length scale or magnification where the first noncontact percolating channel is observed. To discuss this problem, note first that the adhesive interaction between solids *always* increases the area of real contact. However, if the surface roughness or the elastic modulus are large enough, the area of contact still vanishes continuously as the external loading force is decreased towards zero (i.e., $p \to 0$) [17–21]. For systems with less roughness, or for elastically softer materials, the contact area remains finite as $p \to 0$. When the contact area vanish as $p \to 0$, the effective interfacial energy $\gamma_{\rm eff}(\zeta)$, which depends on the magnification ζ, vanishes below some critical magnification $\zeta = \zeta_{\rm c} > 1$, whereas in the opposite case $\gamma_{\rm eff}(1)$ is non-zero. In the former case, the contact mechanics (e.g., the apparent contact area and the interfacial separation) observed at magnification $\zeta < \zeta_{\rm c}$ appear the same as if no adhesive interactions occur, and physical quantities that only depend on the contact mechanics for $\zeta < \zeta_{\rm c}$ are unaffected by adhesive interaction. As mentioned above, such quantities could be the leak rate of seals [22, 23] or interfacial stiffness [24, 25] (and the related electric and thermal contact resistance [26, 27]), which both depend mainly on the long wavelength roughness unless the nominal contact pressure is very high.

Thus, for example, a good approximation for the leak rate of a static seal [28] can be obtained from the size of the narrowest constriction (denoted critical constriction) of the first noncontact percolating channels observed with increasing magnification [22, 23]. In many cases, the noncontact area, as a function of increasing magnification, percolates at a magnification $\zeta < \zeta_{\rm c}$, in which case the leak rate can be accurately predicted without taking into account the adhesive interaction. Other properties, such as sliding friction, depend on the area of real contact and are always influenced by adhesion.

Finally, we note that if a physical quantity is determined only by the long wavelength roughness, say $\lambda > \lambda_{\rm c} = L/\zeta_{\rm c}$, it may be irrelevant whether the materials involved have modified surface layers (e.g., oxide coating on metals) of

thickness $d << \lambda_c$, or whether plastic deformation occurs in the contact regions observed at magnification $\zeta >> \zeta_c$. Note that when two solids make contact, the long wavelength roughness usually deforms elastically, while plastic deformation only occur at short length-scales, involving the roughness observed at sufficiently high magnification.

5 Introduction to Leakage of Rubber Seals

A seal is a device for closing a gap in a mechanical device or making a joint tight with respect to leakage of a fluid. Seals play a crucial role in many modern engineering devices, and the failure of seals can result in catastrophic events, such as the Challenger disaster. In many cases, simple and inexpensive elastomeric seals such as O-rings are used. However, the failure of seals usually results in expensive and time-consuming replacement procedures. Consideration of not only reliability, but also energy saving and environment pollution (resulting from leakage of the fluids), suggests that seals should be handled as thoroughly in the design process as any other crucial machine element, and not treated as a secondary accessory.

Nowadays, the design of seals and sealing systems is mostly based on experimental investigations, which are complex and time consuming because of the wide range of variables involved. Thus, in spite of its apparent simplicity, it is not easy to predict the leak rate and (for dynamic seals) friction forces. The main problem is the influence of surface roughness on contact mechanics at the seal–substrate interface.

5.1 Leak Rate of Static Seals

Consider the fluid leakage through a rubber seal, from a high fluid pressure region to a low fluid pressure region (see Fig. 8). Assume for simplicity that the nominal

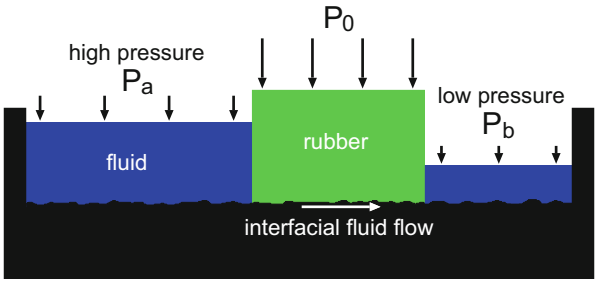

Fig. 8 Rubber seal (schematic). The liquid on the *left* is under the hydrostatic pressure P_a and the liquid on the *right* under pressure P_b (usually, P_b is the atmospheric pressure). The pressure difference $\Delta P = P_a - P_b$ results in liquid flow at the interface between the rubber seal and the rough substrate surface. The volume of liquid flow per unit time is denoted by $\dot{Q}$ and depends on the squeezing pressure P_0 acting on the rubber seal

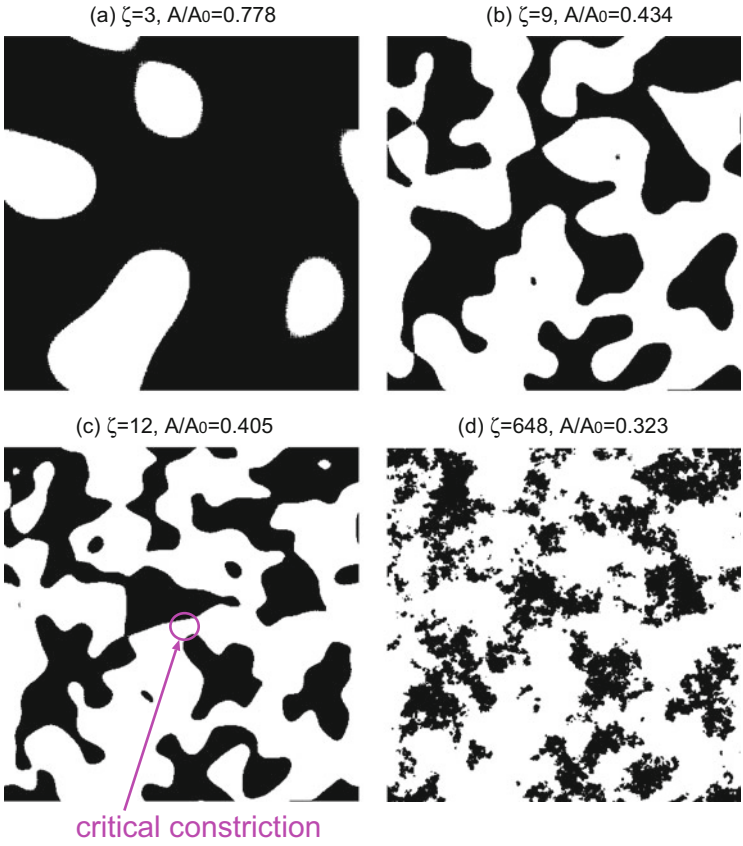

Fig. 9 The contact region (*black*) at different magnifications: (**a**) 3, (**b**) 9, (**c**) 12, and (**d**) 648. Upon magnification of a region in a contact area we observe the appearance of smaller noncontact subareas. When the magnification increases from 9 to 12, the noncontact region (*white area*) percolates, i.e., an open (noncontact) channel extending from one side to the opposite side appears for the first time. At the lowest magnification of $\zeta = 1$, $A(1) = A_0$. The figure is the result of molecular dynamics simulations of the contact between elastic solids with randomly rough surfaces

contact region between the rubber and the hard counter-surface is rectangular with area $L \times L$. Now, let us study the contact between the two solids as we change the magnification ζ. We study how the apparent contact area, $A(\zeta)$, between the two solids depends on the magnification ζ. At the lowest magnification we cannot observe any surface roughness, and the contact between the solids appears to be complete (i.e., $A(1) = A_0$). As we increase the magnification we observe some interfacial roughness and the (apparent) contact area decreases. At sufficiently high magnification, say $\zeta = \zeta_c$, a percolating path of noncontact area is observed, that is, an open (noncontact) channel extending from one side to the opposite side appears for the first time (see Fig. 9). The narrowest constriction along the percolation path,

which we denote the critical constriction, has a lateral size $\lambda_c = L/\zeta_c$ and surface separation u_c. This separation is given by a recently developed contact mechanics theory [11]. As we continue to increase the magnification we find more percolating channels between the surfaces, but these have narrower constrictions than the first channel, which appears at $\zeta = \zeta_c$. As a first approximation, we can neglect the contribution to the leak rate from these channels.

A first rough estimate of the leak rate is obtained by assuming that all leakage occurs through the critical percolation channel and that the whole pressure drop $\Delta P = P_a - P_b$ occurs over the critical constriction. Assuming the shape of the critical constriction to be that of a rectangular block of width and length $\lambda_c = L/\zeta_c$ and height u_c, and assuming an incompressible Newtonian fluid, the volume flow per unit time through the critical constriction is (Poiseuille flow):

$$\dot{Q} = \frac{u_c^3}{12\eta}\Delta P, \tag{8}$$

where η is the fluid viscosity. In deriving this equation we assumed laminar flow and that $u_c << \lambda_c$, which is always satisfied in practice.

To complete the theory, we must calculate the separation u_c of the surfaces at the critical constriction. We first determine the critical magnification ζ_c by assuming that the apparent relative contact area at this point is given by percolation theory. Thus, the relative contact area is given by $A(\zeta)/A_0 \approx 1 - p_c$, where p_c is the so-called site percolation threshold. Computer simulations (and analytical arguments) have shown that $p_c \approx 0.6$, so that $A(\zeta_c)/A_0 \approx 0.4$ determines the critical magnification $\zeta = \zeta_c$. Knowing the critical magnification ζ_c, the separation u_c at the critical junction can be obtained using the Persson contact mechanics theory as follows (see also [16]):

Let $u_1(\zeta)$ be the (average) height separating the surfaces that appear to come into contact when the magnification decreases from ζ to $\zeta - \Delta\zeta$, where $\Delta\zeta$ is a small (infinitesimal) change in the magnification. If $\bar{u}(\zeta)$ denotes the average separation between the surfaces when the interface is studied at magnification ζ, the empty volume between the surfaces that appear to be in contact at magnification $\zeta - \Delta\zeta$ is given by $\bar{u}(\zeta - \Delta\zeta)A(\zeta - \Delta\zeta)$. But, this volume must be the sum of the volume $\bar{u}(\zeta)A(\zeta)$ between the surfaces that appear to be in contact at magnification $\zeta$and the additional volume $u_1(\zeta)[A(\zeta - \Delta\zeta) - A(\zeta)]$ that results from the increase in apparent contact area as the magnification decreases from ζ to $\zeta - \Delta\zeta$:

$$\bar{u}(\zeta - \Delta\zeta)A(\zeta - \Delta\zeta) = \bar{u}(\zeta)A(\zeta) + u_1(\zeta)[A(\zeta - \Delta\zeta) - A(\zeta)]$$

or

$$u_1(\zeta) = \bar{u}(\zeta) + \bar{u}'(\zeta)A(\zeta)/A'(\zeta). \tag{9}$$

In a mean-field type of approximation, $u_c \approx u_1(\zeta_c)$. For more accurate treatment (see [11]), one should take into account that the interfacial separation in the

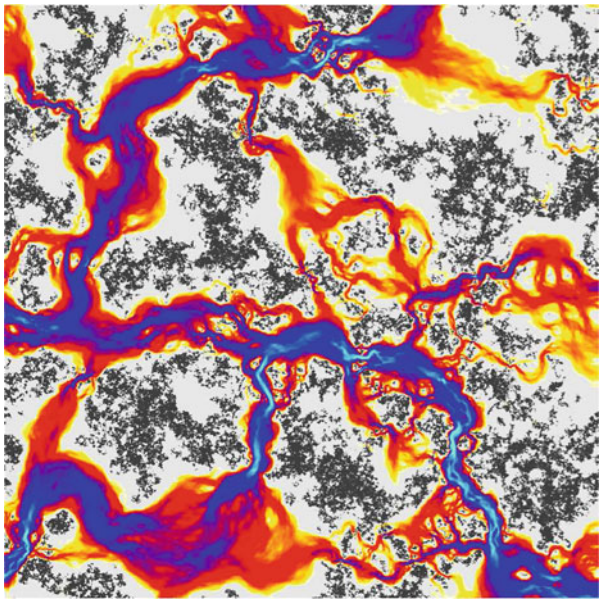

Fig. 10 *Top view* of the contact interface of a rubber seal squeezed against a rough self-affine fractal surface. The simulated seal has only about 20% of its surface in contact (*dark gray region*), yet the flow of liquid (*in color*) across the seal is largely restricted to a few channels. Most of the fluid pressure drop occurs over the narrowest constrictions. Adopted from [28]

noncontact area that appears when the magnification is increased from $\zeta - \Delta\zeta$ to ζ, is not constant but fluctuates as a result of the short wavelength roughness that is observed if the magnification is increased beyond ζ.

We call the theory presented above the "critical junction theory." We have also developed a more accurate theory in which we use the Bruggeman effective medium theory to obtain the leak rate [23]. This theory depends not only on the surface separation at the critical junction, but on the whole probability distribution of interfacial separations, $P(u)$. However, in application we have found that both theories give almost the same results.

5.2 Computer Simulation Tests of the Theory

Exact numerical simulations of the interfacial fluid flow and the leak rate of seals have been performed on small systems to test the predictions of the Persson contact mechanics theory [28]. In these simulations, the Navier–Stokes equations of fluid flow and the theory of elasticity have been used to calculate numerically the flow of fluid in the gap between two elastic solids squeezed together with some given nominal pressure. These calculations were performed using the supercomputer in Jülich in collaboration with the group of Müser [28]. In spite of the very complex fluid flow pattern (see Fig. 10), the leak rates obtained in the numerical simulations agreed very well with the predictions of the Persson contact mechanics theory.

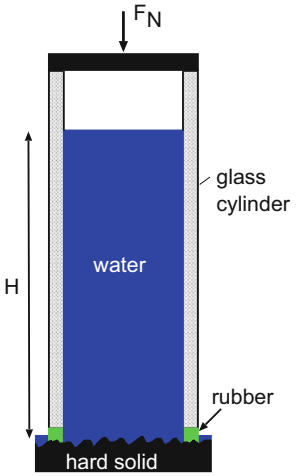

Fig. 11 Experimental setup for measuring the leak rate of seals. A glass (or PMMA) cylinder with a rubber ring attached to one end is squeezed against a hard substrate with well-defined surface roughness. The cylinder is filled with water, and the leak rate of the water at the interface between rubber and counter-surface is detected by the change in height of the water in the cylinder

5.3 Experimental Tests of the Theory

Based on methods and experiments previously developed [29], we performed several experiments to test the theory presented above. In Fig. 11 we show our setup for measuring the leak rate of seals. A glass (or PMMA) cylinder with a rubber ring (of rectangular cross-section) attached to one end is squeezed against a hard substrate with well-defined surface roughness. The cylinder is filled with water and the leak rate of the fluid at the interface between the rubber and hard counter-surface is detected by the change in the height of the fluid in the cylinder. In this case, the pressure difference $\Delta P = P_a - P_b = \rho g H$, where g is the gravitation constant, ρ the fluid density, and H the height of the fluid column.

Figure 12 shows the measured leak rate for different rubber–counter-surface (squeezing) pressures. The red and green solid lines are the calculated leak rates using critical junction theory and the Bruggeman effective medium theory, respectively. Results are shown for sandpaper and sandblasted PMMA surfaces. In the calculations we have used the measured surface topography and the measured rubber elastic modulus.

6 Introduction to Rubber Friction

Soft materials, such as rubber or gel, in lubricated sliding contact have many important applications in science and technology. Examples from biology are the human eye and the synovial joints lubricated by synovial fluid, a viscous non-Newtonian fluid whose main purpose is to reduce friction between the articular cartilages during movement. Lubricated rubber contacts occur in many

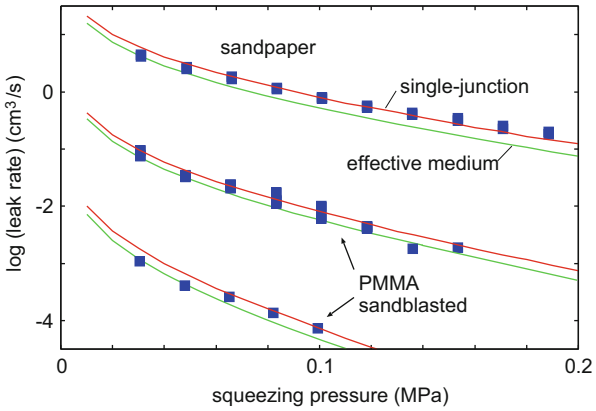

Fig. 12 Measured leak rates (*square symbols*) for different rubber–counter-surface (squeezing) pressures. The *red* and *green solid lines* are the calculated leak rates using the critical junction theory and the Bruggeman effective medium theory, respectively. Results are shown for sandpaper and sandblasted PMMA surfaces. The measured surface topography and the measured rubber elastic modulus were used in the calculations

technological applications; examples are syringes, where the (rubber) stopper–barrel interface is usually lubricated by a high-viscosity silicon oil, and dynamic rubber seals typically lubricated by hydrocarbon oils. Other important applications are tires on wet or contaminated (in particular the smear produced by water + dust) road surfaces or on icy road surfaces where the frictional energy can result in a thin melt-water film acting as a lubricant.

The contact mechanics and friction between rubber and a lubricated counter-surface is a complex topic involving several fundamental processes:

(a) fluid squeeze-out, which depends on the fluid viscosity;
(b) dewetting, which depends on the surface (or interfacial) energies and the elastic properties of the solids;
(c) confinement of fluid in sealed-off regions, which occurs when the area of real contact percolates, which effectively smoothes the surface profile and reduces the area of real contact;
(d) adhesive interaction between rubber and counter-surface in dry contact regions;
(e) shearing of a thin fluid film (in general involving high shear rates and non-Newtonian fluid behavior);
(f) viscoelastic deformations of the rubber surface by substrate asperities;
(g) scratching of the substrate surface by hard rubber filler particles; and
(h) wear processes.

Rubber friction on rough surfaces has been studied both experimentally [30–40] and theoretically [4, 5, 41–50]. Here, we are interested in lubricated rubber friction on rough surfaces. Particular interesting and detailed studies on this topic were performed by Bongaerts and colleagues with silicon rubber lubricated by water

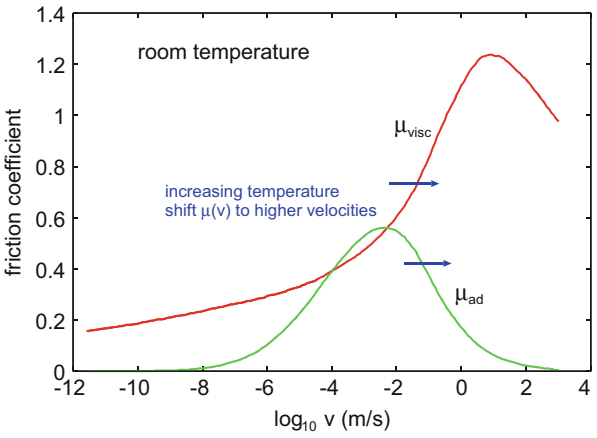

Fig. 13 Adhesive $\mu_{ad}(v)$ and viscoelastic $\mu_{visc}(v)$ contributions to rubber friction. An increase in temperature shifts both $\mu_{ad}(v)$ and $\mu_{visc}(v)$ towards higher sliding speeds

+ glycerol mixtures [40], and more recently with suspensions of small (micrometer-sized) glass balls [51] in water + glycerol mixtures. Other important work was performed by Roberts and coworkers [52–54] and Klein and colleagues [55, 56].

On dry surfaces, there are two contributions to rubber friction, one from the area of real contact and one from the pulsating deformations of the rubber surface as a result of substrate asperities. The latter contribution depends on the internal friction of the rubber. We assume that the friction force can be written as the sum of the viscoelastic contribution F_{visc} and a contribution from the area of real contact, which we assume is proportional to the contact area A:

$$F_f = F_{visc} + \tau_f A, \tag{10}$$

where τ_f is the frictional shear stress acting in the area of contact. If we write the normal force as $F_N = p_0 A_0$, where p_0 is the nominal contact pressure and A_0 the nominal contact area, we obtain:

$$\mu = \mu_{visc} + \frac{\tau_f}{p_0}\frac{A}{A_0}. \tag{11}$$

Figure 13 shows qualitatively the velocity dependency of the two contributions to the friction coefficient $\mu(v)$. In the next two sections we discuss the viscoelastic contribution to the friction and the origin of the frictional shear stress τ_f.

We present experimental friction results and theoretical analyses for tire tread rubber sliding on smooth and rough surfaces. The experiments were performed using a simple Leonardo da Vinci setup, and the data was analyzed using the Persson rubber friction and contact mechanics theory.

7 Viscoelastic Contribution to Rubber Friction

Two different theories have been used to calculate the area of real contact and the viscoelastic contribution to rubber friction. Here, we consider the simplest case of sliding at a constant speed and at such low speed that frictional heating can be neglected.

In the theory of Persson, the friction force acting on a rubber block squeezed with a stress p_0 against a hard randomly rough surface is given by [4, 33, 46, 49]:

$$\mu_{\rm visc} \approx \frac{1}{2}\int_{q_0}^{q_1} dq\ \ q^3 C(q) S(q) P(q) \int_0^{2\pi} d\phi\ \ \cos\phi\ \ {\rm Im}\frac{E(qv(t)\cos\phi, T_0)}{(1-\nu^2)p_0}, \tag{12}$$

where T_0 denotes the temperature, and

$$P(q) = \frac{1}{\sqrt{\pi}}\int_0^{\sqrt{G}} dx\ \ e^{-x^2/4} = {\rm erf}\left(\frac{1}{2\sqrt{G}}\right), \tag{13}$$

where

$$G(q) = \frac{1}{8}\int_{q_0}^{q} dq\ \ q^3 C(q) \int_0^{2\pi} d\phi\ \ \left|\frac{E(qv\cos\phi, T_0)}{(1-\nu^2)p_0}\right|^2. \tag{14}$$

Note that $P(q) = A(q)/A_0$ is the (normalized) contact area observed at magnification $\zeta = q/q_0$ (see Sect. 3).

The factor $S(q)$ in (12) is a correction factor that takes into account the fact that asperity-induced deformations of the rubber are smaller than if complete contact occurs in the (apparent) contact areas observed at magnification $\zeta = q/q_0$. For contact between elastic solids, this factor reduces the elastic asperity-induced deformation energy. Including this factor gives a distribution of interfacial separation in good agreement with experiments and exact numerical studies [11]. The interfacial separation describes how an elastic (or viscoelastic) solid deforms and penetrates into the roughness valleys. It is stressed here that these (time-dependent) deformations cause the viscoelastic contribution to rubber friction. We assume that the same $S(q)$ reduction factor as found for elastic contact is also valid for sliding contact involving viscoelastic solids. For elastic solids, it has been found that $S(q)$ is well approximated by:

$$S(q) = \gamma + (1-\gamma)P^2(q), \tag{15}$$

where $\gamma \approx 1/2$. Here, we use the same expression for viscoelastic solids, being a geometric parameter. Note that $S \to 1$ as $P \to 1$, which is an exact result for complete contact. In fact, the expression (12) is exact for complete contact.

The more general case of nonuniform sliding and including frictional heating has also been studied [33].

In the theory of rubber friction [4, 5], the viscoelastic contribution to friction depends on the surface roughness power spectrum $C(q)$, where $q = 2\pi/\lambda$ is the wavenumber of a particular frequency component (with wavelength λ) of the roughness profile. Most surfaces have a self-affine fractal -like topography, where $C(q) \propto q^{-2(1+H)}$. Here the Hurst exponent is typically in the range $0.7 < H < 1$, corresponding to a fractal dimension $D_f = 3 - H$ between 2 and 2.3 (see [57, 58]). Most surfaces have a roll-off region for $q < q_r$, where $C(q)$ is approximately constant. In calculating the rubber friction we include all the roughness components with wavenumber $q_0 < q < q_1$. Here $q_0 = 2\pi/L$, where L is the linear size of the rubber block in the sliding direction. If $q_0 < q_r$, as is usually the case, the contact area and the viscoelastic contribution to the friction are nearly independent of q_0. We define the magnification as $\zeta = q/q_0$. When we study the interface at magnification ζ we do not observe roughness components with wavenumber $q > q_0\zeta$. Physical quantities observed at this magnification therefore depend on the magnification.

Note that when calculating the viscoelastic contribution to rubber friction (and the contact area) it is necessary to introduce a large wavenumber cut-off, $q_1 = 2\pi/\lambda_1$, where λ_1 is the shortest surface roughness wavelength included in the contact mechanics calculation. For smooth surfaces, λ_1 can be of the order of atomic distances or the average distance between crosslinks (i.e., $q_1 \approx 10^9 - 10^{10}$ m^{-1}). For very rough surfaces such as road surfaces, the cut-off may be related to the onset of rubber bond-breaking and wear processes, which appear in the contact regions at high-enough magnifications as a result of large stresses and high temperatures. For road surfaces, this typically gives the cut-off $q_1 \approx 10^6 - 10^7$ m^{-1}.

The theory above is based on a full three-dimensional (3D) treatment of viscoelastic contact mechanics. The theory of Klüppel and Heinrich is based on an approximate 2D description of the sliding problem. The rubber friction coefficient is given by [5]:

$$\mu_{\rm visc} = q_0\delta_0 \int_{q_0}^{q_1} dq \;\; q^2 C_{1D}(q) {\rm Im} \frac{E(qv, T_0)}{p_0}, \tag{16}$$

where C_{1D} is the 1D surface roughness power spectra, which can be calculated from the 1D height profile $z = h(x)$ measured along a straight line (x-coordinate). In (16), δ_0 is a length parameter proportional to what Klüppel and Heinrich denote as the mean thickness of the excitation layer, which they assume to be proportional to the mean penetration depth of the asperities in the rubber. As in the Persson theory, the lower cut-off wavenumber is given by $q_0 \approx 2\pi/L$. In the Persson theory, the upper cut-off q_1 is attributed to the formation of a modified surface layer on the rubber

surface (as a result of the high stresses and temperatures that prevail in the contact area at high magnification); however, in the theory of Klüppel and Heinrich [5, 45] q_1 is determined by an energy condition that we do not fully understand.

Klüppel and Heinrich [5] state that δ_0 can be estimated from experiments or FEM calculations. Comparing (12) and (16) one should note that:

$$2\pi\int_0^\infty dq\ qC(q) = \int_{-\infty}^{\infty} dq\ C_{1D}(q) = \langle h^2\rangle, \tag{17}$$

where $\langle h^2\rangle$ is the mean square surface roughness amplitude. Thus, the main difference between (12) and (17) is the factor $S(q)P(q)$ occurring in (12). Because the contact area, $P(q) = A(q)/A_{0,}$ depends very strongly on the wavenumber q (and on the sliding speed v) the two theories predict rather different results.

Finally, we note that Popov and coworkers [59] have presented a theory of rubber friction where the full 3D model is mapped onto an effective 1D model. However, one of us has shown [60, 61] that this mapping, when applied to rough surfaces, results in qualitatively wrong results for all contact mechanical properties, including rubber friction.

8 The Contribution from the Area of Contact

Let us consider the contribution from the area of real contact to the friction force. The six most important friction processes are:

(1) For dry sliding contact, the rubber molecules and the substrate atoms interact as indicated in Fig. 14. In many cases one expects weak interfacial interactions, (e.g., van der Waals interactions). For stationary contact, the rubber chains at the interface adjust to the substrate potential to minimize the free energy. This bond formation may require overcoming potential barriers and does not occur instantaneously but requires some relaxation time. During sliding at low velocity, thermal fluctuations help to break the rubber–substrate bonds, resulting in a friction force that approaches zero as the sliding velocity goes to zero. At high velocity, there is

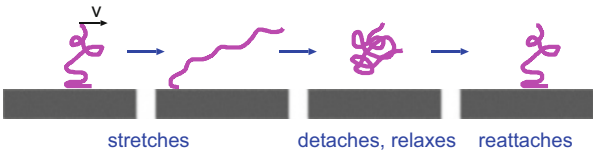

Fig. 14 Classical description of a polymer chain at the interface between a rubber block and counter-surface. During lateral motion of the rubber block the chain stretches, detaches, relaxes, and then reattaches to the surface to repeat the cycle. In reality no detachment in the vertical direction is expected, but only a rearrangement of molecule segments (in nanometer-sized domains) parallel to the surface from pinned (commensurate-like) to depinned (incommensurate-like) domains

not enough time for the rubber molecules to adjust to the substrate interaction potential; that is, the bottom surface of the rubber block "floats" above the substrate, forming an incommensurate-like state with respect to the corrugated substrate potential. Thus, the frictional shear stress is also small for large sliding speeds. We expect the frictional shear stress as a function of the sliding speed to have a maximum at some intermediate velocity v^*. This friction mechanism was first studied in a highly simplified model by Schallamach [42] and later by Leonov and colleagues [43, 50], and in a more realistic model by Persson and Volokitin [44]. The theory predicts that the frictional shear stress is a Gaussian-like curve as a function of $\log_{10} v$, with a width of four (or more) frequency decades and centered at a sliding speed typically of $v^* \approx 1$ cm/s (see the $\mu_{ad}(v)$ curve in Fig. 13). This frictional shear stress law is very similar to that observed (measured) by Grosch [31, 32] for rubber sliding on smooth surfaces (glass or steel).

We found that using the following frictional shear stress law $\tau_f(v, T)$ resulted in good agreement between theory and measurements [30]:

$$\tau_f = \tau_{f0} \ \exp\left(-c\left[\log_{10}\left(\frac{v}{v^*}\right)\right]^2\right), \tag{18}$$

where $c = 0.1$, $v^* = 6 \times 10^{-3}$ m/s and $\tau_{f0} = 6.5$ MPa. The full width at half maximum of $\tau_f(v)$ as a function of $\log_{10} v$ is $2(\ln 2/c)^{1/2} \approx 5.3$.

The master curve (18) is for the reference temperature $T_{ref} = 20°C$ but the frictional shear stress at other temperatures can be obtained by replacing v by va_T', where a_T' is the shift factor obtained when constructing the master curve (18):

$$\ln \ a_T' = C_1'\left(\frac{1}{T} - \frac{1}{T_g} + C_2'\right), \tag{19}$$

where T_g is the glass transition temperature, $C_1' = 1.1 \times 10^4$K, and $C_2' = 8.4 \times 10^{-4}$ K^{-1}. We have found that using these values for C_1' and C_2' gives good agreement with a large set of measured friction data. Nevertheless, one cannot expect C_1' and C_2' to be universal constants because they depend slightly on the rubber compound. The situation is similar to the (bulk viscoelasticity) WLF shift factor:

$$\log_{10} a_T = \frac{-C_1(T - T_g)}{C_2 + T - T_g}$$

For many polymers, $C_1 \approx 15$ and $C_2 \approx 50$ K but these values are not universal because they depend slightly on the polymer used.

We also found that the maximum τ_{f0} in the $\tau_f(v)$ relation varies slightly according to the studied system. Thus, for τ_{f0} we used slightly different values

for different compounds and road surfaces but always in the range $\tau_{f0} = 5.3 - 8.3$ MPa.

The contribution to rubber friction from the area of real contact depends sensitively on contamination by particles and fluids. Thus, on a wet road surface at sufficiently high sliding (or rolling) speed, the surfaces in the apparent contact regions are separated by a thin fluid film (see next section), in which case the viscoelastic deformations of the rubber give the most important contribution to the friction.

(2) For dry contact, there may be a contribution to friction from interfacial crack propagation. Thus, during sliding at each substrate asperity contact region there is a closing interfacial crack at the front (in the sliding direction) and an opening crack at the back [62]. The energy to propagate an opening crack $G(v)$ can be strongly enhanced by energy dissipation in the rubber in the vicinity of the opening crack, and can also enhance the contact area [62–64]. However, it is not clear at present how important this mechanism is when the contact regions are very small (see Appendix 1). Note that processes (1) and (2) generally act together.

The energy to propagate an opening crack (per unit surface area formed) is $G(v) = G_0 a(v)/a_0$, where the crack tip radius a is given by [9, 64, 65]:

$$\frac{a_0}{a} = 1 - \left(1 - \frac{E_0}{E_\infty}\right) \frac{\int_0^{2\pi v/a} d\omega \ \frac{F(\omega)}{\omega} \mathrm{Im}\frac{1}{E(\omega)}}{\int_0^{\infty} d\omega \ \frac{1}{\omega} \mathrm{Im}\frac{1}{E(\omega)}}$$

where $E_0 = E(0)$, $E_\infty = E(\infty)$, and

$$F(\omega) = \left[1 - \left(\frac{\omega a}{2\pi v}\right)^2\right]^{1/2}$$

In the equations above, G_0 and a_0 are the crack propagation energy and crack tip radius, respectively, for an infinitesimally slowly moving crack tip.

(3) There is a contribution to rubber friction from the interaction between filler particles at the rubber surface and the road or substrate surface. Basically, during slip the hard filler particles scratch the road surface. This can give an almost velocity-independent background contribution $\Delta\mu \approx 0.1$ to the rubber friction coefficient, which depends on the filler concentration (for tread rubber it is usually rather high, around 25% of the rubber compound volume) and dispersion. Figure 15a shows the atomic force microscopy (AFM) topography of a glass surface after a rubber tread block has been slid many times on the surface. The surface has strongly anisotropic roughness, in particular for the roughness components with wavelength of a few micrometers, which exhibit very large local Tripp number γ (see Fig. 15b). The Tripp number is a measure of the surface roughness anisotropy, with $\gamma = 1$ corresponding to isotropic roughness [66]. The glass surface root-mean-square (rms) roughness amplitude of approximately 6 nm is much larger

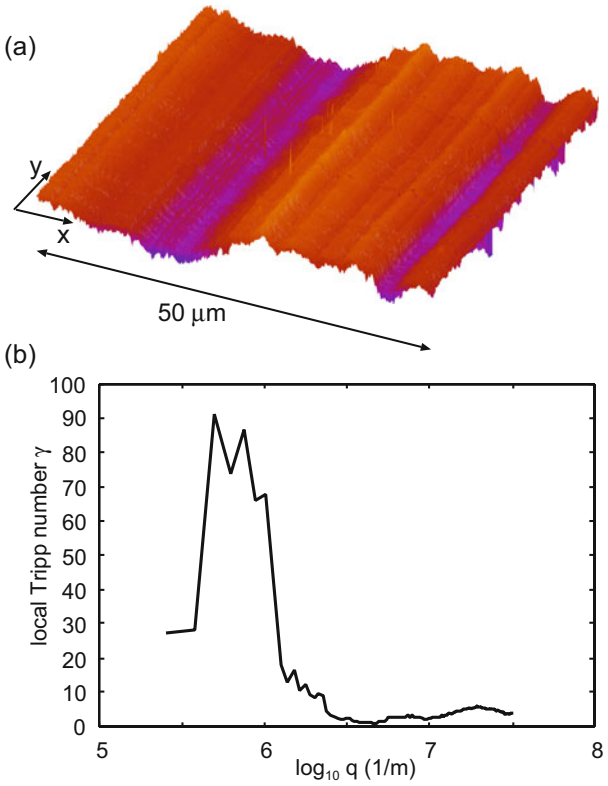

Fig. 15 (**a**) Surface topography (AFM measurement over a 50×50 μm surface area) of a glass surface scratched by a rubber block with silica filler (many sweeps). The surface has a rms-roughness amplitude of ≈ 6 nm and rms-slope of 0.022. Measuring over a larger surface with higher (atomic) resolution increases both quantities. (**b**) The local Tripp (anisotropy) number γ as a function of the logarithm of the wavenumber

than for unused surfaces (about 0.8 nm when measured over the same surface area). The contribution to the friction from scratching (plowing) can be estimated as follows: Assume that A_c is the total cross-section (in the xz-plane) of the wear tracks after one sweep. The contribution to the friction force coefficient from plowing is $\Delta\mu \approx A_c\sigma_Y/F_N$, where σ_Y is the stress necessary to plastically deform the glass surface. The cross-section A_c can be estimated from AFM pictures of the glass surface after one sweep.

(4) If a lubricant or contamination fluid (e.g., water, fragments of rubber molecules, or oil from the rubber) is present at the sliding interface, process (1) might be replaced by shearing a thin (nanometer thick) fluid film. Note that the rheological properties of such a nanometer-thick confined fluid film are in general very different from those of the bulk liquid. Experiments [67] and theory [68, 69] show that the frictional shear stress depends only very weakly on the shear

rate $\dot{\gamma}$ (shear thinning), and that different liquids exhibit similar properties. Thus, for many liquids (or contamination fluids), the frictional shear stress [67, 68] is given by $\tau_f \approx B\dot{\gamma}^{\alpha}$, where $\alpha \approx 0.1$ at room temperature and (in SI units) $B \approx 10^5$.

(5) If contamination particles (e.g., stone dust) are present, the frictional shear stress in the contact area can be similar to that of a hard material sliding on a hard material (e.g., stone on stone). This situation is similar to the influence that filler particles have on the frictional shear stress. Note that if the contamination particles roll rather than slip at the interface, their influence on friction is different.

(6) There is a contribution to friction from rubber wear processes. This can be particular important for rubber sliding on sandpaper (and other surfaces with sharp surface roughness), where strong wear occurs and where one can often observe wear scars extending from one side of the rubber block to the other as a result of scratching by the sharp substrate asperities.

9 Rubber Friction on Dry and Wet Surfaces

In this section, we present a short overview of rubber friction on lubricated (hard) surfaces. Figure 16 compares the contact between dry and wet surfaces, assuming low sliding speed, where the fluid inertia, and also to a large extent the fluid viscosity, are unimportant. With respect to the long-wavelength roughness, fluid squeeze-out (see Fig. 16b) from the interface between a rubber block and a road surface occurs rapidly, with negligible fluid pressure buildup, and the contact mechanics appear the same as on a dry surface (compare Fig. 16a, b). However, on a wet surface, as the magnification is increased and shorter wavelength roughness is observed, one finally observes (at some magnification ζ^*) the influence of the fluid on contact mechanics. For low sliding speed, one can distinguish between three possibilities (see Fig. 16b1–b3), namely:

(b1) The rubber–road contact is separated by a thin fluid film that is not removed because of the fluid viscosity and/or because the spreading pressure $S > 0$. The spreading pressure is given by $S = \gamma_{S_0S_1} - \gamma_{S_0L} - \gamma_{S_1L}$, where $\gamma_{S_0S_1}, \gamma_{S_0L}$, and γ_{S_1L} are the interfacial energies between solids S_0 and S_1, between the liquid and solid S_0, and the liquid and solid S_1, respectively. If $S > 0$, the minimum free energy configuration (for low-enough contact pressure) corresponds to a system with a thin (usually in the order of nanometers) fluid slab separating the surfaces. This implies that a (short-ranged) repulsive force acts between the surfaces when immersed in the fluid.

(b2) If $S < 0$, dewetting may occur and result in dry contact regions [70–72]. At the same time, fluid may be confined (sealed off) in road (or substrate) cavities, inhibiting the rubber from penetrating into the cavities and reducing the viscoelastic contribution to friction [73].

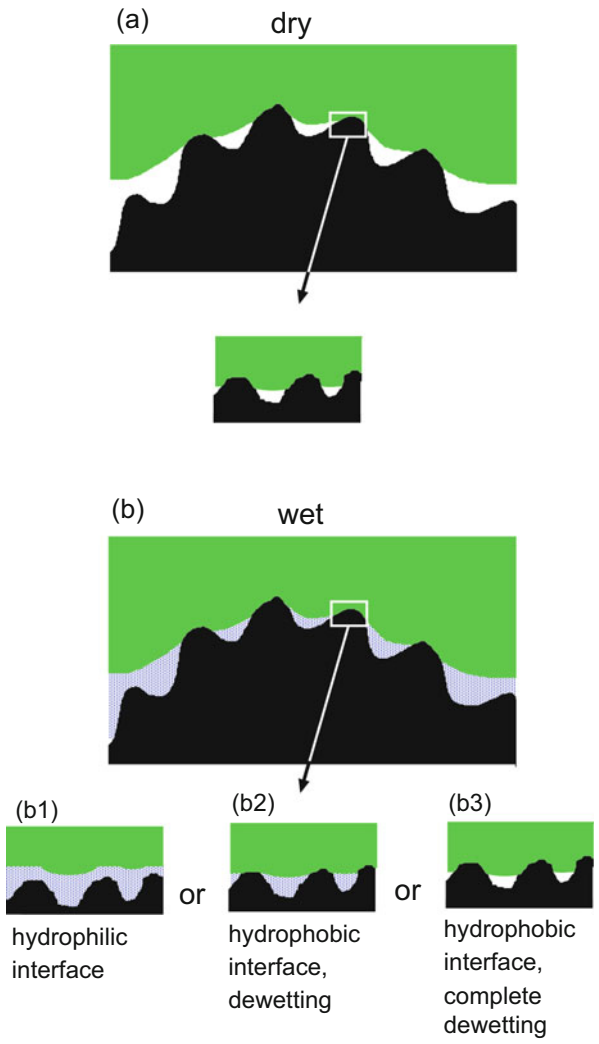

Fig. 16 Rubber friction on (**a**) dry and (**b**) wet road surfaces, for low sliding speeds where the fluid inertia and to a large extent the fluid viscosity are unimportant. (**b1**–**b3**) Three different possibilities at low sliding speed

(b3) If $S < 0$ and if the expel pressure p_c, which depends on the interfacial energies $\gamma_{S_0S_1}, \gamma_{S_0L}$, and γ_{S_1L} and on the surface separation in the noncontact regions, is larger than the fluid pressure, then the noncontact area may also be dry [74].

In the case shown in Fig. 16b1, the adhesive contribution to rubber friction is replaced by a contribution from shearing a thin fluid film, and the viscoelastic contribution is reduced (as compared with the dry case) because the large wavenumber cut-off is reduced: $q^* = \zeta^* q_0 < q_1 = \zeta_1 q_0$ (where q_1 is the cut-off wavenumber on the dry surface). In the case shown in Fig. 16b2, some asperity contact areas are dry but nevertheless both the viscoelastic contribution and the

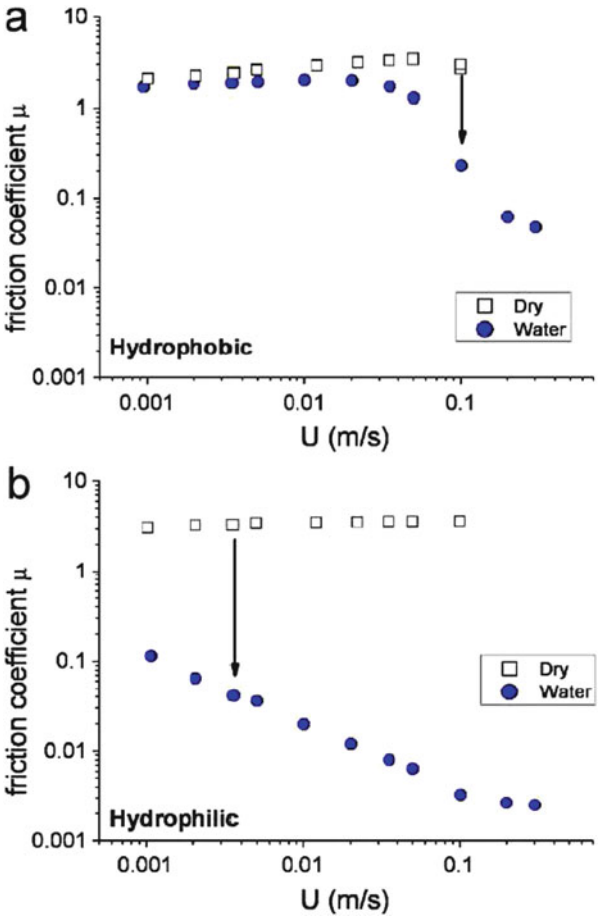

Fig. 17 Comparison of dry and lubricated contact for (**a**) hydrophobic and (**b**) hydrophilic tribopairs. The *open squares* are for dry surfaces, and the *filled circles* in water. The sliding system consisted of a poly (dimethylsiloxane) (PDMS) ball sliding on a PDMS disc. The disc has surface roughness obtained by molding the PDMS rubber against a rough surface. The hydrophilic tribosystem was obtained by exposing the rubber to oxygen plasma. From [36, 39, 40]

contribution from the area of contact are generally reduced. In the case shown in Fig. 16b3, the fluid has negligible influence on the friction.

The role of the wetting properties of the interface on sliding friction has been reported in several studies [36, 39, 40]. As an example, Fig. 17 shows the dry and lubricated contacts for hydrophobic and hydrophilic tribopairs. The sliding system consisted of a poly(dimethylsiloxane) (PDMS) ball sliding on a PDMS disc. The disc had surface roughness obtained by molding the PDMS rubber against a rough surface. The hydrophilic tribosystem was obtained by exposing the PDMA rubber surfaces to oxygen plasma.

Note that for the lubricated (water) hydrophobic interface, the friction coefficient rapidly approaches the dry surface case as the sliding speed decreases. This indicates that the fluid is completely removed from the asperity contact regions as the sliding velocity approaches zero, corresponding to the cases shown in Fig. 16b2, b3. For the hydrophilic tribosystem, the friction is much smaller than for dry surfaces, even at very low sliding speeds. This corresponds to the case shown in

Fig. 16b1, where a thin water film separates the surfaces even in the (apparent) area of contact. For high sliding speeds, where no direct contact occurs between the solids (because the fluid pressure buildup keeps the surfaces separated), the $\mu(v)$-relations are the same for both tribosystems [36, 39, 40].

10 Rubber Friction on Wet, Lubricated Surfaces: Experiment and Analysis

We now present experimental results for three rubber compounds A, B, and C on smooth and rough surfaces. All the compounds were supplied by the Yokohama Rubber Company and were supposed to be standard tire tread rubber compounds. Rubber A is a standard reference compound with (by volume) approximately 20% carbon black, compound B is a summer compound with approximately 15% silica and 5% carbon black, and compound C is an all-season compound with approximately 20% carbon black.

The measured data were obtained using the Leonardo da Vince setup shown in Fig. 18. The slider consists of two rubber blocks glued to a wooden plate. One block is at the front of the wooden plate and the other at the end of the wooden plate. The blocks are 5 mm thick, and of lengths $L_y = 4$ cm orthogonal to the sliding direction and $L_x = 1.25$ cm in the sliding direction, giving a total nominal contact area of $A_0 = 2L_xL_y = 10$ cm^2. The normal force is generated by adding lead blocks (M in Fig. 18, of total mass M) on top of the wooden plate, up to $M \approx 30$ kg. Similarly, the driving force is generated by adding small (0.25 kg) lead blocks in the container M′ shown in Fig. 18. Before each test the rubber blocks were run-in, first on sandpaper and then on the actual road surface used in the experiments. This resulted in the removal of a thin surface layer on the rubber block, which was necessary for obtaining reproducible results.

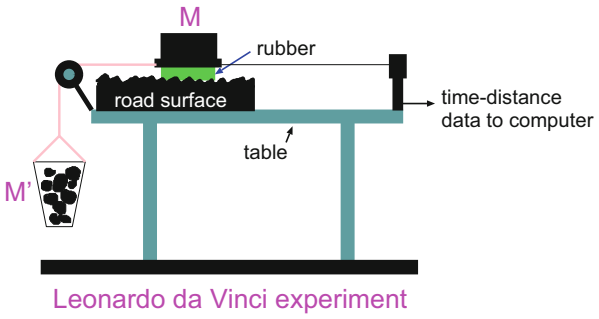

Fig. 18 Simple friction tester used for obtaining the friction coefficient $\mu = M'/M$ as a function of the sliding speed. The sliding distance is measured using a distance sensor, and the sliding velocity obtained by dividing the sliding distance by the sliding time. This setup can only measure the friction coefficient on the branch of the $\mu(v)$ curve where the friction coefficient increases with increasing sliding speed v

The simple friction tester shown in Fig. 18 can be used for obtaining the friction coefficient $\mu = M'/M$ as a function of the sliding speed. The sliding distance is measured using a distance sensor, and the sliding velocity obtained by dividing the sliding distance by the sliding time. This setup can only measure the friction coefficient on the branch of the $\mu(v)$-curve where the friction coefficient increases with increasing sliding speed v.

10.1 Surface Roughness Power Spectra and Rubber Viscoelastic Modulus

We next studied rubber friction for compounds A, B, and C on several smooth and rough surfaces. The surface roughness power spectra of the surfaces are given in Figs. 19 and 20. The PMMA and glass surfaces used in Sect. 10.2 are very smooth and, in these cases, the rubber block has much greater roughness and mainly determines the contact area. The opposite is true for concrete and asphalt road surfaces and in these cases the roughness of the rubber block is not important for the contact mechanics. In Fig. 20 we show the large wavenumber cut-off q_1 as obtained from the condition that the rms-slope of the surface, including the roughness components with wavenumber $q < q_1$, equals 1.3 (which we have found gives viscoelastic friction coefficients in good agreement with experiments). For asphalt surfaces b and c (Fig. 20) it was necessary to extrapolate the measured power spectra to larger wavenumbers, and the results for q_1 in these cases are therefore somewhat uncertain.

The viscoelastic moduli of the three rubber compounds A, B, and C were measured using dynamic mechanical analysis (DMA) in elongation mode. In the measurements, the samples were prestrained with 125 % of the dynamic strain amplitude. The red curves in Fig. 21 shows the low-strain (0.04 %) viscoelastic modulus master curve for compound A. They are obtained by measuring the rubber properties over a small frequency interval (here we used 28–0.25 Hz) and at

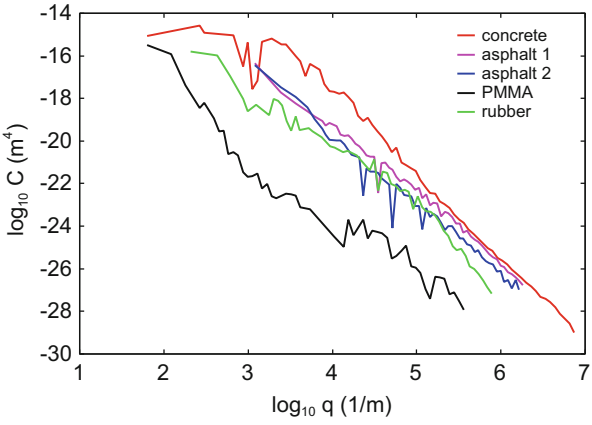

Fig. 19 Surface roughness power spectra of several surfaces used in Sects. 10.2 and 10.3

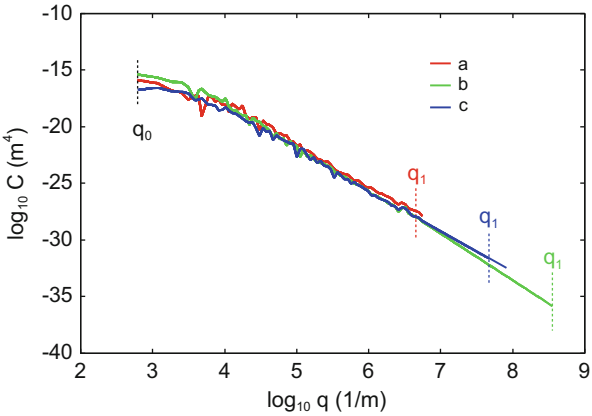

Fig. 20 Surface roughness power spectra for asphalt road surfaces *a*, *b*, and *c* used in Sect. 10.4. Here q_1 indicates the large wavenumber cut-off used for rubber friction calculations. Note that for surfaces *b* and *c* it was necessary to extrapolate the measured power spectra

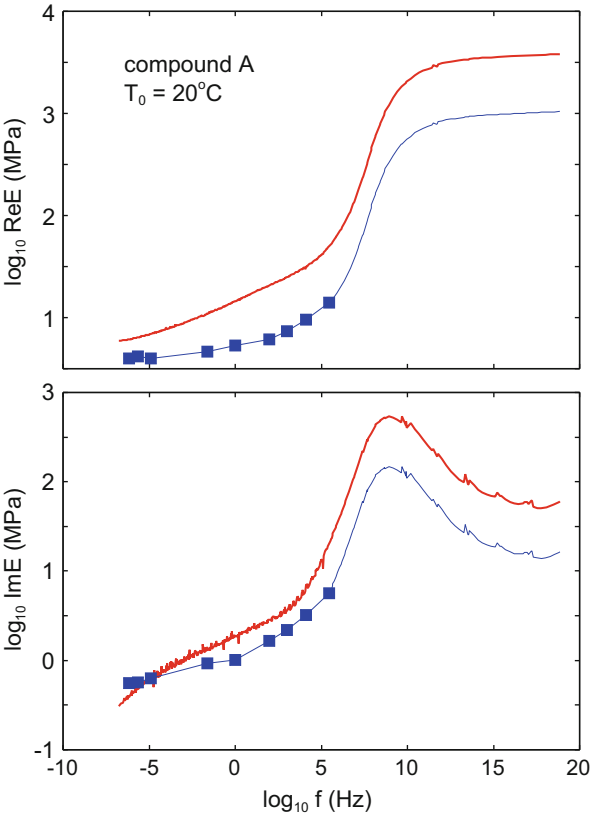

Fig. 21 Low-strain (0.04 %) viscoelastic modulus master curve for compound A (*red curve*). *Blue squares* indicate the large strain (70 % strain) modulus from strain sweep data. The top and bottom figures show the real and the imaginary part of the viscoelastic modules. The reference temperature is 20°C

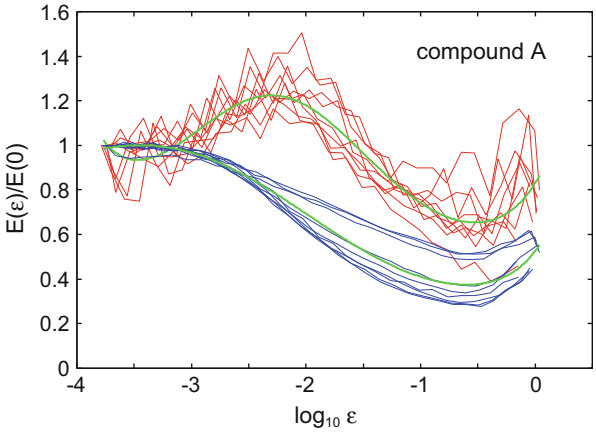

Fig. 22 The ratio Re $E(\varepsilon)$/Re $E(0)$ (blue lines) and Im $E(\varepsilon)$/Im $E(0)$ (red lines) for rubber compound A as a function of the dynamic strain amplitude ε up to large strain $\varepsilon \approx 1$ (or 100% strain). The rubber prestrain was 1.25 times larger than the dynamic strain amplitude. The rubber sample cross-section used in defining the stress was chosen as the cross-section of the prestrained rubber sample. The results are for different temperatures and frequency $f = 1$ Hz

different temperatures (typically from -60°C to 120°C). The results are then shifted along the frequency axis to obtain a broad (in frequency space) master curve at a particular reference temperature. The blue squares in Fig. 21 indicate results for the large strain (70 % strain) modulus obtained from strain sweep data.

The nonlinear properties of the rubber compounds were obtained from strain sweeps performed at different temperatures and for frequency $f = 1$ Hz. Figure 22 shows the ratio Re $E(\varepsilon)$/Re $E(0)$ and Im $E(\varepsilon)$/Im $E(0)$ for compound A as a function of the dynamic strain amplitude ε up to large strains of $\varepsilon \approx 1$ (or 100% strain).

In calculations of the viscoelastic contribution to friction and the area of contact, we take into account the nonlinear effects either by scaling the low strain modulus with the relevant strain-sweep factor $E(\varepsilon)/E(0)$ or by using the blue curve in Fig. 21 obtained for a typical strain value expected in the asperity contact regions (typical strain of approximately 100%). Both procedures give very similar results.

Extrapolation of the nonlinear modulus to high frequencies (blue fit-lines in Fig. 21) is very uncertain because the exact nonlinear viscoelastic properties of filled rubber in the high frequency region is not known. In the DMA experiments, fracture of the sample takes place at large strain and low temperature, which in the context of rubber friction corresponds to large wear. However, for the velocity region for which experimental friction data are presented below (mainly $v < 1$ mm/s), only the frequency region where we measured the E-modulus is used. For higher sliding speeds, part of the extrapolated region is also important, but when frictional heating is included only a region rather close to the highest frequency blue squares in Fig. 21 is relevant. Thus, we believe that the way in which we extrapolate the viscoelastic modulus is not very important in most practical cases. However, there is need for better ways of obtaining the rubber viscoelastic properties for large strain and high frequencies.

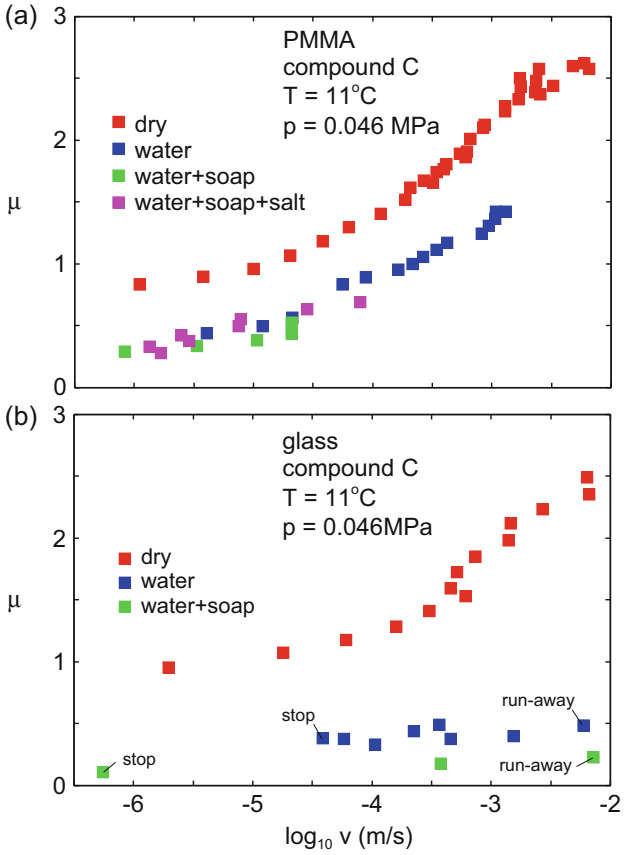

Fig. 23 Measured friction for tread rubber compound C sliding on surfaces of (**a**) PMMA and (**b**) glass. Results are for dry surfaces (*red squares*), in water (*blue squares*), and in soap + water (*green squares*). For the PMMA surface, results were also obtained for water + soap + salt (NaCl) solution (*pink squares*). The rubber surface had previously been run-in on sandpaper and asphalt road surfaces, resulting in a roughened rubber surface

Finally, we note that in the nonlinear response region, if the applied strain oscillates as $\varepsilon(t) = \varepsilon_0 \cos(\omega t)$ the stress is a sum involving terms $\sim \cos(n\omega t)$ and $\sim \sin(n\omega t)$ where n is an integer. The DMA instrument used defines the modulus $E(\omega)$ in the nonlinear region using only the component $f(\varepsilon_0, \omega)\cos(\omega t) + g(\varepsilon_0, \omega)\sin(\omega t)$ in this sum, which oscillates with the same frequency as the applied strain. Thus $\mathrm{Re}E(\omega) = f(\varepsilon_0, \omega)/\varepsilon_0$ and $\mathrm{Im}E(\omega) = g(\varepsilon_0, \omega)/\varepsilon_0$. Note that with this definition the dissipated energy during one period of oscillation ($T = 2\pi/\omega$) is given by

$$\int_0^T dt\sigma(t)\dot{\varepsilon}(t) = \pi\varepsilon_0^2 \mathrm{Im}E(\omega),$$

just as in the linear response region.

10.2 Rubber Friction on Smooth PMMA and Glass Surfaces

Figure 23 shows the measured friction coefficient (μ) for tread rubber compound C sliding on PMMA and glass surfaces. Results are given for dry surfaces, in water, and in soap + water. For the PMMA system, results were also obtained for a water + soap + salt (NaCl) solution. Prior to the study, the rubber surface had been run-in on sandpaper and asphalt road surfaces, resulting in a roughened rubber surface.

It is interesting to note that the friction values for the dry surfaces are very similar for both the PMMA and glass surfaces. However, reproducible results were obtained only after a (relatively short) run-in time period. During this time, it appeared that a very thin contamination film was transferred from the rubber to the counter-surface, and it is possible that shearing this thin film explains the very similar frictional behaviors. The PMMA–water–rubber system is probably hydrophobic or very close to hydrophobic, and for this reason friction in the dry state and in water are rather similar, (as expected if the cases shown in Fig. 16b2, b3 prevail). The reduction in friction in water could reflect a change in the contact area because of adhesion (see below).

Adding soap to the water has only a small influence on the friction for PMMA in the low velocity region. However, it strongly reduces the velocity where the friction has its (first) maximum. In Fig. 23a this is given by the highest velocity data point in all cases (i.e., in the dry state, in water, and in water + soap). We interpret the maximum in the friction coefficient for the lubricated surfaces as the transition to mixed lubrication, where the friction decreases with increasing sliding speed. Clearly, this transition occurs earlier for the water + soap system than when only water is used. We observed a similar effect for concrete lubricated by glycerol (see later in this section): Friction for the lubricated surface was the same as for the dry surface for the velocity region where stable sliding occurs, but the friction coefficient maximum was found at a much lower speed (about 10^{-5} m/s) for the glycerol-lubricated surface than for the dry surface, where the maximum was at about 20-fold higher sliding speed.

The glass–water–rubber system is probably hydrophilic, and in a large fraction of the apparent contact regions we expect the surfaces to be separated by a very thin (maybe about 1 nm) water layer, even at the lowest sliding speed, as expected if the situation shown in Fig. 16b1 prevails. In Fig. 23b for water and for water + soap we also include data points where the sliding motion stops (lowest blue and green data points), and for accelerated motion denoted as run-away (highest blue and green data points). For the water + soap case, Fig. 24 shows the position of the rubber block as a function of time for these two different cases (no motion and run-away motion).

We also measured (after run-in) the surface topography and calculated the surface roughness power spectrum of the rubber tread block used in the study above. Using the contact mechanics theory with adhesion (Ref. [17]), we calculated the contact area as a function of magnification for an elastic solid with the measured power spectrum and elastic modulus $E = 5$ MPa, squeezed against a flat surface

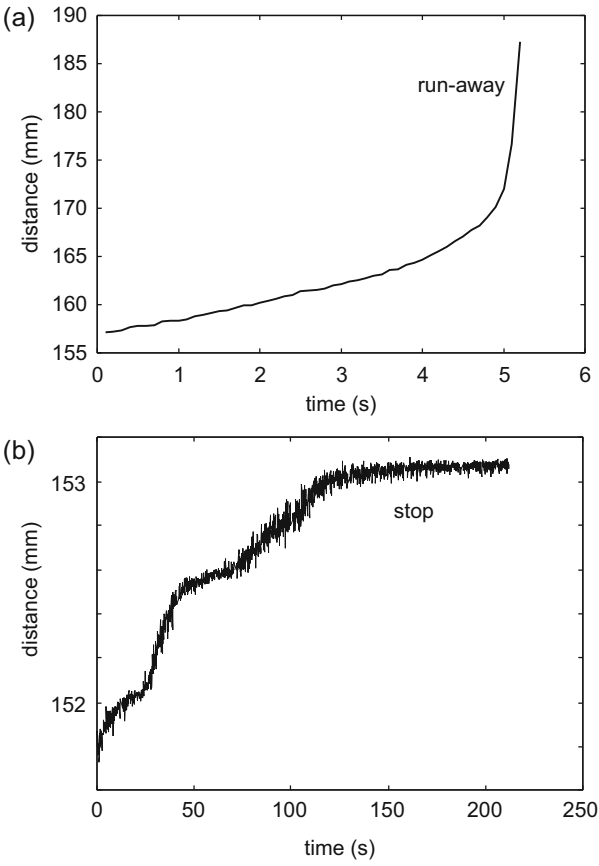

Fig. 24 Position of the rubber block as a function of time for (**a**) the most *right* (run-away), and (b) the most *left* (stop) *green* data points in Fig. 23b

with and without adhesion (see Fig. 25). The result with adhesion is calculated using the (adiabatic) work of adhesion $w = 0.06$ MPa, which is typical for rubber in contact with glass. Note that with adhesion included we get $A/A_0 \approx 0.1$. For rubber on glass (see Fig. 23b) at sliding speed $v = 1$ mm/s we have $\mu \approx 1.5$ for the dry contact, giving the frictional shear stress $\tau_f = \mu p A_0/A \approx 0.75$ MPa, which is similar to the observation of Roberts and Tabor for very smooth rubber and glass surfaces ($\tau_f \approx 0.3$ MPa), where the nominal contact area is probably equal to the actual contact area. Note, however, that the rubber compound used in our study differs from that used in the study of Roberts and Tabor. For the interface lubricated by water and by water + soap (Fig. 23b), $\mu \approx 0.4$ and $\mu \approx 0.2$, respectively. Assuming $A/A_0 \approx 0.05$ (no adhesion), we estimate the frictional shear stress in the area of contact to be ≈ 0.4 MPa and ≈ 0.2 MPa for water and water + soap, respectively.

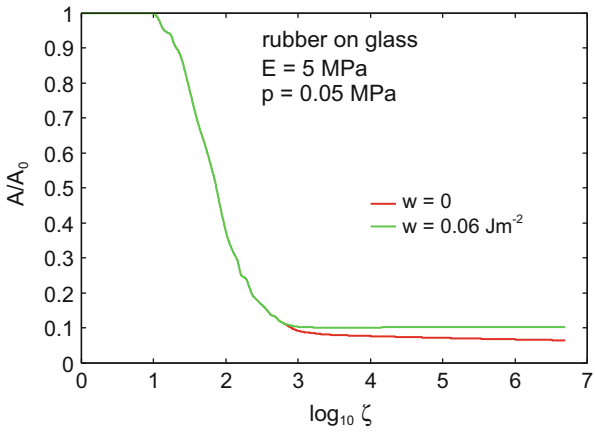

Fig. 25 Calculated contact area for an elastic solid with the surface roughness power spectrum of a rubber tread block (after run-in), as a function of the logarithm of the magnification. Results are shown with (*green curve*) and without (*red curve*) adhesion

Roberts and Tabor studied the contact between a rubber ball and a smooth glass surface in water. The ball was squeezed against the glass surface and it was observed that when the thickness of the water film was below 40 nm, the surfaces suddenly snapped together at various points, leading to adhesive contact over most of the contact region. The contact first occurs at some protrusions (defects) near an edge of the contact zone where the film thickness is smallest; once a point of contact is established, this pulls the rest of the rubber into contact. This dewetting transition depends on the interfacial energies (see above). With a low viscosity fluid such as water as lubricant, surfaces seal together exceedingly quickly at the stage of film collapse.

If, instead of distilled water, a dilute solution of a negatively charged soap (sodium dodecyl sulfate, SDS) is used, a drastically different result ensues. The surfaces no longer snap together trapping islands of liquid (Fig. 26, top left), but at the nominal contact pressure ($p \approx 0.02$ MPa) the surfaces remain apart at an almost uniform separation of about $d \approx 20$ nm (Fig. 26, top right). In this case, the film does not collapse with time but is stabilized by electrical double-layer repulsive forces (osmotic pressure) that support the normal load, even when the squeezing pressure in the contact region equals about 0.1 MPa. The SDS is absorbed on the rubber surface (see Fig. 27) with its negative polar end groups in the water. The glass itself most probably acquires a negative charge through reactions between water molecules and the Si–O groups on the glass surface to form $HOSiO^-$. The two negatively charged surfaces attract positive ions from the solution, establishing a double layer of charge, resulting in repulsive forces between the surfaces at small wall–wall separation. One manifestation of this thin liquid layer is its lubrication effect: sliding at $v = 1$ mm/s results in frictional shear stress $\tau_f \approx 30$ Pa in water + soap, whereas in the dry state or in distilled water $\tau_f \approx 0.3$ MPa. The frictional shear stress in water + soap is what one expects from shearing a water film of 20 nm thickness: $\eta v/d \approx 50$ Pa for $\eta = 0.001$ Pas (the viscosity of water) and $v = 0.001$ m/s.

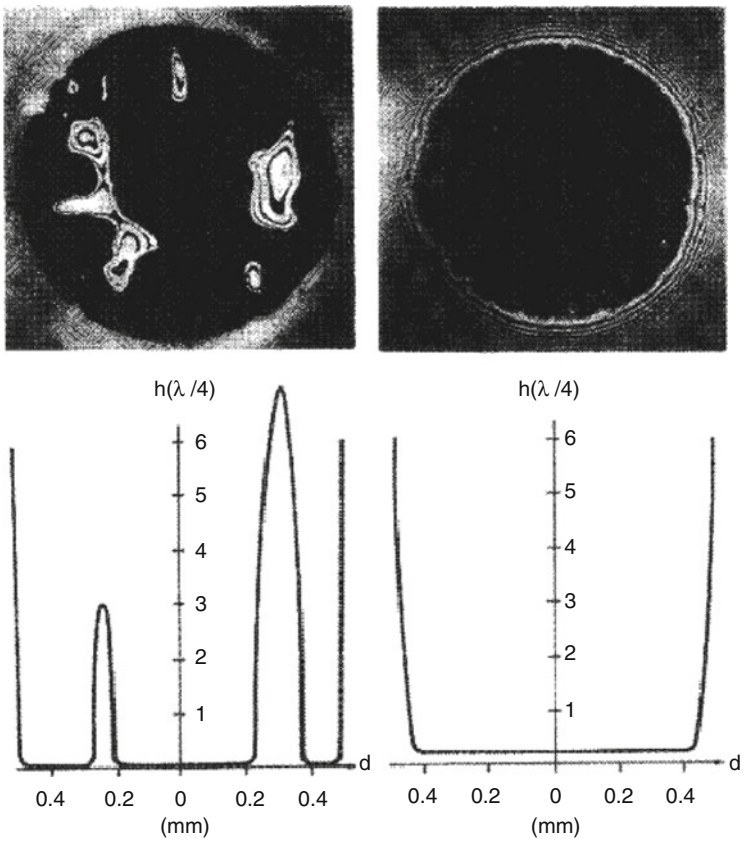

Fig. 26 *Top*: Optical pictures of the contact between a rubber ball with a smooth surface and a glass surface. *Bottom*: Separation between the ball and the glass surface. *Left*: If the rubber ball is squeezed against a glass surface in water, when the surface separation reaches about 100 nm they snap together very fast as a result of adhesion, trapping some fluid islands (which slowly disappear). *Right*: If a negatively charged soap is added to the water, a short range repulsion (osmotic pressure) prevails and the surfaces are separated by about 20 nm when the nominal (applied) pressure is $p_0 \approx 0.02$ MPa. From [52–54]

The friction we observe for rubber on glass in water + soap is much larger than observed by Roberts and Tabor. This probably results from the higher contact pressures that prevailed in our study (about 1 MPa in the asperity contact regions, as compared with $p \approx 0.02$ MPa in the experiments of Roberts and Tabor). This resulted in contact regions where the local pressure was high enough to remove the fluid between the glass and rubber surface. This conclusion is also consistent with the higher friction we observed in soap + water experiments when the rubber surface was contaminated by small rubber particles, where the local contact pressure was even higher than without contamination particles (see Fig. 28).

For a water-lubricated glass surface, Roberts and Tabor observed similar friction as for a dry surface, whereas we observed a reduction in the friction coefficient by a

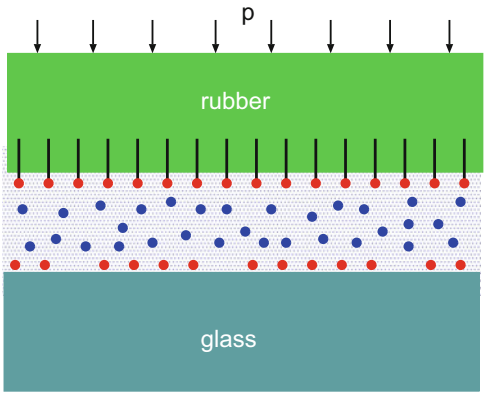

Fig. 27 Rubber–glass contact in soapy water (tentative scheme). Lipid molecules bind to the rubber surface with the hydrocarbon tail in the hydrophobic rubber and the charged head groups in water. The glass surface also becomes charged by ionized surface groups. The water contains counter-ions that balance the charge on the surfaces. During approach, the surfaces first repel each other as a result of osmotic pressure, resulting in a very small contribution to the sliding friction from shearing of the thin confined fluid film. At large applied pressure p, direct contact between the surfaces occurs and results in higher friction. At even larger load, the grafted lipid molecules may be damaged or removed from the contact region, resulting in similar friction as for dry surfaces

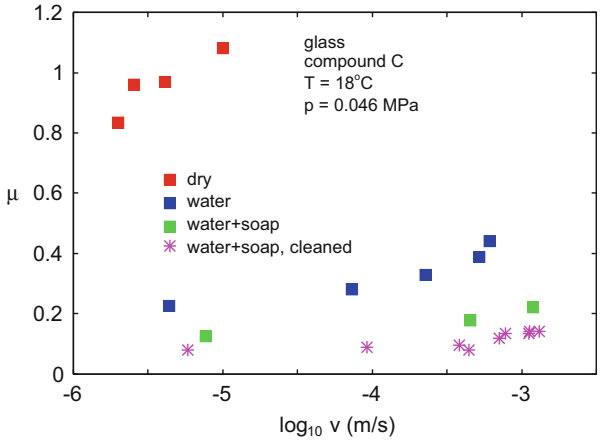

Fig. 28 Measured friction for tread rubber compound C sliding on a dry glass surface (*red squares*), in water (*blue squares*), and in soap + water (*green squares*). The rubber surface had previously been run-in on sandpaper and asphalt road surfaces, resulting in a roughened rubber surface. The substrate surface was not cleaned when going from dry to water to soap + water. Visual inspection of the surface after the soap + water experiment showed that rubber fragments were present on the rubber surface. Removing the rubber fragments resulted in lower friction (*pink asterisks*) in the soap + water

factor of approximately five for the water-covered surface. Part of this may simply reflect the change in contact area as a result of adhesion (see above). Taking this into account, we deduced a frictional shear stress of about 0.4 MPa, which is close to the result obtained by Roberts and Tabor. We note, however, that in the Roberts–Tabor experiment strong adhesion was also observed in water between the rubber and the glass surface, resulting in dewetting and probably near complete atomic contact between the surfaces. In our case, adhesion was probably strongly reduced as a result of surface roughness on the rubber block, which influences the dewetting process. In addition, the rubber compounds differed, which could influence the work of adhesion in the wet state.

It is important to note that even if the surfaces are covered by the highest possible concentration of charges (monolayers of charges), the osmotic pressure can only support applied pressures up to about 1 MPa. If the contact pressure becomes higher than this, which is almost always the case at some locations when rubber is in contact with a hard rough substrate (e.g., asphalt or concrete road surfaces), most of the water is squeezed out. However, hydration lubrication can still result in a small contribution to friction from the area of real contact. Here, hydration shells surrounding charges act as lubricating elements in boundary layers. This has been invoked to account for the extremely low sliding friction in aqueous media, for example, between mica surfaces [75] or more complex systems such as the cartilage in human joints [55]. According to this (see also Appendix 2), hydration shells formed by water molecules are tenaciously attached to the charges they surround, and are not easily squeezed out under compression (even at contact pressures as high as several megapascals), yet they are labile and respond to shear in a fluid manner [56]. Nevertheless, at sufficiently high local pressure p the grafted lipid molecules can be removed from the contact region, resulting in large friction that may be similar to that found for dry surfaces.

10.3 Rubber Friction on Rough Surfaces I

In the following sections we present sliding friction results for the rubber compounds A, B, and C on several different substrate surfaces. As substrates we used a concrete surface and two asphalt road surfaces (denoted 1 and 2). Asphalt 2 contains large stone particles exposing very flat and smooth (almost mirror-like) surfaces. Asphalt 1 is the same as asphalt 2 but with the surfaces slightly roughened with sandpaper. In Sect. 10.4 we also consider rubber friction from three "normal" asphalt road surfaces denoted a, b, and c.

Analysis of the friction data presented below uses the Persson rubber friction theory. As discussed above, there are contributions to friction from (i) viscoelastic energy dissipation in the rubber, and (ii) shearing the area of real contact (frictional shear stress $\tau_f(v, T)$). In the following figures we show the viscoelastic contribution (i) and the total friction (i) + (ii) for dry contact, calculated as described in detail in the literature [30].

10.3.1 Compound A

Figure 29 shows the measured and calculated friction coefficient as a function of sliding speed for rubber compound A sliding on a concrete surface. The background temperature is $T_0 = 10°C$ and the nominal contact pressure is $p = 0.1$ MPa. Measurements were performed for dry contact (red squares) and with the contact lubricated by glycerol (blue squares). The upper green lines are the total calculated rubber friction coefficient and the lower green lines the viscoelastic contribution. The solid lines are without flash temperature and the dashed lines with flash temperature.

Note that the dry and lubricated surfaces exhibit the same friction in the common velocity range. The viscosity of glycerol is about 1000 times higher than that of water, but the low sliding speeds ($v < 10^{-5}$ m/s for the lubricated surface) allow the fluid to squeeze out from the contact regions so that the rubber can make molecular contact with the substrate. If this was not the case (e.g., even if just a few nanometers of fluid separated the surfaces), there would be no reason to obtain the same friction as for the dry surfaces. Note that from the point of view of hydrodynamic lubrication, a sliding speed of $v = 10^{-5}$ m/s in glycerol is equivalent to a sliding speed of $v \approx 10^{-2}$ m/s in water, because the theory of hydrodynamic lubrication predicts that everything depends on the velocity and the fluid viscosity as the product ηv. Thus, for a rubber block sliding on a concrete surface in water, one expects a negligible influence of water on the friction force if $v < 10^{-2}$ m/s. This is consistent with observations we have made in the past.

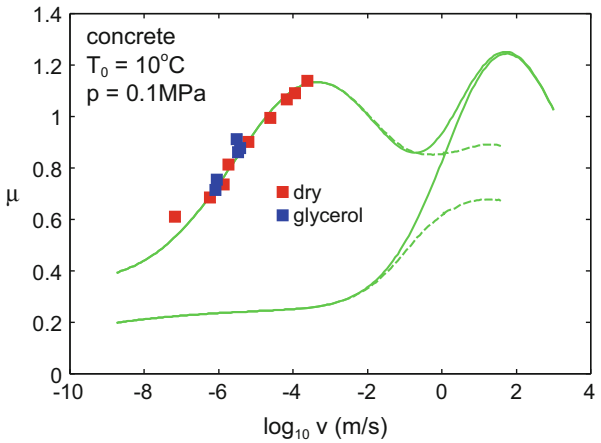

Fig. 29 Measured and calculated friction coefficients as a function of sliding speed for a concrete substrate and rubber compound A. Measurements were performed for dry contact (*red squares*) and a contact lubricated by glycerol (*blue squares*). The *upper green lines* are the total calculated rubber friction coefficient and the *lower green lines* the viscoelastic contribution. The *solid lines* are without flash temperature and the *dashed lines* with flash temperature

The highest velocity data points for both the dry and lubricated contact in Fig. 29 correspond to the highest sliding speed possible before the onset of sliding instability. That is, if the driving force is increased above the values of the highest velocity data points in Fig. 29, the block accelerates and no (low velocity) steady sliding state prevails. With the present experimental setup, in which the driving force rather than the (driving) speed is prescribed, it is not possible to study the rubber friction for higher velocities than shown in Fig. 29. Note that for dry contact, the highest stable sliding speed agrees perfectly with the theoretical prediction (green line), which exhibits a maximum at this sliding speed. This is not the case for the lubricated surface where the (first) maximum in the friction curve occurs at a lower speed (about 10^{-5} m/s). This must result because of a transition from boundary lubrication to mixed lubrication, where the friction decreases with increasing sliding speed for $v > 10^{-5}$ m/s.

Just as for the system studied above, in all the following diagrams, unless otherwise stated, the highest velocity data points correspond to the highest velocities before the onset of sliding instabilities, where the block starts to accelerate. Thus, unless otherwise stated, the highest measured data points correspond to a local maximum in the $\mu(v)$ curves.

Figure 30 shows the measured and calculated friction coefficient as a function of sliding speed for rubber compound A on asphalt road surface 1. Measurements were

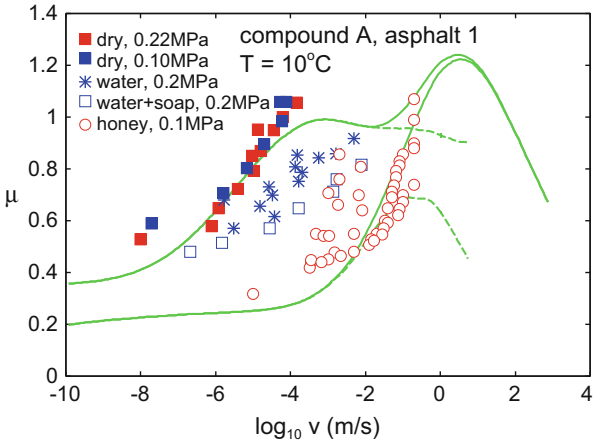

Fig. 30 Measured and calculated friction coefficients as a function of sliding speed for asphalt road surface 1 and rubber compound A. Measurements were performed for dry contact (*red* and *blue squares* for nominal contact pressures of $p = 0.22$ MPa and 0.10 MPa, respectively) and contact lubricated by water (*blue asterisks*, nominal contact pressure 0.20 MPa), water with about 1% soap (dish detergent; *blue squares*, nominal contact pressure 0.20 MPa), and a very thin film of honey (*red circles*, nominal contact pressure 0.10 MPa). In spite of extensive cleaning with water, a very thin honey film must have been left on the surface and resulted in the observed strong reduction in the friction coefficient. For a thick honey film, no steady sliding was observed above $v \approx 10^{-5}$ m/s, indicating that the transition to hydrodynamic lubrication occurs at very low sliding speeds

performed for dry contact (red and blue squares for the nominal contact pressures $p = 0.22$ MPa and 0.10 MPa, respectively), contact lubricated by water (blue asterisks, nominal contact pressure 0.20 MPa), and for water with about 1% soap (dish detergent; blue squares, nominal contact pressure 0.20 MPa). Note that, for dry contact, measurements at the nominal contact pressure $p = 0.22$ MPa give almost the same friction as for $p = 0.10$ MPa. Thus, the friction coefficient for the low sliding speeds studied here is almost independent of the nominal pressure in the pressure range relevant for tire applications. For higher sliding speeds, frictional heating results in a dependency of the friction coefficient μ on the nominal contact pressure. In addition, close to the first maximum of $\mu(v)$ as a function of increasing sliding speed v, $\mu(v)$ depends on the nominal contact pressure as a result of the viscoelastic coupling between the macroasperity contact regions [76]. Asphalt road surface 1 contains large, smooth stone particles, and this is (in contrast to the concrete surface) the reason why the water-covered surface exhibits lower friction than the dry surface. The even lower friction for the water + soap surface could result from adsorbed monolayer films on the road and rubber surfaces (see below).

We also performed measurements with honey as lubricant (red circles, nominal contact pressure 0.10 MPa). When the honey film was thick (several millimeters) only unstable (accelerating) sliding motion prevailed. Thus, the data points shown are for a system where most of the honey was removed by cleaning the surface with water. However, in spite of extensive cleaning with water a very thin honey film must have been left on the surface, resulting in the observed strong reduction in the friction coefficient. For the thick honey film no steady sliding was observed at sliding speeds above the lowest $v \approx 10^{-5}$ m/s data point. This indicates that a transition to the mixed (or hydrodynamic) lubricated sliding state must occur at very low sliding speeds, where $\mu(v)$ is a decreasing function of the sliding speed v. For the washed surface, the honey film thickness must be so small that no mixed (or hydrodynamic) lubrication region exists where the surfaces are separated by a relatively thick fluid (honey) film. Indeed, touching the surface with a finger did not result in a sticky feeling, which would be the case if the honey film was thicker. It is interesting to note that the measured friction coefficient for the thin-film honey-covered surface is close to that predicted from the viscoelastic contribution to the friction (i.e., it seems that the thin honey layer removes the adhesive contribution to friction). However, there should be a contribution to the friction force from shearing the thin honey film (The viscosity of honey may be of the order of 10^3 Pa s but depend on the water content of the honey, which depend on the water humidity in the air.)

After measurements on the surface covered with the thin honey film, the rubber and road surfaces were cleaned extensively with a brush using water containing soap (dish detergent) and then clean water. After drying the surfaces, we again measured the dry sliding friction. Figure 31 shows the results together with the original data from Fig. 30 (red and blue squares). The new data overlaps with the old data in the common velocity region, but the new measurements could be performed to higher sliding speeds before the onset of sliding instability. The green data points were obtained first and the black and pink data points 1 day

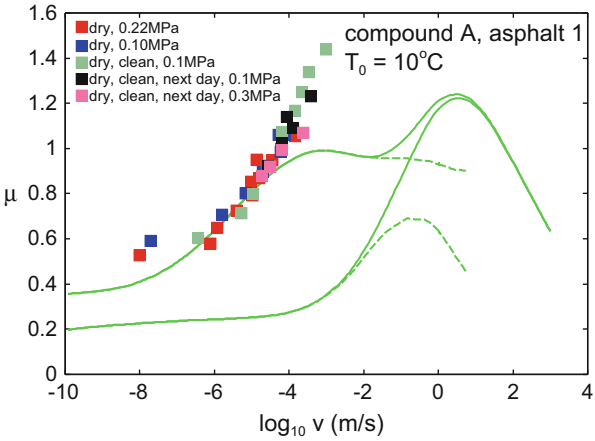

Fig. 31 Measured and calculated friction coefficients as a function of sliding speed for asphalt road surface 1 and rubber compound A. Measurements were performed for dry contact (*red* and *blue squares* from Fig. 30). The other *square symbols* are for the same asphalt road surface after extensive cleaning with water and soap (dish detergent)

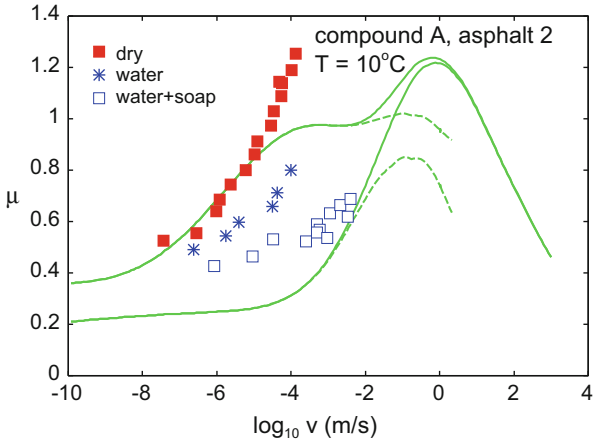

Fig. 32 Measured and calculated friction coefficients as a function of sliding speed for asphalt road surface 2 and rubber compound A. Measurements were performed for dry contact (*red squares*), in water (*blue asterisks*), and in water + soap (dish detergent) (*open blue squares*). The background temperature was $T_0 = 10°C$ and the nominal contact pressure $p = 0.18$ MPa

later. Note that the first measurements (green data points) give the largest maximal friction. We interpret the increase in friction as a result of the influence of adhesion, which may be strongest for the cleanest surface.

Figure 32 shows the measured and calculated friction coefficients as a function of sliding speed for compound A on asphalt road surface 2. Measurements were performed for dry contact (red squares), in water (blue asterisks), and in water + soap (dish detergent, open blue squares). For the dry surface, high frequency noise could be noticed, indicating that local slip events occur at the rubber–road interface.

10.3.2 Compound B

Figure 33 shows the measured and calculated friction coefficient as a function of sliding speed for rubber compound B on asphalt road surface 2. Measurements were

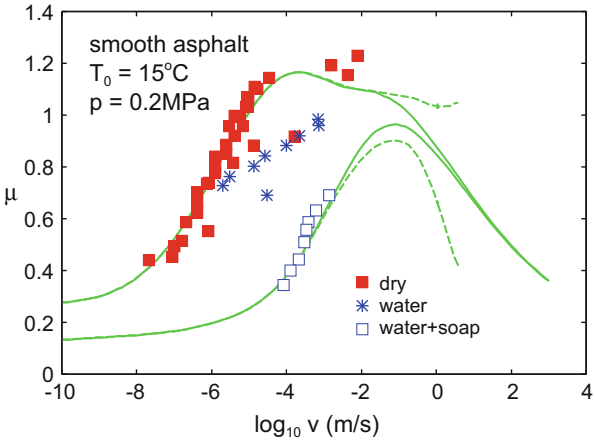

Fig. 33 Measured and calculated friction coefficients as a function of sliding speed for asphalt 2 substrate and rubber compound B. Measurements were performed for dry contact (*red squares*), in water (*blue asterisks*), and in water + soap (*blue open squares*)

performed on dry contact (red squares), in water (blue asterisks) and in water + soap (blue open squares). The upper green lines show the total calculated rubber friction coefficient and the lower green lines the viscoelastic contribution. The three highest velocity data points for the dry surface (red squares) are above the sliding instability point. Accelerated motion occurs, and the quoted velocities are the average over a sliding distance of about 30 cm.

The asphalt road surface used in Fig. 33 contains large stone particles with very flat and extremely smooth surfaces, and in this case adding water results in a drop in friction for sliding speeds larger than about 10^5 m/s. Adding soap (anionic detergent) to the water (open blue squares) results in a strong reduction in friction, which now comes very close to the prediction of the viscoelastic contribution alone (lower green curve). The soap has negligible influence on the fluid viscosity, so the strong reduction in friction must relate to a strong reduction in the frictional shear stress in the area of real contact. This is indeed expected. Thus, the lipid molecules bind to the rubber and probably also to the bitumen, with the hydrocarbon tail in the hydrophobic rubber and the bitumen surfaces, and with the charged head groups in water. The soap we use is (mainly) an anionic detergent, with (in water) negatively charged head groups and Na^+ counter-ions in the water surrounded by water hydration shells. The stone surfaces also become negatively charged by ionized surface groups (see Sect. 10.2). The water contains counter-ions that balance the charge on the surfaces. During approach, the surfaces first repel each other as a result of osmotic pressure, resulting in a very small contribution to the sliding friction from shearing the thin, confined fluid film. For higher contact pressures, most of the fluid is squeezed out but the contribution to friction from the area of contact could still be small as a result of hydration lubrication (see Appendix 2).

In the velocity range between about 1 μm/s and 1 mm/s, we believe that the most important contribution to friction for dry surfaces involves polymer chains at the interface between the rubber block and counter-surface performing stick–slip

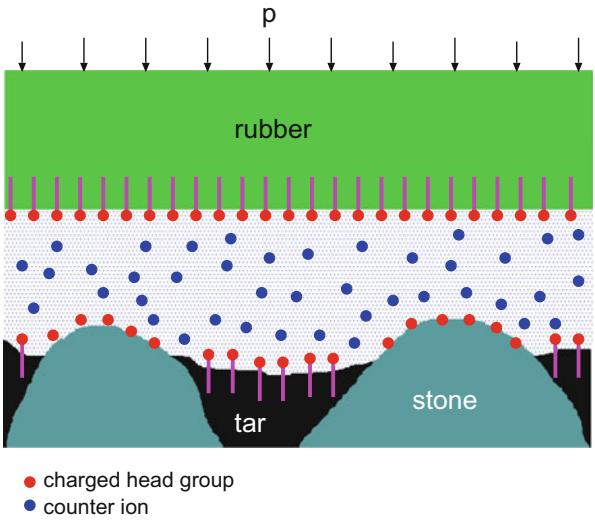

Fig. 34 Rubber–road contact in soapy water (tentative scheme). Lipid molecules bind to the rubber and bitumen, with the hydrocarbon tail in the hydrophobic rubber and bitumen surfaces and the charged head groups in water. The stone surfaces also become charged by ionized surface groups. The water contains counter-ions that balance the charge on the surfaces. During approach, the surfaces first repel each other as a result of osmotic pressure, resulting in a very small contribution to the sliding friction from shearing the thin, confined fluid film. At large applied pressure p, direct contact between the surfaces occurs and results in higher friction. At even larger load, the grafted lipid molecules may be damaged or removed from the contact region, resulting friction similar to that seen for dry surfaces

motions as indicated in Fig. 14. In water, the soap (fatty acid) molecules bind to both the rubber and the road surface (see Fig. 34) so that the process shown in Fig. 14 cannot occur. As a result of the small shear stress of the interface when the surfaces are separated by a thin fluid film, the contribution to friction from the area of contact becomes very small. Without soap, if the water is completely removed in the contact regions between the rubber and the road, the contribution from the area of real contact may be similar to that of dry surfaces, as is indeed observed at low sliding speeds for wet road surfaces.

10.4 Rubber Friction on Rough Surfaces II

We now present the results of measurements for rubber compounds A, B, and C on asphalt road surfaces a, b, and c. For these surfaces it was not always possible to increase the velocity such that the (first) maximum in $\mu(v)$ could be reached.

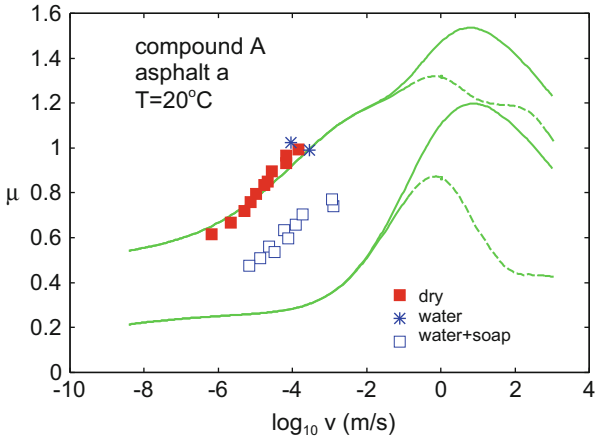

Fig. 35 Measured and calculated friction coefficients as a function of sliding speed for compound A on asphalt road a. The background temperature is $T_0 = 20^\circ$C and the nominal contact pressure $p = 0.1$ MPa

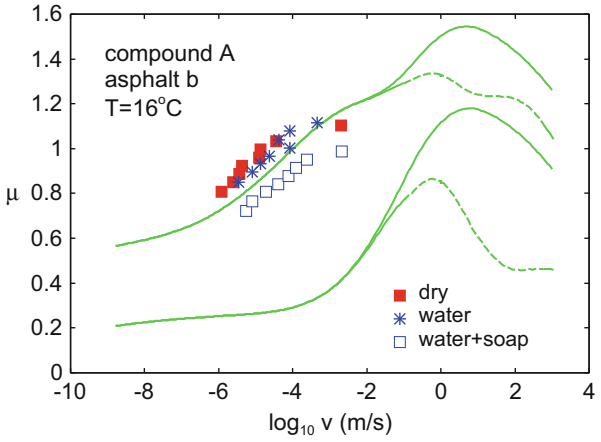

Fig. 36 Measured and calculated friction coefficients as a function of sliding speed for compound A on asphalt road b. The background temperature is $T_0 = 16^\circ$C and the nominal contact pressure $p = 0.1$ MPa

10.4.1 Compound A

In Fig. 35 we show the measured and calculated friction coefficients as a function of sliding speed for compound A on asphalt road a. The upper green lines are the total calculated rubber friction coefficient and the lower green lines the viscoelastic contribution. The solid lines are without flash temperature and the dashed lines

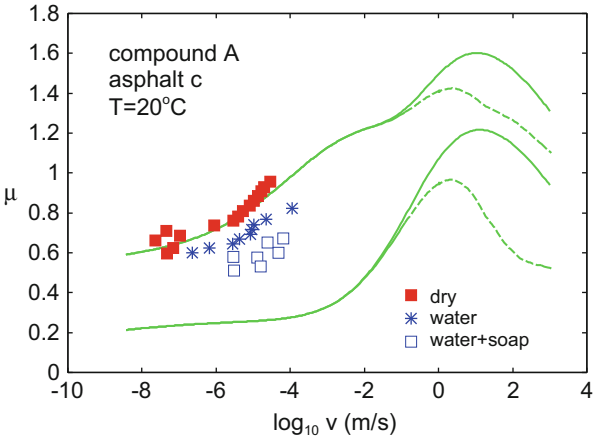

Fig. 37 Measured and calculated friction coefficients as a function of sliding speed for compound A on asphalt road c. The background temperature is $T_0 = 20^\circ$C and the nominal contact pressure $p = 0.1$ MPa

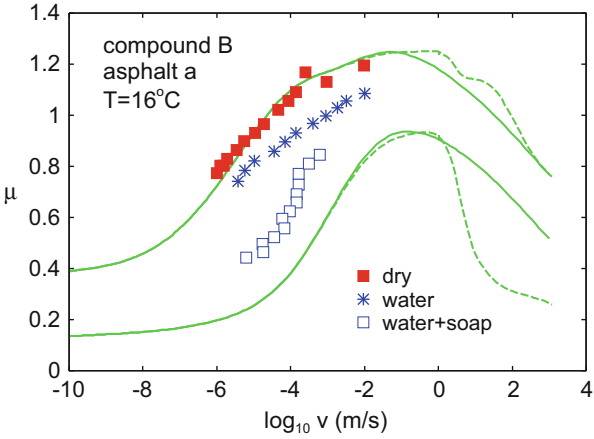

Fig. 38 Measured and calculated friction coefficients as a function of sliding speed for compound B on asphalt road a. The background temperature is $T_0 = 16^\circ$C and the nominal contact pressure $p = 0.1$ MPa

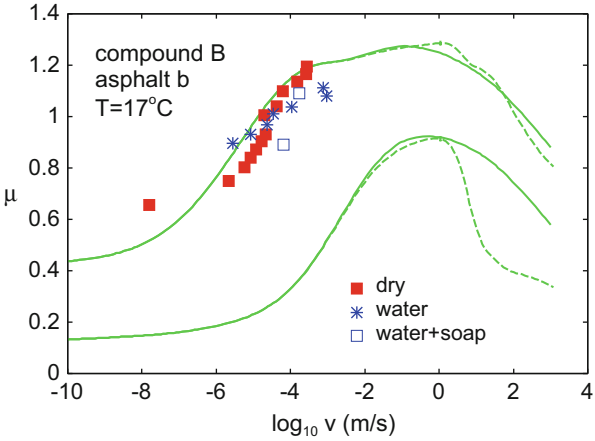

Fig. 39 Measured and calculated friction coefficients as a function of sliding speed for compound B on asphalt road b. The background temperature is $T_0 = 17^\circ$C and the nominal contact pressure $p = 0.1$ MPa

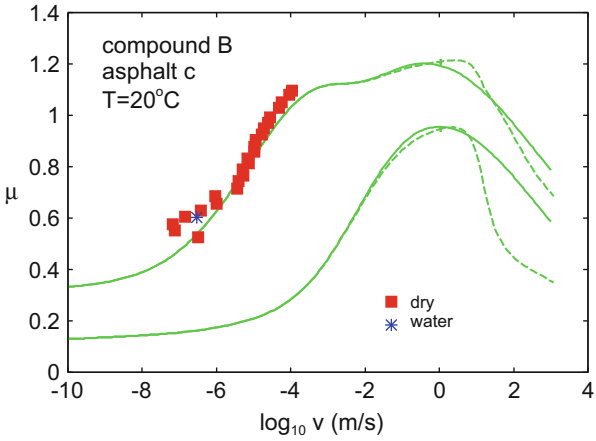

Fig. 40 Measured and calculated friction coefficients as a function of sliding speed for compound B on asphalt road c. The background temperature is $T_0 = 20^\circ$C and the nominal contact pressure $p = 0.1$ MPa

with flash temperature. The background temperature is $T_0 = 20^\circ$C and the nominal contact pressure $p = 0.1$ MPa.

The red squares in Fig. 35 are the results for the dry surface and the blue asterisks the results when the surface is in water. The blue squares are for water with a small amount (less than 1 %) of soap. Note that the water has a negligible influence on friction in the studied low-velocity range. This is in contrast to the results for the very smooth asphalt road surface 2 in Sects. 10.3.1 and 10.3.2 (see Figs. 32 and 33), where water resulted in a strong reduction in friction. For rubber compound B on asphalt road surface 2 (see Fig. 33), the water + soap completely removes the contribution from the area of contact. In the present case too, the soap results in a relatively large reduction in friction. As discussed in Sect. 10.2, this is not a result of changes in the viscosity of the fluid (the small amount of soap results in only a small change in fluid viscosity). The soap molecules form grafted monolayers (or multilayers) on the solid surfaces, which may strongly reduce the frictional shear stress in the area of contact.

Figures 36 and 37 show similar results as Fig. 35, but for asphalt road surfaces b and c, respectively. Again, water has a negligible influence on the observed friction for surface b, although some reduction is observed for surface c. The influence of soap on friction is smaller for road surface b than for road surfaces a and c.

10.4.2 Compound B

Figures 38, 39, and 40 show similar results for compound B as those presented for compound A. Qualitatively, the results for compounds A and B are similar, with a stronger influence of water + soap on friction for road surface a.

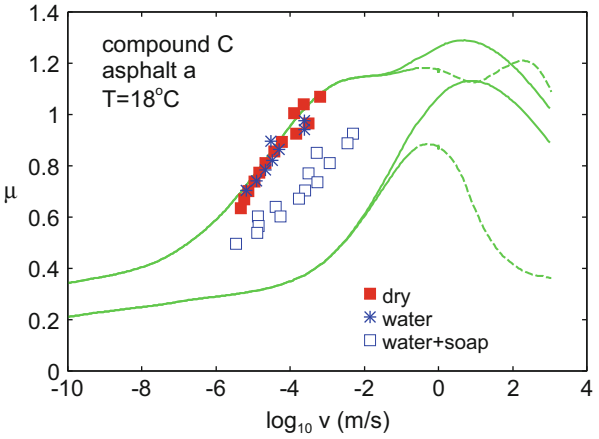

Fig. 41 Measured and calculated friction coefficients as a function of sliding speed for compound C on asphalt road a. The background temperature is $T_0 = 18^\circ$C and the nominal contact pressure $p = 0.1$ MPa

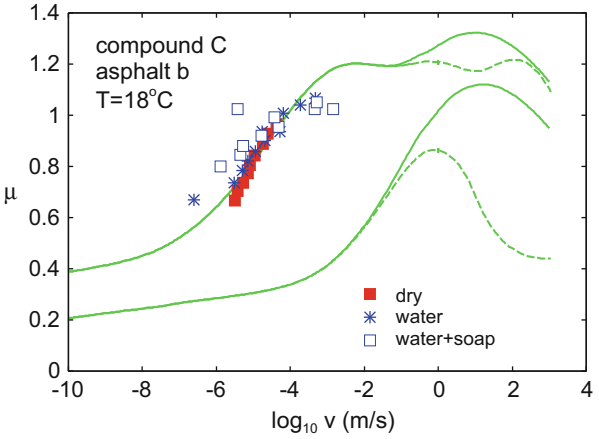

Fig. 42 Measured and calculated friction coefficients as a function of sliding speed for compound C on asphalt road b. The background temperature is $T_0 = 18^\circ$C and the nominal contact pressure $p = 0.1$ MPa

10.4.3 Compound C

Figures 41 and 42, show similar results for compound C. Again, when soap is added to water, asphalt road surfaces a and c exhibit a stronger reduction in friction than surface b. For both surfaces a and b, the dry and wet (pure water) surfaces exhibit the same friction within the accuracy of the experiments. Thus, the difference observed for the water + soap case (where a clear reduction in friction is observed for surface a but not for surface b) is not related to fluid squeeze-out (which clearly happens on both surfaces), but must be caused by larger local stresses in the contact area on surface b than on surfaces a and c. This could be a result of the larger kurtosis for surface b (kurtosis = 4.8) than for surfaces a (4.0) and c (3.9) (Fig. 43).

It is very interesting to note that for the very smooth asphalt road surfaces used in Sects. 10.3.1 and 10.3.2 the maximum friction was larger than predicted by theory, using the value for maximum adhesive frictional shear stress found in this study and

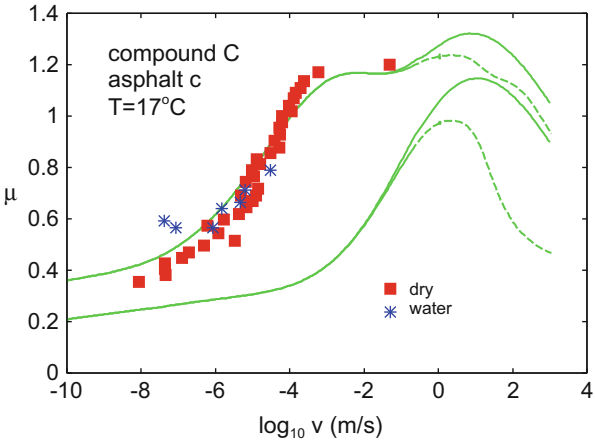

Fig. 43 Measured and calculated friction coefficients as a function of sliding speed for compound C on asphalt road c. The background temperature is $T_0 = 17^{\circ}\mathrm{C}$ and the nominal contact pressure $p = 0.1$ MPa

in an earlier study for rougher asphalt road surfaces and concrete surfaces. In addition, the maximum value was very sensitive to how clean the surface was. This indicates that for the very smooth asphalt surfaces in Sects. 10.3.1 and 10.3.2 adhesion becomes very important (it manifest itself as a finite pull-off force), tending to increase the contact area beyond the value predicted by the viscoelastic contact mechanics used in this study.

11 Discussion

We have compared experimental data obtained at very low sliding speeds with the results of rubber friction calculations for dry contact where the friction was assumed to be the sum of a viscoelastic contributions from asperity-induced deformations of the rubber surface, and a contribution from the area of real contact. Thus, the theoretical calculations are not directly valid for wet (lubricated) surfaces. However, for very smooth surfaces (and hydrophilic interfaces) a thin fluid film may separate the surfaces in the (apparent) contact regions, and in that case the viscoelastic contribution dominates friction. We have observed this to be the case, even at low sliding speeds, for asphalt road surfaces with large and very smooth stone particles in a fluid consisting of water + soap. At higher sliding speeds, even clean water can result in a thin fluid film separating the sliding surfaces everywhere, and in this case too the viscoelastic contribution dominates friction. However, the large wavenumber cut-off q_1 is less than for dry surfaces, because the water can effectively smooth the surface roughness profile at short length scales as a result of fluid pressure buildup caused by the fluid viscosity. Indeed, experiments by Ueckermann et al. [77], at sliding speeds of approximately 10 m/s, show friction coefficients in the range of about 0.3–0.6, which are similar to the calculated viscoelastic contribution to friction for this sliding speed. Ueckermann et al. also

found very good correlation between the measured friction coefficients and the calculated viscoelastic contribution to the friction coefficients for a large number of rubber–road surface combinations.

As discussed above, rubber friction on dry and lubricated road surfaces is a highly complex topic. There are four fundamental problems, briefly mentioned in Sects. 8 and 9, that must be understood in order to understand the nature of rubber friction for lubricated surfaces:

1. Mixed lubrication and fluid squeeze-out. This involves studying fluid flow at the interface between the tire tread blocks and the road surface on many length scales. At short length scales, fluid flow occurs in narrow channels with complex geometry. This is illustrated in Fig. 10, which shows fluid flow at the interface from a high-pressure region on the left to a low-pressure region on the right [28]. The picture is the result of a numerical study, but in the context of rubber friction such an approach is not easy to implement. However, an approximate treatment is possible using Persson contact mechanics theory and the Reynolds equations of fluid flow (these are simplified Navier–Stokes equations) [78]. It is important to note that percolation of the contact area can result in confined fluid regions, which would carry part of the external load and reduce friction. Even if the nominal contact pressure was not sufficiently high for the contact area to percolate globally, it could percolate in the macroasperity contact regions or at shorter length scales, which could strongly reduce friction.
2. Dewetting. When the water film becomes very thin a dewetting transition can occur, resulting in dry contact regions. The dewetting transition occurs only if the interfacial free energy is lowered when the contact becomes dry, which depends on the rubber–water, road–water, and rubber–road interfacial energies. Interfacial energies can be estimated from contact angle measurements using standard methods. Although interfacial dewetting has been studied in detail for stationary contact, the topic is much more complex for sliding contacts and very few studies exist.
3. Fluid film rheology. Water can probably be treated as a Newtonian liquid down to nanometer thickness, but this is not the case with most other fluids. Depending on the type of fluid, one may need to take into account non-Newtonian liquid behavior such as shear thinning. Much is now known about this topic because of surface forces apparatus (SFA) measurements.
4. The influence of water on frictional heating. Clearly, on wet road surfaces the water has a cooling effect on the tire tread block rubber, which will influence rubber friction.

12 Summary and Conclusion

In this paper we have briefly reviewed the processes that determine rubber friction on dry and lubricated smooth and rough substrate surfaces. We have presented experimental friction results obtained using a simple Leonardo da Vinci setup. We

have measured the rubber friction for three tire tread compounds on several substrate surfaces, including five asphalt road surfaces, smooth PMMA, and glass. The study was performed at low sliding speeds ($v < 5$ cm/s) so that frictional heating could be neglected. The road surface topographies were measured using a stylus instrument, and the rubber compounds characterized using DMA. The data was analyzed using the Persson rubber friction and contact mechanics theory.

For wet surfaces at sufficiently high sliding speed (above a few meters per second) a thin water film separates most rubber–road (apparent) contact regions, in which case rubber viscoelasticity is the main contribution to friction. At the low sliding speeds considered in this paper ($v < 0.05$ m/s) water mostly causes only a small reduction in friction. However, for very smooth asphalt road surfaces, we observed that water + soap can remove most of the contribution to friction from the area of contact, and the friction is, to a good approximation, given by the viscoelastic contribution alone.

Acknowledgments This work was performed within a Reinhart–Koselleck project funded by the Deutsche Forschungsgemeinschaft (DFG). We would like to thank DFG for project support under the DFG grant MU 1225/36-1. The research work was also supported by DFG grant PE 807/10-1. This work is supported in part by COST Action MP1303.

Appendix 1

When a hard ball is in contact with a smooth rubber surface, a circular contact region forms with a radius r_0 that depends on the applied normal load and the adhesive ball–rubber interaction. When the ball is removed from the substrate, the radius $r_0(t)$ of the contact region decreases with time. The bond-breaking process can be considered as an opening crack propagating with velocity $v = \left|\dot{r}_0(t)\right|$ (see Fig. 44a). For a viscoelastic material such as rubber, the energy to propagate an opening crack at a finite speed v can be much larger than for an adiabatic (infinitely slowly) moving crack. This effect is a result of energy dissipation inside the rubber because of the time-dependent stress field from the moving crack. For an infinitely

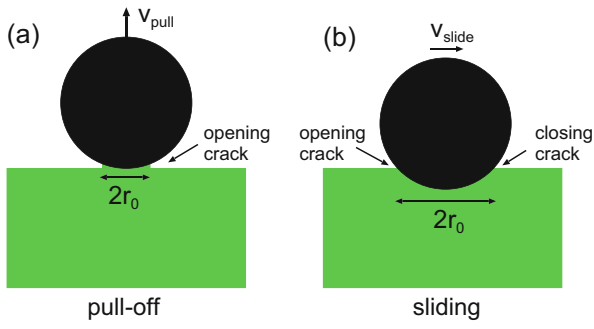

Fig. 44 Pull-off (**a**) and sliding (**b**) of a hard, smooth ball in contact with a smooth rubber surface

long crack moving with velocity v one usually writes the energy per unit area to propagate the crack as [9, 64, 79–81]:

$$G(v,T) = G_0(T)[1 + f(v,T)], \tag{20}$$

where $f(v,T)$ is the viscoelastic enhancement factor. Note that $f \to 0$ as $v \to 0$, so G_0 is the energy per unit area to form the crack surfaces in the adiabatic limit. For an infinitely long crack in an infinitely extending media, f may increase by a factor of about 1000 as v increases from zero to a high value. For a particular rubber and counter-surface combination, $G(v,T)$ is often measured by pulling a rubber strip in adhesive contact with the counter-surface [81].

We assume that the viscoelastic loss function $\mathrm{Im}E^{-1}(\omega)$ is maximal for $\omega = \omega_c$. When an opening crack propagates at some speed v, the time-dependent deformations of the rubber at distance r from the crack tip are characterized by the deformation frequency $\omega = v/r$. Thus, most of the viscoelastic energy dissipation occurs in a region centered a distance $r \approx v/\omega_c$ away from the crack tip.

Let us now consider opening cracks of finite size, for example, a circular opening crack with radius $r_0(t)$ formed during removal of a ball from the substrate. If $r_0 > v/\omega_c$ one can still (approximately) use expression (20) to calculate the energy and force necessary to remove the ball (which depends on the pull-off speed). However, if the ball has a small enough radius (such that the radius of the contact region r_0 is small enough), or if the pull-off speed is large enough (so the crack tip velocity v is large enough), then this inequality is not valid and the viscoelastic enhancement factor decreases (B. Persson, unpublished). This important fact is usually overlooked in the interpretation of adhesion experiments.

When a hard ball slides on the surface of a rubber block, an opening crack is formed at the back (see Fig. 44b). In this situation too, when calculating the contribution of viscoelastic energy dissipation to the friction force, one needs to take into account the possibility that f is reduced because of finite-size effects. This is particularly important for sliding of a rubber block on a hard rough substrate, where the substrate asperities act on the rubber block in the same way as on the ball in Fig. 44b. Here, the linear size of the contact regions may be very small (e.g., of micrometer size) and the value of $f(v,T)$ derived or measured for long cracks may give a much larger viscoelastic enhancement factor than the actual factor, particularly for high sliding speeds (B. Persson, unpublished).

Note that for rubber friction on very rough surfaces such as road surfaces, the cut-off length λ_1 (related to the wavenumber cut-off $q_1 = 2\pi/\lambda_1$) is typically abound 1 μm. Because the slip velocity in tire applications is about 1 m/s and the maximum of $\mathrm{Im}E^{-1}(\omega)$ is typically for $\omega_c = 10^6\ \mathrm{s}^{-1}$, we obtain $r_0 = v/\omega_c \approx 1$ μm. Thus, in tire applications or for road surfaces the reduction in f (and in the adhesive contribution to friction) because of finite-size effects may not be very important.

Appendix 2

In this appendix we briefly describe hydration lubrication [55, 56], which is the hypothesis that hydration shells surrounding charges act as lubricating elements in boundary layers, resulting in extremely low sliding friction in aqueous media, (e.g., between mica surfaces) [75]. This highly fluid behavior under extreme confinement and shear is in direct contrast to the performance of nonassociating simple liquids (e.g., octamethylcyclotetrasiloxane (OMCTS), cyclohexane, or toluene) under similar conditions. These nonassociating liquids undergo liquid-to-solid phase transition, resulting in a finite yield stress once confined to six to nine molecular layers. It has been suggested that the lubricity of hydrated films of Na^+ relies upon two factors: (i) the capacity of water to retain its bulk fluidity under confinement and in hydration layers around charged species, and (ii) the strong binding of water molecules within the hydration shell around Na^+. The latter supports an applied load, therefore preventing primary minimum contact (which is adhesive and leads to high shear forces) between the mica surfaces. The shear lubricity of these load-bearing hydrated films has been rationalized in terms of the rapid kinetics of exchange of water molecules within hydration spheres with adjacent water molecules, as well as the rapid rotational dynamics and diffusivity of the water molecules within the thin film. The bulk water exchange rate, k_{ex}, for a water ligand in the primary hydration sphere of Na^+ is approximately 10^9 s^{-1}. In addition, the rotational relaxation time of water molecules (about 10^{-11} s in bulk water) is thought to be a factor in the persistent fluidity of the confined hydration layers.

In general, two conditions must be satisfied in order for hydration lubrication to take place [56]: (i) ions must remain bound to the shearing surfaces under confinement, and (ii) the surface-bound ions must retain their hydration shell under confinement and applied load. When these conditions are fulfilled, hydration lubrication is mediated by the (thermodynamically) bound and fluid-like hydration layers attached to interfacial charged species. With respect to contact mechanics and friction, we can qualitatively consider the hydrated Na^+ ions as slippery elastic balls. Note that hydration lubrication is also likely to occur in more complex, strongly hydrated interfaces, such as occur in synovial joints and mucosal surfaces.

Finally, we note that at very large applied pressure p the grafted lipid molecules may be removed from the contact region. The result is increased friction, which may be similar to that found for dry surfaces.

References

1. Persson BNJ (1998) Sliding friction: physical principles and applications. Springer, Berlin
2. Heinrich G (1997) Rubber Chem Technol 70:1
3. Persson BNJ (1998) Surf Sci 401:445
4. Persson BNJ (2001) J Chem Phys 115:3840
5. Klüppel M, Heinrich G (2000) Rubber Chem Technol 73:578

6. Heinrich G, Kluppel M, Vilgis TA (2000) Comput Theor Polym Sci 10:53
7. Berger HR, Heinrich G (2000) Kautschuck Gummi Kunststoffe 53:200
8. Heinrich G, Schramm J, Kluppel M, Muller A, Kendziorra N, Kelbch S (2003) Tire - chassis - roads. VDI Ber 1791:47
9. Persson BNJ, Albohr O, Heinrich G, Ueba H (2005) J Phys Condens Matter 17:R1071
10. Persson BNJ (1998) Sliding friction - physical principles and practical applications. Springer, Berlin
11. Almqvist A, Campana C, Prodanov N, Persson BNJ (2011) J Mech Phys Solids 59:2355
12. Campana C, Müser MH (2007) Europhys Lett 77:38005
13. Hyun S, Pei L, Molinari J-F, Robbins MO (2004) Phys Rev E 70:026117
14. Persson BNJ (2008) J Phys Condens Matter 30:312001
15. Persson BNJ (2007) Phys Rev Lett 99:125502
16. Yang C, Persson BNJ (2008) J Phys Condens Matter 20:215214
17. Persson BNJ (2002) Eur Phys J E 8:385
18. Persson BNJ, Sivebaek IM, Samoilov VN, Zhao K, Volokitin AI, Zhang Z (2008) J Phys Condens Matter 20:395006
19. Pastewka L, Robbins MO (2014) Proc Natl Acad Sci 111:3298
20. Persson BNJ, Scaraggi M (2014) J Chem Phys 141:124701
21. Carbone G, Scaraggi M, Tartaglino U (2009) Eur Phys J E 30:65
22. Persson BNJ, Yang C (2008) J Phys Condens Matter 20:315011
23. Lorenz B, Persson BNJ (2010) Eur Phys J E 31:159
24. Campana C, Persson BNJ, Müser MH (2011) J Phys Condens Matter 23:085001
25. Akarapu S, Sharp T, Robbins MO (2012) Phys Rev Lett 106:204301
26. Barber JA (2003) Proc R Soc Lond A 495:53
27. Persson BNJ, Lorenz B, Volokitin AI (2010) Eur Phys J E 31:3
28. Dapp WB, Lücke A, Persson BNJ, Müser MH (2012) Phys Rev Lett 108:244301
29. Lorenz B, Persson BNJ (2010) Europhys Lett 90:38003
30. Lorenz B, Oh YR, Nam SK, Jeon SH, Persson BNJ (2015) J Chem Phys 142:194701
31. Grosch KA (1963) Proc R Soc Lond Ser A 274:21
32. Grosch KA (1997) Rubber Chem Technol 69:495
33. Lorenz B, Persson BNJ, Fortunato G, Giustiniano M, Baldoni F (2013) J Phys Condens Matter 25:095007
34. Lang A, Klüppel M (2014) In: Book of abstracts KHK 11th Fall Rubber Colloquium, 26–28 Nov 2104, Hanover. DIK, Hanover
35. RodrÃ-guez NV, Masen MA, Schipper D-J (2013) Proc Inst Mech Eng J J Eng Tribol 227:398
36. de Vicente J, Stokes JR, Spikes HA (2006) Food Hydrocoll 20:483
37. Vorvolakos K, Chaudhury MK (2003) Langmuir 19:6778
38. Westerman S, Petry F, Boes R, Thielen G (2004) Kautschuk Gummi Kundstoffe 57:645
39. de Vicente J, Stokes JR, Spikes HA (2005) Tribol Lett 20:273
40. Bongaerts JHH, Fourtouni K, Stokes JR (2007) Tribol Int 40:1531
41. Persson BNJ (2000) Sliding friction: physical principles and applications, 2nd edn. Springer, Heidelberg
42. Schallamach A (1963) Wear 6:375
43. Cherniak YB, Leonov AI (1986) Wear 108:105
44. Persson BNJ, Volokitin AI (2006) Eur Phys J E 21:69
45. Gal AL, Yang X, Klüppel M (2005) J Chem Phys 123:014704
46. Persson BNJ (2006) J Phys Condens Matter 18:7789
47. Fortunato G, Ciaravola V, Furno A, Lorenz B, Persson BNJ (2015) J Phys Condens Matter 27:175008
48. Carbone G, Putignano C (2014) Phys Rev E 89:032408
49. Scaraggi M, Persson BNJ (2015) J Phys Condens Matter 27:105102
50. Leonov AI (1990) Wear 141:137

51. Yakubov GE, Branfield TE, Bongaerts JHH, Stokes JR (2015) Tribology of particle suspensions in rolling-sliding soft contacts. Biotribology 3:1–10
52. Richards SC, Roberts AD (1988) J Nat Rubber Res 3:210
53. Roberts AD, Tabor D (1971) Proc R Soc A 325:323
54. Roberts AD (1971) In: Hays DF, Browne AL (eds) The physics of tire friction: theory and experiment. New York, Plenum
55. Ma L, Gaisinskaya-Kipnis A, Kampf N, Klein J (2015) Nat Commun 6:6060. doi:10.1038/ncomms7060
56. Perkin S, Goldberg R, Chai L, Kampf N, Klein J (2009) Faraday Discuss 141:399
57. Persson BNJ (2014) Tribol Lett 54:99
58. Persson BNJ, Albohr O, Tartaglino U, Volokitin AI, Tosatti E (2005) J Phys Condens Matter 17:R1
59. Li Q, Popov M, Dimaki A, Filippov AE, Kürschner S, Popov VL (2013) Phys Rev Lett 111:034301
60. Lyashenko I, Pastewka L, Persson BNJ (2013) Phys Rev Lett 111:189401
61. Persson BNJ (2015) Tribol Lett 58:1
62. Carbone G, Mangialardi L (2004) J Mech Phys Solids 52:1267
63. Krick BA, Vail JR, Persson BNJ, Sawyer WG (2012) Tribol Lett 45:185
64. Persson BNJ, Brener EA (2005) Phys Rev E 71:036123
65. Knauss WG (2015) Int J Fract 196:99
66. Persson BNJ (2010) J Phys Condens Matter 22:265004
67. Yamada S (2002) Tribol Lett 13:167
68. Sivebaek IM, Samoilov VN, Persson BNJ (2012) Phys Rev Lett 108:036102
69. Thompson PA, Grest GS, Robbins MO (1992) Phys Rev Lett 68:3448
70. Brochard-Wyart F, de Gennes PG (1994) J Phys C 6:A9
71. Martin A, Buguin A, Brochard-Wyart F (2001) Langmuir 17:6553
72. Persson BNJ, Volokitin AI, Tosatti E (2003) Eur Phys J E 11:409
73. Persson BNJ, Tartaglino U, Albohr O, Tosatti E (2005) Phys Rev B 71:035428
74. Lorenz B, Rodriguez N, Mangiagalli P, Persson BNJ (2014) Eur Phys J E 37:57
75. Sakuma H, Otsuki K, Kurihara K (2015) J Traffic Transportation Eng (English Edition) 2:59
76. Braun O, Steenwyk B, Warhadpande A, Persson BNJ (2016) Europhys Lett 113: 56002
77. Ueckermann A, Wang D, Osser M, Steinaner B (2015) Int J Pavement Eng 16:646
78. Persson BNJ, Scarggi M (2011) Eur Phys J E 34:113
79. Gent AN, Schultz J (1972) J Adhes 3:281
80. Maugis D, Barquins M (1978) J Phys D 11:1989
81. Gent AN (1996) Langmuir 12:4492

Adv Polym Sci (2017) 275: 157–186
DOI: 10.1007/12_2016_3

Published online: 24 July 2016

Multiscale Modeling Approach to Dynamic-Mechanical Behavior of Elastomer Nanocomposites

Ievgeniia Ivaneiko, Vladimir Toshchevikov, Stephan Westermann, and Marina Saphiannikova

Abstract Rubber composites based on an elastomeric matrix filled with rigid fillers such as carbon black or silica remain important materials for technical applications and everyday life. Targeted improvement of the mechanical properties of these materials requires a deep understanding of the molecular mobility over broad time and temperature scales. We focus here on recent studies of the dynamic properties of rubber composites with the aid of a physically motivated multiscale theoretical approach. Rubber compounds, based on a solution-polymerized styrene butadiene rubber filled with precipitated silica, have been investigated. The construction of master curves for the storage and loss moduli over more than 15 decades of frequencies is presented. The master curves over the whole frequency range are analyzed with the aid of a new multiscale approach, which includes contributions from the relaxation processes described in rigorous theoretical studies for different scales of motion. It takes into account the long-scale motions of dangling chain ends, Rouse-like dynamics and bending motions of semiflexible chain fragments in the intermediate frequency range, and the specific nonpolymeric relaxation at very high frequencies. The modification of molecular mobility of polymer chains on the surfaces of filler particles and the contribution of the percolation network built by the filler are discussed. The proposed theoretical approach allows fitting of the dynamic moduli of filled and unfilled rubbers in the linear viscoelastic regime with

---

The authors declare no competing financial interests.

I. Ivaneiko, V. Toshchevikov, and M. Saphiannikova (✉)
Leibniz-Institut für Polymerforschung Dresden e. V., Hohe Strasse 6, 01069 Dresden, Germany
e-mail: grenzer@ipfdd.de

S. Westermann
Goodyear Innovation Center Luxembourg, Avenue Gordon Smith, 7750 Colmar-Berg, Luxembourg

a limited set of parameters (relaxation times, scaling exponents, molar mass of the Kuhn segment, etc.) having reasonable values. The slowing down of the relaxation processes in the vicinity of the filler particles is demonstrated.

Keywords Dynamic moduli • Multiscale theoretical approach • Polymer localization • Rigid fillers • Rubber composites

Contents

1 Introduction

The present review article focuses on recent research conducted in the area of modeling the linear dynamic-mechanical properties of elastomer nanocomposites [1, 2]. The authors devote this article to Prof. Dr. Gert Heinrich, without whose tremendous expertise in the theoretical and experimental aspects of polymers, elastomers, and rubbers this work would not have been successful.

It is well established that knowledge of fundamental structure–property relationships are essential for the development of high-performance materials for specific products. Technical elastomer products such as tires, conveyor belts, automotive mats, or even shoe soles typically use rubbery components with tailor-made properties to ensure optimum performance of the products for the customer. Due to increasing customer demand for better product performance at lower and lower prices, it is essential to develop new approaches for screening material properties as early as possible in the development process. It is therefore of key importance to develop a consistent set of approaches and knowledge that enables the connection of fundamental structural and dynamic properties with product performance (see for example [3–11]).

Despite the undisputed relevance of dynamic-mechanical properties (e.g., for tire performance), it is also appreciated that a full understanding of rubber viscoelasticity and its connection to the underlying chemistry still requires deeper research. The main reasons for this current status are the richness of the dynamic processes originating from the multiscale nature of polymer mobility and the

complex chemical and physical interactions of the macromolecules with the surfaces of different fillers, such as silica and carbon black [3, 12]. However, in certain subsets of the viscoelastic spectrum of polymers and filled elastomers, significant progress has been made for specific types of motion.

In general, an understanding of the dynamics of pure network domains is of great importance for the description of molecular mobility either in unfilled rubbers or in network domains far from the filler surfaces in rubber composites. In this respect, the classical Rouse-like dynamics of flexible Gaussian chain fragments between network junctions was described theoretically and investigated experimentally as early as the 1950s [13, 14]. The non-Gaussian dynamics on scales shorter than the Kuhn segments of polymer chains can be associated with the bending motions of semiflexible chain fragments [15, 16]. The specifically nonpolymeric glassy-like high-frequency dynamics on the scales of chemical bonds has the character of torsional vibrations, which can be described by the models of rotators [17–20]. The low-frequency dynamics on scales longer than the distance between topological entanglements and network junctions includes the contributions of collective motions of polymer chains in a network structure [21–24], sliding motions of chains along the confining tube [25], and the disentanglement motions of dangling chains [26, 27]. In the terminal low-frequency regime, the storage modulus tends to a limiting value that corresponds to the static modulus of a polymer network. The static modulus as a function of the degree of crosslinking and the degree of entanglements has been successfully described by the extended tube model of Gert Heinrich and coworkers [3, 28–30].

Modification of molecular mobility in the vicinity of filler particles has also been discussed in the literature. A new theoretical understanding was generated to predict the modifications of Rouse dynamics for elastomer filled by nanofillers, where the polymer segments become more localized [31, 32]. Evidence was published that these predictions are in agreement with experimental data [3, 10, 12]. The mobility at long scales is characterized by the slowing down of polymer dynamics in the vicinity of filler surfaces. The contribution of the mobility of the percolation network formed by filler particles was introduced to describe the low-frequency dynamics as well as the Payne effect in rubber composites [3, 33, 34].

Thus, several dynamic regimes of unfilled and filled elastomers are already quite well understood. The aim of the research presented in this review was to assess whether it would be possible to integrate these different pieces into a single picture that allows a description of the linear viscoelastic response of unfilled and filled rubbers. The proposed picture would include the contributions of relaxation processes over the full frequency range from the low-frequency range, dominated by dangling chain ends and strong filler–filler interactions, up to the dynamic glass transition dictated by the very local relaxation processes of monomer subunits. For this purpose, the superposition principle for different types of motions can be applied, according to which the contributions of all interacting modes in a polymer network can be well described by a superposition of modes for independent relaxation processes on different scales [21–24].

The article is organized as follows: After presenting the materials used for experimental validation of the proposed model, the experimental process applied

to obtain linear dynamic-mechanical properties is discussed, with specific focus on the shifting process used to construct master curves. Next, modeling of the dynamic-mechanical behavior of unfilled rubbers is detailed. The theoretical piecewise power-law approach is introduced and the individual dynamic ranges are assigned to specific molecular relaxation processes of known relaxation behavior. Application of the new model to experimental data is discussed and the results from nonlinear least-squares fitting are given. It is shown that very consistent molecular information for all dynamic scales is derived. On the basis of this new model for unfilled rubbers, the extension to rubbers filled by nanoparticles is presented. Well-established laws for hydrodynamic reinforcement, dynamics of localized chain segments, and long-time relaxation of filler–filler bonds are integrated. The consistency of this extended model is validated against the dynamic-mechanical data for solution-polymerized styrene butadiene rubber (S-SBR) compounds filled with different volume fractions of silica filler. The resulting fit parameters are assessed for their molecular validity and their consistency with knowledge available from literature. It is shown that, on the basis of the suggested piecewise power-law approach, a significant understanding of the rich dynamics in filled nanocomposites can be achieved. This new baseline can be further extended and refined for additional relaxation processes that are missing from the present study.

2 Materials and Experimental Data

2.1 Materials

The rubber samples prepared for this investigation were based on S-SBR provided by Lanxess (Leverkusen, Germany) with a microstructure of 50% vinyl, 25% styrene, 8% *cis*-polybutadiene (PB), and 17% *trans*-PB (Buna VSL5025-0). Three unfilled crosslinked samples were produced from the unvulcanized S-SBR using different amount of sulfur. The curing package consisted of 1.0, 1.5, and 2.75 phr sulfur and 1.2, 2.3, and 3.3 phr CBS (*n*-cyclohexyl-2-benzothiazolesulfenamide), respectively.

Structural parameters of S-SBR rubbers such as the crosslink density, ν_c, and the density of entanglements were obtained from the modeling of stress–strain measurements using the extended tube model of the rubber elasticity [3, 28–30]. For the entanglement modulus, G_e, no change with crosslink density was observed. Its value, $G_e = 0.32 \pm 0.02$ MPa, averaged over all three samples, corresponds to the number density of entanglement strands $\nu_e = 2G_e/k_BT = 0.156$ nm^{-3} (where k_B is the Boltzmann constant and T is temperature). The number of Kuhn segments in an entanglement strand, N_e, can be estimated as $N_e = ck_BT/2G_e$, where c is the number density of Kuhn segments. Using the value of $ck_BT = 7.7$ MPa, which is extracted from the dynamic-mechanical measurements in Sect. 3.2, we obtained a value for

Table 1 Unfilled S-SBR samples

Sample	Sulfur (phr)	G_c (MPa)	v_c (nm^{-3})	N_c	T_g (°C)
S-SBR950	1.0	0.112	0.027	69	−16.3
S-SBR953	1.5	0.152	0.037	51	−14.3
S-SBR956	2.75	0.243	0.059	32	−11.0

N_e of approximately 12. The diameter of a confining tube, d_{tube}, can be calculated from N_e as follows [16]:

$$d_{tube} = \sqrt{N_e} l_s, \tag{1}$$

where $l_s = 1.4$ nm is the length of the Kuhn segment for the studied S-SBR [1]. This provides $d_{tube} \simeq 5$ nm, which is a typical value for a pure polymer matrix (see table 9.1 in [16]). The crosslinking modulus G_c and, hence, the number density of network strands, $v_c = G_c/k_BT$, was found to increase linearly with the sulfur content. The number of Kuhn segments in a network strand can be estimated as $N_c = ck_BT/G_c$ from the values of G_c and ck_BT. The length of network strands decreases noticeably with an increase in crosslink density. Table 1 summarizes the structural parameters of unfilled S-SBR rubbers and shows the glass transition temperature, T_g, which increases slightly with the crosslink density.

Elastomer nanocomposites based on the S-SBR matrix and silica were also investigated. As a reference system, we chose the S-SBR953 sample with a crosslink density of 0.037 nm^{-3}. The S-SBR matrix was filled with different amounts of precipitated silica (Zeosil 1165 MP; Solvay, Lyon, France): 30, 50, 70, and 90 phr. This filler is characterized by an average diameter of primary particles of 20 nm and an average aggregate size of approximately 50 nm. A silane coupling agent (TESPD) was used at a level of 8 phf (parts per hundred parts of filler). The volume fraction of silica, ϕ, was calculated from the mass fractions of constituents, taking the mass density of S-SBR as 0.93 g/cm^3 and that of silica as 2.0 g/cm^3. Table 2 shows the relevant parameters for all filled samples and for the corresponding unfilled reference sample.

2.2 *Linear Dynamic-Mechanical Measurements*

Dynamic-mechanical measurements were performed in tensile mode using an Eplexor 2000 N dynamic measurement system (Gabo Qualimeter, Ahlden, Germany). The complex tensile modulus, E^*, was measured in the temperature region from −60°C to 120°C, with steps of 5°C at five frequencies, $F = 0.5$, 1.58, 5, 15.8, and 50 Hz. For measurement of the complex modulus, E^*, a static load of 1% prestrain was applied, modulated by a superimposed small dynamic load of 0.5% strain at linear response conditions. From the initial slope of the stress–strain curves

Table 2 Filled S-SBR samples with corresponding unfilled matrix

Sample	Sulfur (phr)	ν_c (nm^{-3})	Silica (phr)	ϕ
S-SBR953	1.5	0.037	0	0
S-SBR938	1.5	0.037	30	0.13
S-SBR169	1.5	0.037	50	0.20
S-SBR172	1.5	0.037	70	0.26
S-SBR941	1.5	0.037	90	0.31

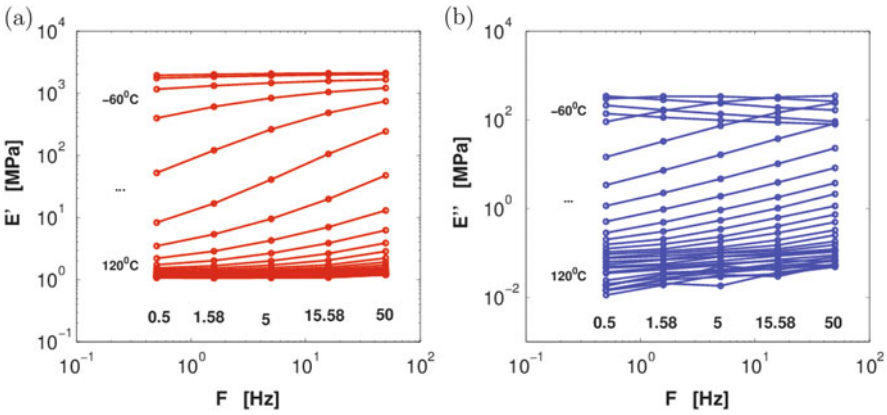

Fig. 1 Combined temperature–frequency sweep of the (**a**) storage E' and (**b**) loss E'' moduli of unfilled S-SBR953 sample

(not shown here), it was verified that the test conditions used in this study (i.e., total strains between 0.5% and 1.5%) were safely within the linear regime.

Figure 1 shows examples of unmastered experimental data for the small strain storage $E'(F)$ (Fig. 1a) and loss $E''(F)$ (Fig. 1b) moduli measured for the unfilled sample S-SBR953. Similar unmastered data were obtained for all samples used in this review. To enlarge the frequency range, master curves were constructed as described in the next section.

2.3 Master Curve Construction

The construction of master curves for uncrosslinked melts usually uses a few experimental curves measured with temperature steps of about 10–15°C and covering up to four decades of frequency. However, it is not possible to measure the dynamic-mechanical response of crosslinked rubbers at frequencies above 50 Hz because of the hardware limitations of the Eplexor 2000 N. The artifact-free experimental window for the rubber testing devices is usually limited to two decades of frequency. To compensate for this limitation, a different procedure can be applied [12, 35]: a large number of experimental curves is measured with

a small temperature step, usually 5°C. This provides a good overlapping of experimental curves and is equivalent to the first procedure in the case of thermorheologically simple materials when the time–temperature superposition (TTS) principle is valid.

2.3.1 Time–Temperature Superposition with Simultaneous Vertical and Horizontal Shift Factors

The TTS principle [14, 16, 36] states that the shape of the relaxation curves remains the same at decreasing temperature, whereas the characteristic relaxation time, τ_0, of the polymer increases. For τ_0, the relaxation time of the Gaussian chain fragment can be chosen, which will be introduced in Sect. 4.2. The TTS principle follows naturally from the molecular models of polymer dynamics [16], which imply that all relaxation times have the same dependence on the absolute temperature, T, as $\tau_0(T)$. The characteristic relaxation time diverges below T_g and, hence, all other relaxation times of the polymer diverge below T_g.

The TTS method [14, 16, 36] allows the determination of linear dynamic-mechanical behavior over a substantially increased range of frequencies. The dependences of the storage E' and loss E'' moduli on the angular frequency, $\omega = 2\pi F$, and on the absolute temperature T can be presented as:

$$\begin{aligned} E'(\omega) &= nk_BT \cdot f_1(\omega\tau_0(T)), \\ E''(\omega) &= nk_BT \cdot f_2(\omega\tau_0(T)), \end{aligned} \tag{2}$$

where n is the number density of polymer chains, k_B is the Boltzmann constant, and $f_1(x)$ and $f_2(x)$ are dimensionless functions. According to Eq. (2), the change in temperature from the reference value T_{ref} to the current value T is equivalent to the shift of both $E'(\omega)$ and $E''(\omega)$ in a double logarithmic scale by the horizontal factor $\log a_T$ and by the vertical factor $\log b_T$, where $a_T = \tau_0(T)/\tau_0(T_{ref})$ and $b_T = nk_BT_{ref}/nk_BT$. Thus, both the horizontal and the vertical shifts should be applied to construct the master curves. The vertical shift factors are calculated in our studies as $b_T = T_{ref}/T$ assuming a negligible change in polymer number density with temperature. They are in the range of 0.9–1.4 for the reference temperature $T_{ref} = 25$°C. After vertical shifting, the horizontal shift factor is applied as described in detail in the next section. Application of both horizontal and vertical shift factors results in smooth master curves for E' and E'' for all samples, filled and unfilled. The mastering procedure is quite accurate as all molecular parameters, which are extracted below, appear to have reasonable values.

The vertical shifting procedure, when applied to filled samples with the same rubber matrix, results in master curves that overlap in the high-frequency glassy region. In particular, the position of the high-frequency peak is found to be the same for unfilled and filled systems, even at very high concentrations of silica. This is closely related to other experimental studies [37–39], where the location of the glass transition peak in the S-SBR composites was found to be independent of silica

concentration. Note that in the study by Klüppel [37] the master curves for silica-filled samples were constructed using the same horizontal shifts as for the unfilled sample and introducing adjustable vertical shifts to obtain good overlapping. Nevertheless, despite a difference in the mastering procedure, a similar result was obtained – the high frequency (glass transition) region stays unaffected by the addition of filler.

2.3.2 The Horizontal Shifting Algorithm

The combined temperature–frequency sweep (an example is shown in Fig. 1) is performed at N different temperatures, T_k, where k runs over integer values from 1 to N. The experimental frequency window of 0.5–50 Hz is the same at each temperature and contains M frequencies, $F_{k,n}$, where n runs over integer values from 1 to M. The horizontal shifting algorithm described here was developed for the particular case when the number of frequencies in the experimental window is small. For example, $M = 5$ was used in the sweep shown in Fig. 1.

Master curves can be constructed using the raw data of the storage E' or the loss E'' modulus. The shifting procedure based on the raw data for $\tan\delta = E''/E'$ is also possible. In the present work, we chose to use the raw data for the E'' modulus and then to apply the same horizontal shifts to the E' modulus. Applying the vertical shifting with the factor $\log b_T$ we obtain the rescaled moduli $E'_{k,n}$ and $E''_{k,n}$. After that, the horizontal shift procedure is performed as follows. The frequencies at the reference temperature, which corresponds to some number k, $T_k = T_{\text{ref}}$, are fixed and unchanged giving $\log a_k = 0$. Values for the loss modulus, measured at the temperature $T_k = T_{\text{ref}}$, are fitted in the double logarithmic scale using the following quadratic function:

$$\log E''_{k,n} = a(\log F_{k,n})^2 + b\log F_{k,n} + c, \tag{3}$$

where a, b, and c are the fitting coefficients. Then, the points $(F_{k+1,n}, E''_{k+1,n})$, measured at the temperature T_{k+1}, are shifted along the frequency axis by the factor $\log a_T\,(T_{k+1}) = \log a_{k+1}$ in such a way that the difference ΔE is minimal:

$$\Delta E = \sum_{n=1}^{M} \left[\log E''_{k+1,n} - a(\log F_{k+1,n} + \log a_{k+1})^2 - b\left(\log F_{k+1,n} + \log a_{k+1}\right) - c\right]^2 \tag{4}$$

This is done by the least-squares method.

Figure 2a schematically presents the first shifting step. Similarly, we obtain the horizontal factor $\log a_{k+2}$ for the values of loss modulus, measured at temperature T_{k+2}, to shift them to temperature T_{k+1}. Note that the coefficients a, b, and c for the data at T_{k+1} have different values from those at T_k. After that, the total factor $\log a_T(T_{k+2}) = \log a_{k+1} + \log a_{k+2}$ is applied to shift the values of the loss modulus,

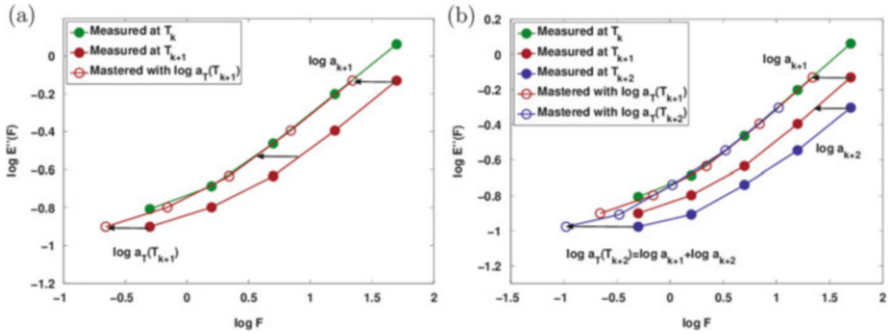

Fig. 2 Horizontal shifting procedure to the reference temperature $T_k = T_{\text{ref}}$: (**a**) the first shift from T_{k+1} and (**b**) the second shift from T_{k+2}

measured at temperature T_{k+2}, to temperature T_k. Figure 2b presents the second shifting step. Applying this procedure step by step to all raw data, measured at different temperatures, a smooth master curve for the loss modulus can be constructed. Note that the data measured at $T_k < T_{\text{ref}}$ should be shifted to lower frequencies and the data measured at $T_k > T_{\text{ref}}$ to higher frequencies.

One example is shown in Fig. 3, which presents master curves for the unfilled sample S-SBR953 (which is used as the reference sample in Sect. 4) obtained with the shifting algorithm described above. The dependence of the horizontal shift factor a_T on temperature is usually fitted with different empirical expressions. One of them was proposed by Williams, Landel, and Ferry and is known as the WLF equation [40]:

$$\log a_T(T) = \frac{-C_1(T - T_{\text{ref}})}{C_2 + (T - T_{\text{ref}})}, \tag{5}$$

where C_1 and C_2 are empirical constants. Another well-known expression is the Arrhenius dependence:

$$a_T(T) = \exp\left[\frac{E_a}{R}\left(\frac{1}{T} - \frac{1}{T_{\text{ref}}}\right)\right], \tag{6}$$

where E_a is the activation energy and R is the universal gas constant. The Arrhenius equation is generally used when the temperature is at least 100°C above T_g. This is nearly out of the temperature range used in the present study. Therefore, the WLF equation was applied to fit the horizontal factors obtained with respect to the reference temperature $T_{\text{ref}} = 25$°C. Figure 4 shows the fit according to the WLF equation with the parameter values $C_1 = 8.86$ and $C_2 = 101$°C. From Eq. (5) one can see that the relaxation times diverge at the temperature $T_\infty = T_{\text{ref}} - C_2 = -76$°C. The value of T_∞ is 60°C below T_g. This result is in agreement with a classical feature of the WLF equation [14], that the interval

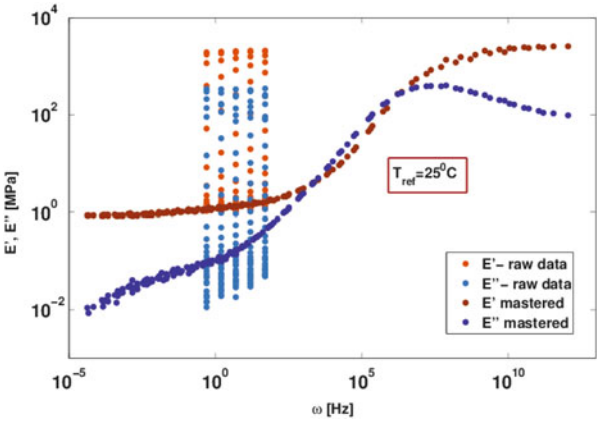

Fig. 3 Storage and loss moduli: raw data and master curves obtained with the shifting procedure

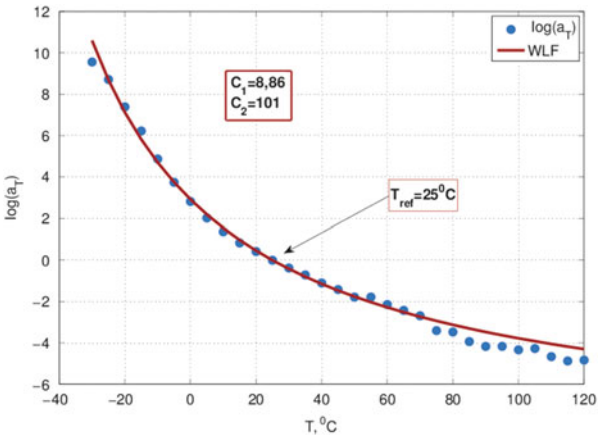

Fig. 4 Horizontal shift factor $\log a_T$ for unfilled S-SBR953 sample fitted using the WLF equation

between T_∞ and T_g is usually about 50°C. Such an agreement confirms that the mastering was performed correctly.

Using the shifting algorithm described above, the master curves for all unfilled and filled samples used in the present review were obtained. Importantly, the chosen mastering procedure provides very smooth master curves, which can be used for further research into dynamic-mechanical behavior.

3 Modeling of Dynamic-Mechanical Behavior of Unfilled Rubbers

3.1 Theoretical Piecewise Power-Law Approach

Analysis of the dynamic-mechanical behavior of unfilled rubbers uses a method based on the distribution function of the relaxation times, $H(\tau)$. The dynamic moduli E' and E'' can be rewritten in terms of the spectral density function $H(\tau)$ as follows [14]:

$$E'(\omega) = E_{eq} + \int_0^\infty H(\tau)\frac{(\omega\tau)^2}{1+(\omega\tau)^2}d\ln(\tau),$$
$$E''(\omega) = \int_0^\infty H(\tau)\frac{(\omega\tau)}{1+(\omega\tau)^2}d\ln(\tau). \quad (7)$$

Here E_{eq} is the plateau modulus, which corresponds to the limiting value of the storage modulus at low frequencies: $E_{eq} = E'(\omega \to 0)$. As mentioned in the Introduction, there are different types of motions in a randomly crosslinked polymer network. In order to account for this scale-dependence of chain dynamics, a piecewise power-law approach was proposed by us [1, 2] for the relaxation time spectrum $H(\tau)$:

$$H(\tau) = \frac{ck_BT}{\pi}\begin{cases}(\tau/\tau_b)^{\beta}(\tau_b/\tau_0)^{-3/4} & \tau < \tau_b,\\ (\tau/\tau_0)^{-3/4}, & \tau_b < \tau < \tau_0,\\ (\tau/\tau_0)^{-1/2}, & \tau_0 < \tau < \tau_e,\\ (\tau/\tau_e)^{-\alpha}(\tau_e/\tau_0)^{-1/2}, & \tau_e < \tau < \tau_{max},\end{cases} \quad (8)$$

The spectral density function is schematically presented in Fig. 5a by the solid line. It is built piecewise from the four power-law regions with widely separated time boundaries, which are defined by the four characteristic relaxation times: τ_b, τ_0, τ_e, and τ_{max}. For times above τ_{max}, the function $H(\tau) = 0$. One can see that each power-law region $H(\tau) \sim \tau^{-\alpha}$ transforms into a power law in the moduli $E'(\omega) \propto E''(\omega) \propto \omega^{\alpha}$ in a broad frequency domain.

Let us start from very high frequencies, or very short relaxation times $\tau < \tau_b$. As can be seen from Fig. 5, $\omega = \tau_b^{-1}$ marks the high-frequency maximum for the dependence $E''(\omega)$. The dynamics at $\omega > \tau_b^{-1}$ is characterized by small high-frequency vibrations of chain fragments of a size comparable with that of monomers. In this glassy regime, the relaxation modulus is known to obey the Kohlrausch–Williams–Watts time behavior $E(t) \sim \exp[-(t/\tau_b)^{\beta}]$ with $0 < \beta < 1$ [17–20, 41]. For short times, the exponential function can be expanded into a series, $E(t) \sim 1 - (t/\tau_b)^{\beta}$, and the corresponding spectral density can be approximated by the power law $H(\tau) \sim (\tau/\tau_b)^{\beta}$.

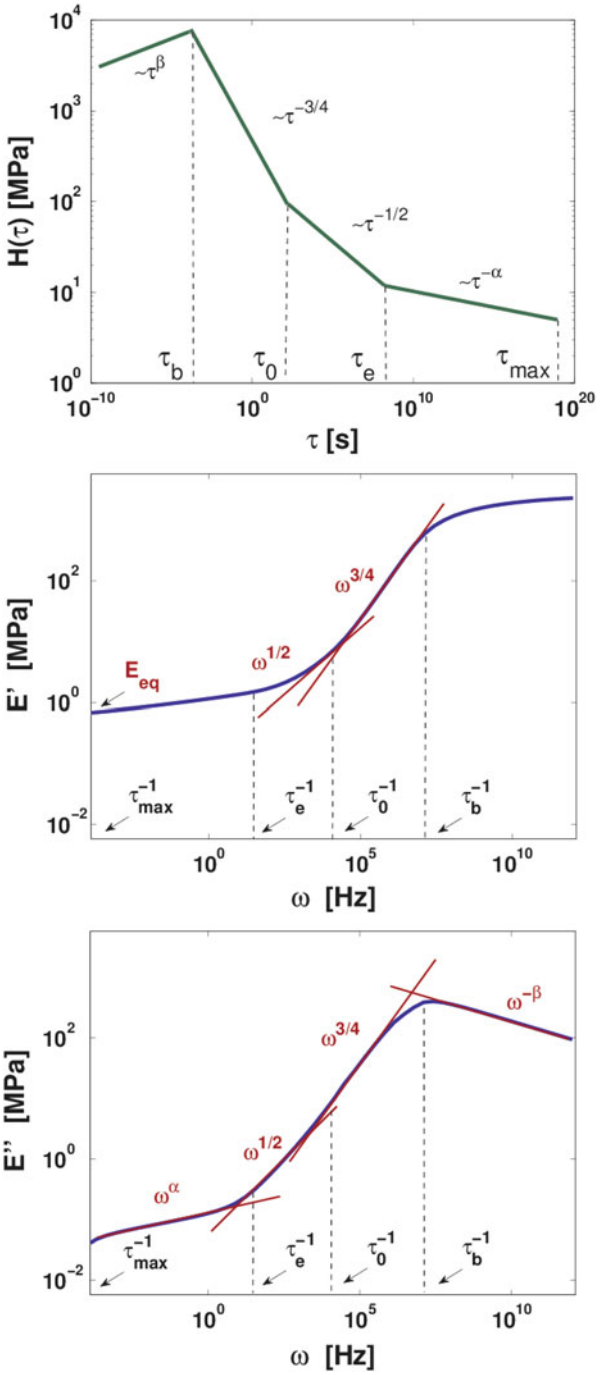

Fig. 5 Logarithmic spectral density $H(\tau)$ as a continuous, piecewise power-law function. Storage E' and loss E'' moduli calculated on the basis of $H(\tau)$ using Eqs. (7) and (8)

The next frequency domain, $\tau_0^{-1} < \omega < \tau_b^{-1}$, is characterized by the power law exponent 3/4. This exponent is known to be a fingerprint of the bending rigidity of polymer chains [15, 16], which manifests itself at shorter times comparable with the relaxation time of a Kuhn segment. Thus, it makes sense to assign the shortest relaxation time τ_b to the smallest length scale at which the bending rigidity comes into play. This scale corresponds approximately to two rigid monomers that can bend around the joining group. The relaxation time τ_0 is assigned to the largest length scale at which the bending rigidity is still noticeable, which corresponds approximately to three Kuhn segments. It was shown [42] that such chain fragments obey Gaussian statistics in good approximation, and they are therefore called Gaussian springs.

In the intermediate frequency domain, $\tau_e^{-1} < \omega < \tau_0^{-1}$, the dynamic moduli exhibit power-law behavior with the exponent 1/2. This is a typical Rouse-like behavior, which arises from the motion of Gaussian springs comprising the entanglement strand. The relaxation time τ_e marks the end of the Rouse-like asymptotic behavior and is roughly proportional to the relaxation time of the subchain between entanglements. In the Rouse-like regime, the spectral density function obeys the following asymptotic behavior [1, 14]:

$$H_{\text{Rouse}}(\tau) = \frac{c k_B T}{\pi} \left(\frac{\tau}{\tau_0} \right)^{-1/2}. \tag{9}$$

Note that the number density of Kuhn segments in this equation can be expressed as $c = N_e \nu_e$, where N_e/n is the number of Gaussian springs comprising the entanglement strand and ν_e is the number density of entanglement strands.

Finally, let us consider the low-frequency regime, $\omega < \tau_e^{-1}$. In this regime, unfilled rubbers exhibit an extremely long power-law decay with exponent α, the value of which depends on the crosslink density. Physically motivated explanation of the power-law decay in randomly crosslinked networks is still a controversial issue. For the unfilled S-SBR samples used in this study, $\alpha \leq 0.3$ was found. This result allows exclusion of some relaxation processes, proposed in literature for the explanation of this low-frequency tail. For example, the sliding motion of entangled network strands between chemical junctions is given by the asymptotic behavior for the moduli with $E' \propto E'' \propto \omega^{1/2}$ [25] and cannot describe experimental data for the S-SBR samples with an exponent of $\alpha \leq 0.3$ for the moduli. Random connectivity of network junctions in the framework of phantom Gaussian chains leads to another asymptotic behavior, with $E' \propto E'' \propto \omega^{d/2}$, where $d \geq 1$ is a spectral dimension of the network structure [22, 43]. For randomly crosslinked networks, the index d can be approximated to a large value of 4 [43]. Thus, the random connectivity of network strands is not able to provide an exponent $\alpha \leq 0.3$.

Randomly crosslinked networks have a number of defects, most of which belong to dangling chains and uncrosslinked chains comprising the sol fraction [44, 45]. Reptation of the latter would lead to an additional maximum in the low-frequency domain for E'', which is not observed experimentally. Because the

dangling chains can be as long as one and a half times the length of network strands at low crosslink densities, the low-frequency dynamics is dominated by the relaxation of highly entangled dangling chains, whose constrained dynamics were first described by Curro and Pincus [26]. Based on the exact numerical result obtained by Curro et al. [27], we showed [1] that the entangled dangling chain concept predicts the following asymptotic behavior for the logarithmic spectral density function:

$$H_{\text{dang}}(\tau) \simeq v_{\text{dg}} k_{\text{B}} T (\tau/\tau_{\text{e}})^{-\alpha}, \tag{10}$$

where v_{dg} is the number density of entanglement strands in the dangling chains and the relaxation time τ_{e} is roughly the Rouse time for a subchain between two entanglements [27]:

$$\tau_{\text{e}} \simeq \tau_0 N_{\text{e}}^3. \tag{11}$$

Importantly, Curro and Pincus [26] predicted that both the exponent α and the longest relaxation time of the dangling chains $\tau_{\max}$ depend on the crosslink density: $\alpha \propto v_{\text{c}}$ and $\ln(\tau_{\max}) \propto 1/v_{\text{c}}$.

The final form of the logarithmic spectral density function, as given by Eq. (8), is determined by the condition of continuity between all four relaxation regimes. The dynamic-mechanical behavior of the unfilled rubbers is characterized by eight parameters: E_{eq}, $ck_{\text{B}}T$, α, β, τ_{b}, τ_0, τ_{e}, and $\tau_{\max}$. In the modeling procedure, all these parameters should first be predefined manually. The fitting procedure was made in two steps. First, all fitting parameters were allowed to vary. Here we note that $E'' < E'$ in the Rouse-like regime of elastic networks $\left(\omega < \tau_0^{-1}\right)$, whereas $E'' > E'$ in the region with an exponent 3/4 $\left(\omega > \tau_0^{-1}\right)$, as follows from the features of the power-type behavior of the moduli [14, 36]. This means that the values τ_0 and $ck_{\text{B}}T$ should be in the vicinity of the point where $E' = E''$. Thus, the initial value for $ck_{\text{B}}T$ was taken as the cross-point $E' = E''$ at the middle frequencies $\omega = \tau_0^{-1}$ and for the exponent β as a slope of the very high-frequency region. As we found, $ck_{\text{B}}T$ and β do not change with the crosslink density. Therefore, at the second step, these two parameters were fixed and only the manually adjusted values of six other parameters E_{eq}, α, τ_{b}, τ_0, τ_{e}, and $\tau_{\max}$ were used as the initial values for the nonlinear fitting routine of the Matlab software.

3.2 *Fitting Results for Storage and Loss Moduli*

Figure 6 presents the master curves for the storage and loss moduli for the differently crosslinked S-SBR rubber samples modeled using the multiscale theoretical approach, as described in the previous section. The corresponding fitting

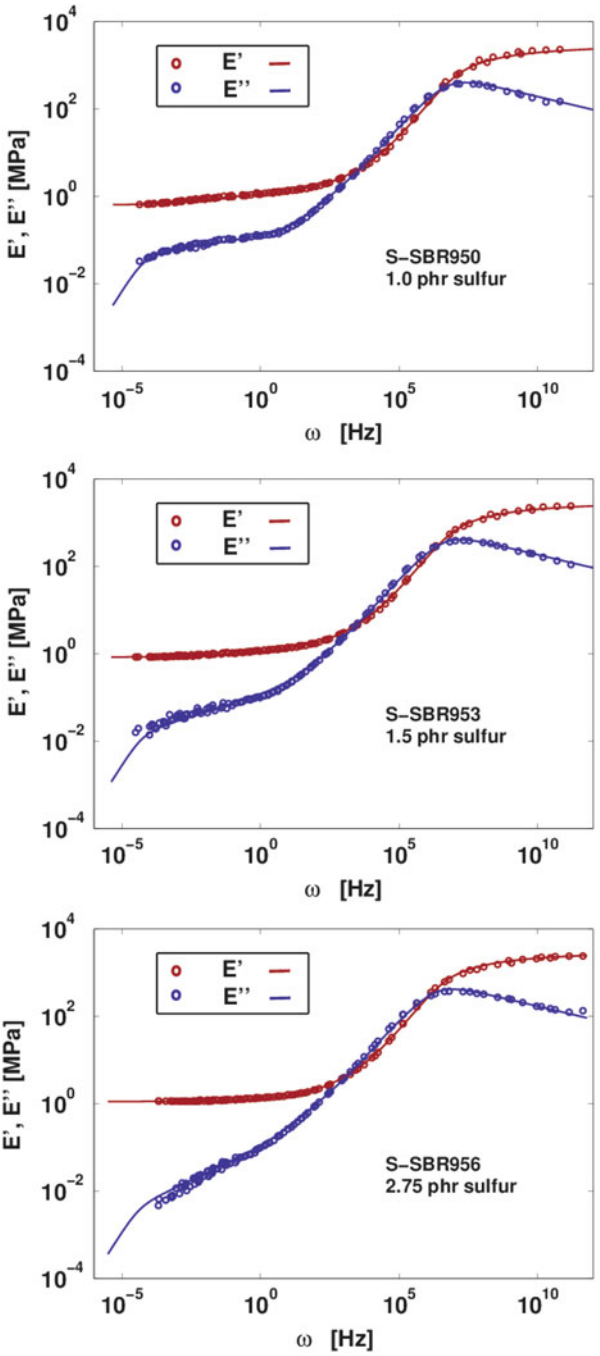

Fig. 6 Fits of the master curves for the storage and loss moduli for the samples S-SBR950, S-SBR953, and S-SBR956 using the multiscale approach based on Eqs. (7) and (8)

Table 3 Fitting parameters for unfilled S-SBR samples

ν_c (nm^{-3})	ck_BT (MPa)	α	β	τ_b (s)	τ_0 (s)	τ_e (s)	τ_{max} (s)	E_{eq} (MPa)
0.027	7.7	0.1	0.15	1.2×10^{-7}	8.82×10^{-5}	4.68×10^{-2}	2.1×10^{4}	0.651
0.037	7.7	0.2	0.15	1.71×10^{-7}	1.29×10^{-4}	4.48×10^{-2}	2.4×10^{4}	0.849
0.059	7.7	0.3	0.15	3.35×10^{-7}	2.58×10^{-4}	1.58×10^{-1}	3.18×10^{4}	1.131

parameters are summarized in Table 3. All parameters have reasonable values, as discussed next.

As can be seen from Table 3, the shortest relaxation time τ_b slightly increases with the degree of crosslinking. This can be explained by the increase in the monomeric friction coefficient as a result of the gradual increase in T_g by 5°C (see Table 1). Similarly, Marzocca et al. [46] related the increase in the monomeric friction coefficient with the crosslink density and the network structure of unfilled sulfur-cured natural rubber vulcanizates.

Further, let us consider a relation between the relaxation times τ_b and τ_0, which defines the region dominated by the bending rigidity on the scales between two monomer lengths $2l_m$ and three lengths of the Kuhn segment $3l_s$. In the bending regime, the relaxation time of a bending unit is known to be proportional to the fourth power of the unit length [15, 16] so we can write the following approximate relation:

$$\frac{\tau_0}{\tau_b} \simeq \left(\frac{3l_s}{2l_m}\right)^4. \tag{12}$$

Hence, the ratio $(\tau_0/\tau_b)^{1/4}$ is independent of the crosslink density and can be used to extract the ratio of the Kuhn and monomer lengths. In the present study, $l_s/l_m \approx 3.5$, as can be seen in Fig. 7a. This is very close to the value of 4.4, as defined from the chemical composition of S-SBR [1]. Note that for flexible hydrocarbon polymers the ratio l_s/l_m changes from 2.5 for poly(ethylene oxide) to 5 for polystyrene [47], demonstrating that the present analysis derives a realistic value of this parameter, which indicates that the mastering at high frequencies was very accurate.

As discussed in Sect. 3.1, the dangling chain picture predicts the characteristic scaling dependences for the exponent $\alpha \propto \nu_c$ and the terminal relaxation time $\ln(\tau_{max}) \propto 1/\nu_c$ as functions of the crosslink density ν_c [26, 27]. Indeed, both tendencies were observed for our systems, as shown in Fig. 7b, c. The value of τ_{max} was normalized to the corresponding value of τ_e in order to eliminate a small shift to larger values, observed for all relaxation times upon crosslinking as a result of an increase in T_g. As shown [1], the dangling chain picture provides plausible values of material parameters such as the relative fraction, f_{dg}, of dangling chains and the average number, N_{dg}, of Kuhn segments in dangling chains:

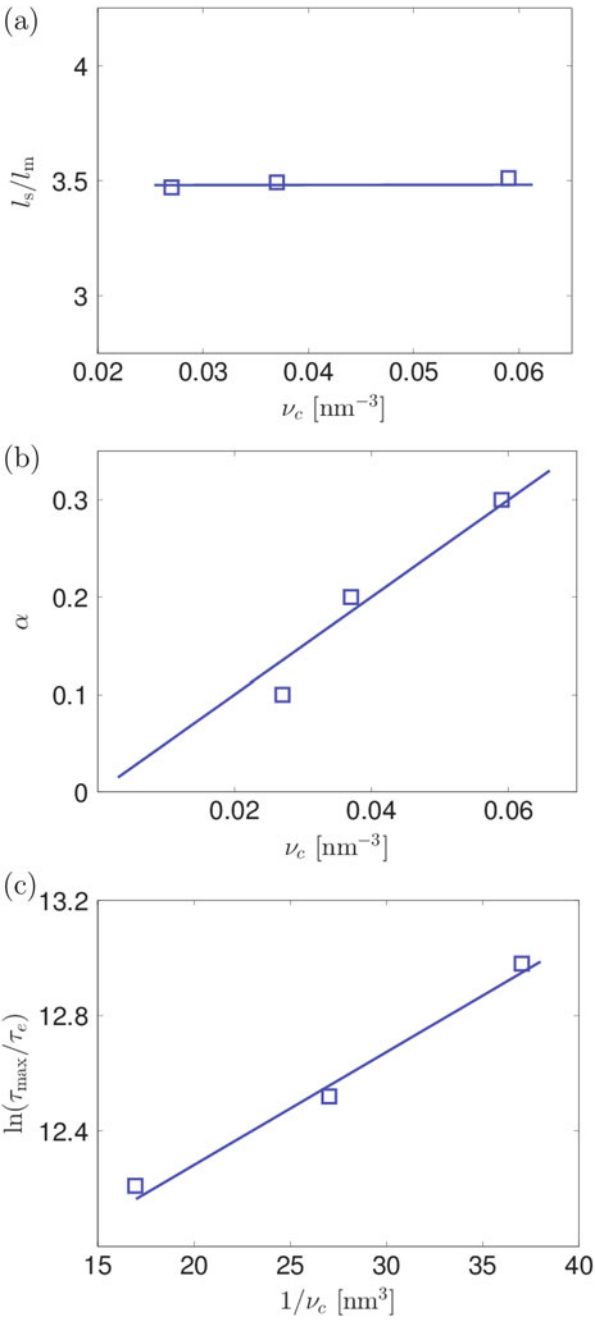

Fig. 7 Fitted parameters and relations between them as functions of the crosslink density: (**a**) l_s/l_m, (**b**) α, and (**c**) $\ln(\tau_{max})/\tau_e$

Table 4 Fraction and length of dangling chains

Sample	α	f_{dg}	N_{dg}	N_{dg}/N_c
S-SBR950	0.1	0.50	206	3.0
S-SBR953	0.2	0.21	100	2.0
S-SBR956	0.3	0.09	66	2.1

$$N_{dg} = N_e/(\alpha\nu'). \tag{13}$$

Here $\nu' \simeq 0.6$ is the material constant [16, 27] and $N_e \simeq 12$ is the number of Kuhn segments in the entanglement strand, as estimated in Sect. 2.1. The dangling parameters are summarized in Table 4, showing that both the volume fraction of dangling chains f_{dg} and their average length N_{dg} decrease with increasing crosslink density.

The plausibility of the values obtained in the frame of the dangling chain picture can be established by comparing them with estimates provided by molecular theories describing the random crosslinking process. A rigorous consideration of network defects in randomly crosslinked networks was carried out by Lang and coworkers [44, 45]. Following these studies, we showed [1] that the fraction of dangling chains in a randomly crosslinked network can reach, at some extent of the crosslinking reaction, a maximal value of 0.60. Table 4 shows that the volume fraction of dangling chains, f_{dg}, estimated from the modeling of master curves always satisfies the condition that follows from rigorous molecular theories: [44, 45], $f_{dg} < 0.6$. Furthermore, the theory [44] predicts that the length of dangling chains can be as long as 1.5 times the length of the network strands at low extents of reaction. The ratios N_{dg}/N_c obtained for our samples are in qualitative agreement with theoretical estimations (see Table 4), although slightly exceeding the maximum theoretical value of 1.5. Presumably, this discrepancy is the result of a sol fraction that contains long primary chains with extremely slow reptation motions.

In conclusion, the fitting parameters provide values for the molecular characteristics that are reasonable for the studied rubber matrices and are in a good agreement with rigorous theoretical calculations. Let us turn now to the modeling of filled rubbers.

4 Modeling of Dynamic-Mechanical Behavior of Filled Rubbers

On the basis of the model for unfilled rubbers discussed in the previous section, an extended concept was developed to describe the dynamic-mechanical behavior of filled rubbers. To achieve this, the first extension step was to include a hydrodynamic reinforcement factor into the model. Second, the piecewise power-law approach was generalized, taking into account the modified dynamics for chain fragments of different length scales, especially for semiflexible and Gaussian chain fragments in the vicinity of the filler surface.

4.1 Hydrodynamic Reinforcement Factor

The rigid filler particles in viscoelastic composite materials are known to increase the average mechanical strain in the matrix as compared with the applied strain [48–50]. This pure hydrodynamic effect results in increases in the dynamic moduli and viscosity of the composite material with respect to the matrix values of these mechanical characteristics. A contribution of the hydrodynamic reinforcement effect can be excluded from the storage and loss moduli using a vertical rescaling of these moduli on a so-called hydrodynamic reinforcement factor h. It is defined as $h = E/E_0$, where E and E_0 are the tensile moduli of an elastomer nanocomposite and an elastomer matrix, respectively. The hydrodynamic reinforcement factor was derived by Chen and Acrivos for volume fractions of hard spherical particles of up to approximately $\phi \sim 0.1$ [51]:

$$h(\phi) = 1 + 2.5\phi + 5.0\phi^2. \tag{14}$$

Quite often, a considerably steeper dependence with a second order prefactor of 14.1 is used in studies of reinforced rubbers:

$$h(\phi) = 1 + 2.5\phi + 14.1\phi^2. \tag{15}$$

This expression, obtained originally by Gold in his thesis on viscous suspensions [52, 53], was taken over a priori by Guth for linear elastic solids [54]. It is known now that the Gold formula, Eq. (15), contradicts established results for viscous suspensions [49] and can only be considered as a phenomenological result. Nevertheless, both expressions were applied in the present study to calculate the vertical rescaling. Figure 8a presents the master curves rescaled according to Eq. (14) and Fig. 8b shows the master curves rescaled using Eq. (15). It is clearly seen that the phenomenological Guth–Gold equation overpredicts the hydrodynamic reinforcement effect in the high-frequency region: the reduced moduli of the filled rubber compounds become smaller than the moduli of the matrix. In contrast, the rigorous Chen–Acrivos equation does not lead to this unphysical result: the reduced moduli overlap at very high frequencies. In conclusion, only the rigorous Eq. (14) provides a physically meaningful value for the hydrodynamic reinforcement factor $h(\phi)$ and is therefore used further. Note that the dynamic moduli rescaled with $h(\phi)$ still contain other reinforcement effects arising as a result of the presence of filler clusters/networks [3, 33, 55] or chain localization on the filler surface [3, 31, 32]. These effects are considered in detail in the next section.

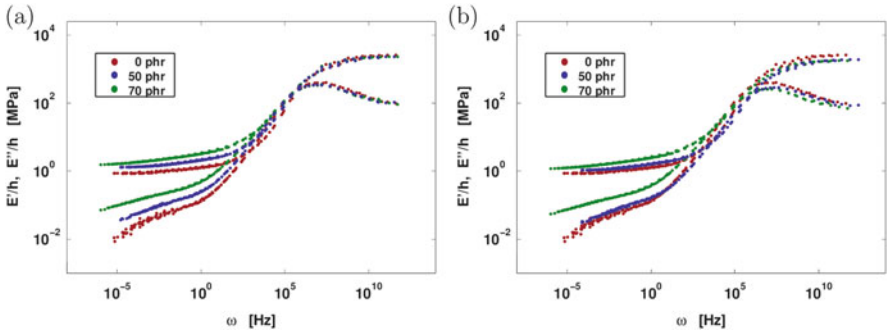

Fig. 8 Dependences of the reduced storage E' and loss E'' moduli for samples with 0, 50, and 70 phr of filler after rescaling with the hydrodynamic reinforcement factor $h(\phi)$ using (**a**) Eq. (14) and (**b**) Eq. (15)

4.2 Piecewise Power-Law Approach for Filled Rubbers

After rescaling with the hydrodynamic reinforcement factor $h(\phi)$, the reduced values of the dynamic moduli take the following form:

$$\frac{E'(\omega)}{h(\phi)} = \frac{E_{\mathrm{eq}}}{h(\phi)} + \int_0^\infty H(\tau)\frac{(\omega\tau)^2}{1+(\omega\tau)^2}d\ln(\tau),$$
$$\frac{E''(\omega)}{h(\phi)} = \int_0^\infty H(\tau)\frac{(\omega\tau)}{1+(\omega\tau)^2}d\ln(\tau), \tag{16}$$

where the logarithmic spectral density $H(\tau)$ describes the mechanical properties of the rubber matrix in an elastomer nanocomposite. Similarly to the unfilled rubber [see Eq. (8)], $H(\tau)$ for the filled rubbers is built from the four power-law regions with widely separated time boundaries:

$$H(\tau) = \frac{ck_{\mathrm{B}}T}{\pi}\begin{cases}(\tau/\tau_{\mathrm{b}})^{\beta}(\tau_{\mathrm{b}}/\tau_0)^{-\gamma} & \tau < \tau_{\mathrm{b}}\\ (\tau/\tau_0)^{-\gamma}, & \tau_{\mathrm{b}} < \tau < \tau_0\\ C_{\mathrm{R}}(\tau/\tau_0)^{-1/2} + (1-C_{\mathrm{R}})(\tau/\tau_0)^{-3/8}, & \tau_0 < \tau < \tau_{\mathrm{e}}\\ (\tau/\tau_{\mathrm{e}})^{-\alpha}\left(C_{\mathrm{R}}(\tau_{\mathrm{e}}/\tau_0)^{-1/2} + (1-C_{\mathrm{R}})(\tau_{\mathrm{e}}/\tau_0)^{-3/8}\right), & \tau_{\mathrm{e}} < \tau < \tau_{\max}.\end{cases} \tag{17}$$

The specific form of prefactors in the above equation is determined by the condition of continuity of $H(\tau)$ at the crossover points. We assume that the number density of Kuhn segments, c, in Eq. (17) remains insensitive to the presence of filler particles. It is calculated as $ck_{\mathrm{B}}T = \rho_{\mathrm{p}}RT/M_{\mathrm{s}} = 6.52$ MPa (where R is the gas constant) from the density $\rho_{\mathrm{p}} = 0.93$ g/cm^3 of S-SBR and the mass of the Kuhn segment $M_{\mathrm{s}} = 353.5$ g/mol [1] and is fixed for all samples.

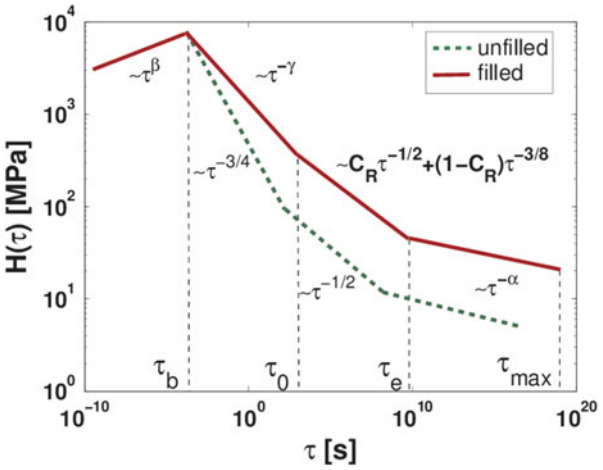

Fig. 9 Logarithmic spectral density $H(\tau)$ for elastomer nanocomposites (*solid red line*) in comparison with $H(\tau)$ for unfilled rubbers (*dashed green line*)

Figure 9 illustrates schematically the main changes in the shape of $H(\tau)$ for elastomer nanocomposites compared with its shape for unfilled rubbers. First, we note that the high-frequency regime stays unchanged, as discussed in the previous section. The low-frequency regime also keeps its functional form, although the values of exponent α and the terminal time $\tau_{\max}$ become dependent on the volume fraction of filler. In the time domain $\tau_b < \tau < \tau_0$, the fixed bending exponent 3/4 can no longer be used because of the influence of the filler on the dynamics of semiflexible Kuhn segments. Instead, the relaxation exponent γ is used as a new fitting parameter for this region. Furthermore, in the time domain $\tau_0 < \tau < \tau_e$ a gradual change in the Rouse-like 1/2 exponent to the exponent 3/8 with an increase in the volume fraction of filler was found. Such a change in dynamic-mechanical behavior is typical for Rouse polymer chains in the vicinity of the energetically and/or geometrically rough surfaces of filler clusters and aggregates [3, 31, 32]. To describe this process, we assume that there are two kinds of network strands in the elastomer nanocomposites:

free strands, far away from the filler surface, which initially keep Rouse dynamics;
localized strands, found near the filler surface, which show changed dynamics with the 3/8 exponent

If C_R is the fraction of free network strands, the free and localized network strands contribute with their power laws weighted with the coefficients C_R and $1 - C_R$, respectively. This is similar to superposition approaches proposed for the rheology of filled polymer melts [56, 57]. The dynamic-mechanical behavior of elastomer nanocomposites is characterized by nine parameters: C_R; E_{eq}; three exponents α, β, and γ; and four relaxation times τ_b, τ_0, τ_e, and $\tau_{\max}$. The initial values of most fitting parameters are identified from the master curves automatically using a software tool (see Fig. 10). The exponents α and β are taken as the slopes of E'' at very high and very low frequencies, respectively. The relaxation times τ_b and τ_0 are determined from the cross-points of storage E' and loss E'' moduli. The value of the plateau

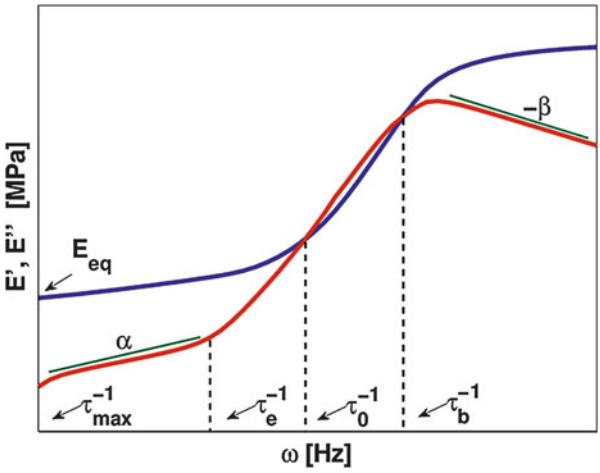

Fig. 10 Initial values of the fitting parameters identified automatically

modulus is taken from the minimal value of the storage modulus E'. The relaxation times τ_e and τ_{max} are taken from those points where the master curves change curvature (see Fig. 10).

The final values of the fitting parameters, found by the optimization routine of the Matlab software, are quite insensitive to the initial values and can differ considerably from the latter. Therefore, to find the values of the fraction of free chains C_R and the exponent γ, we started from the sample with the lowest filler loading (30 phr) and used $C_R = 1$ and $\gamma = 3/4$, which characterize the unfilled reference sample, as initial values. The final values of C_R and γ, obtained for the sample with the lowest filler loading, serve as initial values for the sample with the next higher filler loading. The procedure is repeated until all samples are fitted satisfactorily.

4.3 Fitting Results for Storage and Loss Moduli

Figure 11 presents master curves for the storage and loss moduli for the elastomer nanocomposites modeled with the multiscale theoretical approach, as described in the previous section. A very good agreement of fit lines with the experimental data over the whole frequency range of more than 15 decades is observed. This agreement shows the versatility of the proposed multiscale approach. The final values of the fitting parameters are summarized in Table 5. Note that for the unfilled reference sample S-SBR953 we obtained somewhat different values to those shown in Table 3, as we used the value of ck_BT calculated from the chemical structure of S-SBR. However, these two sets of fitting parameters are very close and give no difference in a physical interpretation. Because the multiscale approach is physically based, with each parameter having a well-defined physical meaning in an

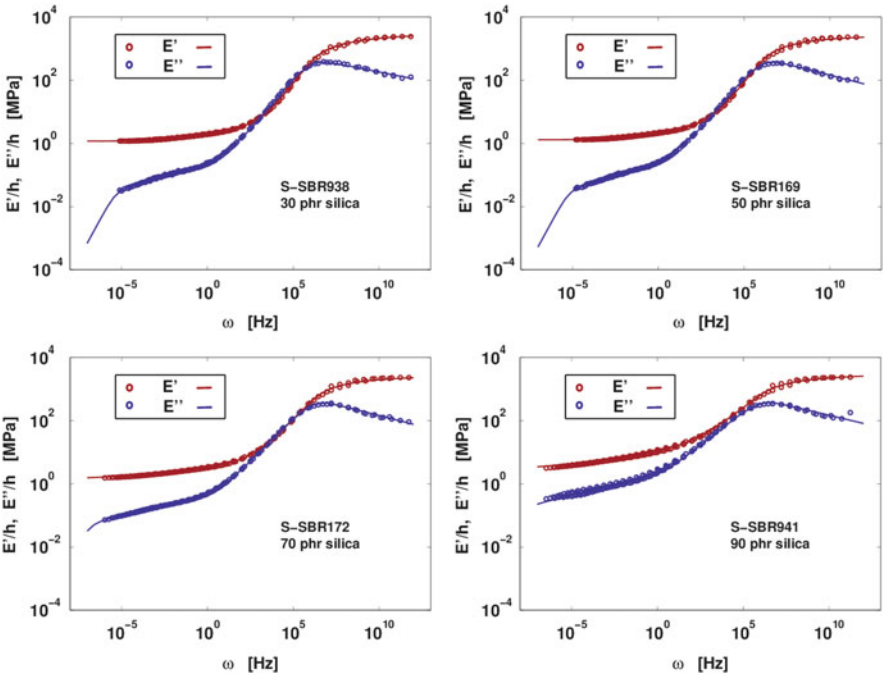

Fig. 11 Fits of the master curves for the vertically rescaled storage E' and loss E'' moduli for four different S-SBR/silica samples using the multiscale approach based on Eqs. (16) and (17)

Table 5 Fitting parameters for elastomer nanocomposites based on S-SBR matrix

ϕ	C_R	α	β	γ	τ_b (s)	τ_0 (s)	τ_e (s)	τ_{max} (s)	E_{eq} (MPa)
0	1	0.153	0.16	0.75	4.6×10^{-7}	4.7×10^{-4}	0.30	9.0×10^{4}	0.86
0.13	0.61	0.150	0.11	0.72	7.0×10^{-7}	7.1×10^{-4}	0.21	2.9×10^{5}	1.79
0.20	0.59	0.153	0.14	0.69	6.6×10^{-7}	9.3×10^{-4}	0.29	2.1×10^{5}	2.61
0.26	0.59	0.128	0.14	0.56	4.7×10^{-7}	3.3×10^{-3}	0.22	$\sim 10^{7}$	3.69
0.31	0.04	0.134	0.13	0.42	7.7×10^{-7}	8.9×10^{-2}	0.17	$\sim 10^{8}$	7.72

appropriate frequency regime, all determined parameters have reasonable values at the end of the fitting procedure.

Let us now discuss how the increase in volume fraction ϕ of silica nanoparticles influences the characteristics of elastomer composites. As can be seen from Table 5, the shortest relaxation time τ_b and the exponent β, which characterize the high-frequency regime $\omega > \tau_b^{-1}$, do not show a clear tendency with an increase in ϕ but scatter around the average values of $\tau_b = (6 \pm 2) \times 10^{-7}$ s and $\beta = 0.14 \pm 0.03$. This observation indicates unchanged dynamics of the S-SBR matrix upon addition of silica particles at very short times, $\tau < \tau_b$, and is explained by the insensitivity of nonpolymeric relaxation processes (such as fast local motions around the main chain bonds) to the presence of particles [58–60]. Thus, the only influence of the

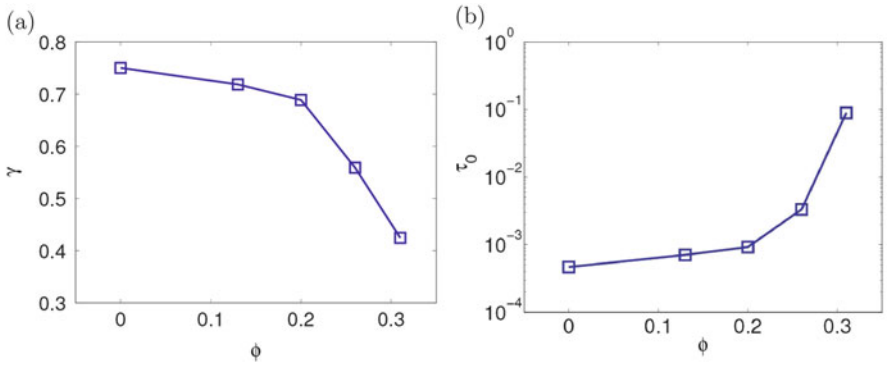

Fig. 12 (**a**) The exponent γ and (**b**) the relaxation time of the Gaussian chain fragment τ_0 as functions of the filler volume fraction ϕ. Reprinted from Ivaneiko et al. [2], Copyright 2016, with permission from Elsevier

filler particles on the dynamic-mechanical behavior in the high-frequency regime results from a purely geometric effect of the hydrodynamic reinforcement, as discussed in Sect. 4.1.

The next frequency domain, $\tau_0^{-1} < \omega < \tau_b^{-1}$, is characterized by the exponent γ. For unfilled S-SBR samples, γ is equal to 3/4 and has the meaning of the bending exponent for motions on smaller scales that are comparable with the length of a Kuhn segment [16]. As can be seen from Fig. 12a, with an increase in the volume fraction of silica, γ gradually decreases from 3/4 to approximately 0.4 for the highly filled sample with $\phi = 0.31$. Such a decrease in the exponent γ probably indicates that the bending relaxation modes is slowed down by addition of silica particles. For example, it was shown by Doi and Edwards [36] that the stretching of relaxation spectra leads to the flattening of frequency dependences for the storage and loss moduli and is characterized by decreases in the characteristic exponents. Together with the decrease in γ, there is a noticeable increase in the relaxation time τ_0, as shown in Fig. 12b. This again indicates a considerable stretching of the bending relaxation spectrum in the presence of silica particles.

Very interesting behavior was found for the intermediate frequency domain, $\tau_e^{-1} < \omega < \tau_0^{-1}$, where the dynamic moduli of unfilled rubbers exhibit power-law behavior with the exponent 1/2. In this regime, progressive localization of network strands on the particle surface is expected with an increase in filler volume fraction ϕ [3, 31, 32]. It can be seen in Fig. 13a that the fraction of free network strands C_R indeed rapidly decreases with an increase in ϕ, so that there are virtually no free chains in the highly filled sample with $\phi = 0.31$. The thickness of the layer of localized strands L can be roughly estimated from the average radius of filler particles, $R_p = 10$ nm, as follows:

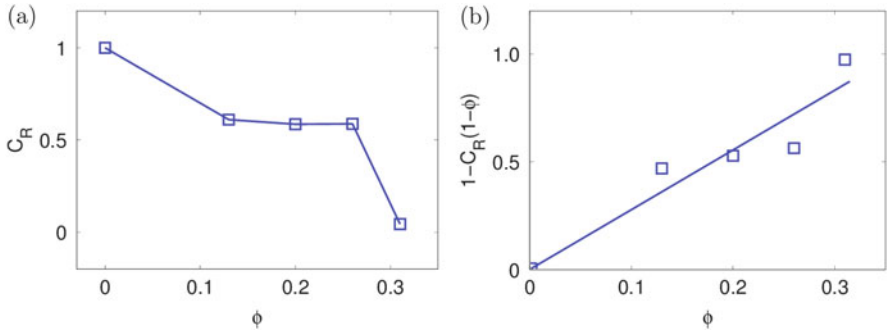

Fig. 13 (**a**) The fraction of free network strands C_R and (**b**) the factor $1 - C_R(1 - \phi)$ as functions of the filler volume fraction ϕ

$$1 + \frac{\phi_{loc}}{\phi} = (1 + L/R)^3, \tag{18}$$

where $\phi_{loc} = (1 - \phi)(1 - C_R)$ is the volume fraction of a localized polymer layer. Using Eq. (18) and the definition of ϕ_{loc}, the following relation can be obtained:

$$1 - C_R(1 - \phi) = \phi(1 + L/R)^3. \tag{19}$$

The left side of this relation is a linear function of ϕ (see Fig. 13b). From its slope we can calculate the thickness of the localized layer, which has the reasonable value of $L = 4.1 \pm 0.4$ nm.

Let us turn now to the low-frequency regime, $\omega < \tau_e^{-1}$. As can be seen from Fig. 14, the plateau modulus E_{eq} increases gradually with an increase in volume fraction of the filler. This increase in E_{eq} includes two contributions:

$$E_{eq}(\phi) = h(\phi)E_{eq}(0) + E_f(\phi), \tag{20}$$

where the first term describes the hydrodynamically reinforced contribution from the polymer matrix and the second term arises as a result of the presence of filler clusters. The latter can form a percolating filler network at high-enough volume fraction of particles, as explained in detail in the book by Vilgis et al. [3]. The presence of filler clusters/network is known to cause an additional upward shift of the low frequency values of the storage modulus. In a first approximation, such behavior can be effectively described by the frequency-independent elastic modulus of the filler network, E_f [61, 62]. As can be seen from Fig. 14, E_f increases from about 0.5 MPa for $\phi = 0.13$ to about 3.5 MPa for $\phi = 0.3$ and is considerably lower than the Young's modulus of a single silica particle, $E_p \simeq 90$ GPa [63].

The relaxation time τ_{max}, which marks a transition from the low-frequency regime to a trivial terminal behavior, increases by orders of magnitude upon addition of silica. For the two highly filled samples, the value of τ_{max} corresponds

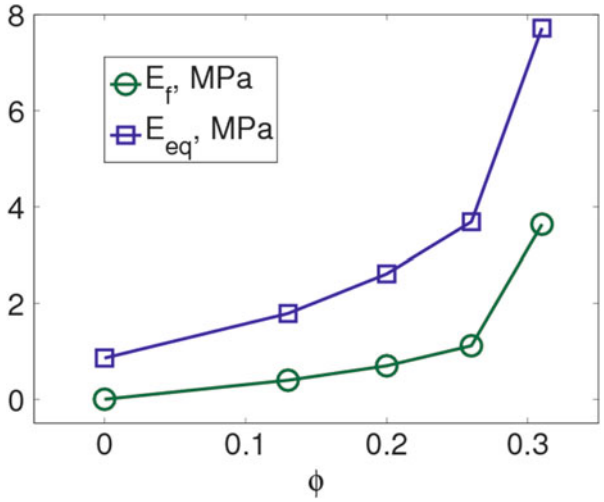

Fig. 14 The plateau modulus E_{eq} and the modulus of filler network E_f as functions of the filler volume fraction ϕ. Reprinted from Ivaneiko et al. [2], Copyright 2016, with permission from Elsevier

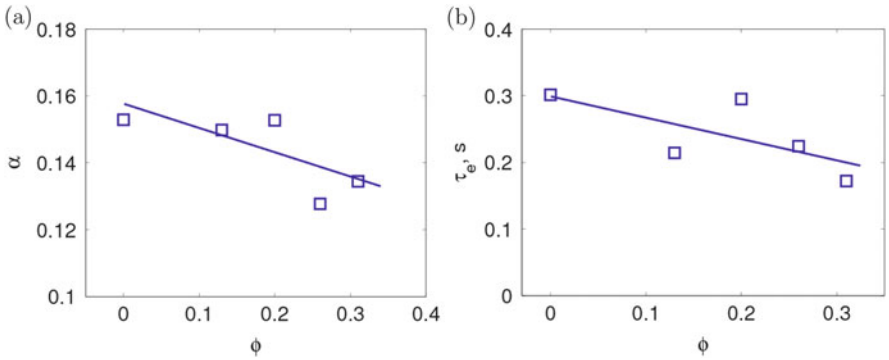

Fig. 15 (**a**) The low-frequency exponent α (**b**) and the relaxation time τ_e as functions of the filler volume fraction ϕ. Reprinted from Ivaneiko et al. [2], Copyright 2016, with permission from Elsevier

to years and is a signature of frozen-like behavior, typical for polymer compounds reinforced with filler clusters and networks [64–66]. The appearance of extremely long times in the low-frequency spectrum upon inclusion of filler particles was also predicted theoretically [23, 67, 68]. At the same time as the increase in terminal relaxation time τ_{max}, there was a slight decrease in the relaxation exponent α (see Fig. 15a). At the end of Sect. 3.2 we showed that the low-frequency regime can be explained by the entangled dangling chain concept [1, 26, 27]. According to Eq. (13), the exponent α is proportional to the ratio of the length of the entanglement strand N_e to the length of the dangling chain N_{dg} (i.e., $\alpha \sim N_e/N_{dg}$). It is

plausible to assume that the chemical structure of the localized polymer chains remains similar to that of the free chains, so that the value of N_{dg} does not change with an increase in the volume fraction of silica. Thus, the decrease in the low-frequency exponent α from 0.15 for the unfilled S-SBR to 0.13 for the two highly filled samples can be explained by a relative decrease in the entanglement length N_e of 13%. According to Eq. (1), the diameter of the confining tube scales as $d_{tube} \sim \sqrt{N_e}$, which results in a relative change in d_{tube} of about 7%, corresponding to a slight decrease in the tube diameter from 5 nm (estimated in Sect. 2.1 for the unfilled S-SBR) to approximately 4.6 nm for samples filled with 70 and 90 phr silica.

The complex influence of hard nanoparticles on the diameter of the confining tube has been discussed in a number of studies [58, 60, 69–71]. As early as in 1993, Heinrich and Vilgis found that the entanglement modulus of rubbers filled with carbon black decreases by about 20%. This was explained by a slight increase in the tube diameter as a result of shortening of network strands with increasing filler content [69, 70]. Recently, a decrease in the tube diameter upon addition of silica nanoparticles to polymer melts, investigated by the neutron spin echo (NSE) method, was reported by Richter and co-authors [71]. The authors proposed two types of entanglement constraints: (1) polymer entanglements resulting from the presence of other chains and (2) geometric entanglements resulting from the presence of nanoparticles. The *apparent* tube diameter, as found in NSE experiments, was related to the polymer tube diameter and the geometric tube diameter through a simple phenomenological relation. Applying this relation at different volume fractions of filler, Richter and co-authors [71] predicted that polymer entanglements become weaker with increasing ϕ, in agreement with Heinrich and Vilgis [69, 70], whereas the geometric entanglements become stronger. Total disentanglement of chains in highly filled polymer melts was explained by a local stretching of polymer chains induced by the narrow voids between filler particles [58, 71]. Our results for the S-SBR filled with nanometer-sized silica particles can be interpreted on the basis that the particles impose strong geometric constraints that dominate the reduced entanglement constraints. This leads to a reduction in the apparent tube diameter, as estimated from the decrease in exponent α at higher filler content, in agreement with the proposal of Richter and co-authors [71] and other researchers [58, 60].

The decrease in entanglement length N_e naturally explains the decrease in the relaxation time of entanglement strands, τ_e. According to Eq. (11), $\tau_e \sim N_e^2$, meaning that the decrease in N_e by 13% should be accompanied by a decrease in τ_e of 26%. As can be seen in Fig. 15b, this is in a good agreement with the experimentally observed decrease from 0.30 to 0.22 s when the volume fraction of filler increases from 0 to 0.31.

5 Conclusions

The multiscale approach, presented in this review article, unifies the ideas developed in multiple theoretical studies of uncrosslinked and crosslinked polymers for different types of relaxation processes. The influence of the disordered filler surface on the chain relaxation at different time scales is also taken into account. The proposed theoretical approach allows simultaneous and precise modeling of the frequency dependences of the storage and loss moduli of elastomer nanocomposites across a whole frequency domain that stretches over more than 15 decades.

The multiscale approach has been tested on SBRs with different crosslink densities and containing different amounts of precipitated silica. For these compounds, four frequency regimes have been identified and described: (1) monomer relaxation at very high frequencies, (2) bending relaxation of semiflexible chain fragments for frequencies in the rubber–glass transition region, (3) relaxation of free and localized flexible strands between the entanglements at intermediate frequencies, and (4) extremely slow relaxation of dangling chains at low frequencies. Only the fastest processes at very high frequencies are found to be insensitive to the presence of silica. All other processes, including the bending modes, are slowed down, which manifests in a noticeable decrease in the corresponding relaxation exponents.

The proposed approach can be applied to a wide range of materials showing dynamic-mechanical behavior close to that of SBRs and that have dynamic processes in each of the four frequency regimes similar to the S-SBRs. In the case of materials exhibiting some additional dynamic relaxation processes (for example, polymer networks with a high heterogeneity of the spatial or mass distribution of crosslinks), the proposed multiscale approach should be extended and refined to include new dynamic effects.

The fitting parameters obtained in the present study for SBRs provide molecular characteristics that are reasonable for the studied rubber and filler materials and are in a good agreement with rigorous theoretical calculations. This demonstrates the great potential of the multiscale approach for use in future investigations of the molecular mobility and structure of other filled elastomer materials of high interest for the automobile industry and for everyday applications.

Acknowledgements The authors gratefully acknowledge a technical support from T. Götze, K. Scheibe, and R. Jurk (Leibniz-Institut für Polymerforschung Dresden e.V.).

We wish to thank Dr. K. W. Stöckelhuber (Leibniz-Institut für Polymerforschung Dresden e. V.) for inspiring discussions, Dr. F. Petry (Goodyear Innovation Center Luxembourg) for his outstanding support and collaboration, and the Goodyear Tire and Rubber Company for permission to publish this paper.

The authors would like to cordially express their gratitude to Prof. Dr. G. Heinrich for all the outstanding collaborations and discussions during the past years. Be it in conjunction with elastomer physics, polymer and rubber viscoelasticity, rubber friction, contact mechanics, fracture mechanics, or any other scientific subject, the discussions were always shaped by respect, honesty, integrity and an impressive level of scientific competence. Prof. Heinrich is an undisputed authority in his field, from fundamental science and polymer theory up to the tire-related

applications of rubber technology. He unifies the leadership traits of a scientific director, academic teacher, and institutional manager. It has always been a great pleasure to collaborate and work with him.

References

1. Saphiannikova M, Toshchevikov V, Gazuz I, Petry F, Westermann S, Heinrich G (2014) Macromolecules 47:4813–4823
2. Ivaneiko I, Toshchevikov V, Saphiannikova M, Stöckelhuber K, Petry F, Westermann S, Heinrich G (2016) Polymer 82:356–365
3. Vilgis TA, Heinrich G, Klüppel M (2009) Reinforcement of polymer nanocomposites: theory, experiments and applications. Cambridge University Press, Cambridge
4. Grellmann W, Heinrich G, Kaliske M, Klüppel M, Schneider K, Vilgis T (2013) Fracture mechanics and statistical mechanics of reinforced elastomeric blends. Springer, Heidelberg, New York, Dordrecht, and London
5. Heinrich G (1997) Rubber Chem Technol 70:1–14
6. Klüppel M, Heinrich G (2000) Rubber Chem Technol 73:578–606
7. Heinrich G, Vilgis TA (2015) Poly Lett 9:291–299
8. Heinrich G, Dumler BD (1998) Rubber Chem Technol 71:53–61
9. Heinrich G, Vilgis TA (2008) Kautschuk Gummi Kunststoffe 61:368–376
10. Westermann S, Petry F, Boes R, Thielen G (2004) Tire Technology International: Annual review. p 68
11. Westermann S, Petry F, Boes R, Thielen G (2004) Kautschuk Gummi Kunststoffe 57:645–650
12. Stöckelhuber KW, Svistkov AS, Pelevin AG, Heinrich G (2011) Macromolecules 44:4366–4381
13. Mooney M (1959) J Polym Sci 34:599–626
14. Ferry JD (1980) Viscoelastic properties of polymers, 3rd edn. Wiley, New York
15. Morse DC (1998) Macromolecules 31:7044–7067
16. Rubinstein M, Colby RH (2003) Polymer physics. Oxford University Press, Oxford
17. Shore JE, Zwanzig RJ (1975) Chem Phys 63:5445–5458
18. Mansfield MJ (1983) Polym Sci Polym Phys Ed 21:773–786
19. Gotlib YY, Toshchevikov VP (2001) Polym Sci A 43:525–534
20. Gotlib YY, Toshchevikov VP (2001) Polym Sci A 43:1074–1083
21. Gurtovenko AA, Gotlib YY (2000) Macromolecules 33:6578–6587
22. Gurtovenko AA, Blumen A (2005) Adv Polym Sci 182:171–282
23. Toshchevikov VP, Blumen A, Gotlib YY (2007) Macromol Theory Simul 16:359–377
24. Toshchevikov VP, Gotlib YY (2009) Macromolecules 42:3417–3429
25. Edwards SF, Takano H, Terentjev EMJ (2000) Chem Phys 113:5531–5538
26. Curro JG, Pincus P (1983) Macromolecules 16:559–562
27. Curro JG, Pearson DS, Helfand E (1985) Macromolecules 18:1157–1162
28. Heinrich G, Straube E, Helmis G (1988) Adv Polym Sci 85:33–87
29. Edwards SF, Vilgis TA (1988) Rep Prog Phys 51:243–297
30. Kaliske M, Heinrich G (1999) Rubber Chem Technol 72:602–632
31. Migliorin IG, Rostiashvili VG, Vilgis TA (2003) Eur Phys J B 33:61–73
32. Vilgis TA (2005) Polymer 46:4223–4229
33. Klüppel M (2003) Adv Polym Sci 164:1–86
34. Leblanc JL (2010) Filled polymers: science and industrial applications. CRC, Boca Raton
35. Rooj S, Das A, Stöckelhuber KW, Wang D-Y, Galiatsatos V, Heinrich G (2011) Soft Matter 9:3798–3808
36. Doi M, Edwards SF (1988) The theory of polymer dynamics. Oxford University Press, Oxford

37. Klüppel M (2009) J Phys Condens Matter 21:035104
38. Otegui J, Schwartz G, Cerveny S, Colmenero J, Loichen J, Westermann S (2013) Macromolecules 46:2407–2416
39. Kummali M, Miccio L, Schwartz G, Alegria A, Colmenero J, Otegui J, Petzold A, Westermann S (2013) Polymer 54:4980–4986
40. Dealy JM, Larson RG (2006) Structure and rheology of molten polymers. Hansa, Cincinnati
41. Williams G, Watts DC (1970) Trans Faraday Soc 66:80–85
42. Toshchevikov VP, Heinrich G, Gotlib YY (2010) Macromol Theory Simul 19:195–209
43. Sommer J-U, Schulz M, Trautenberg HLJ (1993) Chem Phys 98:7515–7520
44. Lang M, Göritz D, Kreitmeier S (2003) Macromolecules 36:4646–4658
45. Chasse W, Lang M, Sommer J-U, Saalwächter K (2012) Macromolecules 45:899–912
46. Marzocca AJ, Steren CA, Raimondo RB, Cerveny S (2004) Polym Int 53:646–655
47. Chatenay D, Cocco S, Monasson R, Thieffry D, Dalibard J (eds) (2005) Multiple aspects of DNA and RNA: from biophysics to bioinformatics. Lecture notes of the Les Houches Summer School 2004, session LXXXII. Elsevier, Amsterdam
48. Westermann S, Kreitschmann M, Pyckhout-Hintzen W, Richter D, Straube E, Farago B, Goerigk G (1999) Macromolecules 32:5793–5802
49. Domurath J, Saphiannikova M, Ausias G, Heinrich G (2012) J Non-Newtonian Fluid Mech 171–172:8–16
50. Domurath J, Saphiannikova M, Férec J, Ausias G, Heinrich G (2015) J Non-Newtonian Fluid Mech 221:95–102
51. Chen HS, Acrivos A (1978) Int J Solids Struct 14:349–364
52. Gold O (1936) Beiträge zur Hydrodynamik der zähen Flssigkeiten. Dissertation, Wien University
53. Guth E, Gold O (1938) Phys Rev 53:322–324
54. Guth E (1945) J Appl Phys 16:20–25
55. Huber G, Vilgis TA (1999) KGK, Kautschuk Gummi Kunststoffe 52:102–107
56. Simhambhatla M, Leonov A (1995) Rheol Acta 34:329–338
57. Sarvestani AS, Jabbari E (2007) Macromol Theory Simul 16:378–385
58. Li Y, Kröger M, Liu W (2012) Phys Rev Lett 109:118001
59. Glomann T, Schneider G, Allgaier J, Radulescu A, Lohstroh W, Farago B, Richter D (2013) Phys Rev Lett 110:178001
60. Kalathi J, Kumar S, Rubinstein M, Grest G (2015) Soft Matter 11:4123–4132
61. Sobhanie M, Isayev A (1999) J Non-Newtonian Fluid Mech 85:189–212
62. Costa F, Saphiannikova M, Wagenknecht U, Heinrich G (2008) Layered double hydroxide based polymer nanocomposites. Adv. Polym. Sci. 210:101–168
63. Odegard G, Clancy T, Gates T (2005) Polymer 46:553–562
64. Richter S, Saphiannikova M, Jehnichen D, Bierdel M, Heinrich G (2009) Express Polym Lett 3:753–768
65. Richter S, Saphiannikova M, Stöckelhuber K, Heinrich G (2010) Macromol Symp 291–292:193–201
66. Richter S, Kreyenschulte H, Saphiannikova M, Götze T, Heinrich G (2011) Macromol Symp 306–307:141–149
67. Toshchevikov V, Gotlib Y (2006) Polym Sci Ser A 48:649–663
68. Toshchevikov V, Gotlib Y (2013) Polym Sci Ser A 55:556–569
69. Heinrich G, Vilgis T (1993) Macromolecules 26:1109–1119
70. Heinrich G, Vilgis T (1993) Kautschuk Gummi Kunstoffe 46:283–289
71. Schneider G, Nusser K, Willner L, Falus P, Richter D (2011) Macromolecules 44:5857–5860

Adv Polym Sci (2017) 275: 187–234
DOI: 10.1007/12_2016_6

Published online: 24 July 2016

Networks: From Rubbers to Food

B.I. Zielbauer, N. Schönmehl, N. Chatti, and T.A. Vilgis

Abstract Many soft materials can be viewed as networks of different structure and complexity. Their (statistical) physics determine their elastic deformation behavior, fracture, and failure. In food systems, similar properties are of importance. This contribution discusses some of the common points between elastic materials and food gels. Topics range from fundamental physics to some applications in materials science and food science.

Keywords Food networks • Gluten • Hydrogels • Phase separation • Polymers • Protein crosslinking • Reinforced elastomers • Rubbers • Salt

Contents

B.I. Zielbauer, N. Schönmehl, N. Chatti, and T.A. Vilgis (✉)
Max Planck Institute for Polymer Research, Ackermannweg 10, 55128 Mainz, Germany
e-mail: vilgis@mpip-mainz.mpg.de

1 Introduction

The physics of networks and the statistical thermodynamics of heterogeneous networks are longstanding problem areas in the context of soft matter physics, which ranges from basic theory to very profound applications in engineering.

Considerations are typically based on calculation of the appropriate partition function (as customary in statistical mechanics) of a network with permanent, randomly distributed crosslinks, which give rise to the inherent inhomogeneity of the network. To treat such permanent (or "frozen") disorder in the system, one needs a special technique, the "replica trick," as suggested in the seminal paper by Deam and Edwards [1]. This approach has been developed further within the more comprehensive statistical physics context of permanent or chemical gels [2], as shown in Fig. 1.

According to de Gennes [3], the elastic modulus G of permanently crosslinked gels is given by a simple relation:

$$G \simeq \frac{k_B T}{\xi^3} \tag{1}$$

The physics of this naïve equation can be understood very simply: the basic energy of soft matter systems is the thermal energy, which defines the order of magnitude of the elastic shear modulus, which corresponds physically to an energy density, $k_B T$. Therefore, the only relevant volume governing the modulus is given by the mean distance between two adjacent crosslink points, ξ. Indeed, it has been shown experimentally that even swollen hydrogels follow this basic scaling ansatz in a reasonable manner.

The rigorous theory of networks was mainly founded by Deam and Edwards in their seminal paper [1], where it was shown that networks belong to the class of systems containing "quenched disorder." Their elasticity is governed basically by the

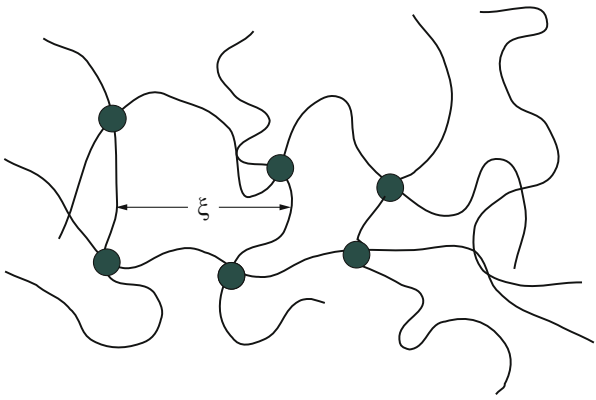

Fig. 1 Representation of a permanent gel with permanent crosslinks between monomers, which define quenched disorder in the gel. The average number of crosslinks determine the mean mesh size ξ

actual configuration of the crosslinks, which does not change during rupture-free deformations. This is true for all networks and gels, even complex food gels. It is interesting to note that the physics of food networks were also considered by Edwards' group 30 years ago [4]. We discuss some important works by Edwards before turning to ideas in food networks and gels. Soft matter physics covers both nano-reinforced rubber materials and food at various time and length scales, as illustrated in Fig. 2. The hierarchical structure of reinforced polymer systems is governed by flexible polymer chains, consisting of certain monomers that interact with the surface of the filler particles (e.g., carbon black or functionalized silica). The filler particles form aggregates and clusters, creating large heterogeneous surfaces within a matrix of crosslinked polymer chains [5]. Similar arrangements can be found in food networks such as wheat dough. The polymers are proteins, showing certain conformations according to the arrangement (primary structure) of the amino acids. The chains are heterochains, which interact in a specific way with the surfaces of starch granules. Both are "filled networks," although their structures and properties are different [6].

This paper is organized as follows: First, simple polymer notation is outlined, defining the terminology used in this paper. Then, simple theories for rubbers are discussed, including dense systems (rubbers). As a short excursion, we look at the

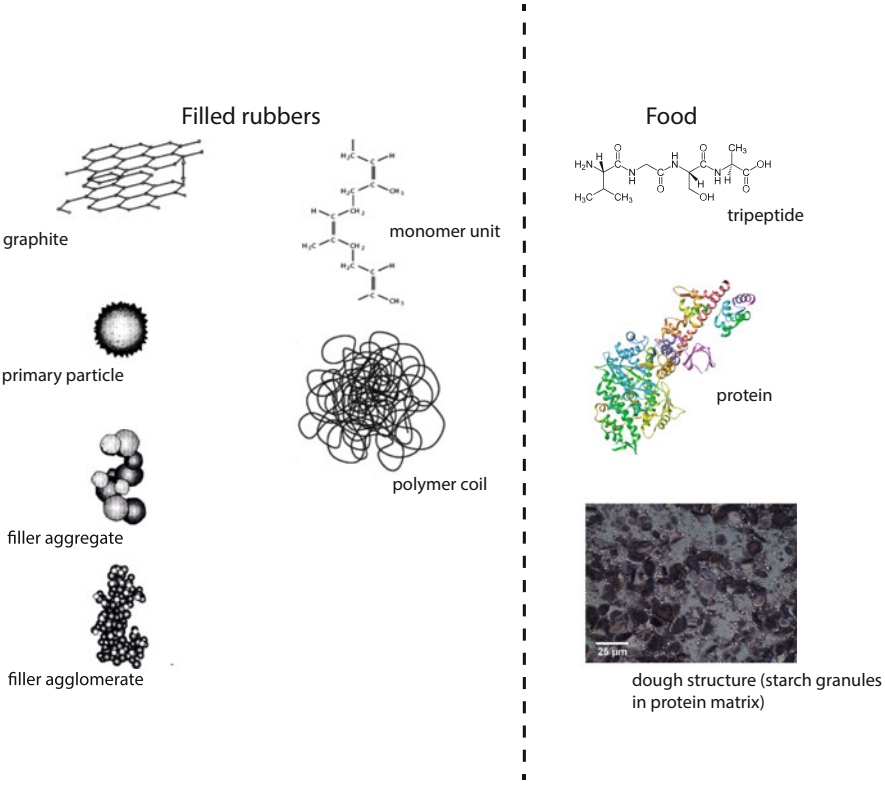

Fig. 2 Different relevant length scales in reinforced rubbers (*left*) and food systems, for example, dough systems (*right*)

effect of the finite extensibility of swollen gels, which leads to very simple material laws and constitutive equations [7]. We show that proteins and carbohydrates follow, to some extent, the ideas developed in polymer physics. Food systems are in most cases swollen systems, in contrast to rubber materials. A good solvent is water; thus, many effects are known from the physics of amphiphilic molecules. Proteins consist of hydrophilic and hydrophobic amino acids, and their behavior with respect to the solvent water determines most of the structural properties of foods. Because most foods contain salt, the effects of charge screening and the related conformational and structural changes become important [3]. Such effects have a huge impact on taste and food structure, and indicate that the nutritional demands of reduced salt intake are not only a challenge for taste perception, but also for understanding the basic physics of the food system. Finally, pure agarose gels are discussed. Their modulus surprisingly follows the simple scaling prediction given in Eq. (1). Mixtures of agarose and gelatin are typical examples of gel-forming polymer blends and interpenetrating networks, which show micro- and macrophase separations at different concentrations.

However, this contribution discusses only some simple but important physics ideas. Novel applications to engineering and materials science are not described.

2 Polymers: Basic Remarks

Homopolymers are long (linear) macromolecules that contain one repeat unit, the monomer, which is polymerized to form long chain molecules. The monomers determine the local "chemistry" of the entire polymer, for example, the local stiffness or the solution behavior in a corresponding solvent. The most important breakthrough in the statistical physics of polymers was discovery of the "universality." The shape of very long polymers is independent of the monomer properties [3]. In consequence, the mean size R of very long polymers, measured by their mean square radius of gyration (R_g^2), shows a scaling behavior:

$$R = bN^{\nu} \tag{2}$$

where ν is independent of all local properties, such as the detailed structure of the monomers, provided the chain is long enough; hence, the degree of polymerization is high. The quantity b corresponds to the Kuhn length and is assigned to the mean length of independent statistical units (in fact, this is an ill-defined cut-off), where the number of such units is N [7]. The condition that relates both is $L = bN$, where L is the "real" length of the polymer chain.

Having accepted this fundamental idea, it appears plausible to construct simple, but more systematic, theories for polymer chains. The basic models are freely jointed chains, where N segments each of length b are linked together. Assuming that each segment can take arbitrary spatial orientations and do not hinder each

other (the segments can pass through each other like phantoms), all possible states can be calculated exactly [7] as the average of:

$$P\left(\{\mathbf{b}_i\}_{i=1}^{N}\right) = \prod_{i=1}^{N} p(\mathbf{b}_i), \tag{3}$$

where the probability $p(\mathbf{b}_i)$ is given by:

$$p(\mathbf{b}_i) = \frac{1}{4\pi b^2}\delta\left(|\mathbf{b}_i| - b\right), \tag{4}$$

where $\delta(x)$ denotes Dirac's delta function and fixes the length of the bond vectors to their strict value b. The evaluation of this expression is straight-forward [7] and leads to the well-known Gaussian distribution of the end-to-end distance, $\mathbf{R} = \sum_{i=1}^{N} \mathbf{b}_i$,:

$$P(\mathbf{R}) = \left(\frac{3}{2\pi b^2 N}\right)^{3/2} \exp\left(-\frac{3\mathbf{R}^2}{2b^2 N}\right) \tag{5}$$

Therefore, suitable models of the polymer chains are based on random walks. The exponent, which defines the mean size of the polymer chain, can be immediately read off from the distribution or obtained by calculation of the mean square size. It is given by $R = bN^{1/2}$, which defines $\nu = 1/2$. Obviously, the distribution given by Eq. (5) corresponds to the number of states that realize the end-to-end vector $\mathbf{R}$, and thus to the entropy of the chain, $S = k_\mathrm{B}\ \ln P$, where k_B is the Boltzmann constant. Because the Gaussian polymer chain is non-interacting, the free energy $F = -T\ S$, and the chain size physically corresponds to the balance between chain stretching and chain compression:

$$F = k_\mathrm{B}T\left(\frac{3R^2}{2b^2 N} + \frac{2b^2 N}{\pi R^2}\right). \tag{6}$$

Minimization with respect to R leads immediately to the correct scaling relation, $R \propto N^{1/2}$, when the free energy is minimized with respect to the chain radius R. The second term in Eq. (6) comes from another part of the probability, which is not derived here. Its origin is in compressed and confined polymer chains (i.e., entropy loss of fluctuations as a result of compression rather than elongation) [7, 8]. Of course, such models are oversimplified. Real polymers cannot be described by random walks, because real polymers cannot cross themselves. Thus, "excluded volume" needs to be taken into account, which is usually described by the repulsive potential between two polymer segments. In theory, the excluded volume of two segments is modeled by pseudo-potentials:

$$V\left(\mathbf{R}_i - \mathbf{R}_j\right) = \upsilon\delta\left(\mathbf{R}_i - \mathbf{R}_j\right) \tag{7}$$

where υ is of the order of the volume of a segment b^3, which allows estimation of the scaling relation of excluded volume chains. The potential, Eq. (7), is of the order of $V \simeq \upsilon/R^3$. Because the total excluded volume of the chain is given by the summation over the chain indices i; j, the total free energy of the chain is given by:

$$F = k_B T \left(\frac{3R^2}{2b^2 N} + \upsilon \frac{N^2}{R^3} \right), \tag{8}$$

After minimization, one obtains the scaling exponent of a "swollen chain," $R \simeq bN^{3/5}$, which is very close to the correct value ($\nu = 0.588$) for chains in good solvent [3]. High-accuracy values have been reported recently [9].

In concentrated solutions, when the chains start to overlap at typical concentrations, $c^* = N/R^3 = N^{-2/5}$, the excluded volume interactions become screened. Interchain contacts cannot be distinguished from intrachain contacts, and excluded volume correlations become lost in three dimensions (but remains marginal in two space dimensions).

When polymer chains are immersed in poor solvent, collapsed states appear. The polymer protects itself from the poor solvent by exclusion. Figure 3 illustrates a scaling approach proposed by de Gennes [3]. The collapsed chain can be represented by a collapsed string of n_p blobs of diameter ξ_p that are densely packed, $R^3 = n_p \xi_p^3$. At the lowest order in a virial expansion, the free-energy term from Eq. (8) needs to be extended by a three-body repulsion term of the order $b^6 N^3/R^6$, because the two-body interaction becomes effectively attractive. From the balance of the attractive two-body interactions and the repulsive three-body term, the blob size can be readily calculated as $\xi_p = b/\tau$, where τ is given by the quotient of the (temperature-dependent) excluded volume and the third virial coefficient. The size of the collapsed chain is then:

$$R = b\tau^{-1/3} N^{-1/3}, \tag{9}$$

which means that the chain is densely packed at scales larger than the blob size ξ_p.

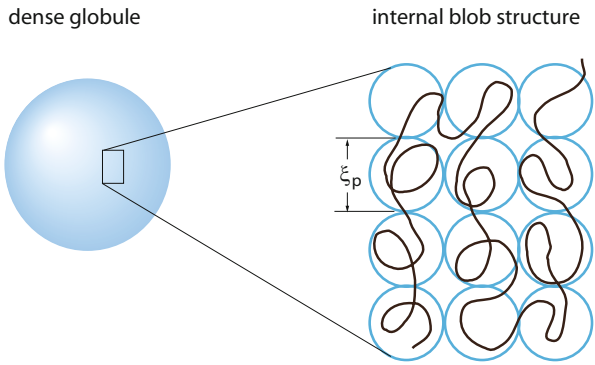

Fig. 3 Collapsed chains in poor solvent form dense globules with internal structure. The blob size ξ_p is mainly determined by the "poorness" of the solvent (e.g., the distance from the critical temperature)

The exponents define the basic boundaries for the size of homopolymer chains in solvents of different qualities in three dimensions:

$$1/3 \leq \nu \leq 3/5 \tag{10}$$

The Gaussian chain behavior $\nu = 1/2$ can be realized in a so-called theta solvent, where the excluded volume is $v = 0$, which occurs for certain solvents at a given temperature.

A later (Sect. 6) of this paper considers food polymers and gels. Food homopolymers (or quasi-homopolymers) have either polar monomers (some hydrocolloids) or are ionizable polyelectrolytes. Both of these dissolve in water. For polar food polymers, similar statements as given above also hold. Water is a good solvent for polar polymers.

For polyelectrolytes [10], similar scaling theories can be developed. When monomers along the chain repel each other by strong electrostatic forces, the potential between the monomers can be approximated by a Coulomb potential. The mean field free energy then becomes:

$$F = k_B T \left(\frac{3R^2}{2b^2 N} + \frac{l_B f^2 N^2}{R} \right), \tag{11}$$

where l_B is the Bjerrum length, $l_B = e^2/(4\pi\ k_B T\epsilon)$, and f the fraction of charged monomers along the contour of the chain. Eq. (11) shows immediately that the chains are stretched; their size scales as:

$$R = b \left(\frac{l_B f^2}{b} \right)^{1/3} N. \tag{12}$$

When salt is added, the electrostatic interactions become screened [11]. The chain conformation becomes less and less stretched and tends towards self-avoiding walk conformations.

Polyelectrolytes in poor solvent and their stretching behavior have been discussed in detail [12]. For these cases, repulsive electrostatic and attractive excluded volume forces balance themselves. The chains form necklaces, as indicated in Fig. 4.

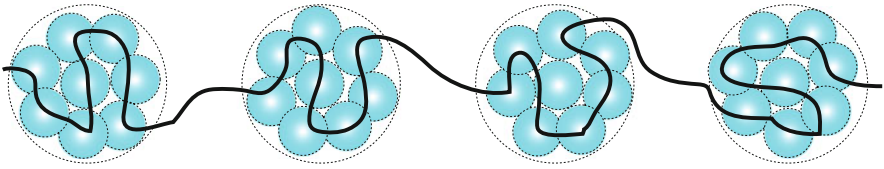

Fig. 4 Pearl-necklace conformations of polyelectrolytes in poor solvent. The chain forms charged collapsed regions, which repel each other

Long food proteins (e.g., glutenin) can be viewed as "random copolymers," which form permanent networks. Proteins are heteropolymers; their "monomers" consist of the 20 proteinogenic amino acids, which are hydrophopic, polar, and positively or negatively charged. Thus, interaction of the monomers is a position-dependent, complex function that is both short- and long-ranged. Simple models hardly exist. The primary structure of long food proteins defines the folding and, thus, the shape and function of the proteins. In their denatured form, polymer properties can be used to design food materials, as can be seen by the examples of glutenin in baking products or of gelatin in gels. These cases are discussed in more detail below (see Sect. 6).

3 Theory of Ideal Rubber

3.1 The Standard Edwards Formulation: Non-Gibbsian Statistical Physics

The standard rubber model was introduced by Edwards in the context of quenched disorder [1, 13] formed by the fixed crosslinks, which introduce a non-Gibbsian statistical physics. The partition function of a given (quenched) crosslink configuration of the chain is given by:

$$Z(\mathrm{C}) = \int_V \mathcal{D}R e^{-\beta(H_W+H_I)} \prod_{e=1}^{M} \delta\left(\mathbf{R}_{i_e} - \mathbf{R}_{j_e}\right), \tag{13}$$

where the monomer positions are given by a set of vectors $\mathbf{R}_i$ and the index i runs over all monomers along the contour (i.e., $i = 0,\ldots, N$). The term β denotes the inverse temperature, $\beta = 1/k_\mathrm{B}T$. There are M crosslinks, which join monomers i_e and j_e ($e = 1, 2,\ldots M$), so that $\mathbf{R}_{i_e} = \mathbf{R}_{j_e}$. The network partition function now depends on the crosslink distribution $\{i_e, j_e\}$. The Edwards Hamiltonian contains two important contributions. The first defines the connectivity of the chain and is expressed by a discrete Wiener measure:

$$\beta H_\mathrm{W} = \frac{d}{2a^2} \sum_{i=1}^{N} (\mathbf{R}_i - \mathbf{R}_{i-1})^2. \tag{14}$$

The second contribution is defined by the excluded volume of the different monomers:

$$\beta H_I = v \sum_{0 \le i < j}^{N} \delta\left(\mathbf{R}_i - \mathbf{R}_j\right). \tag{15}$$

The main issue is the handling of the crosslink constraints, which are expressed by the multiple delta function in Eq. (13). This hard constraint represents the quenched disorder, which imposes the condition that the monomer at the position vector $\mathbf{R}_{i_e}$ is always linked to the monomer at $\mathbf{R}_{j_e}$. Thus, the free energy of the network depends on the actual crosslink configuration, $C\{i_e, j_e\}$ [i.e., $F(\mathrm{C}) = -k_\mathrm{B}T \ln Z(\mathrm{C})$], and must then be averaged over its distribution:

$$F = \langle F(C)\rangle_\mathrm{C} = -k_B T \langle \ln Z(\mathrm{C})\rangle_\mathrm{C} \tag{16}$$

The usual way to treat the crosslink term is to employ the so-called replica trick, which allows one to average the quenched system (i.e., the system with a frozen disorder). Use of the formal mathematical identity $\ln Z = \lim_{n\to 0} \frac{1}{n}(Z^n - 1)$ allows averaging a power of the partition function and evaluation of the generalized partition function:

$$\exp(\beta F(n)) = \langle Z^n(\mathrm{C})\rangle_\mathrm{C} = \int_V \prod_{\alpha=1}^{n} \mathcal{D}\mathbf{R}^\alpha \frac{1}{2\pi i} \oint \frac{d\mu M!}{\mu^{M+1}} \exp^{-\beta H_{\mathrm{eff}}(n,\mu)} \tag{17}$$

The effective Hamiltonian, H_{eff}, is given by:

$$\begin{aligned} H_{\mathrm{eff}} = \; & \sum_{\alpha=1}^{n} \left(\frac{d}{2a^2} \sum_{i=1}^{N} \left(\mathbf{R}_i^\alpha - \mathbf{R}_{i-1}^\alpha\right)^2 + \upsilon \sum_{0\le i<j}^{N} \delta\left(\mathbf{R}_i^\alpha - \mathbf{R}_j^\alpha\right) \right) \\ & -\mu \sum_{0\le i<j}^{N} \prod_{\alpha=1}^{n} \delta\left(\mathbf{R}_i^\alpha - \mathbf{R}_j^\alpha\right) \end{aligned} \tag{18}$$

In Eq. (17), the grand canonical representation for the crosslink constraints has been used, $(A)^M = (M!/2\pi i) \oint d\mu \exp(\mu A)/\mu^{M+1}$, where $A = \sum_{0\le i<j}^{N} \delta\left(\mathbf{R}_i^\alpha - \mathbf{R}_j^\alpha\right)$ and μ stands for the chemical potential. In order to calculate the free energy in Eq. (17) one has to evaluate the functional integral over configurations $\{\mathbf{R}_i^\alpha\}$. This is a formidable task and, therefore, one should transform the problem into a more tractable one by going to a field theoretical representation followed by a mean field treatment. Amorphous solid state formation [14], density correlation functions in heterogeneous structures of networks during stretching, and some other interesting issues have been discussed in detail by Panyukov and Rabin [2].

However, for practical reasons, the evaluation of partition function, Eq. (17), can only be carried out in very limited cases. For practical use, simplification is necessary. The first step is the Gaussian network. Despite its simplicity, it contains some essential ideas for experimental purposes [15].

3.2 Gaussian Networks

Historically, the theory of "neo-Hookian" elasticity of rubbers was developed in the 1940s and is reviewed in a book by Treloar [15]. The theory is based on some basic assumptions:

- Each subchain forming the network is "phantom," that is, all surrounding polymers do not restrict conformations that are compatible with the end-to-end distance of the subchain under study.
- The statistics of all subchains is Gaussian. This assumption can be justified by the fact that networks are usually rather concentrated systems (e.g., in a concentrated solution), in which chains are governed by Gaussian statistics [3].
- Deformations on the nanoscale are the same as on the macroscale. This property is usually referred to as the affine deformation of rubber networks.
- The density of the network is well behaved.

The Gaussian theory for an ideal polymer chain is expressed in Gaussian statistics of the conformations at a given end-to-end distance vector **R** as:

$$P(\mathbf{R}) = \left(\frac{3}{2\pi N b^2}\right)^{3/2} \exp - \left(\frac{3R^2}{2Nb^2}\right) \tag{19}$$

As a result, in Gaussian network theory the elasticity is defined by the entropy contribution of subchains (i.e., chain fragments between two crosslinks). The entropy of a subchain with an end-to-end vector **R** is given by:

$$S(\mathbf{R}) = k_{\mathrm{B}} \ln P_N(\mathbf{R}) \tag{20}$$

where P_N (**R**) is the end-to-end vector distribution function for a Gaussian chain with a chain length N [3]. Note that because the internal energy U can be neglected, the total free energy $F(\mathbf{R}) = -TS(\mathbf{R})$ and we have:

$$F(\mathbf{R}) = k_{\mathrm{B}}T \frac{3R^2}{2Nb^2} - \frac{3}{2} k_{\mathrm{B}}T \ln\left(\frac{3}{2\pi b^2 N}\right) \tag{21}$$

The corresponding deformation force is then given by:

$$\mathbf{f} = \frac{\partial F}{\partial \mathbf{R}} = k_{\mathrm{B}}T \frac{3}{b^2 N} \mathbf{R} \tag{22}$$

Although this is a very simple formula it has some interesting features. First, it resembles Hooke's law, where the force is proportional to the extension. Second, the force increases with increasing temperature. This is in contrast to ordinary elasticity (e.g., in metals) where the force decreases with temperature. The physical

reason for this is the entropic nature of elastic effects, such that more conformations are normally accessible for higher temperatures . Moreover, Eq. (22) shows that the elasticity modulus is proportional to ~1/N (i.e., is very small).

In the same way as for chain extension, chain compression costs entropy. Confining a chain of a natural size $R \simeq bN^{1/2}$ to any other (smaller) size R can be estimated by the entropy penalty [3]:

$$F_{\text{conf}} = k_{\text{B}}T\frac{b^2N}{R^2} \tag{23}$$

The combination of this equation with Eq. (21) leads to the total free energy:

$$F(\mathbf{R}) = k_{\text{B}}T\left(\frac{R^2}{b^2N} + \frac{b^2N}{R^2}\right) \tag{24}$$

The minimum of this free energy occurs at the well known size $R \simeq bN^{1/2}$.

This simple preliminary consideration based on single chain deformation behavior enables the construction of a theory of Gaussian networks. To this end, we introduce a diagonal deformation matrix:

$$\boldsymbol{\lambda} = \begin{pmatrix} \lambda_x & 0 & 0 \\ 0 & \lambda_y & 0 \\ 0 & 0 & \lambda_z \end{pmatrix} \tag{25}$$

where the deformations $\lambda_{x,y,z}$ correspond to the three principal axes. Each of these parameters describes the ratio of the final length of the rubber to the initial length, as well as the individual deformation of chains on the nanoscopic length scale:

$$\mathbf{R}(\boldsymbol{\lambda})_i = \boldsymbol{\lambda} \cdot \mathbf{R}_i \tag{26}$$

where $\mathbf{R}_i$ is the undeformed end-to-end distance of the i-th chain in the network. Then, the free energy of a deformed rubber consisting of n_{c} crosslinked chains can be described as:

$$F(\{\boldsymbol{\lambda} \cdot \mathbf{R}_i\}) = k_{\text{B}}T\frac{3}{2b^2N}\sum_{i=1}^{n_c}(\boldsymbol{\lambda} \cdot \mathbf{R}_i)^2. \tag{27}$$

Note that the free energy as it stands in Eq. (27) still contains "microscopic" variables (i.e., the individual chain end-to-end distances $\mathbf{R}_i$). To obtain the free energy of the total network, one should average the free energy over all subchains (this actually corresponds to non-Gibbsian statistical mechanics, as discussed in Sect. 3.1). Taking into account that $\left\langle \mathbf{R}_i^2 \right\rangle = b^2N/3$, we arrive at the following expression :

$$F(\boldsymbol{\lambda}) = \frac{1}{2} k_{\mathrm{B}} T n_{\mathrm{c}} \boldsymbol{\lambda} \cdot \boldsymbol{\lambda}^{\mathbf{T}}. \tag{28}$$

Because a simple diagonal form of the deformation matrix was chosen, the final equation can be written in a standard form:

$$F(\boldsymbol{\lambda}) = \frac{1}{2} k_{\mathrm{B}} T n_{\mathrm{c}} \left(\lambda_x^2 + \lambda_y^2 + \lambda_z^2 \right) \tag{29}$$

This free energy enables us to calculate a simple equation of state, which is here a force–extension relationship. Note that the crosslinked polymer materials are (in the absence of any solvent) incompressible. Therefore, we can use the following relation for a uniaxial deformation experiment:

$$\begin{array}{rcl} \lambda_z & = & \lambda \\ \lambda_x & = & \lambda_y = \lambda^{-1/2} \end{array} \tag{30}$$

which yields the force extension relation:

$$f = n_{\mathrm{c}} k_{\mathrm{B}} T \left(\lambda - \frac{1}{\lambda^2} \right). \tag{31}$$

Equation (31) is one of the main results of classic rubber elasticity theory [15]. It is interesting that this formula predicts not only the linear deformation regime (for $\lambda - 1 << 1$) but also some nonlinear properties. In a more general case, one could also take into account the compression term, which make the free energy function more complicated. Here, we only mention that in this case the additional terms $1/\lambda_x^2 + 1/\lambda_y^2 + 1/\lambda_z^2$ and $\lambda_x^2/\lambda_y^2\lambda_z^2 + \mathrm{perm}\,(x, y, z)$ appear. In the more general mathematical theory it is postulated that the deformation free energy depends only on the three tensor deformation invariants $I_1 = \lambda_x^2 + \lambda_y^2 + \lambda_z^2$, $I_2 = \lambda_y^2\lambda_x^2 + \lambda_y^2\lambda_z^2 + \lambda_x^2\lambda_z^2$, and $I_3 = \lambda_x^2\lambda_y^2\lambda_z^2$, which resemble the trace, the sum of products of the off diagonals, and determinant of the deformation tensor, respectively. Note that for incompressible rubber systems, $I_3 = 1$ and the second invariant reduces to the sum of the inverse square deformation parameters.

The free energy function discussed above ignores the defects shown in Fig. 5. The realistic crosslinked polymer melt can be made solid by adding a reagent that joins each chain to neighbors. With network formation, however, many structural elements such as entanglements, loops, and dangling ends (i.e., subchains that are crosslinked only once) become frozen-in, as shown in Fig. 5.

The lack of the excluded volume forces suggests that the phantom networks collapse [as also suggested by the Hamiltonian Eq. (17)]. For example, the phantom chain model does not take into account any topological constraints or chain entanglements. Moreover, the chain has a maximum extension of $\lambda_{\max} = \sqrt{N}$, which often appears far larger than measured in reality. As soon as the deformation $\lambda \to \lambda_{\max}$, the force becomes very large, a fact ignored in Gaussian theory.

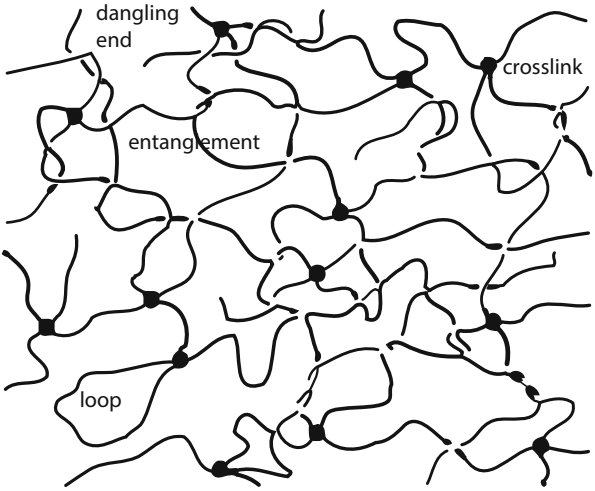

Fig. 5 Different structural elements in a network. Entanglements and knots contribute to the elasticity, dangling ends and self-crosslinked loops do not

4 Simple Material Laws

4.1 Finite Extensibility

The first step towards more realistic models is to consider chains with finite extensibility. Gaussian chains can be stretched to infinity; the Gaussian distribution in Eq. (19) allows unrealistic and unphysical overstretched chain conformations, $R > Nb$. These problems were resolved in the early days of network physics and the main ideas are summarized in a book by Treloar [15]. The exact result shows implicit force–extension relations, which involve inverse Langevin functions, $\widetilde{R}\left(\widetilde{f}\right) = \coth\left(\widetilde{f}\right) - \widetilde{f}^{-1}$, where $\widetilde{R} = R/Nb, \widetilde{f} = fb/k_{\mathrm{B}}T$ [16]. This is very difficult to handle for explicit calculations. Especially for swelling experiments, when a non-volume-conserving, three-dimensional deformation of the network takes place through the uptake of a good solvent, the finite extensibility limits the swelling. The nonlinear rise in the force acting at the meshes between crosslinks strongly limits the swelling. These effects become especially important in food networks and hydrogels, where a large concentration of water (good solvent) is taken up.

Swelling of polymer networks corresponds to equitriaxial deformation. In the frame of a Flory-type calculation for the equilibrium polymer size R, the free energy of the polymer chain is composed of two parts, $F(\alpha) = F_{\mathrm{elas}}(\alpha) + F_{\mathrm{int}}(\alpha)$. Here, $\alpha = \sqrt{R^2/R_0^2}$ is the swelling parameter of the model. The elastic free energy is of entropic origin and tends to coil the polymer chain for more configurational entropy. In Flory's classic theory, it takes the form $F_{\mathrm{elas}}(\alpha) = \frac{3}{2}(\alpha^2 - 1) - 3\ln\alpha$, by which the state of $\alpha = 1$ is taken to be the reference state of the polymer chain with $F_{\mathrm{elas}} = 0$. The interaction free energy F_{int} is the driving force for chain swelling, which can be the result of any repulsive-type interactions between monomers.

For $F_{\text{int}}(\alpha) = cz\alpha^{-3}$, the constant $c = 134/105$ is chosen to be consistent with the perturbation theory of polymer swelling [17] and the parameter $z = \upsilon N^{1/2}/b^3\widetilde{\upsilon}N^{1/2}$ with the scaled $\widetilde{\upsilon}$, which is the effective interaction parameter characterizing the strength of the driving force for swelling the chain. Minimizing $F(\alpha)$ with respect to the swelling parameter α suggests the equilibrium value α_* as the solution of the relation:

$$\alpha_*^5 - \alpha_*^3 = cz. \tag{32}$$

To go beyond Flory's treatment, a suitable form takes into account the finite-extensibility appropriately, which requires the introduction of a singularity at the maximum stretching $R_{\max} = Nb$, which corresponds to $\alpha_{\max} = \sqrt{R_{\max}^2/R_0^2} = N^{1/2}$. The elastic free energy is modified to the following:

$$F_{\text{elas}} = \frac{3}{2}\left(\frac{\alpha^2 - 1}{1 - \alpha^2/N}\right) - 3\ln\alpha \tag{33}$$

whereas the short-ranged excluded volume term remains unchanged. The swelling equilibrium is then given by:

$$\frac{\alpha_*^5}{\left(1 - \alpha_*^2/N\right)}\left(1 - \frac{1}{N}\right) - \alpha_*^3 = z \tag{34}$$

which recovers Flory's classic equation exactly at the limit $N \to \infty$.

Although the effect vanishes for long chains, the effect on the swelling properties is significant [18]. The mesh size in densely crosslinked rubbers or hydrogels based on gelatin, agarose, or other hydrocolloids is much smaller than the chain length. The forces induced by the swelling pressure increase strongly and limit the uptake of solvent, as shown in Fig. 6.

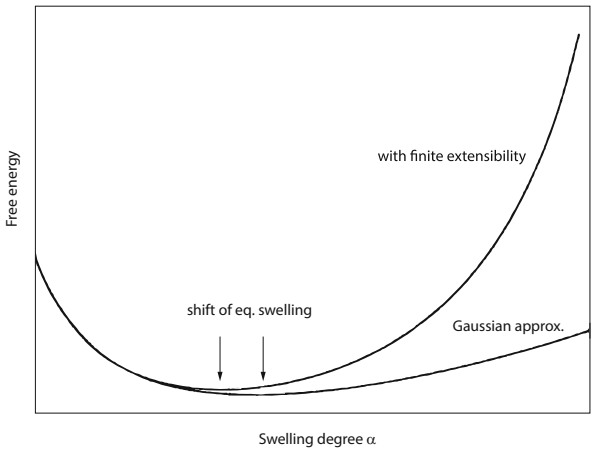

Fig. 6 Shift of the swelling equilibrium to smaller values by the effect of finite chain extensions

4.2 *Entanglements and a Simple Tube Model: A Material Law*

The tube model goes back to de Gennes and Edwards and is a relatively simple representation of topological restrictions in a crosslinked melt [3, 7]. It introduces a new length scale, the tube diameter or the mean distance between entanglements, which governs physical behavior (cf. Fig. 7).

On the other hand, the entanglement can be seen as a local topological constraint, as pictured in Fig. 8. The two conformations shown in Fig. 8 are not equivalent because they cannot be transformed into each other. This is a result of excluded volume, which makes chains of a finite thickness. This must have strong

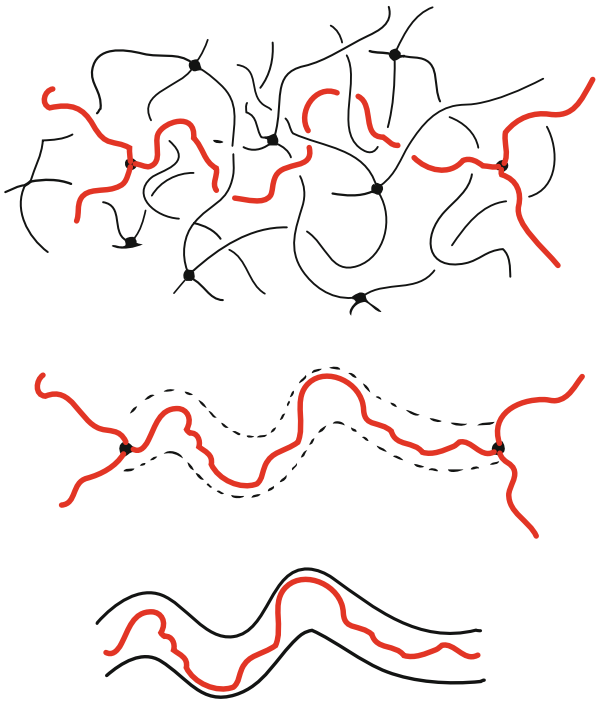

Fig. 7 Chains trapped in tubes as a simple mean field model for entangled states in networks. Figures (from *top* to *bottom*) show successively how the notion of a tube can be defined. It corresponds to a mean field confinement formed by other chains

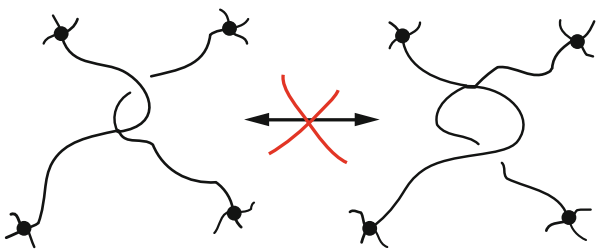

Fig. 8 Locally constrained chains. There is no way to transform the two chains conformations into each other

influences on the mechanical behavior. One could expect that these topological constraints act at two different regimes. At small deformations the sliding of entanglements is relevant, whereas at larger deformations the tube geometry governs the mechanical behavior. These two points are the subject of the rest of this section, where we mainly follow the publications by Edwards and Vilgis [19, 20].

4.2.1 Entanglement Sliding

The effects of entanglement at low deformation can be mainly described by entanglement sliding. As mentioned before, we have already intuitively seen that entanglement can be seen as a kind of "soft crosslink." Schematically, this can be drawn as in Fig. 9. Here, the crosslinks at the end of subchains act as full constraints, whereas the entanglement acts as a ring that can slide along the chains a certain distance a. This distance a is of the order of the mean distance between entanglements. Such sliding could happen anywhere in the network and, initially, we assume that there are N_s such slip-links in the rubber. The number N_s of slip-links and the number of crosslinks N_c are assumed to be given, so that we are dealing with a two-parameter theory. Recently, a powerful new numerical development has been described using a detailed primitive path analysis (which also enables the calculation of N_c) [21].

The mathematical description of the statistical mechanics of this model is rather complicated and beyond the scope of this article. Instead, a more simplified version is described. This kind of approach is easier to generalize when one also needs to discuss the finite extensibility of chains. We assume that the chain is Gaussian, with an end-to-end separation probability written in the form:

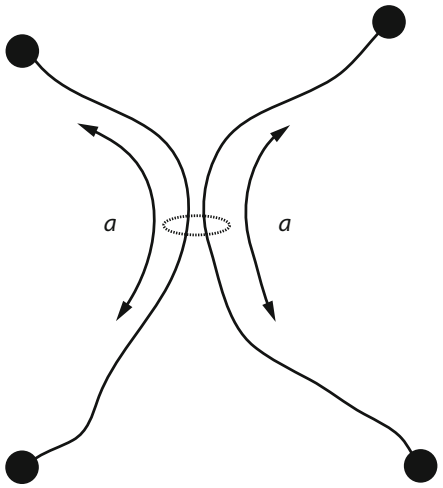

Fig. 9 Locally constrained chains. The chains are trapped and the conformation cannot be resolved

$$P(\mathbf{R},N)=\prod_{i=x,y,z}\int d\tau\chi(\tau)\left(\frac{3}{2\pi b^2(N+\tau)}\right)^{3/2}\exp\left(-\frac{3R_i^2}{2b^2(N+\tau)}\right) \tag{35}$$

The variable τ describes the number of segments that are gained or lost as a result of the slippage. The distribution $\chi(\tau)$ describes the probability of the slippage, which for simplicity can be taken as a rectangular function:

$$\chi(\tau)=1 \quad \text{for} \quad -a<\tau<a \tag{36}$$

Then we may write:

$$P(\mathbf{R},N)=\prod_{i=x,y,z}\frac{1}{2a}\int_{-a}^{+a}d\tau\left(\frac{3}{2\pi b^2(N+\tau)}\right)^{3/2}\exp\left(-\frac{3R_i^2}{2b^2(N+\tau)}\right) \tag{37}$$

The free energy of the deformed network is then given by calculating the "quenched average":

$$F=-\mathrm{k_B}T\int d^3RP(\mathbf{R},N)\ln P(\boldsymbol{\lambda}\cdot\mathbf{R}) \tag{38}$$

where $\boldsymbol{\lambda}$ is the deformation tensor. After some calculation this gives:

$$\frac{F}{\mathrm{k_B}T}=\frac{1}{2}N_\mathrm{c}\sum_{i=x,y,z}\lambda_i^2+\frac{1}{2}N_\mathrm{s}\sum_{i=x,y,z}\left\{\frac{(1+\eta)\lambda_i^2}{1+\eta\lambda_i^2}+\log\left(1+\eta\lambda_i^2\right)\right\} \tag{39}$$

In Eq. (39) we have added the crosslink and slip-link contributions. The parameter η is proportional to a. This result is consistent with the more complicated theory by Ball et al. based on non-Gibbsian statistical physics [22].

The free energy relation Eq. (39) is quite a simple result. The main effect is a reduced macroscopic slip variable η, which is proportional to the mesoscopic variable a. Assuming that the slip takes place between two neighboring crosslinks, estimation of η suggests values between zero and one. Two limiting cases should be discussed. First, if the slippage becomes zero ($\eta=0$), the slip-link turns into a crosslink and fully contributes to the modulus. The free energy is then:

$$\frac{F}{\mathrm{k_B}T}=\frac{1}{2}(N_\mathrm{C}+N_\mathrm{s})\sum_{i=x,y,z}\lambda_i^2 \tag{40}$$

The other significant limit is given by infinite slippage, $\eta\to\infty$. For large values of η the constraints are less severe. Such cases can be treated as swollen networks in which the chain segments are pushed away from each other as far as possible. Then, the free energy reads apart from a deformation independant constant:

$$\frac{F}{k_B T} = \frac{1}{2} N_c \sum_{i=x,y,z} \lambda_i^2 + \frac{1}{2} N_s \ln \prod_{i=x,y,z} \lambda_i \tag{41}$$

and the modulus depends mainly on the number of crosslinks.

Discussion of the physical behavior should now clarify major counterintuitive points. The intuitive picture of the behavior of a slip-link under stress is that it will respond by moving until it locks onto another entanglement or crosslink and behaves as a crosslink of perhaps higher functionality. This means that a slip-link hardens, but a finite value of η in Eq. (39) suggests softening. This result is reasonable if one accounts for the increase in phase space during deformation for the slippage a. As the slipping distance increases, the more conformations become accessible, so that the link weakens. This is, of course, only true if the deformation is not too large, (i.e., long before the polymers are drawn taut).

5 Filled Rubbers

For many applications, rubbers are reinforced with nanoparticles such as carbon black or functionalized silica particles [5]. Filler particles act on different levels, depending on their concentration in the rubber matrix. At low concentrations, filler particles do not interact with each other and contribute only by their volume. This regime is usually called hydrodynamic reinforcement. When the filler particles form irregular, fractal clusters, the reinforcement is still hydrodynamic, but stronger than for simple (spherical) particles. The most important cases are those in which the particles interact to form larger clusters, and form a percolation threshold on connected networks. In addition, the detailed interactions between filler particles and the polymer chains that form the rubber matrix give rise to other universal contributions to the modulus [23]. Figure 10 summarizes the different regimes of

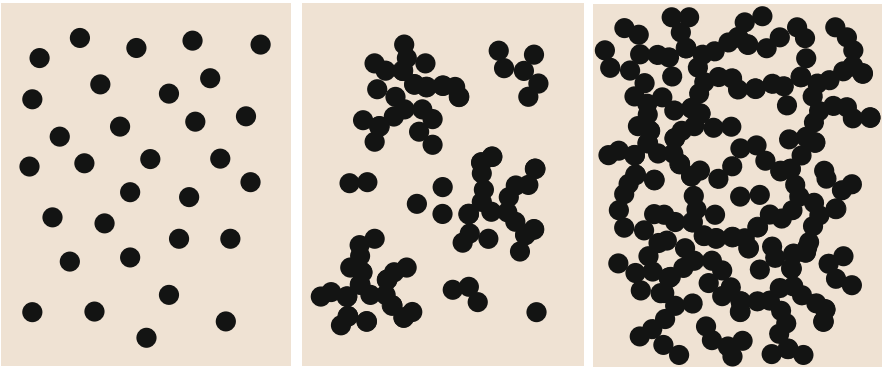

Fig. 10 Three main concentration regimes of filler reinforcement: low concentration (*left*); clusters are formed (*middle*); concentrations are larger than the overlap concentration (*right*)

reinforcement mechanisms. At low concentrations (Fig. 10, left), the particles do not interact with each other. When clusters are formed (middle), the hydrodynamic reinforcement becomes structure dependent. At concentrations larger than the overlap concentrations (right), the fillers form cluster–cluster aggregates and a percolating network.

An overview of some applications of the deformation aspects has recently been published [24].

5.1 Hydrodynamic Reinforcement: Spherical Particles

The rubber matrix contributes to the elastic background as described in the previous sections. The filler adds different contributions, depending on the concentration of the filler particles, their interactions between each other and their interactions with the rubber matrix. Most well known are volume effects, also called hydrodynamic interactions (analogous to enhancement of the viscosity of liquids by the addition of particles). The classic approach for rubbers was presented in 1944 by Smallwood [25], who showed that addition of randomly dispersed, spherical filler particles to a rubbery matrix yields an elastic reinforcement of the form:

$$G = G_{\mathrm{m}}(1 + 2.5\phi). \tag{42}$$

where G is the modulus of the reinforced material and G_{m} the modulus of the pure rubbery matrix; ϕ is the volume fraction of the filler particles. The physical conditions for this result are (1) freely dispersed particles (i.e., low volume fraction), (2) spherical shape (leading to the constant 2.5), and (3) entirely nonelastic filler particles, (i.e., their elastic modulus is infinitely large). Although the assumptions are very strict and idealized, the Einstein–Smallwood equation contains very essential physics. Basically, Eq. (42) is nothing but the first term in a series in powers of the volume fraction ϕ. More importantly, it is a special case of a more general effective medium theory [26]. Note that in one equation given by Huber and Vilgis [26] there is an important misprint. The results given in their figures remain valid, which will be reported in a forthcoming errata.

The general theory for such systems has been derived by Felderhof and Iske [27]. Their general result for the effective shear modulus is given by:

$$\frac{G}{G_{\mathrm{m}}} = 1 + \frac{[\mu]\phi}{1 - \frac{2}{5}[\mu]\phi}, \tag{43}$$

where $[\mu]$ is the intrinsic modulus, defined as:

$$[\mu] = \lim_{x \to 0} \phi^{-1}(G - G_{\mathrm{m}})/G_{\mathrm{m}}$$

This results from a mean field approximation, which corresponds to the Lorentz local field method in the theory of dielectrics, leading to the famous Clausius–Mosotti equation for the effective dielectric constant. For rigid and spherical filler particles at low volume fraction, the Einstein–Smallwood formula is recovered, because $[\mu] = 5/2$ (the intrinsic modulus $[\mu]$ follows from the solution of a single-particle problem). However, the result clearly goes beyond the limits of Einstein–Smallwood, because two-body interactions (excluded volume) are included, leading to a strong increase in the modulus at high volume fraction.

For uniform soft filler particles with elastic modulus $G_\mathrm{f} > G_\mathrm{m}$ there are several methods for calculating the intrinsic modulus (e.g., see Christensen [28]). The result as given by Jones and Schmitz [29, 30] is:

$$[\mu] = 5\frac{1 - G_\mathrm{m}/G_\mathrm{f}}{2 + 3G_\mathrm{m}/G_\mathrm{f}}. \tag{44}$$

Inserting this into Eq. (43) leads to:

$$\frac{G}{G_\mathrm{m}} = 1 + \frac{5}{2}\phi\frac{G_f/G_\mathrm{m} - 1}{G_\mathrm{f}/G_\mathrm{m} + 3/2 - \phi(G_\mathrm{f}/G_\mathrm{m} - 1)} \tag{45}$$

Figure 11 shows how the reinforcement factor rises with the volume fraction and the hardness of the particles. Indeed, it can be shown that, for holes, when the ratio $G_\mathrm{f}/G_\mathrm{m} < 1$, the material softens strongly. For rubbers, such cases should be avoided. For food materials like dough, many air bubbles are present after dough mixing and have a significant effect on the elastic and rheological properties of the dough network, as described later (see Sect. 6.1.2).

For rubbers, coated particles are important and correspond to a first approximation of "bound" rubbers, a direct consequence of particle–polymer interactions, which are discussed in detail in ref. [26]. For food networks, such effects are of lesser importance. Reinforcement with fractal clusters appears more important, because the precise structure of the cluster has an influence.

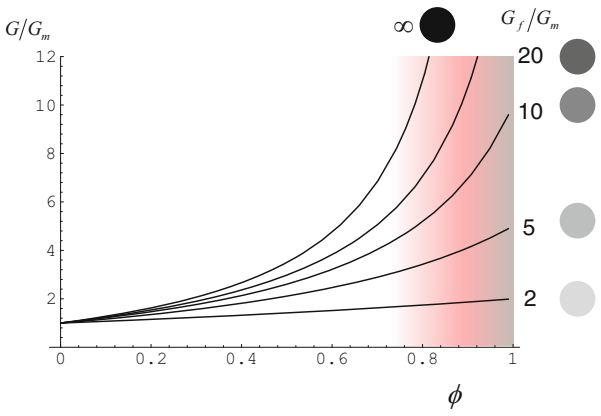

Fig. 11 Uniform soft filler particles with theoretical (mean field) elastic modulus G_f: relative increase of the elastic modulus as a function of the ratio G_f/G_m for different values of the filler volume fraction. The *shaded area* is beyond the close-packing volume fractions

5.2 Reinforcement by Fractal Aggregates

These results allow prediction of the reinforcement factor as a function of the volume fraction $\phi = b^3 c$. To bring the results into a more useful form, we replace the linear cluster size L by its spatial dimension $R = bL^{\nu}$. To do so, the hydrodynamic reinforcement theory needs to be embedded in a general framework such as an effective medium theory, known for example from the hydrodynamic theory for polymers. Local stresses between filler particles and clusters are transformed via the elastic rubber matrix, whose modulus depends on the local spatial coordinates. The local moduli, which formally take the role of "propagators" between local stresses and deformations, become spatially dependent and follow local elastic laws. It becomes useful to solve the corresponding equations between local stresses and local deformations by using Fourier transformations in reciprocal **k** space. The final macroscopic modulus corresponds then to the large scale limits, $k \to 0$, as outlined in the appendix of the publication in ref. [26]. The results of these lengthy calculations can be summarized as:

$$\frac{G - G_{\mathrm{m}}}{G_{\mathrm{m}}} \overset{k\to 0}{\sim} (kb)\frac{2 - 2\nu - D}{\nu} \times \begin{cases} \left(\frac{R}{b}\right)^{\frac{2+\nu-2D}{\nu}} & c \quad \text{below overlap conc.} \\ \left(\frac{R}{b}\right)^{\frac{2-D}{\nu}} & \frac{2\nu}{c^{3\nu-D}} \quad \text{above overlap conc.} \end{cases} \tag{46}$$

or alternatively by use of $\nu = D/d_{\mathrm{f}}$:

$$\frac{G - G_{\mathrm{m}}}{G_{\mathrm{m}}} \overset{k\to 0}{\sim} (kb)^{2\frac{d_f}{D} - d_f - 2} \times \begin{cases} \left(\frac{R}{b}\right)^{2\frac{d_f}{D} - 2d_f + 1} & \phi \quad \text{no overlap } \phi \le \left(\frac{R}{b}\right)^{d_f - 3} \\ \left(\frac{R}{b}\right)^{2\frac{d_f}{D} - d_f} & \phi^{\frac{2}{3-d_f}} \quad \text{with overlap } \phi \gg \left(\frac{R}{b}\right)^{d_f - 3} \end{cases} \tag{47}$$

For the case of a realistic modeling of carbon black aggregates by diffusion-limited aggregation (DLA) clusters [31, 32] with $d_{\mathrm{f}} \approx 2.5$ and $D \approx 4/3$:

$$\frac{G - G_{\mathrm{m}}}{G_{\mathrm{m}}} \sim \begin{cases} R^{-1/4}\phi & \text{for } \phi < \phi_c \text{ (a)} \\ R^{5/4}\phi^4 & \text{for } \phi > \phi_c \text{ (b)} \end{cases} \tag{48}$$

where $\phi_{\mathrm{c}} = (R/b)^{-1/2}$ denotes a critical overlap volume fraction for the branched filler aggregates. Thus, the two different regimes correspond to (a) nonoverlapping clusters and (b) overlapping clusters, depending on filler volume fraction. In the nonoverlapping regime, the behavior is similar to Eq. (42) as guessed earlier (i.e., the reinforcement is proportional to the volume fraction). In regime (b), the hydrodynamic reinforcement is highly dependent on the universal aggregate structure.

In the nonoverlapping regime, the filler contribution to the modulus is always proportional to the filler concentration and a geometrical factor. As a result of the fractal nature of the filler aggregates, this factor depends on the mean aggregate

size. This stems from the general concept of fractal elasticity [32]. Equation (48) determines that the aggregate size dependence of the reinforcement to be weak without overlap, but almost linear with overlap. This again is a result of the branched structure of the filler aggregates. Disadvantages of this model are the small range of application and the idealizations introduced to enable analytic calculation. Advantages are the successful derivation of a structure–property relationship, the possibility of explicitly including the fractal filler structure, and its universality (transfer to all types of branched aggregates). Refinements of the present model require the inclusion of local properties such as particle–particle binding between the primary filler particles.

The dependence of the hydrodynamic reinforcement contribution on the universal aggregate structure is found to be weak at small filler concentration, but very strong for high filler content. Similar results have been found and confirmed by experimental data [5].

5.3 *Filler Network Breakdown: Payne Effect*

Another important case is the breakdown of the filler network at large deformations, which shows an important and general structure–property relationship and is strongly related to the Payne effect (see, for example, the reviews [5, 24]). Experimentally, an increase in strain amplitude results in a decrease in the storage modulus G' from G'_0 to a plateau value G'_∞. This peculiar behavior is known as the Payne effect and appears to be "universal" for any filled rubber systems. Payne [33] interpreted the decline in storage modulus as the result of dynamic breakup of the filler network described above: (van der Waals) bonds between aggregates are continuously broken and re-formed in dynamic equilibrium. Consequently, at low deformations the energetic elastic contribution of the rigid filler network is dominant, whereas at high deformations the filler has only a small remaining effect, which is hydrodynamic and caused by interactions between the rubber and carbon black filler [34].

Kraus [35] developed a useful phenomenological model to describe these phenomena, and started from the assumption that the dynamic breakup of the filler network can be described by a breaking and (re-)agglomeration rate under a shear amplitude γ. Then, it is assumed that the breaking rate r_b is proportional to the number of remaining contacts N and to a power m of the amplitude:

$$r_b = k_b \gamma^m N. \tag{49}$$

In a similar way, the (re-)agglomeration rate R_a should be proportional to the number of broken bonds $N_0 - N$ (N_0 is the number of the contacts existing in the undeformed state):

$$r_a = k_a \gamma^{-m}(N_0 - N), \tag{50}$$

where the quantities k_b and k_a are reaction rates taken as phenomenological rate constants. In the rate balance, both rates are equal and the equations can be solved for N.

It is assumed that the excess storage modulus is given by the portion of momentary existing contacts, whereas the excess loss modulus is proportional to r_b, leading to the following formulae:

$$\begin{aligned} \text{storage modulus} \quad & \frac{G'(a) - G'_\infty}{G'_0 - G'_\infty} = \frac{N}{N_0} = \frac{1}{1 + \left(\frac{\gamma}{\gamma_c}\right)^{2m}}, \\ \text{loss modulus} \quad & \frac{G''(a) - G''_\infty}{G'_0 - G'_\infty} \sim k_b \gamma^m N_c \sim \frac{\gamma^m}{1 + \left(\frac{\gamma}{\gamma_c}\right)^{2m}}. \end{aligned} \tag{51}$$

where $\gamma_c = (k_a/k_b)^{(1/2m)}$ is used for abbreviation.

All information about the process is contained in the parameters m, γ_c, and G'_0; $G'_\infty \cdot \gamma_c$ marks the maximum of G'' and m characterizes the form of the functions G' and G''. The Kraus model has been successfully applied many times to describe the dynamic mechanical behavior of filled rubbers. It was shown that the exponent m is universal (i.e., it is to a large extent independent of temperature, frequency, carbon black content, and the type of carbon blacks and rubber mixtures used). By fitting to the experimental data, one finds a value of $m \approx 0.6$ for rubbers filled with carbon black, independent of temperature, frequency, filler concentration (above the percolation threshold), and filler type [36, 37].

A suitable model for interpreting the Kraus concept uses the breakdown of the filler network directly, as shown in Fig. 12. The structure of the filler network can be approximated by clusters, which have fractal nature (even though the formation of filled rubbers corresponds to a number of nonequilibrium processes). The filler

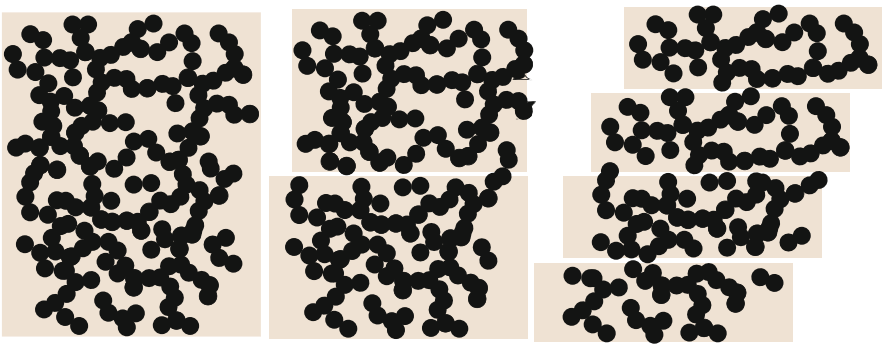

Fig. 12 Successive breakdown of the filler network under shear with increasing deformation

network of fractal dimension d_f is likely to break first at its weakest bonds. Because shear stresses are transported by the shortest connected path, with a dimension $d_{\min}$, network breaking can be related to the fractal structure of the network [38, 39]. The length h of a cluster ensemble created by break-off of an agglomerate with extension ξ_0 is given by the number of clusters n ($n = N_0 = N$) along the minimum path of the initial agglomerate times the cluster size, where $N_0 \simeq (\xi_0/b)^{d_{\min}}$ is the total number of particles of size b in the initial aggregate and $N \simeq (\xi/b)^{d_{\min}}$ denotes the same number within a cluster. This provides:

$$\frac{h}{\xi_0} \simeq \frac{\xi}{\xi_0}\frac{N_0}{N} \simeq \left(\frac{\xi_0}{\xi}\right)^{d_{\min}-1}. \tag{52}$$

Because the amplitude γ is proportional to the deformation, the width w of the cluster ensemble is obtained as $w \simeq \xi_0 \gamma^{-1/2}$ for uniaxial deformation under the assumption of affine local cluster deformation. The volume occupied by the clusters is $hw^2 \simeq \xi^3(\xi_0/\xi)^{d_f}$. These two expressions together lead to the relation between cluster size and deformation amplitude:

$$\frac{\xi}{\xi_0} \sim \gamma^{-1/\left(d_{\min}-d_f+2\right)}. \tag{53}$$

The elastic energy stored in a volume ξ_0^3 yields together with the total number of clusters [40] the initial modulus:

$$G_0(a) \sim \gamma^{\frac{3d_f-d_{\min}-4}{d_{\min}-d_f+2}}. \tag{54}$$

The viscous part of the modulus can be estimated by the total friction as a measure of energy dissipation [7] and is proportional to the cluster extension ξ/ξ_0. The assumption of a self-similar filler network structure upon breaking at increasing deformation provides the loss and storage moduli of the Kraus form [5]:

$$\frac{G'(a) - G'_\infty}{G'_0 - G'_\infty} = \frac{1}{1 + K^2\gamma^{2/\left(d_{\min}-d_f+2\right)}} \tag{55}$$

$$\frac{G''(a)}{G'_0 - G'_\infty} = \frac{K\gamma^{1/\left(d_{\min}-d_f+2\right)}}{1 + K^2\gamma^{2/\left(d_{\min}-d_f+2\right)}}, \tag{56}$$

where $K = (E_1 + E_0)/(\omega\eta_0)$ is a constant containing the system parameters (frequency, temperature, material properties), which defines the "Kraus exponent":

$$m = 1/\left(d_{\min} - d_f + 2\right). \tag{57}$$

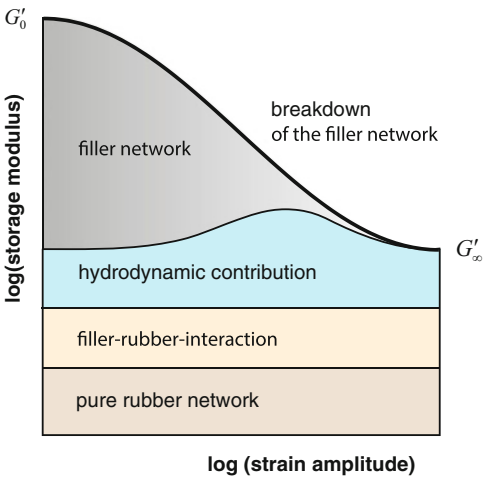

Fig. 13 Different contributions to the modulus as a function of deformations

Using the values $d_f = 1.8$ and $d_{min} = 1.3$ for cluster–cluster aggregates, the Kraus exponent becomes $m = 0.6$, which is in reasonable agreement with many experiments. These ideas have also been recently used and confirmed in detail [41].

The different (deformation-dependent) contributions to the modulus of the entire network can be summarized as shown in Fig. 13. At small deformation amplitudes, all contributions add up to the zero shear modulus. At larger amplitudes, the fragile and fractal particle network successively breaks down and the modulus at "infinitely" large deformations is the sum of the elastic matrix, the filler contributions, and the interaction between particles and matrix polymers. Similar ideas can be used for food networks such as elastic dough, for which starch grains can be modeled as filler particles with no fractal arrangement. Particle networks known from semisolid fats also show similar behavior under shear.

6 Food Polymer Networks

Many of the basic concepts discussed above are also useful for an understanding of food systems made up of food biopolymers. Elasticity, deformability, and fracture play important roles in the production and consumption of foodstuffs. Important classes of food biopolymers are proteins and hydrocolloids, examples of which are discussed in more detail below.

Proteins are biological macromolecules that resemble polymers in their chain-like structure. However, an important difference is the fact that proteins usually need to exist in specifically folded states to fulfill their biological tasks, whereas polymers have many statistically equivalent conformations [3]. The basic building blocks ("monomers") of proteins are the 20 proteinogenic amino acids, which are organic molecules containing amine and carboxylic acid groups as well as side

chains of different chemical functionality. These amino acids can be positively or negatively charged, polar or neutral. Therefore, the sequence (primary structure) of the amino acids in a protein governs their local interactions and, thus, the folding of the protein into its native structure, corresponding to a low energy state. Folding results in very complex structures involving structural elements such as α-helices or β-sheets [42, 43].

The folded state corresponds to the state of lowest energy, and the protein structure is stable. At higher temperatures, parts of the structural elements denature and the protein changes its shape. At sufficiently high temperature, most of the structural elements lose their functional structure and the protein is completely denatured. It can then be viewed as a random copolymer with 20 different monomers of different solubility. Such denatured proteins dissolved in water show similar features: equally charged monomers repel each other, oppositely charged amino acids attract each other, and hydrophobic parts form collapsed, globular structures. The proteins may form pearl-necklace structures, depending on salt concentration, which screen electrostatic interactions. Because amino acids are zwitterionic, their net charge can change and, thus, solubility depends on the pH value. The overall conformation depends on the pH value of the solvent.

Depending on the precise properties of their side groups, amino acids can be roughly classified as hydrophilic or hydrophobic. A protein can thus be assigned a hydrophobicity h, which depends on the number of hydrophobic and hydrophilic amino acids contained. Values can range from $h = 0$, corresponding to good solvent conditions in solvent water, to $h = 1$ corresponding to a poor solvent. Given the complicated specific folding of proteins, one could suppose that they do not obey simple universal laws. However, it has been found that the radius of gyration, R_g, of (denatured) proteins follows a simple scaling law, $R_g \propto N^{\nu}$, which can be compared with that for classic polymers. The lower boundary, the close packing limit, $\nu = 1/3$, remains the same as for polymers. In proteins, this compares to that for closely folded protein globules. Good solvent conditions (i.e., all amino acids are water soluble) yield trivially $\nu = 3/5$ in the mean field Flory limit. For proteins, two other regimes are of interest. The first has been discussed by Hong and Lei [44] in detail. In their work, it was assumed that the ground state of the protein is a globular state, corresponding to a soft elastic solid. To estimate the initial elastic contribution for the globule [12], it is sufficient to estimate the mean number of van der Waals interactions between the nearest neighboring contact points n to $n \propto N$. The elastic free energy of the dense soft globule is $F \propto k_B T \kappa R^2$ (before the blobs in a "poor solvent globule" are pulled apart by a constant force; κ denotes the elastic modulus of the globule. When balanced by the excluded volume contribution:

$$F/(k_B T) \approx \kappa R^2 + \upsilon \frac{N^2}{R^3} \tag{58}$$

a new exponent is predicted to be $\nu = 2/5$, which is larger than for the collapsed state, but significantly below the excluded volume exponent. These states can be

expected for a value of the hydrophobicity h of around 0.5, which occurs for a balanced number of hydrophilic and hydrophobic amino acids [44] (see Fig. 14). For significantly overcharged chains, with charge Q, the excluded volume needs to be replaced by the long-range electrostatic repulsion, $\frac{Q^2N^2}{R}$. This limit suggests a scaling of $v = 2/3$.

Using data from the Protein Data Bank for about 37,000 native proteins under physiological conditions, a scaling exponent of $v = 2/5$ was found, with the limiting borders of $v = 1/3$ and $v = 3/5$ [44] (see Fig. 15). Hong and coworkers related this scaling exponent to the hydrophobicity h of the proteins, showing that there is indeed a correlation. For most proteins, $0.4 < h < 0.6$ and $v = 2/5$ is found. Outside this range, the scaling exponent tends to 3/5 for $h = 0$ and to 1/3 for $h = 1$. This

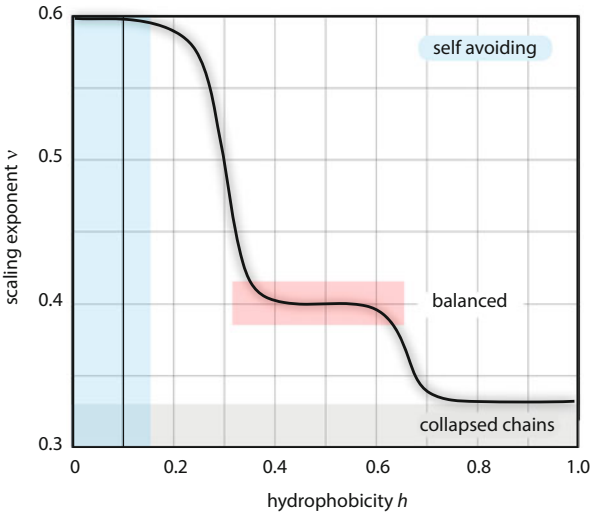

Fig. 14 Range of the scaling exponents of the different regimes according to the simple Flory-type approximation. Actual values scatter around the black line [44]

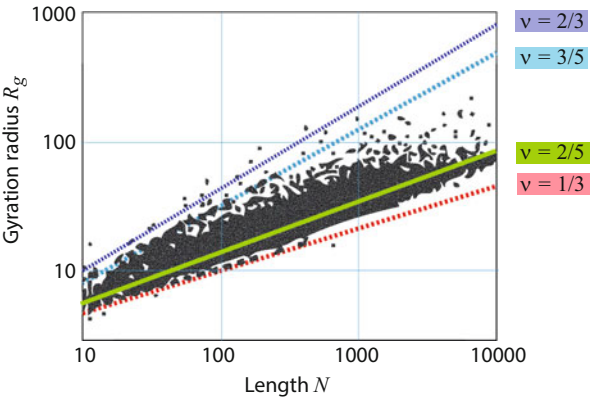

Fig. 15 Scaling law for proteins, with the limits indicated. The limit for overcharged chains $v = 2/3$ is also indicated. Data from Hong and Lei [44]

corresponds to the cases of a good solvent ($h = 0$) and poor solvent ($h = 1$), for which the scaling exponents 3/5 and 1/3 are also found from the Flory theory.

Such scaling approximations provide only a crude idea of the behavior of proteins. However, when proteins denature as a result of processing conditions (e.g., temperature, pH) they lose their native structure and can form networks, where their basic polymer properties become important.

6.1 Wheat Proteins

Wheat proteins are long, to some extent unstructured, protein chains, which can be described by the approximations above. Typical examples of network-forming proteins are wheat storage proteins, also known as gluten. They give wheat dough its unique mechanical properties such as high deformability and strain hardening (e.g., resulting in gas-holding capacity during dough proofing), which are hard to reproduce with substitute materials. Hydration and kneading of gluten results in an insoluble, cohesive mass with viscoelastic properties.

Gluten proteins can be fractionated into gliadins and glutenins [45, 46]. Glutenins can be further divided into two main fractions of high (HMW) and low molecular weight (LMW), with 600–800 and about 300 amino acids, respectively [45]. Almost all glutenins contain the amino acid cysteine, which has a thiol (SH) group and thus enables crosslinking by thiol–disulfide interchange reactions. Depending on the position of cysteines along the protein chain, inter- or intramolecular crosslinks are formed. In gliadins they are placed in such a way that intramolecular disulfide bonds are mainly formed. Gliadins are therefore "self-crosslinked" chains and do not contribute to the elasticity of the gluten network. Instead, they are responsible for its viscous properties. LMW glutenins can form intra- as well as intermolecular crosslinks. In HMW glutenins, the cysteines are placed close to the chain ends and almost exclusively form intermolecular bonds. Glutenins are examples of biopolymers that form "end-linked polymer networks." Thus, they define a network with a large mesh size, leading to the observed large-scale elasticity [47].

This network formation takes place only in the hydrated state of gluten and at higher temperatures. Water is crucial for network formation. It also enables formation of the gluten chains and formation of the network. During kneading, the gluten chains form a transient network, with electrostatic and hydrophobic interactions between the different amino acids, leading to further crosslinks of different strain resistance. The basic structure of a gluten network, including these different interactions, is shown in Fig. 16.

The network structure suggests a complicated rheological behavior [48], because electrostatic and hydrophobic complexes possess different binding energies, which are responsible for different types of breakdown of the network structure during amplitude sweeps in shear experiments.

During the mixing process in dough formation, the network rearranges until the most stable conformation is reached. Also, specific protein structures such as

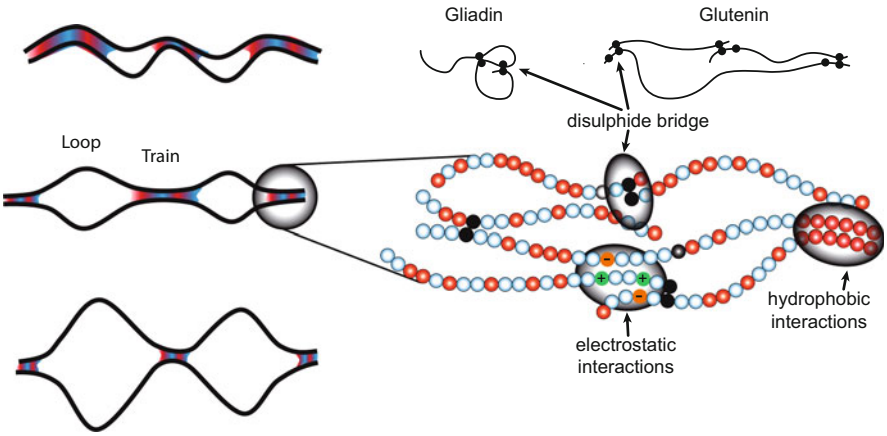

Fig. 16 Representation of the gluten network, including relevant interactions

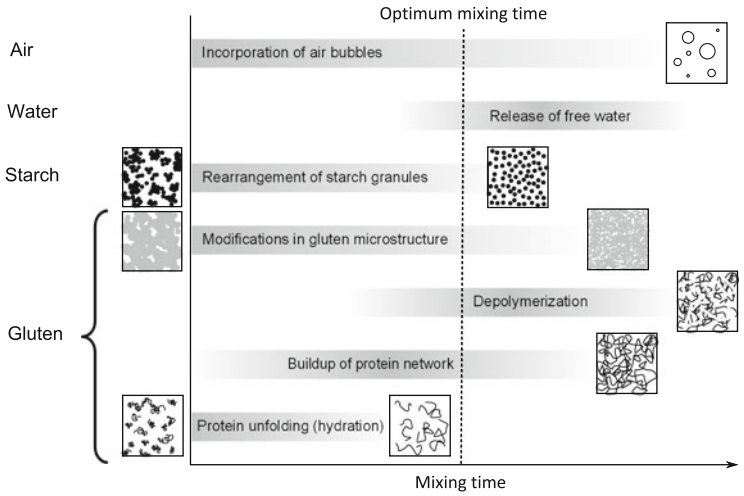

Fig. 17 Processes occurring during dough development for different mixing times. The *dashed line* indicates the optimum mixing time. The *y*-axis represents processes occurring in different constituents at different length scales. The importance of a process at a certain time is indicated by the intensity of *grey*. Adapted with permission from [48]

β-sheets are formed, which may act as spatially more extended transient additional (hydrophobic) crosslinks. After an optimal point is reached, further mixing leads to breakdown of the network. These processes are summarized in Fig. 17 (in the part corresponding to gluten). Simultaneously, changes in the microstructure of other dough constituents also occur. These include the rearrangement of starch granules, redistribution of water, and incorporation of air bubbles (see Fig. 17).

6.1.1 Salt Effects on Gluten Networks

Salt is routinely added to bakery products. This is of course important for the taste, but equally for the viscoelastic properties of the protein matrix. As a result of the ionic properties of amino acids, the addition of salt influences the electrostatic interactions between them and, thus, the resulting conformation of the proteins. Charges can, for example, be screened by the addition of sodium chloride [49]. This hinders strong attraction between oppositely charged amino acids, but also repulsion between similarly charged amino acids. However, the exact molecular processes are not yet fully understood [50].

Recently, the effect of chloride salts with cations of different valency (NaCl, $CaCl_2$, $AlCl_3$) on the formation and rheological properties of the gluten network has been studied for a range of salt concentrations [51]. Pronounced effects on the time scale of network formation (time to optimal dough development; Fig. 18) and on the elastic modulus (Fig. 19) of the gluten network have been found for the different

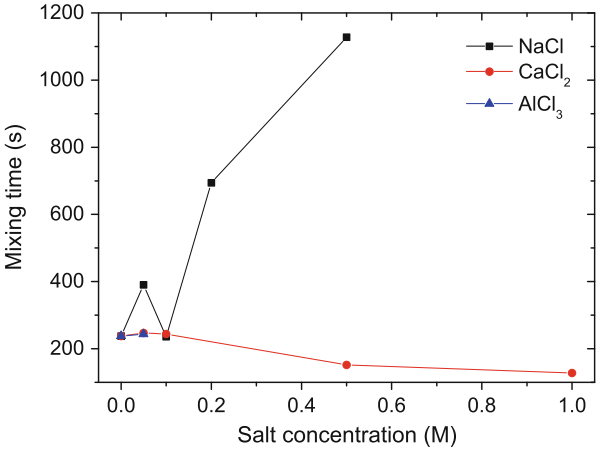

Fig. 18 Dependence of time for network formation on salt concentration and type [51]

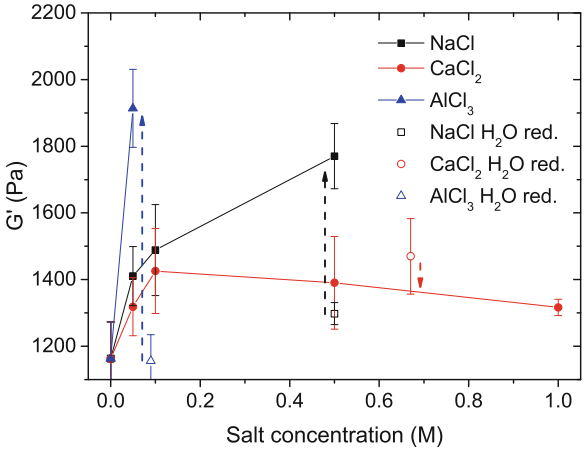

Fig. 19 Dependence of elastic modulus G' of gluten networks on salt type and concentration [51]

cations. Although kosmotropic and chaotropic effects are often used to explain the effect of salt on gluten [52, 53], the effects shown here can be explained qualitatively by electrostatic effects. For increasing concentrations of NaCl, the time until optimum network development increases significantly. This delayed network formation has been reported previously [53, 54] and is accompanied by decreased water absorption by gluten in the presence of NaCl. The Na^+ and Cl^- ions screen the charges of the amino acids and facilitate hydrophobic interactions, leading to a denser, less hydrated protein network [54, 55]. This is in accordance with the increase in the elastic modulus, which is also observed for NaCl.

For $CaCl_2$, the effects are more subtle. The mixing time is slightly decreased; however, this can be almost fully explained by the fact that the effective water content in the dough is reduced as a result of the high molecular weight of $CaCl_2$. Compared with a dough of correspondingly reduced water content, the elastic modulus of gluten dough with added $CaCl_2$ is decreased for higher concentrations. This can be related to excess positive charges that build up along the proteins as a result of the attraction of the divalent calcium cations to negatively charged amino acids. This net positive charge reduces intra- and intermolecular protein attractions and, thus, leads to a looser network.

The most severe effect occurs for $AlCl_3$. For concentrations higher than 0.05 M, no cohesive viscoelastic mass is formed and the elastic modulus increases strongly even at this low concentration. A possible explanation could be that for increasing concentrations of Al^{3+}, as a result of increasing positive charge density, it is more likely that one Al^{3+} ion interacts with several negatively charged amino acids. Because these are probably located on the same protein, a kind of self-crosslinking occurs and hinders the formation of an extended gluten network.

These changes in the network structure are shown schematically in Fig. 20, which shows the dependence on the ionic species of the added salt. It is clear that simple polyelectrolyte effects play an important role, even in such a complicated system as gluten.

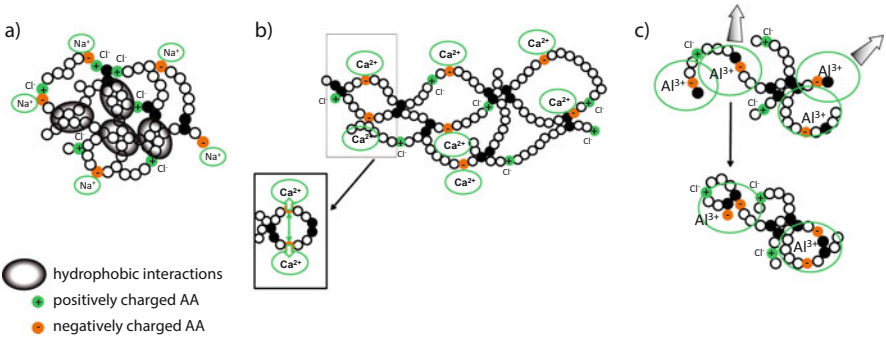

Fig. 20 Effect of cations with different valence on the interactions in a gluten network: (**a**) NaCl, (**b**) $CaCl_2$, and (**c**) $AlCl_3$

6.1.2 Dough: Starch-Filled Gluten Network

As discussed above, gluten is responsible for the large deformability of wheat dough. However, pure gluten dough is very cohesive and is difficult to deform permanently or to separate into pieces by hand. Obviously, this is not the case for dough prepared from flour, which can be easily molded and partitioned to produce bakery products. Wheat flour contains about 80% w/w starch granules, which are elliptical particles with a bimodal size distribution ranging from 2 to 38 μm. During dough formation, these particles become distributed evenly inside the gluten matrix, as shown in Fig. 17. Thus, they can be seen as hard filler particles that reinforce the gluten polymer matrix. In this system, starch–starch and protein-protein interactions play a role and contribute differently to the deformation behaviour of dough on different length scales. The effect of increasing starch volume fractions on dough rheology can be tested by investigating model doughs made from starch and gluten in different proportions [48, 56–60]. Figure 21 shows the strain dependence of the elastic modulus for various starch volume fractions ϕ of up to 0.49 (90% starch, 10% gluten) [48].

Typically, for all starch fractions, the elastic modulus is constant for low amplitudes and then drops at higher deformations. The total modulus can be seen as the sum of contributions resulting from the different components of dough:

$$G(t) = G_{\mathrm{G}}(t) + G_{\mathrm{S}}(t) + G_{\mathrm{SG}}(t) + G_{\mathrm{A}}(t) \tag{59}$$

There is a contribution from the gluten matrix $G_{\mathrm{G}}(t)$ as well as one from the particle–particle interactions of the starch granules $G_{\mathrm{S}}(t)$, which form a particle network at higher volume fractions. Additionally, the protein chains interact directly with the starch granule surfaces, leading to the cross-term $G_{\mathrm{SG}}(t)$. Finally, air bubbles are introduced during mixing (see Fig. 17), which soften the material (contribution G_{A}).

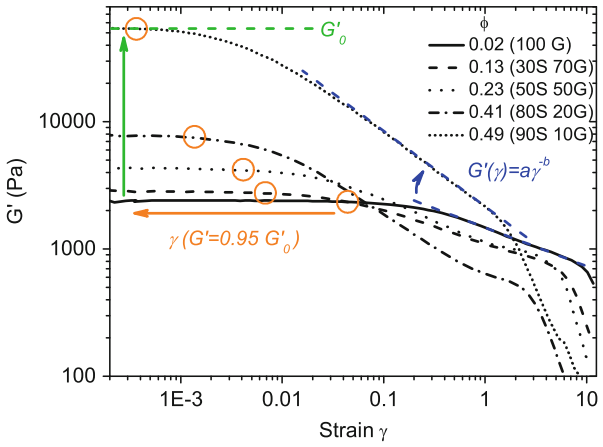

Fig. 21 Dependence of elastic modulus of wheat dough on deformation for increasing starch fraction. Adapted with permission from [48]

G' at low deformations corresponds to the total modulus of the undisturbed dough structure. Because this is not disturbed at small deformations, G' is constant up to a certain amplitude. At larger amplitudes, the arrangement of starch granules is disturbed and their original structure is destroyed. This leads to a decrease in the modulus at higher deformations. The consequence of introducing higher volume fractions of filler particles to the gluten matrix can be evaluated by analyzing the following parameters in the small and large strain regime: for small deformations, the storage modulus $G_0^{'}$ in the linear viscoelastic range (Fig. 22a) and the linear viscoelastic range $\gamma\left(G^{'} = 0.95G_0^{'}\right)$ (Fig. 22b). For large deformations, the definitions of elastic and viscous modulus no longer hold because of the nonlinear relation between stress and strain. However, comparison is still useful because different interactions are probed here than at small deformations. This can, for example, be accomplished by fitting G' to a power law $G^{'}(\gamma) = a\gamma^{-b}$ in the region that appears linear in a double logarithmic representation.

Overall, the introduction of starch leads to reinforcement of G' for small amplitudes, reduction of the linear range, and faster decrease in the modulus for larger amplitudes. The reinforcement effect is similar to that explained in Sect. 5. Several effects can contribute to the decrease in the linear range. Among these are the breakdown of starch aggregates [57, 58, 61] and stress amplification between the particles as a result of decreasing average gap size [56, 62], leading to debonding of the gluten strands from the starch particle surface [60].

The exponent b can then be used as a measure of the decrease in modulus with increasing strain, which gives a hint about the strain-resistance of certain structures. Unlike filled rubbers, starch granules do not form a fractal network and the exponent b cannot be related to self-similar structural changes (as in Sect. 5). The high concentration of starch grains suggests a sliding of grains with respect to each other. The friction between the grains is governed by the loose and inhomogeneous gluten network, which partly disintegrates and ruptures at large deformations. Thus, the protein–protein interactions become weaker, as well as the particle–protein interactions at high shear strains.

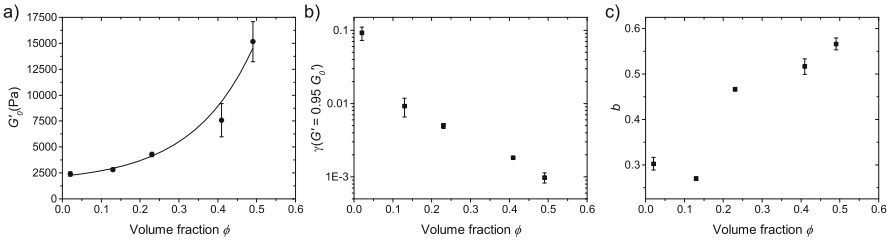

Fig. 22 Dependence of elastic plateau modulus G', linear range, and exponent γ on the starch volume fraction ϕ for artificial model doughs from starch and gluten. Adapted with permission from [48]

6.1.3 Effect of Temperature on Gluten

Instead of changing the environmental conditions for dough formation, as in the case of salt addition, another possibility for modifying the various interactions occurring in wheat dough is via physical modification of the material itself, such as in heat moisture treatments. These are carried out under various process conditions for microbiological safety, inactivation of enzymes, or to influence the textural properties of the final product. For flour, heat treatment may affect different components, depending on the temperature and humidity of the treatment. At high moisture contents, starch granules gelatinize, whereas they are rendered more heat stable at lower moisture contents as a result of an increase in their internal molecular order [63]. As already discussed, proteins denature at elevated temperatures. Starch granules are covered by a thin layer of proteins that may also denature during heat treatment. Indeed, it has been found that the surface of starch granules can become hydrophobic after heat treatment, which is probably caused by the denaturing of its surface proteins [64]. Similarly, gluten proteins denature when heated. Decreased protein solubility is attributed to aggregation via SH–SS interchange reactions [65] as well as decreased surface hydrophobicity [66, 67], which can result from aggregation of unfolded proteins.

Again, use of artificial doughs prepared from starch and gluten offers the possibility of increasing the understanding of processes going on in native wheat flour dough. Heat treatment of the individual components, starch and gluten, can also be carried out separately. This has been studied recently in parallel with a systematic study of the effect of heat treatments at different time–temperature–moisture conditions on native wheat flour [68]. The effects on dough rheology and protein solubility of the unhydrated material were studied. Figure 23 shows the main effects occurring in native and model doughs after the most severe temperature treatment (30 min, 90°C). It can be seen that the typical changes in native flour

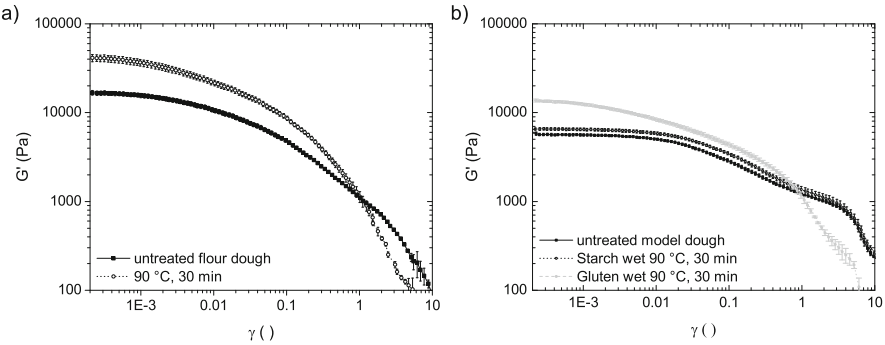

Fig. 23 Strain-dependent elastic moduli for (**a**) flour dough untreated and heat treated at 90°C for 30 min, moisture content of flour 16–17% and (**b**) starch/gluten model dough untreated and prepared with either starch or gluten heat-treated at 90°C for 30 min. Moisture content of starch 15.5%, moisture content of gluten 10%. Adapted with permission from [68]

dough (increase in G', faster decrease in G' with increasing temperature) are reproduced qualitatively in model dough with heat-treated gluten. Using heat-treated starch had less effect on the elastic modulus, namely a slight reinforcement effect despite the high volume fraction of starch present in the composite system. This indicates that changes in gluten are mainly responsible for the observed effects.

To study those changes in more detail, proteins have been extracted from heat-treated flours using acetic acid. Flours heat-treated at three different moisture contents (dry, 6.5–7.0%; normal, 13.2%; and moist, 16.0–17.0%) were analyzed. In general, protein solubility was found to decrease with increasing time and temperature of heat treatments, as well as with increasing moisture content during heat treatment. Gluten [69] and starch are both known to have a moisture-dependent glass transition temperature, T_g, which decreases with increasing moisture content (as known for polymers). Therefore, it is useful to normalize the results by plotting them against the temperature difference from the corresponding T_g at different moisture contents. The T_g values for flour were determined by differential scanning calorimetry (DSC) [70]. Only one T_g was found in the investigated temperature range, which might result from the overlay of several individual transitions corresponding to gluten and starch. Normalizing the solubility results using values for T_g interpolated to the relevant moisture contents, it becomes obvious that changes start to occur only above T_g (Fig. 24).

This finding is understandable, because molecules become more mobile and, thus, more susceptible to conformational changes and reactions above their T_g. Therefore, it is likely that gluten molecules unfold and aggregate with increased probability if exposed to temperatures above their T_g. A schematic representation of changes probably occurring in wheat flour dough prepared from heat-treated flour are shown in Fig. 25, and are in accordance with the observed changes in rheology and protein solubility.

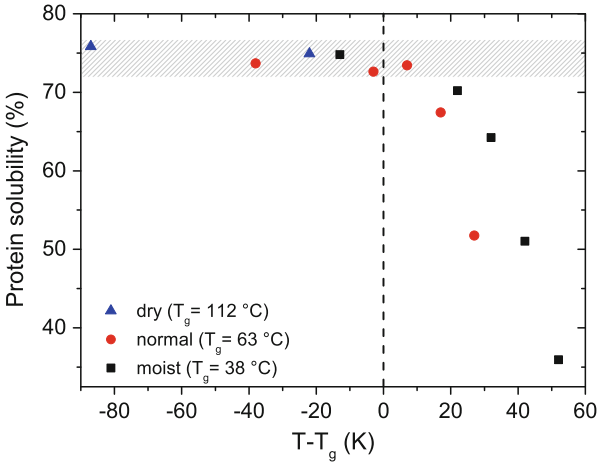

Fig. 24 Changes in protein solubility for heat-treated flours of three different moisture contents (dry, 6.5–7.0%; normal, 13.2%; moist, 16.0–17.0%) [68] plotted against the difference in temperature from the corresponding glass transition temperatures found by Kaletunc and Breslauer [70]

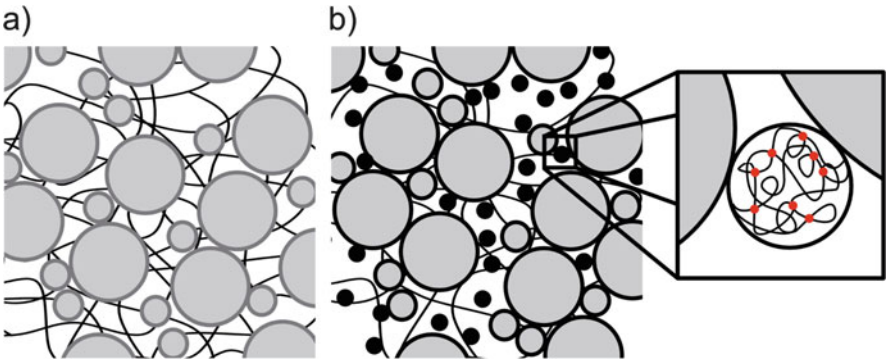

Fig. 25 Wheat flour dough prepared from flour (**a**) without and (**b**) with heat treatment. Changes include modified starch granule surface properties, formation of starch aggregates, and formation of protein aggregates (*black circles*), leading to a less crosslinked gluten network. Reprinted with permission from [68]

Changes in gluten probably involve the formation of protein aggregates permanently crosslinked via S–S bonds. On the one hand, these aggregates can no longer participate in gluten network formation, leading to a weaker network and decreased linear range. On the other hand, they can act as additional filler particles, thus reinforcing the composite and increasing the elastic modulus. Changes in the starch fraction could cause an increased surface hydrophobicity of the granules, which could lead to increased starch agglomeration. Because these agglomerates have a larger effective volume than individual particles, they could further increase the modulus [71]. On the other hand, they also contribute to a decreased strain resistance, because they can be broken up easily at large deformations.

6.2 Water-Based Gels

Water-based gels are certainly simple model systems for many foods. Formation of their exceptional water-binding and soft solid-like character by lowering the thermal energy k_BT is based on a kinetically driven gel-forming mechanism. The common process for most gelling agents originating from plant cell walls is shown in Fig. 26. At high temperature, the gelling agents form a solution and the viscosity is enhanced. By lowering the temperature, the viscosity is increased further and solids are formed in the critical region close to the gel point [5, 72]. The gelation corresponds to a liquid–solid transition and, when it happens in equilibrium, the process can be modeled by a percolation process [3, 40], which is described as a second-order phase transition with critical exponents close to the gelation point. The chains form larger clusters, and the largest grows to an “infinite”

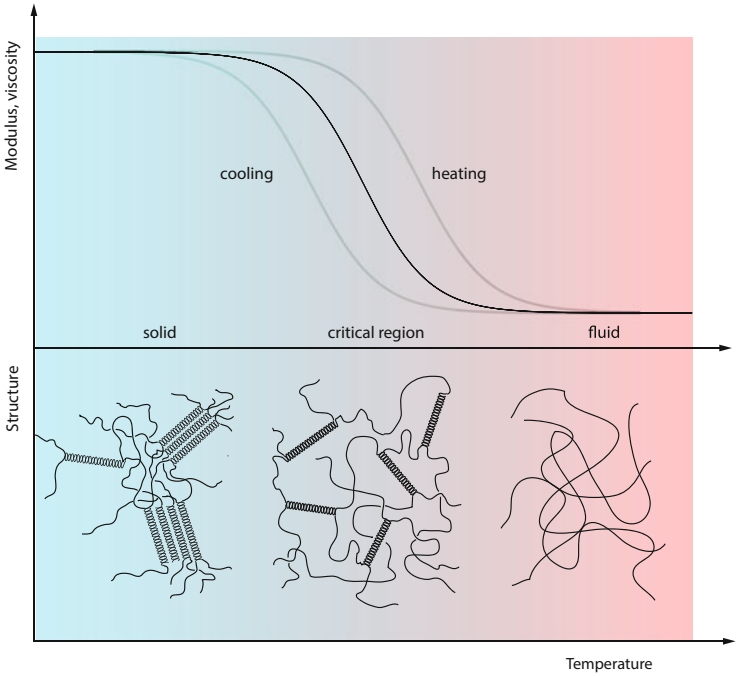

Fig. 26 Typical view of the thermal reversible sol–gel transition of a helix-forming network. At high temperatures (*right*) chains are dissolved. The kinetic origin is responsable for the hysteresis in cooling and heating

cluster. The percolating system shows a solid character with low moduli. Far above the critical point, the gelling system shows a high modulus, with a value determined by the physical properties of the percolating elements (e.g., chain stiffness, bending properties, and the mean distance between the connecting points) [5]. Gels in foods are mostly significantly above the gel point and behave as soft elastic solids, with sufficient brittleness. One of the most commonly used gelling agents from plants is agarose [73, 74], the gel-forming molecule in agar, which stems from the cell walls of algae [75]. An important common point of several gels is the hysteresis during cooling and heating, which corresponds to nonequilibrium phenomena [76]. Helix formation during cooling and its dissolution during heating are associated with coupled helix–coil transitions, whose differences at finite cooling rates are manifested in the hysteresis.

In the liquid state, when fully dissolved at temperatures close to the boiling point, agarose molecules are present as random coils and are distributed homogeneously in the solution [77]. During gelling, when the solution is cooled, this entropically preferred state has to be overcome and the single polysaccharide chains are forced to associate with other chains via hydrogen bonds. Below the gelling

temperature, this is compensated for by a gain in energy as a result of formation of hydrogen bonds between molecules and their subsequent association into double helices (formed from two single agarose chains [78]). It was demonstrated by X-ray diffraction (XRD) [79] and optical rotation measurements that agarose gels are made up of the double-helical structures of single polymer chains. The binding by hydrogen bonds leads to a double-helical combination of two single agarose chains [78]. It has been suggested that this initial helix formation is followed by an aggregation of the helices, leading to a two-step gel formation process [80, 81]. The first step is formation of a gel by joining the randomly distributed coils into a double-helical association by hydrogen bonds, followed by aggregation of the double helices into a tight three-dimensional network. Between the junction zones of this network, meshes are established that enable the enclosure of water molecules by forming hydrogen bonds with the hydroxyl groups of the agarobiose units facing outward [79].

Another well-known gelling agent is gelatin, whose origin is the connective tissue in meat and stromal proteins. Collagen, consisting of triple helices, denatures to gelatin, which is a strongly water-soluble amphiphilic polymer that forms soft and elastic gels [82] when the corresponding preparations are cooled [83]. Gelatin gels have been widely studied [84, 85].

It is tempting to combine the carbohydrate-based agarose and the protein gelatin and study the different gelation phases. However, their intrachain interactions are very different, as well as their kinetics of gel formation. It is well known that the formation of gelatin-based gels requires times [86] that are an order of magnitude higher than for the solidification of agarose gels [6]. Depending on the concentrations, different regimes can be expected.

6.2.1 Agarose

The use of agarose gels for the size-dependent separation of molecules in gel electrophoresis is well known. This application is possible because such gels can be prepared with a wide range of well-defined pore sizes, depending on the agarose concentration. Obviously, this is also important for food applications, because the elastic modulus of a network is determined by its mesh size [3], as described in the Introduction. However, it is not clear whether these basic considerations also hold for a highly swollen network with a complex crosslink structure, as in the case of agarose.

Confocal laser scanning microscopy (CLSM) offers the possibility of determining the pore size of agarose gels directly and noninvasively. This has been done for agarose gels with concentrations of 0.25, 0.5, 0.75, and 1%. To visualize their network structure, agarose molecules are stained covalently with 5-(4,6-dichlorotriazinyl)aminofluorescein (DTAF) [87]. The resulting micrographs are shown in Fig. 27.

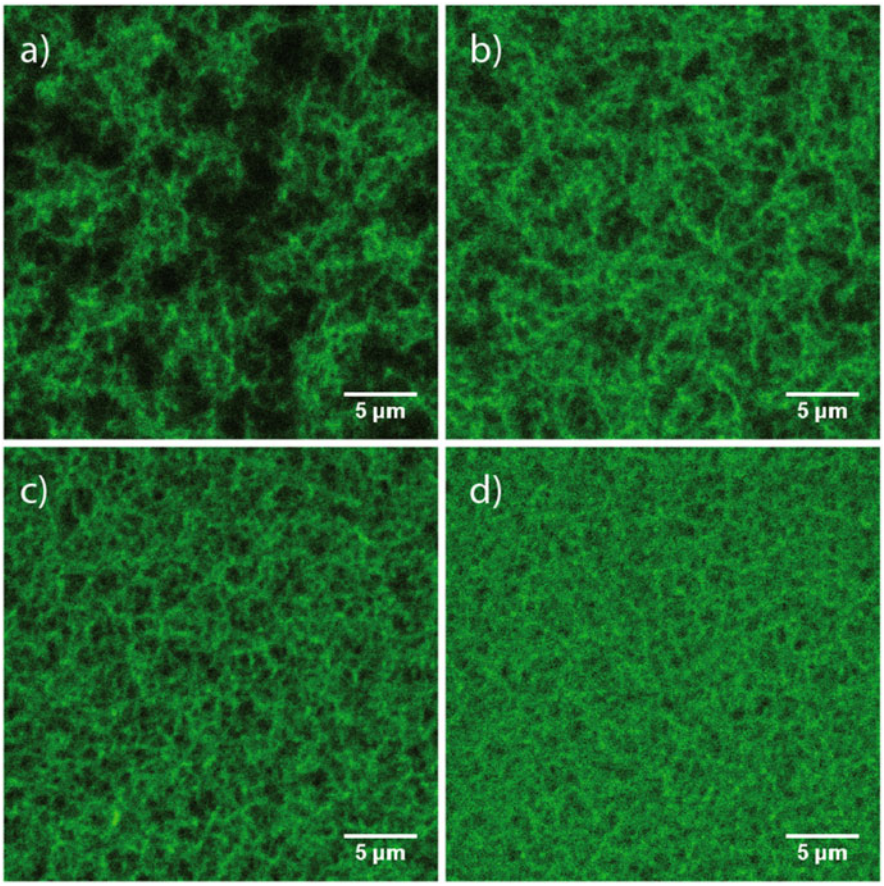

Fig. 27 CLSM images of agarose gels stained with DTAF: (**a**) 0.25%, (**b**) 0.5%, (**c**) 0.75%, and (**d**) 1% agarose concentration. Adapted with permission from [87]

It is clearly visible that the pore size decreases with increasing agarose concentration. The mean pore size has been extracted from the images manually by measuring 150 pores per concentration c. The following values were found: $c = 0.25\%$, pore size 1.55 ± 0.36 µm; $c = 0.5\%$, 0.99 ± 0.21 µm; $c = 0.75\%$, 0.73 ± 0.18 µm; $c = 1\%$, 0.56 ± 0.13 µm. Measurements supporting this trend have also been performed with atomic force microscopy (AFM) [88] and absorbance measurements [89].

The elastic moduli of the gels shown in Fig. 27 have been determined by dynamic oscillatory measurements [87]. From traditional theory, one would expect a relation between the elastic modulus and the mesh size, $G' \propto k_B T/\xi^3$.To test how far this correlation holds for agarose gels, the mean pore size was taken as the mesh size and the normalized values of ξ^{-3} and G' were plotted against the concentration (see Fig. 28). It can be seen that both curves follow a similar trend, although the

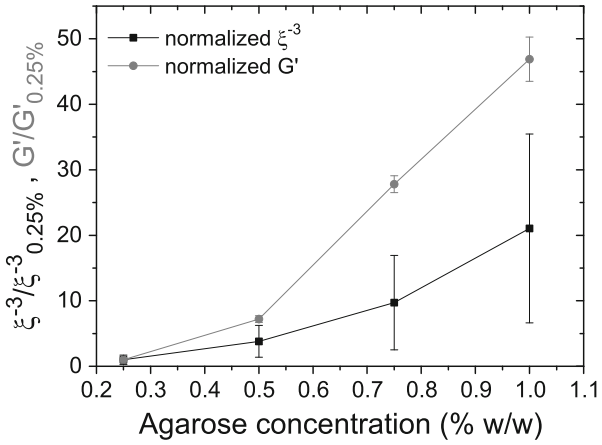

Fig. 28 Dependence of normalized elastic modulus and inverse cubic agarose pore size on agarose gel concentration. Adapted with permission from [87]

elastic modulus increases faster than the reciprocal pore size. However, because the crosslinks in agarose are not point-like and agarose chains are not fully flexible as assumed in the theory, an exact agreement is not expected.

6.2.2 Protein–Polysaccharide Mixtures

Food systems often contain mixtures of biopolymers, especially of proteins and polysaccharides. However, they are usually co-soluble only at low concentrations. At higher concentrations, phase separation is likely to occur. This can be the result of aggregation or segregation, depending on whether the interactions between the different polymers are attractive or repulsive. Segregative phase separation (also called thermodynamic incompatibility) is observed more often [90]. It has its origin in a decreased entropy of mixing (and consequently high positive free energy of mixing) as a result of steric exclusion effects between the polymers [91]. The topic of protein–polysaccharide interactions has been reviewed extensively (e.g., [90–94]). Particularly interesting for food is the possibility of using such effects to tailor the texture of food products [95]. If gelling hydrocolloids are used, structures formed as a result of phase separation can be fixed by gelation of one or both components. Properties such as elasticity, hardness [96, 97], syneresis, susceptibility to fracture [98, 99], thermal stability, [100] and aroma release [100] can be adjusted. This is shown below for the simple example of mixed agarose–gelatin (polysaccharide–protein) gels, containing the two gelling agents in different proportions. Both agarose and gelatin form thermoreversible gels upon cooling. As mentioned, for both gelatin [101, 102] and agarose, a coil-to-helix transition occurs during gel formation. However, the mechanical properties of agarose and gelatin gels are quite different. Gelatin melts at body temperatures, leading to a delicate mouth feel, but agarose gels are stable up to 70°C and can therefore be used in hot

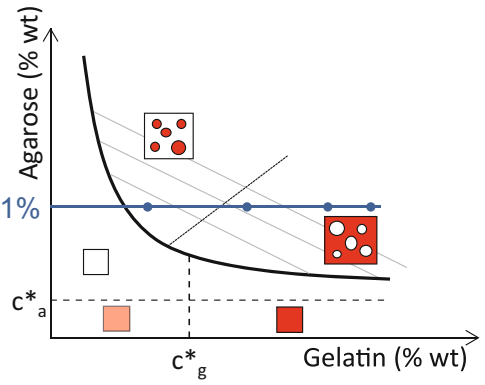

Fig. 29 Phase diagram of an agarose–gelatin mixture. No gel is formed below the critical concentrations c_a^* and c_g^*. The *curved black line* represents the binodal. For compositions above the binodal, phase separation occurs

dishes. However, agarose gels are relatively hard and brittle, so chefs often prepare mixed gels from both materials to balance those features. Investigations of agarose–gelatin systems can be found in the literature [103–105].

Figure 29 shows a schematic phase diagram for an agarose–gelatin system. Detailed explanation of the phase diagram is given in the literature (see, e.g., [106]). The critical gelling concentrations are indicated for agarose c_a^* and gelatin c_g^*, below which no gel is formed. The black curve in Fig. 29 is the binodal, below which the two polymers co-exist and a single phase gel (or liquid if $c < c^*$) is formed. Above the binodal, spontaneous phase separation occurs, leading to filled gels with a continuous phase rich in either agarose or gelatin. The compositions of the continuous and dispersed phases are found by following the so-called tie lines (grey lines in Fig. 29), corresponding to the initial concentrations of the two polymers, until their intersection with the binodal. The dotted line corresponds to the point of phase inversion. As shown, for a continuous phase of agarose it is also possible to have liquid filler particles of gelatin, if the latter is present at concentrations below c_g^*.

To evaluate the macroscopic effects of these phase separations, agarose–gelatin gels were prepared with different compositions. The concentration of agarose was kept constant at 1% while the concentration of gelatin varied from 0.5 to 20%. The resulting gels were dyed with the fluorescent dye Rhodamin B, which preferentially stains the gelatin phase, and subsequently observed by CLSM. Similar pictures can be found in the literature (e.g., [107]) for mixed gels from whey proteins and polysaccharides. Micrographs of the different agarose–gelatin gels are shown in Fig. 30. It was found that for $c_g = 0.5\%$ a continuous phase of agarose contains inclusions of gelatin, whereas a continuous phase of gelatin developed at $c_g = 5\%$ and above. For the lowest concentration of gelatin used here ($c_g = 0.5\%$), closer inspection of the dispersed phase shows sickle-like structures instead of circular structures. This may indicate that, under these conditions, the gelatin phase does not form a gel but remains in its liquid state. For those samples, as well as for a pure agarose gel with $c_a = 1\%$ and pure gelatin gels with concentrations ranging from

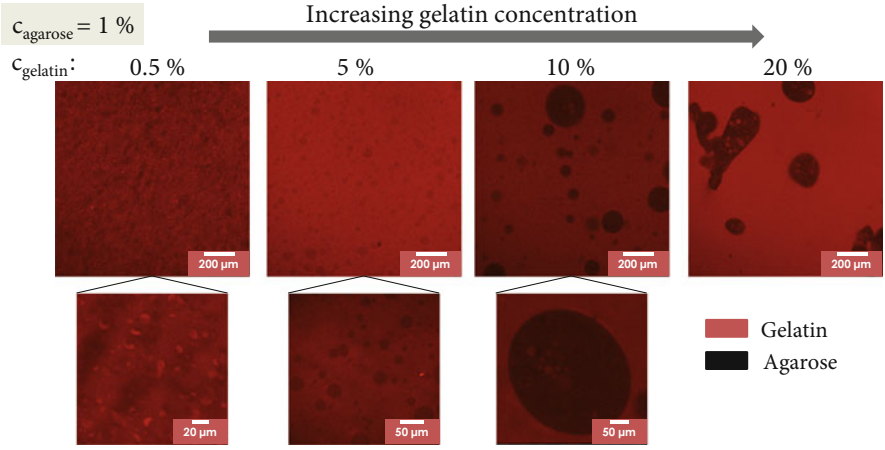

Fig. 30 CLSM images of agarose–gelatin gels ($c_g = 1\%$, $c_a = 0.5$–20%). Samples were dyed with Rhodamin B. Because no quantitative information has been extracted from the images, the contrasts have been optimized using ImageJ software

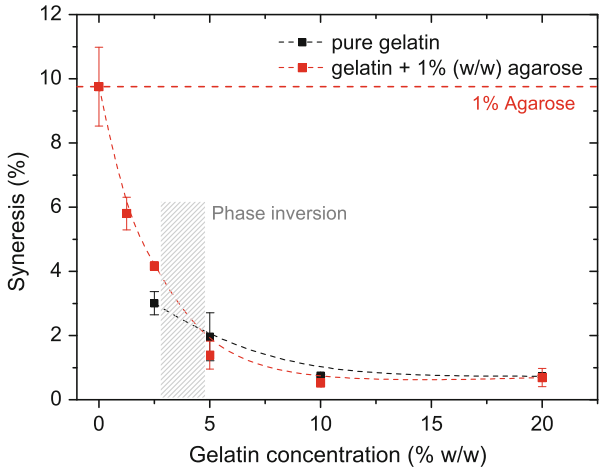

Fig. 31 Syneresis of mixed agarose–gelatin gels ($c_g = 1\%$, $c_a = 0.5$–20%), pure agarose gel ($c_a = 1\%$), and pure gelatin gel (2.5–20%) determined by centrifugation

2.5–20% (no gel is formed at $c_g = 0.5\%$), the syneresis (Fig. 31) and hardness (Fig. 32 normalized by the height of the sample) were determined.

In both cases, the results are dominated by the continuous phase. However, for the hardness, a reinforcement effect is obvious for the agarose-filled gels compared with the pure gelatin gels. This is reasonable, because the elastic modulus of the gelled agarose filler particles is larger than that of the surrounding gelatin matrix. From the measurement of both quantities (syneresis, hardness), it can be

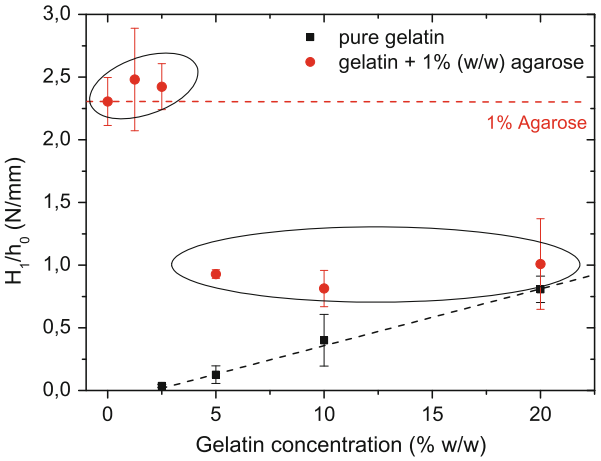

Fig. 32 Hardness of mixed agarose–gelatin gels ($c_g = 1\%$, $c_a = 0.5$–20%), pure agarose gel ($c_a = 1\%$), and pure gelatin gel (2.5–20%) determined by indentation and normalized to the sample height

inferred that the gelatin concentration for which phase inversion occurs is probably between 2.5% and 5%. This is supported by the fact that a CLSM image of the gel with 1% agarose and 2.5% gelatin (not shown here) showed no detectable structural features.

7 Conclusion

Theories describing the behavior of classic polymers are well established and highly developed. The formation of crosslinked networks and their macroscopic properties can be well described using these theories. Biopolymers such as proteins and polysaccharides play a very important role in determining the structure of food materials. However, they are more complicated to describe because they form complicated native structures (e.g., proteins) and the crosslinks are typically of a more extended (e.g., helix formation for agarose and gelatin) and possibly transient nature. Nevertheless, we have shown that ideas from traditional polymer physics are also helpful for the understanding of such systems. Examples are solvent-dependent scaling laws for proteins, the mechanical properties of the filled food polymer system wheat dough, polyelectrolyte effects in salted doughs, mesh size-dependent elastic moduli in agarose, and phase-separated protein–polysaccharide mixtures. Figure 33 compares a classic filled polymer system (tire) with a filled food polymer system (bread) on different length scales, revealing differences and similarities. The details of the interactions and structures appear very different, but many food systems are definitely soft matter or hard matter materials. Their relevant length and time scales are of the same order of magnitude as many polymer and soft matter materials. There is only one fundamental difference from the engineering point of view: if rubbers fail, it becomes a disaster; however, foods

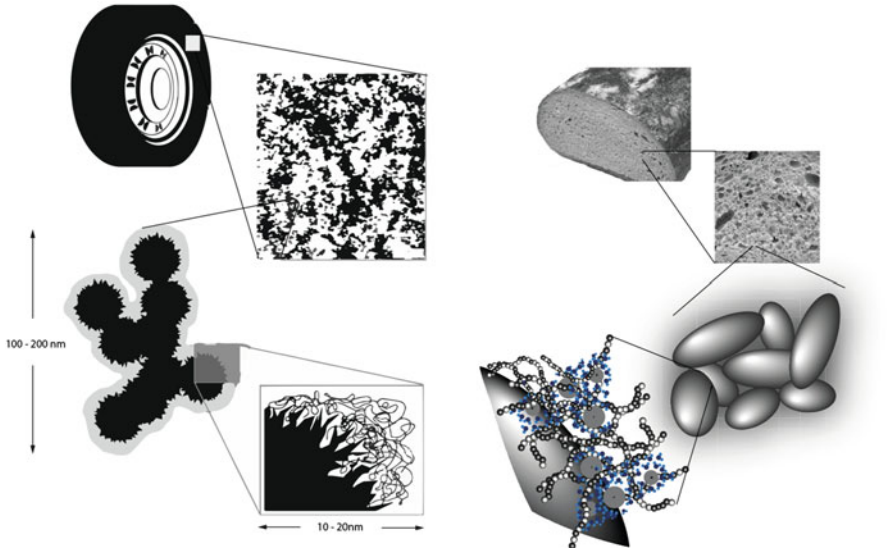

Fig. 33 Comparison on different length scales, from macroscopic to microscopic, of a classic filled polymer system (tire) and a filled food polymer system (bread)

must break down in the mouth, otherwise there is no pleasure from texture, taste, or aroma release.

References

1. Deam RT, Edwards SF (1976) Philos Trans R Soc Lond A Math Phys Eng Sci 280(1296):317
2. Panyukov S, Rabin Y (1996) Phys Rep 269(1):1
3. de Gennes PG (1979) Scaling concepts in polymer physics. Cornell University Press, Ithaca
4. Edwards S, Lillford P, Blanshard J (1987) In: Blanshard JMV, Lillford P (eds) Food structure and behaviour. Academic press, London
5. Vilgis TA, Heinrich G, Klüppel M (2009) Reinforcement of polymer nano-composites: theory, experiments and applications. Cambridge University Press, Cambridge
6. Vilgis TA (2015) Rep Prog Phys 78(12):124602
7. Doi M, Edwards SF (1986) The theory of polymer dynamics. Clarendon, Oxford
8. Rubinstein M, Colby RH (2003) Polymer physics. Clarendon, Oxford
9. Clisby N (2010) Phys Rev Lett 104(5):055702
10. Holm C, Joanny J, Kremer K, Netz R, Reineker P, Seidel C, Vilgis T, Winkler R (2004) Polyelectrolytes with defined molecular architecture II. Springer, Berlin/Heidelberg, pp 67–111
11. Dobrynin AV, Rubinstein M (2005) Prog Polym Sci 30(11):1049
12. Vilgis TA, Johner A, Joanny J (2000) Eur Phys J E 2(3):289
13. Edwards SF (1981) Ann N Y Acad Sci 371(1):210
14. Peng W, Castillo HE, Goldbart PM, Zippelius A (1998) Phys Rev B 57(2):839
15. Treloar LRG (1975) The physics of rubber elasticity. Oxford University Press, Oxford

16. Kuhn W, Grün F (1946) J Polym Sci 1(3):183
17. Grosberg AY, Khokhlov AR, Stanley HE, Mallinckrodt AJ, McKay S et al (1995) Comput Phys 9(2):171
18. Miao B, Vilgis TA, Poggendorf S, Sadowski G (2010) Macromol Theory Simul 19(7):414
19. Edwards S, Vilgis TA (1986) Polymer 27(4):483
20. Edwards S, Vilgis TA (1988) Rep Prog Phys 51(2):243
21. Sukumaran SK, Grest GS, Kremer K, Everaers R (2005) J Polym Sci B Polym Phys 43(8):917
22. Ball R, Doi M, Edwards S, Warner M (1981) Polymer 22(8):1010
23. Vilgis TA (2005) Polymer 46(12):4223
24. Heinrich G, Klüppel M, Vilgis TA (2002) Curr Opinion Solid State Mater Sci 6(3):195
25. Smallwood HM (1944) J Appl Phys 15(11):758
26. Huber G, Vilgis TA (2002) Macromolecules 35(24):9204
27. Felderhof B, Iske P (1992) Phys Rev A 45(2):611
28. Christensen RM (2012). Mechanics of composite materials. Courier Corporation, Dover, Mineola NY
29. Jones R, Schmitz R (1983) Physica A 122(1):105
30. Jones R, Schmitz R (1983) Physica A 122(1):114
31. Kluppel M, Heinrich G (1995) Rubber Chem Technol 68(4):623
32. Bunde A, Havlin S (2012) Fractals and disordered systems. Springer, Berlin/Heidelberg
33. Payne A, Kraus G (1965) Reinforcement of Elastomers, vol 69. Interscience, New York
34. Medalia A (1978) Rubber Chem Technol 51(3):437
35. Kraus G (1984) J Appl Polym Sci Appl Polym Symp 39:75–92
36. Vieweg S, Unger R, Heinrich G, Donth E (1999) J Appl Polym Sci 73(4):495
37. Lion A (2005) KGK-Kautschuk Gummi Kunststoffe 58(4):157
38. Witten T, Rubinstein M, Colby R (1993) J Phys II 3(3):367
39. Huber G, Vilgis TA, Heinrich G (1996) J Phys Condens Matter 8(29):L409
40. Aharony A, Stauffer D (2003) Introduction to percolation theory. Taylor & Francis, London
41. Song Y, Zheng Q (2011) Polymer 52(3):593
42. Finkelstein AV, Ptitsyn O (2002) Protein physics: a course of lectures. Academic, San Diego
43. Yang AS, Honig B (1993) J Mol Biol 231(2):459
44. Hong L, Lei J (2008) J Polym Sci B Polym Phys 47(2):207. doi:10.1002/polb
45. Belitz HD, Grosch W, Schieberle P (2009) Food chemistry. Springer, Wien
46. Wieser H (2007) Food Microbiol 24(2):115
47. Shewry P, Tatham A (1997) J Cereal Sci 25(3):207
48. Schiedt B, Baumann A, Conde-Petit B, Vilgis TA (2013) J Texture Stud 44(4):317
49. Chaikin PM, Lubensky T (2000) Principles of condensed matter physics. Cambridge University Press, Cambridge
50. Tuhumury H, Small D, Day L (2014) J Cereal Sci 69(1):229–237. doi: 10.1016/j.jcs.2014.03.004
51. Schönmehl N (2015) Beeinflussung der viskoelastischen Eigenschaften von Weizengluten unter Zugabe von mono-, di-, sowie trivalenten Metallkationen. Bachelor thesis, SRH Fernhochschule, Riedlingen
52. Bruun SW, Sondergaard IB, Jacobsen S (2007) J Agric Food Chem 55(18):7234. doi:10.1021/jf063680j
53. Melnyk JP, Dreisoerner J, Bonomi F, Marcone MF, Seetharaman K (2011) Food Res Int 44 (4):893. doi:10.1016/j.foodres.2011.01.053
54. McCann TH, Day L (2013) J Cereal Sci 57(3):444. doi:10.1016/j.jcs.2013.01.011
55. Beck M, Jekle M, Becker T (2012) Int J Food Sci Technol 47(9):1798. doi:10.1111/j.1365-2621.2012.03048.x
56. Uthayakumaran S, Newberry M, Phan-Thien N, Tanner R (2002) Rheol Acta 41:162. doi:10.1007/s003970200015
57. Smith J, Smith T, Tschoegl N (1970) Rheol Acta 9(2):239
58. Yang Y, Song Y, Zheng Q (2011) J Food Sci Technol 48(4):489. doi:10.1007/s13197-011-0255-x

59. Khatkar BS (2005) J Food Sci Technol 42(4):321
60. Watanabe A, Larsson H, Eliasson AC (2002) Cereal Chem 79(2):203. doi:10.1094/CCHEM.2002.79.2.203
61. Larsson H, Eliasson AC, Johansson E, Svensson G (2000) Cereal Chem 77(5):633
62. Tanner R, Uthayakumaran S, Qi F, Dai S (2011) J Cereal Sci 54(2):224. doi:10.1016/j.jcs.2011.05.006
63. Jacobs H, Delcour JA (1998) J Agric Food Chem 46(8):2896
64. Seguchi M (1984) Cereal Chem 61(3):248
65. Schofield J, Bottomley R, Timms M, Booth M (1983) J Cereal Sci 1(4):241. doi:10.1016/S0733-5210(83)80012-5
66. Weegels P, de Groot A, Verhoek J, Hamer R (1994) J Cereal Sci 19:39
67. Stathopoulos CE, Tsiami AA, David Schofield J, Dobraszczyk BJ (2008) J Cereal Sci 47(2):134. doi:10.1016/j.jcs.2007.03.002
68. Mann J, Schiedt B, Baumann A, Conde-Petit B, Vilgis TA (2014) Food Sci Technol Int 20(5):341. doi:10.1177/1082013213488381
69. Hoseney R, Zeleznak K (1986) Cereal Chem 63(3):285
70. Kaletunc G, Breslauer KJ (1996) J Therm Anal 47(5):1267. doi:10.1007/BF01992827
71. Shenoy AV (1999) Rheology of filled polymer systems. Kluwer Academic, Dordrecht
72. Seiffert S, Sprakel J (2012) Chem Soc Rev 41(2):909
73. Imeson A (2011) Food stabilisers, thickeners and gelling agents. Wiley, New York
74. Saha D, Bhattacharya S (2010) J Food Sci Technol 47(6):587
75. Armisen R (1997) Thickening and gelling agents for food. Springer, Dordrecht, pp 1–21
76. Aymard P, Martin DR, Plucknett K, Foster TJ, Clark AH, Norton IT (2001) Biopolymers 59(3):131
77. Labropoulos K, Niesz D, Danforth S, Kevrekidis P (2002) Carbohydr Polym 50(4):407
78. Rees DA, Welsh EJ (1977) Angew Chem Int Ed Engl 16(4):214
79. Arnott S, Fulmer ASWE, Scott WE, Dea ICM, Moorhouse R, Rees DA (1974) J Mol Biol 90(2):269
80. Normand V, Lootens DL, Amici E, Plucknett KP, Aymard P (2000) Biomacromolecules 1(4):730
81. Nordqvist D, Vilgis TA (2011) Food Biophys 6(4):450. doi:10.1007/s11483-011-9225-0
82. Johns P, Courts A (1977) The science and technology of gelatin. Academic Press, London, pp 137–177
83. Ross-Murphy SB (1987) Food Hydrocoll 1(5):485
84. Weiss RG, Terech P (2006) Molecular gels. Springer, Dordrecht
85. Ledward D, Phillips G, Williams P et al (2000) Handbook of hydrocolloids. Woodhead, Cambridge, pp 67–86
86. Ross-Murphy SB (1992) Polymer 33(12):2622
87. Russ N, Zielbauer BI, Koynov K, Vilgis TA (2013) Biomacromolecules 14(11):4116. doi:10.1021/bm4012776
88. Pernodet N, Maaloum M, Tinland B (1997) Electrophoresis 18(1):55
89. Narayanan J, Xiong JY, Liu XY (2006) J Phys Conf Ser 28:83. doi:10.1088/1742-6596/28/1/017
90. Doublier JL, Garnier C, Renard D, Sanchez C (2000) Curr Opin Colloid Interface Sci 5(3–4):202. doi:10.1016/S1359-0294(00)00054-6
91. McClements DJ (2006) Biotechnol Adv 24(6):621. doi:10.1016/j.biotechadv.2006.07.003
92. Tolstoguzov VB (1991) Food Hydrocoll 4(6):429. doi:10.1016/S0268-005X(09)80196-3
93. Grinberg V, Tolstoguzov V (1997) Food Hydrocoll 11(2):145. doi:10.1016/S0268-005X(97)80022-7
94. Rodriguez Patino JM, Pilosof AM (2011) Food Hydrocoll 25(8):1925. doi:10.1016/j.foodhyd.2011.02.023
95. Tolstoguzov V (2006) Biotechnol Adv 24(6):626. doi:10.1016/j.biotechadv.2006.07.001
96. Kobayashi M, Nakahama N (1986) J Texture Stud 17(2):161. doi:10.1111/j.1745-4603.1986.tb00402.x

97. Gotlieb AM, Plashchina IG, Braudo EE, Titova EF, Belavtseva EM, Tolstoguzov VB (1988) Food Nahrung 32(10):927. doi:10.1002/food.19880321002
98. Plucknett KP, Pomfret SJ, Normand V, Ferdinando D, Veerman C, Frith WJ, Norton IT (2001) J Microsc 201(Pt 2):279
99. Brink J, Langton M, Stading M, Hermansson A (2007) Food Hydrocoll 21(3):409. doi:10.1016/j.foodhyd.2006.04.012
100. Taylor AJ, Besnard S, Puaud M, Linforth RS (2001) Biomol Eng 17(4–5):143
101. Djabourov M, Maquet J, Theveneau H, Leblond J, Papon P (1985) Br Polym J 17(2):169. doi:10.1002/pi.4980170215
102. von Hippel PH, Wong KY (1963) Biochemistry 2(6):1399
103. Shrinivas P, Kasapis S, Tongdang T (2009) Langmuir 25(15):8763. doi:10.1021/la9002127
104. Sharma D, George P, Button PD, May BK, Kasapis S (2011) Food Chem 127(4):1784. doi:10.1016/j.foodchem.2011.02.060
105. Watase M, Nishinari K (1980) Rheol Acta 19(2):220. doi:10.1007/BF01521934
106. Zasypkin D, Braudo E, Tolstoguzov V (1997) Food Hydrocoll 11(2):159. doi:10.1016/S0268-005X(97)80023-9
107. de Jong S, van de Velde F (2007) Food Hydrocoll 21(7):1172. doi:10.1016/j.foodhyd.2006.09.004

Adv Polym Sci (2017) 275: 235–266
DOI: 10.1007/12_2016_8

Published online: 17 August 2016

Nanostructured Ionomeric Elastomers

Debdipta Basu, Amit Das, Klaus Werner Stöckelhuber, and Sven Wießner

Abstract Driven by the desire to find an alternative way of vulcanizing elastomers without sulfur, researchers have widely explored ionic crosslinking techniques. The opportunity was taken to play with the functionality of the host polymer and its modification process to develop nanostructured ionic elastomers. Neutralization of polar elastomers by various divalent metal cations has been the route most employed for fabrication of this class of material. Ionic association or aggregation on the molecular level results in microphase separation of certain regions and, hence, enables easier processing. Thermally labile ionic domains introduced into the network make the entire material thermoresponsive and, therefore, it is possible to obtain reversible transition of dynamic mechanical properties. The unique network structure of these materials has led to outstanding physical properties that have not been achieved so far for conventional sulfidic networks. Consequently, many multifunctional and smart materials have been envisaged and

D. Basu (✉)
Leibniz-Institut für Polymerforschung Dresden e. V., Hohe Straße 6, 01069 Dresden, Germany

Technische Universität Dresden, Institut für Werkstoffwissenschaft, 01069 Dresden, Germany

Present address: Advanced Engineering Center, Apollo Tyres Limited, Bangalore 560001, India
e-mail: debdipta.basu@apollotyres.com

A. Das
Leibniz-Institut für Polymerforschung Dresden e. V., Hohe Straße 6, 01069 Dresden, Germany

Tampere University of Technology, 33101 Tampere, Finland

K.W. Stöckelhuber
Leibniz-Institut für Polymerforschung Dresden e. V., Hohe Straße 6, 01069 Dresden, Germany

S. Wießner
Leibniz-Institut für Polymerforschung Dresden e. V., Hohe Straße 6, 01069 Dresden, Germany

Technische Universität Dresden, Institut für Werkstoffwissenschaft, 01069 Dresden, Germany

designed using these systems. A detailed overview is provided on the various nanostructured ionic elastomers developed over the years. It would not be exaggerating to mention in the context of the discussion that nanostructured ionic elastomers will definitely open up new horizons in materials research.

Keywords Elastomers • Ionic crosslinking • Self healing rubber

Contents

1 Introduction

Uncrosslinked elastomers behave like viscous materials and the direct application of such materials to engineering fields is rare. Crosslinking transforms the rubber into a semisolid elastic material with higher strength, increased toughness, enhanced hardness, and improved modulus. A crosslinked rubber therefore turns into a highly deformable elastic material in which the macromolecular chains are linked together by chemical or physical bonds. As a result, this crosslinked network structure provides highly elastic properties and, simultaneously, considerably reduces the viscous properties of the materials [1, 2]. The established polymer network structures lead to restricted mobility of the macromolecular chains. Usually, the permanent network structures of raw rubbers are established by covalent crosslinking using sulfur or peroxide [3]. However, supramolecular assembly of relatively small molecules could also lead to the formation of chains and crosslinks and, thus, highly elastic materials can be designed. Furthermore, polymeric compounds with supramolecular assembly capabilities can be physically mixed with commercial rubber to develop rubber compounds with self-healing properties [4]. Similarly, crosslinks can be established by introducing ionic functionalities into the macromolecular chemical structure, which eventually results in a three-dimensional (3D) network structure through ionic association. The elastomers fabricated by such types of crosslinking process

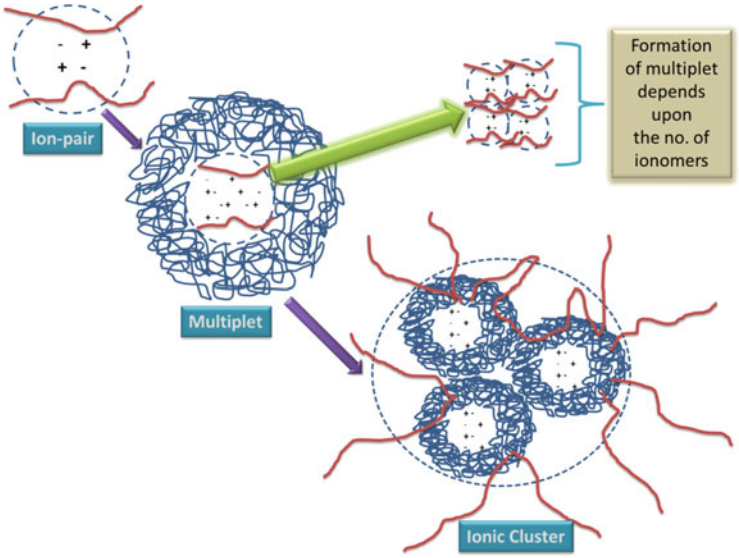

Fig. 1 Hierarchical nature of ionic elastomer formation

are termed ionic elastomers or ionomers. Some elastomers with chemical functional groups attached to the polymer chains (e.g., solution butadiene rubber modified with amine ($–NH_2$) or thiol (–SH) groups) can be further treated with suitable chemicals to form ionic functional groups; however, literature concerning these kind of ionic elastomers is very rare. The term 'ionomer' was introduced as early as 1965 [5] when a special class of thermoplastic polymers comprising ethylene and methacrylic acid partly neutralized by sodium or zinc was produced and commercialized under the name of Surlyn® by Du Pont. Because the ionic aggregates are thermoreversible in nature, the ionomers can be processed by traditional techniques. Surlyn® is reported to offer improved properties compared with those of the parent polyolefin.

Ionomers are generally classified as a special class of polymers, in which the incorporation of a relatively small amount of bound ionic functionalities (10 mol %) in the form of inorganic salts into hydrocarbon chains generates unique and dramatically changed physical properties for the whole material. Ionic elastomers are fabricated when these ionomer units are effectively crosslinked through the ionic association and, in some cases, form ionic multiplets and clusters (see Fig. 1). Initially ion pairs are formed, followed by the formation of multiplets. Multiplets are basically aggregates consisting of several ion pairs (about six to eight) [6].

Multiplets primarily form a physical crosslinking network within the structure. A few parameters are considered to affect the number of ion pairs in a multiplet: the nature of the ion pair (carboxylate, sulfonate, phosphonate), the size of the ion content and the steric effects related to the volume of the polymer chain segments adjoined to the ion pairs, degree of neutralization, and the types of cations and anions [7–9]. Several forms of these multiplets can be realized, such as quadrapoles, hexapoles,

and octapoles. A very important observation is worth emphasizing with respect to ionomers. A relatively low dielectric constant and low glass transition temperature (T_g) of the host polymer favor ionic aggregation, whereas a higher dielectric constant and/or higher T_g prevent multiplet formation [9]. The ionic networking process is also known to be influenced by specific interactions between the plasticizer (if present in the system) and the backbone of the ionic groups. The multiplets generally [9] disperse into the hydrocarbon matrix and, therefore, are restrained from forming a distinct separate phase. With increasing ion content, the average distance between multiplets decreases. As a result, ion clusters are produced.

There exists a striking contrast between multiplets and ionic clusters. The latter typically exhibit the characteristics of phase-separated regions, with their own T_g. The composition of ionic clusters contains a significantly higher number of ion pairs and a considerable amount of nonionic hydrocarbon. Clusters show a unique relaxation behavior at higher temperature, and subsequently act as reinforcing fillers in addition to their function as physical crosslinks [10]. The relative amount of ionic functionalities present in these two forms in any ionic elastomer is determined by the nature of the hydrocarbon backbone and by the concentration of salt groups and their chemical nature [11]. Not only is the glass transition of the macromolecular body affected, but ionic functional groups can also affect other fundamental properties such as the size of clusters, melt rheology, distribution and morphology of domains dispersed in the continuous elastomer phase (matrix polymer), miscibility of polymers, and some mechanical and dynamic properties [12, 13]. The miscibility of two polymer molecules is often determined by categorically selecting the ionomer system (ionic functionality and the counter ion). Ionic association in the ionomers provides unique opportunities for manipulation of various properties by controlling the molecular structure. Elastomers crosslinked by strongly interacting ionic groups have generated a great deal of interest because of their outstanding physical properties resulting from microphase segregation in bulk and in solution [7]. Evidence of the microphase separation has been found where self-assembly of the polymer microstructure with different types of morphologies is feasible [14]. But, the question still arises: What is the driving force for such a phenomenon? Extensive analysis has compelled scientists to conclude that in such types of ionic association in these polymeric units, it is dipole–dipole interactions between ionic pairs in nonpolar media that act as the primary driving force [15].

Ionomers are generally classified into the following types: monochelics, telechelics, telechelic stars, AB block copolymers, ABA triblock copolymers, dendrimers, random copolymers, and ionenes [16, 17]. Monochelic ionomers are the simplest type, comprising a single ion placed at the end of a polymer chain (e.g., polystyrene containing a terminal carboxylate anion). They can be produced by radical polymerization of unsaturated monomer initiated by a polar initiator such as peroxodisulfate. On the other hand, a molecule of telechelic ionomer generally possesses one ion at each end of the polymer chain. Normally, anionic polymerization is the best technique for synthesizing such types of ionomer. Free-radical polymerization of unsaturated monomer can be employed for the preparation of telechelic ionomers, while the termination of growing radicals takes place via the combination mode. Apart from carboxylate end groups, the active part of the ionic ends can be a sulfonate, sulfate, borate, etc. Last in

this series, when a three- or multiple-arm star is tipped at each arm's end by an ionic group, a telechelic star polymer system is formed. AB-type block copolymers consist of nonionic segments and ionic repeat units. ABA-type triblocks comprise one completely nonionic segment and a partly ionic moiety. Several other types of ionomers also exist, such as simple random copolymers, ionenes (in which the ionic groups distribute regularly along the backbone), grafts, and polymer–salt mixtures. Detailed classification based on the chemical structural units and properties are discussed in Sect. 2.

Fabrication of nanostructured ionic elastomers by introduction of various functional nanomaterials such as metal oxides, metal halides [7], and layered double hydroxides [18] has generated some new insights. Thanks to advancement in the large scale production of such nanostructured materials in different geometric forms and of different chemical compositions [19] and their incorporation into various elastomers depending on the application, the field of functional elastomer composites has achieved tremendous commercial viability. A relatively unexplored multifunctional nanostructured material, layered double hydroxides [18], has recently incentivized rubber scientists and technologists to design nanocomposites for smart applications. The unique advantage of such metal-based nanofillers compounded with an elastomer is the production of ionomers exhibiting unique physical properties.

Usually, ionic elastomers are prepared using traditional rubber compounding machines such as internal mixers and two-roll mills. Synthetic elastomers with modified structures thanks to the presence of polar functional groups (carboxylate, sulfonate, maleic anhydrate, etc.) are compounded with metal oxides such as ZnO, MgO, CaO, and ZnO_2; metal halides such as $ZnCl_2$; or Zn-based layered double hydroxide (Zn-Al LDH) at different loadings. Preparation of ionic elastomers in solution has also been reported by several researchers. Copolymerization of a functionalized monomer unit with an unsaturated olefin monomer or direct functionalization of the preformed polymer are methods for fabrication of ionic elastomers by chemical synthesis [8].

2 Types of Ionic Elastomers

Over the decades, several types of ionic elastomers have been produced by varying or modifying the chemical structural units. Functionalization according to specific demands has led to tremendous changes in properties such as melt processability, rheological features, physical properties, and thermal properties [20]. In this section, different ionic elastomers and their distinctive features are discussed.

2.1 Carboxylated Ionic Elastomers

This type of ionic elastomer is classified as a butadiene rubber functionalized with a certain amount (about 6–7 %) of carboxylic groups. Carboxylated ionic elastomers

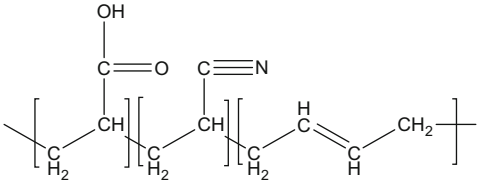

Fig. 2 Nitrile rubber (NBR) is converted to carboxylated nitrile butadiene rubber (XNBR) after chemical modification with acrylic acid (–COOH ~ 7 %)

are produced by employing free-radical copolymerization by direct copolymerization of a relatively small amount of acrylic or methacrylic acid with ethylene or styrene. When this modification is carried out on acrylonitrile butadiene rubber (NBR) to enhance its elastomeric properties, carboxylated acrylonitrile butadiene rubber (XNBR) is obtained. The structural modification is displayed in Fig. 2. Carboxylated ionic elastomers are generally classified into two main categories [8]:

1. Classic carboxylated ionic elastomers: The worldwide production of this type of ionic elastomer is about 0.5 million tons per year [21]. Because of its production in bulk and ease of availability, much research is carried out on this type of ionomer.
2. Telechelic carboxylated ionic elastomers: This special type of ionic elastomer is not produced in abundance. Low molecular weight difunctional carboxyl-terminated butadiene-based elastomers are included in the family of telechelic ionomers.

Functionalization by addition of certain amounts of acidic groups to the hydrocarbon chains of di-ene rubbers improves many properties but does not provide stability to the whole structural unit. Therefore, modified elastomers are in general neutralized with metal oxides such as zinc oxide (ZnO), zinc peroxide (ZnO_2), calcium oxide (CaO), and magnesium oxide (MgO) to generate extraordinary physical properties. A simple example can be given with respect to XNBR rubber neutralized with zinc oxide. A stable and neutral salt in the form of COO–Zn–COO is eventually obtained after such modification (see Fig. 3). As a consequence, an increase in T_g and enhancement of the rubbery modulus at high temperatures (dynamic mechanical property) are observed in these rubber compounds [7].

Uncrosslinked XNBR, once compounded with a divalent metal oxide such as zinc oxide, yields higher green strength than sulfur-vulcanized butadiene elastomers. The 3D network evolved by the ionic association in the system differs from the quasi-irreversible rearrangements of the monosulfidic, disulfidic, and polysulfidic linkages [22]. As a result, higher elastic properties are generated by substantially reducing the viscous properties of such ionomeric systems, which leads to improved physical properties. After neutralization, carboxylate dionomers contain a mixture of free acid and mixed salts. Therefore, the final compound demonstrates fluidity at elevated temperatures, additional transition in the dynamic spectra at elevated temperature, enhanced stress relaxation, and poor compression set. These properties are similar to those obtained with chemically generated crosslinks along with secondary bonding driven by ionic association [23]. Ibarra

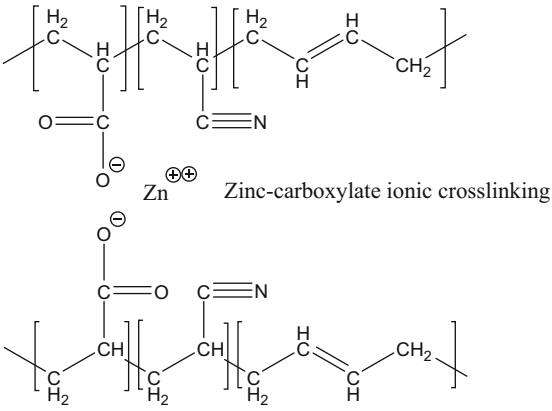

Fig. 3 Zinc carboxylate linkage produced by the reaction between zinc oxide and carboxylic group of carboxylated nitrile butadiene rubber (XNBR)

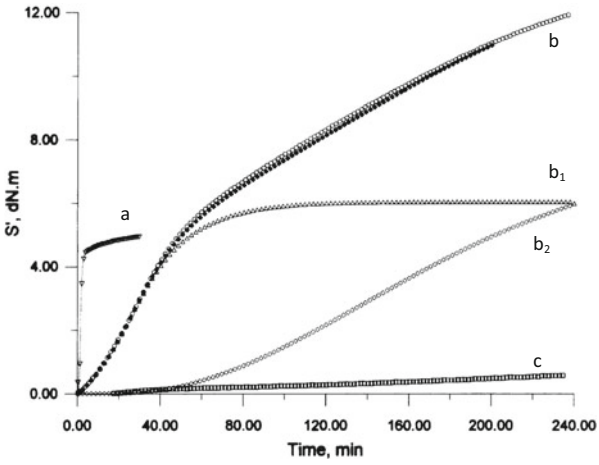

Fig. 4 Rheometer curves for (*a*) XNBR–ZnO system, (*b*) XNBR–ZnO–zinc peroxide system ($b = b_1 + b_2$), and (*c*) NBR–ZnO–zinc peroxide system. *Curves* b_1 and b_2 are obtained by Gaussian fitting of *curve b*. Reprinted with permission from [24]. Copyright 2002 Elsevier

et al. [24] explored different mechanistic pathways in the system of XNBR cured with the dual presence of zinc oxide and zinc peroxide. In XNBR exclusively crosslinked with zinc oxide, a single maximum (Fig. 4, curve a) was obtained, which was attributed to an improvement in the ordering of the ionic association between the carboxylic functionalities of XNBR and the zinc atoms of zinc oxide. As a result of additional crosslinking, covalent in nature, in XNBR treated with both zinc oxide and zinc peroxide, the torque–time curve was split into two distinct and separate contributions (Fig. 4, curves b_1 and b_2).

Apart from zinc oxide and zinc peroxide, Ibarra et al. also exploited other inorganic oxides such as calcium oxide and magnesium oxide to ionically crosslink XNBR. They reported that a marginally excess amount of CaO with respect to the stoichiometric proportion enhances the physical properties of vulcanized samples, irrespective of the temperature of curing [25]. A similar sort of ionic association was also found to take place between XNBR and MgO. This composition leads to

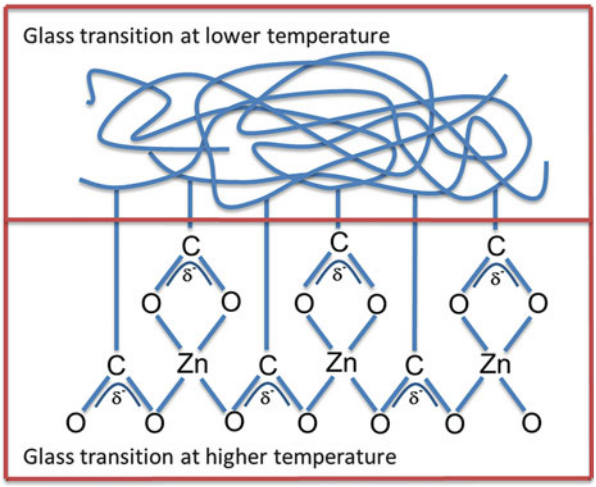

Fig. 5 Crosslinked network formed by 'zinc carboxylate polymer' [7]

formation of a phase-separated morphological structure that ultimately generates an additional high temperature transition as well as the normal T_g. Ibarra et al. [26] termed this type of ionic association "thermally labile."

It is noteworthy that ionic elastomers formed by XNBR and only metal oxide show unique dynamic behavior. Other inorganic compounds made of the same metal fail to produce identical dynamic properties when mixed with rubbers such as XNBR [7]. Most probably, the metal oxides can only form a very specific microstructure with the carboxylic group, but other metal compounds do not seem able to form the same kind of chemical structures. In exploring this topic further, an extensive study by Basu et al. [7] found that zinc carboxylate, which is produced as an ionic aggregate as a result of formation of a special zinc carboxylate polymer (Fig. 5), is primarily responsible for generation of a phase-separated region in the matrix. Therefore, an extra glass transition-like behavior at higher temperature is observed for such compounds. Fourier-transform infrared spectroscopy (FTIR), dynamic mechanical analysis (DMA), and high-resolution transmission electron microscopy (TEM) proved that this high-temperature relaxation behavior does not exclusively originate as a result of ionic crosslinking but is associated with the formation of an additional 3D network of zinc-enriched polymer phase (Fig. 5) that arises through reaction between carboxylic groups and zinc oxide. The existence of a phase-separated morphology for ZnO-cured XNBR was shown by a detailed TEM study, explaining the co-existence of Zn-rich and Zn-poor phases in the XNBR matrix [7].

Tungchaiwattana et al. [27] examined the role of acrylonitrile (–CN) on various properties of a nanostructured film synthesized from core–shell nanoparticles comprising butadiene, acrylonitrile, and methacrylic acid. When mixed with ZnO, three types of crosslinking networks were established in these ionomeric films. Covalent crosslinking from the unsaturation in the butadiene moiety, physical crosslinking induced by the ionic association of COO^- (from methacrylic acid) and

Zn^{2+}, and another relatively weaker physical crosslinking involving –CN and Zn^{2+} [28]. Elasticity, toughness, and tensile modulus (as demonstrated by mechanical tests) were increased by the introduction of –CN functionality without affecting the ductility of the system.

Carboxylated styrene butadiene rubber reinforced with soy protein isolate was synthesized by Jong [29]. Ionic aggregates produced in such a system are composed of submicron-sized protein moieties. Interestingly, soy protein-reinforced ionic elastomers demonstrate a better elastic modulus than carbon black-reinforced samples, which is attributed to the formation of a stronger filler network in the former.

Malmierca et al. [30] employed a very sophisticated method in the light of ^{1}H low-field NMR spectroscopy to investigate the complexities of XNBR and MgO-based ionomeric elastomers. The influence of the concentration of MgO on the ionomeric properties was explored by the means of multiple-quantum (MQ) spectroscopy. The key observation from their study was that incorporation of metal oxide exceeding the stoichiometric amount improved physical properties such as the stress–strain behavior of the ionomer by establishing a significant number of relatively small ionic clusters that played the role of dynamic crosslinks. The authors claimed that alteration of the network structure created by the dynamically heterogeneous crosslinks and the phase-separated morphology directly influences the dynamics of the entire system and, hence, the behavior of such materials at higher temperature resembles that of thermoplastic elastomers [30].

2.2 EPDM-Based Ionic Elastomers

Ethylene propylene diene terpolymer (EPDM) is a commercial elastomer possessing excellent resistance to oxidation and weathering, primarily as a result of the presence of a saturated macromolecular backbone. A fair amount of research work has been carried out on the zinc salt of sulfonated ethylene propylene terpolymers containing some norbornene as unsaturated units. The structure of this rubber molecule is exhibited in Fig. 6. In contrast to other cationic elements

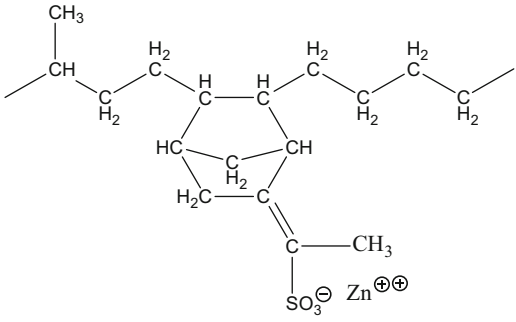

Fig. 6 Sulfonated EPDM neutralized by zinc ion

Table 1 Physical data for SEPDM neutralized with different metals [32]

Metal	Tensile strength (MPa)	Elongation at break (%)
Mg	2.2	70
Ca	2.8	90
Co	8.1	290
Li	5.2	320
Ba	2.3	70
Na	6.6	350
Pb	11.6	480
Zn	10.2	400

Base polymer CR-2504, sulfonate content 31 meq/100 g EPDM. Dissolved in 100 g of free acid in 1000 mL hexane–150 mL isopropanol; neutralized with 90 meq acetate in 25 mL water

such as sodium (Na), the zinc ion (Zn^{2+}) is a very popular choice for EPDM molecules because of its higher capability of forming ionic crosslinks with the host rubber, especially at lower temperatures. Zinc sulfonated EPDM-based ionomers (SEPDMs) show some typical melt-flow behavior at higher temperatures, similar to common thermoplastics. Hence, SEPDM behaves as a thermoplastic elastomer and can be processed by techniques employed to shape this class of polymers [31]. In this report, the authors explore the role of reinforcing filler on SEPDM. Electrophilic reaction of the sulfonating group on the double bond of the elastomer unit produces SEPDM. The details of SEPDM production and its reaction mechanism have been reported by Markowski et al. [32]. They explored the influence of various metal cations on the physical properties of SEPDM, as depicted in Table 1. It is evident that only zinc and lead, along with establishing the ionic crosslinking network in the system, also act as reinforcing fillers at ambient temperature. Tensile strengths and elongation at break are improved to a significant extent after addition of zinc salts to SEPDM. Their work also claims that the melt processability and rheological features such as apparent viscosity, melt flow index, and melt fracture at higher shear rates are also greatly enhanced by crosslinking zinc and lead cations with SEPDM.

Both clay [33] and carbon black [31] are reported to enhance the final physical properties of SEPDM. It is noteworthy that neither hard clay nor carbon black could inhibit the appearance of a second transition in the DMA spectra, apart from the normal T_g relaxation for such systems (see Fig. 7a). The explanation of such phenomenon is attributed to the realization of multiplets and clusters in the SEPDM ionomer [34].

The rubber–filler interactions are the result of weak van der Waals' forces acting in the nonpolar elastomer backbone; however, the ionic associations are of much stronger type, as proposed in Fig. 7b. The conclusions made from these studies are pretty obvious: The fillers do not influence the ionic association process induced by zinc salts but instead stiffen the final compounds to impart reinforcing strength.

The existence of an extra transition for the SEPDM ionomers in addition to the usual glass transition is also observed in dielectric thermal analysis. The dielectric spectra of the SEPDM ionomer (Fig. 8b) shows two transitions compared with the

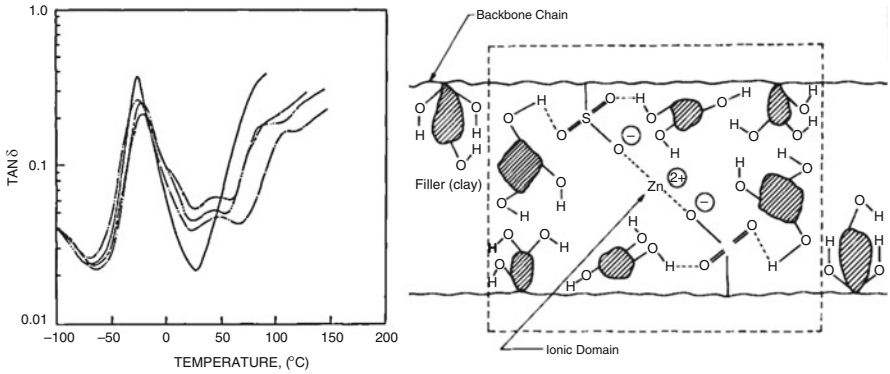

Fig. 7 *Left*: Plot of tan δ versus temperature for the SEPDM system, showing an extra transition at higher temperature. *Right*: Interactions of filler particles with the elastomer backbone and with ionic aggregates. Reprinted with permission from [33]. Copyright 1995 Elsevier

single transition seen for uncrosslinked EPDM (Fig. 8a). The single transition at 118°C in the tan δ versus temperature plot corresponds to the melting transition of the crystalline block of the polyethylene units. In the case of the SEPDM ionomer, the higher temperature transition at 125°C is attributed to melting of the crystalline polyethylene block and the lower temperature transition at 60°C is driven by the ionic association [33, 35–37].

An important question arises about the stability of the second transition peak at higher temperatures. Mandal et al. [38–40] concluded that a basic source such as ammonia can play the role of plasticizer for ionic aggregates, resulting in solvation of the hard phase in the high-temperature region of the dynamic mechanical spectrum. Basu et al. [7] showed that ammonia can cause disappearance of the second transition peak in DMA spectra because the alkaline medium neutralizes the acidic zinc carboxylate, which forms an in-situ polymer phase in the ionomer. Both these studies were carried out on XNBR-based systems that were neutralized by zinc sources. EPDM-based ionomeric elastomers neutralized by a zinc source are also reported to show a similar kind of behavior. The ionic aggregates formed in SEPDM are assumed to be solvated after treatment with dimethyl sulfoxide [41, 42], glycols, amines, and even water [43, 44]. In all cases, treatment of the ionomers results in formation of a complex linked with the cation, or hydrogen bonds linked with the anions, which eventually leads to solvation of the hard phase. Because of its more polar in nature, this solvation effect is much more pronounced in the case of XNBR-based ionomers than in EPDM-based ionomers. However, FTIR studies carried out by the aforementioned researchers conclusively showed that the hard phase formed as a result of ionic aggregation at elevated temperatures for both these systems becomes complexed and masked while treated with selective solvents such as ammonia. Hence, the original biphasic structure collapses, giving rise to a single transition in the corresponding DMA spectra or dielectric analysis. After a series of creep experiments, Agarwal et al. [45] came to the speculative

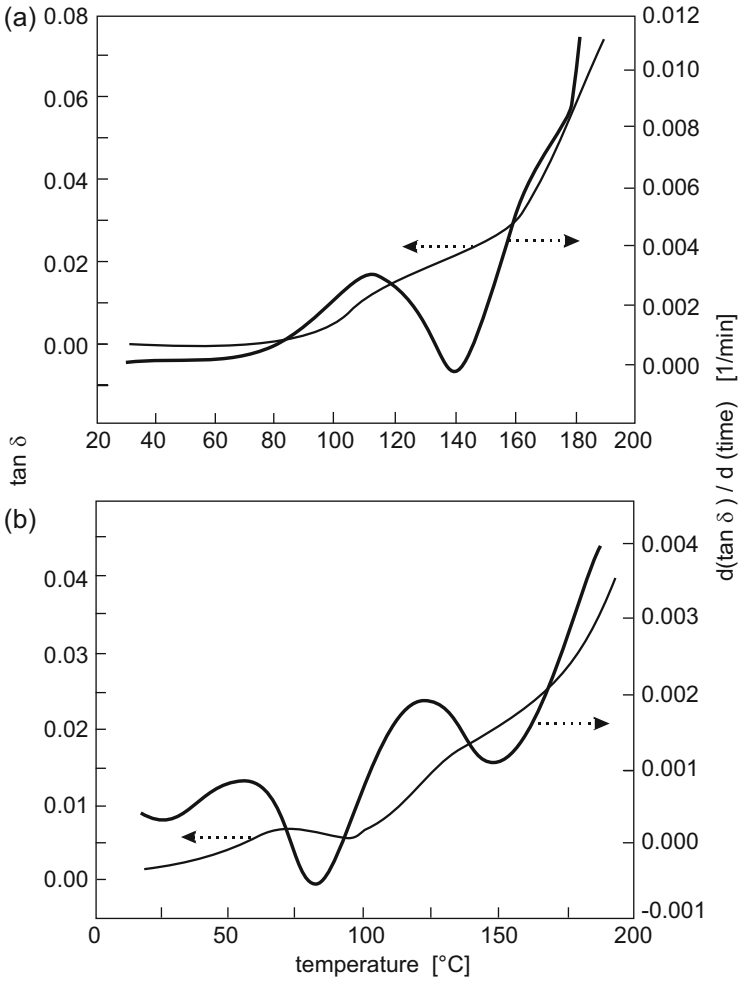

Fig. 8 Dielectric analysis plots (tan δ versus temperature) for (**a**) uncrosslinked EPDM and (**b**) SEPDM ionomer. Adapted from [31]. Copyright Elevier Ltd, 1995

conclusion that nonionic components such as the hydrocarbon polyolefin restrict the 'ion-hopping' phenomenon in the structure and that this has a direct impact on the physical properties of the SEPDM system. Small angle X-ray scattering (SAXS) studies by van der Meeet al. [46] confirmed that microphase separation in the maleic anhydride-grafted EPDM is greatly influenced by the choice of cation. For example, microphase separation is predominantly noticed for a monovalent cation such as K^+, as shown by the sharp scattering peak, whereas this effect is less pronounced for a bivalent cation such as Zn^{2+} (Fig. 9).

Unfavorable bonding between the Zn^{2+} cation and the two carboxylates because of structural distortion induced by specific co-ordination chemistry is primarily

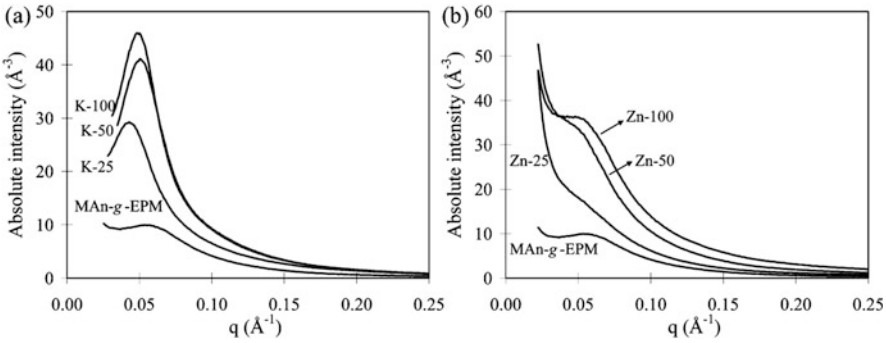

Fig. 9 Small angle X-ray scattering (SAXS) data for maleic anhydride-grafted EPDM-based ionomers produced with (**a**) monovalent cation K^+ and (**b**) bivalent cation Zn^{2+} under certain conditions. Reprinted with permission from [46]. Copyright 2008 American Chemical Society

responsible for such phenomenon. Lightly sulfonated SEPDM foam was produced by Brenner et al. [47]. The foaming process developed by them using EPDM-based ionomer is claimed to be much easier and straightforward than with polyurethane-based foam. As a result of the physical crosslinking, such ionomers can be recycled and, hence, rapidly processed to any shape at higher temperatures. SEPDM coating is used in agricultural applications. Urea fertilizers are sometimes coated with such ionomers to assist maximum release of manure during growing seasons [48].

2.3 Polyurethane Ionic Elastomers

Processability of any elastomeric ionomer is a challenging task. Polyurethane (PU)-based systems are classified in the category of ionomers whose synthesis and characterization are of significant interest. This class of ionomers combines the advantages of both PUs and ionomers. The hydrophobicity of the pure PUs can be easily overcome by introducing certain ionic hydrophilic groups, creating dispersions or emulsions [49]. A series of articles have reviewed this class of ionomer [50–53]. Basically, three types of PU ionomers exist: cationic, anionic, and zwitter PU ionomers, as depicted in Fig. 10.

Details of the synthesis of these three classes of PU ionomers have been elaborately described by Jaudouin et al. [49]. The authors claim that the synthesis of all three PU ionomers can easily be carried out in aqueous medium, which provides a unique advantage in dealing with such compounds by taking care of environmental issues related to pollution. The morphology and mechanical and thermal properties of PU block copolymers have been major areas of research for a long time [54–59]. This interest has grown significantly because of the phenomenon of phase separation of the urethane hard blocks into microdomains, primarily induced by the strong intermolecular force between aromatic urethane groups.

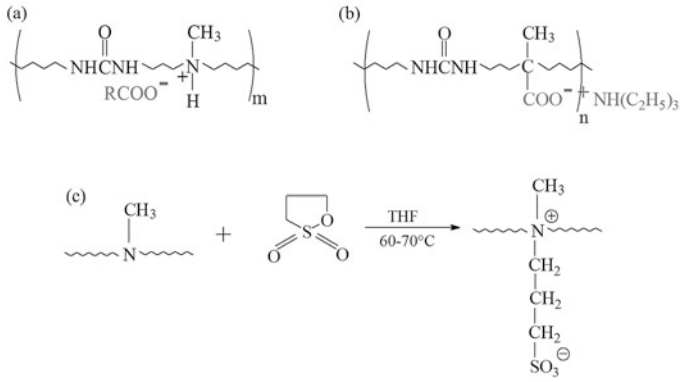

Fig. 10 (**a**) Cationic, (**b**) anionic (*m* and *n* are degrees of polymerization) [50], and (**c**) zwitter polyurethane ionomers [49]

These groups can easily form hydrogen bonds within the structure. It is well known that the hard domains in the PU unit are crystalline in nature and essentially provide strength by being separated from the rubbery soft segment matrix. Incorporation of ionic groups into the macromolecular backbones substantially affects this intermolecular bonding and morphology.

The dual presence of hydrogen bonds and ionic bonds subsequently influences other properties such as the T_g and the mechanical and thermal properties of the polymeric unit. Two contrasting phenomena have been observed with respect to the T_g and are related to the amount of ionic groups introduced into the PU chain. The T_g drops with the introduction of ionic functionalities into the PU units because the overall crystallinity decreases and, subsequently, microphase separation of the soft and hard domains increases [60, 61]. On the other hand, a few studies suggest that T_g increases with the amount of ionic groups introduced into PU units [62–64]. Nierzwicki et al. [64] reported the same result. The authors considered that the ionic group being solubilized in the soft domains could influence the chain mobility as a result of the physical crosslinking of ionic groups. Various chemical interactions such as hydrogen bonding between carbamoyl groups and dipole–dipole interactions in the aromatic groups are also reported to restrict the free motion of the polymer chains and, hence, cause an increase in T_g [63, 65]. Introduction of ionic groups also influences the mechanical properties of PU ionomers. Tensile strength and elongation at break are significantly enhanced as a result of physical crosslinking between the macromolecular chains [66, 67]. The degree of enhancement of mechanical properties generally depends on the nature of the ionic functionality, counter ions, etc. PU ionomers find a wide range of sophisticated applications such as shape memory polymers and biomedical tools. The dilute solution nature of such ionomers also opens fields of application in paints, coatings, and adhesives.

The diverse types of structure–property relationships that can be easily managed provide the opportunity to develop shape memory polymers. Usually, a broad range

of operating temperatures between −40°C to +80°C can be selected as the shape recovery temperature, depending on the application. Kim et al. [68] designed a PU ionomer system based on polycaprolactonediol, 4,4′-diphenylmethane diisocyanate, 1,4-butanediol, and dimethylolpropionic acid to explore the shape memory effect. PU elastomers are very biocompatible [69–73] because polyether-based PUs are resistant to hydrolysis by biological fluids and are nontoxic. They are used in biomedical applications such as artificial hearts, connector tubing for heart pacemakers, and hemodialysis tubes, without any sort of surface treatment [71–73].

2.4 Block Copolymer Ionic Elastomers

Kennedy and Faust first discovered block copolymer ionic elastomers in 1986 when isobutylene units were polymerized using cationic polymerization techniques [74]. Architecturally, this type of ionomer can be classified into five types: diblock (AB type) [75], triblock (ABA type) [76], comb type [77], star block [78], and dendrimer type [79]. Weiss et al. [76] synthesized triblock copolymer ionomers based on poly[styrene-*block*-(ethylene-*co*-butylene)-*block*-styrene] (SEBS) by sulfonating the polystyrene end. Sulfonation is reported to take place only on the phenyl rings. Moreover, these ionomer blocks possess two distinct microstructures: (1) block copolymer domains (ethylene-*co*-butylene) of length scale of about 20–30 nm and (2) polystyrene microdomains of length scale of about 3–4 nm induced by ionic aggregation. Storey et al. [78] reported the synthesis of a new class of block copolymer ionomers composed of a three-arm star branched structure. Multiple numbers of ionic groups forming an ionic block are introduced at the extreme end of each macromolecular chain. The corresponding reaction scheme is shown in Fig. 11. The ionomer is prepared in two steps. First, the three-arm star block copolymer ionomer precursor is prepared using living anionic polymerization (Fig. 11a). This is followed by post-polymerization to finally synthesize the block copolymer ionomer. The final structure of the block copolymer ionomer produced by Storey et al. [78] is depicted in Fig. 11b. The sulfonate dionomer prepared in this way is reported to gain mechanical rigidity, especially in the crystalline sample compared with the amorphous sample. In the DMA spectra, an enhancement in the storage modulus with temperature clearly indicates that the ionomer compound was in a nonequilibrium state and that reorientation of the ionic aggregates takes place at elevated temperature. Vargantwar et al. [80] prepared a solvated block copolymer ionomer network based on a styrene-based triblock copolymer. An electroactive-responsive polymer was designed with such a system. Styrene-based block copolymers are used as dielectric elastomers because of their tremendous actuation strains, which approach almost 300%, as well as high electromechanical coupling efficiencies (Fig. 12). This group showed how altering different solvents improves the blocking stress and yields remarkably high energy densities; therefore, a robust and versatile class of electroactive smart functional polymeric materials was developed.

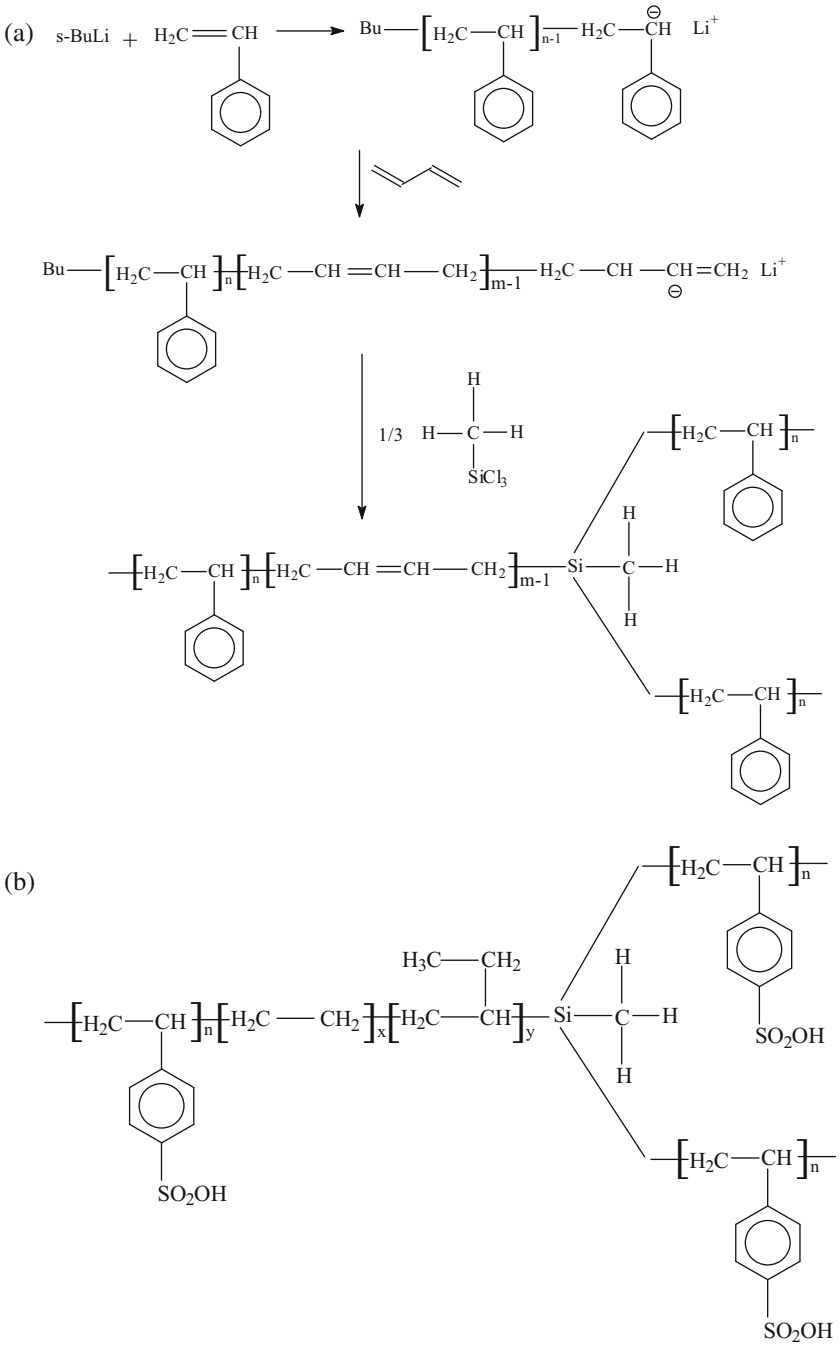

Fig. 11 (**a**) Reaction scheme for synthesis of precursor material for three-arm star block copolymer. (**b**) Final three-arm star block copolymer produced [78]

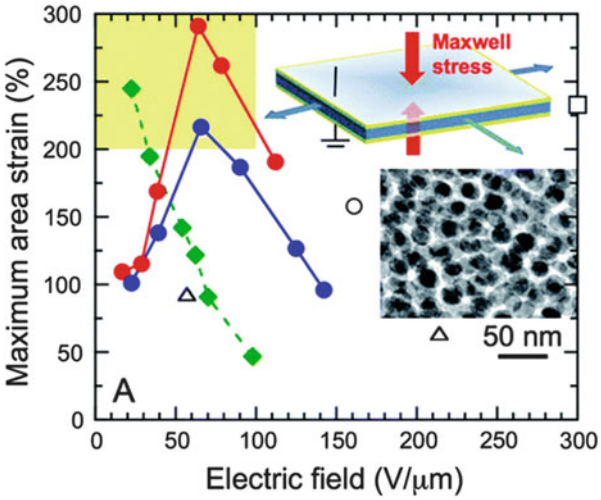

Fig. 12 Plot of actual strain versus electric field for mineral oil solvated SEPS (*red circles*), SEEPS (*blue circles*), and SEBS (*green squares*) copolymers. Silicone elastomers (*triangle*), acrylic-based adhesive (*circle*), and interpenetrating network (*square*) are also provided for comparison. *SEPS* poly[styrene-*b*-(ethylene-*alt*-propylene)-*b*-styrene)]; *SEEPS* poly[styrene-*b*-(ethylene-*co*-{ethylene-*alt*-propylene}]; *SEBS* poly[styrene-*b*-(ethylene-*co*-butylene)-*b*-styrene)]. The *yellow box* indicates the area of low dielectric fields and high performance. Reprinted with permission from [80]. Copyright 2011 Royal Society of Chemistry

2.5 *Liquid Crystalline Ionic Elastomers*

Liquid crystal polymers (LCP) are well known for their outstanding strength at high temperature; resistance to weathering, radiation, and most chemicals; and flame retardant properties. These polymers maintain a high degree of ordered structure in the melt as well as in solid forms. Similar to LCP, a unique combination of liquid crystalline phase and rubber-like elasticity produces liquid crystalline elastomers (LCEs). LCEs are therefore footprint elastomers for a number of functional properties such as optoelectricity and piezoelectricity. The rubber-like elasticity of such elastomers provides the necessary mechanical robustness. Functionalization of LCEs with ionic moieties opens up new horizons of research. A few recent studies [81–83] have shown that microphase separation of the ionic domains in the liquid crystalline ionic elastomers, which is a typical feature of ionomers, results in outstanding mechanical orientability [82, 83]. Therefore, from a purely technological point of view, ionic LCEs possessing the characteristics of mechanical orientability and other sophisticated smart properties are of great interest to industrial manufacturers. Meng et al. [84] synthesized a series of siloxane-based LCEs comprising biphenyl benzoate mesogenic units modified with Brilliant Yellow ionic functionalities. FTIR spectra provide clear evidence that the monomer, namely sodium 2,2′-(1,2-ethenediyl)bis{5-{4-{9-{[4′-(4-allyloxybenzoyl)-

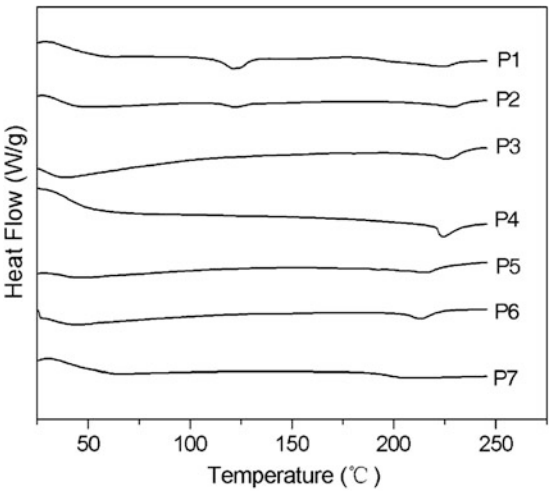

Fig. 13 Differential scanning calorimetry plots for ionic liquid crystalline elastomers. As the amounts of ionic groups gradually increase (*P1* to *P7*), the melting point (~230°C) seems to vanish [80]. Reprinted with permission from [84]. Copyright 2005 Nature Publishing Group

oxybiphenyl-4-yl]oxycarbonyl}nonanoyloxy}phenyl}azo}-benzenesulfonate, was successfully converted to the corresponding polymeric unit. Stretching bands of O = S = O along with C–O and Si–O were observed to overlap at wave number 1,000–1,300 cm^{-1} in the spectra. Crosslinking density values calculated by a swelling technique using dimethyl sulfoxide (DMSO) solvent confirmed that the ionic elastomer with the highest siloxane content was highly crosslinked.

The Brannon–Peppas model was employed to determine the crosslink density values. This model was proposed as a modification of the classical Flory–Rehner theory. The former illustrates the phenomenon of equilibrium swelling of the ionic hydrogel in aqueous medium, whereas the latter is proposed for macromolecular chains reacting in solid state. Nevertheless, in both the models the network chain lengths have a Gaussian distribution. Ionic crosslinking was also reported to influence the thermal properties of the LCE. The T_g and melting point shifted to a higher temperature. Another work by the same group noticed the thermotropic effect of LCE ionomers. The melting temperature of the corresponding compound vanished with an increase in ionic moieties in the polymeric structure [84], as shown in Fig. 13.

3 Smart Properties and Applications

Ionic elastomers find a wide range of sophisticated applications. The outstanding physical properties induced by the unique type of crosslinking in this class of material are exploited to a significantly large extent in modern technologies. In addition to traditional applications such as roofing [85], flooring, and photochemical cells [86], the thermoreversibility of the crosslinking enables ionic elastomers

to be designed for use in self-healing tires, dielectric actuators, shape memory elastomers, etc.

3.1 Self-Healing Rubber

A flat car tire while driving can cause huge annoyance. It is a well-known fact that rubber is made of long macromolecular chains or strands, which are crosslinked by sulfur to ensure that rubber is durable and elastic – a process known as vulcanization. When a tire is punctured, the rubber is deformed to break by pieces of glass or any sharp object and the strands are irreversibly ruptured; thus, the rubber cannot be patched for long-term use. A recent development by Das et al. [22] showed how designing a self-healing rubber can solve this issue. Smaller holes can be patched faster and damage can be healed sooner. The authors introduced a simple approach for tuning a commercially available and widely used rubber into a highly elastic material with extraordinary self-healing properties, avoiding use of the typical vulcanizing agents. Ionic modification of butyl rubber, which is commonly used as the inner liner in tires because of its excellent air impermeability, with a carbon–nitrogen compound converts it into self-healing rubber (Fig. 14). This allows the material to link itself again and again after the initial hydrocarbon chains are separated by a tear or hole (Fig. 15).

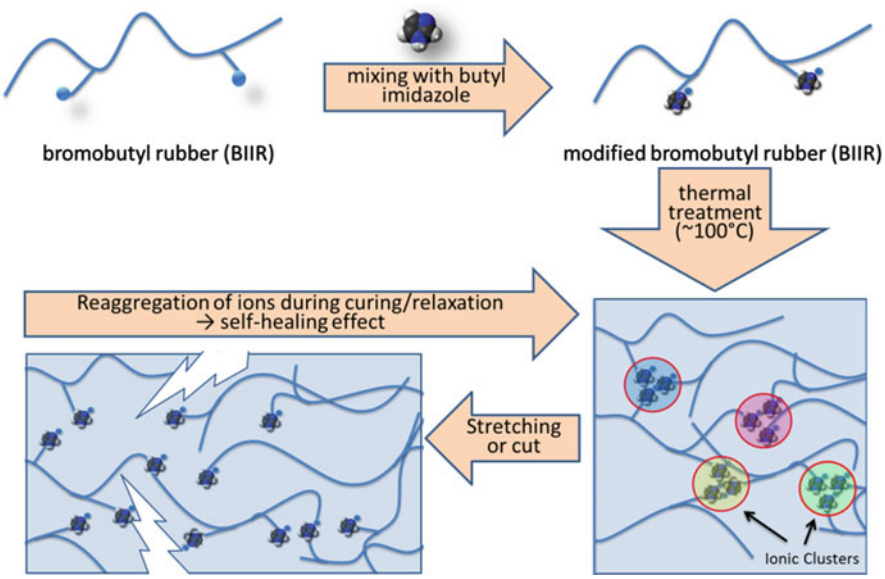

Fig. 14 Modification of bromo-butyl rubber by butyl imidazole. The ionic imidazolium bromide groups thus developed can associate to form a crosslinked-type network structure. This network is broken during damage and rebuilt during healing

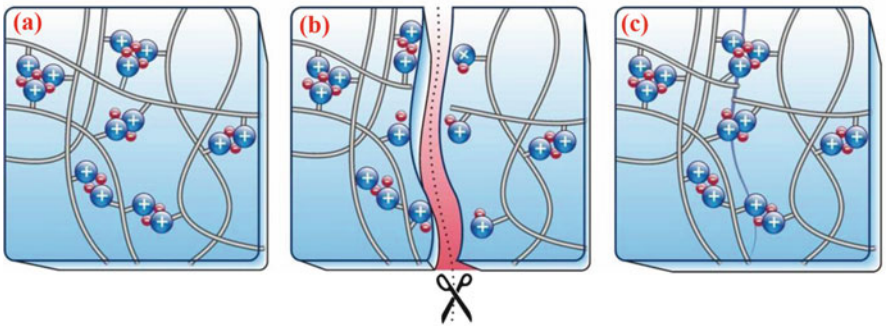

Fig. 15 The self-healing effect demonstrated by re-formation of ionic associates to produce a crosslinked network: (**a**), uncut, (**b**) cut, and (**c**) healed samples [22]

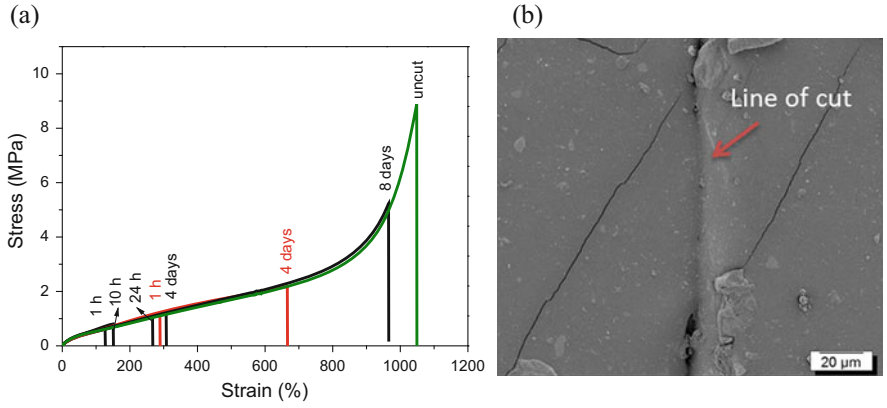

Fig. 16 (**a**) Mechanical data for ionic elastomers. The *green curve* is for an uncut sample; *black curves* represent samples healed for different time periods at room temperature; and the *red curves* are for samples kept at 100°C for first 10 min of their total healing time. (**b**) SEM image of a sample after being healed for 24 h at room temperature. Reprinted with permission from [22]. Copyright 2015 American Chemical Society

After the material is broken or cut, the elastic deformation behavior of the healed sample can be revived again without it being heated or glued. At the same time, the newly developed material is still elastic, stretchable, and tougher than the starting material. Minor damage can be repaired under laboratory conditions within just 1 h at room temperature. The self- healing process of the modified rubber is depicted in Fig. 15. The ionic elastomer shows less hysteresis in the cyclic stress–strain plot than the sulfur-cured rubber. In the quasi-static stress–strain plot (Fig. 16a), the sample elongates up to 960% at a stress of 5.2 MPa (black curves) after 192 h of annealing. In an effort to improve the healing capability, the cut and restored sample was kept at 100°C for the first 10 min of the total healing time (red curves). The healing time substantially drops as a result. The mended sample eventually

showed elongation at break of 630% after 96 h of healing. The corresponding stress–strain plot is demonstrated in Fig. 16a. Figure 16b shows an SEM image of the surface of a sample after a healing period of 24 h at room temperature. It is clear from this image that the cut is almost repaired. However, after healing a clear mark is prominently visible along the line of damage. Mechanical cutting can make an incision in both the ionic associates and the polymer chains and therefore complete healing of the cut is not possible. However, a closer look at this cut shows that the sharp line of the cut is almost filled by polymer.

In addition to the damaged areas (line of cut) some other fine cracks are also observed throughout the surface. These fine cracks arise as a result of the sensitivity of butyl rubber chains to high energy electron irradiation during SEM imaging and preparation of the sample by the gold-sputtering technique. This is very typical of butyl rubber [87].

As well as highly important commercial rubbers such as butyl rubber, XNBR-based ionic elastomers have also been explored for self-healing ability. It was mentioned earlier that the network induced by ionic crosslinking between zinc source and polar XNBR matrix leads to microphase separation and that such a phenomenon is accountable for a thermally reversible network. As a result, dynamic bonds are created in the system that generate self-healing ability in such ionomeric elastomers. Hohlbein et al. [88] reported a potential self-healing rubber based on XNBR that showed extraordinary mechanical, thermal, and dynamic properties. In their study, temperature-dependent dynamic mechanical analysis clearly indicated a positive shift of the crossover point to higher frequencies at higher temperature, whereas a shift of the ionic transition towards higher temperatures with elevated frequency was also noticed.

3.2 Dielectric Actuation

Their versatile nature, unique physical properties, facile processability, and easy modification have made ionic elastomers well-researched materials for cutting-edge technologies. Design of dielectric elastomers based on ionomers has been explored to a significant extent. Ionogels synthesized by Chen et al. [89] based on acrylic elastomers show remarkable dielectric actuation. Ionogels are defined as a 3D network of macromolecular chains in an ionic liquid. A schematic of the fundamental difference between a solution and an ionogel is depicted in Fig. 17. This system attained an electrical conductivity of 0.2 S m^{-1}. Electromechanical transducers with voltage-induced areal elongation of 140% have been designed using the ionogel and an acrylic-based dielectric elastomer. An additional feature of this functional system is transparency, which enables the development of smart and sophisticated materials such as noise-reducing windows [90], tunable lenses [91], etc.

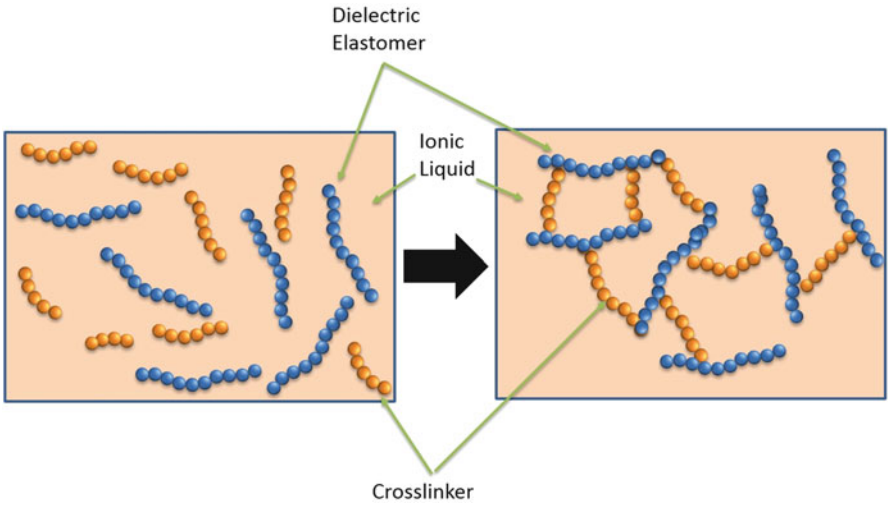

Fig. 17 Solution (*left*) and ionogel (*right*)

Yu et al. [92] investigated how to reduce the large driving voltages of the dielectric elastomers to make them industrially viable. As a remedy, this group developed an interpenetrating network (IPN) based on amino- and carboxylic-functionalized inorganic silicone rubber. High permittivity without compensating the elastic modulus was obtained with such system, leading to fabrication of a satisfactory dielectric elastomer actuator. The dielectric permittivity as a function of frequency (0.1 Hz) is exhibited in Fig. 18. It is clearly revealed from this ternary plot that ionic networks possess a higher dielectric permittivity (~7.49×10^3) than pure polydimethylsiloxane (PDMS) (~3.17) and IPN (~2.05×10^3). Dielectric permittivity is reported to increase linearly with increased ionic concentration in the macromolecular structure. The primary reason for this is that the ionic groups in the IPN bestow a relatively higher dielectric permittivity, whereas the host elastomer (i.e., silicone rubber) imparts a substantially high mechanical strength [92].

3.3 Shape Memory Behavior

Motivated by the potential use of nanostructured ionic elastomers as dielectric actuators, researchers also explored these materials for the development of intelligent shape memory polymers (SMPs). SMPs are generally defined as polymers that are capable of altering their shape in response to external stimuli such as heat, light, electric or magnetic fields, and pH [93]. Heat-induced SMPs are mostly studied in the branch of elastomeric materials. Because of their crosslinked network, SMPs possess a stable and permanent structure. But, when heated above a critical temperature, denoted T_c, they can be deformed to a temporary shape, yielding a

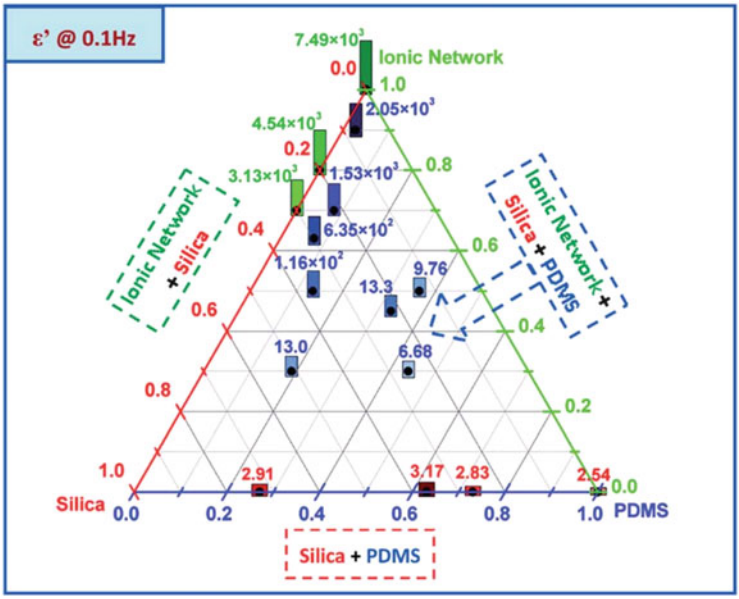

Fig. 18 Dielectric permittivity of the ionic network, PDMS, and the interpenetrating network as a function of frequency (0.1 Hz) [92]

reversible network. This semipermanent shape is retained until the sample is reheated to a temperature higher than T_c, without using any external stress to recover its original and primary structure. Malmierca et al. developed an ionic elastomer based on XNBR neutralized with zinc and magnesium oxides that shows remarkable promise as an SMP [94]. A mixed crosslinking system comprising covalent and ionic networks effectively generates the shape memory effect in this system. Vulcanization with dicumyl peroxides (unsaturation of the XNBR chains) yields a covalent network, which influences the ionic network formed by the interaction of $–COO^-$ and Zn^{2+} or Mg^{2+} ions to fabricate an intelligent material. Peroxides influence the recovery step, whereas a more dynamic network created by the ionic association amends the elastic force to fix the semipermanent shape.

Cai et al. [95] reported a shape memory effect possessing a shape-memory ratio of around 99.5% in a poly(glycerol–sebacate) (PGS)-based elastomer. The PSG elastomer is a straight strip at room temperature in its initial state (Fig. 19). However, with only slight changes in temperature and deformation, the samples continuously undergo changes in shape. Within 20 s of elevating the temperature, the soft rubber strip regains its original shape (~99% recovery). The ionically crosslinked segments in the network impart rigidity, whereas the amorphous part generates reversibility.

Zia et al. [96] synthesized an SMP based on a PU elastomer compounded with chitin and other chemicals. Dimethylol propionic acid was one of the chemicals used to fabricate this type of ionic elastomer. It contains two primary hydroxyl

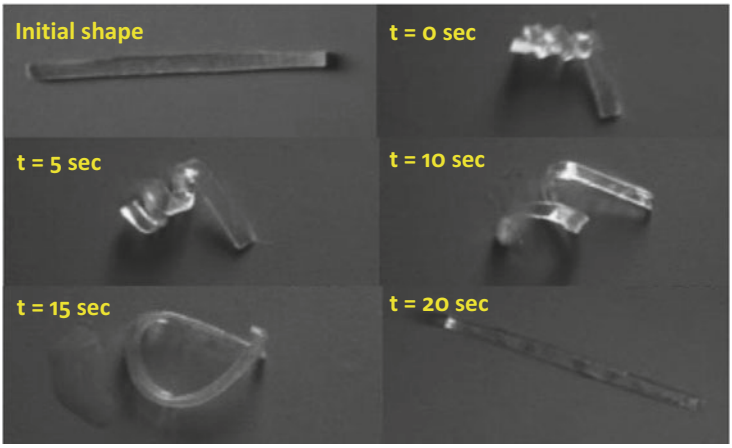

Fig. 19 Shape memory effect of poly(glycerol sebacate)-based elastomer at different exposure times. Reprinted with permission from [95]. Copyright 2008 Elsevier

groups and one tertiary carboxyl group in its chemical structure, which essentially work as the ionic centers. The ionic centers govern the availability of functional polar groups, making the PUs hydrophilic, and eventually enhances the surface free energy of elastomer. By contrast, chitin makes the surface more hydrophobic.

The end properties of the SMP can be controlled by tuning the contents of the two contrastingly featured chemicals in the PU elastomers. Weiss et al. [97] designed a novel SMP system based on ionic elastomers comprising sulfonated EPDM and low molar mass fatty acids and their salts (e.g., zinc stearate). The novelty of such SMPs lies in the variation in critical temperature (T_c), providing an opportunity to develop a thermoresponsive smart elastomeric material. Below the T_c, the physical crosslinking developed by the ionomeric network imparts the necessary bond strength. On the other hand, melting of the fatty acids above T_c enables reshaping of the material according to demand.

In another report, Dong et al. [98] explored the shape memory effect of zinc oleate-based SEPDM ionic elastomer. Fine particles of zinc oleate dispersed in sulfonated ionic EPDM construct a semipermanent or temporary network, as shown in Fig. 20. By contrast, driven by a strong ionic association by the zinc carboxylate linkage for relatively longer relaxation times, physical crosslinking is formed that is permanent in nature [24]. The shape memory path displayed in Fig. 21 demonstrates the entire effect with respect to temperature. In cycle 1, the temperature of the specimen was raised to ~100°C in the absence of any external stress and, as a result, about 36% elongation was gained (cycle 2). The specimen then was cooled down to ambient temperature and elongation reached approximately 70% as a result of crystallization of the fatty acids (zinc stearate) (cycle 3). Then, the stress was released (cycle 4) to obtain a semipermanent elongation of about 67%. From this point, the temperature of the specimen was once again raised to ~70°C (path 5) and this immediately started the dimensional recovery. A temperature of 70°C was

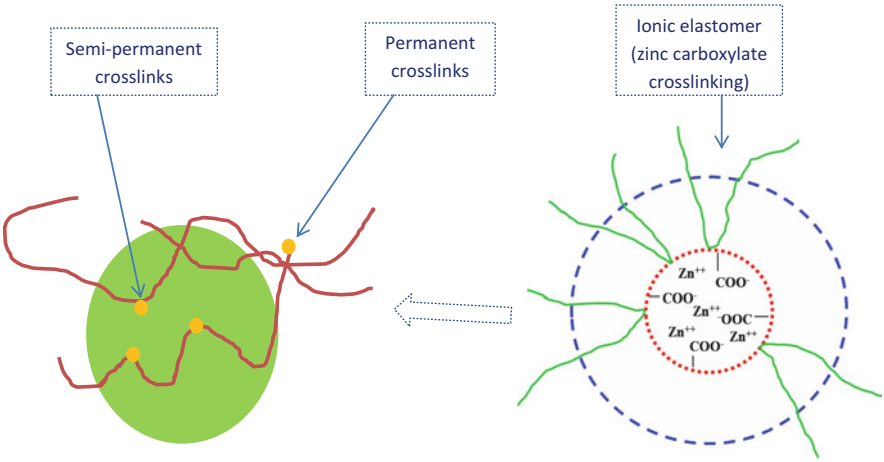

Fig. 20 Representation of an 'ionic crosslinked elastomer' in the fabrication of shape memory polymers based on Zn-SEPDM [98]

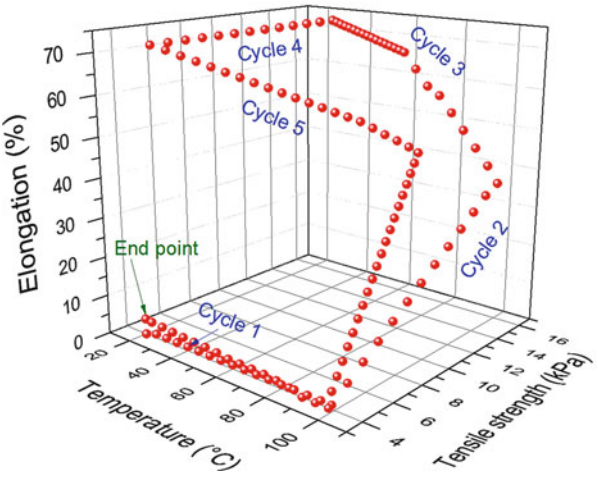

Fig. 21 Entire shape memory cycles for a zinc sulfonated EPDM specimen during stress–strain experiments under the influence of temperature [98]

therefore designated as the critical temperature (T_c) for this system. The temperature was further increased to 100°C and the specimen kept at this temperature for 30 min to reach equilibrium, followed by cooling to room temperature. About 104% dimensional recovery was reported for this ionomeric elastomer at the end point of the entire experiment (indicated in Fig. 21).

4 Summary and Outlook

Nanostructured ionic elastomers have, over the years, been one of the most vigorously researched materials worldwide. The ever-growing interest in such materials is a result of their architectural versatility, which provides the opportunity to tune the structure–property relationship according to demand. Simple modification of the chemical structure, addition of polar functionalities in the host elastomers, or neutralization of the functional polymer with suitable metal cations have had a profound impact on rubber research. As a consequence, function-integrated properties have been achieved for such materials. Besides the remarkable enhancement in conventional properties such as mechanical reinforcement, dynamic properties, thermal properties, processability, and dielectric properties, some sophisticated features are also seen in these materials. Nanostructured ionic elastomers can be distinguished from conventionally crosslinked elastomers in the light of their dynamic and reversible crosslinking, which is physical in most cases in contrast to chemical covalent crosslinks. The long-range elasticity created via sulfur or peroxides as a result of the network of covalent crosslinks between chains is usually permanent and irreversible; hence, recycling of such systems is a challenging task to be addressed. Incorporation of metal cations is primarily responsible for development of ionic character in the polymer backbone, leading to ionic association of the groups, which ultimately leads to formation of a network structure of the rubber chains. The ionic domains created in this way can be destroyed (melting) at elevated temperatures. The higher magnitude of the activation energy obtained in case of ionic elastomers is also ascribed to the availability of less free volume (required for the mobility of chains), that is, to more restricted mobility of the polymers in comparison with covalently cured rubbers.

Crack propagation, a very significant property for commercial vehicle tires, is improved in ionically modified rubbers, as shown by tear fatigue experiments. As a result of the presence of ionic clusters, the crack propagation rate is significantly lower in ionic elastomers. The ionic clusters present in the crack tip can be dissociated into smaller aggregates, but these aggregates are not completely destroyed. Moreover, the ion hopping phenomenon causes further re-aggregation or re-association of the ion pairs, leading to a higher crack resistance. Novel nanostructured ionomers based on different elastomers (e.g., XNBR, sulfonated EPDM, PU, liquid crystalline elastomers) have been discussed in detail, focusing on their structure–property relationships and their applications. In spite of the challenges involved in characterizing these heterogeneous materials because of the involvement of multiple length and time scales, various novel methods such as SAXS, high-resolution TEM, and multiple quantum NMR spectroscopy have been employed to gain insight into the fundamental mechanisms. The know-how obtained was utilized to design smart materials out of these nanostructured elastomeric ionomers. The result is SMPs, dielectric actuators, self-healing polymers etc., which are being developed to raise our quality of life.

However, there is still a long way to go to comprehensively understand the various complex mechanisms involved in different systems of ionic elastomers. The existence of multiplets, ionic clusters as speculated by a number of researchers, is yet to be evidenced by direct experimental analysis. Various other complicated properties of nanostructured ionic elastomers related to the labyrinthine structure–property issue make life challenging for researchers. Real-life application of such materials at a large scale is still a dream and needs to be converted into a feasible reality. Nevertheless, the rising potential and promise that these materials have shown means that there is very little doubt among academicians and industrialists that this is going to be an exciting topic to explore in the future.

5 Personal Note of Debdipta Basu

I started studying for my Ph.D. in department of elastomer at IPF, Dresden in May 2011 and was awarded my Ph.D. in November 2015. My experience of studying at IPF was extremely soothing. The department was extremely supportive in creating a suitable atmosphere for me to carry out my research by providing me access to a good infrastructure and mechanisms of support from all my colleagues. Collaborative framework and cross-functional culture at the institute made my job pretty easy.

Prof. Gert Heinrich, my supervisor was brilliant. He is truly an ocean of knowledge in the discipline of elastomer. Being a student, I tried my level best to soak in all the incandescent glow of wisdom he offered in this period of time. In-depth analysis, accuracy, proficiency, pin-point explanations, innovativeness are some of the key virtues I learned from him. Prof. Heinrich always encouraged me to explore new fields in order to get a broader perspective and bring together innovative ideas and methodologies to the cutting-edge research projects to solve the current problems. Apart from the scientific aspects, his humbleness, simplicity and sincerity taught me a great lesson in life. He was sensitive to my needs as an international student and supported me to be able to study well at IPF. He also encouraged and supported me to attend various conferences, apply for grants and subsequently plan my future after my research.

Presently being involved in a job as a scientist, I want to practice the same philosophy inculcated from him to solve the technical issues relevant to the organization and bring in a lot of positive energy to expedite the system.
On this auspicious occasion of his 65th birthday, I wish Prof. Heinrich a happy birthday and pray to the Omnipotent for his good health and prosperity.

Debdipta Basu, Bangalore, India

References

1. Treloar LRG (2005) The physics of rubber elasticity. OUP, Oxford
2. Flory PJ (1985) Molecular theory of rubber elasticity. Polym J 17:1–12
3. Hofmann W (1989) Rubber technology handbook. Oxford University Press, Oxford
4. Schüssele AC, Nübling F, Thomann Y, Carstensen GB, Speck T, Mülhaupt R (2012) Macromol Mater Eng 297:411–419
5. Rees RW, Vaughan DJ (1965) Polym Prepr (Am Chem Soc Div Polym Chem) 6:287
6. Eisenberg A (1970) Clustering of ions in organic polymers—a theoretical approach. Macromolecules 3:147–154
7. Basu D, Das A, Stöckelhuber KW, Jehnichen D, Formanek P, Sarlin E, Vuorinen J, Heinrich G (2014) Evidence for an in-situ developed polymer phase in ionic elastomers. Macromolecules 47(10):3436–3450
8. MacKnight WJ, Lundberg RD (1984) Elastomeric ionomers. Rubber Chem Technol 57 (3):652–663
9. Eisenberg A, Hird B, Moore RB (1990) A new multiplet-cluster model for the morphology of random ionomers. Macromolecules 23:4098–4107
10. Hird B, Eisenberg A (1992) Sizes and stabilities of multiplets and clusters in carboxylated and sulfonated styrene ionomers. Macromolecules 25:6466–6474
11. MacKnight WJ (1987) Available ionomers. In: Pineri M, Eisenberg A (eds) Structure and properties of ionomers. NATO science series C: mathematical and physical sciences, vol 198. Reidel, Dordrecht, pp 1–9
12. MacKnight WJ, Earnest TR (1981) Macromol Rev 16:41
13. Bazuin GC, Eisenberg A (1981) Ind Eng Chem Prod Res Dev 20:271
14. Khokhlov AR, Dormidontova EF (1997) Self-organization in ion-containing polymer systems. Phys Usp 40:109–124
15. Nyrkova IA, Khokhlov AR, Doi M (1993) Microdomains in block copolymers and multiplets in ionomers: parallels in behavior. Macromolecules 26:3601–3610
16. Eisenberg A (1967) Ionic forces in polymers. Adv Polym Sci 5:59–112
17. McGrath JE (ed) (1981) Anionic polymerization: kinetics, mechanisms, and synthesis. ACS Symposium Series, vol 166. American Chemical Society, Washington
18. Basu D, Das A, Stöckelhuber KW, Wagenknecht U, Heinrich G (2014) Advances in layered double hydroxide (LDH)-based elastomer composites. Prog Polym Sci 39:594–626
19. Masala O, Seshadri R (2004) Synthesis routes for large volumes of nanoparticles. Annu Rev Mater Res 34:41–81
20. Lundberg RD, Markowski HS (1980) A comparison of sulfonate and carboxylate ionomers. In: Eisenberg A (ed) Ions in polymers. ACS advances in chemistry series, vol 187. American Chemical Society, Washington, pp 21–36
21. Jenkins DK, Duck EW (1975) In: Holliday L (ed) Ionic polymers. Halstead Press, Wiley, New York (chap. 3)
22. Das A, Sallat A, Böhme F, Suckow M, Basu D, Wiessner S, Stöckelhuber KW, Voit B, Heinrich G (2015) Ionic modification turns commercial rubber into a self-healing material. ACS Appl Mater Interfaces 7:20623–20630
23. Basu D (2015) Role of zinc containing compounds in nitrile rubber based micro-and nanocomposites. Thesis in TU Dresden, Germany
24. Ibarra L, Marcos-Fernández A, Alzorriz M (2002) Mechanistic approach to the curing of carboxylated nitrile rubber (XNBR) by zinc peroxide/zinc oxide. Polymer 43:1649–1655
25. Ibarra L, Alzorriz M (2003) Ionic elastomers based on carboxylated nitrile rubber and calcium oxide. J Appl Polym Sci 87:805–813
26. Ibarra L, Alzorriz M (2007) Ionic elastomers based on carboxylated nitrile rubber and magnesium oxide. J Appl Polym Sci 103:1894–1899

27. Tungchaiwattana S, Musa MS, Yan J, Lovell PA, Shaw P, Saunders BR (2014) The role of acrylonitrile in controlling the structure and properties of nanostructured ionomer films. Soft Matter 10:4725–4734
28. Chakraborty SK, Bhowmick AK, De SK (1981) Mixed cross-link systems in elastomers. J Macromol Sci Polym Rev 21:313–332
29. Jong L (2005) Viscoelastic properties of ionic polymer composites reinforced by soy protein isolate. J Polym Sci B Polym Phys 43:3503–3518
30. Malmierca MA, González-Jiménez A, Mora-Barrantes I, Posadas P, Rodríguez A, Ibarra L, Nogales A, Saalwächter K, Valentín JL (2014) Characterization of network structure and chain dynamics of elastomeric ionomers by means of 1H low-field NMR. Macromolecules 47:5655–5667
31. Kurian T, Khastgir D, De PP, Tripathy DK, De SK, Peiffer DG (1995) Reinforcement of EPDM-based ionic thermoplastic elastomer by carbon black. Polymer 36:3875–3884
32. Markowski HS, Lundberg RD, Westerman L, Bock J (1980) Synthesis and properties of sulfonated EPDM. In: Eisenberg A (ed) Ions in polymers. ACS, vol 187. American Chemical Society, Washington, pp 3–19
33. Kurian T, De PP, Tripathy DK, De SK, Peiffer DG (1996) Effect of clay on properties of ionic thermoplastic elastomer based on EPDM. J Appl Polym Sci 62:1729–1734
34. Ghosh SK, Bhattacharya AK, De PP, Khastagir D, De SK (2001) Effect of zinc stearate on properties of melt processable ionomer based on sodium salt of sulfonated maleated EPDM rubber. Plast Rubber Compos 1:16–22
35. Yano S, Nagao N, Hattori M, Hirasawa E, Tadano K (1992) Dielectric relaxations of ethylene ionomers. Macromolecules 25:368
36. Yano S, Tadano K, Nagao N, Kutsumizu S, Tachino H, Hirasawa E (1992) Dielectric relaxation studies on water absorption of ethylene ionomers. Macromolecules 25:7168
37. MacKnight WJ, McKenna LW, Read BE (1968) Properties of ethylene-methacrylic acid copolymers and their sodium salts: mechanical relaxations. J Appl Phys 38:4208
38. Mandal UK, Tripathy DK, De SK (1995) Effect of silica filler on dynamic mechanical properties of ionic elastomer based on carboxylated nitrile rubber. J Appl Polym Sci 55:1185–1191
39. Mandal UK, Tripathy DK, De SK (1993) Moving die rheometry and dynamic-mechanical studies on the effect of reinforcing carbon-black filler on ionomer formation during cross-linking of carboxylated nitrile rubber by zinc-oxide. Polymer 34:3832–3836
40. Mandal UK, Tripathy DK, De SK (1995) Effect of reinforcing carbon black fillers on dynamic mechanical properties of ionic elastomer based on carboxylated nitrile rubber. Plast Rubber Comp Proc Appl 24:19–25
41. Datta S, De SK, Kontos EG, Wefer JM (1996) Ionic thermoplastic elastomer based on maleated EPDM rubber. I. Effect of zinc stearate. J Appl Polym Sci 61:177–186.
42. Navratil M, Eisenberg A (1984) Ion clustering and viscoelastic relaxation in styrene-based ionomers. III. Effect of counterions, carboxylic groups, and plasticizers. Macromolecules 7:84–89
43. Weiss RA, Fitzerald JJ, Kim D (1991) Viscoelastic behavior of plasticized sulfonated polystyrene ionomers. Macromolecules 24:1064–1070
44. Lundberg RD (1987) Ionomer solution behavior. In: Pineri M, Eisenberg A (eds) Structure and properties of ionomers. NATO science series C, vol 198. Reidel, Dordrecht, pp 387–397
45. Agarwal PK, Peiffer DG (1987) Viscoelastic behaviour of blends of ionic thermoplastic elastomers and their precursors. Polym Commun 28:186–190
46. van der Mee MAJ, I'Abee RMA, Portale G, Goossens JGP, van Duin M (2008) Synthesis, structure, and properties of ionic thermoplastic elastomers based on maleated ethylene/propylene copolymers. Macromolecules 41:5493–5501
47. Brenner D, Lundberg RD (1977) Novel flexible foams based on an ionic elastomer. J Cell Plast 13:270–275
48. Drake EN (1994) Polym Prepr Am Chem Soc Div Polym Chem 35:14

49. Jaudouin O, Robin JJ, Lopez-Cuesta JM, Perrin D, Imbert C (2012) Ionomer-based polyurethanes: a comparative study of properties and applications. Polym Int 61:495–510
50. Dieterich D, Keberle W, Wilt H (1970) Polyurethane ionomers, a new class of block polymers. Angew Chem Int Ed Engl 9:40–50
51. Hwang KKS, Yang C-Z, Cooper SL (1981) Properties of polyether-polyurethane zwitterionomers. Polym Eng Sci 21:1027–1036
52. Yang C-Z, Hwang KKS, Cooper SL (1983) Morphology and properties of polybutadiene-and polyether-polyurethane zwitterionomers. Makromol Chem 184:651–668
53. Lee JC, Kim BK (1994) Basic structure–property behavior of polyurethane cationomers. J Polym Sci A Polym Chem 32:1983–1989
54. Estes GM, Cooper SL, Tobolsky AV (1970) J Macromol Sci Rev Macromol Chem 4:313
55. Agganval SL (ed) (1970) Block polymers. Plenum Press, NewYork
56. Noshay A, McGrath JE (eds) (1973) Block copolymers. Wiley, New York
57. Cooper SL, Estes GM (eds) (1979) Multiphase polymers. Adu. Chem. Ser. 176, American Chemical Society, Washington
58. Clough SB, Schneider NS (1968) J Macromol Sci Phys B2:553
59. Clough SB, Schneider NS, King AO (1968) J Macromol Sci Phys B2:641
60. Lee D, Register RA, Yang C, Cooper SL (1988) MDI-based polyurethane ionomers. 1. New small-angle X-ray scattering model. Macromolecules 21:998–1004
61. Lee D, Register RA, Yang C, Cooper SL (1988) MDI-based polyurethane ionomers. 2. - Structure-property relationships. Macromolecules 21:1005–1008
62. Kim B, Yang J, Yoo S, Lee J (2003) Waterborne polyurethanes containing ionic groups in soft segments. Colloid Polym Sci 281:461–468
63. Mondal S, Hu JL (2006) Structural characterization and mass transfer properties of nonporous segmented polyurethane membrane: Influence of hydrophilic and carboxylic group. J Memb Sci 274:219–226
64. Nierzwicki W, Rutkowska M (1986) Ionic interactions and microphase separation in urethane elastomers. Polym Commun 27:327–329
65. Lee BS, Chun BC, Chung YC, Sul KI, Cho JW (2001) Structure and thermomechanical properties of polyurethane block copolymers with shape memory effect. Macromolecules 34:6431–6437
66. Chwang CP, Lee SN, Kuo YM, Chao S, Chao DY (2002) On the study of polyurethane ionomer-Part I. Polym Adv Technol 13:285–292
67. Chwang CP, Lee SN, Kuo YM, Chao S, Chao DY (2002) On the study of polyurethane ionomer-Part II. Polym Adv Technol 13:293–300
68. Kim BY, Lee SY, Lee JS, Baek SH, Choi YJ, Lee JO, Xu M (1998) Polyurethane ionomers having shape memory effects. Polymer 39:2803–2808
69. Gogolewski S (1989) Selected topics in biomedical polyurethanes: a review. Colloid Polym Sci 267:757–785
70. Barbucci R, Benvenuti M, Dal Maso G, Nocentini M, Tempesti F, Losi M (1989) Synthesis and physicochemical characterization of a new material (PUPA) based on polyurethane and poly(amido-amine) components capable of strongly adsorbing quantities of heparin. Biomaterials 10:299–308
71. Barbucci R, Magnani A (1989) Physiochemical characterization and coating of polyurethane with a new heparin-adsorbing material. Biomaterials 10:429–431
72. Bakker D, Van Blitterswijk CA, Hesseling SC, Koerten HK, Kuijpers W, Grote JJ (1990) Biocompatibility of a polyether urethane, polypropylene oxide, and a polyether polyester copolymer. A qualitative and quantitative study of three alloplastic tympanic membrane materials in the rat middle ear. J Biomed Mater Res 24:489–515
73. Bruin P, Jonkman MF, Meijer HJ, Pennings AJ (1990) A new porous polyetherurethane wound covering. J Biomed Mater Res 24:217–226
74. Faust R, Kennedy JP (1987) Living carbocationic polymerization IV. Living polymerization of isobutylene. J Polym Sci Polym Chem Ed 25:1847

75. Allen RD, Yilgor I, McGrath JE (1986) Studies on synthetic block ionomers. In: Eisenberg A, Baily FE (eds) Coulombic interactions in macromolecular systems. ACS symposium series, vol 302. American Chemical Society, Washington, pp 79–92
76. Weiss RA, Sen A, Willis CL, Pottick LA (1991) Block copolymer ionomers: 1. Synthesis and physical properties of sulfonated poly(styrene-ethylene/butylene-styrene). Polymer 32:1867–1874
77. WolImann D, Williams CE, Eisenberg A (1990) Small-angle X-ray scattering in "bottlebrush" ionomers. J Polym Sci Polym Phys Ed 28:1979
78. Storey RF, George SE, Nelson ME (1991) Star-branched block copolymer ionomers: synthesis, characterization, and properties. Macromolecules 24:2920–2930
79. Vanhest JCM, Baars MWPL, Elissan-Roman C, Van Genderen MHP, Meijer EW (1995) Acid-functionalized amphiphiles, derived from polystyrene-poly(propylene imine) dendrimers, with a pH-dependent aggregation. Macromolecules 28:6689–6691
80. Vargantwar PH, Shankar R, Krishnan AS, Ghosh TK, Spontak RJ (2011) Exceptional versatility of solvated block copolymer/ionomer networks as electroactive polymers. Soft Matter 7:1651–1655
81. Meng FB, Zhang BY, Liu LM, Zang BL (2003) Liquid-crystalline elastomers produced by chemical crosslinking agents containing sulfonic acid groups. Polymer 44:3935–3943
82. Vuillaume PY, Galin JC, Bazuin CG (2001) Ionomer and mesomorphic behavior in a tail-end, ionic mesogen-containing, comblike copolymer series. Macromolecules 34:859–867
83. Bualek S, Kapitza R (1988) Orientability of crosslinked and of chiral liquid crystalline polymers. Mol Cryst Liq Cryst 155:47–56
84. Meng FB, Zhang BY, Jia YG, Yao DS (2005) Effect of ionic aggregates of sulfonated groups on the liquid crystalline behaviours of liquid crystalline elastomers. Liq Cryst 32:183–189
85. Paeglis AU, O'Shea FX (1988) Thermoplastic elastomer compounds from sulfonated EPDM ionomers. Rubber Chem Technol 61:223–237
86. Nogueira AF, Alonso-Vante N, De Paoli M-A (1999) Solid-state photoelectrochemical device using poly(o-methoxy aniline) as sensitizer and an ionic conductive elastomer as electrolyte. Synth Met 105:23–27
87. Telnov AV, Zavyalov NV, AKhokhlov Y, Sitnikov NP, Smetanin ML, Tarantasov VP, Shadrin DN, Shorikov IV, Liakumovich AL, Miryasova FK (2002) Radiation degradation of spent butyl rubbers. Radiat Phys Chem 63:245–248
88. Hohlbein N, Pelzer T, Nothacker J, von Tapavicza M, Nellesen A, Datta H, Schmidt AM (2013) Self-healing processes in ionomeric elastomers. In: ICSHM 2013: Proceedings of the 4th international conference on self-healing materials, Ghent, Belgium, 16–20 June 2013. Magnel Laboratory for Concrete Research, Ghent, pp 680–683
89. Chen B, Lu JJ, Yang CH, Yang JH, Zhou J, Chen YM, Suo Z (2014) Highly stretchable and transparent ionogels as nonvolatile conductors for dielectric elastomer transducers. Appl Mater Interfaces 6:7840–7845
90. Yu X, Rajamani R, Stelson K, Cui T (2006) Carbon nanotube-based transparent thin film acoustic actuators and sensors. Sens Actuat A 132:626–631
91. Shian S, Diebold RM, Clarke DR (2013) Tunable lenses using transparent dielectric elastomer actuators. Opt Express 21:8669–8676
92. Yu L, Madsen FB, Hvilsted S, Skov AL (2015) Dielectric elastomers, with very high dielectric permittivity, based on silicone and ionic interpenetrating networks. RSC Adv 5:49739–49747
93. Lendlein A, Kelch S (2002) Shape-memory polymers. Angew Chem Int Ed 41:2034–2057
94. Malmierca MA, Mora-Barrantes I, Posadas P, González-Jiménez A, Rodríguez A, Ibarra LM, Valentín JL (2013) Development of ionic elastomers with shape memory effect. In: Gil-Negrete N, Alonso A (eds) Constitutive models for rubber VIII. CRC, Boca Raton, pp 689–692
95. Cai W, Liu L (2008) Shape-memory effect of poly (glycerol-sebacate) elastomer. Mater Lett 62:2171–2173

96. Zia KM, Zuber M, Barikani M, Bhatti IA, Khan MB (2009) Surface characteristics of chitin-based shape memory polyurethane elastomers. Colloids Surf B Biointerfaces 72:248–252
97. Weiss RA, Izzo E, Mandelbaum S (2008) New design of shape memory polymers: mixtures of an elastomeric ionomer and low molar mass fatty acids and their salts. Macromolecules 41:2978–2980
98. Dong J, Weiss RA (2011) Shape memory behavior of zinc oleate-filled elastomeric ionomers. Macromolecules 44:8871–8879

Adv Polym Sci (2017) 275: 267–318
DOI: 10.1007/12_2016_5

Published online: 10 July 2016

Graphene-Based Elastomer Nanocomposites: Functionalization Techniques, Morphology, and Physical Properties

Titash Mondal, Anil K. Bhowmick, Ranjan Ghosal, and Rabindra Mukhopadhyay

Abstract Understanding the fundamentals involved in the fabrication of an elastomer nanocomposite is crucial for the development of high performance materials. Despite a plethora of studies of different types of elastomer nanocomposites, work related to the development of graphene-based elastomer nanocomposites has only gained precedence in recent years. Because the inherent structure of graphene often limits its processability inside a high molecular weight elastomer matrix, various strategies have been adopted to control the dispersion of graphene in an elastomer. In this chapter, representative and commercially important elastomers are selected for discussion. The effect of different processing routes for the preparation of elastomer/graphene nanocomposites and their correlation with dispersion of the graphene-based filler in the elastomer matrix are discussed in detail. Parameters controlling strength, thermal stability, barrier properties, and dielectric behavior are discussed. This chapter gives a comprehensive review of the preparation of graphene/elastomer nanocomposites and also provides an idea of the structure–property relationships that exist for such nanocomposites.

Keywords Functionalization • Graphene • Graphite • Rubber

T. Mondal and A.K. Bhowmick (✉)
Rubber Technology Centre, Indian Institute of Technology Kharagpur, Kharagpur 721302, India
e-mail: anilkb@rtc.iitkgp.ernet.in

R. Ghosal
SKI Carbon Black (Birla Carbon) R&D, Taloja, Mumbai 410208, India

R. Mukhopadhyay
HASETRI, J. K. Tyre & Industries Ltd., Kankroli 313342, India

Contents

1 Prelude to Graphite and Graphene

Research related to the development of elastomer or polymer nanocomposites based on graphite or graphene is gaining widespread popularity in the polymer science and technology community because of the unique properties exhibited by these two nanofillers [1–5]. The distinctive structures of graphite and graphene molecules play a crucial role in determining the properties of the nanocomposite. Although a plethora of research work has been carried out with other carbon nanomaterials such as carbon nanotubes and fullerene, there has been an exponential growth of research work relating to graphene and graphite in the last decade [6–10]. Graphene, although the newest member of the carbon allotrope family, is nevertheless often referred to as the mother of all carbon nanomaterials. Zero-dimensional fullerenes, one-dimensional (1D) carbon nanotubes, and three-dimensional (3D) graphite can be generated through the wrapping, rolling, and stacking, respectively, of the graphene sheet.

The use of graphite was noted as early as the fourth millennium BCE, as a constituent of paint used for pottery decoration [11]. The term "graphite" was coined from the Greek term *grapho* meaning the ability to write/draw. Whenever graphite is used for writing or marking a surface, a layer of graphene is expelled onto the marked surface, a fact that has generally remained un-noticed for generations. The reason that graphite marks any surface it is rubbed against can be attributed to the structure of graphite. Its layered structure, with stacks of graphene sheets held together by means of van der Waals interactions, results in the deposition of some of these layers onto the marked surface whenever any mechanical force is applied to the graphite.

Apart from being used as a material for painting purposes, graphite was the subject of chemical research in the eighteenth century, when the first intercalated compound of graphite was reported [12]. A mixture of sulfuric acid and nitric acid was used for exfoliation of graphite [13]. The eminent scientist Brodie took an interest in determining the molecular weight of graphite. He used strong oxidants such as potassium perchlorate for his reaction recipe. Serendipitously, he discovered a new type of compound, graphite oxide [14]. Following his research, there

were a series of experiments by stalwarts such as Staudenmaier, Hummers, and Offeman [15, 16].

In the nineteenth century, Brodie's method of oxidation was coupled with the additional step of reduction, as described by Boehm [17]. Chemicals such as hydrazine and hydrogen sulfide were utilized as reducing agents. The products obtained after reduction were subjected to transmission electron microscopy (TEM). The thickness of the material obtained was different to that generally reported for graphite. Such an observation led Boehm to surmise that the product isolated had the structure of a single carbon layer. Boehm proposed to name the material "graphene." The "ene" part indicates the fused polyaromatic structure and the "graph" part indicates its roots in graphite [18]. Later, the terminology was recognized by the International Union of Pure and Applied Chemistry (IUPAC) [19].

In the twentieth century, the graphene "gold rush" began when it was first observed to exist as a 2D crystal. The micromechanical exfoliation technique was developed by researchers based at the University of Manchester. Scotch tape was used to peel off layers of highly oriented pyrolitic graphite (HOPG) [8]. Under the microscope, these materials demonstrated a single-layer structure and had exceptional properties, which were normally impossible to achieve using graphite.

It is crucial to acquaint readers with the different terminologies involved when discussing problems related to graphene and graphite. *Graphene* refers to the single-atom thick sheet of sp^2 hybridized carbon atoms arranged in a hexagonal array of infinite size (the lateral dimension being limited to the order of a few nanometers to micrometers). *Multilayer graphene* refers to the presence of two to nine layers of graphene sheets. When the number of layers of graphene is limited to between two and five, it is commonly referred to as *few-layer graphene*. These three materials are essentially 2D in nature. *Graphite* is a 3D material. Commonly encountered terms such as *graphite nanoplates, graphite nanosheets*, and *graphite nanoflakes* refer to 3D materials with a thickness or lateral dimension that is less than 100 nm. *Expanded graphite* refers to the class of materials prepared by partial exfoliation of graphite using thermal, chemical, or mechanical techniques that do not sacrifice the 3D nature of the precursor material [20–24].

1.1 Insight into the Structure and Properties of Graphene

Graphene demonstrates a 2D hexagonal lattice system, as shown in Fig. 1a. This hexagonal lattice (with chemically equivalent carbon atoms) ideally does not belong to the Bravais lattice system because of the dissimilarity in the symmetry of the carbon atoms. Such hexagonal lattice systems can be considered to be composed of two triangular lattices with a two-atom basis (a and b in Fig. 1a). Each carbon atom is immediately linked to three other carbon atoms, with a carbon–carbon distance of 0.142 nm. The 2D crystal belongs to the *P6mm* plane group. The rigid structural framework of graphene is attributed to the σ-bond

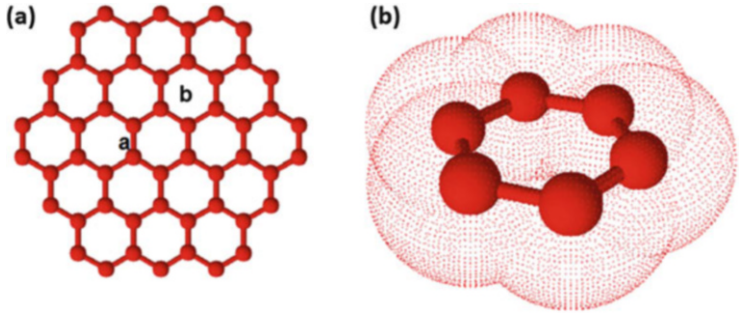

Fig. 1 (**a**) Fragment of a graphene lattice with two triangular sub-lattices, marked *a* and *b*. (**b**) Example of the out-of-plane p_z-orbitals forming a delocalized π-system above and below the graphene plane

formed as a result of the participation of three half-filled valance orbitals. The other half-filled orbital protrudes out of the plane. These out-of-plane orbitals form a delocalized π-cloud over the graphene structure, as shown in Fig. 1b.

Graphene is also well known for its mechanical properties. It is predicted to be 100 times stronger than a hypothetical steel film of similar dimensions [25]. The Young's modulus for graphene is reported to be around 0.5–1 TPa and it has a large spring constant of 1–5 N m^{-1}. The high order of stiffness is attributed to the strong C–C σ-bonds dispersed over a wide area. Two seminal reviews on modification of carbon nanomaterials and the relevant structure and properties of these materials have been published by Bhowmick and coworkers [5, 7].

1.2 Different Strategies for Synthesis of Graphene

With the advent of new chemistries, different strategies have been adapted for the synthesis of graphene and few-layer graphene. Recently, researchers from our group have successfully synthesized graphene using a non-conventional precursor material, styrene butadiene rubber (SBR), in a chemical vapor deposition (CVD) reactor. Distinct flake-like features were observed, as shown in Fig. 2. A similar strategy was extended by us for fabrication of a doped graphene variety from polyurethane acrylate.

The synthesis of graphene and few-layer graphene can be broadly classified into top-down and bottom-up techniques. These are discussed in detail below.

1.2.1 Top-Down Techniques

Long before the scotch tape technique came into the limelight, several efforts were made to isolate graphene using exfoliation and intercalation of graphite [26]. Alkali

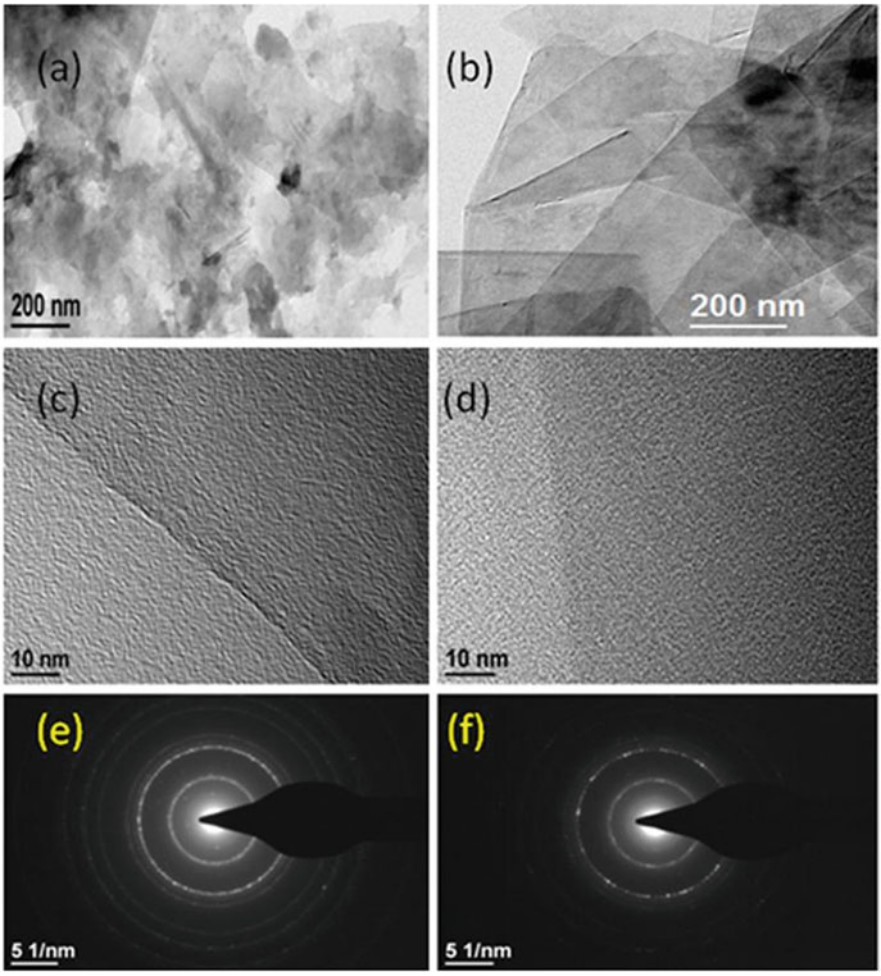

Fig. 2 (**a**, **b**) TEM micrographs, (**c**, **d**) high resolution TEM micrographs, and (**e**, **f**) selected area electron diffraction (SAED) patterns of (**a**, **c**, **e**) nitrogen-doped graphene and (**b**, **d**, **f**) graphene. [Reprinted (adapted) with permission from [9], Copyright 2015, American Chemical Society]

metal ions such as potassium are often employed in the intercalation process. A mixture of graphite and potassium ions is annealed under vacuum. Further treatment of the isolated product with aqueous media gives rise to the exfoliated graphite structure. This is attributed to the formation of potassium hydroxide in the aqueous medium. Apart from this methodology, Falcao et al. [27] reported the possibility of exfoliation of graphite to graphene using microwave irradiation.

The most widely recognized and highly appreciated top-down technique is the micromechanical exfoliation method. In 2004, Novoselov et al. utilized ordinary scotch tape to peel off layers of graphite from the HOPG surface [8]. Further, the graphite stuck to the scotch tape was repeatedly subjected to further peeling. This

resulted in the formation of the world's thinnest crystal. Scalability and cost-effectiveness were matters of concern associated with this technique.

1.2.2 Bottom-Up Techniques

Despite a wide range of successful efforts using the top-down approach, it also has many shortcomings. The need for highly crystalline graphene for electronic purposes was not fulfilled using this experimental protocol. Thus, bottom-up techniques gained popularity. CVD is the most important methodology for the preparation of well-structured, highly crystalline graphene [28]. Gases such as methane, ethane, and propane are circulated inside a reactor in the presence of a metallic substrate [29]. The size of the hydrocarbon precursor, temperature, and pressure were found to be crucial in determining the number of layers of graphene formed [30]. Additionally, polymeric precursors and carbon waste have been reported to be used for generation of high-quality graphene inside the CVD reactor [31–33].

An alternative route, which is equally popular for the generation of structurally well-defined graphene, is the epitaxial growth of graphene on SiC [34]. The production step involves thermal degradation of a single crystal of silicon carbide. The Si atom preferentially sublimes under the experimental conditions and the remaining carbon atoms reorganize to form a graphene structure under high temperature. The preparation, characterization, and properties of graphene have been reviewed in a recent publication [35].

1.3 Functionalization of Graphene and Graphite

Functionalization of carbon nanomaterials has been a matter of wide interest in our laboratory for several years. Sengupta et al. performed the amination of carbon nanotubes using hexamethylenediamine for the development of a polyamide-6,6 nanocomposite [36]. Silane modification and oxidation of carbon nanotubes were also reported by Bhowmick and coworkers for preparation of an ethylene vinyl acetate (EVA) system reinforced with functionalized carbon nanotubes [37]. They further extended the strategy to a graphite/EVA system [38, 39]. It is worth mentioning that the inherent curvature present on the surface of a carbon nanotube plays a pivotal role in any covalent modification. However, such an effect is not active for graphite and graphene. Thus, functionalization of graphite and graphene becomes difficult. From the discussion in Sect. 1.1, it should be noted that the out-of-plane p_z-orbital of graphene forms a delocalized π-cloud. As a result, a self-passivating network is formed over the graphene surface. This causes most organic solvents to have negligible interaction with it (except for *N*-methyl-2-pyrrolidone and *o*-dichlorobenzene). As a result, poor solubility of the pristine material is observed. Further, these p_z-orbitals of graphene are also responsible for the

formation of agglomerative structures through π–π interactions. Thus, poor processing characteristics are associated with the pristine material. Hence, there are reasons why functionalization of graphene is advantageous. In addition, some important pursuits are tailoring of the electrochemical properties of graphene [40], preparation of solution-processable graphene derivatives [41], and synthesis of graphene-based energy materials [42].

1.4 Reactivity of Graphene and Graphite

As discussed in Sects. 1.1 and 1.3, the self-passivating network that is formed over the surface of graphene hinders any kind of chemical modification of its surface. This creates an immense challenge for modification of the basal plane of graphene with any foreign chemicals. In general, factors such as localized charge, weak dangling bonds, and localized orbitals play pivotal roles in surface modification of any material. Unfortunately, graphene lacks all of these properties. Furthermore, any kind of disruption on the surface of graphene results in the formation of high energy radicals on the basal plane of graphene. Such a phenomenon is thermodynamically unfavorable. Apart from the thermodynamic barrier, kinetic constraints also come into play whenever there is any basal plane modification of graphene. Any covalent modification on the surface of graphene induces a change of sp^2 hybridized carbon atoms (planar) to sp^3 (tetrahedral) [43]. As a result of such a change in hybridization, a geometric constraint is introduced over multiple lattices, as shown in Fig. 3a. This causes an increase in the energy barrier at the transition state and effectively hinders the process.

Despite the presence of such shortcomings, covalent modification of graphene is still achievable. In our earlier review, we discussed several possible techniques for functionalization of graphite and graphene [7]. However, in this review, we primarily focus on some typical methods for functionalization of graphite and graphene. The edges of graphene host dangling bonds that react very efficiently with external chemicals, as described by Mondal et al. [44]. A typical example of edge functionalization is shown in Fig. 3b. The most commonly observed edges of graphite and graphene have a zigzag or armchair configuration, as shown in Fig. 4 [45]. There is a striking resemblance between the electronic structures of armchair and zigzag graphenes with those of benzyne and carbene. Thus, zigzag graphene is reported to be more reactive than armchair graphene [46]. Irrespective of its configuration (armchair or zigzag), the edges of graphite and graphene are the most vulnerable sites for modification. Furthermore, these edges are also embedded with internal stress [47]. As a result, such edges readily react with different chemicals to relieve the stress, as described by Mondal et al. [44]. These edges are so reactive that they are also reported to react between two active layers of graphene sheet to form a closed edge multilayer graphene. Such observations were reported by Liu et al., who observed the closure of edges of graphite during thermal treatment [48].

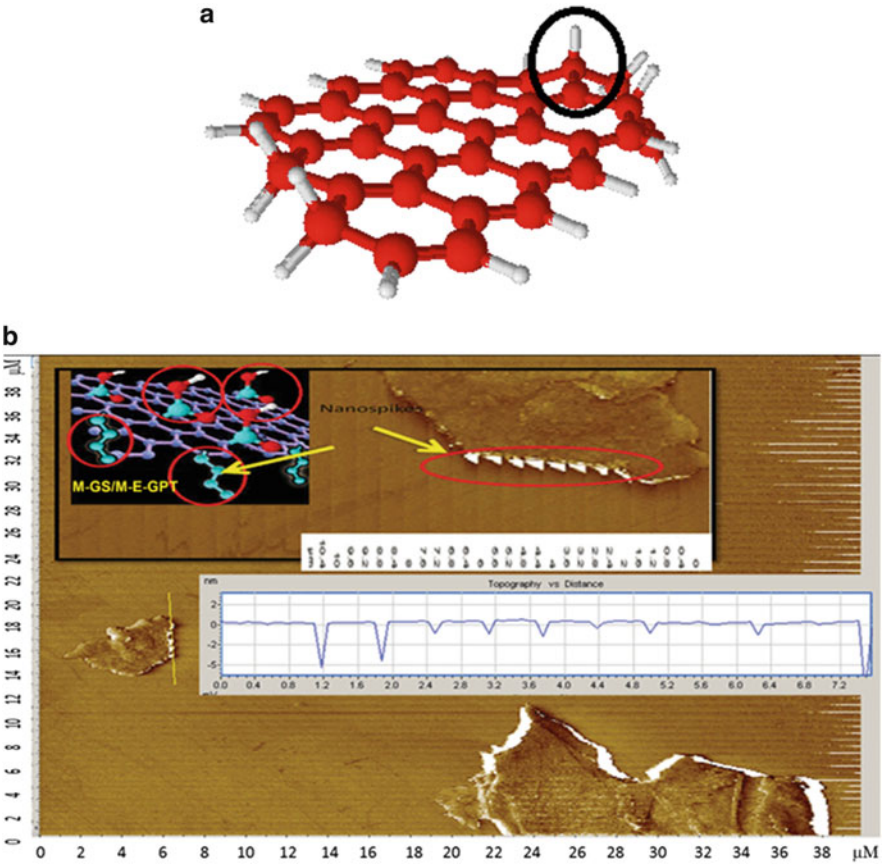

Fig. 3 (**a**) Typical distortion in the lattice of graphene as a result of conversion from sp^2 to sp^3 hybridized carbon atom. (**b**) Contact mode AFM of edge-functionalized graphene, highlighting the nanospikes formed. A typical height profile across the nanospike region is also displayed (*inset* shows a 3D model and high resolution image of edge-modified graphene). [Reprinted (adapted) with permission from [44], Copyright 2013, Royal Society of Chemistry]

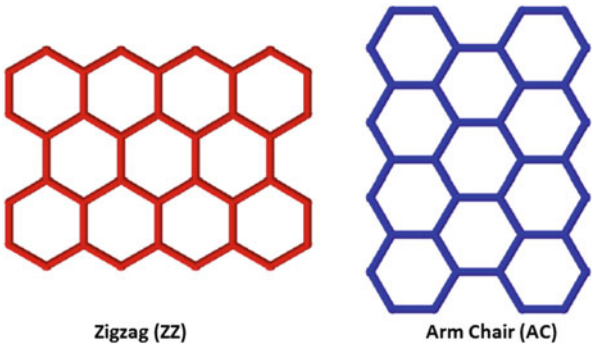

Fig. 4 Typical edges of graphite and graphene in zigzag (ZZ) configuration and armchair (AC) configuration

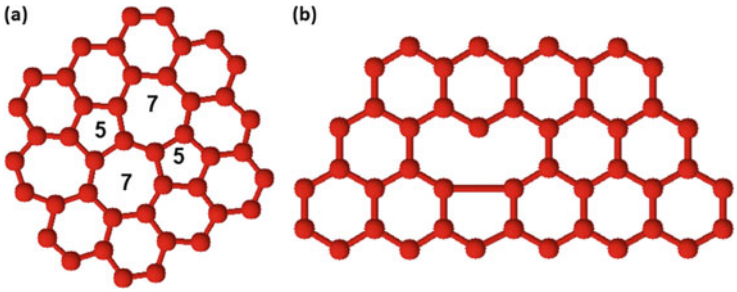

Fig. 5 (**a**) Ball-and-stick model for Stone–Wales defect SW (55–77). (**b**) Atomic structure of the single vacancy type of defect obtained using density functional theory

The intrinsic structural defects that are present are also reactive towards functionalization. The most prominent type of defect that is present in graphene is the Stone–Wales (SW) defect [49]. This defect does not involve any removal or addition of any atom from the graphite or graphene. Two pentagons and two heptagons [SW (55–77) defect] are formed from four hexagons by rotation of one C–C bond by 90°, as shown in Fig. 5a. The formation energy associated with the SW (55–77) defect is of the magnitude of 5 eV [50, 51]. When the transformation occurs via an in-plane bond rotation by simultaneous movement of the two involved atoms, the kinetic barrier is ca. 10 eV [50].

The other major defect that is commonly present in graphite and graphene is a result of the vacancy of an atom from the surface of graphene. Such vacancies can be the result of the absence of single atoms or multiple atoms (coalescence of two single vacancies or more). It is typical for such single vacancies to undergo Jahn–Teller distortion. As a result, two of the three dangling bonds are saturated over the vacant site, while the other dangling bond remains apart because of geometric constraint [51]. This causes the formation of five-membered and nine-membered rings, as shown in Fig. 5b.

These topological defect sites in graphite and graphene are ideal locations for chemical modification. Based on theoretical studies, it is predicted that the reactivity of graphite and graphene scales up with the presence of defects [52]. The π-orbital electron density changes in these defect sites. As a result, the reactivity increases. Furthermore, based on the π-orbital vector analysis model predicted by Haddon [53], the pyramidalization angle for the defect sites is closer to that for a sp^3 hybridized system than for a sp^2 hybridized system. As a result, whenever there is any scope for transition from an sp^2 to an sp^3 hybridized system for graphite and graphene, it takes place. Thus, minimization of geometric strain is a crucial contributory factor in the functionalization of graphitic materials. Although our discussion is mainly focused on graphene, the same modification methodology is expected to be relevant for expanded graphite, few-layer graphene, natural graphite, graphene nanoribbons etc.

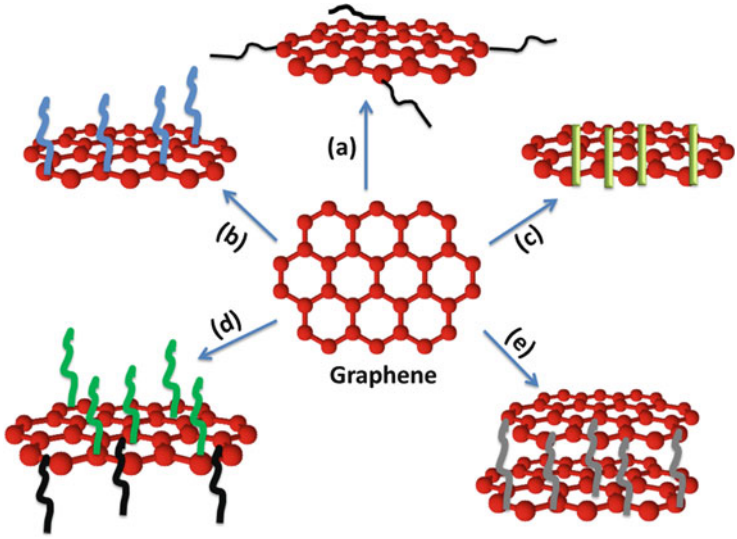

Fig. 6 Different functionalization routes for modification of graphene: (*a*) edge functionalization, (*b*) functionalization on the basal plane, (*c*) noncovalent modification, (*d*) asymmetrically modified basal plane, and (*e*) self-assembly of modified graphene sheets

1.5 Covalent Functionalization of Graphite and Graphene

Reports on the use of pristine graphite for bulk scale application are few and far between as a result of its typical structural features, as discussed in Sect. 1.1. To address such limitations, researchers across the globe are developing various covalent and noncovalent modification routes [54]. Generally, the covalent route is selected over the noncovalent method because of the greater range of versatile products that can be achieved after functionalization (see Fig. 6).

For covalent modification of graphite and graphene, there are myriad reactions that can be used, such as radical addition [55–57], nitrene addition [58, 59], 1,3-dipolar cycloaddition [60], Diels–Alder chemistry [56, 61–63], benzyne cycloaddition [64], and graphene oxide (GO) transformations [65, 66]. However, to simplify the situation, such modifications of graphitic materials can be broadly classified into reactions that are either carbon–carbon bond forming or carbon–nitrogen bond forming. These are discussed in reviews by Bhowmick and coworkers [5, 7].

1.5.1 Functionalization of Graphite and Graphene Using Small Molecules

In the field of carbon–carbon bond formation, the contribution of diazonium chemistry has been remarkable [67]. It is the most widely used procedure for

tailoring the properties of graphite and graphene. The reaction pathway is believed to proceed via a free radical mechanism. For the modifier, a substituted aromatic amine is selected according to the end application. The diazotized product generates highly reactive aryl radicals in the medium. When these aryl radicals come into close contact with the graphite and graphene, they are rapidly quenched by the graphite framework.

Following diazonium chemistry, we have successfully grafted chlorophenyl groups onto graphene sheets. Shear/sonication-assisted delamination of the graphite platelets was obtained in situ in the reaction medium. The chlorophenyl radical formed was spontaneously grafted onto the few-layer graphene platelets, as shown in Fig. 7 [68]. Grafting of (*p*-nitrophenyl)diazonium tetrafluoroborate onto epitaxial graphene grown on SiC substrate was reported by Niyogi et al. [69]. Spontaneous electron transfer from the graphene layer and its substrate to the diazonium salts resulted in functionalization. Further, Wang et al. carried out detailed investigation of the reactivity of (*p*-nitrophenyl)diazonium tetrafluoroborate with graphene [70]. A top-down approach was utilized for the preparation of single-layer and multilayer graphene sheets from 3D graphite on silicon wafers. The samples were further annealed and then treated with the diazonium salt. Following this protocol, Wang et al. observed that the top layer and the edges of the graphene sheet reacted specifically.

As discussed earlier, modification of graphite and graphene is expected to tailor the properties of graphitic material. In line with that, Sinitskii et al. [71] proposed a kinetic model to describe the conductivity change for functionalized graphene modified using diazonium chemistry and reported a relatively faster kinetics for this process.

Apart from grafting of aryl radicals onto epitaxial graphene and graphene supported on a substrate, bulk phase grafting onto graphite has also been achieved [72].

Instead of strong acids and free radicals, orangolithium reagents can also be used to functionalize carbon materials via carbon–carbon single bonds. Despite such type of reactions being very common for carbon nanotubes [73–75], reports of such reactions on graphite and graphene are few in number. Worsley et al. [75] were among the first to use *n*-butyl lithium and *n*-hexyl lithium to graft an alkyl group

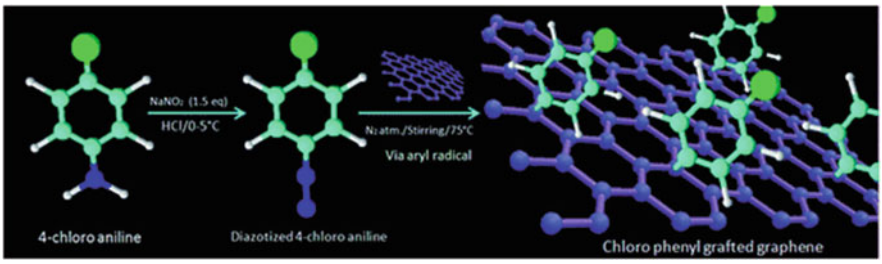

Fig. 7 Grafting of chlorophenyl radicals onto graphene using diazonium chemistry. [Reprinted (adapted) with permission from[68], Copyright 2012, Royal Society of Chemistry]

onto graphene fluoride. Their objective was to solubilize graphite platelets in solvents. Recently, Yu et al. extended this strategy for generation of graphene–fullerene hybrid materials [76]. They proposed that the reaction proceeded via generation of a "living" center of lithium, where subsequent termination could occur by treatment with nucleophiles.

A defect-specific functionalization of graphite platelets was carried out by Mondal et al. [44] using *n*-butyl lithium as the reagent. Concomitant functionalization by a carboxylic group as well as a butyl group was reported to take place. In a different paper, a hybrid material of polyoligomeric silsesquioxane (POSS) and graphene was produced utilizing the same strategy [77].

Carbon–carbon bond forming reactions are also important in preparation of graphite-based hybrid filler materials. Production of most of these hybrid materials is mediated by the formation of GO from graphite. The most widely accepted methodology was proposed by Hummers and Offeman in 1958 [16]. Generally, graphite is treated with a strong oxidant such as potassium permanganate in the presence of strong acids such as sulfuric and nitric acid. The isolated product demonstrates an excellent dispersibility in different organic solvents, as shown in Fig. 8.

Better dispersion is observed as a result of the presence of various oxygen functionalities on the surface of the graphene sheet. Furthermore, these oxygen functionalities react with different modifiers to give rise to functional graphene using simple chemistry such as amidation and esterification reactions.

Structural elucidation of GO has been a matter of debate. However, to date the model proposed by Lerf et al. [79] is the most widely accepted model for GO. It was observed that the structure of GO involves two different kinds of subunits: aromatic regions with unoxidized benzene rings and regions with aliphatic six-membered rings, as shown in Fig. 9a.

The atomic scale resolution of the GO was demonstrated by Navarro et al. [80] using high resolution TEM, as shown Fig. 9b. The micrograph demonstrates that, despite the oxidation reaction, the percentage area of defect-free crystalline graphene is high enough.

Using this protocol, Xue et al. [81] developed a strategy for the synthesis of graphene–silicon hybrid material. The silicon precursor that was selected for this

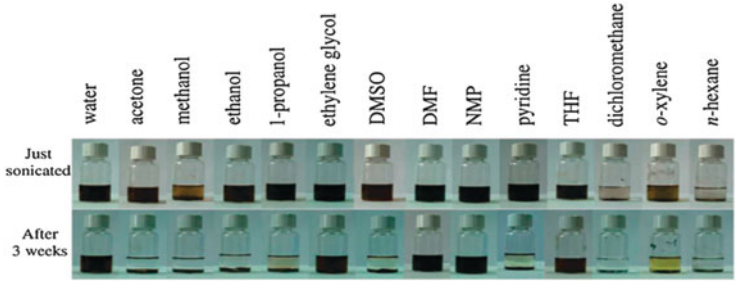

Fig. 8 Dispersion of graphene oxide in different organic solvents. [Reprinted (adapted) with permission from [78], Copyright 2008, American Chemical Society]

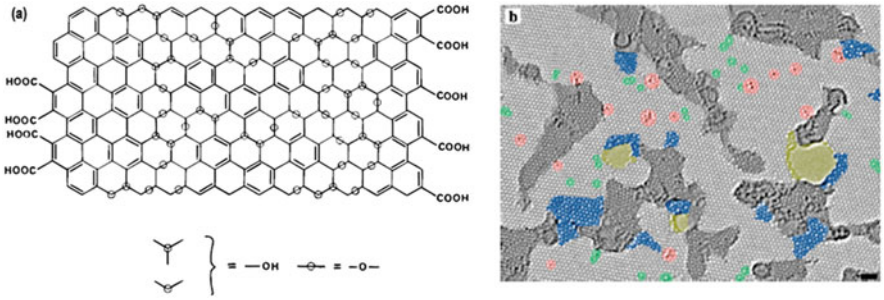

Fig. 9 (**a**) Structure of graphene oxide. (**b**) TEM image of graphene oxide showing defect-free crystalline graphene area (*light gray*), contaminated regions (*dark gray*), disordered single-layer carbon networks (*blue*), ad-atom substitutions (*red*), isolated topological defects (*green*), and holes and their edges (*yellow*). *Scale bar*: 1 nm. [Reprinted with permission from [79, 80], Copyright 1998, 2010 American Chemical Society]

purpose was substituted POSS. The cage-like structure of POSS makes it a material of high interest. Furthermore, the functional group attached to POSS can also enhance the solubility of the material in a wide range of solvents. The surface properties of the graphitic material can also be engineered by grafting of the POSS moiety, thereby imparting amphiphilicty to the hybrid material. This hybrid material was also utilized as hybrid nanofiller for tuning the thermal stability and glass transition temperature of polymethyl methacrylate. Unlike the strategy employed by Xue et al. [81], in our laboratory we adopted direct functionalization of few-layer graphene with a POSS moiety using *n*-butyl lithium [77]. The covalently grafted POSS moiety became attached specifically at the edges of the graphene sheet. The success of the reaction was monitored using different microscopy techniques (see Fig. 10A). A series of studies were also reported by Valentini and coworkers [82, 83] and Wang et al. [84] in which a similar strategy was extended for grafting of POSS onto GO.

In our group, we were also successful in developing a graphene–carbon nanotube hybrid material [40]. The carbon nanotubes and the graphite were linked with each other through carbon-carbon single bond. The hybrid material demonstrated supercapacitance properties at different currents and voltages. The morphology of the hybrid material is shown in Fig. 10B.

1.5.2 Tethering of Macromolecules for Generation of Polymer Nanocomposites

Functionalization of graphite and graphene is not limited to small organic or inorganic moieties. Large organic chemical species such as macromolecules are often utilized for grafting onto graphitic structures for generation of polymer nanocomposites. Polymer nanocomposites can be generated either through physical mixing or via chemical bond formation between the polymer and the filler material.

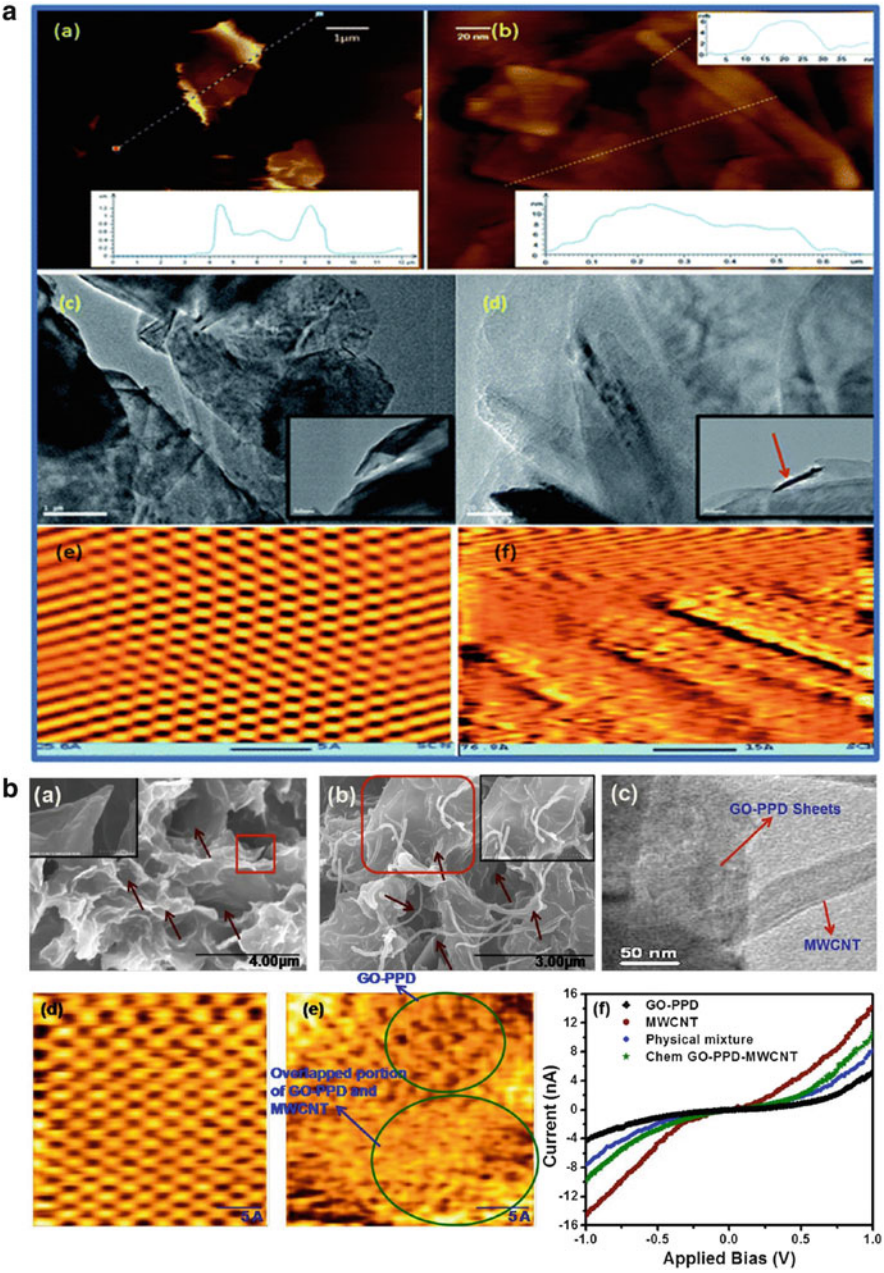

Fig. 10 (**A**) Atomic force microscopy (AFM) images for (*a*) graphene sheet (*inset* shows height profile across graphene sheet) and (*b*) POSS-*g*-graphene sheet (*inset* shows height profile across POSS-*g*-graphene sheet and specifically at the rod-like feature). TEM micrographs for (*c*) graphene sheet (*inset* shows edges across graphene sheet) and (*d*) POSS-*g*-graphene sheet (*inset* shows rod-shaped feature). Scanning tunneling microscopy (STM) images of (*e*) graphene sheet and (*f*) POSS-*g*-graphene sheet. [Reprinted with permission from [77], Copyright 2013, Royal Society of Chemistry]. (**B**) Field emission scanning electron microscopy (FESEM) images of (*a*)

Widespread recognition of the field of nanocomposites came after a group of Toyota Industries researchers developed nanocomposites of clay and nylon-6 [85]. Subsequently, there has been a huge volume of work executed in the field of polymer nanocomposites using a variety of nanomaterials [86–94]. Although a wide range of success has been achieved by physical mixing of modified and unmodified carbon nanomaterials with polymers, the properties of the nanocomposites can be greatly enhanced if the polymer chains are tethered onto the nanomaterials. Thus, methodologies such as "grafting-to" and "grafting-from" are gaining popularity [95–97].

"Grafting-from" Technique

In this case, graphitic precursor materials such as GO or hydroxyl-terminated graphite and graphene are used. The initiator for the polymerization reaction is anchored onto the basal plane and the edges of the functional graphite and graphene. Then, the polymers are allowed to grow from the surface of the graphitic material. As a result, there are no problems of steric hindrance associated with the growth of polymer chains. This makes the situation advantageous. Briefly, different controlled radical polymerization reactions such as atom transfer radical polymerization (ATRP) and reversible addition-fragmentation chain transfer (RAFT) reaction can be carried out [98–103].

Lee et al. [104] utilized a series of monomers for grafting onto functional graphite nanoplates. The initiator used for this purpose was 2-bromo-2-methylpropionyl bromide. Based on their investigation, it was observed that the chain length of the polymer can be controlled by varying the ratio of monomer to initiator-grafted graphitic platelets. A similar strategy has been extended by dozens of researchers for growing polymer brushes from the surface of graphite nanoplates. However, the ATRP technique for functionalization of graphitic materials is mostly limited to acrylates [105].

"Grafting-to" Technique

In grafting-to methodology, a pre-synthesized polymer is tethered onto functional graphitic platelets using reactions such as amide or ester bond forming reactions or click chemistry [95]. The contribution of click chemistry to the pursuit of graphene modification is important. In conjunction with macromolecules, small molecules

Fig. 10 (continued) GO–PPD (*inset* shows wrinkled GO sheets) and (*b*) chem GO–PPD–MWCNT hybrid [*inset* shows individual dispersion of multiwalled carbon nanotubes (MWCNTs) on GO sheets]. (*c*) TEM image of chem GO–PPD–MWCNT hybrid showing the inherent bonding of GO–PPD with MWCNTs. STM imaging of (*d*) GO–PPD and (*e*) chem GO–PPD–MWCNT hybrid (set point 210 pA) on HOPG. (*f*) Representative scanning tunneling spectroscopy (STS) I−V spectra. [Reprinted (adapted) with permission from [40], Copyright 2013, American Chemical Society]

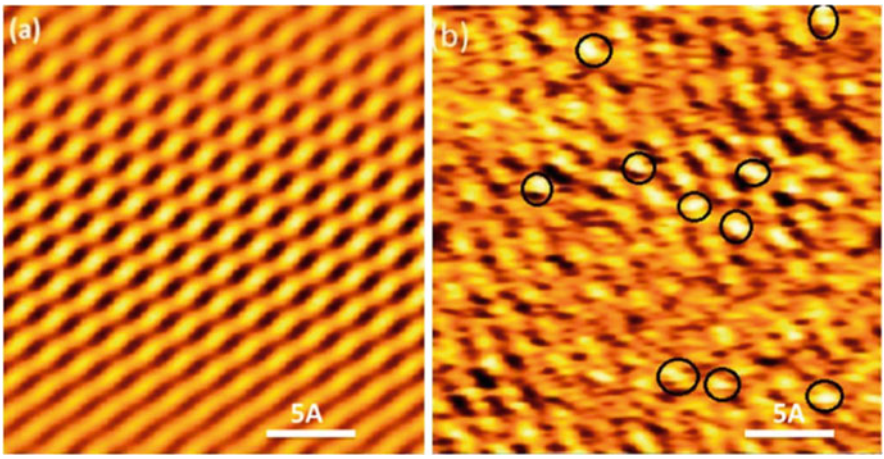

Fig. 11 Atomic level images of (**a**) expanded graphite (scan at 25 × 25 Å area) and (**b**) modified graphene (scan at 25 × 25 Å area), carried out with a bias voltage of −200 mV against a tunneling current of 300 pA using a Pt/Ir tip. *Black circle* in (**b**) indicates the formation of micro-ripples on the surface of modified graphene. [Reprinted (adapted) with permission from [106], American Chemical Society]

are often attached to the graphene sheet using click chemistry. In our laboratory, we have specifically modified graphitic materials at their edges using click chemistry [106]. The direct effect of such stress on the edges of modified graphene is reflected as micro-ripples on the surface of modified graphene, as shown in Fig. 11.

A very good example of a grafting-to experiment was demonstrated in our laboratory, wherein a bifunctionalized graphene was modified with a silane moiety. The resulting composite demonstrated an instant conducting adhesive behavior [97]. Additionally, a hierarchical distribution of the graphitic filler material took place, as shown in Fig. 12. The thermodynamic parameters controlling such a preferential distribution of the filler material inside the matrix are discussed in detail in the cited publication.

Salavagione et al. [107] successfully tethered polyvinyl alcohol onto GO under catalytic conditions. An esterification reaction was utilized for appending the polymer onto the GO. *N*,*N*′-Dicyclohexylcarbodiimide (DCC) was used to activate the carboxylic group of GO, and 4-dimethylaminopyridine (DMAP) acted as catalyst. The nanocomposite prepared in this way demonstrated excellent thermal stability compared with the pure polymer.

"Grafting-from" versus "Grafting-to" Techniques

The grafting-from technique is an excellent methodology for growing polymers with a low polydispersity index (PDI), but it is restricted to those polymers whose initiators can be appended onto the graphitic surface. On the other hand, the grafting-to technique is more versatile for tethering a broad spectrum of polymers.

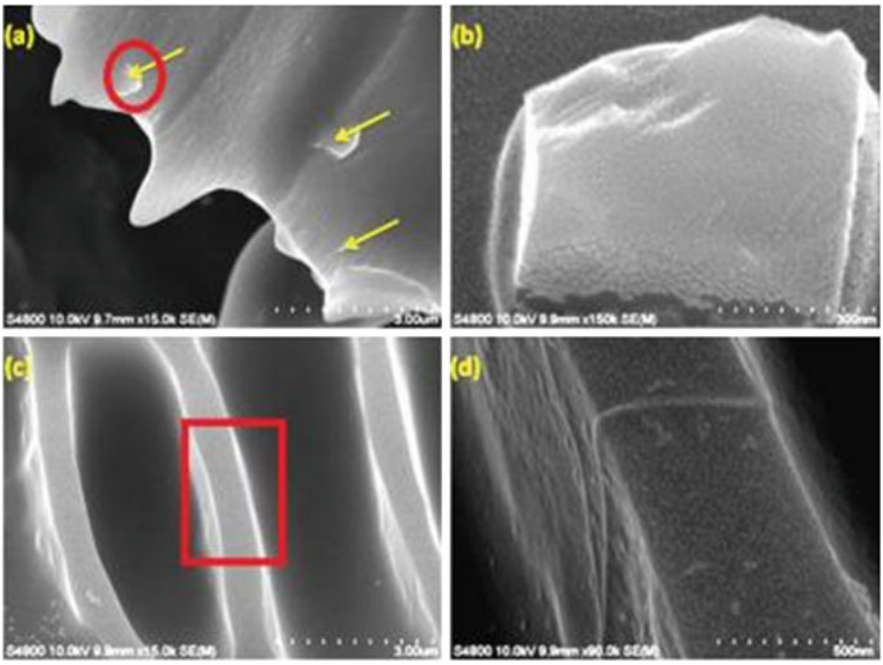

Fig. 12 SEM images of silicone-grafted graphene at different magnifications. (**a**) Surface of silicone-grafted graphene; *yellow arrows* indicate the graphitic particles on the surface of polymer at 15 k magnification. (**b**) Morphology of graphitic plate on the surface of polymer matrix (particle encircled in *red* in **a**) at 150 k magnification. (**c**) Fractured surface morphology of silicone-grafted graphene: the graphitic plates are perpendicular to the polymeric surface at regular intervals, recorded at 15 k magnification. (**d**) Measurement of thickness of *red boxed region* (as shown in **c**) inside the polymeric matrix at 90 k magnification. [Reprinted (adapted) with permission from [97], Copyright 2014, American Chemical Society]

The biggest advantage of the grafting-from technique is that steric hindrance is not prevalent. However, such steric problems are commonly associated with the grafting-to methodology. As a result, a lower degree of functionalization is achieved using grafting-to methodologies. Despite such problems associated with the grafting-to technique, we have successfully tethered high molecular weight poly (ε-caprolactone) onto toluene diisocyanate-modified graphene at adequate grafting density (0.2 chains per square nanometer) [108] Thus, it seems that both techniques are good for modifying graphitic surfaces.

1.6 Modified Graphene and Graphite-Based Elastomer Nanocomposites

This section discusses some commonly used representative graphene/elastomer nanocomposites.

1.6.1 Natural Rubber

The most widely used naturally occurring nonpolar elastomeric material is *cis*-1,4 polyisoprene, isolated in the latex form from *Hevea brasiliensis* through tapping. As a result of its wide importance in both tire and non-tire applications, scientists across the globe are developing nanocomposites based on natural rubber (NR). Recently, the wonder materials graphene and graphite are being used to modulate the properties of pristine NR for multifaceted application. Control over the dispersion and exfoliation of the graphite inside the rubber matrix depends on the processing parameters. Bhattacharya et al.explored the effect of different nanofillers on the properties of NR [109]. Unfunctionalized expanded graphite was one of the fillers tested. However, comparing and contrasting the mechanical properties of NR nanocomposites, it was noted that those containing unfunctionalized expanded graphite exhibited improvement in the 100% modulus (1.09 ± 0.04) compared with neat rubber (0.89 ± 0.01) and carbon black-filled NR (0.92 ± 0.03) under similar loading. Recently, Zhan et al. proposed a new technique wherein uniform dispersion and exfoliation of the graphite nanoplates was achieved in NR latex using ultrasonication [110]. The well-dispersed GO platelets were further reduced in situ through treatment with hydrazine hydrate (to produce reduced graphene oxide; rGO) and then coagulated using formic acid. The master batch so obtained was further diluted with NR in a two-roll mill. The same group extended their concept of "ultrasonication–in situ reduction" to achieve self-assembly of graphene platelets in the rubber matrix. Curing of the rubber composite essentially pushes the graphite nanoplates to the interstitial space of the different rubber particles created during the vulcanization process [111]. Unlike the previous methodology, the latter technique produced a conducting nanocomposite as a result of formation of a conducting filler network in the rubber matrix. Thus, from these observations, it can be reasonably inferred that the properties and performance of the nanocomposites are largely guided by the processing parameters.

In an attempt to understand the underlying phenomenon, Potts et al. [112] utilized the latex coagulation approach and studied the effect of different processing parameters on the properties of the resulting nanocomposite. Two different batches of nanocomposite were prepared by altering the process for incorporation of curing agents into the matrix. In one case, the curing agent was added while masticating the rGO/NR latex in a two-roll mill, whereas the other batch was prepared by mixing crosslinker through traditional solution-casting methodology, wherein the solution phase was the rGO/NR latex coagulated phase. Morphological studies revealed that tactoids of significant dimension (a web-like morphology) were formed by increasing the concentration of rGO in the latex (uncured variety) phase, as shown in Fig. 13a, b. The morphology of the solution phase cured composite demonstrated similar features to those of the uncured sample (Fig. 13c, d). However, the milled sample registered a uniform dispersion of the nanoplatelets in the rubber matrix, as shown in Fig. 13e, f. As a result, the electrical, thermal, and mechanical properties of the composite were greatly affected.

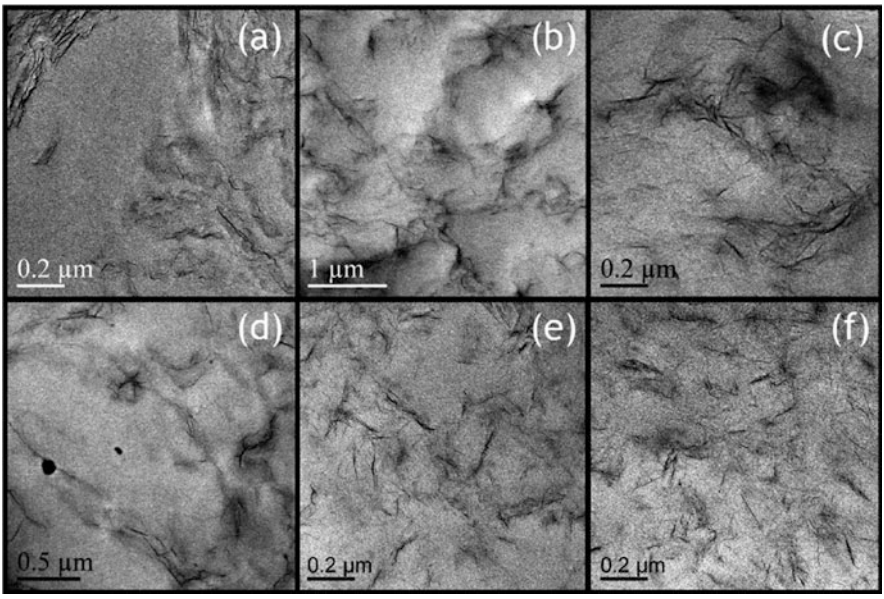

Fig. 13 TEM micrographs of rGO/NR nanocomposite sections. (**a**, **b**) "Weblike" dispersion of rGO platelets in the uncured composites, as obtained directly after latex co-coagulation. (**c**, **d**) Dispersion in the solution-treated samples. (**e**, **f**) Morphology of the milled nanocomposites. [Reprinted (adapted) with permission from [112], Copyright 2012, American Chemical Society]

As well as reducing GO in situ with hydrazine hydrate, it can also be reduced through thermal treatment to form thermally exfoliated graphene oxide (TEGO). In continuation of their earlier work, Potts et al. utilized TEGO as filler phase in the NR matrix and varied its processing parameters [113]. They compared the properties of a composite prepared by direct milling of TEGO with the rubber matrix in a two-roll mill against those of a composite generated by pre-mixing TEGO with NR latex, followed by milling. In line with earlier observations, the latter route gave better dispersion of the nanoplates, thereby resulting in better mechanical properties of the composite. On a similar note, Scherillo et al. [114] observed that latex phase mixing followed by coagulation and milling resulted in the formation of interconnected segregated and nonsegregated assemblies of graphene platelets. Thus, from these observations, it can be reasonably inferred that the processing route can be designed according to the end use of the nanocomposite. For example, an electrically conducting nanocomposite can be achieved via formation of segregated networks, whereas better mechanical properties can be achieved through good dispersion of the nanophase (i.e., through milling of the coagulated latex composite). Following the work of Potts et al., Aguilar-Bolados et al. [115] demonstrated the effect of surfactant on the dispersion of TEGO in the NR latex matrix, followed by coagulating and milling in a two-roll mill. Briefly, two different surfactants were utilized, sodium dodecyl sulfate (SDS) and Pluronic F127. SDS assisted in better dispersion of the graphite nanoplates inside the rubber matrix than

Pluronic F127. Fernandez et al. [116] demonstrated that addition of linseed oil plasticizer at a low loading of ca. 4 parts per hundred rubber (phr) while milling expanded graphite and NR assisted in the formation of favorable interactions between filler and rubber.

As an alternative to the latex phase mixing or coagulation techniques, Wu et al. [117] utilized a solution phase technique to prepare graphene/NR nanocomposites. Additionally, they modified the GO surface with bis (triethoxysilylpropyl)tetrasulfide (BTESPT). The BTESPT moiety acted as a crosslinking agent and actively participated in the formation of covalent bonds with the allylic site of the NR (as shown in Fig. 14). The reproducibility of this procedure was supported by swelling studies. It was noted that an increase in the concentration of modified graphene resulted in a decrease in the swelling ratio of the composite in organic solvent. On a similar note, coating of graphite with acrylate was also reported to improve the dispersiblity of graphite nanoplate filler inside the NR matrix [118].

Recently, Wu et al. [119] designed a pathway for covalent attachment of maleic anhydride-grafted polybutadiene as a modifier for GO. The hybrid so generated assisted in increasing favorable interfacial interactions between the NR matrix and graphene platelets. A tailor-made architecture of graphene inside the NR matrix was also developed by Luo et al. [120]. The GO was modified using poly (diallyldimethylammonium chloride). A co-assembling technique was utilized in a water-borne latex system to develop a 3D interconnected architecture of the modified graphene in the NR matrix. Assembly of the modified graphene platelets was induced by the difference between the surface charges of the modified graphene and the NR latex. Poly(diallyldimethylammonium chloride) induces a positive charge over the surface of the graphene platelets, whereas the NR latex particles are negatively charged. As a result, an assembled product is generated.

Irrespective of the processing route, the main aim is control over dispersion of the graphite nanoplate filler inside the NR matrix, so that better reinforcement can be achieved. However, a phenomenon such as strain-induced crystallization (SIC) makes the situation crucial for NR. Thus, understanding the underlying physics

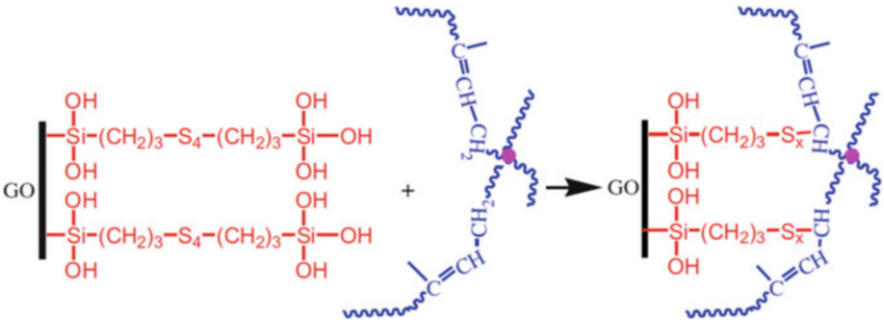

Fig. 14 Reaction of the polysulfide groups of BTESPT with the allyl positions of double bonds in the rubber molecules. [Reprinted (adapted) with permission from [117], Copyright 2012, Elsevier]

involved in the reinforcement of NR by graphene becomes tricky. Stanier et al. [121] proposed two guiding factors that control the reinforcement mechanism: First, reinforcement is provided by the exfoliated anisotropic graphite nanoplates within the elastomeric matrix. Second, the self-reinforcement phenomena active as a result of the formation of a network of polymer chains was held responsible for the reinforcement mechanism. The latter effect is only applicable for NR. An increase in graphite nanoplate content resulted in an upturn at higher strain. This was a result of the formation of SIC. Furthermore, the presence of graphite nanoplates enhanced the crystallization rate (as evident from wide-angle X-ray diffraction, WAXD, studies). As a result, an increase in filler loading resulted in a decrease in strain (as shown in Figs. 15 and 16).

Ozbas et al. [122] monitored the changes in stress and crystallization using synchrotron X-ray scattering measurements of the NR samples loaded with functional graphene sheets during sample stretching. Small-angle X-ray scattering (SAXS) measurements revealed that the functional graphene sheets became oriented in the stretching direction. The anisotropy induced during stretching resulted in the transmission of stress through the filler networks. Furthermore, the in-plane modulus of GO is reported to be higher than the bending modulus [123]. As a result, better reinforcement is seen.

In addition to the above factors, Li et al. [124] combined the concept of SIC with the entangled bound rubber tube (EBT) model to understand the reinforcing effect of graphene on NR polymer chains at low filler loading (0.75 phr). The results were compared and contrasted with those for GO. The EBT model demonstrated that the pristine graphene provided better interaction with the NR matrix. This observation was also in line with the Q_F/Q_G ratio in the Lorenz and Park equation [where Q is the amount of solvent absorbed per gram of rubber for filled (F) and gum

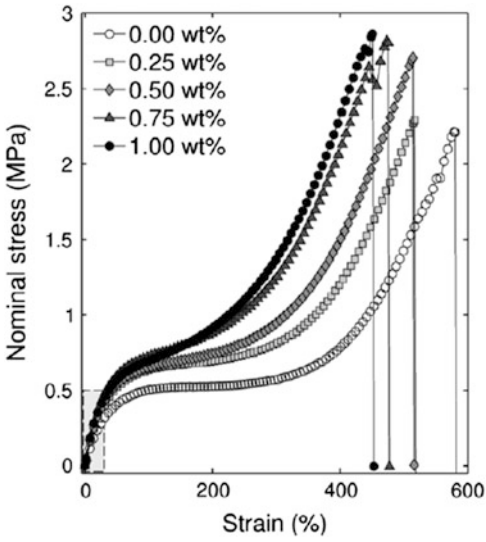

Fig. 15 Tensile properties of GO/NR nanocomposites up to rupture. [Reprinted (adapted) with permission from [121], Copyright 2014, Elsevier]

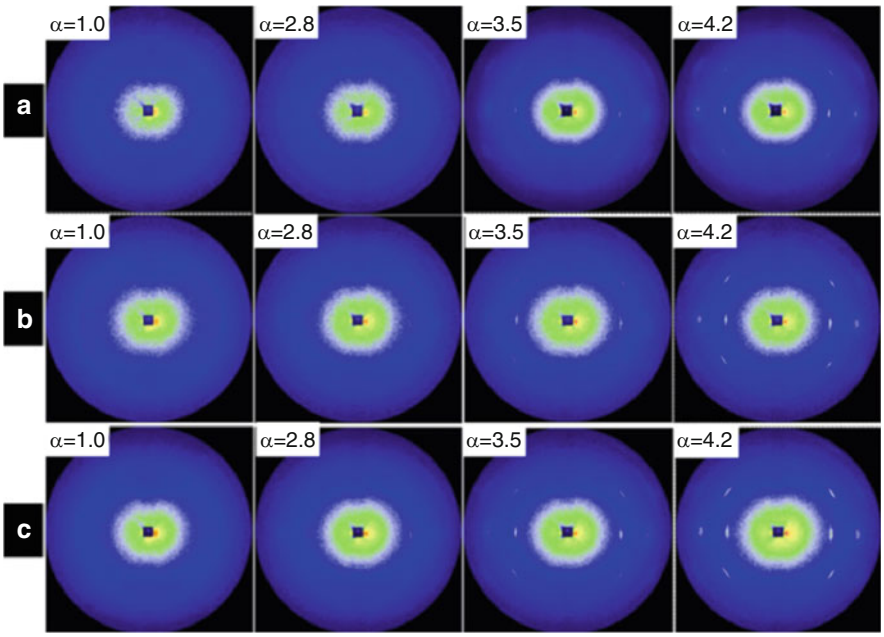

Fig. 16 Sequential changes of WAXD patterns for (**a**) NR (**b**) 0.7 GO/NR, and (**c**) 0.7 graphene/NR. Corresponding strain (α) values are indicated at the *left top* in each pattern. [Reprinted (adapted) with permission from [124], Copyright 2013, John Wiley& Son]

(G) samples]. The Q_F/Q_G ratio for pristine graphene-containing matrix was 0.82, whereas that for the GO/NR matrix was 0.85. This showed that polar GO was incompatible with a nonpolar NR matrix. Wu et al. [125] further demonstrated that variation in the graphite particle size can significantly affect the mechanical properties of NR-based nanocomposites. Unlike the commonly observed phenomena, they reported that a reduction in graphite particle size significantly increased the modulus of the composite. The flexibility of sulfur vulcanized graphene/NR nanocomposites can be greatly affected by the extent of filler loading. Yan et al. [126] carried out a series of SAXS analyses on segregated and nonsegregated graphene-filled NR systems. They showed that polysulfidic linkages give rise to a hump in the high q (scattering vector) value. However, increasing the filler content causes the q_{max} value to shift to a higher q region, thereby indicating a transformation from polysulfidic linkages to monosulfidic linkages. As a result, the flexibility of the matrix is affected.

Safety and reliability during the service life of any nanocomposite can be correlated with the fatigue properties of the material. As a result of the severe service conditions for NR-based nanocomposites, prediction of the fatigue properties of NR becomes very important. Recently, Yan et al. [127] studied the fatigue properties of graphene/NR nanocomposites. At low fatigue strain, graphene platelets accelerated crack growth, whereas retardation was registered at a higher strain. A hypothesis was provided for their observations: At high strain value, SIC

phenomena are active. As a result, the crystallites formed assist in the formation of crack branches. This minimizes the energy and retards the crack growth at higher strain values. In line with the observations made by Yan et al., Dong et al. [128] recently noted that incorporation of GO (as little as 1 phr) successfully resisted fatigue crack growth and propagation.

1.6.2 Epoxidized Natural Rubber

There has been a plethora of work in the field of natural rubber and graphene; however, not many works report using graphene and epoxidized natural rubber (ENR). ENR is a modified version of natural rubber, wherein the double bond of the NR is selectively oxidized using various types of peroxy compounds. Recently, She et al. [129] developed a GO/ENR composite using ultrasonic irradiation-assisted latex coagulation methodology. Both graphene and NR were oxidized in this study. The large number of oxygen functionalities on the edges and basal plane of GO assisted in favorable interaction with epoxy groups of the ENR. WAXD studies provided an insight into the dispersion of GO platelets. The peak corresponding to GO ($2\theta = 8.9^{\circ}$) disappeared in the GO/ENR matrix. It was concluded that the GO platelets were completely exfoliated in the ENR matrix. Strong polymer–filler interactions are bound to affect the glass transition temperature (T_g) of the polymer. As expected, the authors noted that the T_g of the composite was -38.98°C, compared with -41.88°C for neat ENR. Such a favorable interaction is bound to affect the mechanical properties of the composite. In this context, it is worth mentioning that the nonpolar nature of NR makes GO a less favorable filler material. However, the polarity induced in ENR as a result of the presence of epoxy groups greatly enhances the interfacial interactions with GO. Zhan et al. [111] demonstrated that a GO/NR composite with 2% filler content had a tensile strength that was 47% higher than that of pure NR. However, She et al. [129] noted an increase in tensile strength of 72% with a nominal loading of 2% GO. Unlike the observations reported by Potts et al. [112], the mechanical properties of the milled samples (nonsegregated) were found to be inferior to those of the segregated samples for the GO/ENR nanocomposite.

The effect of variation of the ENR epoxidation level on the properties of graphene-based composites was studied by Yaragalla et al. [130]. Two different grades of ENR were examined (25 and 50% epoxidation level). Mixing was carried out in typical open two-roll mill with a 2% filler loading. The shift in the FTIR peak caused by the epoxy ring, compared with neat polymer, suggested significant interaction with the GO particles. From this observation, it can be concluded that several physicomechanical properties of the GO/ENR system are affected. In a different study, Malas et al. [131] developed nanocomposites based on ENR and expanded graphite or GO. In their study, the storage modulus for rubber containing GO was higher than those for neat ENR and ENR containing expanded graphite.

Thus, from the above discussion, it can be reasonably inferred that the mobility of the ENR chains is largely affected by the presence of GO. A proper

understanding of the filler network inside the ENR matrix can provide insights into the structure–property relationships of graphene/ENR composites. In an attempt to address this issue, He et al. [132] carried out rheological and positron annihilation studies on graphene/ENR nanocomposites and showed that the samples adopted a segregated morphology. A polymer–graphene bridged network was recorded at a low filler concentration of 0.17%, whereas a 3D network of graphene platelets was formed with 0.23% filler loading, as shown in Fig. 17. The viscoelastic behavior of neat ENR revealed that the polymer chains remained in an unperturbed relaxed state; however, the graphene/ENR (filler loading 0.14%) composite demonstrated

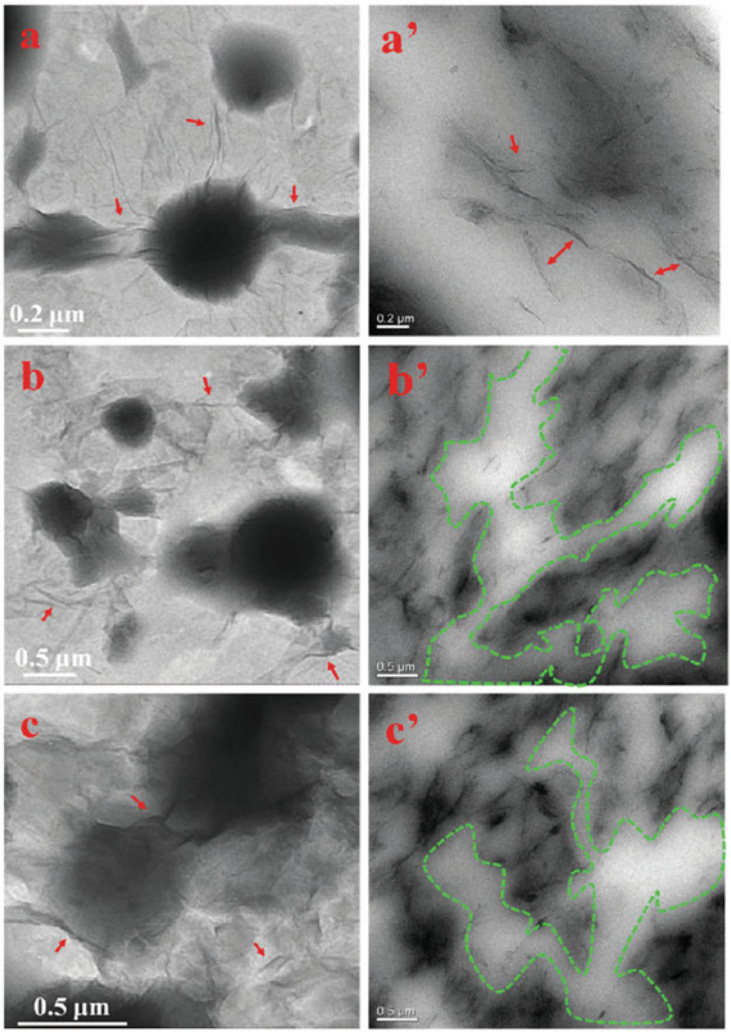

Fig. 17 TEM micrographs of ENR/GO latex (**a**–**c**) and ENR/GO solid composites (**a'**–**c'**) with different GO loadings: (**a**, **a'**) ENR/GO-0.07, (**b**, **b'**) ENR/GO-0.28, and (**c**, **c'**) ENR/GO-0.56. [Reprinted (adapted) with permission from [132], Copyright 2015, Royal Society of Chemistry]

significant perturbation of the polymer chains and exhibited, solid-like viscoelastic properties. Rheological studies were supported by the data obtained from positron annihilation studies. Insight into the segmental chain dynamics and packing at the molecular level can be obtained through positron annihilation studies. The lifetime of an *ortho* positron can be correlated to the amount of "free cavity" present inside the nanocomposite. A decrease in the lifetime value with an increase in filler loading indicates a decrease in the size of the free cavity. Similarly, the authors noted a monotonic decrease in the lifetime value with an increase in filler concentration. Such an observation is the result of the interactions between the modified filler and ENR polymer chains.

1.6.3 Styrene Butadiene Rubber

In the family of the synthetic elastomers, SBR is the most versatile rubber and is used for various tire and non-tire applications. Basically, it is a random copolymer of styrene and butadiene, synthesized using solution (anionic type) or emulsion polymerization (free-radical type). The ratio of styrene to butadiene units can be modulated to different levels. An increase in the styrene content usually makes the rubber harder and vice versa. Because of its high abrasion resistance, SBR finds wide application in the tire industries. In line with current research, scientists are trying to replace the isotropic carbon black with anisotropic carbon nanomaterials as the filler material for tire applications. As a result, there is interest in other carbon- and silica-based nanofillers. The excellent properties demonstrated by graphite and graphene make them unanimous choices as filler material for the strategically important SBR.

The latex coagulation technique employed for composites of NR or ENR and graphene can be also applied for the development of graphene/SBR composites. Schopp et al. [133] reported preparation of graphene/SBR latex composites wherein the efficacies of chemically reduced graphene and thermally reduced GO as filler materials were compared and contrasted with those of reduced carbon black and carbon nanotubes at high loading (25 phr). The uniqueness of this work was that the graphene and its derivatives were dispersed in aqueous medium without the aid of any surfactant. The isolated products were processed in an internal mixer (curatives were added during this step), followed by milling in a two-roll mill ten times (sulfur and *N*-*t*-butyl-2-benzothiazylsulfenamide were added). Morphological analysis using microcomputed tomography revealed that the modified graphitic filler materials were uniformly distributed in the rubber matrix, whereas carbon black, multiwalled carbon nanotubes, and pristine graphite formed agglomerated structures. Enhanced surface area and better dispersion of the modified graphene imparted a better tensile strength to the composite compared with pristine graphite, reduced carbon black, and multiwalled carbon nanotubes. It can be envisioned that the enhanced tensile strength is attributed to the surface morphology of the modified graphene. The crumpled morphology assisted in better interlocking between the

elastomer chains and the filler material. As a result, the tensile strength increased when modified materials were utilized. As an extension of their work, Muelhaupt and colleagues studied the effect of different functionalized graphites, such as wet ground graphite in THF, edge-functionalized graphene, and thermally reduced GO, incorporated into the SBR matrix using a latex coagulation technique [134]. The edge-functionalized graphene was prepared by ball-milling the graphite under an atmosphere of carbon dioxide and argon. Curing of the composite was carried out using a similar process to that described above. Thermally reduced graphene imparted a higher tensile strength than the ball-milled samples, wet ground sample, or pristine graphite. The inferior result obtained for the ball-milled samples is attributed to a reduction in the aspect ratio of the filler material during milling, resulting in poor reinforcement of the elastomer matrix. Furthermore, it was surmised that the carbon dioxide present during ball-milling affected the vulcanization process. Such a hypothesis correlates well with the studies of composite swelling.

Kim et al. [135] reported fabrication of multilayered graphene/SBR nanocomposites using the latex coagulation technique. Differences in the surface charges of the SBR latex and filler material assisted in the heterocoagulation process. Such an approach is very similar to the methodology adopted by Luo et al. [120] in the preparation of graphene/NR nanocomposites. In the former case, multilayer graphene sheets were modified using aluminum chloride and hexadecyltrimethyl ammonium chloride. These positively charged filler materials interact with the negatively charged SBR latex under ultrasonication. The concentration of flocculant was found to play a crucial role during development of the graphene/SBR composite. An extension of this work was carried out by Kim's group, wherein the effect of incorporation of carboxylated graphite into the SBR latex was studied. The composite particles were found to adopt a distinct spherical morphology [136].

A modified latex coagulation technique was developed by Xing et al. [137]. An SBR-based nanocomposite was developed without the use of an ultrasonic field or surfactant. A mechanical agitation technique was employed for preparing nanocomposites with different percentages of filler loading. The in situ reduction process employed for NR-based composites was utilized for reducing GO. The resulting segregated composite was subjected to curing in a two-roll mill with the addition of a curative package. The oriented structure of the graphene was conjectured to result from the milling process. Unprecedentedly, the nanocomposite registered a high mechanical strength. Such an improved mechanical property is attributed to the better interfacial interaction between elastomer and filler. The concept of "bound rubber content" was utilized to estimate the symbiotic effect between the elastomer chains and the filler material. A 33.26% bound rubber content (stemming from the π–π interaction between the styrene unit and the graphene sheet) was estimated to be present at 5 phr filler loading. Furthermore, the presence of graphene gave the resulting material better abrasion resistance than traditional carbon black material.

The same group also reported the ability of graphene to act as an anti-oxidant material for elastomers [138]. The anti-oxidant behavior of graphene sheets inside an SBR matrix was attributed to the ability of graphene to act as a free radical scavenger. Its unique plate-like structure gives excellent barrier properties to the composite. As a result, the percolation of oxygen (the agent responsible for oxidative failure of the products) inside the matrix is greatly inhibited.

The surface chemistry of the filler material plays a pivotal role in determining the extent of interaction of filler material with the elastomer chains. Thus, Tang et al. [139] prepared graphene samples with tailored surface functionalities (GO reduced at different levels by chemical methods). A latex coagulation technique was employed. Dielectric relaxation spectroscopy studies demonstrated that the bulk segmental relaxation of SBR chains was independent of the surface chemistry of the filler material. However, dispersion of the filler material in the elastomer matrix and its interfacial adhesion were largely guided by the surface functionality. Such an observation was supported by the surface energy profiles of the composite materials. Apart from reducing the GO by different degrees, Liu et al. [140] modified the interface of the GO/SBR nanocomposite (prepared by latex coagulation followed by a similar strategy to that mentioned in the preceding reference) by the addition of different amine-based modifiers, such as oleylamine and octadecylamine. Even though both filler materials demonstrated excellent dispersiblity in the SBR matrix, the oleylamine-modified GO demonstrated better mechanical properties than the octadecylamine-modified filler. The enhanced mechanical stability of the oleylamine can be attributed to its structure. The isolated double bonds present in the oleylamine structure actively participate in the crosslinking reaction with sulfur during the vulcanization process. As a result, better mechanical properties are obtained.

Apart from the latex coagulation technique, a solution casting technique can also be used for development of TEGO/SBR nanocomposites, as utilized by Ozbas et al. [141]. Thermally reduced GO was used to obtain a wrinkled morphology of the filler material, which can induce proper interlocking of the elastomer chains with the filler material and avert the possibility of re-stacking of the graphene sheet (from quantum mechanical calculations). The resulting composite demonstrated excellent mechanical properties. A 16-fold increase in the mechanical property of the modulus was obtained compared with samples prepared from carbon black at similar concentrations. It was noted that the superior mechanical properties were governed by the geometry (in line with the Halpin–Tsai equation) and the orientation of the nanofiller, rather than the crosslinking density.

The Young's moduli of the graphene/SBR nanocomposite (prepared using a two-roll mill) was theoretically modeled by Araby et al. [142] using the Guth and the Halpin–Tsai models at low tensile strain. These two models were found to maintain good statistical agreement with experimental values observed at low tensile strain. Recently, Das et al. [143] provided an insight into the nanoscale morphology of graphene/SBR composites using the 3D TEM technique. Carbon

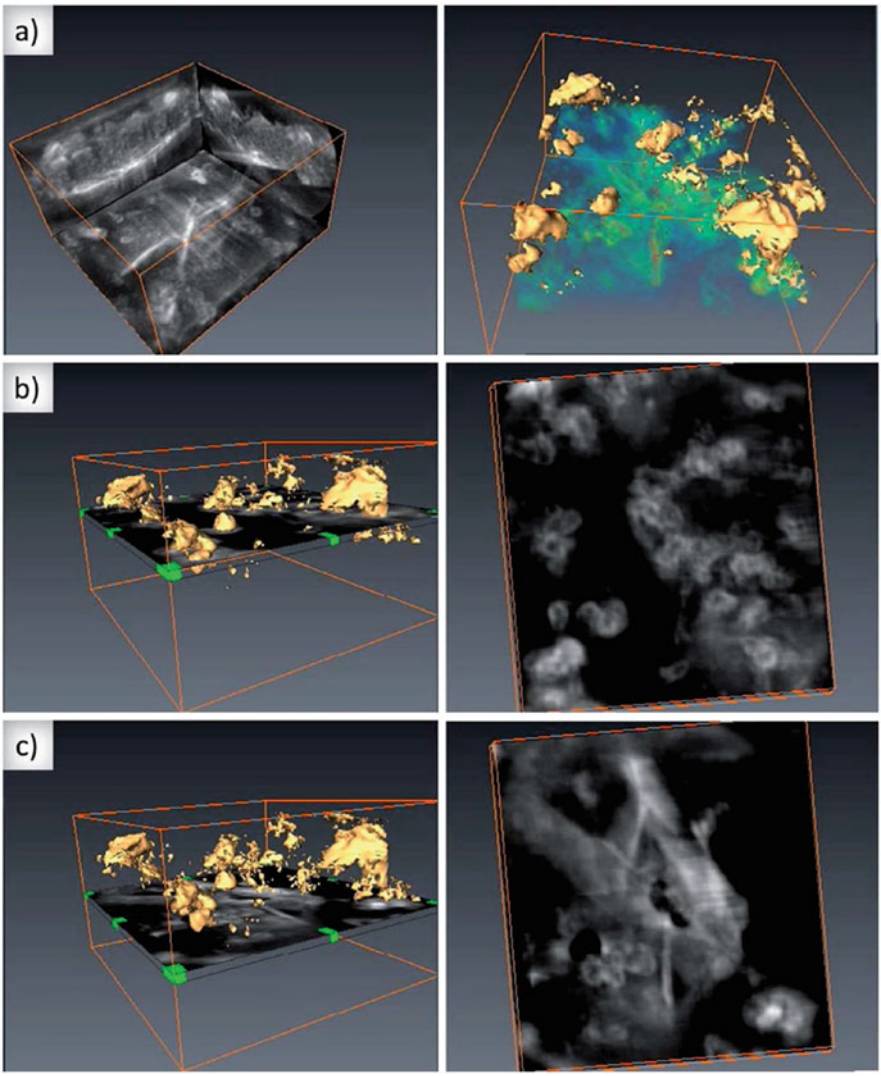

Fig. 18 (**a**) Visualization of the 3D reconstruction of solution SBR filled with 35 phr carbon black and 5 phr graphene; *yellow* and *green regions* represent carbon black and graphene, respectively. (**b**, **c**) Resultant volume on the *left* and a slice in *z*-direction on the *right*. [Reprinted (adapted) with permission from [143], Copyright 2014, Royal Society of Chemistry]

black was used in conjunction with graphene as the filler material. It was proposed that the carbon black moiety assists in de-lamination of the graphene sheet. It was also noted that the graphene sheets are surrounded by carbon black moieties and a few other thin layers of graphene sheet, as shown in Fig. 18. This indicates that the filler morphology inside the elastomer matrix plays an important role.

1.6.4 Butadiene-Styrene-Vinyl Pyridine Rubber

Tire rubber is a very complex composite that utilizes various components, including elastomers, filler material, textiles, and metallic wire/beads. Production of tires also involves the use of various adhesives for binding the elastomer part with the cord/textile part of the pneumatic tire. One commonly used adhesive material is butadiene-styrene-vinyl pyridine rubber (VPR), a random terpolymer of styrene, butadiene, and 2-vinyl pyridine. Currently, researchers are interested in studying the interfacial interaction of GO and this model elastomer. Tang et al. [144] employed a latex co-coagulation technique to prepare a high performance GO/VPR composite to study the interfacial interaction between the elastomer and filler material. The availability of the lone pair of nitrogen atoms from the pyridine unit of the elastomer and the large number of GO hydroxyl groups makes the system ideal for studying interfacial activity. Hydrogen bonding was activated in the system by using calcium chloride as flocculent, and electrostatic interaction using hydrochloric acid. Such interactions can be monitored using high-resolution X-ray photoelectron spectroscopy. The nitrogen 1s electron was analyzed for the pure elastomer and the composite material. Two de-convoluted peaks were noted at 399.1 eV and 400.2 eV for the neat VPR (ascribed to two different chemical environments for the nitrogen atom in the VPR chain). Interestingly, these two de-convoluted peaks were reported to be shifted to 399.0 eV and 399.7 eV for the hydrogen-bonded GO/VPR complex as a result of enrichment of the electron density by hydrogen bonding. An extra peak was observed (in addition to the above two peaks) for the electrostatically interacting GO/VPR composite (399.0, 399.6, and 401.8 eV). The origin of the additional peak at 401.8 eV was formation of a positively charged nitrogen moiety in the VPR elastomer chain. The vulcanization characteristics of both composites were determined with respect to the following parameters: scorch time, optimum curing time, minimum torque, and maximum torque. The optimum cure time was found to increase with GO loading for both composites. The vulcanization process of the electrostatically interacting GO/VPR sample was slower than for the hydrogen-bonded sample. From this, it can be supposed that the VPR chains were confined to a greater extent by GO as a result of electrostatic interaction. Thus, a high storage modulus was registered for the electrostatically interacting GO/VPR sample.

A proper understanding of the reinforcement of elastomer chains by graphene sheets at the molecular level is crucial. In an attempt to understand such phenomena, the same group studied the effect of interfacial interaction on the chain dynamics of the same two composites using dielectric spectroscopy [145]. Two distinct relaxation processes (segmental relaxation and interfacial relaxation) were found to be active in both composites. The dielectric strength of the composites was noted to be higher than that of the neat polymer. Such a difference is attributed to the presence of graphene in the elastomer matrix, which alters the local environment of the elastomer chains. In their study, a distinct difference between the segmental dynamics of the two composites was noted. The electrostatically

prepared composite demonstrated a higher segmental relaxation at a filler loading of 1.5%. However, the hydrogen-bonded sample was nonresponsive to segmental relaxation with a variation in GO loading. The observation was explained in terms of the dispersion of GO inside the matrix. It is worth mentioning that the conductivity of the electrostatically prepared composite was higher than that of the hydrogen-bonded sample. The interfacial relaxation of the composite was monitored from the dielectric loss spectra plot at high temperature. An asymmetrically broad peak was noted for the hydrogen-bonded sample, whereas the electrostatically interacting sample registered two peaks. Such an observation is attributed to the restricted interfacial dynamics induced as a result of better interaction in the case of the electrostatically interacting GO/VPR sample. Thus, it can be concluded that tuning of the properties of elastomer/graphene composites can be achieved through proper modulation of the interfacial interactions.

1.6.5 Acrylonitrile-Butadiene Rubber and Carboxylated Acrylonitrile-Butadiene Rubber

Acrylonitrile-butadiene rubber (NBR) is a random copolymer of acrylonitrile and butadiene, synthesized using emulsion polymerization techniques. Depending on the synthesis conditions (polymerization temperature), two different grades of NBR can be produced (hot and cold varieties). The percentage acrylonitrile content in the NBR is crucial for modulation of the properties of the rubber. Carboxylated NBR (XNBR) is a modified version of NBR. Addition of the carboxylic unit to the butadiene part of the elastomer induces an additional polarity to the elastomer, Furthermore, these carboxylic sites are crosslinkable with metal ions such as zinc. As a result, further improvement in the properties of the elastomer can be achieved.

The chemical constituents in the framework of the NBR impart resistivity of the material toward chemicals (except strong oxidizing agents) and oils. Thus, NBR is widely used for making specialty rubber products such as oil hoses and gloves. Al-Solamy et al. [146] developed a piezo-resistive conducting material based on graphene and NBR (26% acrylonitrile content). Traditional two-roll mixing was adopted for generating the nanocomposite material, followed by compression molding. TEM revealed that an increase in filler loading (from 0.5 to 2%) resulted in a decrease in the aspect ratio of the graphene. Even though the authors failed to provide any suitable explanation for such an observation, we speculate that the processing parameters involved in fabrication of the graphene/NBR composite were responsible. It was also commented by the authors that a decrease in the aspect ratio of the graphene platelets assisted in better dispersion, and helped in the formation of a pressure-sensitive percolating conducting network.

Singh et al. [147] reported the unique ability of a rGO/NBR composite to absorb microwaves over a broad frequency range. The composite was fabricated at different levels of rGO loading (2, 4, and 10%). Waveguide methodology was utilized to measure the complex permittivity and permeability of the material to gain an insight into the microwave absorption properties. A solution-casting technique

was used to produce the nanocomposite. The dihedral angle present in rGO caused the microwave to face a series of reflection. As a result, the microwave got absorbed inside the rGO/NBR matrix. These multiple reflections greatly increase the interactions of the microwaves with the elastomer matrix. As a result, phenomena such as ionic conductance and dielectric relaxation become active and the energy generated is dissipated in the form of heat.

Control over the tribological properties of the composite, especially the wear property, is a very important aspect of rubber-related products. An attempt was made by Wang et al. [148] to understand the mechanical properties and the tribological aspects of composites prepared by either mechanical mixing (microcomposite) or latex phase co-coagulation (nanocomposite). A strong correlation between the dispersion of the graphene and the processing parameter was described. The dispersion of graphene in the rubber matrix was reflected by the mechanical properties. The tensile strength of the nanocomposite was better than that of the microcomposite. The patterns on the worn surfaces of the neat and composite materials were analyzed using SEM through proper understanding of the abraded surfaces (see Fig. 19). Neat NBR was reported to show craters and sharp ridges at a slower velocity. However, at a higher velocity, the virgin elastomer became flat and prominent fatigue cracks were observed on the surface. By contrast, for the microcomposite, direct chipping of graphite was observed under the same experimental conditions. Such an observation was attributed to the poor interfacial interactions between graphite and elastomer. However, the nanocomposite demonstrated a smooth and flat surface as a result of better interfacial interactions between filler and elastomer. Basically, cycles involving chipping of the graphite layers from the matrix, formation and breaking of a lubricant film, concurrent matrix wear, and re-formation of lubricant film acted as a cumulative factor for the wear of GO/NBR composites.

On a similar note, Li et al. [149] studied tribological aspects of the GO/NBR nanocomposite. A solution-casting methodology was adopted for fabrication of the samples. A dramatic decrease in the coefficient of friction (COF) and the specific wear rate for the nanocomposite was recorded. However, the values increased with an increase in filler concentration. It was conjectured by the authors that at low loading, GO was de-bonded from the matrix during the direct sliding test and became deposited over its counterpart. As a result, a thin film was formed and this film assisted in minimizing the COF and specific wear rate. However, at a higher loading, thick graphite layers were chipped off and the equilibrium between the friction couple was perturbed. As a result, an increase in filler content resulted in adhesion and fatigue abrasion.

A melt mixing methodology (Brabender Plasti-Corder) was established by Verghese et al. [150] for the production of pristine graphite/NBR nanocomposites. The reinforcing capability of the pristine graphite was compared with that of carbon black under similar loading. Similar to the observation made by Tang et al. [144] for the GO/VPR system, the cure characteristic parameters were found to increase significantly compared with the virgin elastomer (Fig. 20). By contrast, carbon

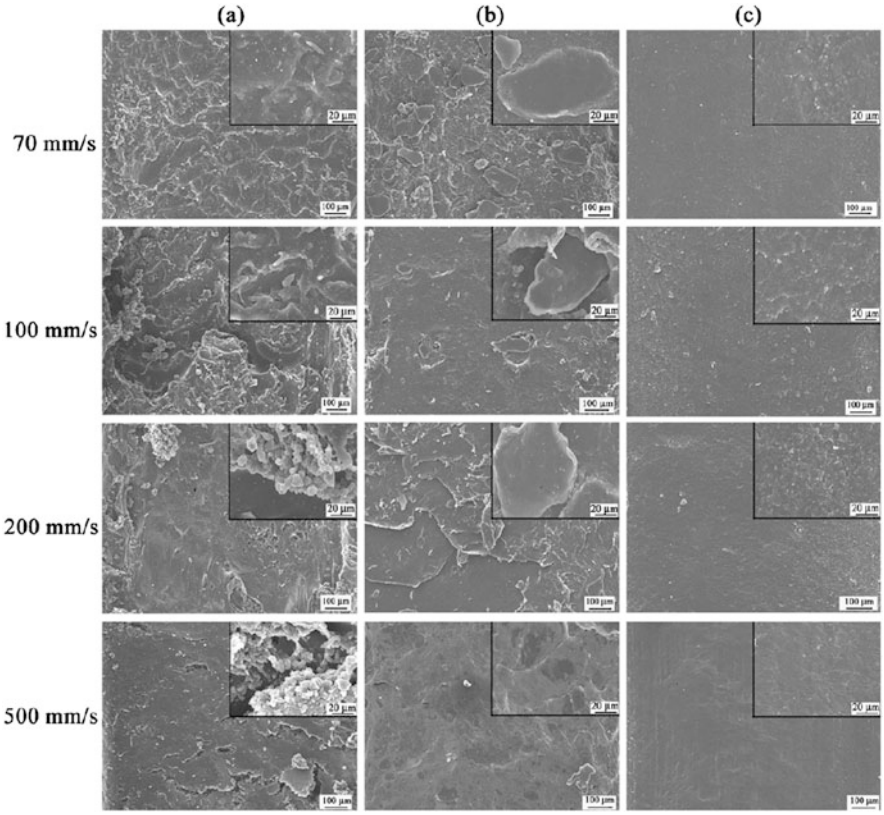

Fig. 19 SEM micrographs of worn surface of (**a**) NBR rubber, (**b**) expanded graphite/NBR (5 phr filler loading) microcomposite, and (**c**) expanded graphite/NBR (5 phr filler loading) nanocomposite at different sliding velocities (60 N). Note: Sliding direction is downward. [Reprinted (adapted) with permission from [148], Copyright 2012, Elsevier]

black-filled samples under similar loading registered higher torque values than the graphene-filled samples. However, the scorch safety of the carbon black-filled samples was poorer than that of graphene-filled samples. The increase in scorch time for graphene/NBR was attributed to the high surface area of the graphene platelets. The plate-like structure of the filler material acted as a barrier against the sulfur-accelerator and zinc-accelerator systems. A 65% increase in the tensile strength was recorded with graphene, where a 35% decrease in tensile strength was registered for the carbon black-loaded sample at a similar filler concentration (1 phr). However, a synergistic effect of both the filler materials was observed when a hybrid of graphene and carbon black was utilized as reinforcing filler for the NBR matrix. The storage modulus was higher than that of the individual filler materials. The observation was explained on the basis that the elastomeric chains become entangled with the void space of the carbon black (physical

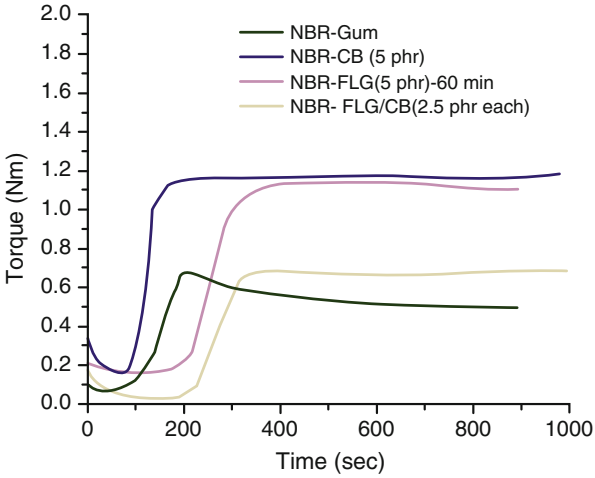

Fig. 20 Comparison of rheograms for NBR/FLG, NBR/carbon black, and NBR/FLG–carbon black compositions (filler loading, 5 phr); *FLG* few-layer graphene. [Reprinted (adapted) with permission from [150], Copyright 2013, Elsevier]

crosslinks), and that the high surface area of the graphene sheet resulted in a high storage modulus in the rubbery region.

The effect of the filler surface activity on the mechanical and dielectric properties of NBR nanocomposites was studied by Moewes et al. [151] using a melt mixing technique (Haake internal mixer). The role of surface porosity and roughness on the formation of high performance NBR-based elastomer composites (acrylonitrile content 39%) was evaluated by the authors. In conjunction with 20% dioctyl phthalate, the graphene sheet in the NBR matrix had an exfoliated structure, as demonstrated by TEM. However, the lateral dimension of the graphene sheets was found to be reduced. This was perhaps a result of the shearing force induced by the internal mixer on the graphene sheet.

Mensah et al. [152] prepared GO/NBR composites using solution casting methodology. The curative package was introduced to the system while milling the sample in a two-roll mill. The interfacial interaction between GO and the NBR chains could be observed in scanning electron microscopy (SEM) images of strained samples of the GO/NBR nanocomposite. An outward protrusion of carbon nanotubes under similar strained conditions for carbon nanotube/elastomer samples has been reported [153]. However, the GO platelets were observed to be embedded in the NBR matrix, even under strained conditions. This shows that the GO matrix demonstrated an excellent interfacial interaction with the elastomer chains.

We note that the graphene-based NBR composites have mostly been developed from pristine graphene or using GO. However, Zhi et al. [154] recently utilized an aminopropyl triethoxysilane (APTES)-functionalized GO to prepare an NBR nanocomposite. The modification of GO by APTES was assisted by ammonia. A latex-based co-coagulation technique was employed to prepare the APTES-functionalized GO/NBR nanocomposite (calcium chloride was the flocculant). A large extent of exfoliation of the functionalized graphene platelets (basal plane spacing of 1.5 nm, as observed from XRD) was observed in the NBR matrix. As

described in the above article, in the present case, the authors noted that the modified GO was deeply embedded inside the rubber matrix, as shown by SEM analysis of the fracture surface of the tensile specimen [154]. In line with the earlier report [144], the maximum torque value of the composite gradually increased with an increase in filler loading. The crosslink density of the composite was calculated using the Flory–Rehner equation. The swelling ratio decreased with an increase in filler volume, as shown in Fig. 21. The authors conjectured that the filler inside the matrix adopted a tortuous structure and that such a structure inhibited the solvent diffusion process. The nanocomposite exhibited a high dielectric constant with a low loss factor.

In a similar attempt, Tian et al. [155] developed a material with high dielectric constant and low dielectric loss that was based on GO and XNBR. The functionalized graphene platelets were encapsulated inside the XNBR latex using ultrasonication coupled with a spin flash drying method. The resulting composite was further molded and vulcanized under compression molding. Encapsulation of the graphene sheet was conjectured to take place via the pathway shown in Fig. 22. To increase the interfacial polarization ability of the functional graphene, it was reduced in situ by a thermal technique at 180°C. As a result, a 3D segregated filler network was formed. In comparison with the virgin elastomer, the dielectric constant of the reduced graphene/XNBR started to increase with a very low loading of the filler material (0.25 phr). Such an observation was attributed to the formation of a percolating network of filler material inside the elastomer matrix. It was also claimed by the authors that the system demonstrated the lowest dielectric constant compared with other graphene/elastomer composites.

In a separate study, Liu et al. [156] modified graphene noncovalently with sodium humate and utilized the modified graphene platelets in the XNBR matrix. Prior to the noncovalent modification, pristine graphite was oxidized and further reduced. The composite was prepared using a latex co-coagulation methodology (calcium chloride was utilized as flocculant). The coagulated matrix was passed through a two-roll mill for incorporation of the curatives and then vulcanized in a

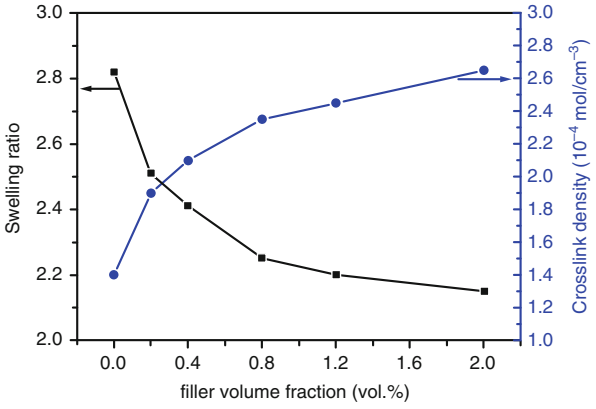

Fig. 21 Swelling ratio and crosslink density of GO-APTES/NBR composites with different GO-APTES loadings. [Reprinted (adapted) with permission from [154], Copyright 2015, Elsevier]

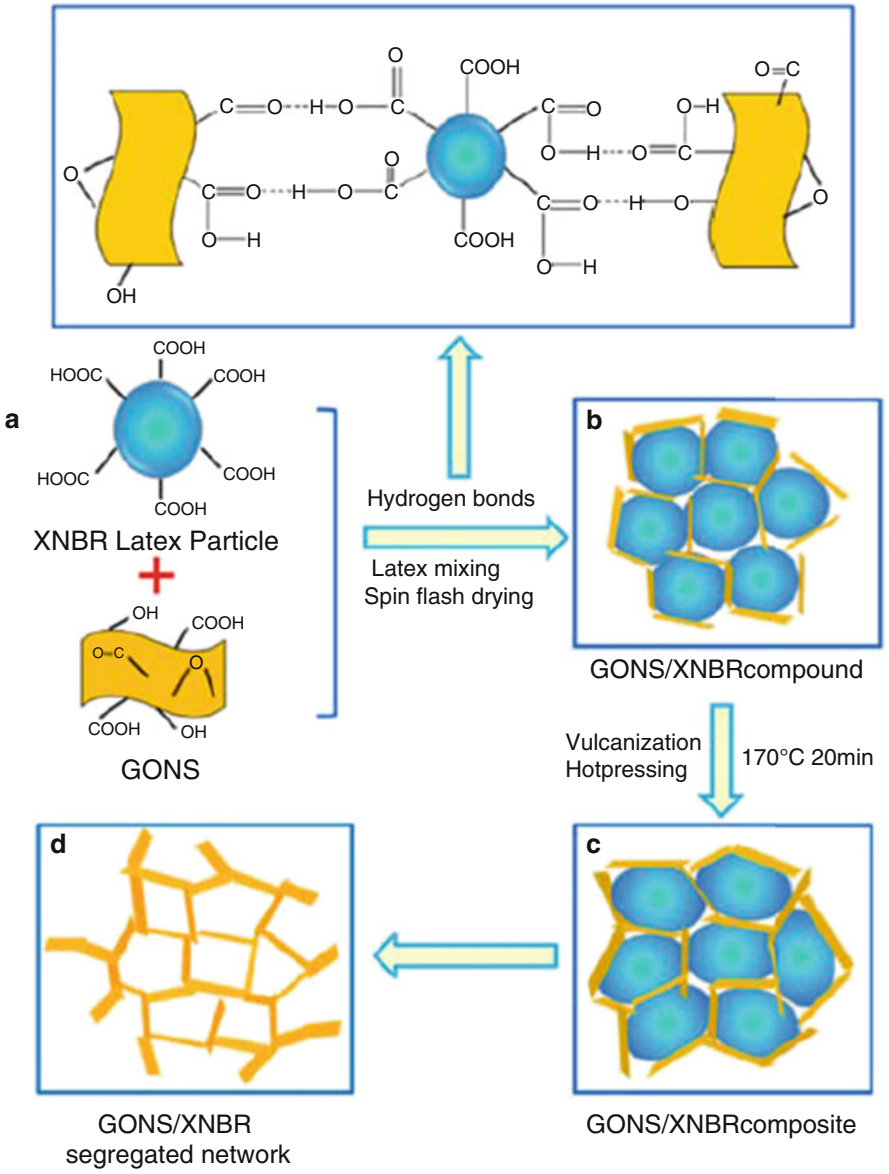

Fig. 22 Preparation of composites of graphene oxide nanosheets and XNBR with segregated network structure. [Reprinted (adapted) with permission from [155], Copyright 2014, Elsevier]

compression molding unit. The thiol unit of the modifier assisted in the formation of additional crosslinks along with the carboxyl group of the XNBR. Such crosslinking was a result of the presence of MgO in the curative package. A chelating effect greatly enhanced the interfacial interaction between filler and elastomer matrix.

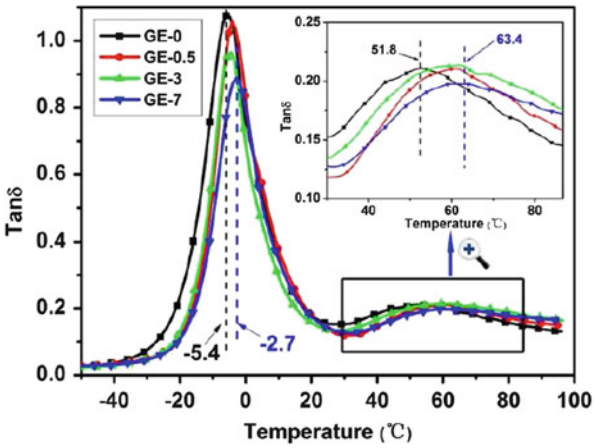

Fig. 23 Tan δ of sodium humate-functionalized graphene/XNBR composites as a function of temperature. [Reprinted (adapted) with permission from [156], Copyright 2013, American Chemical Society]

Such an interfacial interaction was further proved from dynamic mechanical analyses of the neat rubber and nanocomposite. As shown in Fig. 23, the pristine elastomer registered a T_g of about −5.4°C, whereas the T_g shifted to ca. −2.7°C for the nanocomposite. Such a shift of T_g towards a higher temperature is an indication of the restricted chain dynamics of the elastomers as a result of the presence of graphene platelets. Additionally, a secondary peak was also noted around 55°C for the neat polymer as a result of the formation of ionic clusters of carboxylates (ionic transition). Similarly, the secondary peak was also shifted and broadened as a result of the presence of graphene sheets.

The thermal stability, conductivity, and thermal diffusivity of XNBR were modulated by Wang et al. [157] by incorporating functional graphene in the XNBR latex. Incorporation of 1.6 phr of GO greatly enhanced the thermal stability of the XNBR matrix. The maximum degradation of virgin elastomer was noted at 458.9°C, whereas the nanocomposite registered maximum decomposition at 473.5°C. Such an enhanced thermal stability was attributed to better interfacial interactions between filler and elastomer matrix. Increases of 1.4- and 1.2-fold (compared with the neat elastomer) in the thermal conductivity and thermal diffusivity, respectively, for the nanocomposite sample were recorded.

1.6.6 Fluoroelastomers

Fluoroelastomers (FKMs) fall into a special category of elastomer. They exhibit superior properties, even during a harsh service life (exposure to chemicals, high temperature, and oils). Their superior performance is attributed to the unique chemical structure of the C–F bond. Early reports on the development of FKMs were registered by DuPont, who have successfully synthesized a copolymer of hexafluoropropylene and vinylidene fluoride. The service life of an FKM elastomer is determined by the percentage fluorine content. A higher percentage of fluorine

imparts a better performance in extreme conditions. Despite such wonderful properties exhibited by neat FKM rubbers, they are often mixed with different nanomaterials to develop high performance FKM-based elastomeric nanocomposites. For sealing applications in the oil industry, Wei et al. [158] developed a GO/FKM-based sealant material with targeted applications in the petroleum industry. An acetonitrile phase mixing methodology was adopted for preparation of a GO/brominated FKM master batch. The selection of acetonitrile as solvent for developing the nanocomposite was guided by the Hansen solubility parameter. The master batch was mixed at different concentrations with neat FKM and cured using peroxide as the crosslinker. The resulting molded nanocomposite demonstrated remarkable liquid barrier properties when methyl ethyl ketone was selected as the liquid phase. Additionally, the mechanical properties of the nanocomposite were reported to be superior to those of neat FKM rubber. The enhanced performance of the nanocomposite was attributed to the formation of covalent bonds between GO and the brominated FKM rubber. The mechanistic pathway is given in Fig. 24.

It is worth mentioning that rGO was found to interfere with the crosslinking procedure; however, GO facilitated the crosslinking procedure. Such an inference was drawn by the authors based on the cure rate index and crosslink density calculations [158]. On a similar note, Xing et al. [159] studied the mechanical,

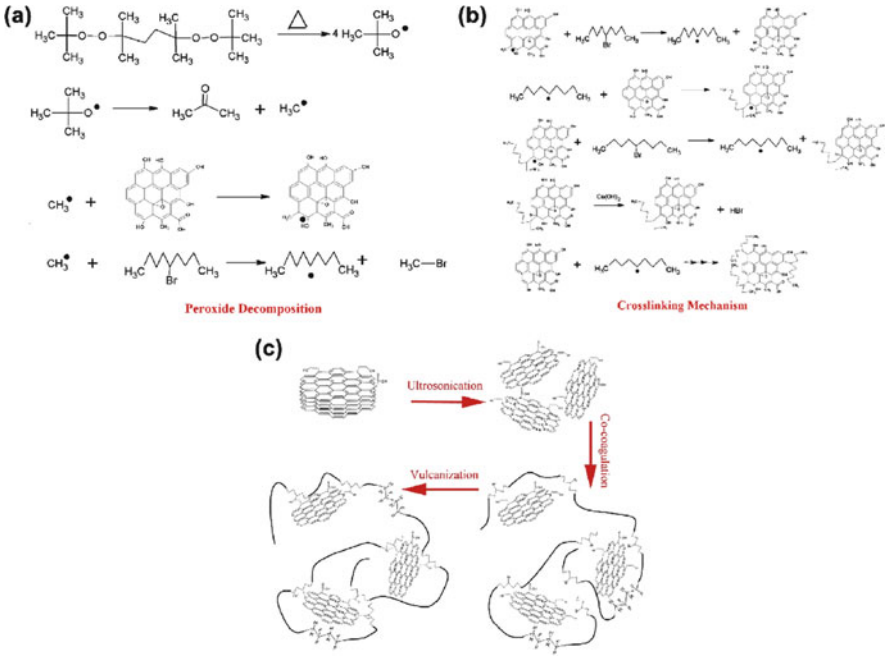

Fig. 24 The proposed (**a**) peroxide decomposition, (**b**) crosslinking mechanism, and (**c**) vulcanization of brominated FKM with GO. [Reprinted (adapted) with permission from [158], Copyright 2014, Elsevier]

thermal conductivity, and dielectric properties of rGO/FKM nanocomposites. *N, N′*-Dimethylformamide (DMF) was selected as the solvent for preparation of the FKM nanocomposite master batch. The GO was reduced in situ thermally during preparation of the master batch. The master batch was further mixed with neat FKM rubber together with the curatives in a two-roll mill. The properties of the rGO/FKM nanocomposite were compared with those of the GO/FKM nanocomposite. Interestingly, Xing et al. reported significant agglomeration at a loading of 1% GO in the nanocomposite. However, the rGO was well dispersed in the FKM matrix up to a filler concentration of 3%. The authors attributed the adsorbed DMF moiety over the rGO sheets to be responsible for preventing re-stacking of the layers. As a result of better dispersion, a higher dielectric permittivity was registered for the rGO/FKM nanocomposite than for the neat FKM.

A nanocomposite of chemically functionalized graphene filler and bromide FKM was demonstrated by Wei et al. [160]. A peroxy curing system was adopted for its preparation. Allyl amine was made to react with GO in the presence of a catalyst. The pre-curing temperature of FKM elastomers (173°C) is close to the thermal degradation temperature of GO (200°C). Thus, reduced allyl-functionalized graphene (better thermal stability than GO) was selected as filler instead of allyl-functionalized GO or GO. Additionally, study of the curing kinetics demonstrated that reduced allyl-functionalized graphene decreased both the scorch time and optimum cure time. Reduced GO hindered the radical reaction between the bromine group of the FKM elastomer and the peroxy curing agent. However, the reduced allyl-functionalized graphene accelerated the vulcanization process. From this, it was inferred that the allyl group actively participates in the vulcanization process, resulting in a higher crosslink density than registered for the other nanocomposites. The vulcanization kinetics were also studied by performing a rheometer test at different temperatures. Calculation of the energy of activation indicated faster kinetics for the reduced allyl graphene than for rGO.

1.6.7 Thermoplastic Polyurethane Elastomer

Polyurethane (PU) is a typical class of polymer and is available both as thermosets and thermoplastics. Generically, most PUs are synthesized by the reaction between substituted isocyanate and polyols through a urethane linkage. As a result, hard and soft segments are imparted to the PU. It is one of the most widely used polymers for multifaceted applications such as foam, seals, and gaskets. Thus, to maximize its potentiality, it is further derivatized by mixing with different nanoparticles. In the field of graphene-based nanocomposites, PU is a topic of research for polymer scientists and in the polymer industry. Some of the interesting reports are discussed in this section.

Quan et al. [161] studied the effect of graphite nanoplates on the thermal degradation behavior of thermoplastic PU. The expanded graphite was developed by annealing graphite intercalated compound. DMF was selected as the solvent for both filler and polymer. Sonication was utilized to homogenize the mixture, which

was then coagulated from alcohol. The isolated nanocomposite powder was treated as a master batch and mixed with neat PU in a Haake rheocord to develop a PU-based nanocomposite. The cone calorimetry test was performed on the developed composite. The heat release rate (HRR) indicated that incorporation of graphite nanoplates improved the flame retardancy of the material.

Khan et al. [162] developed a stiff and tough composite from PU by mixing it with solvent and exfoliated graphene. A mixture of graphene and PU was prepared at different mass fractions in a mixture of DMF and THF and homogenized using ultrasonication. Composite films were generated using a drop-casting methodology. The hard and soft segments of the PU were found to stabilize the graphene and, as a result, the mechanical properties of the composite were superior to those of neat polymer. Two PU moieties of different hard segment chain length were synthesized by Pokharel et al. [163]. The hard segment length of the PU was found to affect the thermal and mechanical properties of GO/PU composites . Additionally, PU was also grafted onto GO. All the sets of nanocomposites so generated demonstrated better mechanical properties than neat PU. The strain hardening of PU was found to improve with an increase in GO loading, as well as with the hard segment length. It was conjectured by the authors that the PU-grafted GO plates and the soft segment of PU were oriented and resulted in improved mechanical properties. Apart from the grafted sample, the PU nanocomposites with longer hard and soft segment lengths registered better mechanical strength than the composites with shorter PU segment length. Such an improvement in mechanical properties was attributed by the authors to be a result of positive interaction between the soft segment and GO.

The dynamic mechanical, rheological, and dielectric properties of the modified graphene and PU were demonstrated by Sadasivuni et al. [164]. The graphite was modified by oxidation. Further, the oxidized graphite was modified with methylenebis(phenyl isocynate). Solvent phase mixing was utilized for development of the nanocomposites. The functional groups of the graphite assisted dispersion of the graphite inside the polymer matrix. However, electron microscopic studies indicated that isocynate-modified graphite demonstrated better dispersion than graphite oxide. The good dispersion was reflected in the increased storage modulus of the nanocomposite compared with the neat polymer. The increase in storage modulus was directly proportional to the filler loading. Incidentally, the isocyanate-modified GO/PU nanocomposite registered a higher storage modulus than the GO-filled system. A similar trend was reported for the loss modulus.

On a similar note, to enhance the dispersion of graphite inside the PU matrix, Yang et al. [165] modified GO with polydopamine using a Micheal addition followed by reduction. A solution phase development of the nanocomposite was adopted. It was observed that polydopamine coating facilitated dispersion of the filler. Further, it also assisted in a stress transfer mechanism that gave the nanocomposite excellent mechanical properties. A 600% increase in the Young's modulus compared with neat PU was observed by loading PU with 0.94% vol. of polydopamine-coated rGO. Such an increase in the Young's modulus was attributed to noncovalent interactions, such as hydrogen bonding between the modified graphene and the hard microdomains of the PU.

The tribological and anticorrosion properties of PU filled with modified graphene or modified GO were demonstrated by Mo et al. [166]. 3-Aminopropyltriethoxysilane was utilized to modify GO and graphene. The samples were prepared using a solution mixing methodology. The tribological properties of the nanocomposites were determined in terms of COF and wear rate. The COF was estimated in terms of dry sliding and seawater-lubricated sliding. Addition of functionalized graphene resulted in an increase in the COF value, followed by stabilization. However, the wear rate initially decreased and then increased. Such a response was suggested to be a result of an interbalance between reinforcement, lubrication by the fillers, and crack generation by the fillers. Of the selected fillers, the oxidized filler generated lesser cracks than the un-oxidized variety. Such an observation was explained in terms of filler dispersion.

A unique solution phase mixing strategy was adopted by Liu et al. [167] for the development of GO/PU and rGO/PU nanocomposite foams. PU foams were cut into blocks and soaked in GO solution (concentration of filler material was 2 mg/mL) for 1 h. The foams were isolated and vacuum dried for 24 h at 30°C. The authors also developed rGO/PU foams by in situ reduction of GO with hydrazine and then soaking the PU foam in the solution. Following this strategy, porous structures were formed, as shown in Fig. 25. The rGO-containing foam system demonstrated better compressive strength than both the GO-filled system and the neat PU system. Additionally, the rGO-containing foam system behaved as a super-hydrophobic and super-oleophilic material. Thus, it can be utilized as an oil adsorber. A similar strategy for development of GO/PU-based flexible foam materials was also reported by Hodlur and Rabinal [168]. The GO-containing foam was reduced in situ to form rGO/PU foam. Interestingly, the latter foam demonstrated a pressure-sensitive conducting behavior. With an increase in pressure from 1 to 1.5 atm, the conductivity of the foam increased fivefold. The reason for such a pressure-sensitive conductivity of the nanocomposite foam was related to the self-assembly of graphene sheets inside the PU foam matrix.

Liang et al. [169] utilized the solution casting technique to develop infrared-triggered actuators from a nanocomposite of chemically functionalized graphene and thermoplastic PU. Three different functionalization schemes were adopted. Graphene was sulfonated, as well as modified with an isocyanate group. Additionally, rGO was utilized as a potential nanofiller. Of all the fillers utilized, the sulfonated variety demonstrated repeated infrared actuation properties for the resulting PU nanocomposite. It is also interesting to note that Kim et al. [170] demonstrated that graphene/PU nanocomposites exhibited self-healing properties when subjected to near infrared radiation (NIR). A solvent casting technique was adopted for production of the nanocomposite. GO was modified with phenyl isocyanate and then blended with the PU solution. The healing process was attributed to the intermolecular diffusion of polymer chains, assisted by thermal energy and infrared radiation. The modified graphene sheets absorb NIR and provide thermal energy for the healing process to take place quickly.

Apart from the solution phase mixing technique, Valentini et al. [171] employed a melt mixing technique for the development of nanocomposites based on

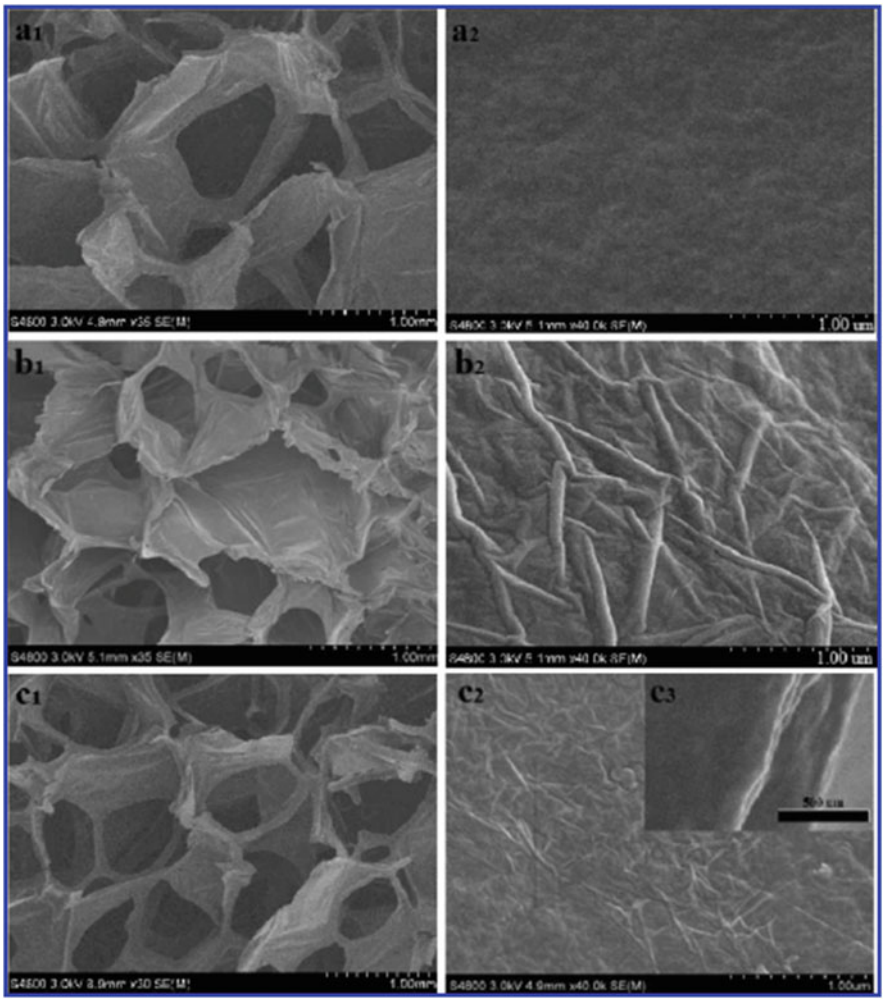

Fig. 25 SEM micrographs of ($\mathbf{a_1}$, $\mathbf{a_2}$) PU, ($\mathbf{b_1}$, $\mathbf{b_2}$) graphene oxide-containing foam, and ($\mathbf{c_1}$, $\mathbf{c_2}$) reduced graphene oxide-containing foam. [Reprinted (adapted) with permission from [167], Copyright 2013, American Chemical Society]

thermoplastic PU and exfoliated graphite using a twin-screw microcompounder. The resulting materials were subjected to microwave irradiation to test their electromagnetic properties. The electromagnetic property of the composite was directly related to the filler concentration. It was proposed by the authors that significant microstructures were formed inside the nanocomposite. Such microstructure formation resulted in the capacitative nature of the nanocomposite. Thus, it can be reasonably inferred that, by adjusting the microstructure of the nanocomposite, it is possible to achieve composites with tunable electric properties.

Kim et al. [172] comprehensively studied the effects of the surface chemistry of graphene and the processing route for nanocomposites based on PU and graphene. Isocyanate-treated graphene and thermally reduced graphene were selected as filler materials. Melt mixing, in situ grafting, and solution phase mixing were selected as processing routes. The electrical conductivity and gas barrier properties of the composites were evaluated. It was noted that with a nominal loading of 0.5% thermally reduced graphene, electrical conductivity of the composite was achieved. X-ray characterization of the melt samples prepared with pristine graphite indicated the presence of a tactoid-like structure of the filler units. From this, it was inferred that exfoliation of graphene sheets was not possible in the melt compounder. However, thermally reduced graphene demonstrated better dispersion than the pristine material when mixed in an internal mixer (at low filler concentration). Interesting observations were made on the basis of TEM analysis. The filler moiety was found to be oriented in the melt mixed samples, unlike the situation in solution blended samples and in situ polymerized samples. In contrast to the thermally reduced graphene filler, the isocyanate-modified filler material was better dispersed and intercalated in the polymer matrix. Additionally, there was a 10% increase in tensile stiffness and 90% decrease in nitrogen gas permeability in response to 3 wt % loading of isocyanate-modified graphene.

1.6.8 Ethylene Vinyl Acetate

The impact of incorporation of graphite as a nanofiller inside commercially important ethylene vinyl acetate (EVA) rubber, with 60% acetate content, was demonstrated in our laboratory [38]. A solution phase mixing of the nanofiller and elastomer was carried out. A peroxy-based curing system was adopted. The potentials of naturally occurring graphite and expanded graphite as filler materials were tested. The expanded graphite demonstrated a higher surface area (0.32 m^2/cm^3) than the natural graphite (0.15 m^2/cm^3). A variation in filler proportion from one part to eight parts was adopted for expanded graphite, whereas natural graphite was only tested at four parts. Neat EVA registered a tensile strength of 5.5 MPa, whereas the sample loaded with 4 phr expanded graphite demonstrated a tensile strength of 7.5 MPa. It is interesting to note that 4 phr of natural graphite resulted in a tensile strength of 4.6 MPa, which was lower than that of neat EVA. Such an observation was attributed to the dispersion of filler inside the EVA matrix. Expanded graphite was well dispersed in the EVA matrix, whereas natural graphite mainly formed agglomerated microstructures inside the matrix. The reinforcing ability of graphite as a filler material was explained in terms of the Kraus plot. The composites were subjected to swelling in toluene at room temperature for 72 h. From the slope of the Kraus plot, a negative value of the slope was obtained. As a result, it was surmised that the filler–polymer interaction was very high, as shown in Fig. 26a. The thermal conductivity of the samples were also examined. Addition of expanded graphite enhanced the thermal conductivity compared with the system filled with natural graphite. Incorporation of 4 phr of expanded graphite increased the thermal

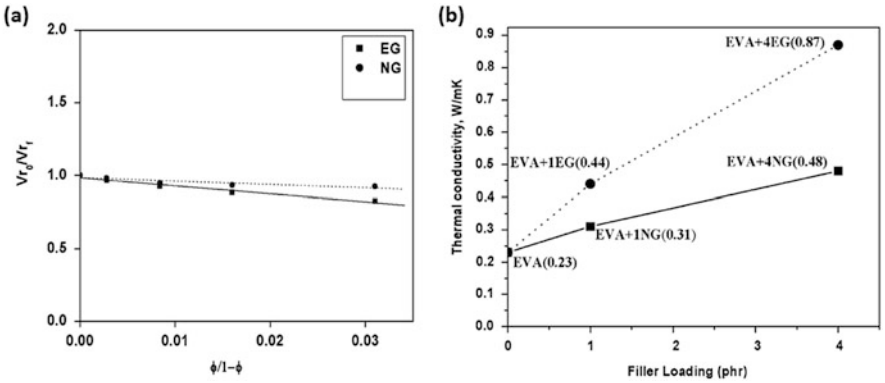

Fig. 26 (**a**) Kraus plots of EVA + expanded graphite (EG) and EVA + natural graphite (NG). (**b**) Thermal conductivity of EVA + EG and EVA + NG. [Reprinted (adapted) with permission from [38], Copyright 2008, Springer]

conductivity from 0.24 to 0.87 W/mK, as shown in Fig. 26b. From this, the authors concluded that a conducting filler network was formed inside the EVA matrix when expanded graphite was added to it.

Additionally, in a different project, we explored the effect of modification of graphite and studied the physical properties of the resulting EVA-based nanocomposites [39]. Briefly, three different modifications of naturally occurring graphite were adopted: (a) mixed acid treatment, (b) potassium permanganate and mixed acid treatment, and (c) amine modification. A solution casting technique was adopted for the preparation of the EVA-based nanocomposite. The properties of EVA containing modified graphite were compared with those of neat EVA and of a commercially available nanocomposite of EVA filled with expanded graphite. .The modified graphite demonstrated better dispersion in the EVA matrix than unmodified filler, as shown in Fig. 27. As a result, better dynamic mechanical properties were also recorded. It was also noted that expanded graphite formed a filler network inside the EVA matrix.

Yuan et al. [173] reported the development of conducting EVA nanocomposites. Reduced GO decorated with polyaniline was utilized as the filler material in their study. In situ polymerization of aniline monomer was carried out in the presence of rGO filler. A solution mixing technique was adopted for generation of the nanocomposite. SEM studies suggested that rGO/EVA nanocomposites demonstrated isolated island-like structures, whereas a networked structure was obtained for the composite containing rGO-polyaniline. Such formation of a network structure contributed to the conducting behavior of the EVA nanocomposite.

The impact of surface functionalization of graphite on the thermal and mechanical properties of EVA nanocomposites was demonstrated by Kuila et al. [174]. GO was modified with octadecyl amine. A solution casting methodology was adopted for the preparation of EVA-based nanocomposite. A 1% loading of the modified filler material resulted in a 74% increase in the tensile strength compared with the

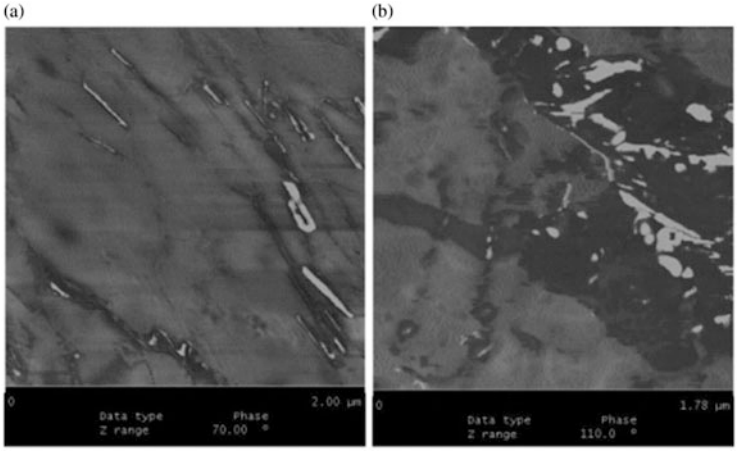

Fig. 27 (**a**) AFM phase image of modified graphene/EVA nanocomposite (2 phr filler loading). (**b**) AFM phase image of unmodified graphene/EVA nanocomposite (2 phr filler loading). [Reprinted (adapted) with permission from [39], Copyright 2008, John Wiley & Son]

neat EVA. Such an improvement in mechanical properties was attributed to the good dispersion of the nanophase inside the EVA matrix. The nanocomposite was found to be thermally more stable than the neat EVA by 42°C.

Apart from performing the covalent modification of graphite to have better dispersion of the nanofiller inside the EVA matrix, Sefadi et al. [175] utilized surfactants, instead of covalent modification of graphite, to obtain better dispersion of the nanofiller inside the EVA matrix. SDS was used to noncovalently modify the surface of expanded graphite. The nanocomposites were prepared in an internal mixer. The properties of EVA containing noncovalently modified graphene were compared with a nanocomposite of EVA containing unfunctionalized expanded graphite. An insight into the changes in crystallinity in the presence of graphite was obtained. A 20% increase in the crystallinity of EVA was noted (compared with neat EVA) in the presence of noncovalently modified graphene; however, a reverse trend was seen in the presence of unmodified filler. A 20% decrease in the percentage crystallinity was noted compared with neat EVA.

1.6.9 Other Miscellaneous Elastomers

The surface energy and mechanical, damping, and thermal properties of GO/ethylene propylene-diene rubber (EPDM) and a blend of EPDM and petroleum resin were studied by Chen et al. [176]. A combination of solution blending and mixing in two-roll mill was adopted for preparation of the composites. Electron microscopy studies showed that GO was well dispersed in both EPDM and the EPDM/petroleum resin blend. The good dispersion was attributed to matching of

the surface energy and low interfacial energy of GO and EPDM elastomer. A 50% increase in tensile strength of the nanocomposite was registered compared with the neat EPDM. A laboratory scale two-roll mill was utilized by Allahbakhsh et al. [177] for the preparation of nanocomposites based on EPDM and GO. The cure kinetics of composite formation were studied and it was noted that the incorporation of GO significantly reduced the activation energy compared with neat EPDM. The cure kinetics were combined with WAXD studies to help understand the underlying mechanisms. The XRD trace for un-compounded sample showed an X-ray diffraction peak at $2\theta = 11°$. This was primarily a result of the presence of GO. However, no such peak was observed for the compounded sample. From this, it was inferred that, during compounding, EPDM macromolecule chains become intercalated through the gallery spacing of GO at 170°C.

Butyl rubber (IIR) is one of the most commercially important elastomers because of its widespread application in the automotive industries. Lian et al. [178] reported the development of modified graphene/butyl rubber nanocomposites and studied their mechanical properties. Cetyltrimethylammonium bromide was adopted to modify GO. The resulting modified graphene was blended with butyl rubber using solution mixing for production of the nanocomposite. For comparison of the properties, pristine graphite was also blended with butyl rubber under similar conditions. Electron microscopy revealed that modified graphene sheets were well dispersed in the butyl rubber matrix, whereas pristine graphite exhibited stacked structures in the polymer matrix. The effect of dispersion was reflected in the mechanical properties of the nanocomposites. The modified graphene/butyl rubber nanocomposite demonstrated a 16-fold higher tensile strength than neat butyl rubber.

Brominated butyl rubber (BIIR) is an equally important derivative because of its faster cure kinetics and better adhesion properties than neat IIR. Xiong et al. [179] studied the thermal conductivity and stability of a GO-filled BIIR system. For this purpose, GO modified with an ionic liquid was selected as the filler material. The ionic liquid modifier became intercalated inside the basal spacing of the GO. As a result, better exfoliation of the modified graphene sheet was reported to take place in the elastomer matrix. A marginal increase of 5°C in the thermal stability of the nanocomposite compared with neat BIIR was obtained using 4% loading of the filler. Such an improvement in the thermal stability was attributed to a physical barrier induced by GO, which prevented the loss of low molecular weight fragments.

A grafting-to approach for the formation of high-performance graphene/BIIR nanocomposites was developed by grafting BIIR onto a simultaneously functionalized and reduced GO surface (BIIR-*g*-GO-PPD), as shown in Fig. 28a. The grafted graphene was then dispersed in the BIIR matrix. BIIR grafted onto an unmodified graphene surface was studied for comparison (see in Fig. 28b) [180].

Modification of graphene resulted in exfoliation of the nanoparticles, and the average thickness of the grafted BIIR on the GO-PPD and graphene surfaces was found to be 5 nm and 3 nm, respectively, as obtained from the height profile AFM analysis. This led to stronger interactions, imparting remarkable enhancement in

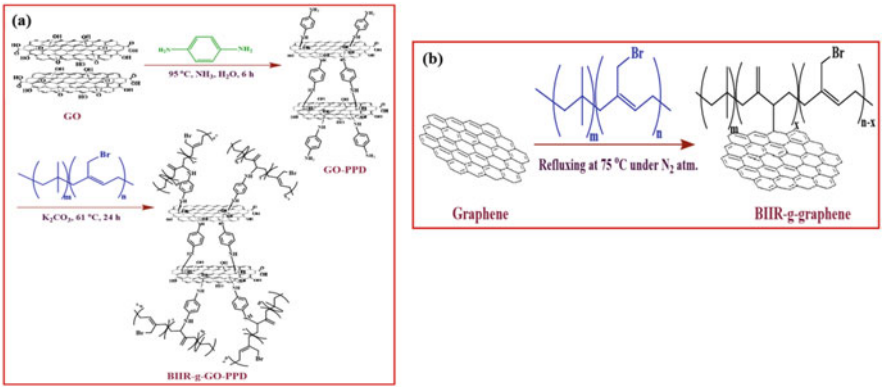

Fig. 28 Scheme for the tethering of BIIR on (**a**) phenyl amine-functionalized graphene (BIIR-*g*-GO-PPD) and (**b**) graphene (BIIR-*g*-graphene). [Reprinted (adapted) with permission from [180], Copyright 2016, Elsevier]

tensile strength (96%), storage modulus (89%), thermal stability (17°C), and permittivity (460%) and a significant decrease in gas permeability (41%) in the nanocomposites compared with neat BIIR (Fig. 29).

Biocompatible elastomers such as silicone rubber are of immense importance for the development of biocompatible scaffolds and implants. However, because of the poor mechanical strength of the virgin elastomers, they are often combined with different nanofillers. Recently, Tian et al. [181] reported development of a nanocomposite of polydimethyl siloxane (PDMS) and thermally expanded graphene. The nanocomposites were fabricated using a solution mixing technique. A tremendous increase in the dielectric constant for the composite was recorded when 2% graphene-based filler material was incorporated. Neat PDMS showed a dielectric constant of 3.1 at 10^3 Hz, whereas the value increased to 89.5 at 2% filler loading. Uniform dispersion of nanofiller accounted for the increase in dielectric constant. Because of the application of PDMS in actuators, the authors also studied the actuated strain of the composite. At a low electric field of 15 V/μm, the actuation strain noted for samples with 2% filler loading was 3.6%, whereas neat PDMS registered an actuation strain of 1.4%. Berean et al. [182] studied some other prospective graphene/PDMS nanocomposites. Enhanced gas permeation of a membrane based on graphene/PDMS, with a good mechanical properties, was achieved by the authors. Gases such as nitrogen, carbon dioxide, methane, and argon were utilized for this study. The authors were successful in developing an agglomeration-free nanocomposite with filler loadings of up to 0.25%. The enhanced gas permeation was attributed to the development of interfacial voids between the graphene filler and the PDMS chains.

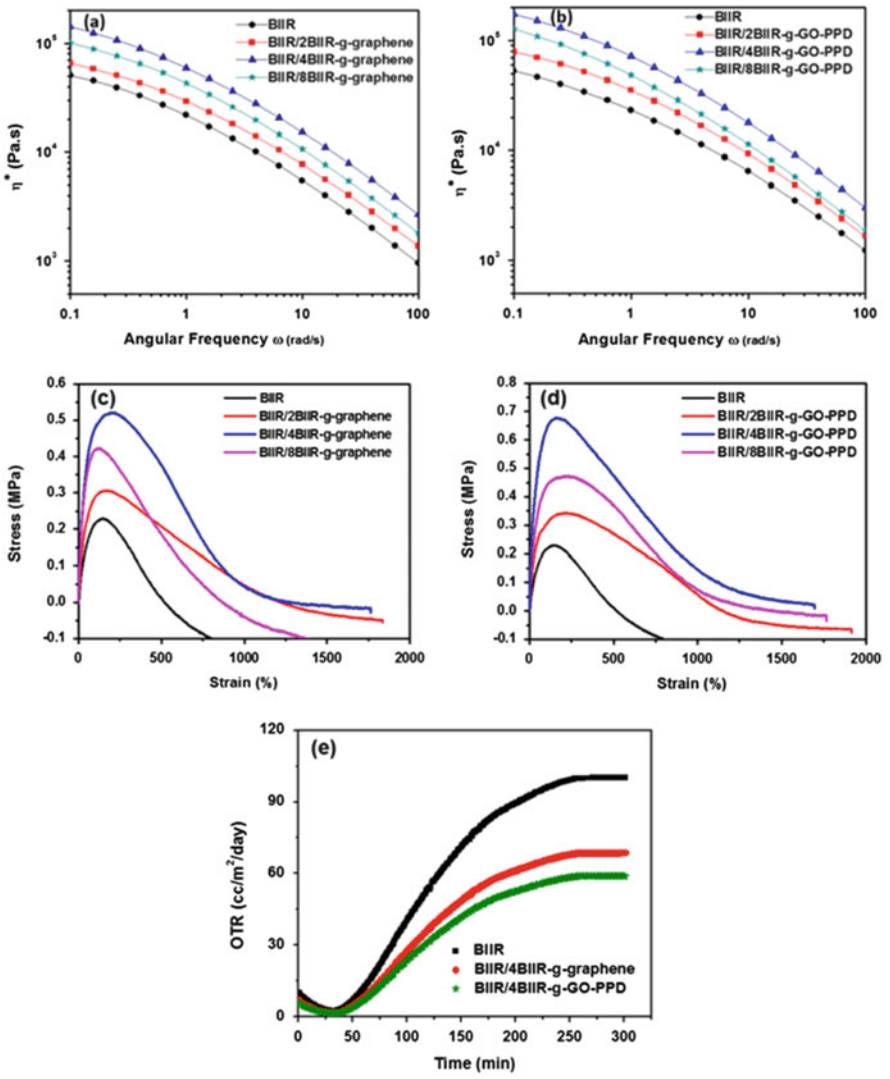

Fig. 29 Influence of (**a**) BIIR-*g*-graphene and (**b**) BIIR-*g*-GO-PPD loadings on complex viscosity (η^*) over a range of angular frequencies (ω) of BIIR nanocomposites. Influence of (**c**) BIIR-*g*-graphene and (**d**) BIIR-*g*-GO-PPD loadings on tensile stress–strain curves of BIIR nanocomposites. (**e**) Oxygen transmission rate (OTR) values for neat BIIR and BIIR nanocomposites with BIIR-*g*-graphene and BIIR-*g*-GO-PPD at 25°C. [Reprinted (adapted) with permission from [180], Copyright 2016, Elsevier]

1.7 Concluding Remarks

This chapter provides an insight into the structure and properties of graphene and graphite, and the nanocomposites incorporating them. The various types of

modification that are possible for graphene are comprehensively reviewed. Special emphasis is laid on understanding the fundamentals involved in the development of graphene/elastomer nanocomposites and their utility. The processing route adopted for the preparation of the graphene/elastomer nanocomposites is crucial in determining the dispersion of the graphene-based filler in the elastomer matrix. The correlations between dispersion of the filler and properties such as mechanical strength, thermal stability, and barrier and dielectric properties are reported and discussed. Additionally, the effects of covalent modification of graphene with different functional groups on the structure–property relationship of elastomer nanocomposites are examined in detail. The elastomers discussed in this chapter are representative of commonly used materials of high industrial importance.

References

1. Ajayan P (1999) Chem Rev 99:1787
2. McCreery RL (2008) Chem Rev 108:2646
3. Ijima S (1991) Nature 354:56
4. Kroto HW, Allaf AW, Balm SP (1991) Chem Rev 91:1213
5. Sengupta R, Bhattacharya M, Bandhopadhyay S, Bhowmick AK (2011) Prog Polym Sci 36:638
6. Allen MJ, Tung VC, Kaner RB (2010) Chem Rev 110:132
7. Roy N, Sengupta R, Bhowmick AK (2012) Prog Polym Sci 37:781
8. Novoselov KS, Geim AK, Morozov SV, Jiang D, Zhang Y, Dubunos SV, Grigorieva IV, Firsov AA (2004) Science 306:666
9. Mondal T, Bhowmick AK, Krishnamoorti R (2015) Chem Mater 27:716
10. Chatterjee T, Jackson A, Krishnamoorti R (2008) J Am Chem Soc 130:6934
11. Spons' Workshop Receipts (1921) Electro-plating on non-metallic substances, vol II: Dyeing to japanning. Spon, London, p 132
12. Schafhaeutl C (1840) J Prakt Chem 21:129
13. Schafhaeutl C (1840) Philos Mag 16:570
14. Brodie BC (1859) Philos Trans R Soc 149:249
15. Staudenmaier L (1898) Ber Dtsch Chem Ges 31:1481
16. Hummers WS, Offeman RE (1958) J Am Chem Soc 80:1339
17. Boehm HP, Clauss A, Fischer GO, Hofmann UZ (1962) Nature 17:150
18. Boehm HP, Setton R, Stumpp E (1986) Carbon 24:241
19. IUPAC (1997) Compendium of chemical terminology, 2nd edn. Blackwell Scientific, Oxford
20. Bianco A, Cheng HA, Enoki T, Gogotsi U, Hurt RH, Koratkar N, Kyotani T, Monthioux M, Park CR, Tascon JMD, Zhang J (2013) Carbon 65:1
21. Bonaccorso F, Lombardo A, Hasan T, Sun Z, Colombo L, Ferrari AC (2012) Mater Today 15:564
22. Ruoff R (2008) Nat Nanotech 3:10
23. Compton OC, Nguyen ST (2010) Small 6:711
24. Ruan M, Hu Y, Guo Z, Dong R, Palmer J, Hankinson J, Berger C, de Heer W (2012) MRS Bull 37:1138
25. Suk JW, Piner RD, Ruoff RS (2010) ACS Nano 4:6557
26. Viculis LM, Mack JJ, Kaner RB (2003) Science 299:1361
27. Falcao EHL, Blair RG, Mack JJ, Viculis LM, Kwon CW, Bendikov M, Kaner RB, Dunn BS, Wudl F (2007) Carbon 45:1367

28. Edwards RS, Coleman KS (2013) Acc Chem Res 46:23
29. Li XS, Cai WW, An JH, Kim S, Nah J, Yang DX, Piner R, Velamakanni A, Jung I, Tutuc E, Banerjee SK, Colombo L, Ruoff RS (2009) Science 324:1312
30. Mattevi C, Kim H, Chhowalla M (2011) J Mater Chem 21:3324
31. Sun Z, Yan Z, Yao J, Beitler E, Zhu Y, Tour JM (2010) Nature 468:549
32. Tiwari RN, Ishihara M, Tiwari JN, Yoshimura M (2012) Polym Chem 3:2712
33. Primo A, Atienzer P, Sanchez E, Delegado JM, Garcia H (2012) Chem Commun 48:9254
34. de Heer WA, Berger C, Ruan M, Sprinkle M, Li XB, Hu YK, Zhang BQ, Hankinson J, Conrad E (2011) Proc Natl Acad Sci U S A 108:16900
35. Papageorgiou DG, Kinloch IA, Young RJ (2015) Carbon 95:460
36. Sengupta R, Ganguly A, Sabharwal S, Chaki TK, Bhowmick AK (2007) J Mater Sci 42:923
37. George JJ, Sengupta R, Bhowmick AK (2007) J Nanosci Nanotechnol 8:1
38. George JJ, Bhowmick AK (2008) J Mater Sci 43:702
39. George JJ, Bandyopadhyay A, Bhowmick AK (2008) J Appl Polym Sci 108:1603
40. Kotal M, Bhowmick AK (2013) J Phys Chem C 117:25865
41. Kelly KF, Billups WE (2013) Acc Chem Res 4:4
42. Yu D, Dai L (2010) Chem Mater 1:467
43. Johns JE, Hersam MC (2013) Acc Chem Res 46:77
44. Mondal T, Bhowmick AK, Krishnamoorti R (2013) J Mater Chem A 1:8144
45. Zhang X, Xin J, Ding F (2013) Nanoscale 5:2556
46. Yan L, Zhen YB, Zhao F, Li S, Gao X, Xu B, Weiss PS, Zhao Y (2012) Chem Soc Rev 41:97
47. Branicio PS, Jhon MK, Gan CK, Srolovitz DJ (2011) Modelling Simul Mater Sci Eng 19:054002
48. Liu Z, Suenaga K, Harris PFJ, Ijima S (2009) Phys Rev Lett 102:015501
49. Stones AJ, Wales DJ (1986) Chem Phys Lett 128:501
50. Li L, Reich S, Robertson J (2005) Phys Rev B 72:1841109
51. Ma J, Alfe D, Michaelides A, Wang S (2009) Phys Rev B 80:033407
52. Ugeda MM, Brihuega I, Guinea F, Gomez-Rodriguez JM (2010) Phys Rev Lett 104:096804
53. Haddon RC (2001) J Phys Chem A 105:4164
54. Loh KP, Bao Q, Ang PK, Yang J (2010) J Mater Chem 20:2277
55. Liu H, Ryu S, Chen Z, Steigerwald ML, Nuckolls C, Brus LE (2009) J Am Chem Soc 131:17099
56. Yuan J, Chen G, Weng W, Xu Y (2012) J Mater Chem 22:7929
57. Sarkar S, Bekyarova E, Haddon RC (2012) Angew Chem Int Ed 51:4901
58. Strom TA, Dillon EP, Hamilton CE, Barron AR (2010) Chem Commun 46:4097
59. Liu LH, Lerner MM, Yan MD (2010) Nano Lett 10:3754
60. Quintana M, Spyrou K, Grzelczak M, Browne WR, Rudolf P, Prato M (2010) ACS Nano 4:3527
61. Sarkar S, Bekyarova E, Haddon RC (2012) Acc Chem Res 45:673
62. Bian S, Scott AM, Cao Y, Liang Y, Osuna S, Houk KN, Braunschweig AB (2013) J Am Chem Soc 135:9240
63. Seo JM, Jeon I-Y, Baek J-B (2013) Chem Sci 4:4273
64. Zhong X, Jin J, Li S, Niu Z, Hu W, Li R, Ma J (2010) Chem Commun 46:7340
65. Stankovich S, Dikin DA, Piner RD, Kohlhaas KA, Kleinhammes A, Jia Y, Wu Y, Nguyen ST, Ruoff RS (2007) Carbon 45:1558
66. Stankovich S, Piner RD, Chen XQ, Wu NQ, Nguyen ST, Ruoff RS (2006) J Mater Chem 16:155
67. Englert JM, Dotzer C, Yang G, Schmid M, Papp C, Gottfried JM, Steinruck H-P, Spiecker E, Hauke F, Hirsch A (2011) Nat Chem 3:279
68. Mondal T, Bhowmick AK, Krishnamoorti R (2012) J Mater Chem 22:22481
69. Niyogi S, Bekyarova E, Hong J, Khizroev S, Berger C, de Heer W, Haddon RC (2011) J Phys Chem Lett 2:2487

70. Wang QH, Jin Z, Kim KK, Hilmer AJ, Paulus GLC, Shih C-J, Ham M-H, Sanchez-Yamagishi JD, Watanabe K, Taniguchi T, Kong J, Jarillo-Herrero P, Strano MS (2012) Nat Chem 4:724
71. Sinitskii A, Dimiev A, Corley DA, Fursina AA, Kosynkin DV, Tour JM (2010) ACS Nano 4:1949
72. Ren L, Huang S, Zhang C, Wang R, Tjiu WW, Liu TJ (2012) Nanopart Res 14:940
73. Maeda Y, Kato T, Hasegawa T, Kako M, Akasaka T, Lu J, Nagase S (2010) Org Lett 12:996
74. Tessonnier J-P, Villa A, Majoulet O, Su DS, Schlögl R (2009) Angew Chem Int Ed 48:6543
75. Worsley KA, Ramesh P, Mandal SK, Niyogi S, Itkis ME, Haddon RC (2007) Chem Phys Lett 445:51
76. Yu D, Park K, Durstock M, Dai L (2011) J Phys Chem Lett 2:1113
77. Mondal T, Bhowmick AK, Krishnamoorti R (2014) RSC Adv 4:8649
78. Paredes JL, Villar-Rodil S, Martinez-Alonso A, Tascon JMD (2008) Langmuir 24:10560
79. Lerf A, He H, Forster M, Klinowski J (1998) J Phys Chem B 102:4477
80. Navarro CG, Meyer JC, Sundaram RS, Chuvilin A, Kurasch S, Burghard M, Kern K, Kaiser U (2010) Nano Lett 10:1144
81. Xue Y, Liu Y, Lu F, Qu J, Chen H, Dai L (2012) J Phys Chem Lett 3:1607
82. Valentini L, Bon SB, Kenny JM (2012) J Mater Chem 22:6213
83. Valentini L, Bon SB, Cardinali M, Monticelli O, Kenny JM (2007) Chem Phys Lett 445:51
84. Wang X, Song L, Yang H, Xing W, Kandola B, Hu Y (2012) J Mater Chem 22:22037
85. Usuki A, Kojima Y, Kawasumi M, Okada A, Kurauchi T, Kamigaito O (1993) J Mater Res 8:1174
86. Maiti M, Bhattacharya M, Bhowmick AK (2008) Rubber Chem Technol 81:384
87. Bhowmick AK, Bhattacharya M, Mitra S, Maji PK, Choudhury A, George JJ, Basak GC, Kumar KD (2010) Kaunt Gumm Kunst 63:192
88. Mitchell CA, Krishnamoorti R (2007) Macromolecules 40:1538
89. Mitchell CA, Krishnamoorti R (2005) Polymer 46:8796
90. Clark MD, Krishnamoorti R (2009) J Phys Chem C 113:20861
91. Shanmugharaj AM, Bhowmick AK (2004) Rad Phys Chem 69:91
92. Roy N, Bhowmick AK (2012) J Mater Sci 47:272
93. Mondal T, Bhowmick AK (2012) J Mater Sci 47:4178
94. George JJ, Bhowmick AK (2008) Nanoscale Res Lett 3:508
95. Krishnamoorti R (2011) MRS Bull 32:341
96. Fang M, Wang K, Lu H, Nutt S (2010) J Mater Chem 20:1982
97. Mondal T, Bhowmick AK, Krishnamoorti R (2014) ACS Appl Mater Interfaces 6:16097
98. Gu R, Xu WZ, Charpentier PA (2014) Polymer 55:5322
99. Fang M, Wang K, Lu H, Yang Y, Nutt S (2009) J Mater Chem 19:7098
100. Layek RK, Samanta S, Chatterjee DP, Nandi AK (2010) Polymer 51:5846
101. Yang Y, Wang J, Zhang J, Liu J, Yang X, Zhao H (2009) Langmuir 25:11808
102. Kou L, He H, Gao C (2010) Nano Micro Lett 2:177
103. Magenau JDA, Strandwitz NC, Gennaro A, Matyjaszewski K (2011) Science 332:81
104. Lee SH, Dreyer DR, An J, Velamakanni A, Piner RD, Park S, Zhu Y, Kim SO, Bielawski CW, Ruoff RS (2010) Macromol Rapid Commun 31:281
105. Salavagione HJ, Martinez G, Ellis G (2011) Macromol Rapid Commun 32:1771
106. Mondal T, Bhowmick AK, Krishnamoorti R (2014) ACS Appl Mater Interfaces 6:7244
107. Salavagione HJ, Gomez MA, Martinez G (2009) Macromolecules 42:6331
108. Mondal T, Ashkar R, Butler P, Bhowmick AK, Krishnamoorti R (2016) ACS Macro Lett 5:278
109. Bhattacharya M, Maiti M, Bhowmick AK (2008) Rubber Chem Technol 81:782
110. Zhan Y, Wu J, Xia H, Yan N, Fei G, Yuan G (2011) Macromol Mater Eng 296:590
111. Zhan Y, Lavorgna M, Buonocore G, Xia H (2012) J Mater Chem 22:10464
112. Potts JR, Shankar O, Du L, Ruoff RS (2012) Macromolecules 45:6045
113. Potts JR, Shankar O, Murali S, Du L, Ruoff RS (2013) Compos Sci Technol 74:166

114. Scherillo G, Lavorgna M, Buonocore GG, Zhan YH, Xia HS, Mensitieri G, Ambrosio L (2014) ACS Appl Mater Interfaces 6:2230
115. Aguilar-Bolados H, Brasero J, Lopez-Manchado MA, Yazdani-Pedram M (2014) Compos Part B 67:449
116. Fernandez SS, Kunchandy S, Ghosh SK (2015) J Polym Environ 23:526
117. Wu J, Huang G, Li H, Wu S, Liu Y, Zheng J (2013) Polymer 54:1930
118. Ma L-X, Yan H-Q, Ke J-N, He Y (2012) Key Eng Mater 501:10
119. Wu L-M, Liao S-Q, Zhang S-J, Bai X-Y, Hou Z (2015) Chinese J Polym Sci 33:1058
120. Luo Y, Zhao P, Yang Q, He D, Kong L, Peng Z (2014) Compos Sci Technol 100:143
121. Stanier DC, Patil AJ, Sriwong C, Rahatekar SS, Ciambella J (2014) Compos Sci Technol 95:59
122. Ozbas B, Toki S, Hsiao BS, Chu B, Register RA, Aksay IA, Prud'homme RK, Adamson DA (2012) J Polym Sci Polym Phys 50:718
123. Suk JW, Piner RD, An JH, Ruoff RS (2010) ACS Nano 4:6557
124. Li F, Yan N, Zhan Y, Fei G, Xia H (2013) J Appl Polym Sci 129:2342
125. Wu X, Lin TF, Tang ZH, Guo BC, Huang GS (2015) eXPress Polm Lett 9:672
126. Yan N, Buonocore G, Lavorgna M, Kaciulis S, Balijepalli SK, Zhan Y, Xia H, Ambrosio L (2014) Compos Sci Technol 102:74
127. Yan N, Xia H, Zhan Y, Fei G (2013) Macromol Mater Eng 298:38
128. Dong B, Liu C, Zhang L, Wu Y (2015) RSC Adv 5:17140
129. She X, He C, Peng Z, Kong L (2014) Polymer 55:6803
130. Yaragalla S, Chandran CS, Kalarikkal N, Subban RHY, Chan CH, Thomas S (2015) Polym Eng Sci 55:2439
131. Malas A, Das CK, Das A, Heinrich G (2012) Mat Des 39:410
132. He C, She X, Peng Z, Zhong J, Liao S, Gong W, Liao J, Kong L (2015) Phys Chem Chem Phys 17:12175
133. Schopp S, Thomann R, Ratzsch K-F, Kerling S, Alstaedt V, Muelhaupt R (2014) Macromol Mater Eng 299:319
134. Beckert F, Trenkle S, Thomann R, Muelhapt R (2014) Macromol Mater Eng 299:1513
135. Kim JS, Yun JH, Kim I, Shim SE (2011) J Ind Eng Chem 17:325
136. Kim JS, Hong S, Park DW, Shim SE (2010) Macromol Res 6:558
137. Xing W, Tang M, Wu J, Huang G, Li H, Lei Z, Fu X, Li H (2014) Compos Sci Technol 99:67
138. Tang M, Xing W, Wu J, Huang G, Xiang K, Guo L, Li G (2015) J Mater Chem A 3:5942
139. Tang Z, Zhang L, Feng W, Guo B, Liu F, Jia D (2014) Macromolecules 47:8663
140. Liu X, Kuang W, Guo B (2015) Polymer 56:553
141. Ozbas B, O'Neill CD, Register RA, Aksai IA, Prud'homme RK, Adamson DH (2012) J Polym Sci Polym Phys Part A 50:910
142. Araby S, Zhang L, Kuan H-C, Dai J-B, Majewski P, Ma J (2013) Polymer 54:3663
143. Das A, Boldt R, Jurk R, Jehnichen D, Fischer D, Stoeckelhuber KW, Heinrich G (2014) RSC Adv 4:9300
144. Tang Z, Wu X, Guo B, Zhang L, Jia D (2012) J Mater Chem 22:7492
145. Wu S, Tang Z, Guo B, Zhang L, Jia D (2013) RSC Adv 3:14549
146. Al-solamy FR, Al-Ghamdi AA, Mahmoud WE (2012) Polym Adv Technol 23:478
147. Singh VK, Shukla A, Patra MK, Saini L, Jani RK, Vadera SR, Kumar N (2012) Carbon 50:2202
148. Wang L, Zhang L, Tian M (2012) Wear 276:85
149. Li Y, Wang Q, Wang T, Pan G (2012) J Mater Sci 47:730
150. Verghese TV, Kumar HA, Anitha S, Ratheesh S, Rajeev RS, Rao VL (2013) Carbon 61:476
151. Moewes MM, Fleck F, Klueppel M (2014) Rubber Chem Technol 87:70
152. Mensah B, Kim S, Arepalli S, Nah C (2014) J Appl Polym Sci 131:40640
153. Nah C, Lim JY, Cho BH, Hong CK, Gent AN (2010) J Appl Polym Sci 118:1574
154. Zhi Y, Mao Y, Wen S, Li Y, Zhang L, Chan TW, Liu L (2015) Compos Part A 76:194

155. Tian M, Zhang J, Zhang L, Liu S, Zan X, Nishi T, Ning N (2014) Colloid Interface Sci 430:249
156. Liu X, Sun D, Wang L, Guo B (2013) Ind Eng Chem Res 52:14592
157. Wang J, Ja H, Tang Y, Ji D, Sun Y, Gong X, Ding L (2013) J Mater Sci 48:1571
158. Wei J, Jacob S, Qiu J (2014) Compos Sci Technol 92:126
159. Xing Y, Bai X, Zhang Y (2014) Polym Compos 35:1779
160. Wei J, Qiu J (2014) Polymer 55:3818
161. Quan H, Zhang B-Q, Zhao Q, Yuen RKK, Li RKY (2009) Compos Part A 40:1506
162. Khan U, May P, O'Neill A, Coleman JN (2010) Carbon 48:4035
163. Pokharel P, Choi S, Lee DS (2015) Compos Part A 69:168
164. Sadasivuni KK, Ponnamma D, Kumar B, Strankowski M, Cardinaels R, Moldenaers P, Thomas S, Grohens Y (2014) Compos Sci Technol 104:18
165. Yang L, Phua SL, Toh CL, Zhang L, Ling H, Chang M, Zhou D, Dong Y, Lu X (2013) RSC Adv 3:6377
166. Mo M, Zhao W, Chen Z, Yu Q, Zeng Z, Wu X, Xue Q (2015) RSC Adv 5:56486
167. Liu Y, Ma J, Wu T, Wang X, Huang G, Liu Y, Qiu H, Li Y, Wang W, Gao J (2013) ACS Appl Mater Interfaces 5:10018
168. Hodlur RM, Rabinal MK (2014) Compos Sci Technol 90:160
169. Liang J, Xu Y, Huang Y, Zhang L, Wang Y, Ma Y, Li F, Guo T, Chen Y (2009) J Phys Chem C 113:9921
170. Kim JT, Kim BK, Kim EY, Kwon SH, Jeong HM (2013) Eur Polym J 49:3889
171. Valentini M, Piana F, Pionteck J, Lamastra FR, Nanni F (2015) Compos Sci Technol 114:26
172. Kim H, Miura Y, Macosko CW (2010) Chem Mater 22:3441
173. Yuan NY, Ma FF, Fan Y, Liu YB, Ding JN (2012) Compos Part A 43:2183
174. Kuila T, Khanra P, Mishra AK, Kim NH, Lee JH (2012) Polym Test 31:282
175. Safedi SA, Luyt AS, Pionteck J (2015) J Appl Polym Sci 132:41352
176. Chen B, Ma N, Bai X, Zhang H, Zhang Y (2012) RSC Adv 2:4683
177. Allahbakhsh A, Mazinani S, Kalaee MR, Sharif F (2013) Thermochim Acta 563:22
178. Lian H, Li S, Liu K, Xu L, Wang K, Guo W (2011) Polym Eng Sci 51:2254
179. Xiong X, Wang J, Jia H, Fang E, Ding L (2013) Polym Degrad Stab 98:2208
180. Kotal M, Banerjee SS, Bhowmick AK (2016) Polymer 82:121
181. Tian M, Wei Z, Zan X, Zhang L, Zhang J, Zhang J, Ma Q, Ning N, Nishi T (2014) Compos Sci Technol 99:37
182. Berean KJ, Ou JZ, Nour M, Field MR, Alsaif MMYA, Wang Y, Ramanathan R, Bansal V, Kentish S, Doherty CM, Hill AJ, McSweeney C, Kaner RB, Zadeh KK (2015) J Phys Chem C 119:13700

Adv Polym Sci (2017) 275: 319–360
DOI: 10.1007/12_2016_1

Published online: 10 July 2016

Characterization and Application of Graphene Nanoplatelets in Elastomers

M. Klüppel, M.M. Möwes, A. Lang, J. Plagge, M. Wunde, F. Fleck, and C.W. Karl

Abstract The physical performance of elastomer composites based on graphene nanoplatelets (GNPs) was investigated regarding the mechanical and fracture mechanical properties, viscoelastic and dielectric responses, and friction, wear and gas permeation properties. Static gas-adsorption measurements at very low pressures demonstrated that pronounced differences in the surface activity and specific surface area can be observed for different GNPs. The surface activity was shown to be large for GNPs that indicate strong polymer–filler couplings for these systems. This is closely related to the energetic heterogeneity (i.e., the number of highly energetic sites) at the filler surface, which determines the polymer–filler interaction strength and is the main factor determining the reinforcing potential. Based on this information, the stress–strain responses of several GNP types and fine graphite were analyzed in styrene butadiene rubber (SBR) and nitrile butadiene rubber (NBR) with and without softener in relation to standard carbon black. Results demonstrated qualitatively different mechanical behaviors. It was revealed that the mechanical response of the composites under quasistatic cyclic loading can be well understood on the basis of quantitative analysis using a micromechanical

M. Klüppel (✉), M.M. Möwes, A. Lang, J. Plagge, M. Wunde, F. Fleck, and C.W. Karl
Deutsches Institut für Kautschuktechnologie e.V., Eupener Str. 33, 30519 Hannover, Germany
e-mail: Manfred.Klueppel@DIKautschuk.de

Present address:
M.M. Möwes
Continental Teves AG and Co. oHG, Jädekamp 30, 30419 Hannover, Germany

F. Fleck
Applied Research Material Physics, Continental Reifen Deutschland GmbH, Jädekamp 30, 30419 Hannover, Germany

C.W. Karl
Fakultät für Bauingenieurwesen und Geodäsie, Leibniz-Universität Hannover, Appelstr. 9a, 30167 Hannover, Germany

model. Gas permeation is strongly reduced by GNPs and further reduced in anisotropic samples with orientation of GNPs perpendicular to the gas flow direction. In comparison with carbon black, dynamic crack growth under pulsed excitation remains almost unaltered for all GNP types, although the wear behavior under sharp abrading conditions is worse. The dry and wet friction properties of SBR composites are well described by hysteresis and adhesion friction theory for GNPs and for carbon black. The dry friction coefficient on rough granite and especially on smooth glass decreases significantly when GNPs are used instead of carbon black. However, the wet friction coefficient on rough granite increases slightly at small sliding velocities, which correlates with the higher hysteresis of GNP composites in the rubbery plateau region.

Keywords Carbon nanotube (CNT) • Elastomer composite • Fracture mechanics • Friction and wear properties • Gas permeation • Graphene nanoplatelet (GNP) • Multilayer graphene (MLC) • Ultrafine graphite (UG) • Static gas adsorption

Contents

1 Introduction

Graphene and its manufacturing technologies have become increasingly important in recent years [1]. This is largely a result of the fact that graphene possesses remarkable and unique properties. It is 200 times stronger than steel and, at one atom thick, the strongest and thinnest material ever measured. It is also the world's most conductive material. Graphene has a wide range of potential uses, including composite materials. The most prominent features are high Young's modulus, fracture toughness, very high electrical and thermal conductivity, large specific surface area, excellent barrier properties, and the quantum Hall effect even at room temperature. This means that there are a growing number of advanced technological applications such as solar cells, field effect devices, a wide range of practical chemical sensors, highly flexible transparent electrodes, and a variety of nanocomposites [2, 3]. Moreover, recent studies have suggested that graphenes and graphitic carbon can be used in composite materials for reducing friction [4, 5]. Within this scope, graphene nanoplatelets (GNPs) with less than 10 nm thickness and a lateral dimension ranging from 2 to 25 μm have been used to improve tire and technical elastomer performance. As well as the different types of GNPs, ultrafine graphite (UG) has also been applied in a series of composites and compared with traditional fillers such as carbon black (CB). We note that many carbon-based materials and especially newly derived graphene types are described by technical terms, so there is no unique nomenclature. Accordingly, GNPs may also be viewed as multilayer graphenes that mainly differ in their layer thickness and diameter. The morphological and energetic properties of the carbon-based fillers used in this work are described in some detail in Sects. 2.1 and 3. By virtue of their unique combination of mechanical properties and excellent electrical and thermal conductivity, GNPs are predestined to be innovative fillers for elastomer composites. These new nanostructured fillers have been identified, developed, and dispersed in an elastomeric matrix. The influence of the structure and morphology of the carbon nanoscale fillers on the characteristics of elastomers have been investigated [5–8]. According to these works, the interactions between filler and polymer matrix trigger the reinforcing effects of the fillers. It was found that this correlation depends on the properties of both the filler and the polymer.

In general, the performance characteristics of elastomer composites under dynamic-mechanical loading (e.g., stiffness, damping, wear resistance) are closely related to distinctive energy dissipation mechanisms that depend on frequency, temperature, and amplitude. These phenomena can be traced back to specific polymer–polymer, polymer–filler, and filler–filler interactions. Elastomer–filler interaction in turn is significantly influenced by the morphology of the filler surface and the surface energy [9–11]. At the same time, restricted geometries have an impact on the filler surface area and influence the dynamics of polymer chains [12]. This manifests itself, for example, in thin films that are heavily dependent on the relaxation time of polymer film thickness with a reduced glass transition temperature [13]. The improvement in mechanical properties is closely related to

aggregation of filler particles in the rubber matrix and the formation of an energy-elastic filler network. The function of the filler network in the various aspects of elastomer reinforcement was intensively discussed by Payne [14, 15] and has been investigated in more detail by various authors [16–18]. As a result of formation of a filler network above the percolation threshold, there is a pronounced increase in the modulus with rising filler volume fraction, which can be described by a characteristic power law [9, 10, 19, 20]. This has been experimentally verified for various filler–elastomer combinations. The obtained universal exponent can be traced back to the fractal structure of the filler network. However, the structure–activity mechanisms of filler networks in elastomers are not yet fully understood. Control of the above-mentioned interactions, which serves as a basis for modification of viscoelastic properties, is strongly restricted and has been substantially discussed in terms of technology for conventional carbon black and silica-filled elastomer composites.

This is why new nanoscale fillers are currently being investigated for potential applications. Here, the focus is on layered inorganic fillers such as layered silicates, organic materials such as carbon nanotubes (CNTs), and different types of GNPs and UGs. Because of the promising results achieved with CNTs as fillers in elastomer composites [21–26], investigations have also focused on layered structures such as single- and multilayer graphene, expanded graphite, and graphene oxide as possible fillers for polymer nanocomposites [27–36]. However, improved exfoliation and inclusion in a rubber matrix are still challenging issues. To address this, elastomer composites with different fillers (hybrid systems) containing carbon black, silica, GNPs, UGs, and CNTs have been compounded and their properties investigated [5–8, 21–26]. For a deeper understanding of these materials, the relaxation and dissipation behavior has been analyzed over a wide temperature and frequency scale (dielectric relaxation spectroscopy, dynamic mechanical analysis) as well as the dispersion (using transmission electron microscopy; TEM) and permeation behavior. Additionally, the microscopic material parameters of the polymer nanocomposites (polymer and filler network) have been determined on the basis of multihysteresis tension tests at medium and large deformations.

The present review describes the analysis of several GNP types, CNTs, and UGs of different morphology as nanofillers in SBR and NBR composites. These fillers show distinct reinforcing properties compared with conventional fillers such as carbon black. First, we describe characterization of the morphology and surface energy distribution of the fillers by static gas adsorption techniques. Then, the stress–strain responses of the composites, including hybrid-filler systems with and without softener, are considered in some detail using a microstructure-based model to help understand the basic reinforcement mechanisms. Finally, we look at several possible application fields for GNP composites, such as gas permeation membranes, sealings, or wiper blades with reduced friction and wear properties. Therefore, fatigue crack propagation and abrasion rates and the dry and wet friction properties on rough and smooth tracks are discussed using viscoelastic models.

2 Experimental Details and Data Treatment

2.1 Materials

Solution styrene butadiene rubber (S-SBR, Buna VSL-2525-0), delivered by Lanxess, was used as elastomer matrix. The first two digits of the code indicate the vinyl content and the last two the styrene content in percentage weight. The digit "0" denotes non-oil-extended rubber. Nitrile butadiene rubber (NBR, Perbunan 3945) with 39% acryl-nitrile, also delivered by Lanxess, was used. Dioctyl phthalate (DOP) was applied as a softener for NBR.

Because single-layer graphene is not currently available in sufficient amounts at acceptable prices [35, 36], graphene nanoplatelets (GNPs) were used. The following GNP types produced by XG-Science were employed: xg M5 (165.6 m^2/g), xg M15 (101.7 m^2/g), xg M25 (219.1 m^2/g), and xg C750 (810.5 m^2/g). The specific surface area as probed by N_2 adsorption is given in brackets. In addition, special graphites, delivered by Graphit Kropfmühl GmbH, and CNTs, delivered by Nanocyl, were used as carbon-based fillers. The applied CNT was NC 7000 (254 m^2/g) and the ultrafine graphite was UF 198C (23.5 m^2/g). Special graphites SGA 10 M (7.4 m^2/g) and SGB 10 L (11 m^2/g) were also used. Several furnace carbon blacks N121 (117.7 m^2/g), N339 (92.6 m^2/g), and N550 (39.2 m^2/g) delivered by Orion Engineered Carbons, and a highly dispersible silica U 7000 GR (175 m^2/g), delivered by Evonik Industries were chosen as references. Furthermore, the highly conductive carbon black Printex EX 2B (1,050 m^2/g) was chosen because of its much larger surface area compared with conventional CBs. The morphological details of carbon-based filler particles are summarized in Table 1.

Zinc oxide and stearic acid were used as dispersing agents in a weight ratio of 3–1.5 phr (per hundred rubber). Using an internal mixer, these two agents can be converted into zinc stearate, which reduces viscosity and acts as a surfactant. This helps to improve the filler dispersion in the polymer matrix. Likewise, zinc oxide operates as activator of sulfur crosslinking. The vulcanization system consists of ground sulfur. *N*-Cyclohexyl-2-benzothiazolsulfenamide (CBS) was used as accelerator.

2.2 Static Gas Adsorption Measurements

To characterize the morphological and energetic surface structure of the filler materials, static (equilibrium) gas adsorption measurements with N_2 and 1-butene were carried out over a broad pressure range (10^{-6} bar to 1 bar) using the volumetric gas adsorption device BELSORP-max (BEL Japan Inc.). To clean the surface, the different carbon-based fillers were pretreated prior to measurement. The samples

Table 1 Morphological details of carbon-based filler particles used in this study

Distributor	Sample	Filler type	Height (nm)	Diameter (μm)	$S_E - N_2$[a] (m^2/g)
XG Science	xg M5	Graphene nanoplatelets	5–8	5	165.8
XG Science	xg M15	Graphene nanoplatelets	5–8	15	101.7
XG Science	xg M25	Graphene nanoplatelets	5–8	25	219.1
XG Science	xg C750	Graphene nanoplatelets	1–5	2	810.5
Graphit Kropfmühl GmbH	UF 198C	Ultrafine graphite		2	23.5
Graphit Kropfmühl GmbH	SGA 10 M	Special graphite		10	7.4
Graphit Kropfmühl GmbH	SGB 10 L	Special graphite		10	11
Nanocyl	NC 7000	Carbon nanotubes		0.02	254
Orion Eng. Carbons	N121	Carbon black		0.08	117.7
Orion Eng. Carbons	N339	Carbon black		0.12	92.6
Orion Eng. Carbons	N550	Carbon black		0.2	39.2
Orion Eng. Carbons	Printex	Carbon black		0.2	1,050

[a]Surface area measurement based on N_2 gas adsorption measurements

were purged with helium and heated in a vacuum at 300°C for up to 3 h. To obtain reliable data in the low pressure regime, a high vacuum of around 10^{-8} bar was reached. Measurement of the equilibrium adsorption isotherms was initiated at a low pressure, which was then increased in small steps. A turbo molecular pump was working for at least 12 h before measurement was started. The leakage rate without pumping was 10^{-7} bar/min.

2.3 Compounding and Vulcanization

The fillers were incorporated into the polymer matrix by melt mixing techniques using a laboratory-scale compounder. The blending geometry involves two tangential (non-interlocking) rotors in a Banbury mixer. During mixing, the following parameters are documented: torque, rotational speed, mass flow rate, and temperature in the mixing chamber. A laboratory water-cooled rolling mill served to integrate the crosslinking system. The roll gap was adapted according to the volume of composite melt.

Measurement of the vulcanization process (thermally induced formation of the filler network and chemical crosslinking of polymer chains) was carried out on the basis of oscillatory rheology using a cure meter (Alpha Technologies, MDR 2000E) and a rubber process analyzer (Alpha Technologies, RPA 2000). The t_{90} response time is defined as the time required for the torque to reach 90% of the maximum. It serves as basis for the vulcanization time needed for samples to avoid reversion, thermal ageing, and/or excess networking. The vulcanization was conducted at 160°C using a vulcanization press (Rucks Maschinenbau KV 207.00 and Wickert & Söhne WLP63/3,5/3). The molten mass was vulcanized under the influence of pressure and temperature to obtain bubbleless sheets of 2 and 6 mm thickness after placing them in the appropriate rectangular mold.

2.4 Tensile Testing

The universal testing machine (Zwick 1440) was used for uniaxial tensile measurements (i.e., stress response as a function of strain). The measurements were carried out with S2-samples (according to DIN Norm 53504) at room temperature (22°C) with a preload of 0.5 N and a crosshead speed of 200 mm/min. This corresponds to a strain rate of $\dot{\varepsilon} \approx 10^{-1}s^{-1}$. For strain measurement, two reflection marks were placed 15 mm apart. For statistical reasons and to test sample homogeneity, five test samples per composite were measured up to rupture.

Uniaxial multihysteresis tests in tension at 20 mm/min were carried out on dumbbells of 15 mm diameter using the same universal testing machine. Multihysteresis means that up and down cycles are carried out at constant velocity between certain minimum and maximum strains, $\varepsilon_{\min}$ and $\varepsilon_{\max}$. This is done five times for each step, and after every such step the boundaries of deformation are successively raised ($\varepsilon_{\max}$) while $\varepsilon_{\min} = 0$ is kept constant. Only every fifth up and down cycle is evaluated for fitting with the dynamic flocculation model (DFM), which can be regarded as being in an equilibrium state in a good approximation.

2.5 Dynamic Mechanical Analysis

Dynamic mechanical analysis (DMA) was performed with a rheometer (Ares, Rheometric Scientific) using strip specimens with a length of 30 mm, width 10 mm, and thickness 2 mm. The samples were measured by means of a torsional mode under constant normal force (tensile force 120 g) that kept the samples slightly stretched. The complex shear modulus G^* and the loss factor $\tan\delta$ were determined as a function of frequency and temperature, while the deformation amplitude remained constant at $\varepsilon = 2.5\%$. The frequency (f) was varied between

0.02 and 10 Hz at various constant temperatures. The temperature was varied stepwise from higher to lower temperatures between 80°C and −50°C.

2.6 Dielectric Measurements

Dielectric measurements were carried out with a dielectric broadband analyzer (BDS 40) from Novocontrol. The samples were cut with a die punch of 20 mm diameter. The surface was cleaned by 10 min of ultrasonic treatment in an ethanol bath. Afterwards, both sides of the sample were sputtered with gold for 10 min. The real and imaginary part of the impedance was measured and the conductivity calculated as a function of frequency (AC conductivity).

2.7 Dynamic Crack Growth Measurements

The fracture mechanical properties were investigated by analyzing the dynamic crack growth rate under cyclic loading. The tests were executed using the Tear-Fatigue Analyzer System (Coesfeld). Strip samples were used for the measurements, whereby up to ten samples can be measured simultaneously at individual monitoring stations with specified deformation and minor load. Each monitoring station is equipped with its own load cell that fulfills the dual purpose of controlling a steady minor load to tighten up the sample and measuring applied force. The samples were prepared as strips (65 mm × 15 mm × ca. 1.5 mm) carved by a razor blade on one side (1 mm). A camera was used to automatically measure crack depth and contour length in a fixed position. The following semi-empirical equation was used to determine the tearing energy:

$$T = \frac{2\pi}{\sqrt{\lambda}} W_{el}(\lambda) c. \tag{1}$$

Here, c stands for crack contour length, λ is the expansion ratio, and W_{el} is the elastic energy density stored during the expansion cycle, far away from the crack tip. It is defined through numerical integration of the measured tension expansion cycles $\sigma_0 = F/A_0$ towards expansion, where F denotes tensile force and A_0 is the sample section of the non-deformed sample. The tension expansion cycles are measured optically online during the investigation for each 1,200th cycle. The remaining sample section is taken as the reference cross-sectional area A_0 after deduction of the crack area. The investigations were conducted at relatively high expansion rates under pulsed stress, with 50 ms pulse duration and a frequency of 10 pulses/s. This so-called high severity mode is more practically oriented than ordinary harmonic stress at 1 or 10 Hz. The measurements were performed in a heating chamber at 40°C, although heating effects may also have an influence. The

chosen deformation amplitudes correspond to $\varepsilon = 4$, 6, 8, 12, 15, 20, and 22.5%, with the samples in each case having been tightened by applying a preload of 2 N. Two samples at a time were measured at each amplitude and for each elastomer composite.

2.8 Gas Permeation Measurements

The permeation measurements were carried out with a volumetric measuring setup. The measuring equipment consisted of the elastomer membrane to be analyzed (thickness approximately 1 mm), clamped in front of a pressure chamber. Measurement of volumetric flow behind the sample is based on optical detection of the movement of a riser driven by the gas flow inside a capillary. The measurements were performed with air at 70°C and a pressure difference of 4 bar. The permeability coefficient Q is defined by the volume flow V per unit time t, the thickness d, and the cross-section A of the sample:

$$V = Q \cdot t \cdot \frac{\Delta p}{d} \cdot A. \tag{2}$$

There are two processes controlling the permeation process: First, the solubility of the gas in the sample, i.e. the amount of gas molecules, and second, the diffusion speed. Then, the permeation flow can be detected as steady flow with constant flow rate V/t, from which the permeability coefficient Q can be evaluated.

2.9 Friction Measurements

Stationary friction measurements were performed on glued samples with a thickness of 2 mm and cross-section of 50×50 mm using a specially designed linear tribometer available at the DIK. This is a unique piece of equipment for investigating the friction coefficient between a sliding rubber block and a flat substrate. The samples move along the substrate (rough granite, glass) in dry and wet (with 5% detergent) conditions with a stationary velocity ranging from 5 μm/s to 15 mm/s at room temperature. The normal force is kept constant, delivering a moderate pressure of 24 kPa in the contact zone. For each velocity, the friction force is measured with a laterally sensitive force transducer by stationary linear movement of the sample relative to the substrate. Plateau forces over the sliding time are evaluated to calculate the friction coefficient μ, given as the ratio of friction force to normal force.

3 Characterization of Filler Surface Structure by Static Gas Adsorption

A frequently used technique for investigation of filler surfaces in terms of surface area and energy is static gas adsorption. Typically, the sample (e.g., carbon black) is cooled to the boiling point of the adsorbate (e.g., nitrogen). Then, the sample cell is evacuated and a known amount of adsorbate is added. Adsorbate molecules act as molecular probe, first occupying the accessible, energetically favorable spots on the surface of the sample (adsorbent). Adsorbed molecules do not contribute to the pressure inside the sample cell, which allows calculation of the amount of adsorbed gas from the difference between the expected pressure and the measured pressure. Repeating this process for different pressures, we can plot the adsorbed amount of gas against pressure to obtain the adsorption isotherm. In general, there is a strong increase in adsorption with pressure for very low pressure values, because there is enough surface for every molecule trying to make contact. At higher pressures, the surface is almost fully occupied, which results in a plateau-like adsorption isotherm. As the pressure approaches atmospheric pressure, the adsorbate condenses and the isotherm diverges.

In this work we used nitrogen (N_2) and 1-butene (C_4H_8) as adsorbates. Nitrogen is a small molecule that can be used to explore small structures of the sample. It is a widely used gas, especially known for the determination of BET-surface area, as given in Table 1. Butene is a much larger molecule and is chemically similar to many organic polymers, as it has a C=C double bond. It can be considered a polymer-analogous gas and therefore can serve as a molecular probe to investigate the interaction of polymers with the nanoscopic surface of fillers. From a microscopic point of view, the filler–polymer interaction is a key parameter in understanding filled rubber composites as a whole. In most compounds, filler and polymer are connected via physical bonds such as van der Waals forces. In this section, we show that GNPs and other carbon-based fillers show distinct differences in adsorption energies, which can give valuable hints for understanding the different reinforcement characteristics of the fillers.

3.1 Theory of Gas Adsorption on Energetically Heterogeneous Surfaces

The first theory describing multilayer adsorption (e.g., condensation) was the BET theory derived by Brunauer, Emmet, and Teller. One of their main assumptions was an energetically homogeneous surface. In physical reality, surfaces are energetically heterogeneous. Energetic heterogeneities can be of chemical or morphological origin. The latter is represented by structures of the same scale as the test molecule (e.g., cavities or summits), which can favor or hinder interaction [37–39].

The experimental adsorption isotherm cannot be reproduced by a single BET model, but has to be constructed by superposition of BET models corresponding to different adsorption energies. We start by writing the original BET model:

$$\Theta(h,W) = \frac{N(h,W)}{N_m} = \frac{1}{1-h} - \frac{1}{1+(C(W)-1)h} \quad \text{with} \quad h = \frac{p}{p_0} \quad \text{and} \quad C(W) = K_{FG}(W,\theta)\, p_0. \tag{3}$$

Here, $N(h,W)$ is the adsorbed amount of substance at relative pressure h, N_m is the monolayer capacity, and $\theta(h,W)$ represents the surface coverage of the surface fraction with adsorption energy W. The Langmuir constant is given, in good approximation [40], as:

$$K(W) = \frac{N_a \sigma \tau}{\sqrt{2\pi\, mRT}} e^{\frac{W}{RT}}. \tag{4}$$

Following Fowler and Guggenheim [40], we include the interaction with adsorbed neighboring molecules by introducing:

$$K_{FG}(W,\theta) = K(W)\, e^{\frac{\theta\, z\, \Omega}{R\, T}}. \tag{5}$$

Here, z denotes the number of neighboring adsorption sites and Ω is the interaction energy of two adsorbed molecules, which can be calculated in good approximation by the heat of evaporation. Note that K_{FG} is now dependent on the surface coverage fraction θ, because binding affinity increases with increasing amount of adsorbed molecules. Because of this we have to numerically solve Eq. (3) for θ. This is done via Brent's method.

Our goal is to express the experimentally obtained isotherm $N_{exp}(h)$ as a superposition of basic (BET) isotherms $\theta(h, W)$. Formally:

$$N_{exp}(h) \cong N_{mod}(h) = \int_{W_{min}}^{W_{max}} \theta(h,W)\, F(W)\, dW. \tag{6}$$

Here, N_{mod} represents the model isotherm, which has to be as close as possible to the experimentally obtained isotherm. The function we are looking for is the energy distribution $F(W)$. This is a Fredholm integral equation of the first kind. A method designed for exactly this problem is the expectation maximization algorithm described by Stanley and Guiochon [41]. The iteration is given by:

$$F^{k+1}(W_i) = F^k(W_i) \frac{\sum_j \theta(h_j, W_i) \frac{N_{\exp}(h_j)}{N_{\mathrm{mod}}(h_j)}}{\sum_j \theta(h_j, W_i)}, \tag{7}$$

where h_i and W_i denote the discretized relative pressure and energy, respectively. It is obvious that $N_{\exp}(h_j) = N_{\mathrm{mod}}(h_j)$ for all j is a fixed point of iteration.

To obtain an energy distribution in the sense of an energy frequency distribution we have to normalize $F(W)$:

$$f(W) = \frac{F(W)}{\Sigma} \quad \text{with} \quad \Sigma = \int_0^\infty dW\, F(W). \tag{8}$$

From Σ, we can calculate the specific surface area (S_{E}) of the sample via the following equation:

$$S_{\mathrm{E}} = \Sigma N_{\mathrm{A}}\, \sigma, \tag{9}$$

where N_{A} is the Avogadro constant and σ is the surface area of the adsorbing molecule. It is worth mentioning that the surface area calculated here is slightly different to the BET surface area listed in Table 1, because here the energetic heterogeneity is included.

For fitting the experimentally measured adsorption isotherms, Eq. (6) must be solved by means of the iteration scheme given by Eq. (7). With sufficient iterations, the experimental result can be reproduced to almost arbitrary precision (because the unknown continuous function $F(W)$ can be seen as infinite degrees of freedom). Unfortunately the experimental data contain measurement errors, ideally Gaussian fluctuations around a correct mean line. A frequently used method is to keep iterating until the difference between the fitted line and experimental data is of the order of measurement precision. This cannot be done here, because the measurement precision is not known and the BET model does not take into account some major effects that occur at high pressures (e.g., capillary condensation). This effect naturally generates deviations in the experimental data such that the scheme described above is not applicable. Hence, we perform 1,000 iterations in the relative pressure range of 2×10^{-6} to 0.3 after sampling the data equidistantly in log-log space using a cubic spline interpolation algorithm.

3.2 Adsorption Isotherms and Energy Distribution Functions

Figure 1 shows the surface coverage of various samples with nitrogen (N_2) and 1-butene against the relative pressure p/p_0, where p_0 is the saturation vapor pressure of N_2 and 1-butene at adsorption temperatures of 77 K and 267 K, respectively. Here, the adsorption isotherms of different GNPs, ultrafine graphite (UF 198C), and CNTs

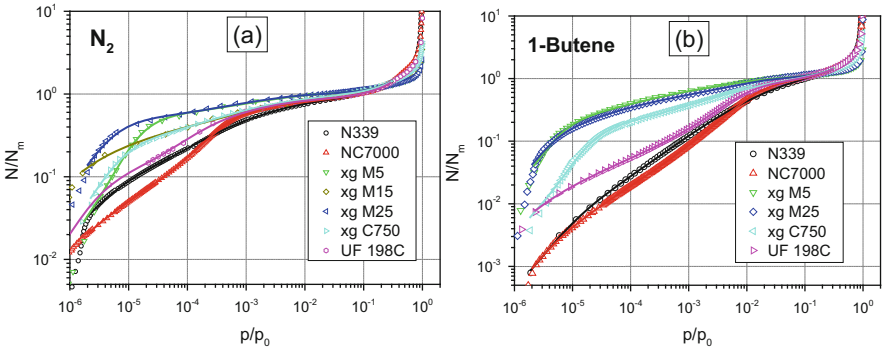

Fig. 1 Nitrogen (**a**) and 1-butene (**b**) adsorption isotherms (*symbols*) normalized to monolayer capacity and corresponding fits (*solid lines*) based on Eq. (6)

are compared with the furnace CB N339. It is obvious that the adsorption strength in the low pressure regime is large for all GNPs, indicating that the surface activity of GNPs is high compared with that of CNTs or CB. The highest adsorption strength is found for GNPs of M-type, followed by the C-type, and the ultrafine graphite (see Table 1 for characteristics). We also observe that the low pressure adsorption behaviors of the furnace CB and CNTs are quite similar, reflecting a surface activity lower than that of the GNPs. At low pressures ($p/p_0 = 10^{-6}$ to 10^{-2}), the coverage obtained from the isotherms reflects the amount of highly energetic adsorption sites at the surface. Previous investigations [37–39] have shown that the surface coverage in the low pressure range allows evaluation of the energy distribution of adsorption sites, which is a measure of the homogeneity and activity of the surface. For energetic homogeneous surfaces, one would expect a Langmuir–Freundlich behavior of the isotherm, stating that the slope of the isotherm in a double logarithmic plot is equal to one. In contrast, the slope of the adsorption isotherms of the GNPs in the low pressure range (p/p_0 of 10^{-5} to 10^{-3}) is significantly smaller, indicating that a large amount of highly energetic adsorption sites are present at the surface. Such sites can be edges or slit-like cavities between adjacent graphitic layers, or other types of defects. Table 1 lists characteristic data for the investigated carbon nanoparticles, including the N_2-surface area obtained from BET plots and other morphological details.

Figures 2 and 3 show the energy distribution of various fillers obtained by Eq. (6) with regard to nitrogen and 1-butene, respectively. The energy distribution of the standard CB N339 is widespread and essentially peaks around a maximum at about 8 kJ/mol (nitrogen) or 23 kJ/mol (1-butene), which can be attributed to the graphitic planes. In comparison with ultrafine graphite UF 198C, it is noticeable that the high-energy regimes are quite similar, but the low-energy regime of N339 is much more pronounced. This could be a result of the roughness, with large-scale cavities in the N339 surface allowing condensation at pressures far below p_0. CNTs NC7000 show greater peaks at around the same value, which is not surprising because they should mainly consist of rolled graphene layers.

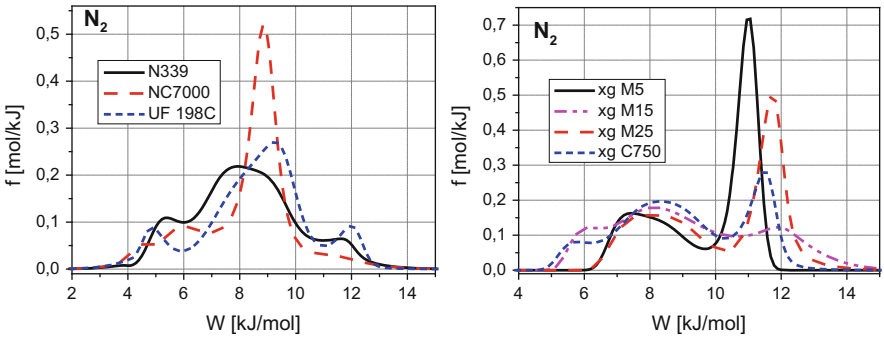

Fig. 2 Adsorption energy distributions of nitrogen for different fillers, as indicated

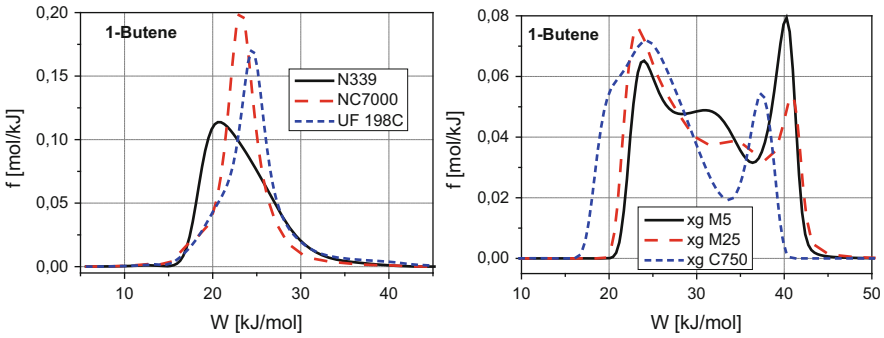

Fig. 3 Adsorption energy distributions of 1-butene for different fillers, as indicated

The distributions of all GNP samples have two peaks, at about 8 and 11 kJ/mol for nitrogen (Fig. 2) and 23 and 40 kJ/mol for 1-butene (Fig. 3). The first peak can be identified with the graphitic planes in both cases. The second peak corresponds to an energetically favorable geometric structure such as interplane cavities or stairway-like graphene stacks. This structure seems to be easily accessible by nitrogen molecules, because the second peak is much larger than the first. In contrast, the peak-to-peak ratio for 1-butene is much smaller, probably because 1-butene molecules are larger than nitrogen and cannot enter the structure in question so easily. This effect is especially prominent in the M-type GNP samples xg M5 and xg M25, whereas the C-type sample xg C750, with very high specific surface area (Table 1), shows a less pronounced peak ratio shift. We point out that the energy scale for 1-butene is about one order of magnitude greater than the thermal energy at room temperature. This indicates a strong adsorption of elastomer chains at the surface of the GNPs, which is even stronger than the interaction with CB. Accordingly, from the high binding affinities and large surface areas of the GNP samples, a strong reinforcement can be expected.

In conclusion, it has been shown that the energy distributions of special nanofillers fit those expected from their geometric structure: CNTs (NC7000)

Table 2 Specific surface areas obtained with Eq. (9)

Sample	$S_E - N_2$ (m^2/g)	S_E– 1-butene (m^2/g)	Ratio
N339	87	64	0.74
NC7000	238	252	1.06
UF 198C	25	14	0.56
xg M5	163	84	0.51
xg M15	102	–	–
xg M25	224	125	0.56
xg C750	813	512	0.63

show a single well-pronounced peak, the fine graphite UF 198C is similar to CB (N339) but is more peaked about the graphite plane energy, and the GNPs show two peaks. The exact origin of the second peak is not known, but its presence indicates a well-defined geometry. From the high binding affinities and high surface areas of the xg samples, a strong reinforcement can be expected.

3.3 Specific Surface Area

The specific surface areas (S_E) obtained with Eq. (9) from nitrogen and 1-butene adsorption measurements are summarized in Table 2. The equation takes energetic surface heterogeneities into account and corresponds to a generalization of the BET theory. Nevertheless, in the frame of experimental error, the evaluated specific surface areas are almost the same as those obtained from original BET theory (Table 1).

In all cases except CNTs NC7000 the nitrogen surface is larger than the 1-butene surface, as expressed by the ratios listed in Table 2. This is because the small nitrogen molecules are able to explore smaller structures (cavities), which are not accessible for 1-butene molecules. The special case of the CNT sample NC7000 can be attributed to measurement precision. In previous studies [42–44], the scaling of the surface area of CBs obtained with varying size of adsorbed molecules was used to estimate the surface fractal dimension D_s that characterizes the self-similar structure of surface roughness. These results were confirmed by applying the fractal Frenkel–Halsey–Hill (FHH) theory developed by Pfeifer et al. [45] in the multilayer regime, yielding $D_s \approx 2.6$ for all examined furnace CBs. Because the ratio of 1-butene to nitrogen surface is 0.74 for N339 and is between 0.51 and 0.63 for the GNP samples, it can be concluded that the latter samples have an even larger amount of small-scale structure than CB.

4 Stress–Strain Response of GNP Composites

4.1 Effect of GNP Type and Polymer Microstructure

A comparison of the stress–strain responses of SBR and NBR composites with 10 vol% of different fillers is presented in Figs. 4 and 5, respectively. It is apparent that, apart from the C-type GNP (xg C750), in both rubbers the shape of the stress–strain curves for the GNPs differs significantly from that of the reference filler CB (N339 in NBR and N121 in SBR). The C-type GNPs exhibit a similar reinforcement character as the CB although the specific surface area is about ten times larger (Table 1). The stress–strain curves initially increase moderately, but at approximately 150% strain the typical CB upturn with a steep, almost linear increase in

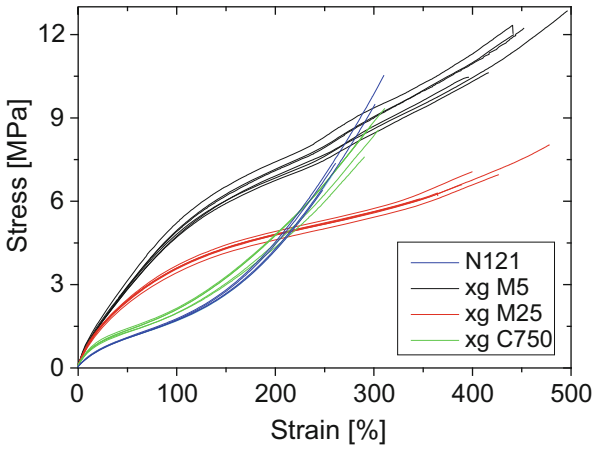

Fig. 4 Stress–strain curves for SBR composites with 10 vol% of different fillers, as indicated

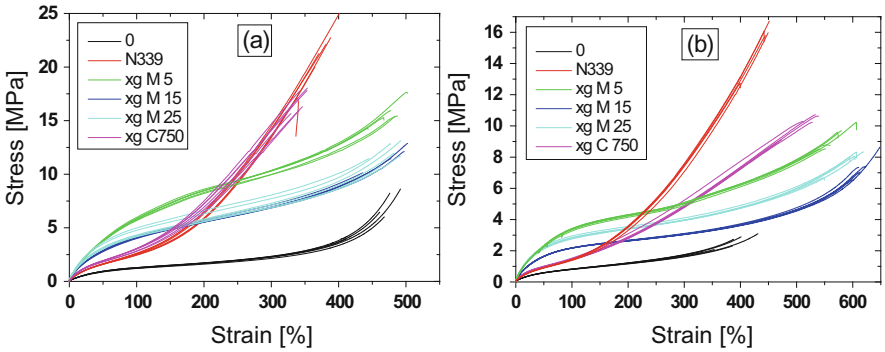

Fig. 5 Stress–strain curves for NBR composites with 10 vol% of different fillers (**a**) and with additional 20 vol% softener (DOP) (**b**)

stress begins delivering high tensile strength values, especially for the NBR samples (Fig. 5a). The M-type GNPs exhibit a totally different behavior: In the first part of the stress–strain curves, the stress increases rapidly and then a more moderate increase in stress is observed. For the NBR samples, a final upturn appears at relatively large strains of about 400%. Up to 200% strain, the stress value of the M-type is higher, but for larger strains the CB and the C-type exhibit significantly higher stress values. Interestingly, Fig. 4 shows that, for the SBR samples, the highest stress and strain values are observed in the case of the M-type GNP xg M5.

We point out that the shape of the stress–strain curves of the M-type GNPs is similar to that of the unfilled rubbers, although the stress values are significantly higher (Fig. 5). This indicates that the main reinforcing mechanism corresponds to strain amplification by the GNPs [46]. By contrast, the very different stress–strain response of CB-filled rubbers during first stretching results from the breakdown of filler network. This has been shown in previous papers by fitting the stress softening and hysteresis behavior observed for quasistatic stress–strain cycles with the dynamic flocculation model [9, 47–49]. It appears that this kind of filler network is not formed for the M-type GNPs, probably because the size of these platelets, with diameters in the micrometer range, is too large (see Table 1). Only the C-type GNP with significantly smaller platelet size seems to be able to form a sufficiently stiff filler network delivering the characteristic stress–strain response of CB-filled rubbers, that is, a flat initial stress increase but the typical steep increase in stress above approximately 150% strain.

The tension tests of NBR/GNP composites containing 20 vol% softeners (DOP) are shown in Fig. 5b. If the results are compared with the data without softener shown in Fig. 5a, one finds that the ranking of stress–strain curves is almost unaffected, although the stress level is significantly decreased as a result of the addition of softener. In both cases, a similar shape of the stress–strain curves is found for the M-type GNPs. The highest stress level is seen for xg M5 followed by xg M25 and xg M15, indicating that the smallest diameter of 5 μm delivers the best mechanical performance. This correlates with the higher adsorption energy of 1-butene (second peak of the energy distribution function) for xg M5, as shown in Fig. 3. Pronouncedly different behavior is observed for the C-type GNPs in comparison with CB, which for the system with softener shows a splitting of stress–strain curves at strains larger than 150% and a less steep increase in stress at large strains, with significant increase in elongation at break. This indicates that in the composite with softener the filler network of the C-type GNP exhibits less stable filler bonds, which break down more readily with increasing strain to deliver lower maximum stress but higher ultimate strain values. Moreover, a small scatter of repetitive measurements is observed for all systems, especially with softener, which may be a sign of unsatisfactory homogeneity and filler dispersion of the samples.

The state of GNP dispersion is visualized in Fig. 6 by a TEM micrograph of the NBR composite with 10 vol% of the M-type GNP xg M5 and 20 vol% softener. It appears that several single GNPs (platelets of approximately 5–8 nm height and 5 μm in diameter; Table 1) were separated and dispersed during mixing, but also that larger stacks of undispersed GNPs seem to be present. Further light microscopy

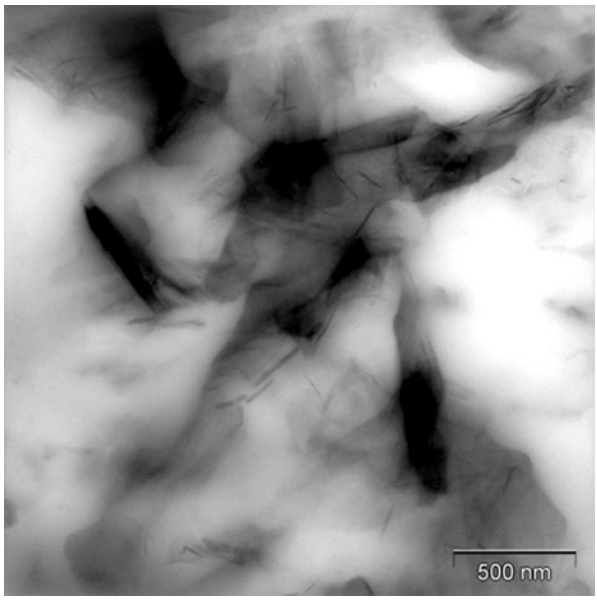

Fig. 6 TEM image of an NBR composite with 10 vol % GNP (xg M5) containing 20 vol% softener (DOP)

investigations have shown that some larger undispersed GNP agglomerates in the range of 50 to 100 μm are also present in the composites. This leads to the conclusion that the dispersion of GNPs is fairly well realized but can be further improved to enable tailoring of mechanical properties for technical applications.

4.2 Hybrid-Filler Systems

In previous studies, hybrid-filler systems have shown to be promising route for improving the mechanical and electrical properties of elastomer composites [8, 22, 23]. We report here on the possibility of obtaining highly conductive GNP composites with improved mechanical properties by adding a small amount of CNTs. This is demonstrated in Fig. 7, where the stress–strain response of SBR hybrid-filler composites with 10 vol% xg C750 partly substituted by 0.5, 1, and 2 vol% CNTs is shown together with the real part of the dielectric conductivity. The stepwise substitution by CNTs led to improved mechanical properties with increased tensile strength, indicating a symbiotic interaction between GNPs and CNTs. For comparison, the response of samples with 1 and 2 vol% pure CNTs are also shown and indicate poor mechanical properties. The conductivity data in Fig. 7b demonstrate that addition of 0.5 and 1 vol% CNTs does not give conductive samples, but 2 vol% is sufficient for obtaining high conductivity, both with and without GNPs. The high conductivity value of the sample with 2 vol% CNTs indicates that the CNTs are not strongly wetted with polymer. Accordingly, the tunneling contacts between adjacent CNTs are well established because the polymer gaps between CNTs are small,

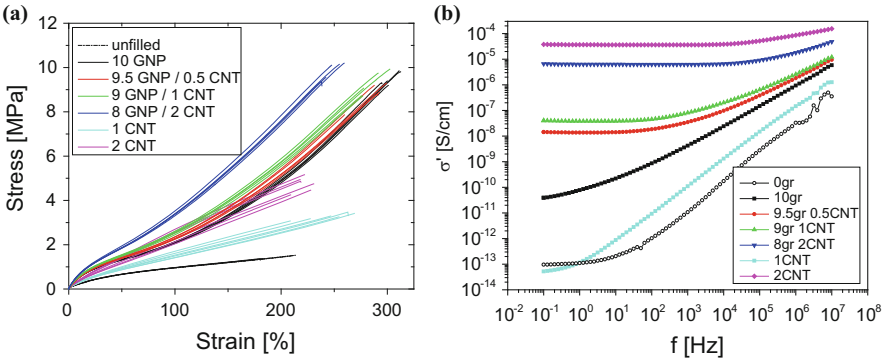

Fig. 7 (**a**) Stress–strain curves for SBR hybrid-filler composites with 10 vol% GNP (xg C750) partly substituted by CNTs. (**b**) Real part of dielectric conductivity

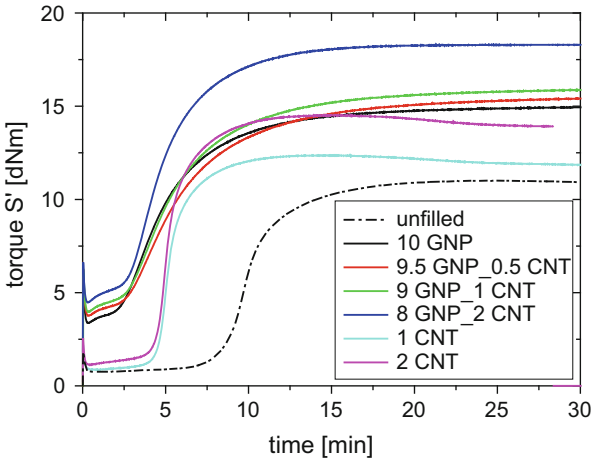

Fig. 8 Curing characteristics at 160°C of SBR hybrid-filler composites with 10 vol% GNP (xg C750) partly substituted by CNTs, as indicated

allowing the electrons to tunnel through these gaps easily [50, 51]. Interestingly, the addition of 8 vol% GNPs to the sample with 2 vol% CNTs decreased the conductivity, indicating that the wetting of CNTs was improved and the polymer gaps between CNTs were larger. This gives some idea of how the symbiotic interaction between GNPs and CNTs works.

The curing characteristics of the same SBR hybrid-filler composites with 10 vol % xg C750 partly substituted by 0.5, 1, and 2 vol% CNTs are shown in Fig. 8. It was found that the incubation time needed for the crosslinking reaction was strongly reduced by the CNTs and even more so by the GNPs. In addition, the samples filled with GNPs showed a pronounced flocculation effect in the first 3 min, when the torque is already quite high and a small side-maximum appears. Obviously, the

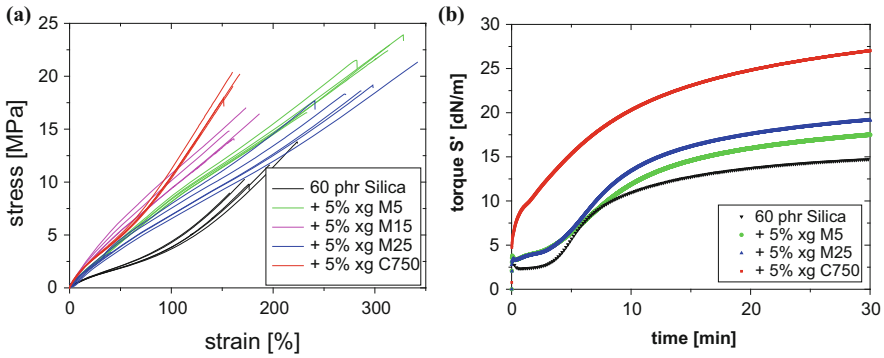

Fig. 9 (**a**) Stress–strain curves of SBR hybrid-filler composites with 60 phr silica (reference) and 5 vol% of various GNPs. (**b**) Curing characteristics of the samples at 160°C

torque increased slightly as a result of formation of a filler network before the crosslinking process became visible. This effect is also often observed for silica-filled rubbers if the particle size is sufficiently small. At longer times, a well-developed plateau was found for the GNP-filled systems whereas the CNT composites showed reversion. In agreement with the stress response shown in Fig. 6a, the largest torque values were found for the hybrid system with 8 vol% GNPs and 2 vol% CNTs. This confirms that material-specific synergetic interactions between the GNP and CNT filler particles deliver improved mechanical and electrical properties, which may serve for future development of tailor-made rubber goods.

Figure 9 shows a typical example where the combination of traditional fillers with GNPs can deliver improved reinforcement and vulcanization properties. In Fig. 9a, the stress–strain response of SBR hybrid-filler composites with 60 phr silica and 5 vol% GNPs is depicted for different GNP types. The greatest stiffness increase was found for the C-type GNPs but the best mechanical performance was observed for the M-types, xg M25 and especially xg M5 with the highest ultimate stress. The xg M15 did not deliver sufficient improvement in mechanical properties, which was probably related to poor dispersion. Figure 9b shows the vulcanization curves of the same combinations of silica/GNP composites, demonstrating that the incubation time as well as the maximum torque strongly depends on the GNP type.

5 Filler-Induced Stress Softening and Hysteresis

5.1 Dynamic Flocculation Model

The dynamic flocculation model (DFM) has been developed to describe the quasistatic stress–strain cycles of filler-reinforced rubbers showing the

characteristic stress softening and hysteresis behavior. It has been shown in various papers that this micromechanical model is well suited to explain the complex mechanical response by referring to a breakdown and re-aggregation of filler clusters under repeated strain. The physical motivation and mathematical treatment of the DFM is explained briefly in this section.

The DFM combines the well-established concepts of rubber elasticity with a micromechanical approach to dynamic filler flocculation in strained rubbers at different elongations. The stress response of filled rubbers as a function of strain can be derived from the following mesoscopic phenomena: A successive breakdown of filler clusters takes place in response to increasing strain of an unconditioned, virgin rubber sample. This process begins with the largest filler clusters and continues up to a minimum cluster size. Upon decreasing the strain, complete re-aggregation of the filler particles takes place. However, the filler–filler bonds, which are formed again after being broken, are significantly weaker than in the virgin sample. During subsequent stress–strain cycles of a pre-strained, reinforced sample, two micromechanical mechanisms can be distinguished:

1. Hydrodynamic reinforcement of the rubber matrix by a fraction of rigid filler aggregates with strong virgin filler–filler bonds, which had not been broken during previous deformations.
2. Cyclic breakdown and re-aggregation of the remaining fraction of softer filler clusters with damaged and, hence, weaker filler–filler bonds.

The fraction of rigid (unbroken) filler clusters decreases with increasing strain, whereas the fraction of soft filler clusters increases. The mechanical action of the soft filler clusters refers primarily to a viscoelastic effect, because any type of cluster that is stretched in the stress field of the rubber stores energy that is dissipated when the cluster breaks. This mechanism leads to a filler-induced viscoelastic hysteresis contribution to the total stress, which significantly affects the internal friction of the filled rubber samples. Note that this kind of hysteresis response is also present in the limit of quasistatic deformations, where no explicit time dependency of the stress–strain cycles is taken into account.

Accordingly, in the DFM the resulting apparent stress consists of two contributions: (1) the stress of the rubber matrix including hydrodynamic reinforcement, and (2) the stress of the strained and broken filler clusters. The free energy density of filler reinforced rubber is given by:

$$W(\varepsilon_\mu) = (1 - \Phi_{\text{eff}})\, W_{\text{R}}(\varepsilon_\mu) + \Phi_{\text{eff}}\, W_{\text{A}}(\varepsilon_\mu), \tag{10}$$

with Φ_{eff} being the effective filler volume fraction of the structured filler particles (e.g., primary carbon black aggregates). The first addend considers the equilibrium energy density stored in the strained rubber matrix, which includes hydrodynamic strain amplification effects that vary with the fraction of relatively stiff filler clusters with strong virgin filler–filler bonds. The second addend considers the

energy stored in the residual fraction of the softer filler clusters with damaged bonds that are deformed in the stress field of the rubber matrix.

The free energy density of the strained rubber matrix is described by a non-affine tube model of rubber elasticity:

$$W_{\mathrm{R}}(\varepsilon_\mu) = \frac{G_c}{2}\left\{\left\{\frac{\left(\sum_{\mu=1}^{3}\lambda_\mu^2 - 3\right)\left(1-\frac{T_e}{n_e}\right)}{1-\frac{T_e}{n_e}\left(\sum_{\mu=1}^{3}\lambda_\mu^2 - 3\right)} + \ln\left[1-\frac{T_e}{n_e}\left(\sum_{\mu=1}^{3}\lambda_\mu^2 - 3\right)\right]\right\}\right. \\ \left. +2G_e\left(\sum_{\mu=1}^{3}\lambda_\mu^{-1} - 3\right)\right., \tag{11}$$

with $\lambda_\mu = 1 + \varepsilon_\mu$. The first bracket term of Eq. (11) considers the interchain junctions, with an elastic modulus G_c proportional to the density of network junctions. The second addend is the result of tube constraints, whereby the tube constraint modulus G_e is proportional to the entanglement density of the rubber. The parenthetical expression in the first addend corresponds to a non-Gaussian extension of the tube model, taking into account the finite chain extensibility of the polymer network. The finite extensibility parameter is chosen as the ratio $n_\mathrm{e}/T_\mathrm{e}$, with n_e being the number of statistical chain segments between two successive entanglements and T_e is the trapping factor characterizing the portion of elastically active entanglements. Because T_e increases with the number of crosslinks in the system ($0 < T_\mathrm{e} < 1$), the finite extensibility parameter decreases with increasing crosslinking density.

The presence of rigid filler clusters, with bonds in the virgin, unbroken state of the sample, gives rise to hydrodynamic reinforcement of the rubber matrix. This is specified by the strain amplification factor X, which relates the external strain ε_μ of the sample to the internal strain ratio λ_μ of the rubber matrix:

$$\lambda_\mu = 1 + X\varepsilon_\mu. \tag{12}$$

In the DFM, the strain amplification factor depends on the pre-conditioning of the sample and gives rise to the well-known stress softening effect of filler-reinforced rubbers. In the case of pre-conditioned samples and for strains smaller than the previous straining ($\varepsilon_\mu < \varepsilon_{\mu,\max}$), the strain amplification factor X is independent of strain and determined by $\varepsilon_{\mu,\max}$, $X = X(\varepsilon_{\mu,\max})$. For the first deformation of virgin samples, it depends on the external strain $X = X(\varepsilon_\mu)$. For fractal clusters, $X(\varepsilon_{\mu,\max})$ or $X(\varepsilon_\mu)$ can be evaluated by averaging over the size distribution of rigid clusters in all space directions. In the case of pre-conditioned samples, this yields:

$$X(\varepsilon_{\mu,\max}) = 1 + c\Phi_{\text{eff}}^{\frac{2}{3-d_f}} \sum_{\mu=1}^{3} \frac{1}{d} \left\{ \int_0^{\xi_{\mu,\min}} \left(\frac{\xi_\mu'}{d} \right)^{d_w - d_f} \varphi\left(\xi_\mu'\right) d\xi_\mu' + \int_{\xi_{\mu,\min}}^{\infty} \varphi\left(\xi_\mu'\right) d\xi_\mu' \right\}. \tag{13}$$

Here, c is a constant of order one, Φ_{eff} is the effective filler volume fraction, ξ_μ is the cluster size, d is the particle size, $d_f \approx 1.8$ is the mass fractal dimension, and $d_w \approx 3.1$ is the anomalous diffusion exponent on cluster–cluster aggregation. $\phi(\xi_\mu)$ is the normalized size distribution that can be derived from the Smoluchowski equation of the kinetics of cluster–cluster aggregation of colloids. With the abbreviation $x_\mu \equiv \xi_\mu/d$ and the normalized mean cluster size $x_0 \equiv \xi_0/d$ it reads:

$$\varphi(x_\mu) = \frac{4x_\mu}{x_0} \exp\left(-\frac{2x_\mu}{x_0} \right) \quad \mu = 1, 2, 3. \tag{14}$$

We point out that, with this distribution function, the integrals in Eq. (13) and (15) can be solved analytically.

The second addend in Eq. (10) considers the energy stored in the substantially strained filler clusters. It delivers a filler-induced hysteresis as a result of cyclic stretching, breakdown, and re-aggregation that can be described by an integral over the soft filler clusters in stretching direction ($\dot{\varepsilon}_\mu > 0$, where the dot denotes the time derivative) with a strain-dependent upper boundary:

$$W_A(\varepsilon_\mu) = \sum_{\mu}^{\dot{\varepsilon}_\mu > 0} \frac{1}{2d} \int_{\xi_{\mu,\min}}^{\xi_\mu(\varepsilon_\mu)} G_A\left(\xi_\mu'\right) \varepsilon_{A,\mu}^2\left(\xi_\mu', \varepsilon_\mu\right) \varphi\left(\xi_\mu'\right) d\xi_\mu'. \tag{15}$$

The sum over stretching directions with ($\dot{\varepsilon}_\mu > 0$) implies that clusters store energy by being stretched and re-aggregate upon contraction. G_A is the elastic modulus and $\varepsilon_{A,\mu}$ is the strain of the soft filler clusters in spatial direction μ. The dependency of these quantities on cluster size ξ and external strain ε_μ can be derived from basic micromechanical consideration of the elasticity and fracture mechanics of fragile filler clusters imbedded into a strained rubber matrix [9, 10]. This analysis has shown that the cluster strain under a certain load rises more strongly with cluster size than the failure strain does. Accordingly, with rising load, large clusters break first followed by smaller ones. The critical size of currently breaking clusters $\xi_\mu(\varepsilon_\mu)$ entering into the upper integration limit of Eq. (15) can be derived. With the abbreviation $x_\mu \equiv \xi_\mu/d$, one obtains:

$$x_\mu(\varepsilon) = \frac{Q_d \varepsilon_{d,b}}{d^3 \hat{\sigma}_{R,\mu}(\varepsilon)} \equiv \frac{s_d}{\hat{\sigma}_{R,\mu}(\varepsilon)} \ . \tag{16}$$

This involves the tensile strength of damaged bonds s_d, which can be expressed by their failure strain $\varepsilon_{d,b}$ and elastic modulus Q_d/d^3, and the stress of the rubber matrix relative to the start of the cycle where $\partial\varepsilon_\mu/\partial t = 0$:

$$\hat{\sigma}_{R,\mu}(\varepsilon) := \sigma_{R,\mu}(\varepsilon) - \sigma_{R,\mu}\left(\partial\varepsilon_\mu/\partial t = 0\right). \tag{17}$$

In a similar way, the tensile strength of virgin bonds s_v governs the minimum size of damaged clusters $\xi_{\mu,,\min}$ ($\varepsilon_{\mu,\max}$) appearing in the integration boundaries of Eqs. (13) and (15):

$$x_{\mu,\min} = \frac{Q_v \varepsilon_{v,b}}{d^3 \hat{\sigma}_{R,\mu}(\varepsilon_{\max})} \equiv \frac{s_v}{\hat{\sigma}_{R,\mu}(\varepsilon_{\max})} \tag{18}$$

The two parameters s_d and s_v are treated as fitting parameters. A more detailed physical description of the DFM and the various experimental tests of the model can be found in the literature [9, 10, 47–49].

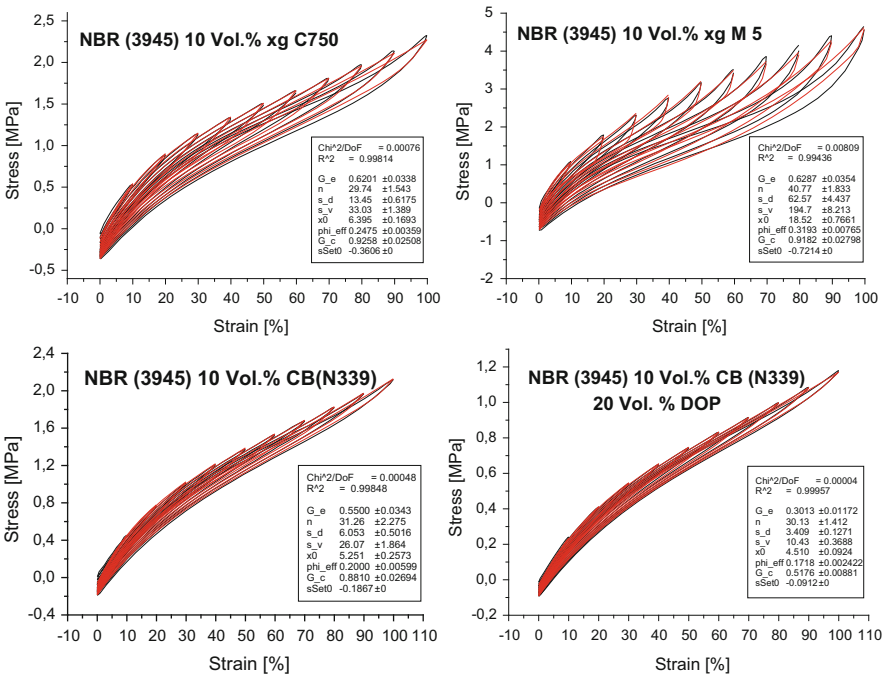

Fig. 10 Comparison of multihysteresis measurements (*black lines*) and fits with the DFM (*red lines*) for four different NBR composites, as indicated. Fitting parameters are given in the *insets*

5.2 Multihysteresis Stress–Strain Cycles

To gain a deeper understanding of reinforcement by GNPs, multihysteresis measurements were made on dumbbell-shaped NBR samples with 10 vol% filler. The ultimate tensile strain was successively increased after each fifth tension cycle. Figure 10 provides paradigmatic examples showing multihysteresis measurements as well as fittings based on the DFM of graphene NBR composites (using different types of GNPs) and of CB N339 (with and without softener). It was ascertained that both hysteresis and the upturn became more pronounced, with the latter occurring significantly earlier in hysteresis curves of the composites with GNPs compared with CB N339. This suggests that the interaction between the polymer and the filler surface is exemplary. Additional mechanical measurements have confirmed this result. An analysis and comparison of the fittings leads to the conclusion that the DFM describes the differently filled samples fairly well, with a correlation coefficient of $R^2 > 0.99$ in all cases. However, some discrepancies are obviously seen for the xg M5 sample at larger strains.

The C-type GNP, with very high specific surface area, delivers the best fits with the DFM. Because the model was developed for CB and silica, which both develop a fractal network, it is likely that the DFM can also describe (to a limited extent) the filler networking of platelet-shaped particles with a high aspect ratio. Seven free fitting parameters were used to carry out the adaptation of the multihysteresis data via the DFM. The set stress σ_{set} was adjusted to the measured setting behavior previous to fitting. The fitting parameters of the different systems are summarized in Table 3.

The microscopic material parameters shown in Table 3 appear physically reasonable. The polymer-specific parameters G_c, G_e, and n_e/T_e vary as follows: The mechanically effective crosslink modulus G_c shows the largest values of about 0.9 MPa for the highly reinforcing fillers and is significantly lower for the two systems with softener. The tube constraint modulus G_e shows a similar trend and, apart from xg M25, is almost independent of filler type at about 0.6 MPa and

Table 3 Fitting parameters of the DFM for NBR composites with 10 vol% of different filler. The physical meaning of the parameters is explained in the text

Parameter	G_e (MPa)	G_c (MPa)	$n = n_e/T_e$	s_d (MPa)	s_v (MPa)	Φ_{eff}	x_0	σ_{set} (MPa)
N121	0.63	0.92	44.2	9.6	30.1	0.19	5.08	−0.23
N339	0.55	0.88	31.3	6.1	26.1	0.20	5.25	−0.19
xg C750	0.62	0.92	29.7	13.5	33.0	0.25	6.39	−0.36
xg M5	0.63	0.92	40.8	62.6	194.7	0.32	18.5	−0.72
xg M25	0.20	0.73	10.4	69.1	244.3	0.37	30.0	−0.59
UF 198C	0.70	0.80	18.8	15.8	64.7	0.19	7.90	−0.23
N339/20% DOP	0.30	0.52	30.1	3.4	10.4	0.17	4.51	−0.09
xg M5/20% DOP	0.26	0.43	63.4	68.6	213.1	0.26	33.2	−0.38

0.3 MPa with and without softener, respectively. This reflects the reduced crosslink and entanglement density as a result of the presence of the softener. Both of these factors drop almost quadratically with the polymer content. Unexpected parameters are found for xg M25, which could not be fitted well, indicating that large-sized platelets are not well described by the DFM. The finite extensibility parameter n_e/T_e varies between 60 and 20 and may be affected by different influencing parameters.

The filler-specific parameters shown on the right side of Table 3 deliver information about filler networking and the in-rubber structure of the different filler systems. On the one hand, the strengths of filler–filler bonds in the virgin and damaged states (s_v and s_d, respectively) are significantly higher for the M-type GNPs, which is responsible for the strong stress-softening and hysteresis effects of these composites. This is accompanied by a relatively large mean cluster size, x_0, which reaches a maximum of about 33 particles in the system with softener. Note that the set stress for these systems is high, indicating that it is closely related to the hysteresis. On the other hand, the sample filled with xg C750 (with very high specific surface area) is more comparable with the CB-filled samples, with s_v and s_d in the range of 30 and 10 MPa, respectively, and a relative cluster size x_0 in the range of 5. This correlates with the very similar stress–strain responses of the samples filled with CB and xg C750, as shown in Figs. 4 and 5. Nevertheless, the strengths of filler–filler bonds in the virgin and damaged states are significantly higher for the GNP system, which results in more pronounced stress-softening and filler-induced hysteresis for xg C750 compared with CB, as observed in Fig. 10.

The effective filler volume fraction Φ_{eff} is again found to be significantly larger for the GNP-filled samples compared with CB or UF 198C, especially for the M-type GNPs. This indicates that the particle shape of the GNPs is quite irregular, showing a pronounced in-rubber structure with a large amount of occluded rubber hidden in voids and cavities. This occluded rubber is not deformed under external straining and acts as additional filler, delivering effective filler loadings much larger than the real loadings. This picture correlates with the irregular shape of the energy distribution functions with very pronounced high energy peaks, found from static gas adsorption measurements for the polymer-analogous gas 1-butene (Fig. 3). It confirms that the polymer–filler interactions for the M-type GNPs are strong enough to deliver a quite stiff filler network that produces the observed high hysteresis of the samples. We point out that this will not necessarily deliver improved ultimate properties or improved fracture mechanical and wear properties of the GNP-filled samples because optimum performance requires a good balance between filler and the polymer network.

6 Gas Permeation Properties

Gas permeability measurements were conducted to characterize gas permeability for application of GNP composites as membranes. The permeability coefficient is defined volumetrically (see Eq. (2), Sect. 2.8). Gas permeability measurements for nitrogen in SBR composites can be seen in Fig. 11. These investigations were

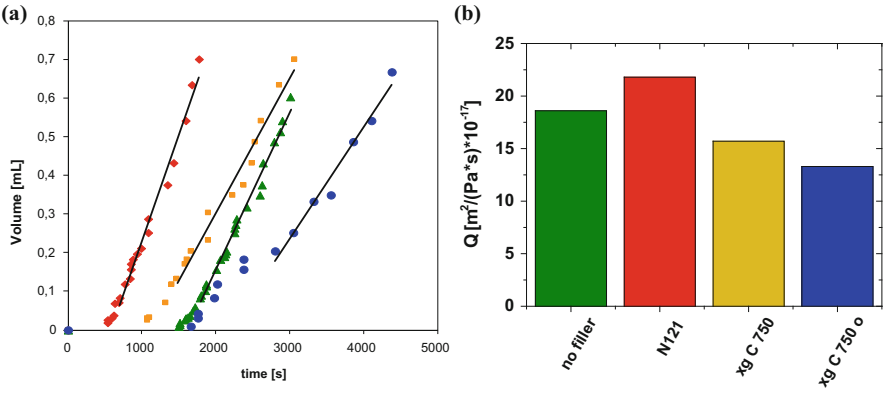

Fig. 11 (**a**) Nitrogen volume flow versus. time with regression lines for the slope. (**b**) The resulting permeation coefficients of SBR composites with 10 vol% of different fillers, as indicated

performed with an experimental setup for volumetric measurements, where a pressure of 5 bar was applied to the SBR membrane. The pressure of the surrounding medium was 1.03 bar at a temperature of 60°C. An unfilled reference solution SBR (S-SBR) elastomer, a CB-filled sample (10 vol% N121), and orientated (indicated by "o") and non-orientated graphene samples (10 vol% xg C750) were scrutinized. Alignment was achieved during processing of the GNP composites by rolling them out fairly thinly and stacking them in the vulcanizing press. The change in nitrogen volume flow over time is plotted in Fig. 11a. The area in which the elastomer sample is exposed to an equilibrium gas flow (diffusion process) facilitating a constant volume flow rate can be explicitly observed here. The permeability coefficient is calculated from the flow gradient using Eq. (2), resorting to test piece geometry (Fig. 11b). Obviously, the system comprising the orientated graphene samples displays the lowest flow gradient, whereas the CB-filled sample shows the gradient with the steepest descent. Hence, the smallest amount of gas flows through the orientated GNP elastomer. As is evident from these results, the use of GNPs significantly reduces gas permeability and an added alignment assists in this reduction.

The permeability coefficients of air for NBR and SBR composites with different filler types were measured at 70°C using a pressure-controlled device at a pressure of 4 bar. Figure 12a compares various NBR composites with 10 vol% of different fillers. Three types of graphene are compared with special graphite and an unfilled sample. As can be seen, the graphene types having the largest (initial) diameter (xg M5, 5 μm; xg M25, 25 μm) display the smallest coefficients and therefore better barrier properties. The xg C750 exhibits a diameter of 2 μm and therefore shows much larger gas permeation. The air permeation coefficients of SBR hybrid systems are depicted in Fig. 12b. Here, normal and oriented systems are compared, demonstrating that orientation delivers small permeation coefficients. The orientated samples exhibit graphene alignment in the elastomer matrix induced by

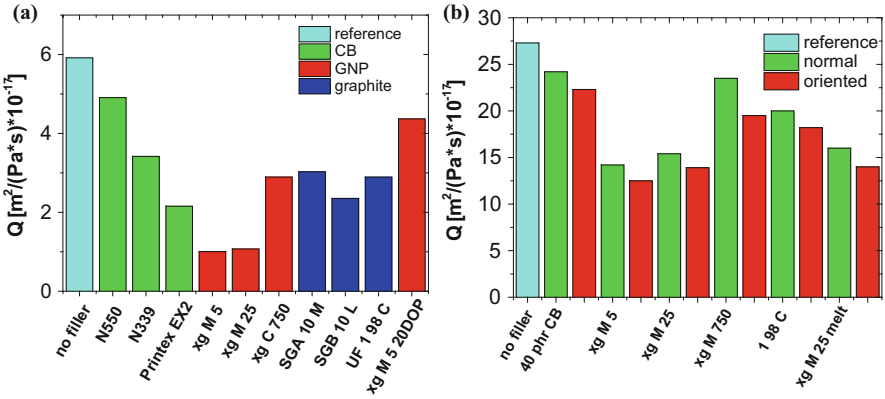

Fig. 12 Gas permeation coefficient of air at 70°C for NBR composites with 10 vol% of different fillers (**a**) and SBR hybrid-filler composites with 16.5 vol% CB N121 partly substituted by 5 vol% GNPs (**b**), as indicated. Samples with oriented and non-oriented GNPs are shown

elongational or shear flow during rolling of thin layers and stacking of the layers in the vulcanizing press. Figure 12b compares unfilled and several filled SBR composites with 16.5 vol% CB (40 phr N121), partly substituted by 5 vol% of GNPs or graphite; the filler content remained unchanged. All substituted systems demonstrate a decreasing permeability coefficient, whereby the M-type GNPs show the lowest permeation whereas those of the C-type xg C750 and the CB-filled SBR are comparable. This effect is very pronounced, especially for aligned samples.

7 Crack Growth and Fracture Mechanical Properties

7.1 Crack Growth Characteristics

The dynamic crack growth rate under cyclic loading is analyzed in Figs. 13, 14, and 15 to determine the fracture mechanical properties of elastomers based on graphene. Each of the examined NBR composites had a concentration of 10 vol %. Two different graphene systems based on the GNP types xg M5 and xg C750 were compared with conventional carbon black (Corax N339). These samples were selected on the basis of mechanical characterization (see Sect. 4.1, 4.2). With the exception of the highly structured carbon black Printex EX2, the GNP-M5 types showed the highest gain values in quasistatic/stress–strain experiments (up to 200% strain plus multihysteresis measurements) and associated with dynamic measurements (storage modulus, activation energy). The GNP type xg C750 has very similar mechanical properties, although its N_2 surface area is pretty high and it differs profoundly from standard carbon blacks.

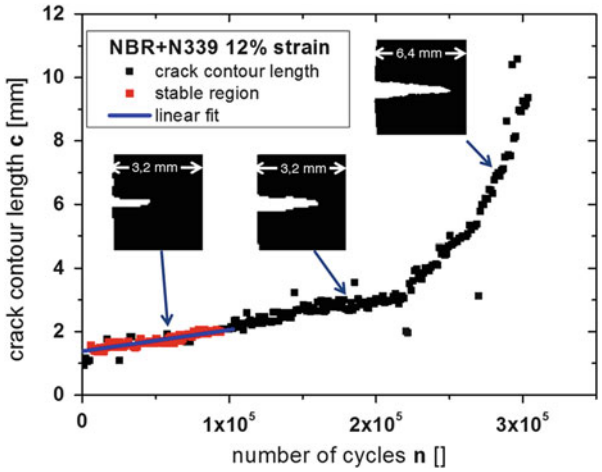

Fig. 13 Crack growth of NBR composite filled with 10 vol% N339 at 12% strain. The region of linear crack growth is shown in *red*. Additionally, three crack images at different crack length are shown

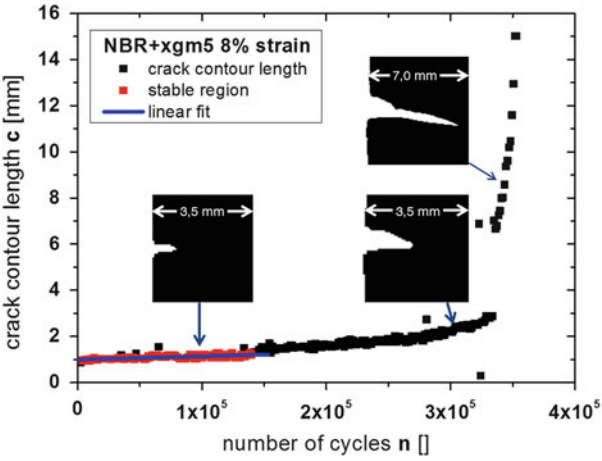

Fig. 14 Crack growth of NBR composite filled with 10 vol% xg M5 at 8% strain. The region of linear crack growth is shown in *red*. Additionally, three crack images at different crack length are shown

Further investigations were performed on the synergetic effects of hybrid systems, whereby 2 vol% of the carbon black N 339 (10 vol%) was substituted by GNPs (xg M5). Increased tension or module values were obtained through quasistatic stress–strain experiments as well as DMA measurements.

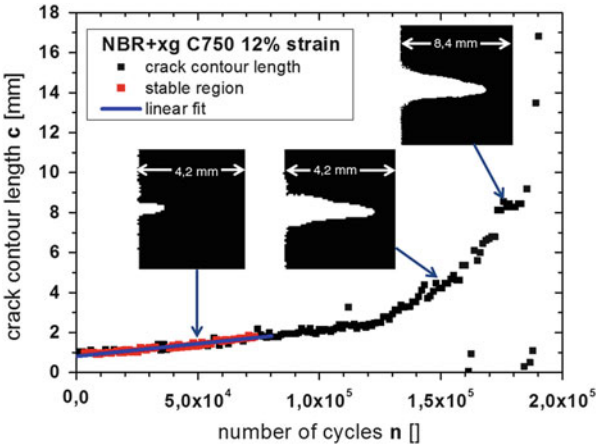

Fig. 15 Crack growth of NBR composite filled with 10 vol% xg C750 at 12% strain. The region of linear crack growth is shown in *red*. Additionally, three crack images at different crack length are shown

7.2 Tearing Energy and Paris–Erdogan Plots

For evaluation of the fracture mechanical properties of the compounds, the crack contour length c was analyzed in a region of linear crack growth (Figs. 13, 14, and 15). Usually, a double-logarithmic plot of the dynamic crack propagation rate (dc/dn) versus the tearing energy T helps empirically describing the crack propagation (see Fig. 16). This so-called Paris–Erdogan plot illustrates the frequently observed power law behavior of elastomers:

$$\frac{dc}{dn} = \alpha^{\beta}. \tag{19}$$

In this context, α and β denote the polymer-specific parameters. The solid lines in Fig. 16 show the fit of this equation to experimental data.

Analysis of the crack growth rates is presented as a function of the tearing energy for two GNPs and a carbon black, each containing 10 vol% of filler. The crack propagation rates as a function of the tearing energy are found within the range of 0.1 and 1 MPa mm for strain values between 4% and 22.5%, as depicted in Fig. 16. Because their rigidity (stiffness) is definitely larger, the GNP composites show measurement points shifted towards higher tearing energies for the same strain values. An extrapolation of the plotted gradients towards lower tearing energies ($T < 0.1$ MPa mm) or smaller deformations (<4%) entails a similar crack growth rate for xg M5 as for the CB-filled sample. The crack growth rates of xg C750 seems to be systematically larger at small strains, but the curves intersect each other at higher strain values and are close together at $T = 0.5$ MPa mm. At high tearing energies ($T > 1$ MPa mm), the sample filled with xg C750 clearly shows the lowest crack propagation rates, which might be important for technical applications. This is even more interesting because GNPs can be oriented and, hence, could serve for

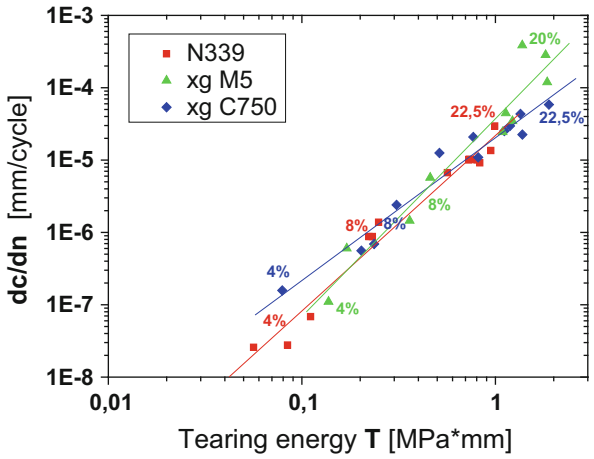

Fig. 16 Dynamic crack propagation rates of NBR composites with 10 vol% of different GNPs (xg M5 and xg C750) and comparison with carbon black N339. Experimental data are indicated by *symbols* and fits to Eq. 19 by *lines*

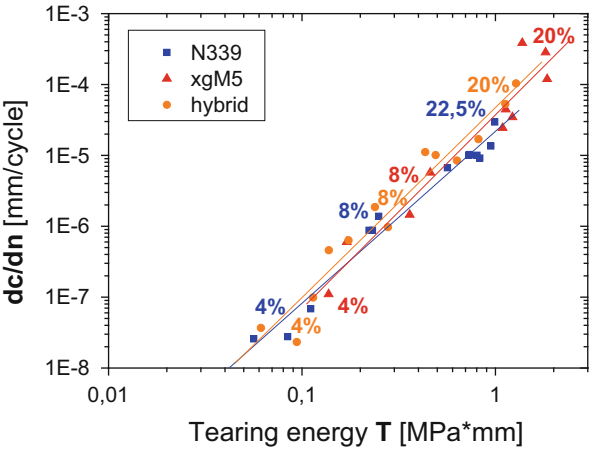

Fig. 17 Dynamic crack propagation rates versus tearing energy of NBR composites with 10 vol% of different filler systems: GNP xg M5, hybrid (8 vol % N339 and 2 vol% xg M5), and carbon black N339, as indicated

crack deflection along the orientation direction in special applications. This could play a role, for example, in truck tire treads, where deep cuts can appear if the tire is operating on unpaved trails or roads with sharp stones. Here, it appears advantageous to avoid crack propagation deep into the tread but to deflect it horizontally. Whether this can be achieved with GNPs remains open and is a task of future work.

The fracture mechanical results for the hybrid-filler system, with 2 vol% of CB replaced by the GNP xg M5, are shown in Fig. 17, where they are compared with the pure CB and GNP samples. As can be expected, a shift towards larger tearing energies at the same strain values is apparent, because the stiffness of the hybrid system exceeds that of the CB values and falls behind the pure GNP values. The crack propagation rates as a function of the tearing energy lie close together and the effect is barely discernible. Within the range of experimental error, no significant differences can be seen between the pure GNP and the hybrid-filler system,

although the pure CB sample seems to show slightly improved tear resistance at higher tearing energies.

8 Friction and Wear Properties

8.1 Rubber Friction Theory

Hysteresis friction of rubber sliding over rough surfaces is the dominant mechanism for slipping tires on wet roads and other lubricated frictional pairings. It results from dissipated energy losses of the rubber as a result of excitations over a broad frequency interval, which is related to the surface roughness on various length scales [52, 53]. In addition, adhesion friction has to be taken into account for friction on dry substrates. This is governed by the true contact area and is mainly a result of molecular interactions in the multiscale contact patches. In this section, we consider the extended Klüppel–Heinrich theory of rubber friction in some detail [53–55], which has been shown to describe experimental friction data on dry and wet substrates very well [56–70].

Both hysteresis and adhesion friction contribute to the total friction force acting on a rubber block sliding over a substrate such as glass or granite. Thus, the friction coefficient, which gives information about the friction force related to the applied normal force, is given by the sum of both contributions:

$$\mu_{\text{tot}} = \mu_{\text{hys}} + \mu_{\text{adh}}. \tag{20}$$

Here μ_{adh} is the adhesion friction coefficient and μ_{hys} is the hysteresis friction coefficient. To determine the individual contributions μ_{hys} and μ_{adh} it is necessary to characterize the surface roughness of the substrates and obtain information about the viscoelastic properties of the rubber compounds.

Most natural and engineered rough surfaces exhibit a self-affine structure within a defined wavelength interval. This means that the surface roughness of such interfaces shows an invariance of the morphology under anisotropic transformation. For such interfaces, a magnification α in the lateral xy-plane corresponds to a magnification α^{H} in the vertical z-direction. The resulting Hurst coefficient H determines the fractal dimension D, which is equal to $3-H$. This self-affinity holds only below the lateral cut-off length $\xi_{\parallel}$ and its corresponding vertical length $\xi_{\perp}$. Both are identified with the largest surface corrugations, corresponding to the limit of the macrotexture. Mathematically, the self-affine character can be derived by the height-difference correlation function:

$$C_z(\lambda) = < (z(x+\lambda) - z(x))^2 > . \tag{21}$$

This function is used to calculate the mean square height differences of all points separated laterally by the distance λ. Below the cut-off lengths, $\xi_{\parallel}$ and $\xi_{\perp}$, the height-difference correlation of self-affine surfaces shows a scaling behavior with slope H. Above the cut-off lengths, no correlation between the analyzed roughness data is found. The linear relationship between C_z and the surface descriptors $\xi_{\perp}$, $\xi_{\parallel}$, and D is given by the following expression:

$$C_Z(\lambda) = {\xi_{\perp}}^2 \cdot \left(\frac{\lambda}{\xi_{\parallel}}\right)^{2H}, \quad \text{for} \quad \lambda < \xi_{||}. \tag{22}$$

Because larger length scales mostly contribute to hysteresis friction, a fine characterization of macrotexture is required in order to obtain relevant contributions in more detail. For that, the height correlation function can be decomposed into two scaling regimes and the formula expanded to two ranges with different Hurst exponents [61, 62].

The hysteresis friction coefficient is obtained by integration of energy dissipation over a range of excitation frequencies corresponding to a multiscale indentation mechanism during the sliding process [53]:

$$\mu_{\text{hys}}(v) \equiv \frac{F_{\text{hys}}}{F_N} = \frac{<\delta>}{2\,\sigma_o v} \cdot \int_{\omega_{\min}}^{\omega_{\max}} \omega \cdot \mathrm{E}''(\omega) \cdot S(\omega) d\omega. \tag{23}$$

The coefficient depends on sliding velocity v and normal force F_N, which is applied on a rubber block. The roughness of the substrate is represented by the Fourier-transformed power spectrum density $S(\omega)$, which can be derived using descriptors obtained from the height difference correlation function:

$$S(\omega) = \frac{(3-D) \cdot {\xi_{\perp}}^2}{2\pi v \xi_{ll}} \cdot \left(\frac{\omega}{\omega_{\min}}\right)^{-\beta}, \quad \text{for} \quad \omega_{\min} < \omega. \tag{24}$$

The minimum excitation frequency $\omega_{\min} = 2\pi v/\xi_{\parallel}$ corresponds to the maximum lateral wavelength $\xi_{\parallel}$. E'' is the loss modulus of the elastomer sample and takes into account the viscosity losses of the material during the sliding process. σ_0 is the applied normal load related to the nominal contact area A_0 and is expected to be constant. δ is the mean layer thickness of the excited volume $V = \delta A_0$ and is assumed to increase linearly with the mean penetration depth z_p of the asperities in the elastomer sample $\Delta = bz_p$.

For dry systems, adhesion effects should be considered in addition to hysteresis friction, because molecular interactions deliver an adhesion force F_{adh}, leading to an adhesion friction coefficient [58–62]:

$$\mu_{\mathrm{adh}} = \frac{F_{\mathrm{adh}}}{F_N} = \frac{\tau_s \cdot A_c}{\sigma_0 \cdot A_0}, \tag{25}$$

with the interfacial shear stress τ_s given by:

$$\tau_s = \tau_{s,0} \cdot \left(1 + \frac{E_\infty/E_0}{(1 + (v_c/v))^n}\right). \tag{26}$$

This corresponds to viscoelastic peeling effects. The static shear stress $\tau_{s,0}$ and the critical velocity v_c, where τ_s converges to a maximum, are free fit parameters. E_∞/E_0 and n are material parameters and can be extracted from the dynamic mechanical material properties in the form of a viscoelastic master curve. The exponent:

$$n = \frac{1-m}{2-m}, \tag{27}$$

is gained from the power law behavior $H = \tau^{-m}$ with exponent m $(0 < m < 1)$ in the glass transition range of the relaxation time spectrum $H(\tau)$. This spectrum can be obtained from the viscoelastic master curves of the storage modulus G' by applying the iteration procedure of Williams and Ferry [71]:

$$\begin{aligned} H(\tau) &= A\,G' \cdot \frac{d\log(G')}{d\log(\omega)}\bigg|_{1/\omega=\tau} \quad \text{for} \quad p < 1 \\ \text{with} \quad A &= (2-p)/2\Gamma\left(2 - \frac{p}{2}\right)\Gamma\left(1 + \frac{p}{2}\right). \end{aligned} \tag{28}$$

Here, p is the local slope of $H(\tau)$ at $\tau = 1/\omega$, which is found to be smaller than 1 in all cases; Γ is the gamma function.

8.2 Materials and Dynamic Mechanical Properties

The friction behavior was analyzed for variously filled S-SBR 2525-0 samples. The elastomer was filled with three different types of sheet-like nanofillers. On the one hand, two types of GNPs, xg M25 (219.1 m^2/g) and xg C750 (810.5 m^2/g), were used and, on the other hand, the ultrafine graphite UF 198C (23.5 m^2/g) was mixed with the rubber. Additionally, the standard furnace carbon black N121 (117.7 m^2/g) served as reference.

To study the friction properties of elastomers, knowledge of how the material behaves under dynamic stress is required. Therefore, temperature- and frequency-dependent dynamic mechanical measurements were carried out at a higher strain amplitude of $\varepsilon = 2.5\%$ and master curves generated, using the Williams–Landel–Ferry (WLF) approach to determine the horizontal shifting factors. Additionally, a vertical shift was applied to consider thermally activated filler effects [60]. As a

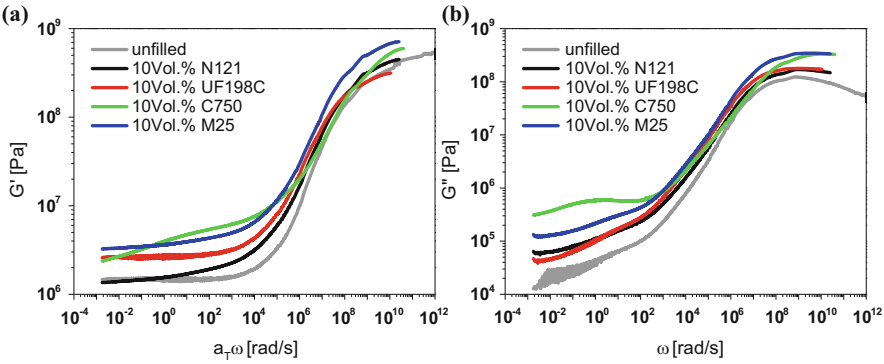

Fig. 18 Master curves of the storage modulus G' (**a**) and loss modulus G'' (**b**) at 2.5% strain amplitude and $T_{ref} = 20°C$ for unfilled and variously filled S-SBR composites, as indicated

reference temperature, 20°C was selected. The WLF factors, which are determined from the horizontal shifting of the branches to obtain reasonable overlap, were $C_1 = -4.56$ and $C_2 = 96.37°C$. The resulting viscoelastic master curves for the different composites are depicted in Fig. 18.

Figure 18a shows the frequency dependence of the shear storage modulus G', which increases with frequency and finally enters a glassy plateau. In the low frequency range, clear differences can be seen between the various composites, whereas at higher frequencies the modulus is almost unchanged as a result of the dominance of the polymer matrix in the glassy state. Compared with the unfilled compound, all filled systems exhibit a higher shear modulus in the rubbery region, with a more or less pronounced frequency dependence. Except for the ultrafine graphite UF 198C, the storage modulus increases with available specific surface area. The loss modulus G'', which is shown in Fig. 18b, delivers information about the internal viscosity losses of the polymer–filler system. In the rubbery region, the losses during dynamic stimulation increase with increasing activity of the filler. The filler with the highest specific surface area (xg C750) exhibits the highest energy dissipation. In addition, G'' shows a local maximum, which is probably caused by confined polymer in graphene clusters. The loss behavior of the other two samples is similar to that of the CB-filled sample, although the storage modulus is significantly higher, especially for UF 198C. The viscoelastic loss modulus $E'' = 3G''$ can be entered into Eq. (23) to perform hysteresis friction simulations.

Figure 19a show the loss tangent of the composites. Addition of filler decreases the maximum slightly, which refers to the polymer–filler interaction. Surprisingly, in the case of xg C750, the location of the maximum is also shifted to significantly higher frequencies. This indicates higher chain mobility, possibly caused by repulsive interactions between polymer and filler. The second low frequency maximum of the xg C750 sample probably results from the confined polymer domains in the highly structured GNP network.

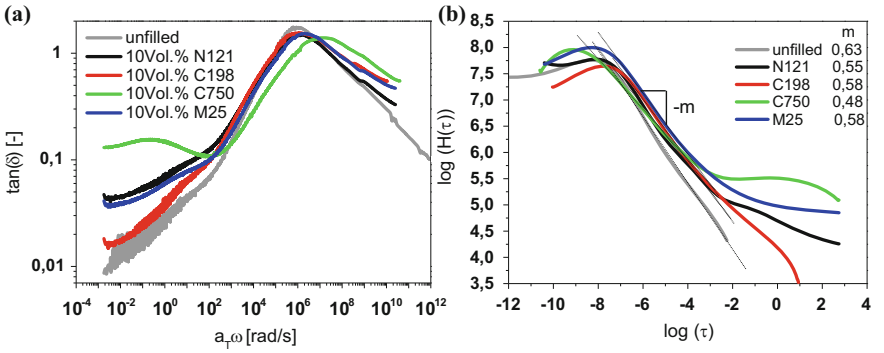

Fig. 19 Loss tangent master curves (**a**) and relaxation time spectra (**b**) at 2.5% strain amplitude and $T_{ref} = 20°C$ for unfilled and variously filled S-SBR composites, as indicated

Figure 19b shows the relaxation time spectra of the five materials, with the slope m of the (dotted) regression line indicated by the inset. As expected, the slope becomes smaller with addition of filler and results in values of m between 0.58 and 0.48 for the filled systems. Using Eq. (27), this gives values of the exponent n close to 0.3, which can be entered into Eq. (26) to perform the adhesion simulations.

8.3 Simulation of Friction Properties

Experimental data and adaptations with the friction theory for the dry and wet friction behavior as a function of sliding speed are shown in Fig. 20 for the CB-filled sample and GNP sample filled with xg M25. The fitting parameters are also shown. A strong velocity dependence is found for both dry and wet conditions as a result of viscoelastic excitation by the substrate asperities during sliding. A closer look at the experimental data shows that the wet friction behavior for both compounds exhibits no major differences and is well reproduced by the simulations. The performance seen under dry condition without any lubricant reveals a complete different picture. Here, the adhesion contribution (green curves in Fig. 20a) dominates the friction properties. Therefore, the friction coefficient for the CB-filled compound reaches a value of about 1.6 at a velocity of 10 mm/s.

In the case of xg M25, the dry friction coefficient is strongly reduced over the whole velocity range, so that the hysteresis contribution (red curve in Fig. 20b) also delivers the main contribution to the friction process in dry conditions and the friction coefficient remains small, $\mu < 1.0$. Nevertheless, in both cases the experimental data are represented quite well by the theoretical concept in the considered velocity range, giving more detailed information about the sliding process of the differently filled rubbers on a rough surface such as granite.

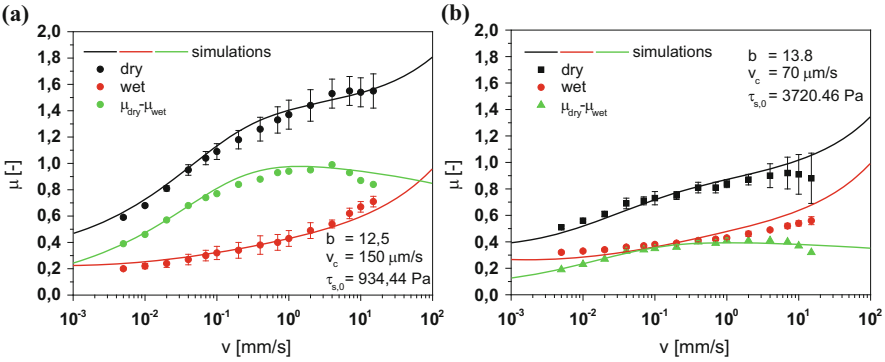

Fig. 20 Friction measurements and simulations for SBR 2525-0 filled with 10 vol% carbon black N121 (**a**) and graphene nanoplatelets M25 (**b**) on rough granite under dry and lubricated conditions. Temperature and load were kept constant at 20°C and 24 kPa, respectively. Experimental data are indicated by *symbols* and adaptations by *lines*

8.4 Dry and Wet Friction on Rough Granite and Glass

Next, we focus on a comparison of experimental friction data for different filler types under dry and lubricated (water plus 5% surfactant) conditions, as shown in Fig. 21. Strong differences can be seen between the different compounds, especially for samples filled with graphene-like fillers. Looking first at the dry measurements (Fig. 21a), the difference between N121 and xg M25 can be clearly seen, as already described in Sect. 8.3. The compound filled with xg C750 also shows a strongly reduced friction behavior on dry granite. Only ultrafine graphite UF 198C with a relatively small specific surface area (23.5 m^2/g) behaves similarly to the reference sample filled with highly structured CB N121. During wet sliding tests (see Fig. 21b), both GNP-filled specimens show same friction performance. At lower sliding speeds, the GNP systems show higher energy dissipation with quite large friction values, which converts into smaller dissipation at higher velocities, compared with the CB-filled samples.

Turning now to measurements on dry glass (shown in Fig. 22), the friction behavior is similar to that on rough granite. It is evident that use of graphene-like fillers results in a strong reduction in the friction coefficient with respect to the reference compound filled with N121. In the measured speed range, the N121 sample provides continuously high friction values of around 3.5 accompanied by strong stick–slip effects. By contrast, the sample filled with xg M25 behaves more stably during friction on dry glass and reveals strongly reduced friction forces over the whole velocity range. Both UF 198C and xg C750 demonstrate improved quite stable friction behavior. At low sliding velocities, both samples generate less friction but show a pronounced increase at a speed of 0.1 mm/s. The coefficient of friction for xg C750 is always below that of the UF 198C sample. The xg M25 sample exhibits quite low friction values for the whole velocity range. This

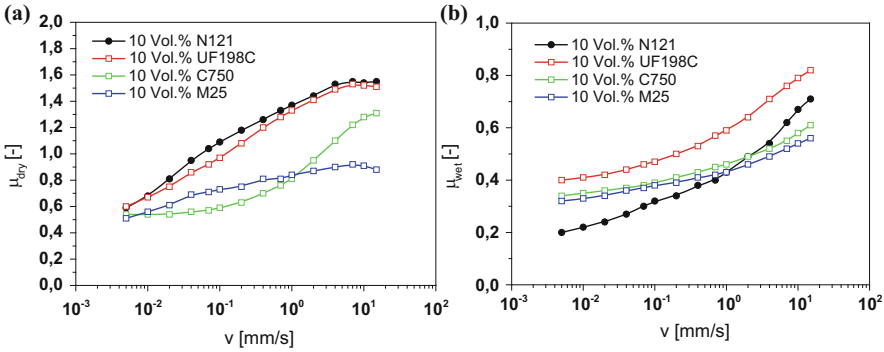

Fig. 21 Dry (**a**) and wet (**b**) friction on granite of SSBR 2525-0 filled with different graphene nanoplatelets, ultrafine graphite, and carbon black N121 at 20°C and 24 kPa load

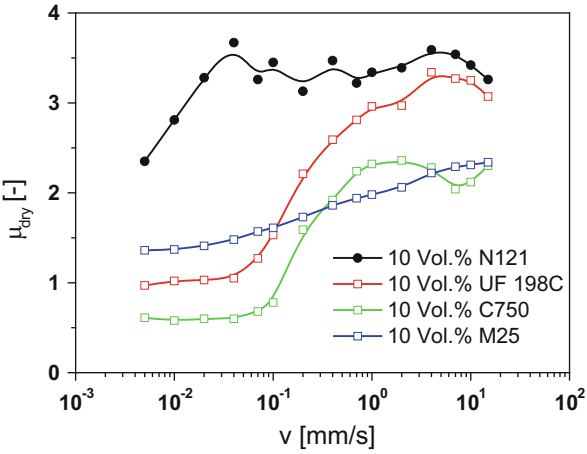

Fig. 22 Velocity-dependent friction coefficient of S-SBR 2525-0 filled with different graphene nanoplatelets, ultrafine graphite, and carbon black N121 at 25°C and 4 kPa load

indicates that GNPs seem to be well suited for delivering improved friction properties (e.g., for wiper blades or rubber seals in dynamic contact with smooth substrates) with less disturbing stick–slip effects.

8.5 Wear Behavior of GNP Composites

In addition to sliding friction measurements, abrasion tests were carried out according to DIN 53516. The results for different polymer compounds are shown in Fig. 23. Solution SBR and NBR composites with different amounts of

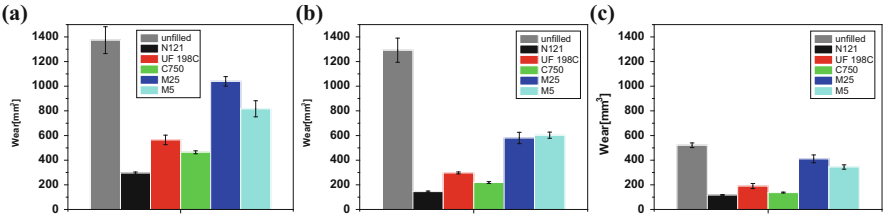

Fig. 23 Wear behavior of S-SBR 2525-0 (**a**), NBR 1846 (**b**), and NBR 3945 (**c**) composites filled with 10 vol% of graphene and graphitic nanoparticles. Carbon black filler N121 was used as reference

acrylonitrile (ACN) were used to figure out how graphene or graphite filler can influence the wear stability. For comparison, N121 was used as a reference.

For all three polymers, it can be seen that for carbon-based filler N121 the wear behavior is best compared with GNPs or other graphitic nanoparticles. However, the best abrasion performance for alternative graphene-like fillers is found for the GNP-type xg C750. Both M-type GNPs exhibit poor wear performance, although the stress–strain-curves (Figs. 4 and 5) suggest high tensile strength values. Finally, we note that the abrasion test according to DIN 53516 is not representative for tire wear but correlates with strong catastrophic abrasion mechanisms that occur, for example, during blocked wheel braking of tires. Accordingly, the effect of GNPs on tire wear remains open at the moment and is a task of future work.

9 Concluding Remarks

This review has demonstrated in some detail that GNPs represent a new class of sheet-like, carbon-based materials that can be used as reinforcing filler in elastomer compounds for improving their specific properties, such as gas permeability or friction properties on dry glass. In particular, the gas permeation coefficient of membranes was found to be strongly reduced for the GNP-filled composites and could be further reduced by orientation of the graphene flakes perpendicular to the direction of gas flow. We also can expect more stable friction properties with less disturbing stick–slip effects for seals operating under non-lubricated conditions or wiper blades sliding on the almost-dry windscreen of a car, as typically realized in slight rain or after the rain has stopped. The fracture mechanical properties of the investigated samples indicate that the lifetime of such GNP-modified rubber goods remains in a reasonable range. However, with respect to several basic properties relevant for technical applications, such as hysteresis as a result of filler networking or wear under strongly abrasive conditions, the data suggest that GNPs are not suitable for replacing traditional fillers such as carbon black or silica. Nevertheless, GNPs will probably be very useful in the future as additives in hybrid-filler systems where small amounts can deliver pronounced effects. The spectrum of possible

applications cannot be fully seen at the moment but we are sure that in future GNPs will appear in many rubber goods as a result of their unique properties and good interaction strength and affinity with elastomers.

Acknowledgements Financial support of the project "Elastomer composites based on graphenes" by the BMBF (grant 03X0110A) is highly appreciated. Special thanks are extended to Prof. Gert Heinrich and Prof. Amit Das fromIPF Dresden for the very fruitful cooperation within this project. Prof. G. Lacayo-Pineda from Continental Reifen Deutschland GmbH is appreciated for performing the gas permeation measurements.

References

1. Geim AK, Novoselov KS (2007) Nat Mater 6:183–191
2. Verdejo R, Mar Bernal M, Romasanta LJ, Lopez-Manchado MA (2011) Graphene filled polymer nanocomposites. J Mater Chem 21:3301–3310
3. Jang BZ, Zhamu A (2008) J Mater Sci 43:5092–5101
4. Li YJ et al (2012) J Mater Sci 47:730–738
5. Lang A, Karl CW, Klüppel M (2012) In: Proceedings of the 10th fall rubber colloquium (KHK), Hanover, 7–9 November 2012, pp 99–105
6. Möwes M, Fleck F, Klüppel M (2013) Effect of filler surface activity and morphology on mechanical and dielectric properties of NBR/graphene nano-composites. Rubber Chem Technol 87:70–85
7. Möwes M, Fleck F, Wunde M, Klüppel M (2013) Graphenes as new active filler in elastomer composites with special features. In: Proceedings of the 6th international conference on carbon nanoparticle-based components (CNPComp), Dresden, 22–25 September 2013
8. Klüppel M, Möwes M, Jungk J (2013) Carbon nano-particle based hybrid filler systems in elastomers. In: Proceedings of the 6th international conference on carbon nanoparticle-based components (CNPComp), Dresden, 22–25 September 2013
9. Klüppel M (2003) The role of disorder in filler reinforcement of elastomers on various length scales. Adv Polym Sci 164:1–86
10. Vilgis TA, Heinrich G, Klüppel M (2009) Reinforcement of polymer nano-composites. Cambridge University Press, New York
11. Vilgis TA, Heinrich G (1994) Macromolecules 27:7846
12. Gay C, de Gennes PG, Raphael E, Brochard-Wyart F (1996) Macromolecules 29:8379
13. Kremer F, Schönshals A (2003) Broadband dielectric spectroscopy. Springer, Berlin, Heidelberg, New York
14. Payne AR (1958) In: Mason P, Wookey N (eds) Rheology of elastomers. Pergamon, London, pp 86–112
15. Payne AR (1965) In: Kraus G (ed) Reinforcement of elastomers. Interscience, New York
16. Wang MJ (1999) Rubber Chem Technol 72:430
17. Klüppel M, Heinrich G (2005) Physics and engineering of reinforced elastomers. Kautschuk Gummi Kunstst 58:217–224
18. Medalia AI (1978) Rubber Chem Technol 51:437
19. Nawaz K, Khan U et al (2012) Observation of mechanical percolation in functionalized graphene oxide/elastomer composites. Carbon 50:4489–4494
20. Klüppel M, Schuster RH, Heinrich G (1997) Structure and properties of reinforcing fractal filler networks in elastomers. Rubber Chem Technol 70:243–255
21. Das A, Stöckelhuber KW, Jurk R, Saphiannikova M, Fritzsche J, Lorenz H, Klüppel M, Heinrich G (2008) Modified and unmodified multiwalled carbon nanotubes in high performance solution-styrene-butadiene and butadiene rubber blends. Polymer 49:5276–5283

22. Lorenz H, Fritzsche J, Das A, Stöckelhuber KW, Jurk R, Heinrich G, Klüppel M (2009) Advanced elastomer nano-composites based on CNT-hybrid filler systems. Compos Sci Technol 69:2135–2143
23. Fritzsche J, Lorenz H, Klüppel M (2009) CNT based elastomer-hybrid-nanocomposites with promising mechanical and electrical properties. Macromol Mater Eng 295:551–560
24. Das A, Stöckelhuber KW, Jurk R, Fritzsche J, Klüppel M, Heinrich G (2009) Coupling activity of ionic liquids between diene elastomers and multi-walled carbon nanotubes. Carbon 47:3313–3321
25. Fritzsche J, Lorenz H, Klüppel M (2011) Elastomer carbon nanotube composites. In: McNally T, Pötschke P (eds) Polymer carbon nanotube composites: preparation, properties and applications. Woodhead, Cambridge
26. Subramaniam K, Das A, Steinhauser D, Klüppel M, Heinrich G (2011) Effect of ionic liquid on dielectric, mechanical and dynamic mechanical properties of multi-walled carbon nanotubes/polychloroprene rubber composites. Eur Polym J 47:2234–2243
27. Patole AS, Patole SP, Jung SY, Yoo JB, An JH, Kim TH (2012) Eur Polym J 48:252
28. Wang L, Zhang L, Tian M (2012) Wear 276–277:85–93
29. Potts JR, Dreyer DR, Bielawski CW, Ruoff RS (2011) Polymer 52:5–25
30. Kuilla T, Bhadra S, Yao D, Kim NH, Bose S, Lee JH (2010) Prog Polym Sci 35:1350
31. Nawaz K, Khan U, Ul-Haq N, May P, O'Neill A (2012) Carbon 50:4489
32. Potts JR, Shankar O, Du L, Ruoff RS (2012) Macromolecules 45:6045
33. Kim H, Abdala AA, Macosko CW (2010) Macromolecules 43:6515
34. Varghese T, Kumar V, Ajith H et al (2013) Reinforcement of acrylonitrile butadiene rubber using pristine few layer graphene and its hybrid fillers. Carbon 61:476–486
35. Dreyer DR, Park S, Bielawski CW, Ruoff RS (2010) The chemistry of graphene oxide. Chem Soc Rev 39:228–240
36. Zhu Y, Murali S, Cai W, Li X, Suk JW, Potts JR, Ruoff RS (2010) Graphene and graphene oxide: synthesis, properties, and applications. Adv Mater 22(35):3906–3924
37. Schröder A, Klüppel M, Schuster RH, Heidberg J (2001) Energetic surface structure of carbon black. Kautsch Gummi Kunstst 54:260–266
38. Schröder A, Klüppel M, Schuster RH, Heidberg J (2002) Surface energy distribution of carbon black measured by static gas adsorption. Carbon 40:207–210
39. Schröder A, Klüppel M, Schuster RH (2007) Characterization of surface activity of carbon blacks and its relation to polymer-filler interaction. Macromol Mater Eng 292:885–916
40. Jaroniec M (1988) Physical adsorption on heterogeneous solids. Elsevier, Amsterdam
41. Stanley BJ, Guiochon G (1993) J Phys Chem 97:8098–8104
42. Schröder A, Klüppel M, Schuster RH (1999) Kautsch Gummi Kunstst 52:814
43. Schröder A, Klüppel M, Schuster RH (2000) Kautsch Gummi Kunstst 53:257
44. Schröder A, Meier J, Klüppel M, Schuster RH (2003) Gummi Fasern Kunststoffe 56:162
45. Pfeifer P, Obert M, Cole MW (1989) Fractal BET and FHH theories of adsorption: a comparative study. Proc R Soc Lond A 423:169–188
46. Heinrich G, Klüppel M (2002) Recent advances in the theory of filler networking in elastomers. Adv Polym Sci 160:1–44
47. Klüppel M, Schramm J (2000) A generalized tube model of rubber elasticity and stress softening of filler reinforced elastomer systems. Macromol Theory Simul 9:742–754
48. Lorenz H, Klüppel M (2012) Microstructure-based modeling of arbitrary deformation histories of filler-reinforced elastomers. J Mech Phys Solids 60:1842–1861
49. Lorenz H, Klüppel M, Heinrich G (2012) Micro-structure based modeling and FE-implementation of filler-induced stress softening and hysteresis of reinforced rubbers. Z Angew Math Mech 92:608–631
50. Meier JG, Klüppel M (2008) Macromol Mater Eng 293:12–38
51. Meier JG, Mani JW, Klüppel M (2007) Phys Rev B 75:054202
52. Persson BNJ (2001) J Phys Condens Matter 115:3840

53. Klüppel M, Heinrich G (2000) Rubber friction on self-affine road tracks. Rubber Chem Technol 73:578–606
54. Heinrich G (1997) Hysteresis friction of sliding rubbers on rough and fractal surfaces. Rubber Chem Technol 70:1
55. Heinrich G, Klüppel M, Vilgis TA (2000) Evaluation of self-affine surfaces and their implication to frictional dynamics as illustrated with a rouse material. Comput Theor Polym Sci 10:53–61
56. Müller A, Schramm J, Klüppel M (2002) Ein neues Modell der Hysteresereibung von Elastomeren auf fraktalen Oberflächen. Kautsch Gummi Kunstst 55:432–436
57. Schramm J (2002) Reibung von Elastomeren auf rauen Oberflächen und Beschreibung von Nassbremseigenschaften von PKW-Reifen. PhD Thesis, University of Regensburg
58. Le Gal A, Guy L, Orange G, Bomal Y, Klüppel M (2008) Modelling of sliding friction for carbon black and silica filled elastomers on road tracks. Wear 264:606–615
59. Le Gal A, Klüppel M (2006) Investigation and modelling of adhesion friction on rough surfaces. Kautsch Gummi Kunstst 59:308–315
60. Le Gal A, Yang X, Klüppel M (2005) Evaluation of sliding friction and contact mechanics of elastomers based on dynamic-mechanical analysis. J Chem Phys 123:014704
61. Le Gal A (2007) Investigation and modelling of rubber stationary friction on rough surfaces. PhD Thesis, University of Hannover
62. Le Gal A, Klüppel M (2008) Investigation and modelling of rubber stationary friction on rough surfaces. J Phys Condens Matter 20:015007
63. Busse L, Le Gal A, Klüppel M (2010) Modeling of wet and dry friction of silica filled elastomers on sef-affine road surfaces, Chapter 1. In: Besdo D, Heimann B, Klüppel M, Kröger M, Wriggers P, Nackenhorst U (eds) Elastomere friction: theory, experiment and simulation, vol 51, Lecture notes in applied and computational mechanics. Springer, Berlin, Heidelberg, New York. ISBN 978-3-642-10656-9
64. Busse L, Klüppel M (2010) Wet and dry friction of elastomers in advanced simulation compared to experiment. In: Heinrich G, Kaliske M, Lion A, Reese S (eds) Constitutive models for rubber VI. A. A. Balkema, Lisse, Abingdon, Exton, Tokyo. ISBN 979-0-415-56327-7
65. Busse L, Bourbakri I, Klüppel M (2011) Friction master curves for rubber on dry and wet granite: experiments and simulations. Kautsch Gummi Kunstst 64(5):35–39
66. Busse L (2012) Investigation, prediction and control of rubber friction and stick–slip: experiments, simulations, applications. PhD Thesis, University of Hannover
67. Lang A, Klüppel M (2013) Hysteresis and adhesion friction of carbon based elastomer composites: theory, experiments and applications. In: Gil-Negrete N, Alonso A (eds) Constitutive models for rubber VIII. Taylor and Francis Group, London, pp 59–64. ISBN 978-1-138-00072-8
68. Heinrich G, Klüppel M (2002) Elastomer friction and adhesion on self-affine interfaces. Theory, experiment and applications in tire industry. In: Proceedings of the IPF-Colloquium, Dresden, 14–15 November 2002
69. Heinrich G, Schramm J, Müller A, Klüppel M, Kendziorra N, Kelbch S (2002) Zum Einfluss der Straßenoberfläche auf das Bremsverhalten von PKW-Reifen beim ABS-nass und ABS-trocken Bremsvorgang. In: Proceedings of the 4 Darmstädter Reifenkolloquium, Darmstadt, 17 October 2002
70. Heinrich G, Klüppel M (2008) Rubber friction, tread deformation and tire traction. Wear 265:1052–1060
71. Williams ML, Ferry JD (1953) J Polym Sci 11:169

Adv Polym Sci (2017) 275: 361–398
DOI: 10.1007/12_2016_10

Published online: 8 September 2016

Tearing Energy as Fracture Mechanical Quantity for Elastomers

Radek Stoček, Thomas Horst, and Katrin Reincke

Abstract The fracture mechanical characterization of elastomeric materials is based on a global energy balance. Tearing energy was introduced in 1953 by Rivlin and Thomas to characterize the energy required for an infinitesimal increase in surface area during crack propagation. Enhancing the contributions of various energy dissipation mechanisms during the process of crack propagation is crucial for the understanding and modification of elastomeric materials with respect to an enhanced service life. Apart from the tearing energy, alternative fracture mechanical quantities based on the global energy balance are reviewed and discussed with respect to various influencing factors such as geometrical constraints of the specimen, specific loading conditions, and the specific material and its structural details. Finally, the application of advanced experimental methods characterizing the stages of crack initiation, propagation, and wear under more practical loading conditions are reviewed.

Keywords Crack initiation • Crack propagation • Energy balance • Fatigue • Fracture • Rubber • Wear

R. Stoček (✉)
PRL Polymer Research Lab, s.r.o., Nad Ovčírnou IV 3685, Zlín CZ-76001, Czech Republic

Centre of Polymer Systems, Trida Tomase Bati 5678, Zlín CZ-76001, Czech Republic
e-mail: radek.stocek@prl-z.com

T. Horst
Westsächsische Hochschule Zwickau, Institut für Produktionstechnik, Dr.-Friedrichs-Ring 2A, Zwickau D-08056, Germany

K. Reincke
Martin-Luther-University Halle-Wittenberg, Halle D-06099, Germany

Polymer Service GmbH Merseburg, Eberhard-Leibnitz-Str. 2, Merseburg D-06217, Germany

Contents

1 Introduction

Failure of structural components is mostly the result of the creation and propagation of macroscopic cracks. In every real material, defects exist as precursors of macroscopic cracks and the mechanical behavior of components containing macroscopic notches or cracks can be analyzed using fracture mechanics. Increasing the fracture resistance by modification of material structure is an important objective of materials science, not only for structural materials such as steel but also for highly deformable elastomeric materials.

Elastomers are weakly crosslinked polymers that exhibit large deformations as a result of the high internal flexibility of polymer chains above the glass transition temperature. To enhance mechanical properties such as strength and stiffness, these materials can be filled with nanoparticles such as carbon black. However, the fracture mechanical behavior is highly influenced by structural details such as the phase morphology, distribution and dispersion of filler, and multiscale structure of the filler. Crack propagation in elastomers and, consequently, fracture is a complex process in which multiple length scales are involved and the interaction of processes taking place at different length scales has a huge influence on the way the material breaks. Increased fracture toughness can be realized by modifying the structure of the material in such a way that as many non-catastrophic dissipative processes as possible on various length scales in a spacious volume are induced in the specimen. This results in an increase in the material's capacity to absorb energy during crack propagation. Generally, these processes can be traced back to specific

polymer–polymer, polymer–filler, and filler–filler interactions in the material. An understanding of these interactions with respect to their influence on the fracture process is a prerequisite, not only for modeling the processes taking place in the vicinity of the crack tip but also for specific optimization of the material's structure.

2 Energy Balance and Fracture Mechanical Characterization of Elastomers by Means of the Tearing Energy

As a consequence of entropy-driven elasticity, elastomers are susceptible to large deformations even under small external forces. Considering a loaded notched or pre-cracked specimen, a pronounced crack blunting can be observed (i.e., the crack opens up if the specimen is loaded; see Fig. 1). However, unlike the plastic crack blunting in metallic materials, crack blunting in elastomers is reversible. Moreover, the stress and strain fields in the vicinity of the crack front are not known beforehand, neither quantitatively nor qualitatively. Therefore, local characterization of fields in the vicinity of the crack front, as can be done for brittle materials, is not appropriate. The fracture mechanical behavior of elastomers is therefore characterized by a global energy balance, as proposed by Rivlin and Thomas [1], which can be seen as a generalization of Griffith's approach [2].

Considering the process of incremental crack propagation in a solid, the global energy balance in quasistatics reads:

Fig. 1 Elastic crack tip blunting in elastomers [3]

$$\frac{dW_{\text{ext}}}{dA} - \frac{dW}{dA} = \frac{dW_{\text{sep}}}{dA} + \frac{dW_{\text{diss}}}{dA} \tag{1}$$

where W_{ext} is the external work, W is the recoverable elastic strain energy, W_{diss} is the macroscopic remote dissipated energy, and W_{sep} is the local work of separation. For the case of plane specimens with a constant thickness B and a straight crack front, the increment in cracked area is $dA = B\,da$, with da being the crack length increment. The left-hand side of Eq. (1) is the elastic energy released per unit cracked area during crack propagation and is therefore called the energy release rate [4]. The right-hand side of Eq. (1) is the energy needed to advance a fracture plane by one unit area, including all energy losses resulting from the various dissipative processes in the vicinity of the crack front and remotely. It is called the critical energy release rate or energy dissipation rate [5–9], also denoted as tearing energy [1] in the case of elastomers.

Considering that the external work is zero (i.e., the clamp distance l is constant during the process of crack propagation), the original deduction made by Rivlin and Thomas [1] for the determination of tearing energy of elastomers T can be derived:

$$T = -\left.\frac{dW}{dA}\right|_{l=\text{const.}} = -\left.\frac{dW}{B\,da}\right|_{l=\text{const.}} \tag{2}$$

However, energy dissipation mechanisms in elastomers are not restricted to the immediate vicinity of the crack front. Moreover, these dissipation mechanisms can be rate dependent or rate independent and are not only caused by crack propagation but also by specific loading conditions. It should be noted that energy dissipation in rubber materials cannot be neglected, even in the case of a non-propagating crack. Thus, various energy dissipation contributions are crucial in the energy balance, especially with regard to the separation of these contributions. This raises the question of whether the presence of these dissipation mechanisms is only related to crack propagation, is more a consequence of specific loading conditions, or is influenced by both.

Closely related to the energy balance during crack propagation is the so-called J-integral introduced by Rice [10] and Cherepanov [11]. The J-integral is a contour integral defined for plane problems in linear-elastic quasistatics by:

$$J = \int_{\Gamma} \left[W_0 n_1 - \sigma_{ji} n_j \frac{\partial u_i}{\partial x_1} \right] d\Gamma \tag{3}$$

where W_0 is the elastic energy density, σ_{ji} is the stress tensor, u_i is the displacement vector, n_j is the outer normal unit vector, and x_i is the position vector. The integration is carried out along a line Γ encircling the crack tip. The J-integral characterizes the elastic energy flux through Γ to the crack tip during infinitesimal crack propagation. Hence, it is identical to the energy release rate, provided that the integration contour encloses all dissipative fields in the vicinity of the crack tip and

under the assumption that these fields are translated in an invariant manner together with the crack tip.

Rivlin and Thomas [1] used three types of specimens: single-edge-notched tension (SENT), trouser, and pure shear (PS) specimens (see Fig. 2). For every specimen type, specific formulae for the determination of tearing energy T were derived, see Eqs. (4)–(6), using the same assumption that is inherent to the J-integral: the invariant translation of near tip fields during crack propagation.

Therefore, it is assumed that the specimen volume can be divided into differently loaded regions [1] (see Fig. 3 for the case of a PS specimen). Complicated stress and strain fields can be found in the vicinity of the crack front (region B). However, the remote fields are assumed to be homogeneous. In front of the crack front there is a region where a homogeneous state of constraint tension (pure shear) can be found (region C). Behind the crack front, the region is almost unloaded (region A). Finally, there is a region that is influenced by the outer boundary (region D). Considering infinitesimal crack propagation in such a specimen, it is assumed that the complicated inhomogeneous state in the vicinity is translated with the crack front. Consequently, the size of the region in the pure shear state is reduced, increasing the unloaded region. Hence, the tearing energy can be determined via the elastic strain energy density in the homogeneous loaded pure shear region (region C), which is measured by the unloading curves from unnotched PS specimens at

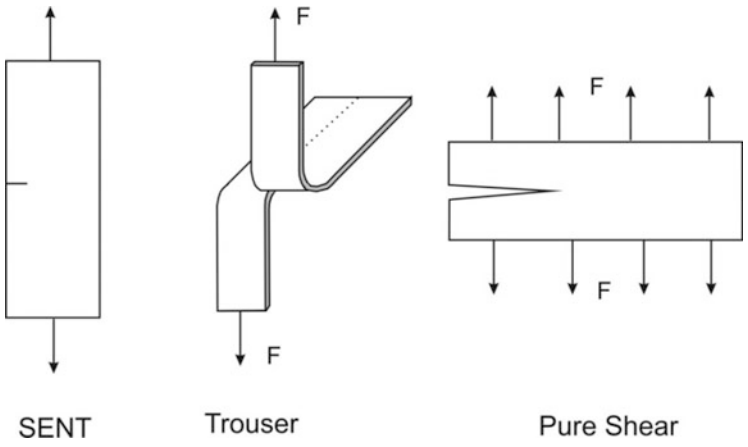

Fig. 2 Typical specimens for the experimental determination of fracture mechanical parameters for elastomers

Fig. 3 Characteristic regions (*A–D*) of a loaded single-edge notched PS specimen [3]

identical boundary displacement where crack propagation occurred in notched specimens. This basic idea leads to a simple formula for the determination of PS specimens:

$$T = W_0 l_0 \tag{4}$$

with W_0 being the elastic energy density in region C and l_0 being the initial length of the specimen, which corresponds to the initial distance of the clamps.

A similar approach can be applied for SENT and trouser specimens, leading for SENT specimens to:

$$T = 2\frac{\pi}{\sqrt{\lambda}} W_0 a \tag{5}$$

with λ being the stretch ratio and W^* being the crack length. For trouser specimens the tearing energy is given by:

$$T = \frac{W_0 A_0 - 2\lambda F}{B} \tag{6}$$

with A_0 being the cross-section area of the non-deformed specimen and F being the external load.

In the past, mainly SENT and the PS specimens have been used for the determination of tearing energy. The advantage of the PS specimen can be seen from Eq. (4) and lies in the independence of the current crack length. For SENT specimens, the current crack length a must normally be taken into consideration, which is not the case for PS specimens. This is of special interest for fracture mechanics tests under cyclic loading (fatigue tests), where the limited width of SENT samples is very disadvantageous.

It was clearly shown in the previous paragraphs that the tearing energy significantly depends on the test specimen's geometry as well as its crack length. Thus, the geometry ratio $l_0{:}Q$ (length to width) and the crack length must be taken into account for an exact determination of the tearing energy. The first evaluations of tearing energy were performed by Yeoh [12], where the geometry ratio $l_0{:}Q = 1{:}5$ was studied and the influence of crack length on tearing energy was observed.

To study the effect of different geometry ratios and the influence of crack length on the tearing energy, test specimens with varied geometry ratios were modeled using nonlinear finite element analysis (FEM) [13]. Additionally, the effect of strain up to 50% was taken into consideration. The results of this study are shown in Fig. 4 for a test specimen based on unfilled styrene–butadiene rubber (SBR), where the width Q was constant and length l_0 was varied (10 and 30 mm) to obtain the required geometry ratios of 1:12 and 1:4. The test specimens were analyzed at strains of 10, 30, and 50% with respect to the length l_0. The structure of the notation

of the specimens in Fig. 4 and Fig. 5 is following: First, the type of rubber is mentioned (e.g. SBR), the next two numbers give an information about the filler content in parts per hundred rubber (e.g 00 means 0 phr). N2 is a code for the used filler. The next two numbers indiacte the initial length l_0 of the specimen in mm and the applied strain with respect to the initial length l_0 in %. The last information given is the geometry ratio, i.e initial length l_0: width Q.

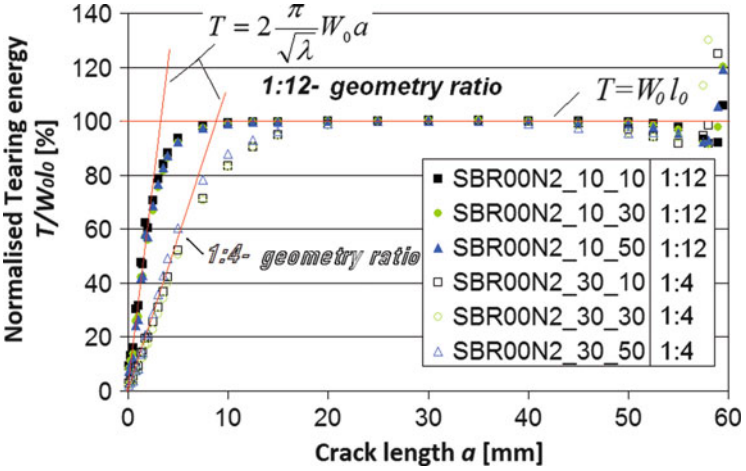

Fig. 4 FEM results showing the dependence of tearing energy on crack length for edge-cracked test specimens with geometry ratios of 1:12 and 1:4 at various strains [13]

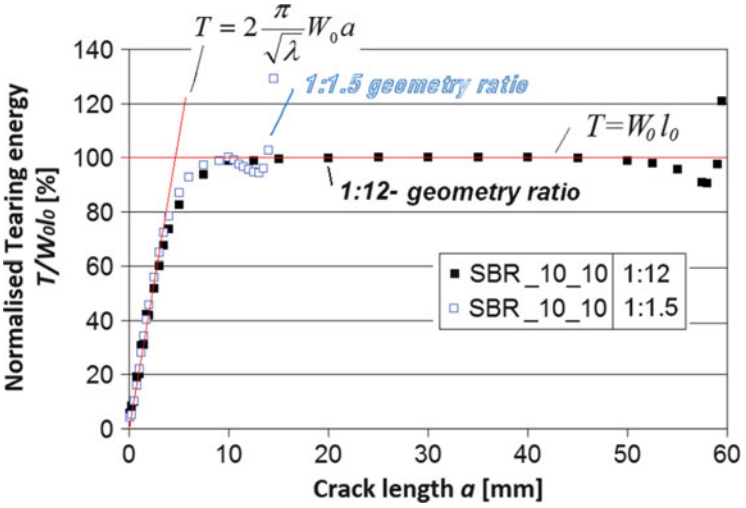

Fig. 5 FEM results showing the dependence of tearing energy on crack length for edge-cracked specimens with geometry ratios of 1:12 and 1:1.5 at strain 10% [13]

Figure 4 shows that the tearing energy is approximately linearly dependent on crack length for small values of crack length, according to Eq. (5), and is independent of the geometry ratio. This narrow range changes into a non-defined dependence of tearing energy on crack length with a slight increase in crack length. Figure 4 also shows a region in the center of the test specimen where the tearing energy is independent of crack length. This region is deformed in the pure shear state and formulated by Eq. (4). The last region, with large crack lengths, varies from the constant state of tearing energy because of the symmetric model of the test specimen. Comparison of the results obtained for the different geometry ratios shows a relatively small central region of the test specimen for a geometry ratio 1:4 that is deformed in the pure shear state. On the other hand, Fig. 4 demonstrates the independence of various strains on the different geometry ratios.

Figure 5 shows the FEM results of edge-cracked test specimens with geometry ratios of 1:12 and 1:1.5 at strain 10 %, where the different geometry ratios were achieved at constant length l_0 and various widths Q. Here, a geometry ratio of 1:1.5 presents the geometry of a SENT specimen. The simulation gave an identical slope of the linear dependence of tearing energy on crack length for small crack lengths, as suggested by Eq. (5), in both specimens with different geometry ratios. This demonstrates that an identical crack growth in the region of availability of Eq. (5) provides the same length l_0 for specimens defined with different geometry ratios. There is no region where tearing energy is independent of crack length in the center of the test specimen with geometry ratio of 1:1.5.

3 Alternative Fracture Mechanical Quantities

As already pointed out, equations provided for specific specimen geometries are mostly used for characterization of fracture mechanical behavior of elastomers because of their simplicity of application. However, there are some other approaches for characterizing fracture toughness. First, methods based on elastic–plastic fracture mechanics (EPFM), which are commonly used for characterization of thermoplastics, can be adapted for fracture toughness characterization of elastomers. Moreover, two methods based on the direct evaluation of energy balance, the dissipation rate concept and experimental determination of the J-integral as a contour integral, are described.

3.1 Methods Based on Elastic–Plastic Fracture Mechanics [14]

By applying fracture mechanical methods, one can obtain a deeper knowledge of a materials' deformation and fracture behavior. The methods of technical fracture

mechanics have proven to be useful tools for establishing structure–property correlations for polymeric materials because of their sensitivity to structural changes [15, 16].

The concepts of EPFM are of great importance for the fracture mechanics of polymers compared with the concepts of linear–elastic fracture mechanics (LEFM). Here, the crack-tip-opening displacement (CTOD) and the *J*-integral concept are often used for evaluation of the crack toughness behavior of various polymeric materials, although these materials are more or less viscoelastic. For this reason, the load–deformation curves are nonlinear. However, during experimental investigations with monotonic increase in loading, the viscoelasticity is often not taken into consideration.

The *J*-integral as fracture criterion is based on an energetic interpretation of the fracture process: A path-independent line integral encloses the plastically deformed area and is used to describe the stress–strain field around the crack tip. Generally, *J* describes this energy flowing under deformation through the closed area around the crack tip, which is not stored but dissipated by crack extension.

Considering a material showing stable crack propagation, the crack resistance curve (*R*-curve) concept of the EPFM can be used for quantitative description of the stable fracture process, including crack-tip blunting, crack initiation, and crack propagation. Figure 6 shows a schematic representation of an *R*-curve with the loading parameter *J* and the damage parameter Δa being the size of the stable crack growth. At the beginning of the stable crack process, blunting of the crack tip with increasing loading takes place. This process is characterized by a linear connection between *J* and Δa, namely the blunting line. At a critical point, the crack is initiated, which means that crack growth begins. For some thermoplastic polymers, a stretch zone can be proven. In this case, the stretch zone width (SZW) can be determined as a critical point where the crack begins to expand and, so, a physical crack initiation value J_{iphys} can be determined. For materials that do not form a stretch zone, the ESIS protocol [17] allows determination of the technical crack initiation value $J_{0.2}$ at a stable crack growth size of 0.2 mm as an alternative crack initiation value. After crack initiation, the crack resistance curve is nonlinear and often flattens with increasing crack growth.

To obtain *R*-curve data, various experimental methods can be applied including single-specimen or multi-specimen methods under quasistatic or impact-like

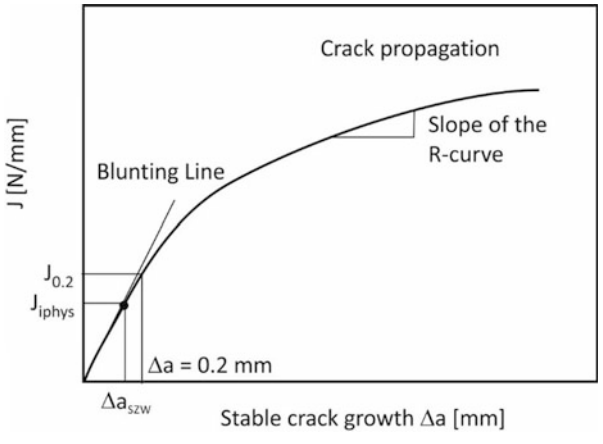

Fig. 6 Representation of a crack resistance curve (*R*-curve)

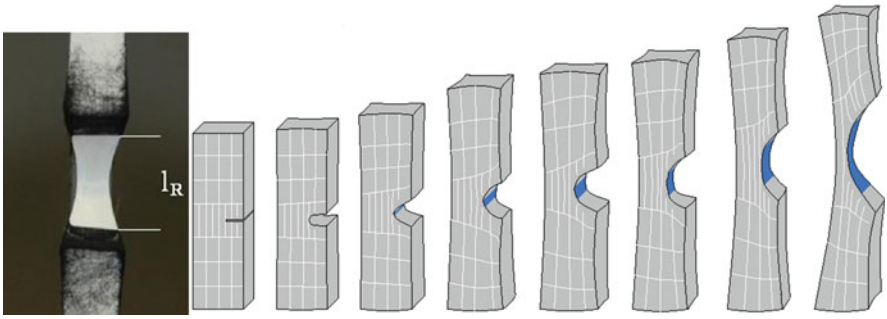

Fig. 7 Increasingly loaded specimen during a fracture mechanics test and definition of the damage parameter crack opening l_R (*blue*)

loading conditions. For thermoplastic polymers, there are several well-known standards for *R*-curve determination. One example is the ESIS TC 4 standard draft "A testing protocol for conducting *J*-crack growth resistance curve tests on plastics" [15–18].

The advantage of the single-specimen method (SSM) lies in the reduced material consumption and, therefore, reduced costs, which allow crack toughness characterization during an early stage of material development [15]. For *R*-curve tests with application of the SSM, only one single specimen is necessary. Most of the previous tests were performed by using SENT specimens (see Fig. 2). Here, the length $l_0 = 100$ mm, width $Q = 25$ mm, thickness $B = 6$ mm, and crack length to specimen width ratio (a:Q) of at least 0.2 were preferred [19, 20]. The notching is realized using a metal blade to ensure a very sharp notch. Before starting the test, the notch tip is prepared with TiO_2 powder (for black materials) to enable examination of the point of crack initiation as well as the crack opening l_R (see Fig. 7). The latter can be used as abscissa for the *R*-curve.

Rice et al. [21] showed that instead of using the energy balance, Eq. (1), the *J*-integral can more easily be determined directly from the load–displacement curve by using the approximate formula:

$$J = \frac{\eta \cdot W}{B \cdot (Q - a)} \tag{7}$$

with η being a dimensionless geometry function of the a:Q ratio of the SENT specimen. However, it should be noted that the geometry function can be assumed to be constant for the limited amount of stable crack propagation in filled elastomers. The deformation energy W was determined by integrating the load–extension diagram (F–l diagram) up to certain deformation values. The intervals must correspond to the times of taking pictures of the crack opening.

The J–l_R data pairs are plotted as an *R*-curve and two fracture parameters can be obtained as a result of experiments (see Fig. 6). The first parameter is the physical crack initiation value J_i, which can be determined through observation of the notch tip and, therefore, a subjective influence cannot be excluded. The second parameter

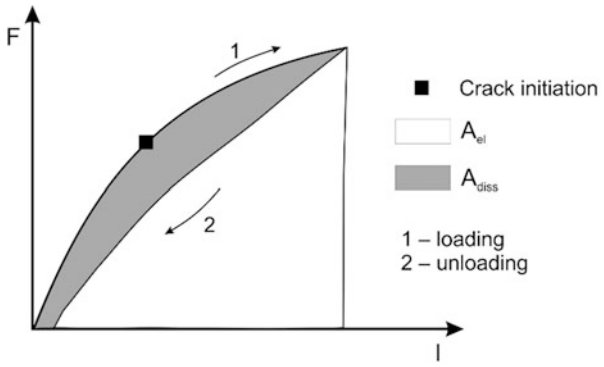

Fig. 8 Load (F)–extension (l) diagram from a quasistatic fracture mechanics test (multiple-specimen method); A_{el} elastic deformation energy, A_{diss} energy corresponding to the area between the loading and unloading cycles, A_{tot} total deformation energy, corresponding to the complete area under the loading curve ($A_{tot} = A_{el} + A_{diss}$)

is a crack propagation value T_J^*, that is taken from the slope of the R-curve at the point $l_R = 0.5$ mm (i.e., at the beginning of the crack propagation process).

In the multiple-specimen method (MSM), a certain number of equal specimens are used. Again, SENT was the previously most frequently used specimen type. Single specimens are loaded in tension up to different load levels, but not to total fracture. In this way, different amounts of stable crack propagation are created. During loading, the load–extension diagram can be recorded, including the loading and unloading cycle (Fig. 8) so that, in addition to J values according to Eq. (7), the determination of J_{diss} according to Eq. (8) is also possible. In this way, the large amount of elastic deformation is disregarded and therefore:

$$J_{diss} = \frac{\eta A_{diss}}{B(Q - a)} \tag{8}$$

with A_{diss} being the energy corresponding to the area between the loading and the unloading cycle, which should be a more precise parameter for quantification of crack resistance.

After the test, the specimens are cut and so that the size of the stable crack growth Δa can be determined using a light microscope. In this way, data pairs of J and Δa are available for the construction of an R-curve, which can be analyzed regarding the slope T_J^* of the curve at a crack growth $\Delta a = 0.1$ mm, which is a measure of the resistance against stable crack propagation.

Examples of crack resistance curves for styrene–butadiene rubber (SBR) vulcanizates and natural rubber (NR) vulcanizates from single-specimen fracture mechanics tests are shown in Fig. 9. The principle recipe of the materials is the same, except for the polymer used. It can be seen that addition of filler and an increase in filler content (in this case carbon black N234) both lead to an increase in J values. Without filler, a very flat R-curve results, indicating a low crack propagation resistance. Comparing the crack resistance curves of SBR and NR

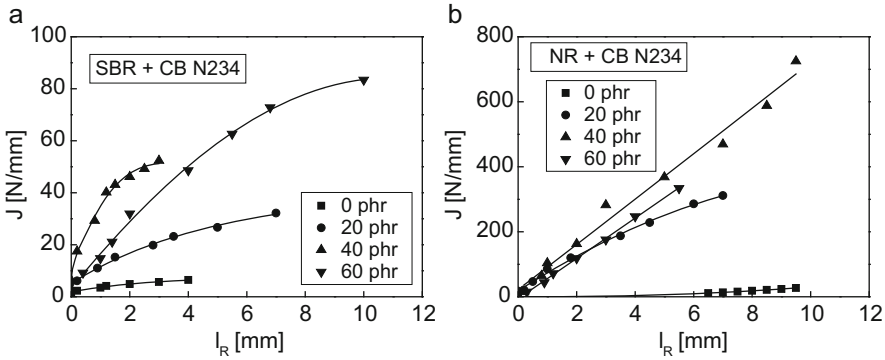

Fig. 9 Crack resistance curves (single-specimen method) for the fracture mechanics test for (**a**) SBR and (**b**) NR elastomers with increasing filler content [14]

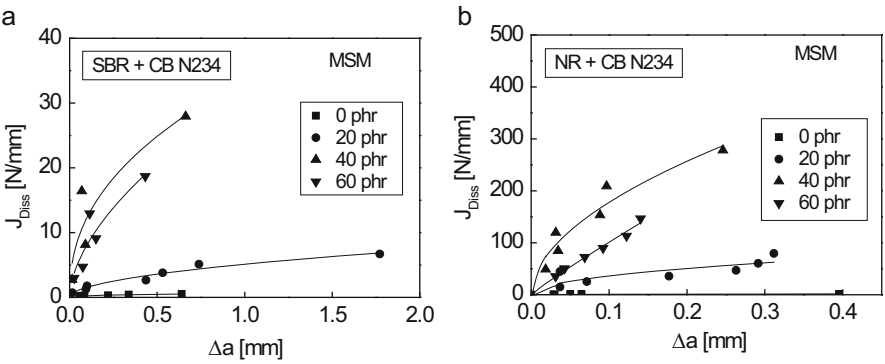

Fig. 10 Crack resistance curves (multiple-specimen method) for (**a**) SBR and (**b**) NR loaded with different amounts of CB N234 [14]

vulcanizates, one can see a very large difference. The J level for NR with filler is much higher than for SBR. This is attributed to the strain-induced crystallization that increasingly appears at higher strains [22]. According to [23], with increasing strain the number of short, stretched polymer chains acting as nucleation sites becomes larger. The distance between chains decreases and, at a certain point, the aligned chains form crystallites. These crystallites contribute to the mechanical response (similar to the effect of filler particles or network nodes) and a self-reinforcement effect is obtained, which is connected to increases in strength, wear, and tear strength. As can be seen from Fig. 9b, the crack propagation resistance is also enhanced.

A similar conclusion can be drawn from Fig. 10, which shows J_{diss}–Δa curves from fracture mechanics tests using MSM for the same two materials. Again, with increasing filler content, an increase in J_{diss} values is observed and the NR vulcanizates have a much higher J_{diss} level than the SBR materials. It should be noted that

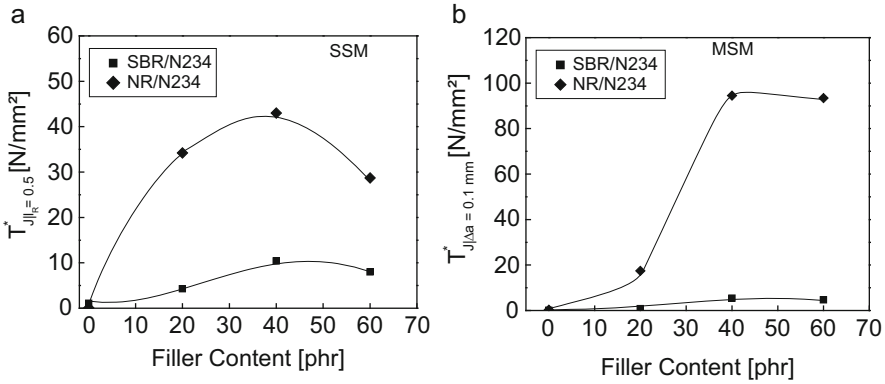

Fig. 11 Crack propagation values T_J^* for SBR and NR materials determined from (**a**) crack resistance curves (single-specimen method) at the point $l_R = 0.5$ mm and (**b**) crack resistance curves (multiple-specimen method) at the point $\Delta a = 0.1$ mm [14]

differences between J and J_{diss} values are a result of disregarding the influence of elastic deformation for J_{diss}. The corresponding crack propagation values determined from the R-curves for tests with SSM and MSM are represented in Fig. 11.

Independently of the fracture mechanical method used, the NR vulcanizates show the largest resistance against crack propagation as a result of strain-induced crystallization, as discussed above. Furthermore, a crack resistance maximum at a filler loading of 40 phr was found. Reasons for this behavior are discussed in the literature [20]. From a practical point of view, such elastomers should be designed with a certain deformability/flexibility so that, even on the molecular length scale, the chains are able to compensate for a higher loading without fracture by elastic deformation. Thus, because the fracture of a polymer begins at the molecular level, the macroscopic fracture also appears at higher external loadings.

3.2 *Dissipation Rate Approach*

Under quasistatic loading conditions, stable crack propagation in elastomeric materials is often characterized by methods based on the R-curve concept of EPFM (see Sect. 3.1). An R-curve acknowledges the fact that the resistance to fracture increases with growing crack size in elastic–plastic materials. Thus, stable crack propagation is characterized by the total energy losses required to produce a certain stable (i.e., subcritical) crack increment.

The global energy balance, Eq. (1), leads to definition of the energy dissipation rate [5–9], which is the energy loss during incremental crack propagation as a result of creation of new fracture surfaces and the energy loss as a consequence of accompanying dissipative processes.

The following two examples demonstrate the dissipation rate approach for elastomers. The first example considers stable crack propagation of a highly filled elastomer, an SBR vulcanizate filled with 40 phr CB N234 [24]. In such highly filled vulcanizates, the amount of stable crack propagation is very limited (i.e., in the micron range) so that stable crack growth can be measured using light microscopy after unloading and cutting the specimen. Consequently, MSM was applied. Identical notched specimens were loaded in a quasistatic manner up to several points above the crack initiation threshold, yet below the point of final specimen fracture. Then, the specimens were unloaded to separate the stored elastic energy from the total energy (see Fig. 8). Finally, the specimens were cut with a razor blade with the aim of measuring the stable crack growth size. Energy dissipation rate was calculated from the left-hand side of Eq. (1).

Moreover, finite element analysis of the MSM was compared with experimentally determined values. It should be noted that, as the result of the quasistatic loading and the very slow stable crack propagation, rate-dependent dissipative effects due to viscoelasticity can be neglected and only rate-independent effects arising from the change in filler structure with increasing strain need to be taken into account by means of a phenomenological model of endochronic plasticity [25]. Material parameters of the model were determined by corresponding cyclic tensile loading of unnotched samples. Comparison of both approaches (i.e., energy contributions derived from experiment and simulation) showed that the limited stable crack propagation in such highly filled vulcanizates has only a very small influence on the amount of energy released during crack propagation. The main contributing factor to the released elastic energy is the development and increase of a dissipation zone around the crack tip with increasing load (see Fig. 12). Therefore, the measured energy losses during stable crack propagation could be related to the development and increase of the dissipative zone. They are not related to the

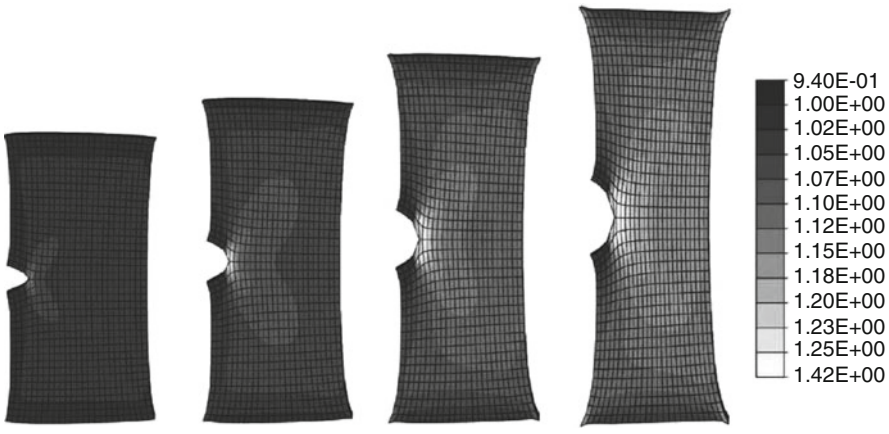

Fig. 12 Development of the dissipation zone during deformation. Values of the phenomenological equivalent plastic variable as a measure of the amount of filler-induced dissipation are depicted [24]

invariant translation of such a dissipation zone, as assumed for steady-state crack propagation. Indeed, for practical applications it is especially desirable to activate distinct dissipative processes in a region that is as large as possible in order to increase the material's ability to absorb energy during crack propagation. However, trying to separate the influences of various dissipation mechanisms on the energy balance during crack propagation could lead to a deeper understanding of the quantities that can be characterized experimentally.

To reach steady-state conditions during crack propagation, in the second example similar experiments were conducted, avoiding the cost-intensive MSM by using single-edge notched PS specimens [3] made of EPDM rubber filled with 60 phr CB N234. Considering the dissipation rate approach, specific quasistatic loading and unloading cycles with a subsequent small increase in maximum displacement were defined. Energy contributions were determined from the loading and unloading curves. Crack increments were measured from digital photographs taken at various instances. To compare the quantities to the conventional approach [see Eq. (4)], the same cycles were conducted with the corresponding unnotched specimen. The elastic energy density of Eq. (4) was determined from unloading curves.

The comparison of both methods of data evaluation (energy dissipation rate and Rivlin–Thomas approach) for an EPDM filled with 60 phr CB N234 can be seen in Fig. 13. The higher energy required for small crack increments can be related either to the initiation of crack propagation or to an increase in the dissipation zone in the vicinity of the crack front rather than to propagation of the crack itself. Such higher values could also be required when the crack must be reinitialized after the crack stops. In contrast, larger crack increments lead to lower energy dissipation rates. These values tend to approach the values determined with the tearing energy approximation [see Eq. (4)] characterizing the steady-state condition during crack propagation, where crack propagation is accompanied by the invariant translation of a dissipation zone.

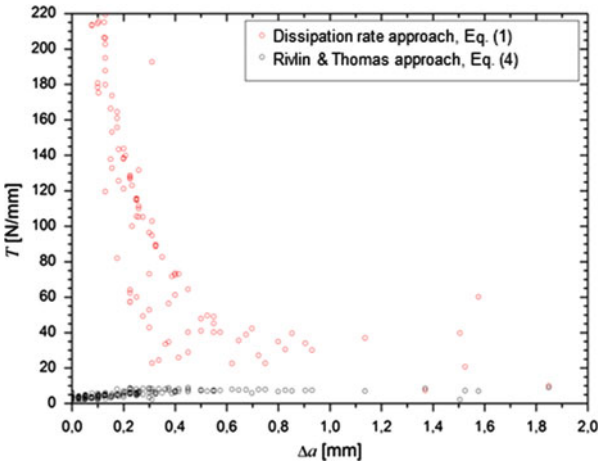

Fig. 13 Dependence of the energy dissipation rate and Rivlin–Thomas approximation on the stable crack increment for EPDM filled with 60 phr CB N234 [3]

Both examples show that the increase in dissipation zone and the initial stages of crack propagation could influence the fracture toughness measurement. Therefore, stable crack propagation in elastomers is not always related to steady-state conditions. Moreover, the proposed combined method based on experimental characterization and a corresponding finite element analysis offers a general way to identify the sources and locations of energy dissipation.

3.3 Experimental Evaluation of the J-Integral

Practical experimental fracture mechanical characterization is based on the Rivlin–Thomas approximation for specific specimen geometries, mainly because of its easy data evaluation. However, these approximations are derived under the assumption of self-similar crack propagation; that is, the crack does not change direction and crack propagation is accompanied by the invariant translation of a dissipation zone. Because crack turning sometimes occurs even under quite simple loading conditions, a change in crack direction is commonly observed in more complex loading situations such as biaxial loading. Hence, an alternative characterization method must be used.

Although mostly used in finite element analysis, the J-integral as a contour integral [see Eq. (3)] in the large strain version [26, 27] can be also used for the experimental fracture mechanical characterization of elastomers. Although stress and strain measures of nonlinear continuum mechanics are used, the interpretation of the large strain J-integral in terms of energy does not change. The experimental method consists of two steps: (1) characterization of the hyperelastic behavior of the corresponding elastomer and (2) plane strain field measurement in the vicinity of the crack tip of a loaded elastomer sheet, with subsequent evaluation of the strain state along an integration contour enclosing the crack tip.

Parameters of the generalized tube model [28] as a hyperelastic material model were fitted considering experimental characterization using unnotched specimens under, preferably, multiple homogeneous loading cases. Subsequent evaluation of the plane strain field measurement in the vicinity of a loaded pre-notched or pre-cracked specimen is based on the local strain field measurement using ARAMIS software [29]. However, evaluation of the J-integral requires not only strain information along a defined path surrounding the crack tip, but also stress and energy density information that can be derived from the fitted hyperelastic model.

Figure 14 shows the results of two approaches, the J-integral approach [large strain version of Eq. (3)] and the Rivlin–Thomas approach, obtained from a PS specimen of an EPDM elastomer filled with 60 phr CB N550 [30]. Specific quasistatic loading and unloading cycles with a subsequent small increase in maximum displacement were also defined in order to reach a small amount of stable crack propagation. It should be noted that, for the Rivlin–Thomas approach, global force and displacement data were used, whereas for the J-integral approach only local strain fields were used for data evaluation. Despite the totally different

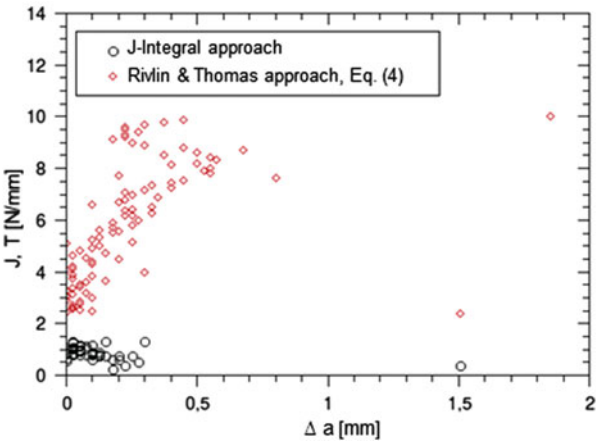

Fig. 14 Characterization of stable crack propagation in EPDM filled with 60 phr CB N550 (PS specimen) comparing the *J*-integral approach with the Rivlin–Thomas approach [30]

data evaluation methods, it is surprising that both approaches led to comparable values of below 10 N/mm, characterizing stable crack propagation. It is evident that values obtained from the *J*-integral approach show less scatter. Furthermore, the *J*-integral approach led to nearly constant values, as predicted for PS specimens. However, the main advantage of the *J*-integral approach is that it is a versatile approach that is not restricted to specific specimen geometries and can be used in more complex loading situations (e.g., under biaxial loading where a crack tends to change its direction) [31]. In this case, the Rivlin–Thomas approximations, Eqs. (4)–(6), cannot be applied.

4 Tearing Energy Under Cyclic Dynamic Loading Conditions

As mentioned previously, there are many factors that affect the fatigue process in rubber and many approaches for analyzing fatigue behavior. Experimental analysis based on mechanical loading is the most common approach. By definition, mechanical fatigue involves crack nucleation and growth caused by cyclic loadings. The driving force of load can be represented by any of various parameters associated with specific analysis approaches: strain, stress, strain energy density, energy release rate, etc. The value of mechanical loading is usually determined as maximum, alternating, minimum, and mean loading and/or the *R*-ratio [32].

The widely used rubber fatigue test at tensile mode or combination of tensile/compression mode by using standard test specimens (ASTM D4712 Type C, dumbbell specimen) monitors the behavior of the material under alternating load. From the results of this test, the difference between a quasistatic load and a fluctuating load is visible. Quasistatic load does not cause fatigue failure, even at

high, subfracture levels. In contrast, fluctuating load can cause fatigue failure, even at low levels. Although quasistatic load does not cause fatigue failures even at high levels it can cause failure as a result of steady, time-dependent crack growth in the case of elastomers that do not exhibit strain crystallization or in the presence of environmental attack [32].

Cyclic dynamic loading conditions are the cause of the loss in stiffness of rubber materials, and this phenomenon has been treated extensively. The rubber material is subjected to a rapid decrease in stiffness during application of the first few loading cycles, which was demonstrated by Mullins [33, 34]. Under cyclic loading beyond the first few cycles, stiffness loss is known to follow a semilogarithmic trend [35]. The rate of this trend is smaller than the initial Mullins effect, at least until the crack nucleation/initiation life is approached. During cyclic loading of the rubber specimen, the growth of the initiated crack accelerates. Thus, the rate of stiffness loss increases until the loading is finished or until the test specimen is totally ruptured [36].

Gent, Lindley, and Thomas [37] determined experimentally the dependence of fatigue crack growth (FCG) rate *da*/*dn* on the crack driving force or tearing energy for rubber materials.

Figure 15 shows the typical relationship for a rubber material in a double logarithmic plot. Lake and Lindley [38] divided this plot into four regions (I–IV) that characterize different tear behaviors. The FCG rate *da*/*dn* depends on the tearing energy *T* in each of the four regions in a characteristic manner.

When the value of tearing energy *T* is lower than T_0, FCG proceeds at a very low constant growth rate *r* and is independent of the dynamic loading, but affected by the environmental attack:

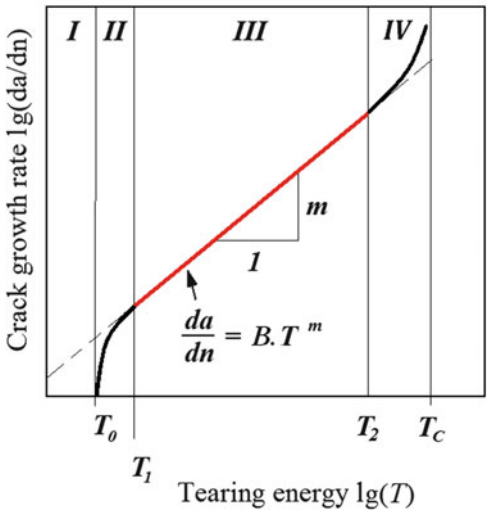

Fig. 15 Double logarithmic plot of FCG rate *da*/*dn* versus tearing energy *T* for a rubber material, indicating four regions (*I–IV*) of different tear behavior; *B* and *m* are material constants [38]

$$T \leq T_0 \rightarrow \frac{da}{dn} = r. \tag{9}$$

In region II between T_0 and T_1 one finds a transition to a higher crack growth rate:

$$T_0 \leq T \leq T_I \rightarrow \frac{da}{dn} = A(T - T_0) + r \tag{10}$$

where A is the crack growth constant.

After this transient state, the crack propagates in a region of stable crack growth between T_1 and T_2, which is denoted as region III. The relationship between FCG rate da/dn and tearing energy is described by Paris and Erdogan [39] with the power law:

$$T_0 \leq T \leq T_2 \rightarrow \frac{da}{dn} = b \cdot T^m \tag{11}$$

where b and m are material constants.

In the last region, IV, as the tearing energy approaches T_2 unstable FCG occurs and the FCG rate becomes essentially infinite:

$$T_2 < T < T_c \rightarrow \frac{da}{dn} = \infty \tag{12}$$

Region III was utilized as the region that corresponds most closely to FCG rates found in the engineering fatigue range. In industrial usage, analyses of SENT and PS specimens are mostly performed in this region to study stable crack growth and, thus, to compare the behavior of crack propagation with respect to rubber composition.

The relationship of crack nucleation/initiation and FCG has been demonstrated to be dependent on rubber type (e.g., [2, 40]) and thereby on the chemical specification of rubber components in experimental fatigue analysis of NR and SBR (see Fig. 16). The results show that in strain-crystallizing rubbers such as NR the FCG is delayed by strain-induced crystallization at the crack tip. On the other hand, non-strain-crystallizing rubbers such as SBR follow time-dependent FCG behavior. With subsequent increase in loading amplitude (i.e., increase in tearing energy), the FCG characteristics of both elastomers analyzed also show differences in the FCG increase. It was observed that the initiation of cracks in SBR starts at higher tearing energy than in NR. However, the FCG following crack initiation shows a counter-phenomenon of more rapid crack propagation in SBR than in the specimen based on NR (see Fig. 16). The results show the hypothetical relationship of crack initiation and propagation for rubber products based on natural or synthetic rubber.

Moreover, the lifetime n_c can be predicted using a fundamental equation [39]. The number of cycles required to develop the crack precursor from its initial size a_0 to a final size a_n is given for SENT specimens by:

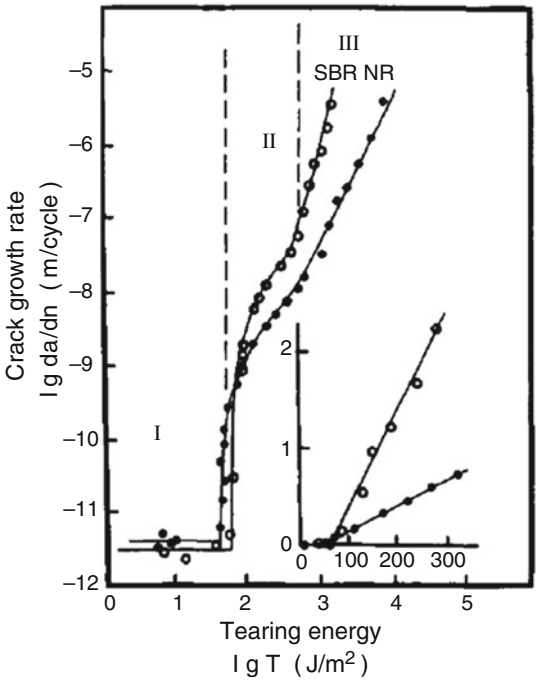

Fig. 16 Double logarithmic plot of FCG rate da/dn versus tearing energy T for NR and SBR materials [2]. The inset shows the same data plotted in a linear scale

$$n_c = \frac{1}{(m-1)\cdot b\cdot (2kW)^m}\cdot\left(\frac{1}{a_0^{(m-1)}}-\frac{1}{a_n^{(m-1)}}\right) \tag{13}$$

whereas the number of cycles required to develop the crack precursor from its initial size a_0 to a final size a_n for PS specimens is given by:

$$n_c = \frac{a_n - a_0}{b(Wl_0)^m} \tag{14}$$

5 Influences on the Fatigue Crack Growth Behavior of Elastomers

There are several researchers [41–44] who have extensively studied the FCG behavior of different rubbers and also the influence of fillers, curing agents, anti-oxidants, environmental conditions (temperature, aging), etc. on FCG behavior.

5.1 Effect of Rubber Type and Filler Content on FCG

A rubber compound consists of a large number of ingredients. Mechanical properties can be improved by varying the type or quantity of each of the ingredients. The type of polymer and the type of filler have the biggest influence on fatigue behavior. Manufacturing processes also affect fatigue behavior through their influence on factors such as ingredient dispersion, state of curing (crosslink density), and the presence and nature of precursor sites for crack initiation [35].

FCG resistance depends on the degree of mechanical hysteresis of the material. The hysteresis is dependent on the square of the strain amplitude and decreases with increasing temperature and increasing mean tensile strain [45]. Elastomers that exhibit strain-induced crystallization are perfectly dissipative at high strains and have good resistance to crack propagation. The minimum value of the FCG exponent m [see Eq. (11)] is about 2. This is because the stress distribution for a sharp crack leads to growth steps that depend on the square of the tearing energy [46]. For relatively elastic materials, m should be significantly greater than 2. Some elastomers that exhibit strain crystallization are natural rubber (NR), isoprene rubber (IR), and polychloroprene (CR). Polymers exhibiting little or no crystallization are styrene–butadiene rubber (SBR), polybutadiene (BR), butyl rubber (IIR), acrylonitrile–butadiene rubber (NBR) and ethylene–propylene rubber (EPDM). The effect of strain-induced crystallinity is time dependent. When the strain is reduced sufficiently, the crystallized structure returns to the amorphous state. In contrast to non-crystallizing elastomers, strain crystallizing rubbers do not show steady crack growth under a quasistatic load [47, 48]. Values of m are dependent not only on the strain level but also on the strain rate. Elastomers that exhibit strain crystallization have a lower m and show superior resistance at high strain rates, relative to other elastomers. NR is the most resistant material at high tearing energy rates and NBR is the worst. In contrast, at lower tearing energies, CR is significantly better regarding the crack resistance than NR. Steady crack growth rate in amorphous elastomers is associated with their viscoelasticity. Mullins found a simple proportionality between the loss modulus and energy release rate at a given crack growth rate. It was shown that a material exhibiting higher loss modulus requires higher energy release rates to drive a crack at constant velocity [34].

The presence of CB in the material influences the fatigue behavior. Furthermore, CB serves as a protection against ultraviolet degradation. The resulting effect depends on the type and volume of filler. The effect of filler on fatigue properties has been attributed to multiple mechanisms. CB causes changes in stiffness and hysteresis properties and has the ability to change crack growth rate as a result of deviation and branching, induced by non-homogeneity at the crack tip. Filled rubber compounds exhibit the Mullins effect, characterized by an initial transient softening of the stress–strain curve [49]. The improvement in the fatigue properties of filled, non-strain-crystallizing elastomers has been attributed to this dissipative mechanism [50]. There are two types of CB. High reinforcing CB considerably improves the cut growth resistance of all vulcanizates except CR. A low reinforcing CB has a beneficial effect on SBR, IIR, and CR [32]. At low tearing energies, close

to the fatigue limit, reinforcing fillers can increase the tearing energy by about 50% [47]. It is necessary to choose the volume fraction of filler according to the required properties of the material. High volume of filler leads to changes in stiffness and hysteresis of the material, which can lead to heat buildup. Unless this heat is dissipated, it can promote further fatigue cracking [38].

5.2 *Effect of Temperature on FCG*

Lake et al. [38] observed a 10^4-fold decrease in fatigue life for unfilled SBR on increasing the temperature from 0 to 100°C, whereas there was only a fourfold decrease for unfilled NR in the same temperature range. Young et al. [51] observed a significant increase in FCG rate in changing from 70 to 100°C for undercured NR belt skim compound. Ghosh et al. [52] showed a temperature dependence of the FCG rate for pure NR-based rubber (see Fig. 17) using temperatures of 30 and 70°C. The compound exhibited a significant increase in FCG rate with temperature increase, which can be explained by the energy-dissipation process. Viscoelastic dissipation at the crack tip is one of the most important mechanisms in the fracture resistance of polymers. As the temperature increases, molecular movements become easier and thereby decrease in viscous dissipation. Thus, the fracture resistance of rubber vulcanizates is reduced as long as more energy is available for crack propagation.

5.3 *Effect of* R*-Ratio on FCG*

The influence of the *R*-ratio (ratio of minimum to maximum amplitude of applied force, strain, etc.) on the FCG characteristics of unfilled NR was extensively studied

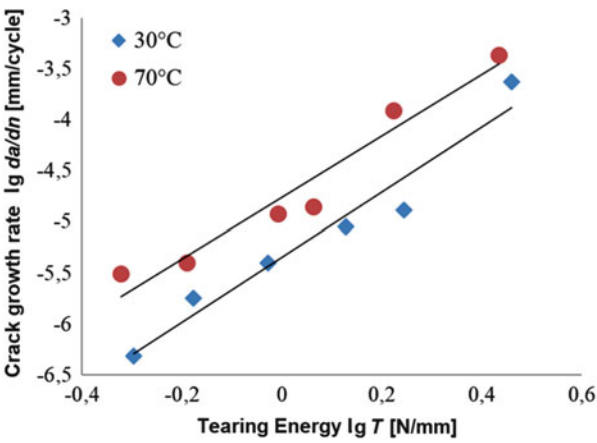

Fig. 17 FCG curves for NR vulcanizate at 30°C and 70°C [52]

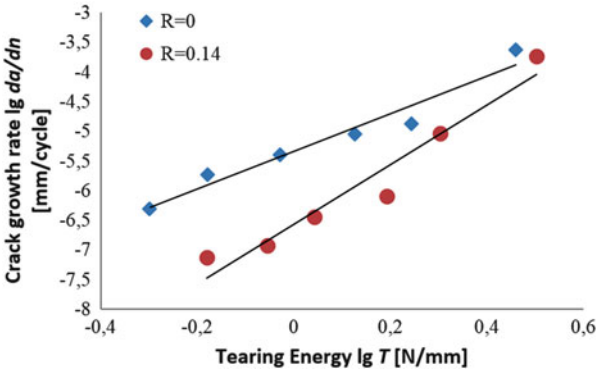

Fig. 18 FCG curves for NR-based rubber at different *R*-ratios [52]

by Lindley [53]. Later, Mars et al. proposed [54] a phenomenological model for the effect of *R*-ratio on the fatigue behavior of strain-crystallizing rubbers using published literature data together with their own data. In normal service, the load is rarely fully unloaded, in contrast to typical laboratory studies. The effect of minimum or mean loading on fatigue life depends on polymer and filler types. There is an important difference between the crack growth behavior of crystallizing and non-crystallizing rubbers. Non-crystallizing rubbers can exhibit steady crack growth under static load, whereas crystallizing rubbers typically exhibit no crack growth. The crack growth rate under cyclic load of non-crystallizing rubbers is given by the sum of contributions of steady and cyclic crack growth rate behavior [32, 55]. Ghosh et al. [52] investigated the effect of the *R*-ratio on FCG for pure rubber based on NR (see Fig. 18). It is evident that, at positive *R*-ratio, the NR exhibited a significant decrease in FCG rate at lower tearing energy, but the rates tended to converge with those at zero *R*-ratio at higher tearing energies. The decrease in FCG rate at higher *R*-ratio is also associated with the strain-induced crystallization phenomena and has been explained by many researchers [53, 56]. Recent work by Saintier et al. [56] explains the influence of strain-induced crystallization of NR material under positive *R*-ratio cyclic loading conditions. It was argued that at $R = 0$, strain-induced crystallization also exists but the crystallites melt at each cycle. In the case of $R > 0$, there is constant pre-load, which helps to prevent the crystallized zones from melting completely.

5.4 Effect of Waveform on FCG

Waveform shape has an influence on FCG, particularly for amorphous polymers. In several research works dealing with FCG, a sinusoidal waveform was used. It is important to adjust the waveform shape to service load conditions corresponding to the tested product. For instance, Gauss-pulse is representative of some tire deformations, whereas sine waveforms occur in engine mounts. The effect depends not only on polymer type, but also on other compound ingredients. The pulse waveform

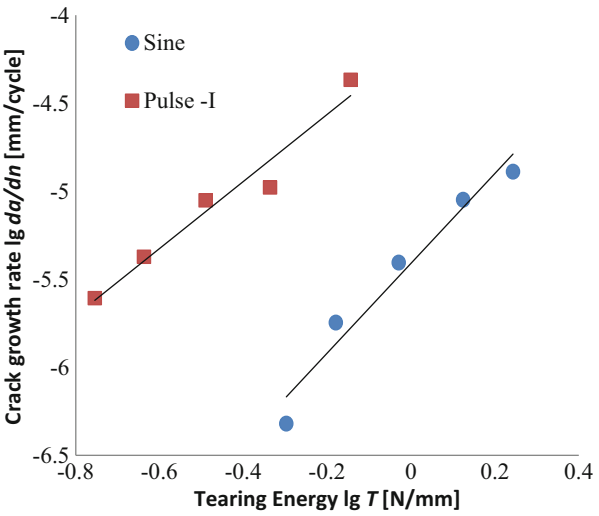

Fig. 19 FCG curves for NR-based rubber for sine and pulse waveforms [52]

led to higher FCG rates than the sine waveform at the same peak energy release rate. This could be caused by the much greater loading rate in the pulse waveform than in the sinusoidal waveform [35, 50].

Several researchers [57–59] also highlighted the effect of waveform on FCG characteristics. Harbour et al. [57] studied the effect of dwell period on FCG characteristics of filled NR and SBR. It was found that SBR showed much higher sensitivity towards the dwell period than NR. Andreini et al. [58] directly compared the effect of sine and pulse waveform on the FCG characteristics of various rubbers. A higher FCG rate was observed in pulse mode compared with sinusoidal loading for NR and BR, but SBR did not show any significant difference between these two waveforms.

Ghosh et al. [52] investigated the effect of waveform on FCG for pure rubber based on NR in pulse mode testing compared with sine mode. The result is shown in Fig. 19, demonstrating that the NR-based rubber showed a higher FCG rate in pulse mode than in sine mode. This observation is in accordance with the findings made by previous researchers [45, 46, 47]. Harbour et al. [56] suggested that in pulse mode testing there is some relaxation time (dwell period), which can assist in time-dependent recovery of rubbery microstructure at the crack tip, leading to a localized and temporary elevated stress state. The re-formation of broken polymer chains, reorganization of the polymer chain network, or redistribution of filler at the crack tip produces stiffer material at the crack tip. This can lead to a localized and temporary elevated stress state, which can account for the higher FCG rate. In contrast to the above findings, no appreciable difference in FCG rate was observed in SBR for pulse and sine waveforms in the work presented by Anderini et al. [58].

5.5 *Effect of Test Specimen Geometry on FCG*

Later work by Andreini et al. [59] compared SENT and PS specimens using NR, BR, and SBR compounds. The results obtained using SENT samples showed a higher FCG rate in pulse mode than in sine mode. A previous study by Stoček et al. [13] using simultaneous analysis of two different test specimen geometries (SENT and PS) showed that there was a dependence of FCG rate on the tearing energy and found identical FCG exponents m for both specimens. Comparison of the results determined in SENT and PS specimens (visualized in Fig. 20) shows that the FCG rate at a given tearing energy is higher in PS than in SENT specimens for non-reinforced and reinforced NR with a filler concentration of 20 phr carbon black. The trends shown by the FCG rate for SENT and PS specimens at the given tearing energy of NR reinforced with 40 phr carbon black are similar [59].

5.6 *Effect of Loading Frequency on FCG*

The effect of loading frequency depends on polymer type. A large frequency effect has been observed for amorphous polymers because of the time-dependent continuous FCG associated with viscoelasticity. This steady component of crack growth is especially important at frequencies below 0.2 Hz. Natural rubber shows very little effect of frequency on FCG over the range of 10^{-3} to 50 Hz. At high frequency, heat generation occurs in the material, especially for thick samples. In this case, heat degradation is the predominant cause of failure. This type of failure is called thermal runaway and often leads to blowout of tires exposed to high speed or overload [13, 60].

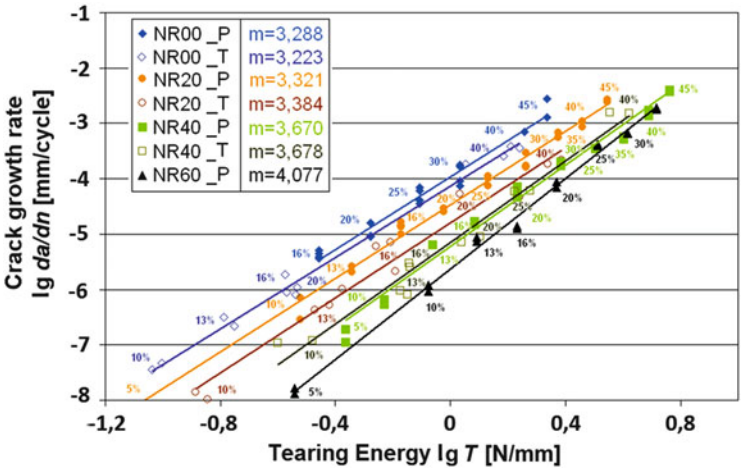

Fig. 20 FCG power law behavior of FCG rate versus tearing energy for SENT (denoted by T) and PS (denoted by P) specimens based on carbon black-filled NR; m FCG exponent [58]

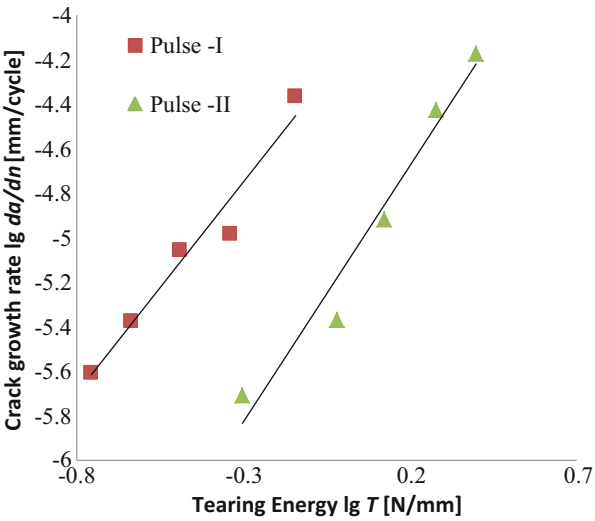

Fig. 21 FCG curves for NR-based rubber for varying loading frequency [52]

Ghosh et al. [52] studied the influence of loading frequency on FCG for pure NR-based rubber in pulse mode testing using frequencies of 10 Hz (pulse I) and 1 Hz (pulse II) (see Fig. 21). The FCG rate for pulse I loading is higher than that for pulse II. The only difference between these two loadings is the relaxation time. This suggests that the reason for a lower FCG rate in pulse II loading is the higher relaxation time of 980 ms compared with 80 ms for pulse I.

6 Advanced Experimental Methods Based on the Concept of Tearing Energy

6.1 Methods for Evaluation of Crack Initiation

The micromechanical mechanisms of crack initiation in rubber materials are subjects of high scientific interest, because at present it is still not known exactly how these processes start and how they proceed under quasistatic and dynamic loading conditions. Therefore, their description can improve the safety, durability, and service life of rubber products. The main scientific aim is to determine the crack driving force at the crack initiation phase from an energy point of view, which is generally dependent on the stored elastic energy in the bulk of the rubber matrix. When this becomes equal to the energy required to create the new crack surface plus the energy required by the viscoelastic dissipation processes near the crack tip, the crack starts to propagate; the characteristic energy is called the tearing energy [1]. However, the subject of current scientific interest is identification of the exact

crack driving force at the instant of crack initiation, as well as propagation, from the point of view of force (i.e., the force actuating at the crack tip orthogonally to the main stress). An appropriate measure for the crack driving force at crack initiation that can be determined using standard laboratory tests and is applicable for arbitrary structures has not yet been found.

Newly developed testing equipment that can evaluate the crack driving force from the both energy and force point of view was introduced by Stoček et al. in 2015 [61]. The testing equipment, denoted the "intrinsic strength tester," and the methodology was developed by PRL Polymer Research Lab. (Zlín, Czech Republic). The measuring principle is based on actuation/cutting of the crack tip in an orthogonal direction to the main strain with a sharp blade. The crack driving force can be exactly applied and controlled, or measured at the microscale during crack initiation and propagation. A diagram of the experimental setup is shown in Fig. 22 and a photograph of the testing equipment in Fig. 23. The measuring principle is based on use of fully instrumented and electrically driven testing equipment, which is able to apply varied waveform loading both statically and dynamically. The test specimen (F) is held in a clamping system (G, H) and is pre-stressed (using the actuator of the *y*-axis, A) by applying a given force (controlled by load cell C) or waveform in strain direction *y*. The tip of the razor blade (I), defined by the sharpness radius of the tip, actuates/cuts (using the actuator of the *x*-axis, B) the loaded test specimen in direction *x*, orthogonal to the main strain. During actuation/cutting of the test specimen with the razor blade, the crack driving force is observed (controlled by load cell D). The crack driving force subjected to the stored elastic energy in the bulk of the rubber test specimen is calculated according to energy criterion defined by Rivlin and Thomas [1].

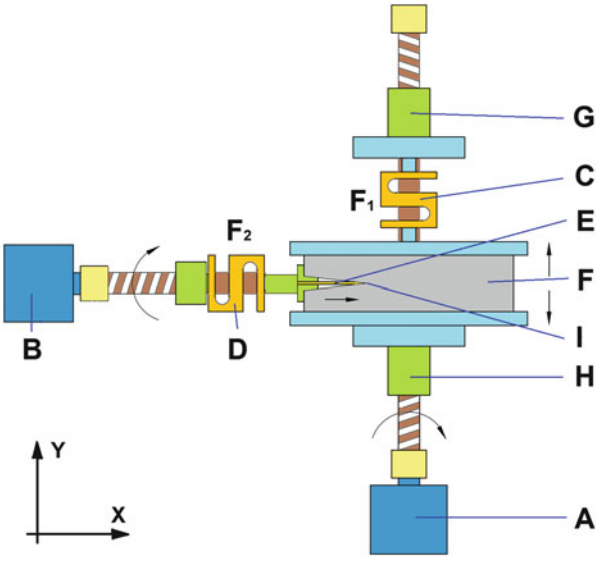

Fig. 22 Functional principle and visualization of testing equipment for experimental characterization of crack initiation: *A* actuator of the *y*-axis, *B* actuator of the *x*-axis, *C* loading cell of the *x*-axis, *D* loading cell of the *y*-axis, *E* razor blade, *F* test specimen, *G* upper clamping system of test specimen, *H* bottom clamping system of test specimen, *I* razor blade tip [61]

Fig. 23 The "intrinsic strength tester" for experimental characterization of crack initiation and propagation

In Fig. 24, the tearing energy T [calculated using Eq. (4) for different loading conditions] is plotted against crack length a resulting from crack driving forces acting on the test specimen at different velocities in the orthogonal direction to the main strain, after the test specimen had been pre-stressed by varying amounts (see Table 1).

Generally, the increase in crack length a is dependent on the increase in tearing energy T. Figures 4 and 5 show that there is a significant increase in crack length at low values of tearing energy, which corresponds to the crack initiation process. The rapid increase in crack length a in the low tearing energy region corresponds to region II of Fig. 15, defining the transition between nucleation and propagation of the crack. At the region of higher tearing energies, crack evolution is more or less linear and defined by a small slope. This behavior corresponds to region III of Fig. 15, defining stable crack growth.

The values of the energy necessary for crack initiation U_{cut} (cutting energy) with respect to various testing conditions (see Table 1) are plotted in Fig. 25. The initial growth of a crack requires an increased cutting energy, whereas the energy rapidly decreases after reaching the maximum and almost drops to zero. Thus, for subsequent propagation of a crack, the system requires lower energy than for crack initiation. It can be seen that the rubber matrix affected by a higher velocity in the direction orthogonal to the main strain requires increased cutting energy. The reason for this phenomenon can be found in the viscoelastic behavior of the rubber matrix, whereby with increased dynamic loading the matrix behavior becomes more elastic.

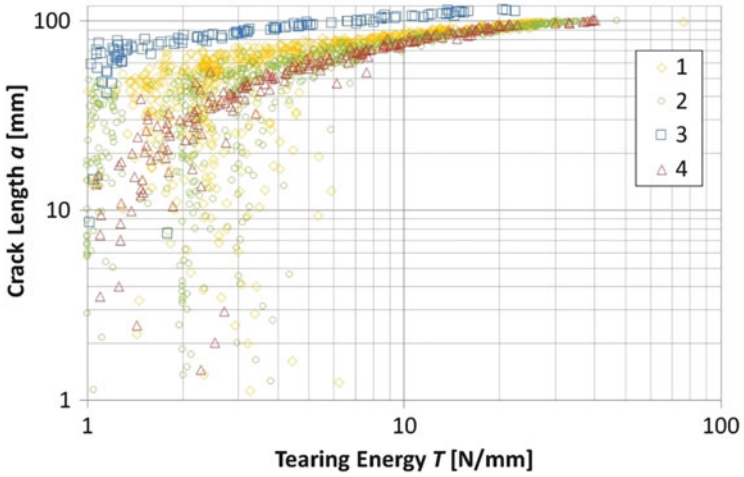

Fig. 24 Tearing energy T versus crack length a for different testing conditions (see Table 1 for details of conditions *1–4*)

Table 1 Applied testing conditions

No. of test	Velocity of razor blade v_x (mm min^{-1})	Pre-force of test specimen F_y (N)
1.	25	50
2.	25	100
3.	100	50
4.	100	100

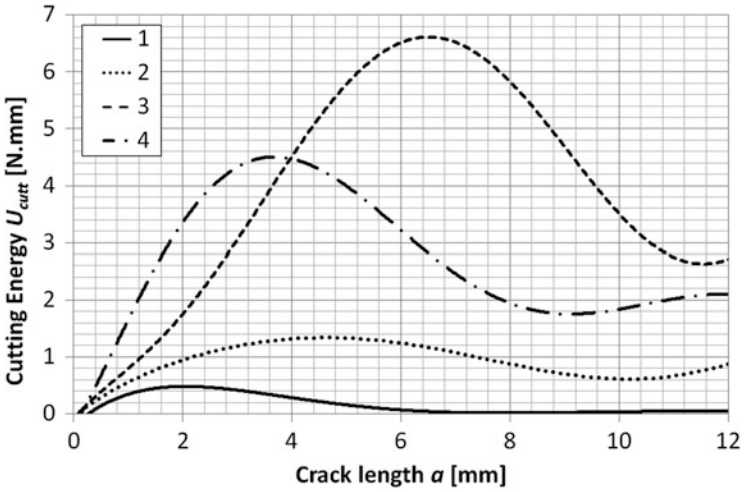

Fig. 25 Cutting energy U_{cutt} of razor blade versus crack length a (see Table 1 for details of conditions *1–4*) [61]

6.2 Methods for Evaluation of Dynamic Wear

Rubber products very often come into contact with different kinds of surfaces to meet their functional requirements. Under dynamic conditions, the repetitive interaction of rubber with a counter-surface leads to a continuous loss of material caused by a dynamic wear process. It is necessary to investigate such behavior in rubber materials used for conveyor belts or tire tread applications, in which the top cover sheet of rubber material is affected by high cyclic dynamic loading and, thus, by dynamic wear processes [62]. Most previous fracture mechanics-based research (e.g., [63–65]) on rubber wear has only considered the frictional force using experimental analysis under quasistatic loading conditions.

Southern and Thomas [65] have correlated the horizontal frictional force $F_{\mathrm{F}(i)}$ with the tearing energy T:

$$T = \frac{F_{\mathrm{F}(i)}}{z} \cdot (1 + \cos\phi) \tag{15}$$

where z is the width of asperity and φ is the angle defining the deflection of crack growth, created on the tread surface, from the y-axis. The equation assumes that the entire frictional force is available to drive the crack [63]. Liang et al. [65] showed that the normal and frictional force between the asperity and the rubber surface also make a significant contribution to the crack driving energy. The relative significance of the normal load $F_{\mathrm{N}(i)}$ and the frictional force $F_{\mathrm{F}(i)}$ on the abrasion process at quasistatic loading is still not exactly clear, and for the dynamic wear there is no significant contribution in scientific publications. Liang et al. [63, 65] introduced a correlation between the wear at steady state and cyclic FCG rate in dependence on tearing energy for NR, SBR, and BR, finding very similar behavior. Thus, it was assumed that the wear process is related to the FCG.

With respect to the process of dynamic loading conditions applied to rubber, Beatty and Miksch [66] have developed laboratory equipment and measuring methodology for the characterization of dynamic wear of rubber used for tire tread applications. Their research publication was the basis for the design of new testing equipment by Manas et al. [67] that enabled variation of the testing parameters. However, the analysis depends only on the impact energy, in a very limited range of energy values, whereas the distance of the affecting penetrator from the rubber surface is uncontrolled. Also, the time of sliding over the rubber surface does not reach the required minimal time on the millisecond scale that is typical for dynamic application during the dynamic wear process.

Thus, new testing equipment has been developed by PRL Polymer Research Lab., s.r.o. (Zlín, Czech Republic) for quantitative analysis of dynamic wear, which is known in the tire industry as the Chip&Cut behavior of rubber compounds in the laboratory. The test equipment works automatically. It controls the user-specified loading conditions over a wide range. Thus, it is possible to simulate the dynamic wear behavior under conditions that occur for real rubber products in operation in a

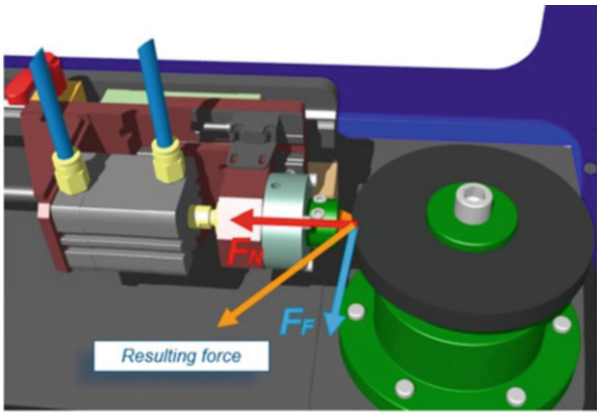

Fig. 26 Functional principle of the testing equipment for analysis of dynamic wear

precise and reproducible manner. Furthermore, all relevant forces and energies that drive the dynamic wear process are measured. The data are correlated to make them available for analytical purposes. The adjustable load parameter field allows tests to simulate real load conditions on different abrasion partners with definable allocations and shapes/sizes of its asperities at the laboratory scale.

The testing principle of the equipment is as follows: the cylindrical test specimen rotates with required velocity up to 1500 rpm and, simultaneously, a penetrator impacts the surface of the test specimen with defined energy given by the normal force F_N, which can be set from 0–500 N. The penetrator impacts the test specimen and slides over its surface. The constant normal force F_N is applied on the penetrator for an exactly defined time, which can be set from the minimal value of 20 ms up to permanent contact. The impact frequency can be set up to 5 Hz. During measurement, the normal and tangential forces, the depth of impact into the test specimen, and the length of sliding are measured. Thus, all the required data and energies defining the dynamic wear process can be separated and evaluated. Because of the broad possibilities for setting the test equipment, both dynamic and quasistatic loading conditions can be simulated by a broad range of loading conditions.

Figure 26 gives a detailed view of the testing equipment and its functional principle for analysis of dynamic wear and Fig. 27 shows a photograph of the Chip&Cut analyzer.

To evaluate the relationship between dynamic wear and cyclic FCG, analyses using the newly developed Chip&Cut analyzer and the Tear and Fatigue Analyzer from Coesfeld GmbH have been performed.

Dynamic wear analysis is based on the relationship between tearing energy T and weight loss rate Δw, which is the weight loss per loading cycle:

$$\Delta w = \frac{dw}{dn} \tag{16}$$

Fig. 27 Photograph of the testing equipment for measurement of dynamic wear

The tearing energy T is calculated from the total force affecting the process, which is a combination of the normal force F_N and frictional force F_F with respect to the thickness of the abrading tool L:

$$T = \frac{\sqrt{F_N^2 + F_F^2}}{L} \tag{17}$$

Figure 28 shows the rate of mass loss plotted against the number of cycles (on logarithmic scales) for the three studied compounds, where compound A is a pure SBR rubber, compound B is based on SBR and contains 10 phr of rubber powder, and compound C contains 30 phr of the same rubber powder. The loading conditions were set as follows: impacting normal force $F_N = 150$ N, loading frequency $f = 4$ Hz, and two varied rotation speeds of 100 and 300 rpm. It is clear that the increasing rotation speed and, consequently, the number of loading cycles n is the reason for the decreasing resistance against abrasion. The abrasion resistance decreases more rapidly as a function of increasing content of rubber powder. The tearing energy T increases with an increase in rotation speed, whereas the content of rubber powder has a marginal effect on the tearing energy.

Cyclic FCG measurements were carried out using the Tear and Fatigue Analyzer under pulse loading conditions using PS specimens. The frequency was set to 4 Hz with a pulse width of 30 ms and strain of 10–40% of the test specimen length. A mini pure shear (mPS) specimen with a geometry ratio of 1:10 was used. Each of the mPS specimens was notched on both sides of specimen considering the required minimal notch length for PS specimens [68]. The tearing energy was calculated using Eq. (4).

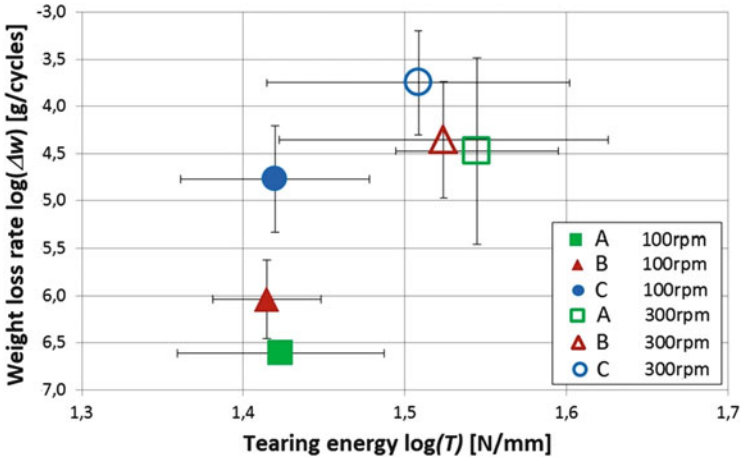

Fig. 28 Double logarithmic plot of tearing energy T versus weight loss rate Δw for compounds A (pure SBR), B (SBR with 10 phr of rubber powder), and C (SBR with 30 phr of rubber powder) using rotation speeds of 100 and 300 rpm

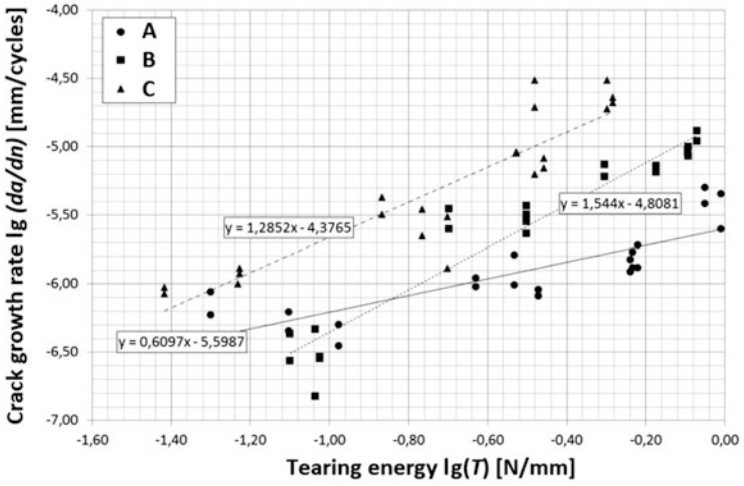

Fig. 29 Double logarithmic plot of tearing energy T versus FCG rate da/dn for samples A, B, and C (see Fig. 28)

In Fig. 29, the influence of the content of rubber powder in SBR on FCG rate becomes apparent. It was found that the FCG rate at a given tearing energy increases significantly with an increase in rubber powder content. Furthermore, the FCG exponent m slightly increases with a higher amount of rubber powder in test specimens. The increase in tear strength independent of rubber powder concentration induces the higher FCG rate.

From Figs. 28 and 29 it is very clear that the content of rubber powder significantly affects dynamic wear as well as FCG, whereby both parameters increase with increasing content of rubber powder. However, both diagrams show that the evaluated tearing energies are significantly different and, therefore, the comparison is only qualitative.

7 Conclusions

The fracture mechanical characterization of elastomeric materials by means of the tearing energy is, despite its introduction in 1953, still commonly used. The derived formulae for the determination of tearing energy for specific specimen geometries containing a notch are attractive to use because of their simple experimental evaluation.

The influence of the specific geometry of the specimen was studied in detail with respect to the reliable experimental determination of tearing energy. Moreover, alternative fracture mechanical characterizations for elastomers have been presented. Methods based on elastic–plastic fracture mechanics that are commonly used for plastics can be adapted for elastomers, leading to reliable characterization of stable crack propagation by means of the *R*-curve. This allows simple comparison of different elastomers and, hence, establishment of relationships between the structural details of the material and the induced properties. Alternatively, energy balance can be evaluated in detail during crack propagation, giving a quantity called the energy dissipation rate. This is a costly method but it leads to more detailed understanding of stable crack propagation in elastomers, especially when experimental fracture mechanical characterization is accompanied by corresponding finite element modeling. Taking into account the fact that cracks often change their direction in loaded specimens, nearly all methods of fracture mechanical characterizations fail. In those cases, determination of the *J*-integral is an appropriate method and involves in line integration along a contour encircling the crack tip. Instead of using approximate formulae commonly used for the determination of tearing energy, it combines previous hyperelastic characterization of the considered elastomer with an appropriate model and the *J*-integral evaluation using a full strain field measurement in the vicinity of the crack tip in an elastomer sheet.

However, taking into account the more practical periodic loading conditions, approximate formulae have utmost relevance, especially those for pure shear specimens. Various influences on the fatigue crack growth behavior have been studied under these loading conditions, not only the influence of rubber type and filler content but also the influences of specific loading and temperature.

Taking into account the whole degradation behavior, from a virgin elastomer specimen to its loss of integrity in more practical situations, advanced experimental methods have been developed to characterize the primary stage of crack initiation and wear behavior.

Acknowledgements The authors dedicate this article to Prof. Dr. Gert Heinrich as successful initiator and coordinator of the DFG Research Unit 597 "Fracture Mechanics and Statistical Mechanics of Reinforced Elastomeric Blends." The authors would like to cordially express their gratitude to Prof. Dr. G. Heinrich for all the open-minded discussions on the theoretical background of physics as well as its pragmatic engineering implementation, and for his personal and scientific support.

We gratefully acknowledge financial support of this work by the Deutsche Forschungsgemeinschaft (DFG) under contracts HE446/3-1, HE4466/3-2, GR 1141/26-1, and GR 1141/26-2; the Ministry of Education, Youth and Sports of the Czech Republic – Program NPU I (LO1504); and the Operational Program Research and Development for Innovations co-funded by the European Regional Development Fund (ERDF) and national budget of the Czech Republic, within the framework of the project CPS - strengthening research capacity (reg. number: CZ.1.05/2.1.00/19.0409).

References

1. Rivlin RS, Thomas AG (2003) Rupture of rubber. I. Characteristic energy for tearing. J Polym Sci 10:291–318
2. Griffith AA (1921) The phenomena of rupture and flow in solids. Philos Trans R Soc Lond Ser A, 163–198
3. Horst T, Heinrich G, Schneider M, Schulze A, Rennert M (2013) Linking mesoscopic and macroscopic aspects of crack propagation in elastomers. In: Grellmann W, Heinrich G, Kaliske M, Klüppel M, Schneider K, Vilgis T (eds) Fracture mechanics and statistical mechanics of reinforced elastomeric blends. Springer, Heidelberg, pp 129–165
4. Kanninen MF, Popelar CL (1985) Advanced fracture mechanics. Oxford University Press, Oxford
5. Sumpter JDG (1999) An alternative view of R-curve testing. Eng Fract Mech 64:161–176
6. Sumpter JDG (2004) The energy dissipation rate approach to tearing instability. Eng Fract Mech 71:17–37
7. Kolednik O, Turner CE (2007) Application of energy dissipation rate arguments to ductile instability. Fatigue Fract Eng Mater Struct 17:1129–1145
8. Memhard D, Brocks W, Fricke S (1993) Characterization of ductile tearing resistance by energy dissipation rate. Fatigue Fract Eng Mater Struct 16:1109–1124
9. Kolednik O (1991) On the physical meaning of the J-Δa-curves. Eng Fract Mech 38:403–412
10. Rice JR (1968) A path independent integral and the approximate analysis of strain concentration by notches and cracks. J Appl Mech 35:379–386
11. Cherepanov GP (1967) Crack propagation in continuous media. Appl Math Mech (PMM) 31:503–512
12. Yeoh OH (2001) Analysis of deformation and fracture of 'pure shear' rubber testpiece. Plastics Rubber Compos 30:391–397
13. Stoček R, Heinrich G, Gehde M, Kipscholl R (2013) Analysis of dynamic crack propagation in elastomers by simultaneous tensile- and pure-shear-mode testing. In: Grellmann W, Heinrich G, Kaliske M, Klüppel M, Schneider K, Vilgis T (eds) Fracture mechanics and statistical mechanics of reinforced elastomeric blends. Springer, Heidelberg, pp 269–300
14. Grellmann W, Reincke K (2013) Technical material diagnostics – fracture mechanics of filled elastomer blends. In: Grellmann W, Heinrich G, Kaliske M, Klüppel M, Schneider K, Vilgis T (eds) Fracture mechanics and statistical mechanics of reinforced elastomeric blends. Springer, Heidelberg, pp 227–268
15. Grellmann W, Seidler S (eds) (2013) Polymer testing. Hanser, München

16. Grellmann W, Seidler S (eds) (2001) Deformation and fracture behaviour of polymers. Springer, Heidelberg
17. ESIS (2001) Standard draft ESIS TC 4: A testing protocol for conducting J-crack growth resistance curve tests on plastics. European Structural Integrity Society
18. Blumenauer H, Pusch G (1993) Technische Bruchmechanik. Deutscher Verlag für Grundstoffindustrie, Leipzig Stuttgart
19. Reincke K, Heinrich G, Grellmann W (2004) Investigation of mechanical and fracture mechanical properties of elastomers filled with precipitated silica and nanofiller based upon layered silicates. Rubber Chem Technol 77:662–677
20. Reincke K, Grellmann W, Lach R, Heinrich G (2003) Toughness optimization of sbr elastomers – use of fracture mechanics methods for characterization. Macromol Mater Eng 288: 181–189
21. Rice JR, Paris PC, Merkle JG (1973) Some further results of J-integral analysis and estimates. Progress in flaw growth and fracture toughness testing. ASTM STP 536:231–245
22. Brüning K, Schneider K, Heinrich G (2013) In-situ structural characterization of rubber during deformation and fracture. In: Grellmann W, Heinrich G, Kaliske M, Klüppel M, Schneider K, Vilgis T (eds) Fracture mechanics and statistical mechanics of reinforced elastomeric blends. Springer, Heidelberg, pp 43–80. ISBN 978-3-642-37909-3
23. Toki S, Fujimaki T, Okuyama M (2000) Strain-induced crystallization of natural rubber as detected real-time by wide-angle x-ray diffraction technique. Polymer 41:5423–5429
24. Netzker C, Horst T, Reincke K, Behnke R, Kaliske M, Heinrich G, Grellmann W (2013) Analysis of stable crack propagation in filled rubber based on a global energy balance. Int J Fract 181(1):13–23
25. Netzker C, Dal H, Kaliske M (2010) An endochronic plasticity formulation for filled rubber. Int J Solids Struct 47:2371–2379
26. Maugin G (1995) Material forces: concepts and applications. Appl Mech Rev 48:213–245
27. Steinmann P (2000) Application of material forces to hyperelastostatic fracture mechanics. I. Continuum mechanical setting. Int J Solids Struct 37:7371–7391
28. Kaliske M, Heinrich G (1999) An extended tube-model for rubber elasticity: statistical-mechanical theory and finite element implementation. Rubber Chem Technol 72(4):602–632
29. GOM (2007) ARAMIS user handbook - software. ARAMIS v6. GOM mbH, Braunschweig
30. Schulze A (2013) Analyse der Verzerrungsfelder gekerbter Elastomerproben unter ein- und zweiachsiger äußerer Belastung. Diploma Thesis, TU Chemnitz, Germany
31. Schneider K, Calabrò R, Lombardi R, Kipscholl C, Horst T, Schulze A, Heinrich G (2014) Charakterisierung und Versagensverhalten von Elastomeren bei dynamischer biaxialer Belastung. Kautschuk Gummi Kunststoffe 67(4):48–52
32. Mars WV, Fatemi A (2004) Factors that affect the fatigue life of rubber: a literature survey. J Rubber Chem Technol 77(3):391–412
33. Mullins L (1947) Effect of stretching on the properties of rubber. J Rubber Res 16:275–289
34. Mullins L (1957) Theoretical model for the elastic behavior of filler-reinforced vulcanized rubbers. Rubber Chem Technol 30:551–571
35. Mars WV, Fatemi A (2004) Observation of the constitutive response and characterization of filled natural rubber under monotonic and cyclic multiaxial stress states. J Eng Mater Technol 126(1):19–28
36. Mars WV, Isasi M, Arriaga A (2013) Loss of stiffness during fatigue and the development of crack precursors. In: Gil-Negrete N, Alonso A (eds) Proceedings of the 8th European conference on constitutive models for rubbers (ECCMR VIII), San Sebastian, 25–28 June 2013. Balkema, Leiden, pp 355–360
37. Gent AN, Lindley PB, Thomas AG (1964) Cut growth and fatigue of rubbers. I. The relationship between cut growth and fatigue. J Appl Polym Sci 8:455–466
38. Lake GJ, Lindley PB (1965) The mechanical fatigue limit for rubber. J Appl Polym Sci 9: 1233–1251

39. Paris P, Erdogan F (1963) A critical analysis of crack propagation laws. J Basic Eng 85: 528–533
40. Persson BNJ, Albohr O, Heinrich G, Ueba H (2005) Crack propagation in rubber-like materials. J Phys Condens Matter 17:R1071–R1142
41. Lake GJ, Lindley PB (1966) Mechanical fatigue limit for rubber. Rubber Chem Technol 39: 348–364
42. Gent AN, Lindley PB, Thomas AG (1965) Cut growth and fatigue of rubbers. I. The relationship between cut growth and fatigue. Rubber Chem Technol 38:292–300
43. Reincke K, Grellmann W, Klüppel M (2009) Investigation of fracture mechanical properties of filler-reinforced styrene-butadiene elastomers. Kautschuk Gummi Kunstoffe 5:246–251
44. Kim JH, Jeong HY (2005) A study on the material properties and fatigue life of natural rubber with different carbon blacks. Int J Fatigue 27:263–272
45. Luchini JR, Peters JM, Arthur RH (1994) Tire rolling loss computation with the finite element method. Tire Sci Technol 22(4):206–222
46. Andrews EH (1961) Crack propagation in strain-crystallizing elastomer. J Appl Phys 32: 542–548
47. Lake GJ, Lindley PB (1964) Cut growth and fatigue of rubbers. II. Experiments on a noncrystallizing rubber. J Appl Polym Sci 8:707–721
48. Beatty JR (1964) Fatigue of rubber. Rubber Chem Technol 37:1341–1364
49. Roland CM (1989) Network recovery from uniaxial extension.I. Elastic equilibrium. Rubber Chem Technol 62:863–879
50. Ellul MD (2012) Mechanical fatigue. In: Gent AN (ed) Engineering with rubber – how to design rubber components. Hanser, Munich, pp 159–203
51. Young DG, Danik JA (1994) Effects of temperature on fatigue and fracture. Rubber Chem Technol 67:137–147
52. Ghosh P, Stocek R, Gehde M, Mukhopadhyay R, Krishnakumar R (2014) Investigation of fatigue crack growth characteristics of NR/BR blend based tyre tread compounds. Int J Fract 188(1):9–21
53. Lindley PB (1973) Relation between hysteresis and dynamic crack growth resistance of natural rubber. Int J Fract 9:449–462
54. Mars WV, Fatemi A (2003) A phenomenological model for the effect of R-ratio on fatigue of strain crystallizing rubbers. Rubber Chem Technol 76:1241–1258
55. Lindley PB (1974) Non-relaxing crack growth and fatigue in a noncrystallizing rubber. Rubber Chem Technol 47:1253–1264
56. Saintier N, Cailletaud G, Piques R (2011) Cyclic loadings and crystallization of natural rubber: an explanation of fatigue crack propagation reinforcement under a positive loading ratio. Mater Sci Eng A 528(3):1078–1086
57. Harbour RJ, Fatemi A, Mars WV (2007) The effect of dwell period on fatigue crack growth rates in filled SBR and NR. Rubber Chem Technol 80:838–853
58. Andreini G, Straffi P, Cotugno S, Gallone G, Polacco G (2010) Comparison of sine versus pulse waveform effects on fatigue crack growth behaviour of NR, SBR and BR compounds. Rubber Chem Technol 83(2010):391–403
59. Andreini G, Straffi P, Cotugno S, Gallone G, Polacco G (2013) Crack growth behaviour of styrene-butadiene rubber, natural rubber and polybutadiene rubber compounds: comparison of pure-shear versus strip tensile test. Rubber Chem Technol 86:132–145
60. Lake GJ, Thomas AG (1988) Strength properties of rubber. In: Roberts AD (ed) Natural rubber science and technology. Oxford University Press, Oxford, pp 731–772
61. Stoček R, Kratina O, Kipscholl R (2015) A new experimental approach to rubber resistance against cutting by sharp objects. In: Maralova B, Petrikova I (eds) Constitutive models for rubber IX: Proceedings of the 9th European conference on constitutive models for rubbers (ECCMR IX), Prague, 1–4 Sept 2015. Balkema, Leiden, pp 357–362

62. Stoček R, Kipscholl R, Euchler E, Heinrich G (2014) Study of the relationship between fatigue crack growth and dynamic chip & cut behavior of reinforced rubber materials. Kautschuk-Gummi-Kunststoffe 67:26–29
63. Liang H, Fukahori Y, Thomas AG, Busfield JJC (2010) The steady state abrasion of rubber: why are the weakest rubber compounds so good in abrasion? Wear 268:756–762
64. Southern E, Thomas AG (1979) Studies of rubber abrasion. Rubber Chem Technol 52:1008–1018
65. Liang H, Fukahori Y, Thomas AG, Busfield JJC (2009) Rubber abrasion at steady state. Wear 266:288–296
66. Beatty J, Miksch B (1982) A laboratory cutting and chipping tester for evaluation off-the-road and heavy-duty tire treads. Rubber Chem Technol 55(5):1531–1546
67. Manas D, Manas M, Staněk M, Pata V (2009) Wear of tyre treads. J Achieve Mater Manuf Eng 37(2):538–543
68. Stoček R, Heinrich G, Gehde M, Kipscholl R (2012) A new testing concept for determination of dynamic crack propagation in rubber materials. Kautschuk Gummi Kunststoffe 65:49–53

Index